



University of Liège
Faculty of Applied Sciences

**Simplified analytical methods for the
crashworthiness and the seismic design of lock gates**

Dissertation submitted for the degree of
Doctor in Applied Sciences

by

Loïc BULDGEN
FRIA Research-Fellow

September 2014

Abstract

The design of navigation lock gates requires to account for accidental loads such as ship impacts or earthquakes, but it is quite difficult to handle with them. The most satisfactory way to investigate their effects is to perform numerical simulations. Such an approach can be justified at the late design stage, but it is quite commonly accepted that it is not well suited during the conception process. This may be justified by the calculation and modeling efforts that are usually prohibitive. Consequently, the aim of this thesis is to develop simplified methods to circumvent these difficulties. The dissertation is divided into two main parts.

The first part is devoted to ship collisions on plane and mitre gates. An analytical procedure is followed to derive the evolution of the impact force with the vessel penetration. Two different solutions are derived to get the collision resistance. The first one is done under the assumption that there is only a crushing of some structural elements in a confined area located near the contact point. This corresponds to a local deforming mode because the damages remain localized in a small part of the gate. Using such an assumption, the resistance is evaluated by the super-elements method. The second calculation is based on the hypothesis that there is an overall bending motion of the structure, which may be seen as a global deforming mode.

Once the local and global solutions are obtained, the final gate resistance is found by combining them. In order to validate this analytical evaluation, comparisons are made with finite element simulations. The agreement with the numerical curves is found to be satisfactory for a pre-design stage, which tends to corroborate the collapse modes considered in this thesis. Although this is already an important achievement, a challenge for the future developments would be to have a better integration of rupture in the global mode.

The second part of the dissertation is devoted to the seismic analysis of lock gates. The preliminary study focuses on fluid-structure interaction in large reservoirs with two opposite flexible walls. As a first step, the Rayleigh-Ritz method is applied by using the dry eigenmodes of plates as generating functions, which leads to the wet modal properties. The virtual work principle then allows for a dynamic analysis of the structure. As a result, the hydrodynamic pressure acting on the flexible walls is computed. Comparisons with finite element solutions show a quite satisfactory agreement in almost all the cases. In addition to all these developments, the influence of various geometrical parameters on the fluid-structure interaction is investigated.

After dealing with reservoirs, the stress is put on plane lock gates with a single plating. The procedure followed during the analytical derivation is nearly the same. The Rayleigh-Ritz method is used this time to get the dry modal properties of the stiffened structure. For a given accelerogram, the time evolution of the hydrodynamic pressure is evaluated by the virtual work principle and validated by comparisons with numerical results. Apart from these developments, some particular points are also investigated, such as the added mass method. The validity of this approach is questioned and some examples are provided as a matter of justification. Finally, a method is proposed for an easier integration of the seismic action in the design of lock gates.

Remerciements

Je souhaite avant tout exprimer ma gratitude au Fonds pour la Formation à la Recherche dans l'Industrie et dans l'Agriculture (FRIA) pour avoir reconnu la viabilité de mon projet de thèse et l'avoir financé durant ces quatre années. Je tiens à souligner ici le rôle important que joue cette institution en soutenant de jeunes chercheurs. Elle a su trouver un équilibre subtil dans le contrôle nécessaire de leurs travaux, sans toutefois tomber dans les travers d'une lourdeur administrative qui freinerait leurs recherches.

J'exprime toute ma gratitude envers mon promoteur, le Pr. Philippe Rigo, qui m'a proposé de me lancer dans la recherche alors que ce n'était pas à priori la voie que j'entrevois au terme de mes études. Ses connaissances dans le domaine des constructions hydrauliques m'ont permis d'appréhender plus facilement mes travaux. De par ses nombreuses relations, il a su m'orienter vers les bonnes personnes pour recueillir ici et là quelques conseils ou informations. Je salue également les autres membres du services ANAST, en particulier François, Olivier, Renaud, Jérôme, Matthieu et Typhaine, dont la bonne humeur et l'amabilité ont égayé ces journées de travail parfois trop longues.

Je tiens à remercier chaleureusement le Pr. Hervé Le Sourné pour son soutien indéfectible durant ces quatre années de doctorat. Il m'a fait découvrir le sujet passionnant des approches analytiques pour le calcul des collisions et a en outre considérablement enrichi ma formation aux méthodes numériques. J'ai eu beaucoup de plaisir à travailler avec lui, non seulement en raison de sa grande compétence scientifique, mais également pour ses nombreuses qualités humaines. Je le remercie aussi pour son encadrement efficace, ses bons conseils, sa motivation et surtout pour toutes les connaissances qu'il a accepté de me transmettre. J'ai beaucoup appris en travaillant avec lui lors de mes nombreux séjours à l'ICAM de Nantes et souhaite bien sûr que cette collaboration ne s'achève pas au terme de ce doctorat.

Je marque aussi ma reconnaissance envers le Pr. Hervé Degée pour m'avoir fait bénéficier de ses connaissances approfondies et de son expertise dans le domaine du calcul sismique. Je lui sais gré également pour son calme et sa patience, tant il est vrai que mon esprit avait parfois des difficultés à s'adapter à la rapidité de ses raisonnements. La pédagogie dont il a su faire preuve dans de pareils cas m'a incontestablement aidé à aborder plus sereinement ce sujet fort ardu.

Je témoigne également ma gratitude au Pr. Eric Delhez et au Dr. Patricia Tossings pour leur soutien ponctuel alors que rien ne les y engageait à priori. Cette spontanéité, alliée bien évidemment à leurs indéniables compétences, m'a fait avancer dans mes recherches en résolvant certains problèmes mathématiques que j'appréhendais difficilement.

Enfin, sans vouloir être exhaustif, je voudrais terminer ces remerciements en soulignant le soutien moral important que m'a apporté ma famille. Je remercie ma mère, ma sœur Bénédicte et mon frère Gaël qui m'ont patiemment supporté dans les moments de découragement et ont parfois (voire souvent) enduré ma mauvaise humeur.

Table of contents

| | |
|--|----|
| CHAPTER 1. General introduction..... | 9 |
| 1.1. Context of the research..... | 10 |
| 1.2. Aim of the research | 12 |
| 1.3. Organization of the thesis..... | 14 |
| - PART I - SHIP IMPACT ON LOCK GATES | |
| CHAPTER 2. Background for the ship collisions on lock gates..... | 16 |
| 2.1. Review of the existing methods..... | 17 |
| 2.1.1. Finite element methods | 17 |
| 2.1.2. Simplified analytical methods | 20 |
| 2.2. Evaluation of the initial kinetic energy..... | 22 |
| 2.3. Evaluation of the internal energy | 24 |
| 2.3.1. Exact theory..... | 24 |
| 2.3.2. Approximate theory..... | 25 |
| CHAPTER 3. Analytical derivation of the collision resistance of plane lock gates..... | 29 |
| 3.1. Introduction | 30 |
| 3.1.1. Description of the impacted gate..... | 30 |
| 3.1.2. Description of the collision scenario | 35 |
| 3.2. General methodology | 38 |
| 3.2.1. Deformation sequence | 38 |
| 3.2.2. Analytical derivation of the resistance | 39 |
| 3.3. Local resistance for super-elements of type 1..... | 45 |
| 3.3.1. Literature review | 45 |
| 3.3.2. Analytical derivation for an impact by the stem | 46 |
| 3.3.3. Analytical derivation for an impact by the bulb..... | 51 |
| 3.3.4. Numerical validation | 55 |
| 3.4. Local resistance for super-elements of type 2..... | 59 |
| 3.4.1. Literature review | 59 |
| 3.4.2. Analytical derivation | 60 |
| 3.4.3. Numerical validation | 67 |
| 3.5. Local resistance for super-elements of type 3..... | 69 |
| 3.5.1. Literature review | 69 |

| | |
|---|------------|
| 3.5.2. Analytical derivation | 69 |
| 3.5.3. Numerical validation | 75 |
| 3.6. Resistance in the global deforming mode | 78 |
| 3.6.1. General procedure | 78 |
| 3.6.2. Elastoplastic solution..... | 81 |
| 3.6.3. Perfectly plastic solution | 85 |
| 3.7. Numerical validations | 92 |
| 3.7.1. Preliminary considerations | 92 |
| 3.7.2. Impact on a gate supported by a sill | 94 |
| 3.7.3. Impact on a gate free at the bottom | 97 |
| 3.8. Conclusions | 99 |
| CHAPTER 4. Analytical derivation of the collision resistance of mitre gates..... | 102 |
| 4.1. Introduction | 103 |
| 4.1.1. Description of the impacted gate..... | 103 |
| 4.1.2. Description of the collision scenario | 106 |
| 4.1.3. General methodology | 107 |
| 4.2. Resistance in the local deforming mode | 109 |
| 4.2.1. Super-elements of type 1 | 109 |
| 4.2.2. Super-elements of type 2 | 113 |
| 4.2.3. Super-elements of type 3 | 120 |
| 4.3. Resistance in the global deforming mode | 124 |
| 4.3.1. Preliminary considerations | 124 |
| 4.3.2. Off-centered impact..... | 126 |
| 4.3.3. Centered impact..... | 131 |
| 4.4. Numerical validations | 135 |
| 4.4.1. Description of the finite element model | 135 |
| 4.4.2. Off-centered impact..... | 136 |
| 4.4.3. Centered impact..... | 137 |
| 4.5. Conclusions | 139 |
| CHAPTER 5. Conclusions about ship impacts on lock gates | 141 |
| 5.1. Scientific developments..... | 142 |
| 5.2. Perspectives | 144 |

- PART II -

SEISMIC ANALYSIS OF LOCK GATES

| | |
|---|------------|
| CHAPTER 6. Literature review on the seismic design of lock gates | 147 |
|---|------------|

| | |
|---|------------|
| 6.1. Dam-reservoir interaction..... | 148 |
| 6.2. Fluid-structure interaction in containers..... | 150 |
| 6.2.1. Hydrodynamic pressure in rigid containers..... | 150 |
| 6.2.2. Hydrodynamic pressure in flexible cylindrical containers..... | 150 |
| 6.2.3. Hydrodynamic pressure in flexible rectangular containers..... | 151 |
| 6.3. Seismic analysis of locks..... | 153 |
| CHAPTER 7. Seismic analysis of large flexible reservoirs | 155 |
| 7.1. Introduction | 156 |
| 7.1.1. Description of the structure | 156 |
| 7.1.2. Evaluation of the hydrodynamic pressure | 157 |
| 7.2. Free vibration analysis of a dry plate..... | 160 |
| 7.2.1. Characteristic equation | 160 |
| 7.2.2. Vibration properties..... | 162 |
| 7.3. Free vibration analysis of an immersed plate | 164 |
| 7.3.1. Characteristic equation | 164 |
| 7.3.2. Rayleigh-Ritz solution..... | 165 |
| 7.3.3. Numerical validation | 170 |
| 7.4. Dynamic analysis of flexible reservoirs..... | 178 |
| 7.4.1. Equilibrium equation | 178 |
| 7.4.2. Virtual work principle | 179 |
| 7.4.3. Numerical validation | 183 |
| 7.4.4. Added mass method | 190 |
| 7.5. Conclusions | 196 |
| CHAPTER 8. Seismic analysis of plane lock gates | 197 |
| 8.1. Introduction | 198 |
| 8.1.1. Preliminary considerations | 198 |
| 8.1.2. Description of the structure | 198 |
| 8.2. Free vibration analysis of a dry gate | 202 |
| 8.2.1. Free vibration analysis of beams | 202 |
| 8.2.2. Rayleigh-Ritz solution..... | 206 |
| 8.2.3. Numerical validation | 209 |
| 8.3. Dynamic analysis of lock gates | 217 |
| 8.3.1. Equilibrium equation | 217 |
| 8.3.2. Virtual work principle | 219 |
| 8.3.3. Numerical validation | 222 |
| 8.3.4. Added mass method | 226 |

| | |
|---|------------|
| 8.4. Conclusions | 229 |
| CHAPTER 9. Conclusions about the seismic design of lock gates..... | 230 |
| 9.1. Scientific developments..... | 231 |
| 9.2. Perspectives..... | 233 |

**- PART III -
APPENDICES**

| | |
|--|------------|
| APPENDIX A. Addendum to Chapter 2..... | 236 |
| A.1. Appendix A.1..... | 237 |
| A.2. Appendix A.2..... | 238 |
| A.2.1. Definition of the strains | 238 |
| A.2.2. Definition of the stresses | 239 |
| A.2.3. Derivation of the internal energy..... | 240 |
| A.2.4. Derivation of the internal energy rate..... | 241 |
| A.2.5. Derivation of the internal energy rate in the plastic regime | 242 |
| APPENDIX B. Additional developments for ship impacts on plane lock gates..... | 245 |
| B.1. Appendix B.1..... | 246 |
| B.1.1. Internal energy rate for stiffened plates..... | 246 |
| B.1.2. Resistance after contact with a lateral support | 246 |
| B.1.3. Resistance after contact with the lower support | 249 |
| B.2. Appendix B.2..... | 252 |
| B.2.1. Subsequent folding | 252 |
| B.2.2. Plastic capacities of a crushed beam | 253 |
| B.3. Appendix B.3..... | 255 |
| B.3.1. Derivation of the resistance for a direct impact | 255 |
| B.3.2. Derivation of the resistance for a subsequent contact | 263 |
| B.4. Appendix B.4..... | 270 |
| B.4.1. Displacement fields before the transition..... | 270 |
| B.4.2. Displacement field after the transition | 271 |
| B.5. Appendix B.5..... | 273 |
| APPENDIX C. Additional developments for ship impacts on mitre lock gates..... | 275 |
| C.1. Appendix C.1 | 276 |
| C.2. Appendix C.2..... | 277 |
| C.2.1. Additional results for SE1 | 277 |
| C.2.2. Additional results for SE2 | 279 |
| C.2.3. Additional results for SE3 | 284 |

| | |
|--|-----|
| C.3. Appendix C.3 | 288 |
| C.3.1. Summary of some cross-section properties | 288 |
| C.3.2. Equilibrium method for a class 1 cross-section | 289 |
| C.3.3. Plastic mechanism after buckling | 291 |
| C.4. Appendix C.4 | 296 |
| APPENDIX D. Additional developments on the seismic analysis of large reservoirs.... | 299 |
| D.1. Appendix D.1 | 300 |
| D.1.1. Derivation of the Rayleigh quotient | 300 |
| D.1.2. Investigation of the fluid-structure interaction | 301 |
| D.1.3. Derivation of the flexible pressure potential | 307 |
| D.2. Appendix D.2 | 309 |
| D.2.1. Dynamic analysis of a rigid reservoir | 309 |
| D.2.2. Investigation of the fluid-structure interaction | 311 |
| APPENDIX E. Additional developments for the seismic analysis of lock gates | 316 |
| E.1. Appendix E.1 | 317 |
| E.1.1. Additional formulae for the Rayleigh quotient | 317 |
| E.1.2. Additional comparisons for gate 2 | 322 |
| E.1.3. Additional comparisons for gate 3 | 325 |
| E.2. Appendix E.2 | 328 |
| E.2.1. Considerations about the wet modes | 328 |
| E.2.2. Considerations about the exactness of the solution | 329 |
| E.2.3. Additional formulae for the external work | 332 |
| E.3. Appendix E.3 | 333 |
| E.3.1. Case of a gate with the real boundary conditions | 333 |
| E.3.2. Case of an asymmetric configuration | 336 |
| E.3.3. Seismic analysis of an entire lock structure | 341 |
| E.3.4. Other components of the seismic acceleration | 345 |
| REFERENCES | 348 |

CHAPTER 1. General introduction

1.1. Context of the research

From statistical data compiled by EUROSTAT¹, it is a fact that the freight transport demand is constantly growing since 1995. According to Figure 1.1a, 76 % of the European goods transit by road and only 6 % by water. Of course such a situation is not viable because the road capacity is progressively reaching a maximum. The modal split has therefore to be changed, and a serious alternative is to develop the river transport. This choice can be motivated by the following reasons:

- The environmental impact is reduced: in Europe, the road traffic is responsible for a quarter of all the CO₂ emissions and also produces a lot of other gases and volatile particles that reduce the air quality. According to the European Environment Agency [56], although stricter international emission standards have been published during the last decades, the pollution emitted by the road sector in terms of CO₂ rejections is still four times higher than the one attributed to waterborne transport (Figure 1.1b).
- Even though it is not easy to have an objective quantification, Rohacs and Simongati [136] estimate that the noise nuisance due to ships is not relevant in comparison with other transport modalities such as trucks, planes or trains. As many people are already leaving in noisy environments, this is a non negligible social advantage.
- From a compilation of statistical data [136], it appears that the number of accidents, fatalities or injuries is very small regarding other transport modes. Consequently, inland waterway ensures a high degree of safety, particularly in case of dangerous goods.
- Unexpected congestion problems are very seldom on inland waterways, which reduce the risk of accident and the energy consumption. Moreover, this allows for a better organization of the transportation, as the time required for conveying goods from one point to another is not influenced by hazardous delays due to potential traffic jams.
- In terms of land take, for a given carrying capacity, waterways are more efficient than road or rail.

In addition to the points listed here above, it is often claimed that the total cost (including infrastructure) is lower if goods are conveyed by water. Nevertheless, this assertion seems to be arguable for short distances because contradictory information is sometimes found when reading articles. So this argument has to be carefully considered.

For the reasons listed above, it appears that waterborne transport is an interesting alternative to road. This is particularly true in Europe, where the five biggest sea ports are all connected to more than 37 000 kilometers of navigable inland waterways. Furthermore, it is a fact that this network is currently under-utilized, so the potential development is not negligible. This policy is precisely the one of the European Commission, who has decided to promote the waterborne transport through the NAIADES I and II action programs. Amongst all the measures suggested by these plans, one of them consists in building new locks or improving the existing ones. On a practical point of view, this can be illustrated by some important achievements such as the "Seine-Nord-Europe" project in France, the "Seine-Scheldt-East" in Wallonia, the Lanaye lock in Belgium...

¹ European Statistics Institute - <http://epp.eurostat.ec.europa.eu>

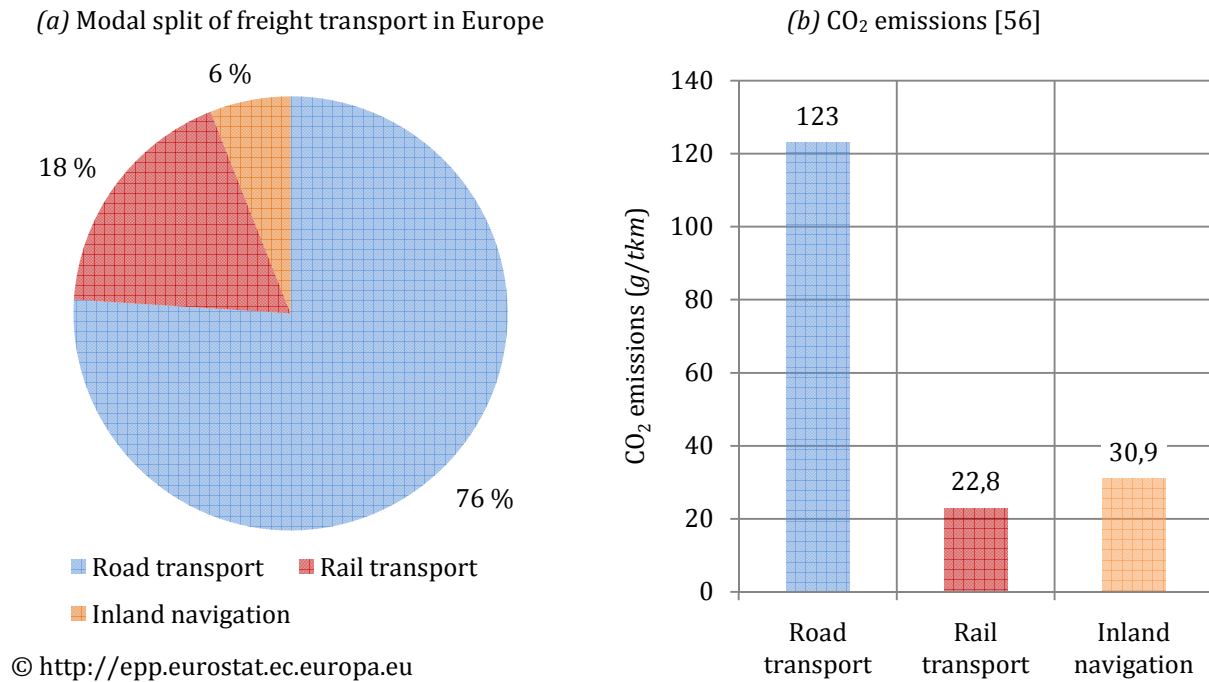


Figure 1.1. Freight transport properties

The direct consequence of such policies should be an increase of the waterborne traffic in the upcoming years. This means that the number of vessels passing through locks will be more important, which is also the case for potential accidents. Therefore, in order to keep a sufficient level of safety and to avoid any unexpected inconvenience for the navigation, locks have to be dimensioned more carefully. To achieve this goal, engineers need to have efficient tools for designing such structures.

From the previous presentation, it can be said that the context of this research is closely linked to the design and the calculation of lock structures, but with due consideration for stricter safety requirements in relation with the future increase of the waterborne traffic.

1.2. Aim of the research

Most of the international standards impose to consider the effects of accidental actions when calculating structures. According to Eurocode 0 [50], these ones are *"usually of short duration but of significant magnitude"* and are *"unlikely to occur on a given structure during the design working life"*. Nevertheless, accounting for them is nowadays more and more required. This is mainly due to exceptional events such as floods, storms, earthquakes... that take place at higher frequencies and therefore increase the probability of damaging the constructions.

This last observation is also valid for locks and is quite problematic in the context exposed in section 1.1. Indeed, as the future development of the waterborne transport requires to improve the safety level of locks, these structures have to be carefully studied within the frame of exceptional loads. This point is particularly sensitive, because any failure may have important economic, environmental and social consequences. More investigations are therefore valuable, but considering all the possible exceptional loads is unfortunately an overwhelming task, so a choice has to be made.

It is known that lock gates are statistically impacted by ships several times per year, but these collisions remain quite negligible. These structures are also involved in major collisions once or twice in their lifespan (20 to 40 years), but there is no consensus on the way to account for them during the design. This is also the case for earthquakes, as their effects remain complicated to integrate in the conception phases, principally because of the difficulty to quantify them. Consequently, these two accidental loads are definitely key issues and this is why we have decided to focus the research on them. For example, they constitute the main difficulties for the new lock gates of the Panama canal, which is one of the most important project of civil engineering in the world.

Of course, the purpose is not to design lock gates such that they are capable to withstand ship impacts or earthquakes without damage. On the contrary, the idea is that the potential consequences of such events have to remain proportionate. To respect this requirement, it is necessary to reach a sufficient security level, but the overall cost has to remain as reasonable as possible. Therefore, one of the crucial phase is the pre-design of the structure, where the general shape and the main geometrical dimensions of the gate are chosen. It is quite intuitive that this operation will be more successfully achieved if it is possible to perform detailed analyses including all the loads acting on the structure. Doing so usually requires the use of finite element software to properly investigate the effects of ship impacts and earthquakes.

However, working with numerical tools is not always possible in the pre-design stage because of time and cost limitations. Indeed, building finite element models, running simulations and post-processing the results may be a quite long procedure. This is particularly true when dealing with ship impacts and earthquakes, for which quite complex dynamic analyses are usually required. In addition, as a structural optimization is often desired, an iterative procedure has to be followed and it is definitely not reasonable to restart numerical simulations at each step.

Another problem is also due to the difficulty of defining the most critical scenario when dealing with accidental loads. In the case of a ship collision for example, once the vessel properties have been chosen, the main questioning point remains to detect the impact location causing the most severe damages to the gate. Usually, many different situations have to be tested separately and using finite element is not always convenient.

Regarding all these difficulties, an option to avoid them could be to neglect accidental loads during the pre-design phase. In this way, the structural configuration is first chosen by considering the main actions and is later checked with the exceptional ones. If these verifications are not successful, then a reinforcement is required. Of course, such an approach could only be efficient in a limited number of cases, where the magnitude of the accidental actions is very small with respect to the others. Furthermore, the problem of finding the most severe scenario is not solved.

The previous considerations point out that an efficient tool is missing for integrating the seismic action and ship collisions in the pre-design of lock gates. The aim of the research is precisely to solve this problem by developing simplified analytical tools allowing for:

- A quick estimation of the force opposed by plane and mitre lock gates when they are impacted by a ship of given shape. The goal is to assess the crushing resistance as a function of the vessel penetration for any impact point.
- A rapid prediction of time evolution of the total hydrodynamic pressure applied on a plane lock gate during a seism. The purpose is to have an analytical evaluation that also accounts for the proper vibrations of structure.

Of course, it is illusory to believe that these simplified tools will provide the same accurate results than finite element software. Nevertheless, such a precision is not really required at the pre-design stage. In fact, the analytical approach is complementary to the numerical one.

1.3. Organization of the thesis

The dissertation is divided into three main parts. The first one is concerned with ship impacts on lock gates, the second one deals with the seismic design, while the last one contains all the appendices.

The first part of the manuscript contains four chapters numbered from 2 to 5. Chapter 2 is entitled *Background for the ship collisions on lock gates* and starts by reviewing some of the methods currently available in the literature to study vessel collisions. It also gives some general indications for the evaluation of the initial kinetic energy and exposes the fundamental theorems that are required to develop an analytical method. These theorems are applied in the Chapter 3 *Analytical derivation of the collision resistance of plane lock gates* to treat the case of a gate with a simple plating and an orthogonal stiffening system. The resistance is first calculated in the local deforming mode by dividing the structure in large components called super-elements. This solution is then coupled with the one evaluated in the global mode to get the final resistance of the gate. As a matter of validation, these analytical results are compared with those provided by finite element software. The same procedure is applied in the Chapter 4 to treat the case of mitre gates. Finally, the conclusions of all these investigations are reported in Chapter 5.

The second part of the manuscript is also divided into four chapters number from 6 to 9. Chapter 6 *Literature review on the seismic design of lock gates* presents a general overview about the fluid-structure interaction in various situations. The case of dams, liquid storage tanks and lock gates are considered. As a preliminary to the seismic analysis of lock gates, Chapter 7 *Seismic analysis of large flexible reservoirs* proposed an analytical method to evaluate the total hydrodynamic pressure in a reservoir made of two parallel rigid walls and two flexible ones. The goal of this chapter is to account for the effect of the structural vibrations on the seismic pressure and to investigate the influence of some geometric parameters. Comparisons with finite element results are made to validate the analytical developments. After that, in the Chapter 8 *Seismic analysis of plane lock gates*, a similar work is done for these structures. The Rayleigh-Ritz method is first applied to evaluate the dry eigenfrequencies and eigenmode shapes. The analytical derivation of the hydrodynamic pressure is then performed through the virtual work principle and is validated by numerical comparisons. In addition, the well-known added mass method is also investigated. Finally, this second part is closed by Chapter 9 that summarizes the conclusions.

The third part contains five appendices numbered from *A* to *E*. All of them are related to one of the chapters mentioned here above. They mainly provide some additional mathematical developments that are included to have a kind of "stand-alone" manuscript.

- PART I -

Ship impacts on lock gates

CHAPTER 2. Background for the ship collisions on lock gates

The purpose of this chapter is to give a general insight about ship collisions on lock gates. As this topic is not really documented in the literature, it seems important to properly expose the methods and the theoretical bases available to study ship impacts on such structures.

To do so, a general review of the existing approaches is first proposed in section 2.1. As they are extensively used in this dissertation, the focus is made on the simplified analytical techniques and on the finite element method. In particular, the problem of defining realistic failure criteria is briefly discussed.

In section 2.2, some indications are given on the way the initial kinetic energy of the striking vessel should be chosen. This is achieved by determining the mass and the striking velocity of the ship. To do so, a detailed compilation of the recommendations available in the literature is proposed to set these two parameters.

Finally, section 2.3 presents the theoretical method followed to evaluate the internal energy dissipated by the gate during the collision. The fundamental theorems used to establish the simplified analytical approach are also exposed in this section.

2.1. Review of the existing methods

The approaches that can be used to study the collision resistance of lock gates are the same as those already listed by Zhang [180] in the field of ship-ship collisions. Amongst them, experimental methods are probably the most reliable way to evaluate the collision resistance. Usually, they consist in studying the structural components (stiffeners, plates...) individually, because performing a true scale experiment is a technical and economical challenge. In the literature, most of the available test results have been realized for the shipbuilding, in order to check the safety of vessel regarding oil spills. Amongst others, experiments were conducted by Akita et al. [3], Amdahl [8], Cho et al. [31], Pedersen et al. [130] or Qvist et al. [131]. In an illustrative purpose, Figure 2.1 shows the deformation of a tanker double side collided by a rigid ball simulating a striking bow.



Figure 2.1. Experimental study of a tanker double side [131]

Apart from experimental approaches, there are two remaining other possibilities to evaluate the collision resistance: the finite element methods and the simplified analytical techniques. Both of them are used in this thesis, numerical solutions being used as a validation for the analytical ones. They are briefly presented hereafter.

2.1.1. Finite element methods

Finite element methods are a powerful tool to study ship collisions on lock gates. They allow for a quite refined study of the local strains and stresses that develop inside the structure, which is always valuable for the design procedure. Most of the time, they lead to accurate and reliable results that are in good accordance with experiments, but this is not always true. Ideally, one should always try to corroborate numerical solutions with physical ones.

Another advantage of finite element methods is the ability of investigating complex models, in which a true representation of the support conditions and of the striking vessel can be included for example. Nevertheless, this has to be nuanced by the computing capacities required to perform very refined analyses, which is particularly true in the field of collisions due to the great number of elements usually required. In addition, such dynamic problems have to be solved using step by step integration solvers, which is also time demanding.

As a matter of illustration, the equivalent Von Mises stresses in a collided lock gate are depicted on Figure 2.2. They have been obtained by using the commercial software LS-DYNA, but many other codes are also available such as ABAQUS or MSC DYTRAN. In the literature, these software have been used in various domains. The purpose here is not to realize a detailed review of all the available publications but to give some typical illustrations of what can be achieved using these numerical tools. For example, in the field of shipbuilding,

numerical simulations were performed by Oh et al. [116] to study ship-ship impacts, by Alsos and Amdahl [7] to investigate ship grounding or by Donner et al. [44] for ship-submarine collisions. In the field of structural engineering, ship impacts on lock gates were considered by Le Sourne et al. [99] or by Buldgen et al. [22] and more recently, the damages caused by an accidental collision between a vessel and the jacket of an offshore wind turbine was studied by Vredeveldt et al. [160].

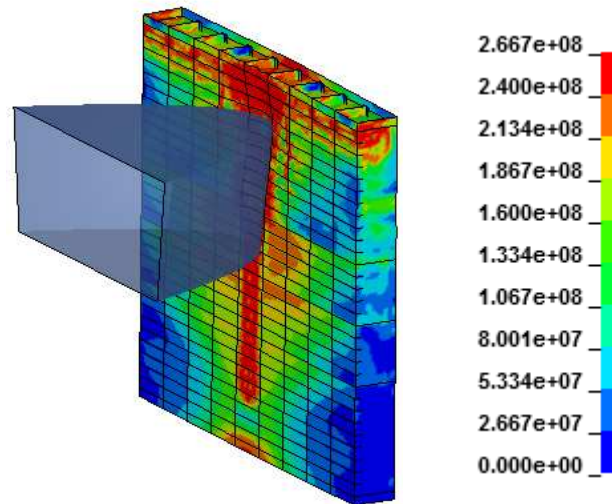


Figure 2.2. Equivalent Von Mises stresses in a collided lock gate (MPa)

Nevertheless, one of the main challenge when working with finite element is to model rupture consistently. This is quite important, because defining realistic failure criteria is closely related to the need of designing crashworthy structures. Therefore, in order to evaluate the collision resistance of the struck gate, it is valuable for engineers to perform realistic finite element simulations and a crucial point is to use material laws that can properly represent the true behavior of steel.

In the literature, this problem has been studied to some extent and is not easy to solve. This can be illustrated by the work performed by Ehlers et al. [47], where the impact responses of three different ship side structures are analyzed by performing finite element simulations using LS-DYNA. The curves showing the crushing force as a function of the penetration are obtained by considering the same non linear stress-strain relation but three different failure criteria defined in accordance with the mesh size. The numerical results are then compared to those collected from large scale experiments. The conclusions of this benchmark study are:

- Considering the same rupture criterion but various mesh sizes leads to different force-penetration curves. This tends to show that the current definitions of the failure criteria are not consistent for all element sizes.
- Considering the same mesh size but various rupture criteria leads to different force-penetration curves, which implies that choosing one or another law is not equivalent.
- There is a contradiction in the fact that the stress-strain curves are independent of the mesh size, while the failure strain is determined in accordance with the elements lengths.

In order to overcome all the previous difficulties, Ehlers and Varsta [48] suggested a new method to get a realistic stress-strain relation until fracture. The material law is obtained by performing a tensile test on steel dog-bone specimens. During this experiment, an optical

measuring system is used to capture the surface displacements over a recorded area, which allows to define the strain reference length as a function of the pixel size (Figure 2.3).

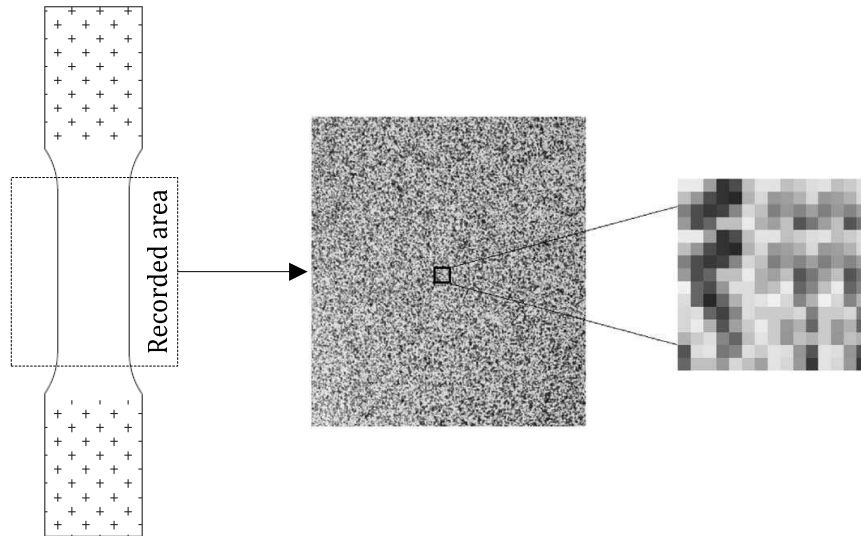


Figure 2.3. Definition of the strain reference length as a function of the pixel size [48]

By post-processing these measurements, it is possible to get the true local deformation as a function of the tensile force applied on the specimen. Furthermore, dividing this force by the actual cross-section area provides an evaluation of the true stress. Combining these results, the material law and the rupture criteria can be derived as a function of the strain reference length. These curves may then be implemented within a finite element software. This was achieved by Ehlers and Varsta [48], who reproduced their tensile tests using LS-DYNA and calibrated the element length in accordance with their previous findings. Doing so, they obtained numerical results that were in incredibly good agreement with the experimental ones.

In another paper, the same operation was performed by Ehlers [46] to study the collision response of a circular plate. Here again, the results were perfectly satisfactory. In addition, it was shown that the numerical rupture pattern was in good agreement with the experimental observations, which indicates that the erosive law consisting in deleting ruptured elements is, in this case, an adequate way to simulate fracture propagation.

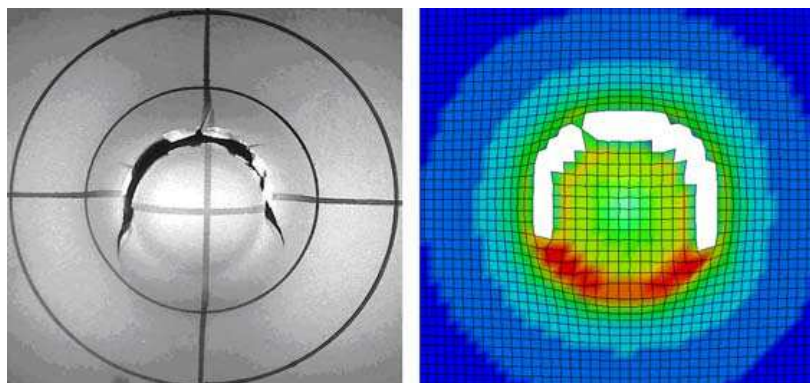


Figure 2.4. Experimental and numerical rupture pattern of the plate specimen [45]

From the previous considerations, it transpires that modeling failure properly is not easy. Of course, the methodology suggested by Ehlers and Varsta [48] is a powerful way to overcome this difficulty. Nevertheless, such an approach requires to perform sophisticated tensile tests and to carefully post-process the measurements, which is not always possible during the pre-

design of lock gates. For this reason, it remains quite common to resort to other easier laws, such as the one suggested by Lehmann and Peschmann [93] for example (see section 3.3.4).

2.1.2. Simplified analytical methods

Simplified analytical methods have been developed to compensate the drawbacks of too time demanding numerical simulations. Therefore, they are typically well suited in the pre-design stage of a structure, when an approximate evaluation of the collision resistance is sufficient. In the literature, the available analytical developments are mainly devoted to evaluate the crashworthiness of individual structural elements, such as plating components, girders, frames, bulkheads... (see sections 2.3, 3.3, 3.4 and 3.5 for more detailed reviews) but some papers have also been published to treat larger entities, such as ship or lock gates.

According to Zhang [180], some of the earliest simplified methods were developed by McDermott et al. [107], Kinkead [86] and Reckling [135] in the field of ship-ship collisions. More recently, Le Sourne et al. [98] also focused on this topic by applying the super-elements approach. Regarding the analytical techniques to evaluate the impact resistance of lock gates, the initial work realized by Le Sourne et al. [99] has been completed and extended by Buldgen et al. to plane [22] and mitre [24] lock gates. Usually, these simplified methods give a reasonable prediction of the resistance in a very short time. They are classically corroborated by comparisons with finite element simulations, but using experimental results is of course more recommended as a matter of validation.

The theoretical basis for developing analytical approaches is nothing else than an energy balance. During the collision on a lock gate, it is assumed that the ship keeps on moving as long as its initial kinetic energy E_0 has not been entirely dissipated by the structure. When the equilibrium is reached, we have:

$$E_0 = E_{int} \quad (2.1)$$

where E_{int} is the internal energy of the gate. At this moment, the vessel does not move anymore. Nevertheless, it is worth noting that the previous energy balance is only valid when there is no other dissipative effect involved in the collision process, which means that two other hypotheses are necessary.

As a first assumption, the striking vessel is assumed to be perfectly rigid. This seems to be reasonable, as the stiffness of the most critical ship is usually attempted to be more important than the one of the gate. Moreover, doing so is conservative, as the total initial kinetic energy of the ship has to be entirely dissipated by the impacted structure. Nevertheless, it is worth noting that some analytical methods have already been established to account for the deformability of the bow. These ones were developed for ship-ship collisions, as the rigidities of the two vessels may be quite similar in this case. A general presentation of the methodology is done by Le Sourne [97] and many other details can be found in references [8], [94], [98], [103], [104] and [130].

The second hypothesis consists in neglecting all the other phenomena that may also dissipate the initial kinetic energy E_0 . These ones have been carefully investigated by Simonsen [140] in the case of ship grounding on rocks. In the present analysis, an additional term that could be potentially included in the energy equilibrium (2.1) is the friction that may appear between the vessel and the gate, but also at the supports of the structure. This is particularly the case if sliding is expected on the lock walls. Equation (2.1) is then modified:

$$E_{int} + E_f = E_0 \quad (2.2)$$

where E_f is the energy dissipated by friction. Nevertheless, the evaluation of E_f is not easy because it is influenced by many other parameters, such as the roughness the lock walls, the seal integrity... Consequently, this additional contribution is neglected in the present method. Doing so is a conservative approach, as it tends to overestimate the structural deformations.

From the previous considerations, it appears that the crucial points of the analytical methods is to consistently derive E_0 and E_{int} . The first one can be evaluated by considering the mass and the velocity of the striking vessel (section 2.2), while the second one may be obtained with help of some fundamental theorems (section 2.3).

2.2. Evaluation of the initial kinetic energy

To evaluate the initial kinetic energy, it is required to define the total mass M_s and the initial velocity V_0 of the striking ship, but there is no clear recommendation on the way these parameters have to be chosen. Of course, when a lock gate has to be checked against collision events, M_s and V_0 can be set by the client according to the security level he wants to reach. As an example, for the new locks that are currently built at the Panama canal, it was contractually imposed [124] to the designers to consider a total displacement of 160000 tons and a velocity of 0.5 m/s for the collisions analysis. Nevertheless, M_s and V_0 are not always so clearly specified. In this case, it is the responsibility of the designers to determine reasonable values, but this is not straightforward. To achieve this goal, some indications are however of interest and are briefly detailed hereafter.

Regarding the mass M_s , it has to be chosen in accordance with the vessels that are currently navigating on the inland waterway where the considered lock is located. A detailed analysis of the traffic could therefore be of precious help. If the required statistical data are not available, some other tools may be used. In Europe for example, the ECMT² has published a resolution [55] in which the waterways are classified according to different parameters (see Table A.1 in Appendix A.1). According to this table, if a new lock has to be built on a class Va waterway for example, then the designer knows that M_s ranges from 1500 to 3000 tons.

Concerning the velocity V_0 , there is no particular recommendation on the way it has to be chosen if not contractually specified. Nevertheless, to have a better idea of V_0 , some information has been collected in the literature or by contact with designers. It is summarized hereafter:

- In 2011, Meinhold [108] investigated numerically the crashworthiness of a mitre gate for the German Federal Waterways Engineering and Research Institute (BAW). All the simulations were conducted by considering an initial velocity of 1 m/s.
- In 2002, Le Sourne et al. [99] performed numerical simulations to investigate plane lock gates crashworthiness. Two different ships were considered for this study. The first one was a carrier travelling at 1 m/s, while the second one was a passenger vessel with velocities of 1 m/s and 2 m/s.
- In a quite old French ministerial circular from 1980 [111], it is claimed that the devices protecting locks against collisions have to be able to withstand an impact at 0.75 m/s.
- According to the German standard DIN 19703:1995-11 [42] dealing with the design of lock gates, the collision protection devices have to be able to withstand an impact by a ship travelling at the speed of 0.9 m/s for motor barges and 1 m/s for pushing units.
- In 2013, the U.S. Army Corp of Engineers (USACE) made different full-scale experiments to study ship impacts on lock walls. The results are described in references [11] and [129]. Even if these analyses are not directly related to the gate, they give however an idea of what could be the speed inside the lock chamber. A total of 44 collisions experiments were performed. The initial velocities for these tests were ranging from 0.15 to 1.2 m/s.

² European Conference of Ministers of Transport

- For the new lock that is currently constructed in Ivoz-Ramet on the Meuse River (Belgium), the design has been done by considering an initial velocity of 0.75 m/s [145].
- According to the CETMEF³ [26], the drawing speed of a vessel is ranging from 0.35 m/s to 1 m/s , depending on its tonnage. This gives an idea of the velocity range near a lock.
- As mentioned earlier, for the design of the set of locks in the Panama canal [124], the striking speed was fixed to 0.5 m/s for a vessel with a displacement of 160000 tons. An additional analysis with a ship of 100000 tons and a velocity of 1 m/s was also required.

Finally, it is worth mentioning that another method for designing lock gates against collision may be to consider an equivalent static force to apply on the structure. Such an approach is followed in the United States for example, where the U.S. Army Corps of Engineers has published several manuals (see references [152] and [153] for more details) providing information dealing with ship collision on lock gates. A similar method is also exposed in the European standard EN 1991-1-7 [51] dealing with accidental actions on structures. The design values of the force are given according to the class of the inland waterways. They were derived for a striking velocity of about 2 m/s and by assuming that the energy dissipated by the structure was negligible. Of course, this is valid for massive structures such as bridge piers for example but is not realistic for lock gates, except in case of minor impacts. Consequently, one has to be extremely careful before applying an equivalent static force method. These approaches are often too conservative or not accurate enough.

As a conclusion, from all the references mentioned here above, it transpires that a reasonable initial striking velocity has to be chosen within a range of 0.15 to 2 m/s . Once M_s and V_0 are fixed, it is suggested in [26] to correct these values to account for the two following phenomena:

- During the motion of the ship inside the lock, some water is also displaced by the vessel, which means that the total mass is no more equal to M_0 but has to be emphasized by a mass coefficient $C_m \geq 1$ to get $C_m M_s$. C_m depends on the shape of the striking stem and a value of 1.2 is recommended in [26].
- When the ship is entering the lock, some water is confined between the stem and the structure, which creates a piston effect and a reduction of the striking velocity. Therefore, V_0 may be reduced by a confinement coefficient $C_c \leq 1$ to get $C_c V_0$. Evaluating C_c is difficult, as it depends on the shape of the bow and on the lock configuration. In [26], it is suggested to choose $C_c = 0.9$.

Finally, accounting for the previous considerations, the total initial kinetic energy E_0 of the striking vessel is given by:

$$E_0 = (C_m M_s) \frac{(C_c V_0)^2}{2} = C_m C_c^2 M_s V_0^2 \simeq 0.97 \frac{M_s V_0^2}{2} \quad (2.3)$$

From equation (2.3), E_0 is only 3 % lower than the uncorrected value $M_0 V_0^2 / 2$. It seems therefore more relevant to carefully choose the values of M_s and V_0 than those of C_m and C_c . It is worth recalling that E_0 has to be entirely dissipated by the deformation of the gate, as the striking bow is assumed here to be perfectly rigid.

³ CETMEF: Centre d'Etudes Techniques Maritimes et Fluviales (France).

2.3. Evaluation of the internal energy

On a theoretical point of view, the problem of evaluating the collision resistance of a lock gate consists in deriving the corresponding collapse load. To do so, one may resort to the theorems of limit analysis in plasticity that are briefly exposed hereafter. It is well known that the exact solution to a problem of the mechanics of deformable solids has to satisfy simultaneously the equilibrium, compatibility and constitutive equations. However, in the frame of limit plastic analysis, two different types of solutions are of interest:

- The lower-bound solutions are those for which only the equilibrium and the yield criterion are verified, so they are said to be statically admissible. Generally, it is possible to find an infinite number of stress states that satisfy these two conditions.
- The upper-bound solutions, for which only the compatibility and equilibrium equations are respected, so they are said to be kinematically admissible. Usually, there are an infinite number of velocity fields that simultaneously respect these two requirements.

2.3.1. Exact theory

Let us now consider a solid of arbitrary shape that is submitted to a collision. Typically, this solid can be a lock gate for example. Because of the impact, one can imagine that this element is progressively transformed from its initial configuration Ω_0 to the current one Ω (Figure 2.5). It is worth noting that Ω is subjectively chosen and does not necessarily describes the real impacted shape of the solid.

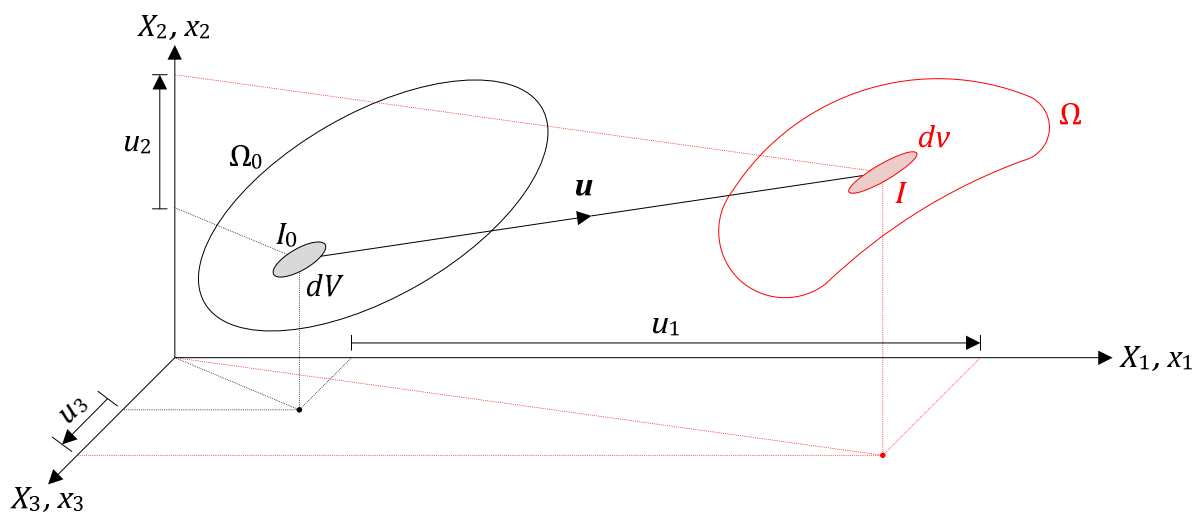


Figure 2.5. Definition of the velocity field

During this deformation from Ω_0 to Ω , a point I_0 with the coordinates (X_1, X_2, X_3) is moved to another point I with coordinates (x_1, x_2, x_3) . The displacement and velocity fields characterizing this movement are respectively designated by \mathbf{u} and $\dot{\mathbf{u}}$. If u_i and \dot{u}_i are the components of \mathbf{u} and $\dot{\mathbf{u}}$ along the axes (X_1, X_2, X_3) , then [157]:

$$x_i = X_i + u_i(X_1, X_2, X_3) \Leftrightarrow \dot{x}_i = \dot{u}_i(X_1, X_2, X_3) \quad (2.4)$$

As Ω is not uniquely defined, \mathbf{u} and $\dot{\mathbf{u}}$ may be arbitrarily selected, provided that they remain kinematically admissible, which implies that they have to respect the compatibility and the boundary conditions.

Let us further analyze the work performed by the external forces acting on Ω . The first ones are the reactions applied at the supports, but they do not work under the assumption that there is no displacement at the boundaries. Another force to consider is the one exerted by the impacting vessel on the deforming solid. By equilibrium, this one is precisely equal to the resistance \mathbf{P} opposed to the penetration of the ship. Consequently, if \mathbf{V} is the striking velocity, the external work rate \dot{W} is simply as follows:

$$\dot{W} = \mathbf{P} \cdot \mathbf{V} \quad (2.5)$$

in which the vector \mathbf{V} is known as the vessel is assumed to move perpendicularly to the gate with an initial velocity V_0 . On the other hand, the internal energy rate \dot{E}_{int} associated to the deformation of the solid can also be evaluated. This one is given by:

$$\dot{E}_{int} = \iiint_v [\sigma] \cdot [\dot{\mathbf{a}}] dv = \iiint_v \sigma_{ij} \dot{a}_{ij} dv \quad \dot{a}_{ij} = \frac{1}{2} \left(\frac{\partial \dot{u}_i}{\partial x_j} + \frac{\partial \dot{u}_j}{\partial x_i} \right) \quad (2.6)$$

In this last expression, v is the volume of Ω , $[\sigma]$ is the Cauchy stress tensor and $[\dot{\mathbf{a}}]$ is the Rivlin-Eriksen rate of the Almansi strain tensor (see Appendix A.2 for more details). In the absence of any other dissipative phenomenon (such as friction), it is clear that the collision energy has to be entirely absorbed by the deforming structure. Therefore, $\dot{W} = \dot{E}_{int}$, which allows for the derivation of the sought collision resistance \mathbf{P} .

As a conclusion, equating (2.5) and (2.6) allows to determine the resistance of any collided structural element. Nevertheless, it is worth recalling that the derivation is performed for a velocity field $\dot{\mathbf{u}}$ that is arbitrarily chosen. In other words, the method exposed here above provides an upper-bound solution to the collision problem, which does not violate the compatibility requirement and the equilibrium equations, but does not respect the yield condition. Furthermore, there is only an overall energy balance that is obtained by equating (2.5) and (2.6). By applying the virtual velocity principle, it can be demonstrated [28] that doing so leads to overestimate the real collision resistance.

In fact, this last assertion is based on the upper-bound theorem. This latter states that [28] *"If a compatible mechanism of plastic deformation is assumed which satisfies the boundary conditions, then the loads determined by equating the rate at which the external forces do work to the rate of internal dissipation will be either higher than or equal to the actual collapse load"*. From this theorem, it also transpires that choosing $\dot{\mathbf{u}}$ in good agreement with the true velocity field characterizing the impacted structure leads to an external force \mathbf{P} that is a closer estimation of the real collision resistance. Consequently, the deformation patterns should be quite properly postulated while evaluating the crashworthiness of an impacted structure.

2.3.2. Approximate theory

The validity of the previous limit theorems of plasticity is in fact limited to the field of small displacements [28]. During a collision, this hypothesis is not realistic as the structure may be subjected to very important damages characterized by large displacements and sometimes large deformations. Unfortunately, no general theory is available to deal with finite displacements. As detailed hereafter, various authors have developed some procedures to treat this kind of situations, but these ones remain quite approximate as they do not have any rigorous theoretical basis. Nevertheless, these solutions are commonly accepted to some

extent because they have been corroborated by numerical and sometimes experimental results. In the literature, two different approaches are singled out for analyzing the crashworthiness of impacted structures submitted to finite displacements. They are referred to as the upper-bound and equilibrium methods.

2.3.2.1. The upper-bound method

The upper-bound method simply assumes that the exact theory presented in 2.3.1 may be extended to structures exhibiting moderate strains and displacements. The procedure is formally similar and kinematically admissible, but some differences lie in the way of evaluating the internal dissipation \dot{E}_{int} . The main modification to equation (2.6) is obtained by performing the integration with respect to the undeformed configuration Ω_0 . This means that the initial volume V is considered in (2.6) instead of the actual one. This simplification is of practical importance, as it avoids having very cumbersome equations that may usually not be solved analytically. Nevertheless, working with respect to Ω_0 implies that the stress and strain rate tensors have to be consistently chosen [157]:

$$\dot{E}_{int} = \iiint_V [S] \cdot [\dot{E}] dv = \iiint_V S_{ij} \dot{E}_{ij} dV \quad \dot{E}_{ij} = \frac{1}{2} \left(\frac{\partial \dot{u}_i}{\partial X_j} + \frac{\partial \dot{u}_j}{\partial X_i} + \frac{\partial u_k}{\partial X_i} \frac{\partial \dot{u}_k}{\partial X_j} + \frac{\partial u_k}{\partial X_j} \frac{\partial \dot{u}_k}{\partial X_i} \right) \quad (2.7)$$

where $[S]$ is the second Piola-Kirshhoff stress tensor and $[\dot{E}]$ is the Green strain rate tensor. It is worth noting that the coordinates (X_1, X_2, X_3) involved in (2.7) are the ones defining the initial configuration Ω_0 and not the actual ones as it was the case in (2.6). Unfortunately, evaluating \dot{E}_{int} by applying (2.7) usually leads to very cumbersome equations that may not be treated analytically. Therefore, in order to overcome this difficulty, the upper-bound method is simplified by making additional hypotheses on the material behavior.

In reality, the stress-strain curve of mild steel in tension is made of a first linear elastic phase (Figure 2.6) that ends when the deformation ϵ_0 is reached. The associated stress is denoted by σ_0 and is the starting point of the plastic phase. During this one, the material is submitted to strain hardening, until necking occurs for a given deformation ϵ_u . Beyond this point, the stress starts decreasing from its maximal value σ_u , but this phase is limited by the material failure in ϵ_r .

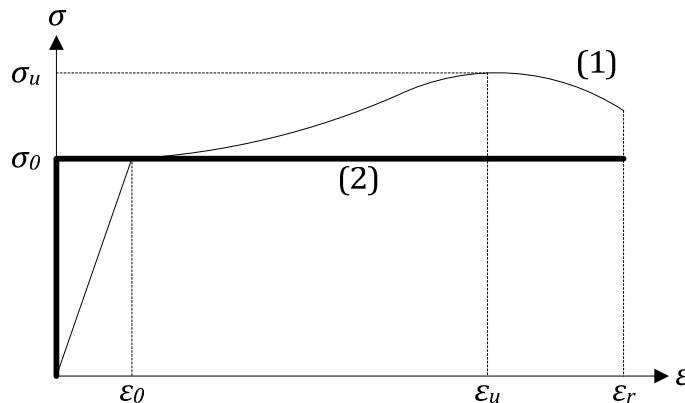


Figure 2.6. Actual (1) and idealized (2) stress-strain curve of mild steel

Of course, it would be too difficult to capture all these successive phases, so the assumption is made of a rigid-plastic material, which implies that the initial elastic regime is disregarded. From the experiments reported by Alsos and Amdahl [6], Cho and Lee [30], Simonsen and Lauridsen [143] or Wang [162], it appears that the plastic deformations largely dominate the

process, so this hypothesis seems to be quite reasonable. Furthermore, doing so also supposes a non-hardening material, but some authors such as Lützen [103], Simonsen [141] or Zhang [180] consider that neglecting the strain hardening by taking a flow stress equal to σ_0 is too conservative. They suggest to work with the mean value $(\sigma_0 + \sigma_u)/2$, but this recommendation will not be followed here. The principal reason is that working with a too high flow stress leads to an increased value of the collision resistance and it is known that applying the upper-bound method already provides an overestimation.

Under the hypothesis of a rigid-plastic material, the plastic flow theory is applicable and it can be shown that in this case, the internal dissipation (2.7) may be evaluated with help of the equivalent Green-Lagrange strain rate \dot{E}_p (see Appendix A.2, section A.2.5):

$$\dot{E}_{int} = \iiint_V \sigma_0 \dot{E}_p dV \quad (2.8)$$

In the literature, the upper-bound method was mainly used for deriving the resistance of plated structures. One of its first application was done by Alexander [71] in 1960 to study the axial crushing of cylinders, but some recent papers show that this upper-bound approach is still of interest. For example, Hong and Amdahl [71] applied it to derive analytically the patch-loading resistance of ship plates, while upper-bound solutions were obtained by Kotelko et al. [89] for various resistance modes of thin-walled structures submitted to compression. Many investigations were also performed on stiffened plates, such as the analytical developments currently achieved by Cho and Lee [30].

The previous references provides only a short illustration on the way the upper-bound method can be applied to determine the collapse load. Other applications dealing with plated components have also been derived by various authors. For clarity, they have not been reported here but are concisely presented in sections 3.3, 3.4 and 3.5.

2.3.2.2. The equilibrium method

Another way to investigate structures submitted to finite displacements is the equilibrium method, which simply uses the translational and rotational static equations to get statically admissible solutions. Most of the time, these ones are written in the deformed configuration and account for the actual shape of the impacted element, but some simplifications are required to get closed-form solutions. One of them consist in postulating that the material is rigid-plastic.

As expressing the equilibrium of plates in finite displacements is usually a quite arduous task, the main applications of this second method are devoted to beams. The analysis is made by assuming that a plastic collapse mechanism is reached. Usually, this latter involves a certain number of plastic hinges where the bending effects concentrate.

One of the first author to consider the problem of large deflection of beams was Haythornthwaite [69] in 1957. Since this pioneer work, many other authors have investigated this question. In particular, Jones [80] pointed out the potential effect of in-plane displacements in case of beams with partial lateral restrains. Similarly, the question of non-symmetrical impacts was addressed by Tin-Loi [148], who also considered some extensional and rotational flexibilities at the supports. A more complicated application of the equilibrium method was done by Jones et al. [82], who treated the case of an impact occurring at the centre of a beam grillage.

An interesting point to note is that applying the equilibrium or the upper-bound method usually does not lead to the same analytical solutions. This may only be the case if a consistent set of equations is used to evaluate the strain rates and to express the equilibrium of the structure. As explained by Jones [79], these ones can be artificially constructed by applying the virtual velocity principle.

CHAPTER 3. Analytical derivation of the collision resistance of plane lock gates

This chapter presents an analytical method to derive the resistance opposed by plane lock gates during a collision involving a vessel of given shape. The striking bow and the structure properties postulated for this study are clearly established in section 3.1.

Before performing any developments, the general methodology followed for the mathematical derivations is first briefly presented in section 3.2.

The resistance is then derived under the assumption of a local deforming mode by applying the super-elements method. Three types of structural components are studied separately. For each of them, the analytical developments are briefly exposed and the corresponding formulae are validated by numerical comparisons in sections 3.3, 3.4 and 3.5.

In section 3.6, the calculation is made for the global deforming mode by dividing the gate into a set of horizontal beams. The derivation is done in both the elastoplastic and rigid-plastic regimes. The resistance obtained in this way is then combined to the local one in order to get the final resistance of the gate.

The results obtained by using the simplified method are validated in section 3.7 by comparing them to finite element solutions. The discrepancies are systematically analyzed and interpreted.

Finally, the main steps and achievements presented in this chapter are summarized in the conclusion. Some additional comments are also provided in this last section.

The developments presented in this chapter have been partly published by Buldgen et al. [22] in the International Journal of Applied Mathematics.

3.1. Introduction

The goal of this chapter is to develop a method that allows for a rapid prediction of the resistance opposed by a plane lock gate impacted by a ship. The basic idea is to derive simplified analytical formulations using the so-called upper-bound method. As a first step, let us start by describing the struck gate and the striking vessel.

3.1.1. Description of the impacted gate

3.1.1.1. Structural properties

This chapter deals with plane lock gates having a single plating and an orthogonal stiffening system. The total height is denoted by h , while the width is designated by l (Figure 3.3). Such a kind of structure may be used for the following cases (see references [38], [170] and [171] for more details):

- Lifting gates (Figure 3.1a and Figure 3.2a), which are raised and lowered vertically to open or close the lock chamber. A tower constructed over the gate allows to pull it out of the water. This motion is achieved by cables, hydraulic cylinders... Counterweights may also be used to assist the hoisting machinery.
- Single leaf gates (Figure 3.2b), which are quite similar to mitre gate (see Chapter 4) but have only one leaf rotating around a vertical axis. They are mainly used for locks having an important head and a small width (i.e. for $h \gg l$) such in the pleasure navigation. The leaf is typically maneuvered by a jack when the upstream and downstream levels are equal.
- Horizontally moving gates (Figure 3.1b), for which many configurations are possible. They are maneuvered perpendicularly to the navigation way and an additional lateral chamber is required for retracting them. In the first configuration (Figure 3.2c), the gate is simply rolling on a track fixed at the bottom of the lock. An alternative solution to this configuration is simply to have a gate sliding on a particular floor placed on the ground (as Hydrolift gate in the Netherlands). In the second case (Figure 3.2d), the structure is still equipped with wheels at the bottom, but is simultaneously held at the rightmost upper corner by a wagon moving on rails. Finally, the last configuration (Figure 3.2e) is a laterally moving gate attached by cables to an additional superstructure (Figure 3.1b).

(a) Vertical lifting gate of the John Day lock on the Columbia River (United States)



© <http://www.kval.com>

(b) Horizontally moving gate of the Lanaye lock on the Meuse River (Belgium)



© <http://www.trekearth.com>

Figure 3.1. Lock gates examples

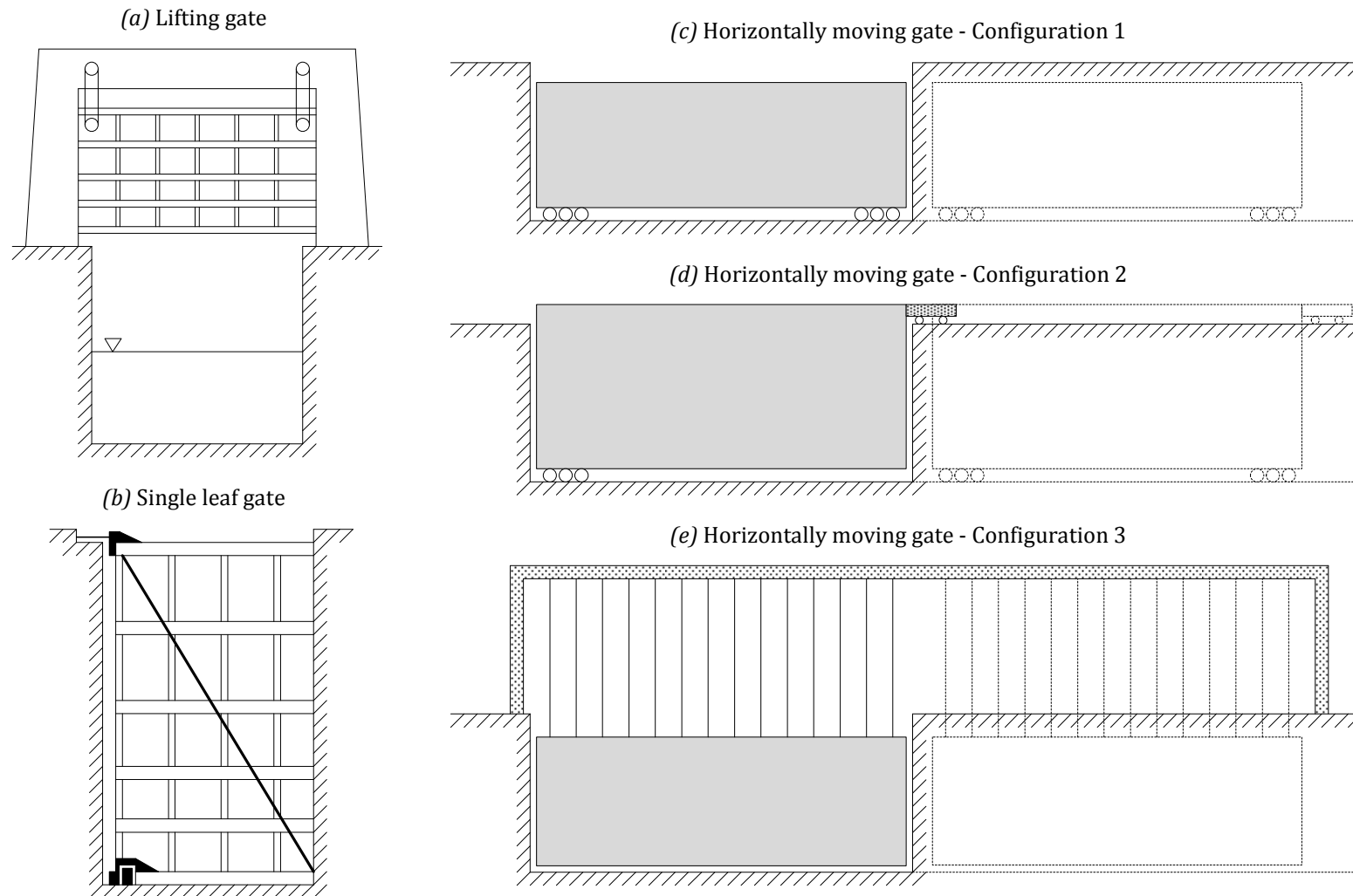


Figure 3.2. Illustration of the different types of gates considered in this chapter

3.1.1.2. Geometrical properties

In order to develop a simplified tool allowing for a quick estimation of the crashworthiness for such gates, a formal description of their configuration is required. To do so, an orthogonal reference frame (X, Y, Z) is placed at the rightmost lower corner of the structure (Figure 3.3). The vertical reinforcing elements (parallel to the Y axis) are called the frames and are placed at different locations Z_i on the horizontal Z axis. Usually, they are regularly spaced along the width l of the gate, but this is not always the case. The total number of vertical components will be denoted by n_v .

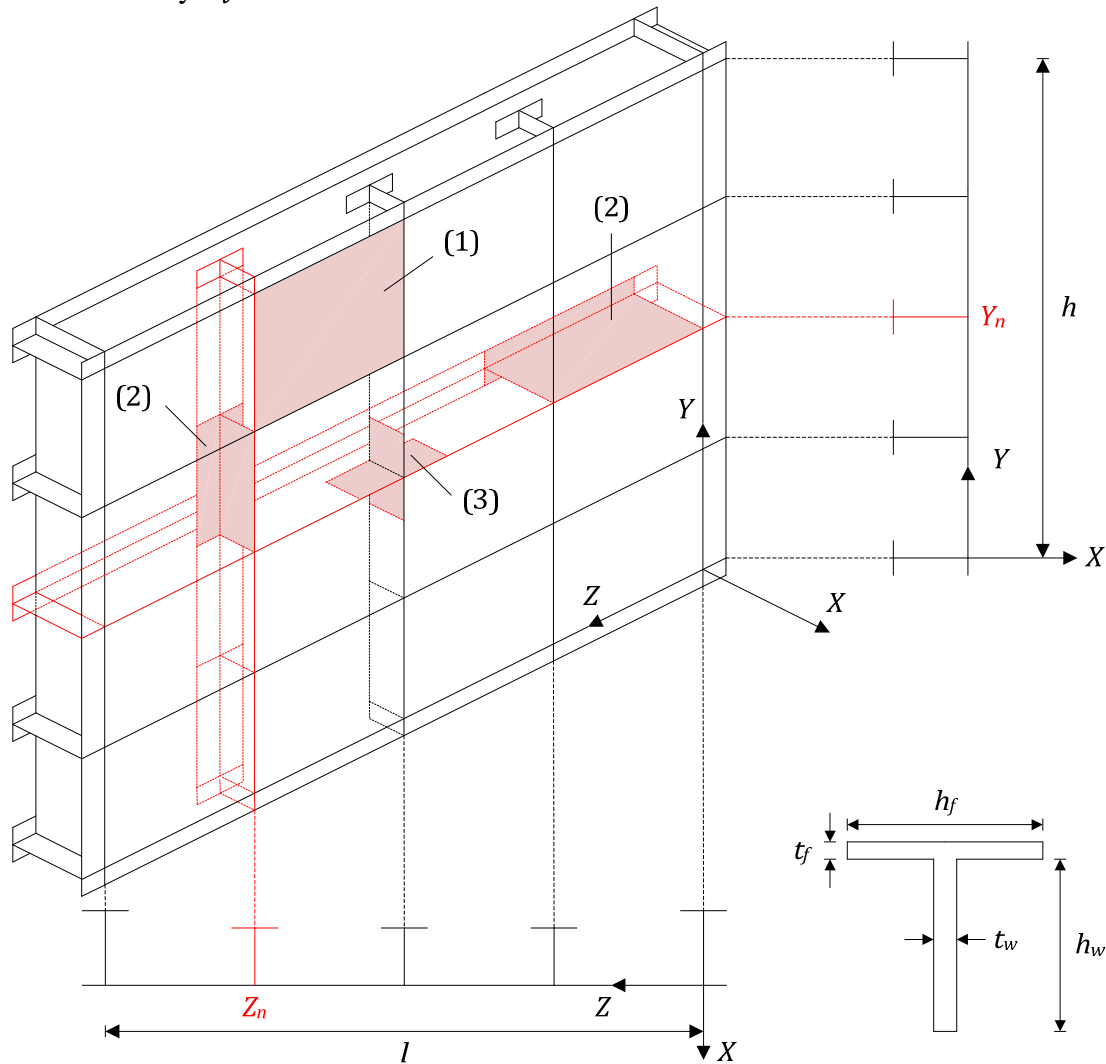


Figure 3.3. General geometry of the reinforced gate

The horizontal reinforcing elements (parallel to the Z axis) are called the girders and are placed at discrete locations Y_i on the vertical Y axis. Most of the time, they are not regularly distributed over the height of the gate. Indeed, the reinforcement is often more important near the bottom of the lock, as the hydrostatic pressure increases with the depth. The total number of horizontal components is called n_h .

In addition to the basic system described above, some horizontal and/or vertical smaller stiffeners may be added to reinforce the portion of the plating located between two frames and two girders. Their role is mainly to avoid the buckling and large deflections of the panels and to provide enough stiffness against light shocks.

All the reinforcing elements are assumed to have a T-shaped cross-section, as depicted on Figure 3.3. The web height and thickness are respectively denoted by h_w and t_w , while the flange width and thickness are designated by h_f and t_f . T-shaped cross-sections are very common for frames and girders, but they may also be replaced by flat bars. This is achieved by choosing $h_f = t_f = 0$. Once again, all the vertical frames usually have similar cross-sections, while it is not always the case for the horizontal girders.

The smaller stiffeners are usually flat plates. Some other cross-sections are however possible, such as those depicted on Figure 3.4. As it will be explained hereafter, defining the precise shape of the stiffeners is not really essential. The only useful properties are their sectional area A_s and their distribution over the height of the gate.

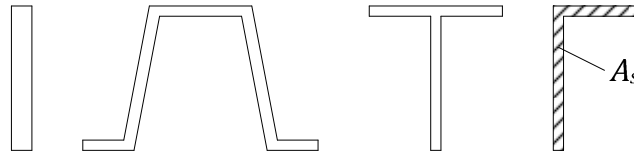


Figure 3.4. Some examples of cross-sections used for the smaller stiffeners

The plating thickness is denoted by t_p . For convenience, it is assumed to be uniform over the gate height. Nevertheless, this is not always realistic, as the plates are commonly thicker near the bottom of the lock (where the pressure is higher). Accounting for such a particularity may be achieved by adapting the present simplified methodology but this has not been done so far. Moreover, the plating thickness has to be corrected to account for the stiffeners. Indeed, for ship-ship collisions, it has been shown in various references (see [121], [122], [144] or [180] for example) that these components mainly resist through an extensional membrane process, the bending effects being negligible. Consequently, it is suggested to smear them over the thickness, as explained in Appendix B.1 (section B.1.1).

3.1.1.3. Boundary conditions

The boundary conditions of a lock gate are particularly difficult to model. Most of the time, they remain quite approximate because a lot of external elements may interfere with their definition.

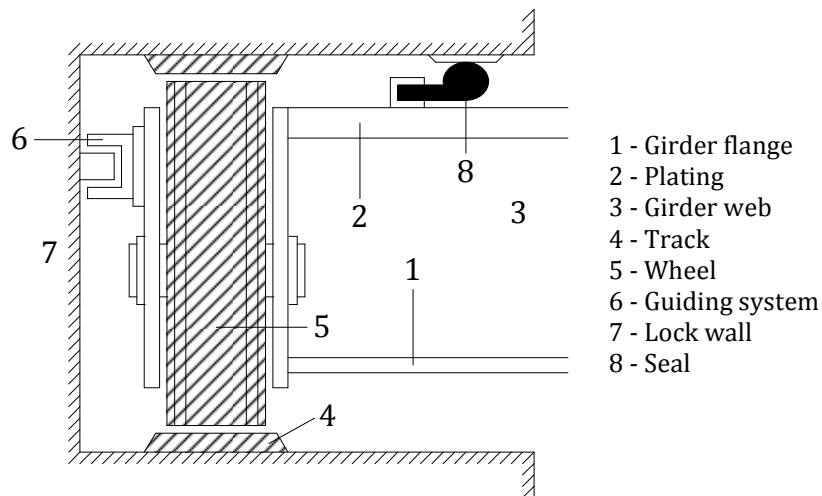


Figure 3.5. Top view of the rolling system attached to a vertical lifting gate

For example, in the case of a vertically moving gate, the support can be provided by fixed wheels attached to the body of the gate and rolling on a track fixed in the lock walls. This is

roughly depicted on Figure 3.5, which is a view in the (X, Z) plane of the rolling system that may equip this kind of lifting structures. Of course, a proper numerical modeling of such boundary conditions is very difficult to achieve, especially when using an analytical approach. Consequently, it is proposed here to work in the following way (Figure 3.6):

- Along the vertical lines located in $Z = 0$ and $Z = l$ (supports 1 and 2 on Figure 3.6), the structure is modeled as being simply supported by the lock walls, which prohibits any displacement in the X direction and allows for free rotations around the Y axis at these locations. It is worth noting that such an assumption also implies that the gate is free to move along the Z axis, but it is clear from Figure 3.5 that this is not necessarily realistic, as the real supports are likely to provide a small lateral restraint. One should also account for the friction appearing between the structure and the lock gate. Consequently, allowing for a free displacement in the Z direction tends to be conservative for both the numerical and analytical models.
- If the gate rests against a sill along the horizontal line in $Y = 0$ (i.e. at the bottom of the lock), then translations in the X direction are prohibited and free rotations around the horizontal Z axis have also to be imposed at this place (support 3 on Figure 3.6).

In addition to the two previous points, it is evident that vertical displacements have also to be forbidden along support 3 (Figure 3.6), as the gate is in contact with the bottom of the lock.

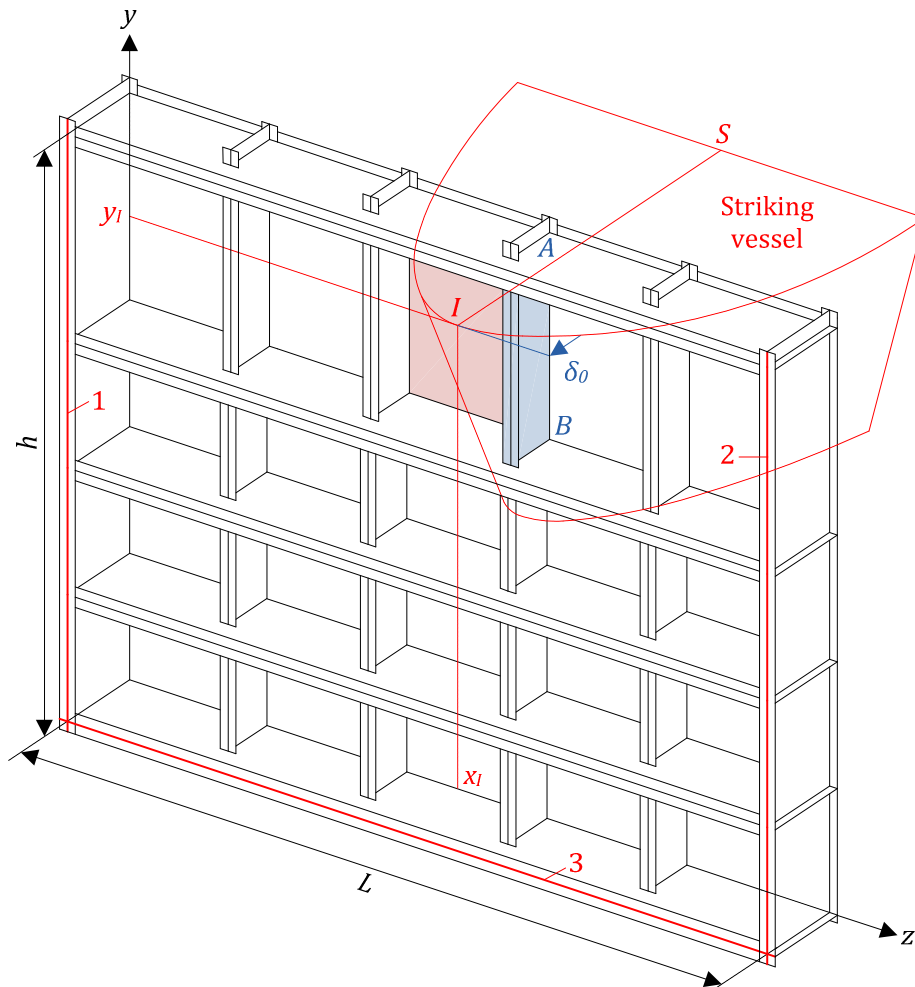


Figure 3.6. Boundary conditions for the gate

3.1.2. Description of the collision scenario

The complete definition of the collision requires first to specify the properties of the striking vessel because the shape of the bow is an important parameter that influences the extent of damages caused to structure. Apart from the definition of the ship, it is also needed to specify its relative position with respect to the struck gate. In the present simplified approach, this is achieved as detailed hereafter.

3.1.2.1. Definition of striking vessel

There are various vessels that may be encountered on inland waterways, such as passenger ships, cargos, barges, yachts... (Figure 3.7). For most of them, the bow has a more or less rounded shape, but it can be seen on Figure 3.7d that this is not the case for barges. Moreover, it is quite common for cargos to have a bulbous bow, in particular if they also have to navigate in the sea. It could be therefore very fastidious to develop a simplified methodology for every possible ship.

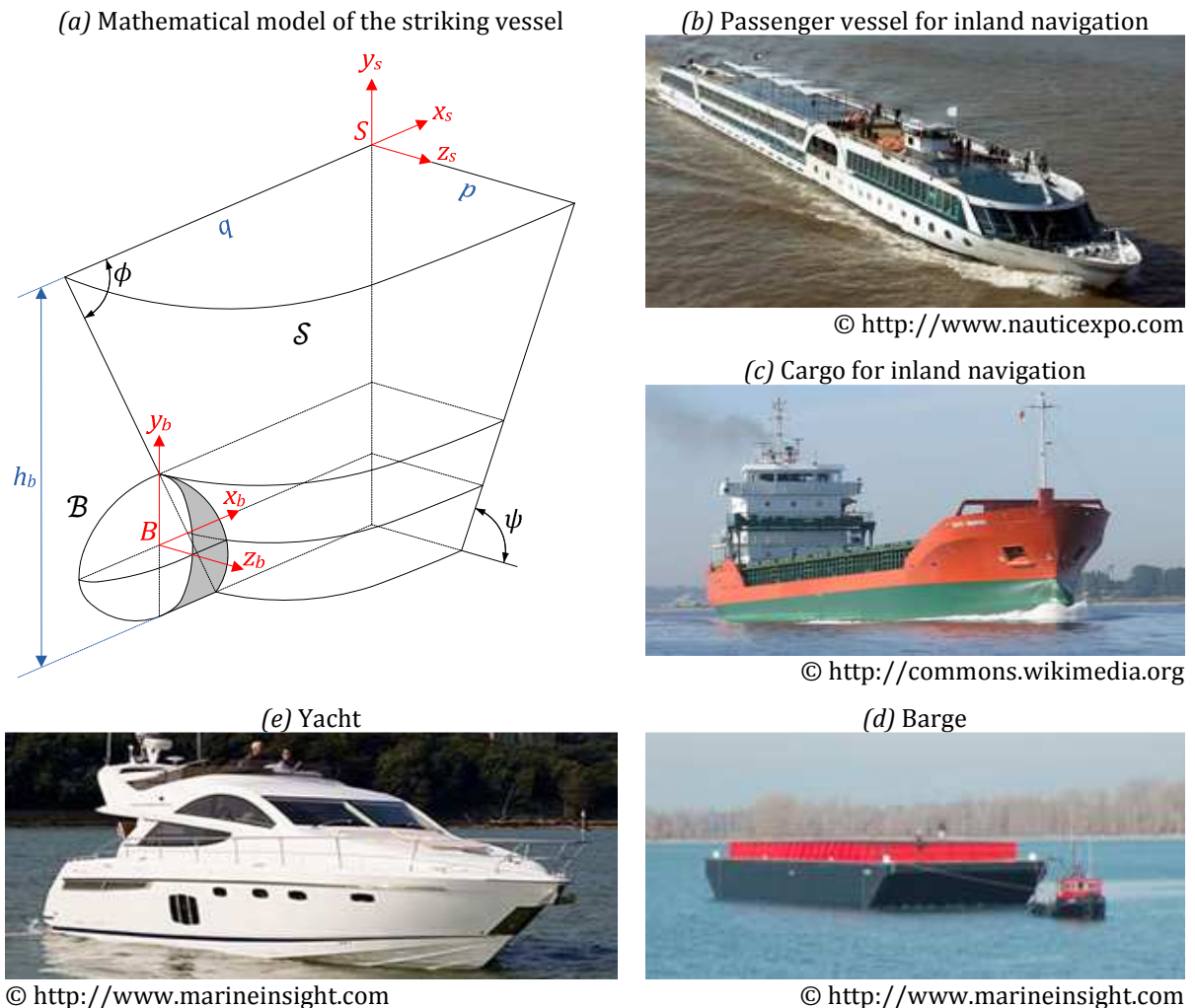


Figure 3.7. Striking vessels

Hopefully, doing so is not really necessary. Indeed, from the investigations performed by Le Sourne et al. [99], it transpires that an impact by a rounded bow is more critical than a collision implying a barge. The main reason is that in the first case, the impact is rather localized in a reduced area of the gate, while it is much more distributed over the structure in

the second case. Consequently, for a given initial kinetic energy of the striking vessel, the total penetration and the damages to the gate are likely to be more severe for a sharp bow than for a flattened one. Nevertheless, it is worth noting that this conclusion has to be nuanced because it is only valid for ships having the same initial kinetic energy. Obviously, a barge with an important mass and a high initial velocity may be more dangerous and should be used for determining the critical collision scenario. This choice has to be done in accordance with the kind of navigation expected in the lock or by accounting for the classification of the inland waterways [55], as detailed in Appendix A.1.

Regarding the arguments exposed here above, the simplified analytical method only considers ships having a rounded stem and an eventual bulb, without accounting for particular vessels such barges. The striking ship is idealized as depicted on Figure 3.7a. It has a total height h_b and is potentially made of two different parts: the stem \mathcal{S} and the bulb \mathcal{B} . Let us denote by S the summit of \mathcal{S} and by (x_s, y_s, z_s) the local coordinate system attached to it. If the stem is limited by a horizontal plane at a given level y_s (with $-h_b \leq y_s \leq 0$), the mathematical equation of \mathcal{S} is assumed to be a parabola:

$$\mathcal{S} \equiv x_s = (q + y_s \cot \phi) \left(\frac{z_s^2}{(p + y_s \cot \psi)^2} - 1 \right) \quad (3.1)$$

where p and q are the radii of \mathcal{S} in the uppermost deck (i.e. for $y_s = 0$), ϕ is the stem angle and ψ is the side angle. Consequently, according to (3.1), \mathcal{S} is nothing else than a set of parabolas whose radii are linearly increasing along the y_s axis.

Similarly, let us denote by B the center of the bulb \mathcal{B} and by (x_b, y_b, z_b) the local coordinate system attached to it. According to Zhang [180], it is more or less realistic to idealize \mathcal{B} as a paraboloid with an elliptic base. Following the same assumption leads to:

$$\mathcal{B} \equiv x_b = R_x \left(\frac{y_b^2}{R_Y^2} + \frac{z_b^2}{R_Z^2} - 1 \right) \quad (3.2)$$

where R_x , R_Y and R_Z are the radii of the bulb respectively measured along the x_b , y_b and z_b axes. It is worth noting that these parameters are not required for all the ships, as some of them may not have a bulbous bow. As a conclusion, the striking vessel is defined by p , q , ϕ , ψ , h_b and eventually by R_x , R_Y , R_Z if necessary (see also Figure 3.8). All these values have to be chosen to get a more or less realistic representation of the hull.

3.1.2.2. Definition of the impact location

There are a lot of possible configurations to define the collision scenario, but most of them are not necessarily relevant. Some considerations have been published by the CETMEF [25] in order to choose an appropriate impact situation. They are briefly summarized hereafter. Considering first the upstream gate, the following conclusions may be drawn:

- In the case of a ship moving *downstream*, the collision takes place at the top of the structure, where it is quite vulnerable. Moreover, if the water levels in the lock chamber and in the reach are not equal, the hydrostatic pressure is acting in the same direction than the impact force, which is unfavorable. However, such scenarios are very rare in practice.
- In the case of a ship moving *upstream*, the collision occurs on the lower part of the gate, where it is usually quite resistant. Moreover, the hydrostatic pressure is favorable and the

ship entering into the lock is slowed down by the piston effect of water. Therefore, even if these accidents are more frequent than in the previous case, they have reduced consequences because of all these mitigating actions.

From the previous considerations, it appears that an upstream collision is usually not the worst scenario to consider. For the downstream gate, the CETMEF [25] conclusions are as follows:

- In the case of a ship moving *downstream*, the contact point is located in the upper part of the structure, where the reinforcement is weak. In addition, the hydrostatic pressure is unfavorable and the piston effect is reduced because of the higher water level. This kind of accident is frequently encountered in practice, because the ships try to keep their velocity as long as possible when entering in the lock chamber to keep their initial direction.
- In the case of a ship moving *upstream*, the impact takes place in the lower part of the gate and the hydrostatic pressure is favorable. Once again, this kind of accident is very rare.

As a conclusion, it can be said that according to the CETMEF [25], the worst and most frequent case to consider occurs when the downstream gate is impacted by a ship entering the lock chamber (Figure 3.8). With this conclusion, it is still necessary to locate the impact point I (Figure 3.6). This is achieved by giving its coordinates Y_I and Z_I in the (X, Y, Z) reference frame. Equivalently, one may also precise the coordinates Y_S and Z_S of point S to position the vessel with respect to the structure (Figure 3.8). This is only true if the ship collides the gate at a right angle, which is almost the case. Only vessels having a rather small size in comparison with the lock dimensions are likely to impact the structure with a certain angle, but such situations are not really critical. Therefore, a right angle collision is considered here.

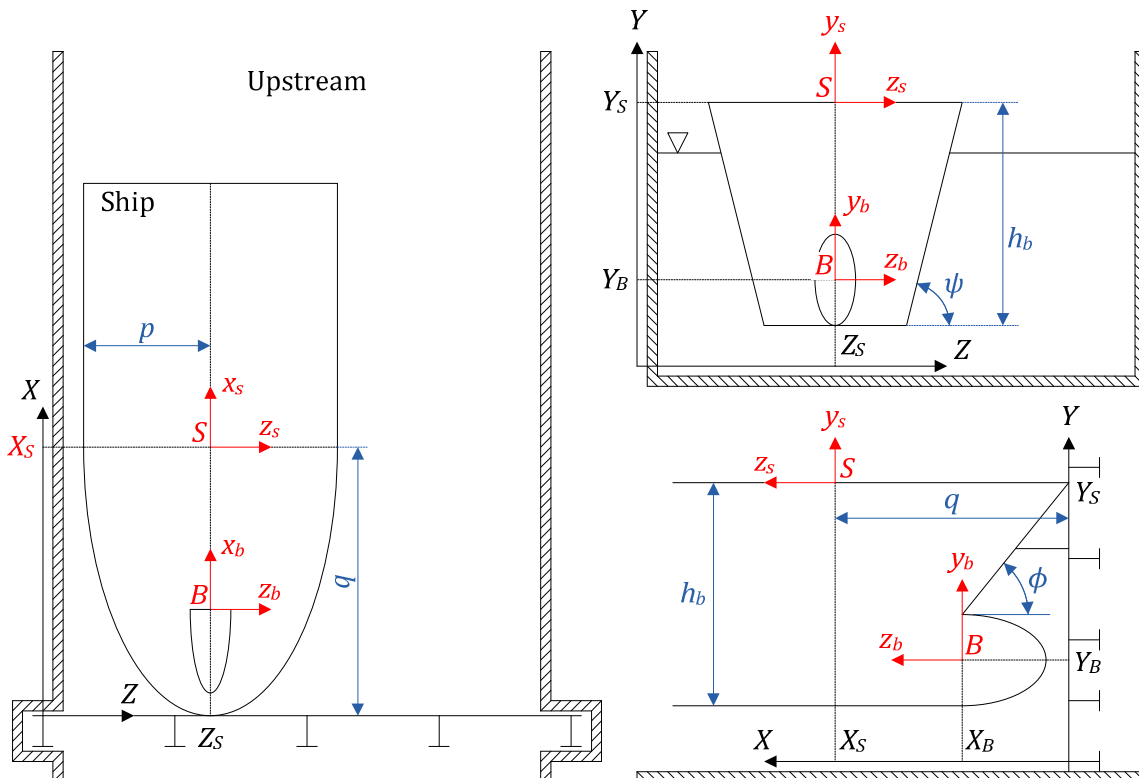


Figure 3.8. Relative position of the ship with respect to the gate

3.2. General methodology

3.2.1. Deformation sequence

According to the hypotheses exposed in section 2.1.2, when the gate is collided by a perfectly rigid vessel, the ship keeps on moving forward as long as the total initial kinetic energy E_0 calculated by (2.3) has not been entirely dissipated. Consequently, simulating the impact behavior of a lock gate requires to determine the internal energy E_{int} absorbed by the structure for a given value of the penetration δ . To do so, one may resort to the general energy theorems presented in section 2.3, but it is now required to have a more detailed overview of the analytical derivation of E_{int} .

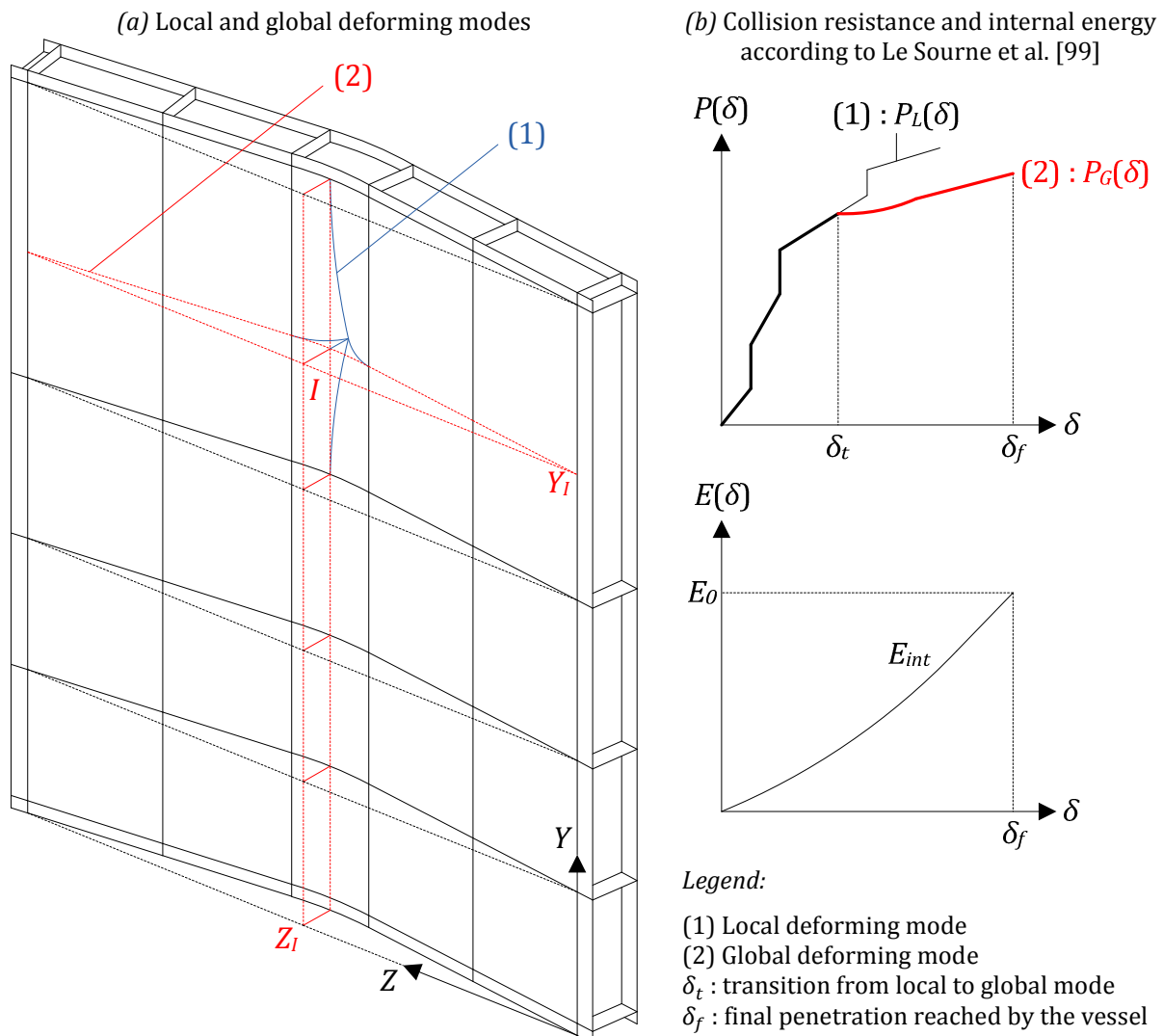


Figure 3.9. Local and global deformation processes

Finite element simulations performed on lock gates show that two different processes are involved during the impact (Figure 3.9). At the beginning of the collision, for low values of penetration δ , the damages caused to the gate remain mainly located in a rather small area confined around the initial contact point I . This region is submitted to important plastic deformations that may sometimes lead to the rupture of some structural elements. Concomitantly, an elastoplastic overall bending motion of the entire gate is superimposed to this localized indentation and is responsible for quite small out-of-plane displacements

affecting the whole structure. In such a case, the gate is said to withstand through a local deforming mode. This is roughly illustrated on Figure 3.9a, where a localized out-of-plane motion of the plating is depicted near point I .

On the other hand, numerical simulations also show that the impact may lead to large out-of-plane displacements affecting the entire structure (Figure 3.9a). In this situation, a generalized rigid-plastic mechanism develops on the entire gate and this second process is called the global deforming mode.

In order to derive analytically the internal energy E_{int} , the structure is first supposed to resist through a local deforming mode. Nevertheless, with increasing values of δ , it becomes more and more difficult for the vessel to keep on moving in this way. Consequently, for a given penetration δ_t , the collision force reaches a sufficient level to activate an overall plastic mechanism and a switch is supposed to occur from the local to the global mode.

Of course, when a lock gate is impacted by a ship, the two aforementioned phenomena are in fact concomitant. The ship moves forward by locally and globally deforming the structure, especially before the activation of an overall plastic mechanism on the entire gate. Unfortunately, accounting for such a particularity is quite arduous when developing an analytical model. To overcome this difficulty, a solution could be to adopt the hypothesis suggested by Le Sourne et al. [99] of having two distinct processes. Doing so, the coupling between the local indentation and the global displacements is neglected and the transition occurs when the resistances in the local and global deforming modes are equal (Figure 3.9b). However, finite element have shown that this approach is not necessarily conservative because it tends to overestimate the resistance when $\delta < \delta_t$ and to anticipate the transition. Consequently, another approach is proposed here in order to approximately account for the elastoplastic coupling between local and global deformations when $\delta < \delta_t$. These particular points, together with the determination of δ_t , are discussed in more details in section 3.6.1.2.

3.2.2. Analytical derivation of the resistance

From the considerations detailed in section 3.2.1, it can be concluded that the main issue is to get a realistic evaluation of the gate resistance $P(\delta)$. Before detailing the procedures followed to get the local and global resistances, it is of prior importance to define them properly:

- The local resistance $P_L(\delta)$ is defined as the one opposed by the gate under the assumption that the striking vessel only moves forward through a localized crushing. It is only derived for a rigid-plastic material by applying the super-elements method described hereafter, but does not account for any overall motion of the gate. It is only a part of the resistance in the local deforming mode (see section 3.6.1.2).
- The global resistance $P_G(\delta)$ is defined as the one opposed by the gate under the assumption that the striking vessel only moves forward by imposing an overall bending motion to the whole structure. An elastoplastic solution of $P_G(\delta)$ is first derived and is combined with $P_L(\delta)$ to get the resistance during the local deforming mode, while a rigid-plastic solution of $P_G(\delta)$ is used to evaluate the resistance during the global deforming mode (see section 3.6.1.2).

The previous definitions of $P_L(\delta)$ and $P_G(\delta)$ are summarized on Figure 3.10 and the method followed for their derivations are respectively explained in sections 3.2.2.1 and 3.2.2.2.

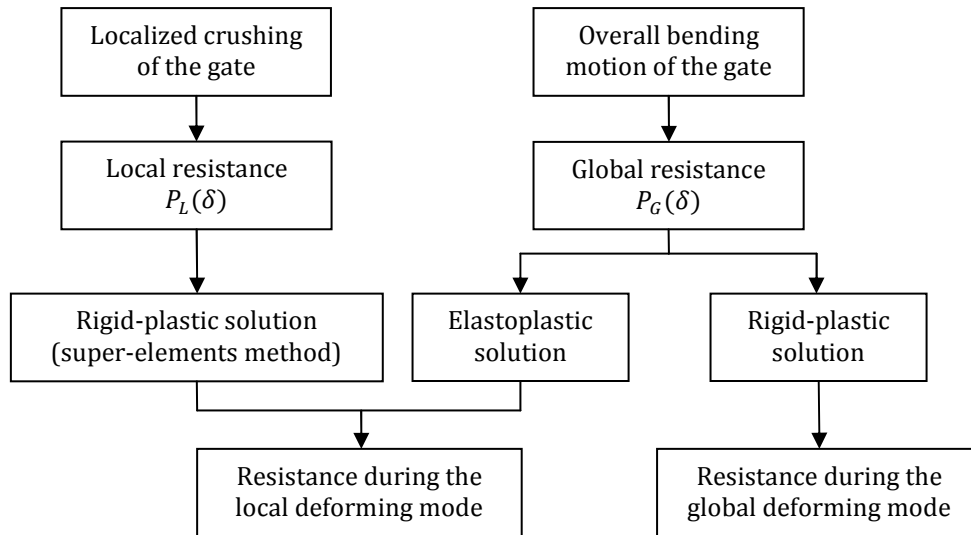


Figure 3.10. Definition of the local and global resistances

More details about the way to combine $P_L(\delta)$ with $P_G(\delta)$ are given in section 3.6.1.2. The method used to evaluate δ_t is also presented there.

3.2.2.1. Local resistance

In order to perform an analytical derivation of $P_L(\delta)$, the architecture of the gate is modeled with a limited number of nodal points and some large-sized structural components. This basic idea was initially suggested by Ueda and Rashed [150] and is often referred to as the idealized structural unit method (ISUM). This one has been applied by Paik and Thayamballi [120] to analyze plated structures, and also by Paik and Pedersen [118] to predict the resistance for ship-ship collisions.

One of the major characteristics of the idealized structural unit method is that the deformations taking place on an individual component have an effect on the surrounding ones, which means that there is a coupling between all of them. Another philosophy is to make the assumption that the structural units are independent. Doing so leads to the simplified technique described by Lützen et al. [104] and called the super-elements method.

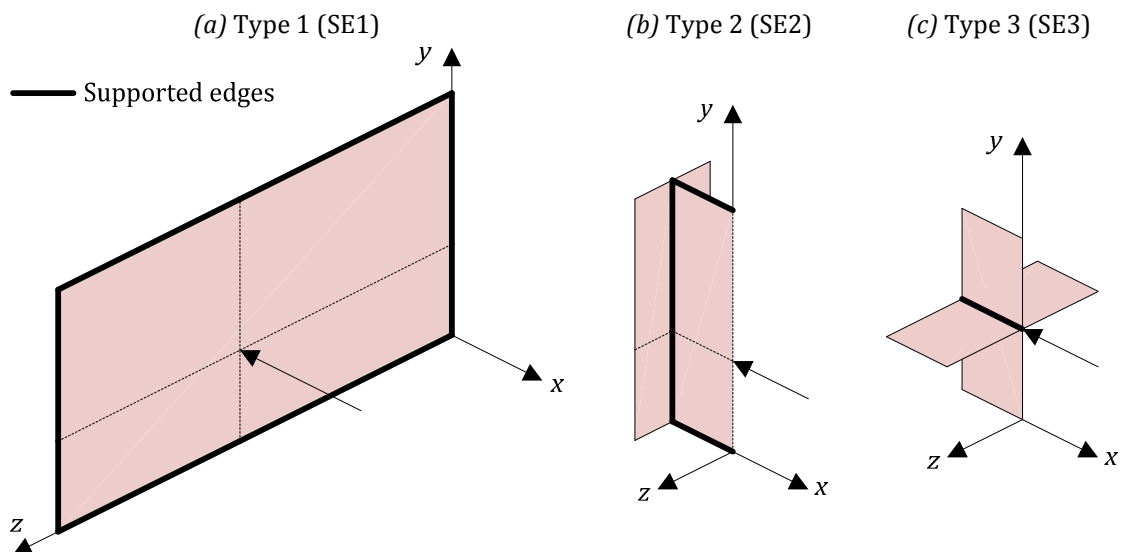


Figure 3.11. Three different types of super-elements used to decompose plane gates

To apply this approach to the impact analysis of lock gates, three different types of super-elements are required for analyzing these plane structures. Each of them is characterized by some geometrical and mechanical properties, but also by a closed-form expression giving their impact resistance as a function of the penetration (see sections 3.3, 3.4 and 3.5). They are represented on Figure 3.3 and briefly detailed hereafter (see Figure 3.11):

- Type 1: the first type of super-element (SE1) introduced here is used to model the portions of the plating that are bounded by two horizontal girders and two vertical frames. The super-elements of this type are treated as plates clamped on their four edges and submitted to an out-of-plane impact load.
- Type 2: the second type of super-element (SE2) designates the portions of the frames limited by two girders, but also the parts of the girders bounded by two frames. In the first case, the super-elements of this type are vertical, while they are horizontal in the second one. They are treated as plates supported on three edges and impacted in their plane.
- Type 3: the third type of super-element (SE3) corresponds to the intersections of the vertical frames with the horizontal girders. They are treated as X or T-shaped elements that are crushed along their axis.

The decomposition of a plane lock gate into super-elements is quite straightforward. As explained in section 3.1.1, the structure is assumed to be made of n_v vertical frames and n_h horizontal girders. Therefore $n_v \times n_h$ nodes can be defined, each of them being located at the intersection of two components. From this point, it can be shown that the gate may be divided into $n_e = (2n_v - 1) \times (2n_h - 1) - 4$ super-elements (see Table 3.1).

| Type | Number | | Type | Number | |
|--------------|------------------------------|------------------------|---------------------|--|------------------------------|
| Type 1 (SE1) | $(n_v - 1) \times (n_h - 1)$ | | Type 3 (SE3) | <i>T-shaped</i> | $2(n_v - 2) + 2(n_h - 2)$ |
| Type 2 (SE2) | <i>Horizontal</i> | $(n_h - 1) \times n_v$ | | <i>X-shaped</i> | $(n_v - 2) \times (n_h - 2)$ |
| | <i>Vertical</i> | $(n_v - 1) \times n_h$ | | <i>Total</i> | $n_v \times n_h - 4$ |
| | <i>Total</i> | $2n_v n_h - n_v - n_h$ | Total number | $n_e = (2n_v - 1) \times (2n_h - 1) - 4$ | |

Table 3.1. Number of super-elements used for decomposing a plane lock gate

As mentioned earlier, all these structural components are assumed to be uncoupled, which means that they do not influence each others. As a consequence, a super-element remains inactive as long as it has not been impacted by the striking bow. As shown by Figure 3.6, this means for example that the vertical SE2 associated to the frame portion AB is not deforming as long as the displacement of the bow is not equal to δ_0 , even though the adjacent SE1 has already been impacted. In fact, for each super-element i (with $1 \leq i \leq n_e$), one may define an activating distance $\delta_{0,i}$ measured from the bow, with $\delta_{0,i} \rightarrow \infty$ if no geometrical contact is possible between the component and the vessel. Consequently, denoting by $P_i(\delta)$ the individual impact resistance associated to super-element i , $P_L(\delta)$ is calculated by summing up all the contributions coming from the activated components:

$$P_L(\delta) = \sum_{i=1}^{n_e} P_i(\delta) \quad \text{with } P_i(\delta) = 0 \text{ if } \delta < \delta_{0,i} \quad (3.3)$$

By following the general methodology explained here above, it is possible to derive $P_L(\delta)$, which is only a part of the resistance during the local deforming mode (Figure 3.10). In fact,

$P_L(\delta)$ has to be corrected to account for the coupling with the elastoplastic overall motion of the gate when $\delta < \delta_t$. As mentioned earlier, the idea developed by Le Sourné et al. [99] of considering only $P_L(\delta)$ during the local deforming mode may lead to unsafe solutions, and this is why another approach is proposed in section 3.6.1.2 to correct $P_L(\delta)$. The next step is now to establish a procedure to evaluate the global resistance. As explained on Figure 3.10, this latter should not be mistaken with the resistance during the global deforming mode.

3.2.2.2. Global resistance

Of course, the super-elements method is not entirely relevant for analyzing impacts on lock gates. Indeed, it is not realistic to imagine that the gate is only made of large structural components that are decoupled from each others. It is clear that many elements located near the impact point are likely to deform, even though they are not in contact with the striking bow. This particular phenomenon is due to the coupling between the different gate components and may therefore not be captured by using only super-elements. However, the method may be improved through the concept of global resistance, which allows for a better representation of the gate behavior.

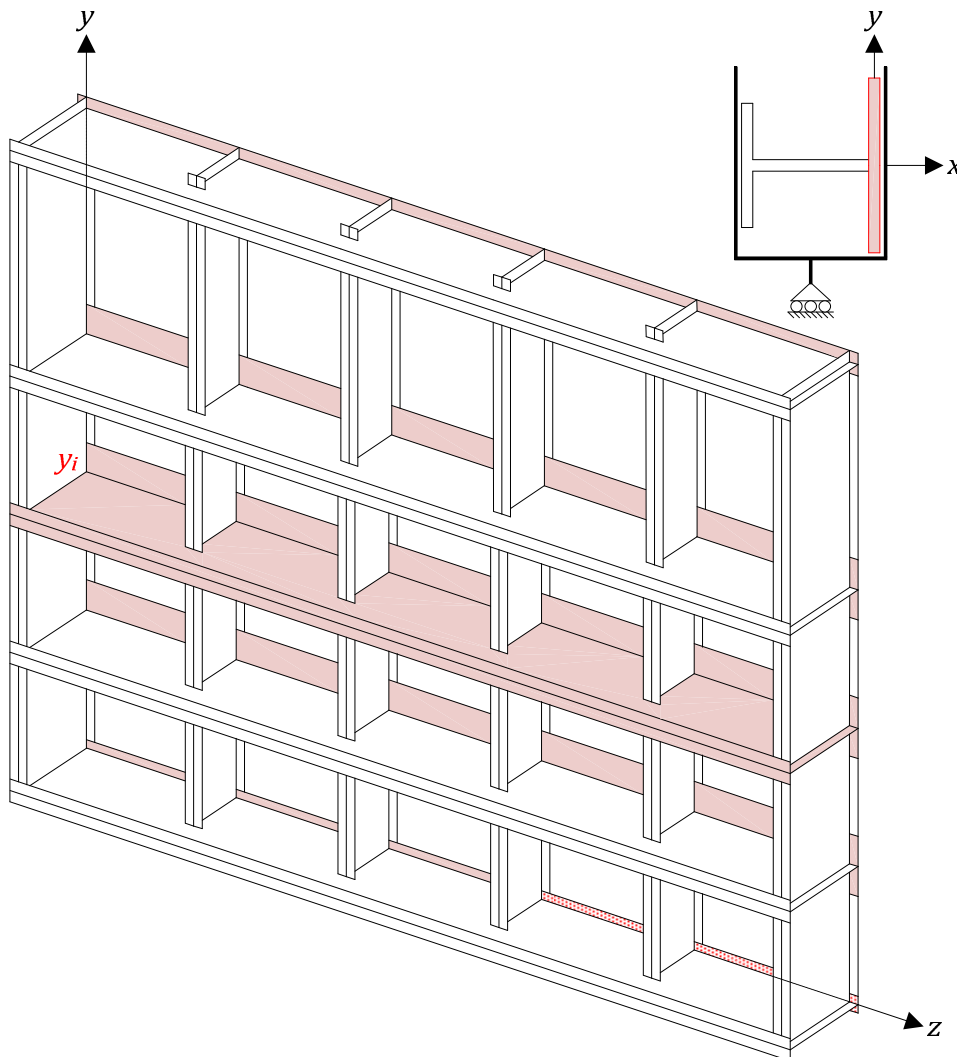


Figure 3.12. Beam grillage used to idealize the gate in the global deforming mode

As mentioned earlier, when the structure exhibits an overall bending motion as depicted on Figure 3.9, the displacements take place over the entire gate and consequently, the

deformations field affects all the gate components. The internal energy E_{int} is therefore calculated as the sum of three different terms:

$$E_{int} = E_p + E_v + E_h \quad (3.4)$$

where E_p , E_v and E_h denote the deformation energy associated to the plating (including the reinforcing small stiffeners if any), the vertical frames and the horizontal girders respectively. In order to derive $P_G(\delta)$ analytically, the main contribution to E_{int} is assumed to come from the horizontal members. This hypothesis seems quite reasonable, as the gate is bent between its lateral supports during the global mode. Consequently, E_v is neglected as compared to $E_p + E_h$ in equation (3.4) and the work consists now in evaluating E_p and E_h .

To do so, one can imagine that the structure deforms through a global mode like a set of horizontal beams weakly connected by the vertical frames. In other words, the structure is supposed to behave like a kind of grillage with the same boundary conditions than the initial gate (Figure 3.12).

In this configuration, I-shaped cross-section beams are defined at the discrete locations Y_i of the girders. Their cross-sections are composed by the girders initial one (Figure 3.3), to which is attached a portion coming from the plating (Figure 3.12). This additional part is supposed to account for the amount of energy E_p dissipated by the overall motion of the gate. During the impact, a beam located at the vertical position Y_i along the Y axis (Figure 3.12) is submitted to a given out-of-plane displacement field $u(Y_i, Z)$, but lateral movements $w_1(Y_i)$ and $w_2(Y_i)$ are also permitted as the gate is likely to slide on the lock walls (Figure 3.13). Regarding the vertical frames, as their internal energy E_v is neglected, they are assumed to remain unaffected by $u(Y_i, Z)$, $w_1(Y_i)$ and $w_2(Y_i)$ but have the following structural functions:

- They provide a kind of collaboration between the beams, which allows for a proper transmission of the displacement field over the whole grillage.
- They are acting as fork supports (Figure 3.12), which prevents the lateral torsional buckling.
- Together with the plating, they exert a small axial restraint on the beams. This means that they have a limiting effect on w_i (Figure 3.13), so the gate is not allowed to move freely on its lateral supports.

The previous points are based on the assumption that the frames are weaker than the girders. Therefore, each horizontal component may be seen as being submitted to a simple bending described by u_i and w_i . Therefore, by applying the classical beam theory, it is possible to evaluate the corresponding internal energy and also the equivalent static force $P_i(\delta)$ as a function of the striking ship penetration (see section 3.6).

In accordance with the previous considerations, it is worth recalling that $P_i(\delta)$ has to be calculated for both the elastoplastic and rigid-plastic regimes. The global resistance $P_G(\delta)$ is then finally obtained by summing up all the individual contributions $P_i(\delta)$ coming from the n_h horizontal beams:

$$P_G(\delta) = \sum_{i=1}^{n_h} P_i(\delta) \quad (3.5)$$

It is worth noting that all the structural components are supposed to be simultaneously involved in the overall bending motion, so there is no need to define an activating penetration as it was the case for the local deforming mode.

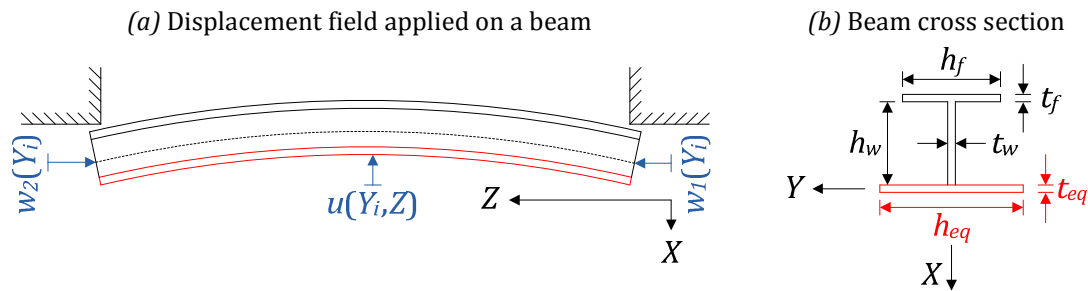


Figure 3.13. Top view and sectional view of a beam

From the brief presentation of the local and global deforming modes that is made here above, it transpires that the crucial point is to determine the individual resistances $P_i(\delta)$ that are involved in equations (3.3) and (3.5) for the derivation of $P_L(\delta)$ and $P_G(\delta)$ respectively. In order to establish closed-form expressions for $P_i(\delta)$, one may of course resort to the theorems of limit analysis in plasticity briefly exposed in section 2.3.

3.3. Local resistance for super-elements of type 1

Before giving some details about the derivation of the local resistance, it is first required to develop the analytical formulae describing the striking vessel in the global reference frame (X, Y, Z) depicted on Figure 3.8. As shown on Figure 3.7a, the ship is composed of the stem \mathcal{S} and the bulb \mathcal{B} , whose vertices are respectively the points S and B . Consequently, at the beginning of the collision, the gate may be first impacted by one of these two parts. From Figure 3.8, it is obvious that the contact first occurs between the stem and the plating if:

$$R_X \leq (h_b - 2R_Y) \cot \phi \quad (3.6)$$

If point S is the vertex of the stem \mathcal{S} and point B the vertex of the bulb \mathcal{B} , it is easy to show that their locations X_S and X_B along the horizontal axis are as follows:

$$\begin{aligned} X_S &= q + \max\{R_X - (h_b - 2R_Y) \cot \phi ; 0\} \\ X_B &= \max\{R_X ; (h_b - 2R_Y) \cot \phi\} \end{aligned} \quad (3.7)$$

Moreover, as explained in section 3.1.2, the definition of the collision scenario requires to specify the coordinates (Y_I, Z_I) of the first contact point I between the gate and the stem (Figure 3.6). From Figure 3.8, it is clear that:

$$Y_S = Y_I \quad Z_S = Z_I \quad Y_B = Y_S - h_b + R_Y \quad Z_B = Z_I \quad (3.8)$$

With the previous relations, it is possible to transform equations (3.1) and (3.2) to get the expressions of \mathcal{B} and \mathcal{S} in the global reference frame. For a given penetration δ , it can be shown that:

$$\mathcal{S} \equiv X = X_S - \delta + (q + (Y - Y_S) \cot \phi) \left(\frac{(Z - Z_S)^2}{(p + (Y - Y_S) \cot \psi)^2} - 1 \right) \quad (3.9)$$

$$\mathcal{B} \equiv X = X_B - \delta + R_X \left(\frac{(Y - Y_B)^2}{R_Y^2} + \frac{(Z - Z_B)^2}{R_Z^2} - 1 \right) \quad (3.10)$$

where all the geometrical parameters have to be specified while defining the striking vessel and the collision scenario (section 3.1).

3.3.1. Literature review

As presented in section 3.2.2.1, the first type of super-element to consider is a vertical plate that is simply supported on its four edges and submitted to an out-of-plane impact (Figure 3.11a). The goal is to derive a closed-form expression relating the resistance opposed by this panel to the penetration δ of the striking vessel. This problem has already been largely studied in the literature by various authors, mainly to assess the strength of plating elements during collisions involving two ships. Very detailed studies have been performed by Zhang [180] and Jones [81], who investigated the plastic collapse of plates submitted to punctual, linear or surface out-of-plane loads. Similarly, Simonsen [141] developed interesting formulae to evaluate the plastic resistance in case of a concentrated load and validated its theoretical approach by experimental data. The influence of other concomitant in-plane forces was treated by Paik et al. [122], but only in the elastic range.

In practice however, the plating of a lock gate is usually reinforced by smaller stiffeners that have to be considered while deriving the resistance of super-elements. The crashworthiness of

stiffened panels was investigated experimentally and theoretically by Cho and Lee [30] or by Alsos and Amdahl [6], amongst others. From these studies, it transpires that the influence of the stiffeners is mainly to increase the membrane resistance of the plates, in particular when these latter are submitted to quite large out-of-plane motions.

All the papers mentioned here above provide a quasi-static evaluation of the resistance, but some dynamic analyses are also available, such as those performed by Jones [81] and Shen [138]. However, regarding the range of velocities involved in collision on lock gates (section 2.2), it is clear that the local acceleration of the impacted area remains quite small, so the corresponding inertia forces may be neglected. Another problem that is more important to assess is to account for the true shape of the striking body. Indeed, for ship-ship collisions, the dimensions of the plating elements may be thought to be sufficiently large to treat collisions on plates as punctual impacts. Nevertheless, this is not necessarily true for lock gates, where the panels are much smaller and may consequently be more deeply influenced by the geometry of the bow. This topic has already been addressed by various authors, such as Simonsen and Lauridsen [143], Wang [162], Wang and Ohtsubo [164] or Zhang [180], who developed some formulae to evaluate the crashworthiness of plates collided by a bulb described by a given mathematical function. This problem was also already investigated by the U.S. Administration [154] in the frame of a research program on ships initiated after an important oil spill in 1995.

3.3.2. Analytical derivation for an impact by the stem

3.3.2.1. Derivation of the displacement field

In the optic of applying the upper-bound method, the first step is to define a kinematically admissible displacement field that more or less represents the true shape of the deformed structure.

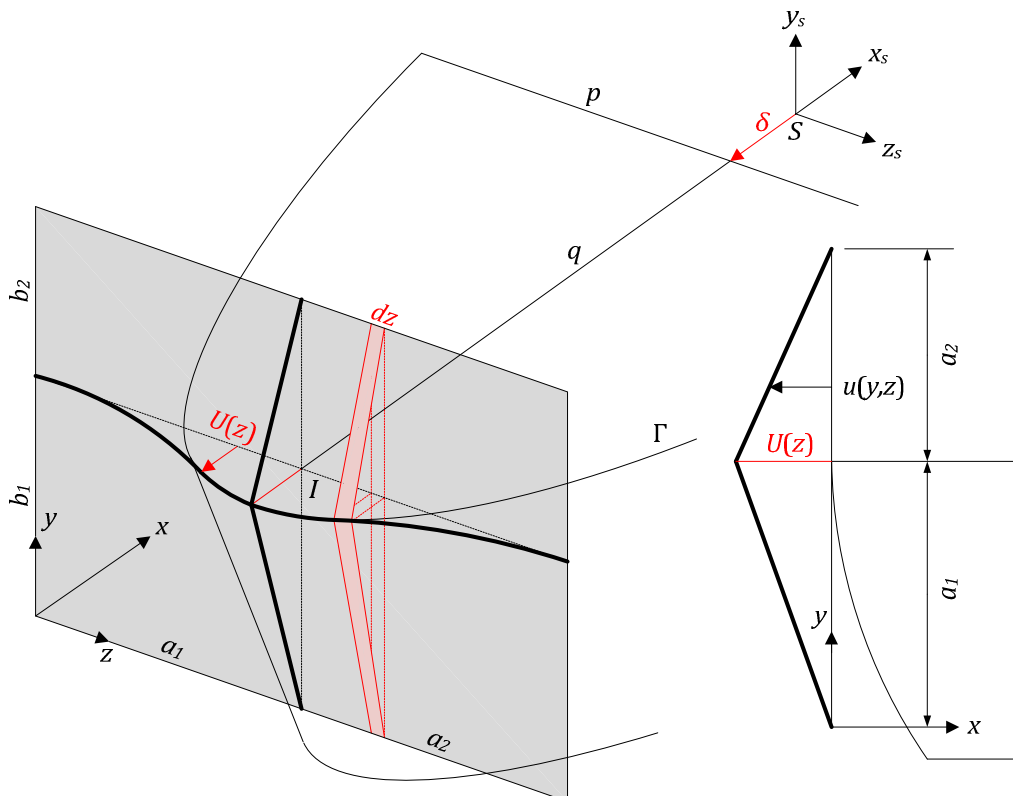


Figure 3.14. Deformation pattern and displacement field $u(y,z)$ for an impact by the stem

To do so, one may start by considering the local reference frame (x, y, z) of the super-element (Figure 3.14) that is parallel to the global one (X, Y, Z) depicted on Figure 3.3. Under the assumption that the out-of-plane displacements $u(y, z)$ are predominant, then each point (y, z) of the plate is assumed to move only along the x axis.

The first contact point with the vessel is denoted by I and has the coordinates (Y_I, Z_I) in the global reference frame (Figure 3.6). It divides the plate in four distinct sub-areas having respectively the dimensions $a_1 \times b_1$, $a_2 \times b_1$, $a_1 \times b_2$ and $a_2 \times b_2$ that can be specified by the relative position between the ship and the super-element. In order to have a better description on the way these surfaces are deforming, it is worth looking at the situation in the horizontal plane $y = b_1$ passing through the uppermost deck of the stem, where the displacement field is denoted by $U(z) = u(b_1, z)$. For a given value of the penetration δ , this one is assumed to be made of two different parts $U_1(z)$ and $U_2(z)$:

- On the portion AB of Figure 3.15, the deformation pattern is supposed to follow the shape of the stem. Consequently, $U_1(z)$ has to be defined in accordance with the parabolic equation of the uppermost deck (3.1).
- On the portions AC and BD of Figure 3.15, the displacements have to respect the support conditions $U_2 = 0$ and $\partial U_2 / \partial z = 0$ at the boundaries C and D of the super-element. Moreover, in points A and B , the compatibility condition requires that $U_1 = U_2$ and $\partial U_1 / \partial z = \partial U_2 / \partial z$. As a consequence, it appears that U_2 has to be a quadratic expression of z .

Even if the impact is not necessarily symmetric (i.e. $a_1 \neq a_2$), it is clear that the displacement field for $0 \leq z \leq a_1$ must be similar to the one over the portion $a_1 \leq z \leq a_1 + a_2$. Consequently, in order to avoid any redundancy, it is sufficient to focus only on one half of the model.

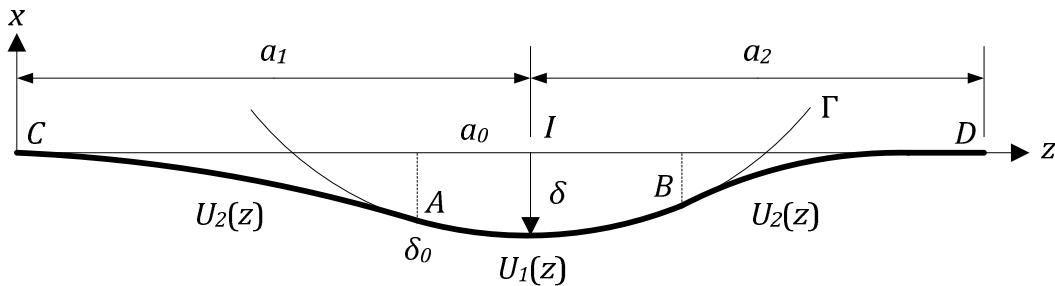


Figure 3.15. Plane view of the out-of-plane displacements imposed by the uppermost deck

As detailed in section 3.1.2.1, the stem \mathcal{S} is idealized as a set of parabolas whose radii are progressively growing along the vertical Y axis, as detailed by equation (3.1). Consequently, the curve Γ describing \mathcal{S} in the plane of the uppermost deck (i.e. for $y_s = 0$) is also a parabola whose radii are p and q . According to (3.9), it is obvious that Γ has the following equation, from which the definition U_1 can be easily derived:

$$\Gamma \equiv x = X_S - \delta + q \left(\frac{(z - a_1)^2}{p^2} - 1 \right) \Rightarrow U_1(z) = q \left(1 - \frac{(z - a_1)^2}{p^2} \right) - X_S + \delta \quad (3.11)$$

Regarding the displacement field over the portion AC , let us denote by δ_0 the out-of-plane displacement of point A and by a_0 the horizontal distance with respect to point I (Figure

3.15). In order to respect the compatibility conditions detailed here above, U_2 has to be given by the following quadratic equation:

$$U_2(z) = \frac{\delta_0}{(a_1 - a_0)^2} z^2 \quad (3.12)$$

In order to have a complete definition of $U(z)$, it is finally necessary to specify how the parameters δ_0 and a_0 are calculated. They have to be such that the continuity is respected at the junction point A . Consequently, one should have:

$$\begin{aligned} \bullet \quad U_1 = U_2 = \delta_0 & \quad \Leftrightarrow \delta_0 = q \left(\frac{a_0^2}{p^2} - 1 \right) - X_S + \delta \quad \Rightarrow a_0 = \frac{p^2}{a_1 q} (q - X_S + \delta) \\ \bullet \quad \frac{\partial U_1}{\partial z} = \frac{\partial U_2}{\partial z} & \quad \Leftrightarrow \frac{\delta_0}{a_1 - a_0} = \frac{q}{p^2} a_0 \quad \Rightarrow \delta_0 = \frac{q}{p^2} a_0 (a_1 - a_0) \end{aligned} \quad (3.13)$$

It is worth noting that a_0 and δ_0 are varying with the penetration. As expected, both are increasing with δ . Once the displacement field is completely characterized by equations (3.11) and (3.12) in the horizontal plane passing through the stem, the goal is to extend its definition over the entire plate. To do so, the hypothesis is made that the deformation pattern may be simply obtained through a linear interpolation of $U(z)$ along the vertical y axis. As the plate is also supported along the horizontal edges $y = 0$ and $y = b_1 + b_2$, the boundary condition $u(y, z) = 0$ has to be respected at these locations. Consequently, the interpolation function $f(y)$ may be chosen as follows:

$$\begin{aligned} \bullet \quad f_1(y) = \frac{y}{b_1} & \quad \text{if } 0 \leq y \leq b_1 \\ \bullet \quad f_2(y) = \frac{b_1 + b_2 - y}{b_2} & \quad \text{if } b_1 < y \leq b_1 + b_2 \end{aligned} \quad (3.14)$$

With the previous definitions, the displacement field is now characterized over the entire surface of the plate. For $0 \leq y \leq b_1 + b_2$ and $0 \leq z \leq a_1 + a_2$, it is simply given by:

$$u(y, z) = U(z)f(y) \quad (3.15)$$

It is worth noting that (3.15) implies that $u(y, z)$ is not kinematically admissible as the slope $\partial u / \partial y$ is discontinuous along $y = b_1$. This is also valid along the supports $y = 0$ and $y = b_1 + b_2$, but such difficulties can be overcome by supposing that horizontal plastic hinges develop at these locations.

3.3.2.2. Derivation of the internal energy rate

The second step of the upper-bound method is now to evaluate the internal energy rate \dot{E}_{int} . This one can be calculated by (2.8), but evaluating \dot{E}_p for the deforming plate of Figure 3.14 leads to very cumbersome equations that are not tractable analytically.

To overcome this difficulty, another mechanical simplification is introduced, which is called the plate strip formulation by Wierzbicki and Simonsen in [154]. The idea is to replace the plate by a set of horizontal and vertical fibers that are still submitted to $u(y, z)$ but are free to move without shearing. Considering first a vertical fiber of length $b_1 + b_2$ and of width dz (Figure 3.14) that is parallel to y axis, according to Jones [81], the internal energy rate (2.8) may be rewritten as follows:

$$d\dot{E}_{int} = \left(2m_0(\dot{\theta}_1 + \dot{\theta}_2) + \int_0^{b_1+b_2} n_0 \dot{E}_{yy} dy \right) dz \quad (3.16)$$

where $n_0 = \sigma_0 t_p$ and $m_0 = \sigma_0 t_p^2/4$, t_p being the plating thickness. The first term in (3.16) corresponds to the bending energy dissipated because of the rotations θ_1 and θ_2 occurring in the plastic hinges located at $y = 0$, $y = b_1$ and $y = b_1 + b_2$ (Figure 3.16a), while the second one is due to the membrane straining E_{yy} along the y axis.

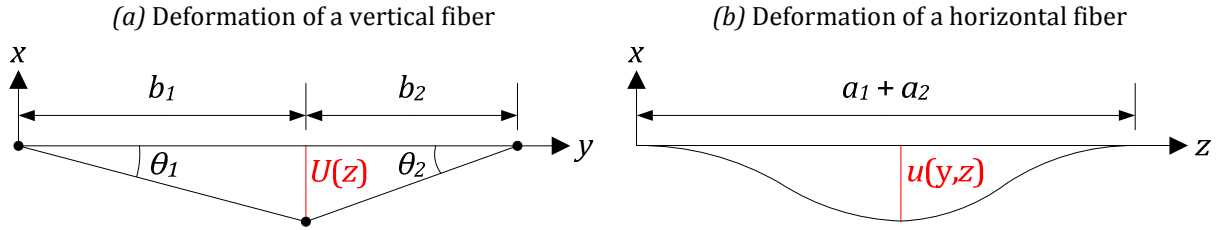


Figure 3.16. Plate strip model

Similarly, for a fiber of length $a_1 + a_2$ and of width dy that is parallel to z axis (Figure 3.16b), the internal dissipation is obtained by summing the contribution coming from the axial straining along the z axis, but also from the continuous change of curvature. Consequently, the corresponding energy writes:

$$d\dot{E}_{int} = dy \int_0^{a_1+a_2} (m_0 \dot{K}_{yy} + n_0 \dot{E}_{zz}) dz \quad (3.17)$$

where \dot{K}_{yy} is the curvature rate. In fact, in (3.16) and (3.17), it is supposed that the maximal unitary bending moment m_0 and tensile force n_0 may be reached simultaneously, which does not respect the plasticity theory (see Appendix A.2, section A.2.5). Theoretically, an interaction formula should be use. Nevertheless, if the thickness is sufficiently small, then m_0 may be neglected with respect to n_0 . Moreover, within the frame of moderate displacements, the membrane effects are largely predominant. For these two reasons, it is suggested to neglect the bending contributions in (3.16) and (3.17). Consequently, according to the plate strip model, the internal energy rate over the entire plate is given by:

$$\dot{E}_{int} = \iint_A n_0 (\dot{E}_{yy} + \dot{E}_{zz}) dy dz \quad ; \quad \dot{E}_{yy} = \frac{\partial u}{\partial y} \frac{\partial \dot{u}}{\partial y} \quad \dot{E}_{zz} = \frac{\partial u}{\partial z} \frac{\partial \dot{u}}{\partial z} \quad (3.18)$$

where A is the area of the initial configuration and the strain rates \dot{E}_{yy} and \dot{E}_{zz} are found by applying (2.7).

3.3.2.3. Derivation of the local resistance

The last step of the upper-bound method consists in evaluating the external power. In the present situation, the only force acting on the plate is the one imposed by the striking vessel, which is in fact equal to the resistance $P(\delta)$ opposed by the super-element. If this force is assumed to be applied at point I with the same direction than the displacement of the vessel (Figure 3.14), then according to (2.5), the external power is simply given by $\dot{W} = P\dot{\delta}$. Consequently, equating \dot{W} with \dot{E}_{int} leads to the sought resistance. Doing so for the four sub-areas of Figure 3.14, it can be shown that the different individual contributions to $P(\delta)$ are given by the following expressions:

$$\bullet P_1(\delta) = \sigma_0 t_p \frac{a_0}{b_1} \left(\delta + q - X_S - \frac{a_0^2}{3R} + \frac{4b_1^2}{9R} + \frac{(a_1 - a_0)^2}{5R} \right) ; a_0 = \frac{R}{a_1} (q - X_S + \delta) \quad (3.19)$$

$$\bullet P_2(\delta) = \sigma_0 t_p \frac{a_0}{b_2} \left(\delta + q - X_S - \frac{a_0^2}{3R} + \frac{4b_2^2}{9R} + \frac{(a_1 - a_0)^2}{5R} \right) ; a_0 = \frac{R}{a_1} (q - X_S + \delta) \quad (3.20)$$

$$\bullet P_3(\delta) = \sigma_0 t_p \frac{a_0}{b_1} \left(\delta + q - X_S - \frac{a_0^2}{3R} + \frac{4b_1^2}{9R} + \frac{(a_2 - a_0)^2}{5R} \right) ; a_0 = \frac{R}{a_2} (q - X_S + \delta) \quad (3.21)$$

$$\bullet P_4(\delta) = \sigma_0 t_p \frac{a_0}{b_2} \left(\delta + q - X_S - \frac{a_0^2}{3R} + \frac{4b_2^2}{9R} + \frac{(a_2 - a_0)^2}{5R} \right) ; a_0 = \frac{R}{a_2} (q - X_S + \delta) \quad (3.22)$$

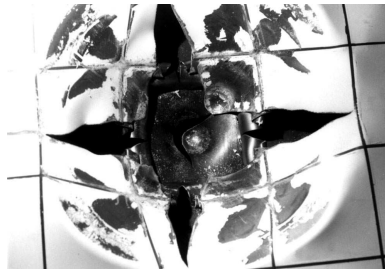
where $R = p^2/q$. As a final result, the total resistance $P(\delta)$ is obtained by summing up the four contributions given by (3.19) to (3.22).

It is worth noting that all these developments are valid as long as there is no failure of the material. Indeed, as depicted on Figure 2.6, the tension in the plate fibers should be released when the rupture strain ϵ_r is reached. Nevertheless, predicting and simulating the failure of structure is quite complex as it is influenced by the type of load. Moreover, as explained by Simonsen [142], the simplified approach exposed here above is only based on an overall hypothetic deformation mechanism, which does not allow for estimating the strains at a detailed level. In other words, this means that the upper-bound method is sufficient for predicting the overall behavior of a super-element, but fails to provide an accurate estimation of local fields such as stresses or strains. Consequently, as suggested by various authors like Zhang [180], Lützen [103] or Wang [162], it is convenient to use the maximum strain failure criteria when developing such analytical models. This latter simply states that rupture will take place when a critical level ϵ_c is reached. In the case of an impacted plate, this writes:

$$\max_A \{E_{yy}, E_{zz}\} = \epsilon_c \quad (3.23)$$

where E_{yy} and E_{zz} are the Green-Lagrange deformations in the horizontal and vertical fibers predicted by the upper-bound method. The main arduous task when using (3.23) consists in choosing an appropriate value for ϵ_c because taking $\epsilon_c = \epsilon_r$ leads to unsafe predictions of failure. Consequently, some unrealistic values are often affected to ϵ_c . According to Amdahl et al. [9] and Mc Dermott et al. [107], ϵ_c should be chosen within a range of 5 to 10 %. In the present case, the selection of ϵ_c is based on finite element simulations (see section 3.3.4).

(a) Front view of a ruptured plate impacted by a cone [163]



(b) Rear view of a ruptured plate impacted by a cone [163]



(c) Theoretical model of a four petals mechanism

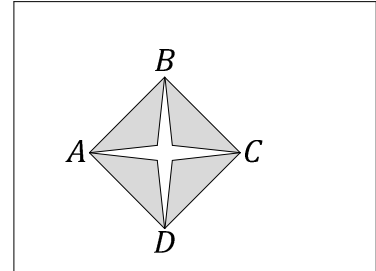


Figure 3.17. Four petals mechanism of a ruptured plate impacted by a cone

As soon as equation (3.23) is satisfied, the plate is assumed to have no resistance anymore and $P(\delta)$ is set to 0. This approach is quite conservative, because numerical simulations (see section 3.3.4) have shown the existence of a residual resistance. This has also been

investigated experimentally by Wang et al. [163], who pointed out that the ruptured plates still dissipated energy through a four petals mechanism (Figure 3.17a and b). Based on these observations, a theoretical model was derived by assuming that plastic dissipation mainly takes place during the rotation of the four petals around the moving plastic hinge lines AB , BC , CD and AD (Figure 3.17c). Of course, these developments could be easily integrated in the present analytical model, but the main difficulty is that they are highly dependent on the shape of the striker. Other types of post-failure mechanism could be observed if other indenters were used. Consequently, it is decided here to neglect the residual strength after rupture.

Another important point to raise is the fact that for most lock gates, the plating is reinforced by additional smaller horizontal and/or vertical stiffeners that also dissipate energy during the impact. These ones may be easily included by smearing them over the plate surface, as exposed in Appendix B.1 (section B.1.1).

As a final remark, it is also worth mentioning that formulae (3.19) to (3.22) are only valid as long as one of the support of the plate has not been impacted by the stem. However, if this is the case, then the resistance is changed and has to be derived in another way. Additional information on this topic may be found in Appendix B.1 (sections B.1.2 and B.1.3).

3.3.3. Analytical derivation for an impact by the bulb

3.3.3.1. Derivation of the displacement field

The displacement field that is postulated for an impact by the bulb \mathcal{B} is more difficult to define than for a collision involving the stem \mathcal{S} . Ideally, $u(y,z)$ should be such that the deforming plate follows the shape of \mathcal{B} (Figure 3.18).

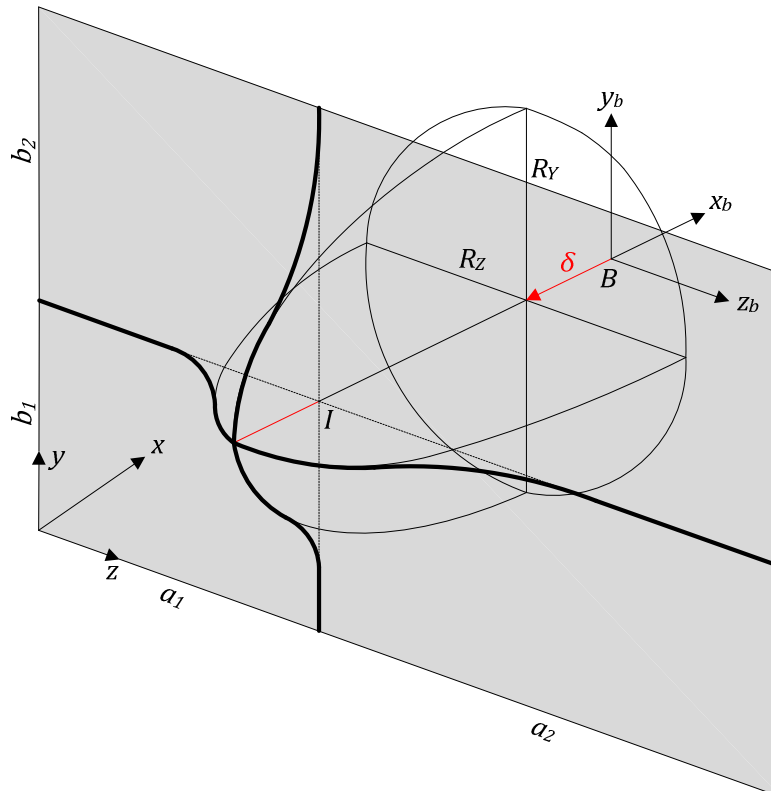


Figure 3.18. Deformation pattern and displacement field $u(y,z)$ for an impact by the bulb

Nevertheless, doing so leads to very cumbersome equations that are not easily tractable within an analytical approach. For this reason, as in section 3.3.2, an approximate formulation will be used for $u(y, z)$. To do so, it is first required to express the equation of \mathcal{B} in the local reference frame (x, y, z) of the super-element. This is easily achieved by considering (3.10), where \mathcal{B} is described in the global (X, Y, Z) axes. Indeed, for a penetration δ , it can be shown that the current description of the striking bulb is as follows:

$$\mathcal{B} \equiv x = X_B - \delta + R_X \left(\frac{(y - b_1)^2}{R_Y^2} + \frac{(z - a_1)^2}{R_Z^2} - 1 \right) \quad (3.24)$$

where R_X, R_Y, R_Z are the three radii (Figure 3.18) and X_B is given by (3.7). As for the case of the stem, this expression could be used to calculate the mathematical expression of the deformation pattern by assuming that this latter has to be tangent to \mathcal{B} . However, as the bulb is usually narrower than the stem, it is not reasonable to think that the entire plate will be involved in the collision process.

Indeed, from numerical simulations (see section 3.3.4), it transpires that only a portion of the plate located near the initial contact point I really deforms during the impact. Of course, this region increases when the ship moves forward and can be defined by considering the intersection curve Γ made by the current description of bulb (3.24) and the initial plane of the plate. As depicted on Figure 3.19, the assumption is made that the resistance only comes from the horizontal and vertical fibers located inside the areas $2\ell_y(a_1 + a_2)$ and $2\ell_z \times (b_1 + b_2)$ respectively.

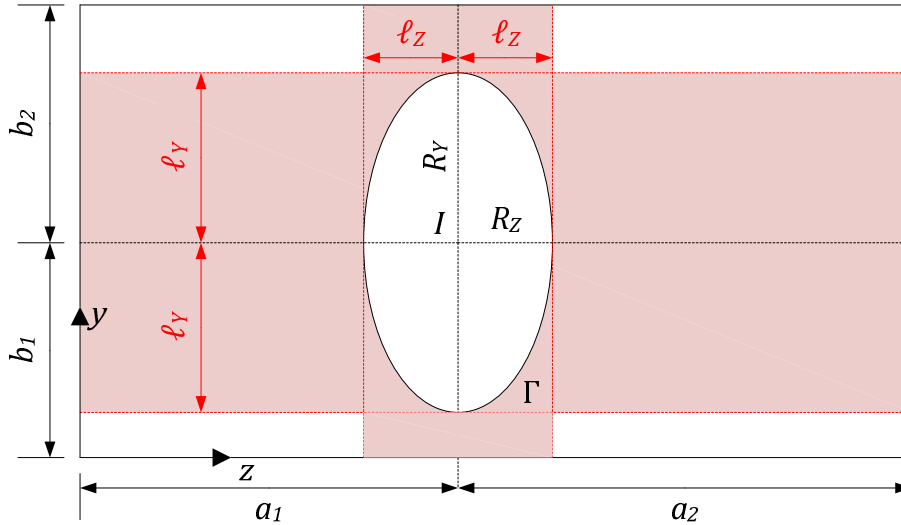


Figure 3.19. Definition of the portions of the plate involved in the collision process

The displacement field $u(y, z)$ is supposed to act only on the shaded parts of Figure 3.19, the other regions being unaffected. For a given penetration δ , the extensions ℓ_y and ℓ_z may be found by considering the mathematical expression of the ellipse Γ . From (3.24), it is easy to show that:

$$\ell_y = R_Y \sqrt{\delta/R_X} \quad ; \quad \ell_z = R_Z \sqrt{\delta/R_X} \quad (3.25)$$

In order to obtain a consistent description of the displacement field, let us start by considering first the deformation pattern for a horizontal fiber (Figure 3.20) located at a certain level y along the vertical axis. For a given value of the penetration δ , it is assumed that the out-of-plane displacements $u(y, z)$ are largely predominant. In order to follow the shape of the bulb,

$u(y, z)$ is split into two different parts $u_1(y, z)$ and $u_2(y, z)$ satisfying the same conditions than $U_1(z)$ and $U_2(z)$ in the case of an impact by the stem (see section 3.3.2.1). The junction between them occurs at point A (Figure 3.20) that is located at a distance $a_0(y)$ from the center of the bulb and submitted to an out-of-plane motion $\delta_0(y)$.

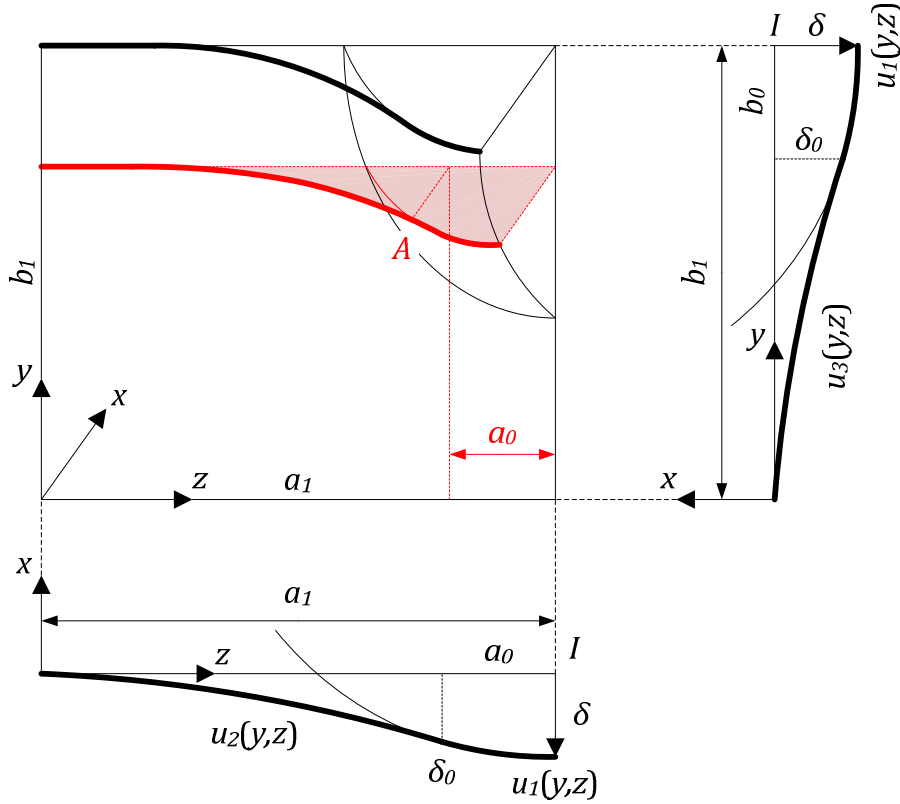


Figure 3.20. Definition of the displacement for a horizontal fiber impacted by the bulb

By following a similar procedure than in section 3.3.2.1 and considering this time equation (3.24), it can be shown that for $b_1 - \ell_Y \leq y \leq b_1$, $u(y, z)$ has the following definition:

- $u_1(y, z) = R_X \left(1 - \frac{(y - b_1)^2}{R_Y^2} - \frac{(z - a_1)^2}{R_Z^2} \right) - X_B + \delta$ if $a_1 - a_0(y) \leq z \leq a_1$ (3.26)

- $u_2(y, z) = \delta_0(y) \frac{(z - a_1)^2}{a_0^2(y)}$ if $0 \leq z \leq a_1 - a_0(y)$ (3.27)

with: $\delta_0(y) = \frac{R_X}{R_Z^2} a_0(y)(a_1 - a_0(y))$; $a_0(y) = \frac{R_Z^2}{R_X a_1} \left(R_X \left(1 - \frac{(y - b_1)^2}{R_Y^2} \right) - X_B + \delta \right)$ (3.28)

Focusing now on a vertical fiber (Figure 3.20), it is obvious that a similar reasoning holds in this case. The displacement field is also divided into two parts: the first one $u_1(y, z)$ is still given by (3.26) and sticks to the bulb, while the second one $u_3(y, z)$ is such that it respects the compatibility requirements with the horizontal supports of the plate. By analogy with the previous equations, for $a_1 - \ell_Z \leq z \leq a_1$, it is found that:

- $u_1(y, z) = R_X \left(1 - \frac{(y - b_1)^2}{R_Y^2} - \frac{(z - a_1)^2}{R_Z^2} \right) - X_B + \delta$ if $b_1 - b_0(z) \leq y \leq b_1$ (3.29)

- $u_3(y, z) = \delta_0(z) \frac{(z - a_1)^2}{b_0^2(z)}$ if $0 \leq y \leq b_1 - b_0(y)$ (3.30)

$$\text{with: } \delta_0(z) = \frac{R_Z}{R_X^2} b_0(z)(b_1 - b_0(z)); \quad b_0(z) = \frac{R_Y^2}{R_X a_1} \left(R_X \left(1 - \frac{(z - b_1)^2}{R_Z^2} \right) - X_B + \delta \right) \quad (3.31)$$

From the previous considerations, it is obvious that $u(y, z)$ is nothing else than a generalization of the developments performed in section 3.3.2.1, but restricted to the areas $2\ell_y(a_1 + a_2)$ and $2\ell_z \times (b_1 + b_2)$ of Figure 3.19. With the previous definitions of $u(y, z)$, it is now possible to evaluate the internal energy rate.

3.3.3.2. Derivation of the internal energy rate

The procedure to get \dot{E}_{int} in the case of a collision involving the bulb is quite similar to the one exposed in section 3.3.2.2 for the stem. If the energy dissipation associated to the bending effects is disregarded, then according to the plate strip model, the internal energy rate comes mainly from the membrane extension of the vertical and horizontal fibers. For the sub-area $a_1 \times b_1$, these latter are respectively given by:

$$\begin{aligned} \bullet \dot{E}_{int}^{(y)} &= \int_{a_1 - \ell_z}^{a_1} n_0 dy \int_0^{b_1 - b_0} \left(\frac{\partial u_3}{\partial y} \frac{\partial \dot{u}_3}{\partial y} + \frac{\partial u_3}{\partial z} \frac{\partial \dot{u}_3}{\partial z} \right) dy \\ \bullet \dot{E}_{int}^{(z)} &= \int_{b_1 - \ell_y}^{b_1} n_0 dz \int_0^{a_1 - a_0} \left(\frac{\partial u_2}{\partial y} \frac{\partial \dot{u}_2}{\partial y} + \frac{\partial u_2}{\partial z} \frac{\partial \dot{u}_2}{\partial z} \right) dz \end{aligned} \quad \Rightarrow \dot{E}_{int} = \dot{E}_{int}^{(y)} + \dot{E}_{int}^{(z)} \quad (3.32)$$

It is worth noticing that there is obviously no energy rate on the portion of the plate sticking to the bulb, which explains why $u_1(y, z)$ does not have to be considered in (3.32). Another point that is important to remember is the fact that (3.32) is valid if the out-of-plane displacements are predominant with respect to the in-plane ones, which is usually true in a collision event.

3.3.3.3. Derivation of the local resistance

According to the upper-bound theorem, the super-element resistance $P(\delta)$ can be calculated by equating the external power \dot{W} to the internal dissipation. If the resistance is acting at point I (Figure 3.18) and has the same direction than the ship velocity, then $P(\delta) = \dot{E}_{int} / \dot{\delta}$, where \dot{E}_{int} is given by (3.32). If the expressions of $u_2(y, z)$ and $u_3(y, z)$ are substituted in (3.32) for the four sub-areas $a_1 \times b_1$, $a_1 \times b_2$, $a_2 \times b_1$ and $a_2 \times b_2$, then the total resistance $P(\delta)$ is obtained by summing up all the corresponding contributions. These latter are as follows:

$$\bullet P_1(\delta) = \frac{8}{3} \sigma_0 t_p \sqrt{\frac{\delta}{R_X}} \left(\frac{R_Y}{a_1} \left(\frac{1}{3} + \frac{1}{5} \frac{R_Z^2}{R_Y^2} \right) + \frac{R_Z}{b_1} \left(\frac{1}{3} + \frac{1}{5} \frac{R_Y^2}{R_Z^2} \right) \right) \delta \quad (3.33)$$

$$\bullet P_2(\delta) = \frac{8}{3} \sigma_0 t_p \sqrt{\frac{\delta}{R_X}} \left(\frac{R_Y}{a_1} \left(\frac{1}{3} + \frac{1}{5} \frac{R_Z^2}{R_Y^2} \right) + \frac{R_Z}{b_2} \left(\frac{1}{3} + \frac{1}{5} \frac{R_Y^2}{R_Z^2} \right) \right) \delta \quad (3.34)$$

$$\bullet P_3(\delta) = \frac{8}{3} \sigma_0 t_p \sqrt{\frac{\delta}{R_X}} \left(\frac{R_Y}{a_2} \left(\frac{1}{3} + \frac{1}{5} \frac{R_Z^2}{R_Y^2} \right) + \frac{R_Z}{b_1} \left(\frac{1}{3} + \frac{1}{5} \frac{R_Y^2}{R_Z^2} \right) \right) \delta \quad (3.35)$$

$$\bullet P_4(\delta) = \frac{8}{3} \sigma_0 t_p \sqrt{\frac{\delta}{R_X}} \left(\frac{R_Y}{a_2} \left(\frac{1}{3} + \frac{1}{5} \frac{R_Z^2}{R_Y^2} \right) + \frac{R_Z}{b_2} \left(\frac{1}{3} + \frac{1}{5} \frac{R_Y^2}{R_Z^2} \right) \right) \delta \quad (3.36)$$

Obviously, equations (3.33) to (3.36) are valid as long as there is no failure in the material, but if the maximal strain arising in the plate exceeds a critical value ϵ_c , then $P(\delta)$ is set to zero. Moreover, these formulae are no longer applicable if one of the supports has been impacted by the bulb. In this case, some additional developments are required. They are very similar to those performed for the impact by the stem (see Appendix B.1, sections B.1.2 and B.1.3) and are therefore not presented here.

3.3.4. Numerical validation

In an attempt to validate the developments performed here above, the analytical results may be confronted to those obtained with finite element. To do so, many collision scenarios were investigated using the LS-DYNA software, involving plates and vessels of various dimensions.

| | | |
|---------------------|--------------|------------------------|
| Young modulus | E_Y | 210000 MPa |
| Poisson coefficient | ν | 0.33 |
| Mass density | ρ | 7850 kg/m ³ |
| Tangent modulus | E_T | 1018 MPa |
| Flow stress | σ_0 | 240 MPa |
| Rupture strain | ϵ_r | Variable |

Table 3.2. Material properties

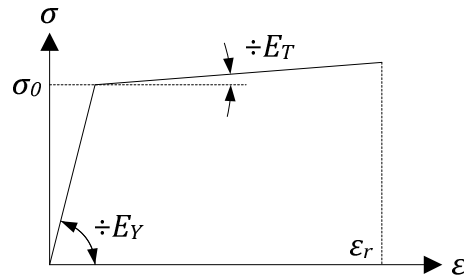


Figure 3.21. Stress-strain curve for the simulations

The material law that is used for the simulations is defined by the stress-strain curve of Figure 3.21. This one is composed of a first elastic phase, characterized by a Young modulus E_Y and a yield stress σ_0 . The second part of the curve corresponds to a linear strain hardening with a tangent modulus E_T . All these parameters have the values listed in Table 3.2. Rupture is assumed to occur when a maximal deformation ϵ_r is reached. Axial tensile test performed for various steel grades have shown that the rupture strain usually ranges from 15 to 25 %.

Nevertheless, simulating correctly the initiation and propagation of failure is still difficult. In the present case, an erosive law based on shear criterion is used, which means that the elements where the effective plastic strain exceeds ϵ_r are simply deleted from the model. Selecting a consistent value for ϵ_r is therefore of prior importance and this choice has to be done in accordance with the mesh size. Indeed, when some elements are removed from the model, a stress concentration appears near the holes that have been created. Obviously, the stresses will increase in a larger proportion if the mesh around the perforated areas is very refined, which will cause the elements to disappear more quickly. Consequently, it can be said that for a same value of ϵ_r , the coarser the mesh, the slower the erosion.

In order to account for this phenomenon, Lehmann and Peschmann [93] suggested to calculate ϵ_r by accounting for the element length l_e and thickness t_e :

$$\epsilon_r = \epsilon_g + \epsilon_e t_e / l_e \quad (3.37)$$

where ϵ_g and ϵ_e are respectively the uniform and necking strains. For mild steel, it is of current practice to choose $\epsilon_g = 0.056$ and $\epsilon_e = 0.54$. This empirical relation was found by performing direct measurements during experimental collision tests and is only valid for mild steel. If another material is used, then the law has to be recalibrated. According to Vredeveldt et al. [160], equation (3.37) has been validated for steel grades having a yield stress ranging from 235 to 355 MPa. Therefore, (3.37) should be convenient for lock gates. Nevertheless,

having a proper simulation of rupture is quite challenging on a numerical point of view. As discussed in section 2.1.1, various laws are available in the literature to define a rupture criteria accounting for the size of the finite element, but they do not necessarily lead to the same results.

As a first validation example, the analytical formulae developed in section 3.3.2 for a collision by the stem are confronted to numerical results given by LS-DYNA. The geometrical data describing the vessel (Figure 3.22) and the impacted structure are listed in Table 3.3. In an illustrative purpose, the equivalent plastic strain in the plate is plotted on Figure 3.22, from which it can be seen that the deformation pattern is more or less similar to the one postulated on Figure 3.14.

| | |
|--------|--------|
| p | 3.5 m |
| q | 7 m |
| h_b | 3.5 m |
| ϕ | 70° |
| ψ | 79° |
| a_1 | 3.5 m |
| a_2 | 1.2 m |
| b_1 | 1.5 m |
| b_2 | 2.5 m |
| t_p | 0.01 m |

Table 3.3. Geometrical properties

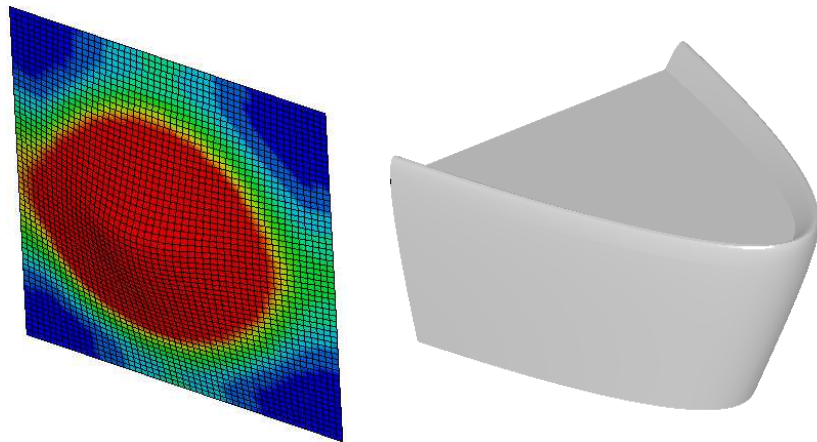


Figure 3.22. Equivalent plastic strain in the plate ; Striking bow used for the simulations

In order to investigate the importance of accounting for the shape of stem, some simulations have been performed without considering failure. The corresponding curves showing the evolution of the force with the penetration are plotted on Figure 3.23a and it can be concluded that using the analytical model is quite satisfactory.

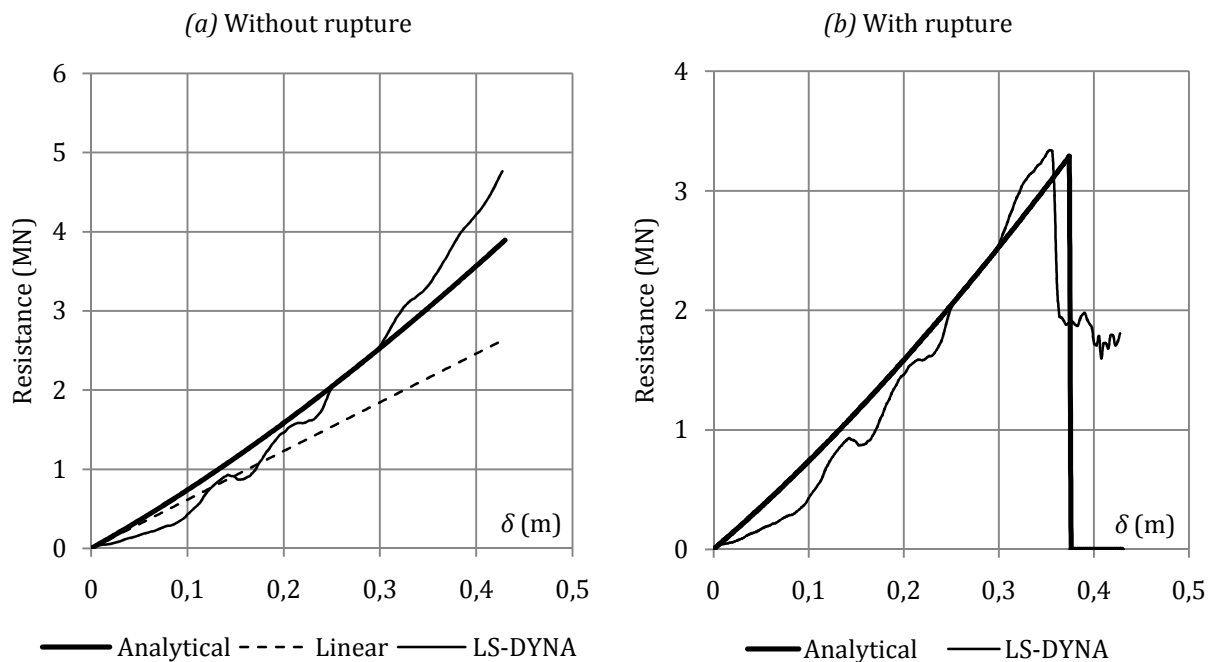


Figure 3.23. Comparison between the analytical and numerical results for an impact by the stem

As a matter of comparison, Figure 3.23a also shows a linear prediction such as the one derived by Zhang [180] for a punctual impact. In this case, it is apparent that the collision resistance is underestimated. This may be explained by the fact that the vessel dimensions are usually much more important than those of the plate. Therefore, the deformations are not correctly assessed if the impact is modeled by a concentrated load. However, a linear formula may be consistent for ship-ship collisions as the plating elements are often larger.

Other simulations were also performed in which failure was taken into account. For the data reported in Table 3.3, the analytical and numerical resistance curves are plotted on Figure 3.23b. Here again, a quite good agreement is found between both of them. In this particular case, the rupture strain ϵ_r is set to 16 % as the element size and thickness are equal to 5 cm and 1.5 cm respectively. Regarding the theoretical model, the value of the critical strain ϵ_c is found to be equal to 7 %, which is quite close to the recommendations made by Lützen [103] or Zhang [180]. It is worth mentioning that this value of ϵ_c is based on many numerical simulations and is chosen to have a satisfactory prediction of failure in most of them.

| | | | |
|-------|--------|-------|---------|
| a_1 | 1.31 m | t_p | 0.015 m |
| a_2 | 1.31 m | R_X | 2 m |
| b_1 | 1.5 m | R_Y | 0.8 m |
| b_2 | 1.5 m | R_Z | 0.3 m |

Table 3.4. Geometrical properties for an impact by the bulb

The case of an impact involving the bulb is now considered. The material used for these simulations is still the one described here above, but the geometrical data are now those listed in Table 3.4. In accordance with (3.37), the failure strain ϵ_r is set to 22 %. The resistance curves with and without rupture are plotted on Figure 3.24, from which it can be seen that the agreement is rather good. As in the case of a collision by the stem, the analytical prediction of Figure 3.24b is obtained by considering $\epsilon_c = 7\%$ in equation (3.23).

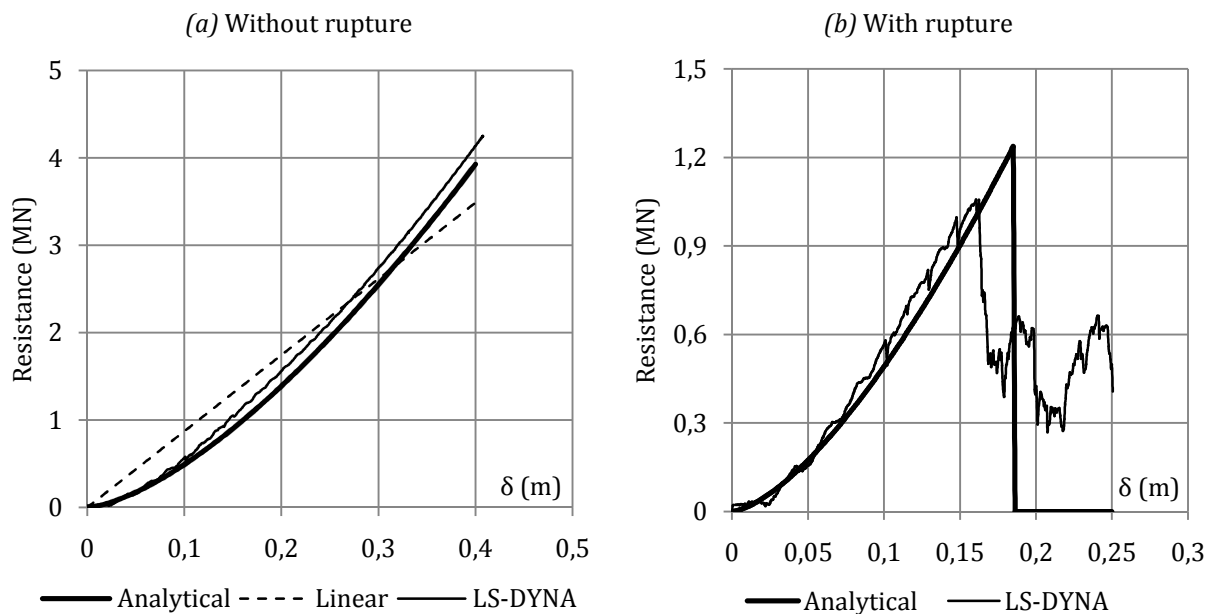


Figure 3.24. Comparison between the analytical and numerical results for an impact by the bulb

From Figure 3.24a, it appears that the linear approximation is much more satisfactory in this case. This is due to the fact that the bulb chosen for this example (Table 3.4) is quite sharp

and the hypothesis of a punctual impact is therefore quite acceptable. Nevertheless, other simulations performed with larger values of R_X , R_Y and R_Z shows that the discrepancy is more important in those cases.

As a final remark, it can be concluded that the results depicted on Figure 3.23 and Figure 3.24 validate the analytical model presented in sections 3.3.2 and 3.3.3 for the first type of super-element.

3.4. Local resistance for super-elements of type 2

As briefly exposed in section 3.2.2.1, the second type of super-element to consider is a horizontal or a vertical plate supported on three edges and impacted in its plane (Figure 3.11b). A major difference with the developments exposed in the previous section is that the shape of the striking bow is assumed to have little effect on the deformation pattern. In other words, a punctual impact is assumed when deriving the local resistance $P(\delta)$.

3.4.1. Literature review

Experiments (Figure 3.25) and numerical simulations have shown that the deformation mode of the component is a folding mechanism. From these observations, some simplified analytical formulations have been derived. This subject was initially investigated by Alexander [5], who studied the collapse of thin cylinders submitted to an axial compressive force. Amdahl [8] was also one of the first to propose a comprehensive model for the crushing of structural elements in offshore platforms.

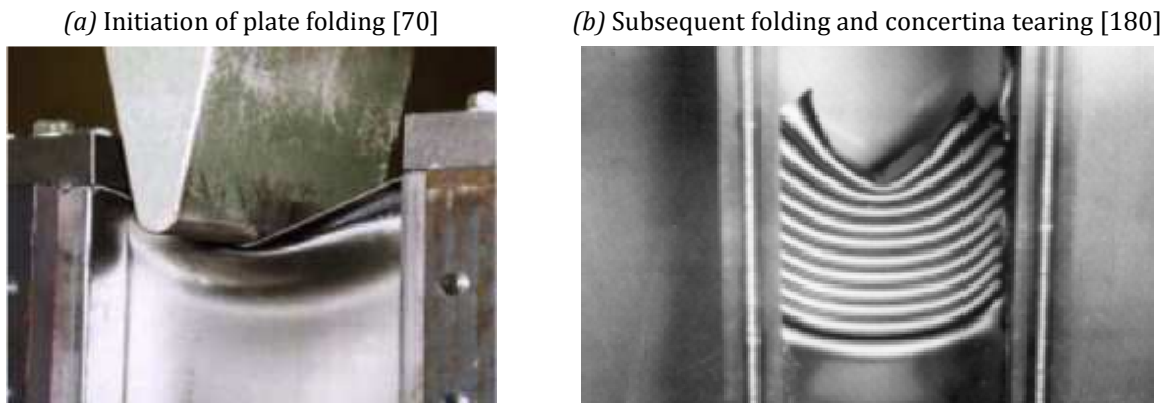


Figure 3.25. Folding mechanism of a plate impacted on its free edge

Since this primary work, the problem has been successfully treated by Simonsen and Ocakli [144], who derived closed-form solutions by assuming a two successive folds deformation mode. Similar developments were also performed by Wang and Ohtsubo [164], Hong and Amdahl [72], Wierzbicki and Abramowicz [168], Simonsen [140], and Zhang [180], but all of them postulated a plastic collapse mechanism involving only one fold. Most of these authors confronted their theoretical predictions with experimental or numerical results. A quite good agreement was found in almost all the cases.

Nevertheless, as pointed out by Wierzbicki and Culbertson-Driscoll [169] in a very comprehensive work, considering only one collapse mode is usually not sufficient because other mechanisms are often involved. Indeed, besides the local folding process, they also investigated global bending and shear failure modes. However, their developments lead to quite cumbersome equations that required numerical tools to be solved.

In all the previous references, an analytical model was derived by assuming that the plate is submitted to a concentrated force. In a very interesting paper, Hong and Amdahl [71] derived the patch-loading resistance of web girders submitted to a uniformly distributed load. The theoretical model was based on two different collapse modes (a "roof-top" and a "double diamond" mechanism) and a good agreement with finite element simulations was found. However, the main drawback of this method is that the equations are not easily tractable within a simplified analytical tool and have to be solved numerically. In addition to all these

theoretical models, a simplified formula was proposed by Choi et al. in references [32] and [33]. They used empirical factors calibrated through a certain number of experiments performed on thin plates. However, this method was restricted to shallow web girders.

Finally, it is worth mentioning that a comparative literature review was recently performed by Hong and Amdahl [70] on the topic of plate crushing. They also proposed a new theoretical model involving a deformation pattern deduced from numerical simulations.

3.4.2. Analytical derivation

This section mainly focus on a horizontal element, but the developments could be easily extended to the case of a vertical one. This component has a total length equal to $a_1 + a_2$ (Figure 3.26). The web height and thickness are denoted by h_w and t_w respectively, while h_f and t_f are the corresponding properties for the flange. It is worth noting that there is no collaborative part coming from the plating, as this latter is treated as a SE1 for the evaluation of the local resistance (section 3.3).

The analytical derivation will be divided into two parts, each of them corresponding to a potential collapse mechanism. In the case of deep plates (i.e. for which h_w is comparable to $a_1 + a_2$), it is sufficient to consider only one folding mode, as it was done by Simonsen and Ocakli [144] for example. For shallow structures, the investigations carried out by Wierzbicki and Culbertson-Driscoll [169] pointed out the need to account for several collapse modes. Therefore, a folding mechanism and a bending collapse mode are introduced in this section.

3.4.2.1. Folding mechanism

A general overview of the folding mechanism is depicted on Figure 3.26. This one is assumed to develop under a localized force, which means that the shape of the striker is disregarded. In particular, there is no need to distinguish between the bulb or the stem, as it was done in section 3.3. This approach may be justified by the need of deriving tractable formulae, which requires to avoid the very difficult deformation patterns postulated by Hong and Amdahl [71] in the case of a distributed contact force.

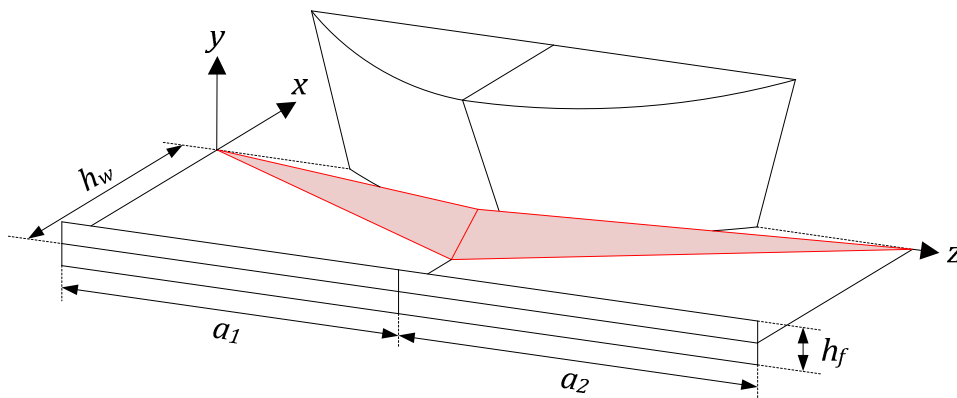


Figure 3.26. Folding mechanism

As depicted on Figure 3.26, one fold may be split into a right and a left wing. The developments are similar for both of them, so it is sufficient to focus on the right one only. This latter has a length equal to a_1 and a height of $2H$ (Figure 3.27), H being kept as a parameter so far. The crushing process involves the extension and the rotation of the two triangles OAB and OBC (Figure 3.27).

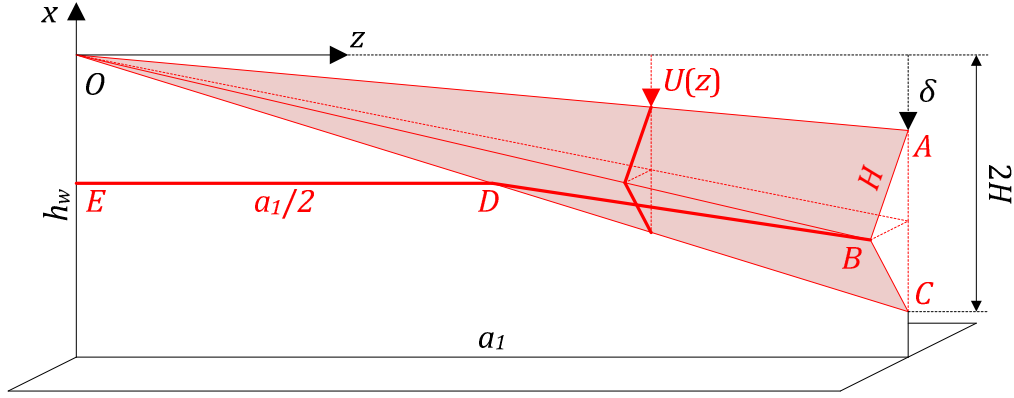


Figure 3.27. Three dimensional view of one wing

In order to apply the upper-bound method, the first step is to postulate a kinematically admissible displacement field. For convenience, this will be done by working with a local coordinate frame (x, y, z) that is parallel to the global one depicted on Figure 3.3. Here again, the plate strip model is invoked, which means that the super-element is seen as set of fibers parallel to the z axis weakly connected to a set of fibers parallel to x axis.

Let us first start by considering a horizontal fiber initially located at a given level $x \in [0 ; 2H]$. There are several admissible displacement fields that could explain how this fiber reaches its current configuration, but the goal is precisely to choose a quite realistic one. From experiments conducted by Choi et al. [32], it appears that the plates are predominantly submitted to axial straining. Consequently, it seems reasonable to suppose that each horizontal fiber is only affected by a displacement $w(y, z)$ parallel to the z axis.

In order to evaluate $w(y, z)$, it is further assumed that the plastic dissipation is restricted to the surface OAC . Consequently, for a horizontal fiber initially located at the level x , this last hypothesis implies that the portion before the line OC remains unaffected, while the part behind OC has to support the total axial extension. In the particular case of EB , this means that only the segment BD is deforming, the part ED keeping the same length. For a given penetration δ , it can be shown that the current lengths \overline{OA} and \overline{BD} are as follows:

$$\overline{OA} = \sqrt{a_1^2 + \delta^2} \simeq a_1 + \frac{\delta^2}{2a_1} \quad ; \quad \overline{BD} = \sqrt{a_1^2/4 + H\delta} \simeq \frac{a_1}{2} - \frac{H\delta}{a_1} \quad (3.38)$$

and are only valid if the fold height H is negligible with respect to a_1 , which is usually the case. Accounting for these results, the displacements of points A and B along the z axis are simply given by:

$$W_A = \overline{OA} - a_1 = \delta^2/2a_1 \quad ; \quad W_B = \overline{OB} - a_1/2 = H\delta/a_1 \quad (3.39)$$

The procedure followed to get W_A and W_B could be generalized to find the displacement $W(x)$ for each point along the line AC (Figure 3.28a), but doing so leads to very cumbersome equations that are not well suited within an analytical approach. Consequently, as suggested by Zhang [180] or Simonsen and Ocakli [144], it can be assumed that $W(x)$ is simply obtained by a linear interpolation:

$$\begin{aligned} W(x) &= W_A \left(1 + \frac{x}{H}\right) - W_B \frac{x}{H} & \text{if } -H \leq x \leq 0 \\ W(x) &= W_B \frac{x + 2H}{H} & \text{if } -2H \leq x \leq -H \end{aligned} \quad (3.40)$$

The displacement field $w(x, z)$ for any point of the surface OAC is then found by postulating that it is simply increasing linearly from 0 along the line OC to $W(x)$ along AB :

$$w(x, z) = W(x) \frac{z + a_1 x / 2H}{a_1 (1 + x / 2H)} \quad (3.41)$$

It is worth mentioning that this last expression of $w(x, z)$ is not kinematically admissible, as it implies different slope discontinuities. The first ones occurs along OB and OC because of the rotations imposed to the triangles OAB and OBC . For similar reasons, there is also a slope incompatibility between the two deforming wings along the edges AB and BC . Therefore, all these lines have to be seen as plastic hinges for the horizontal fibers.

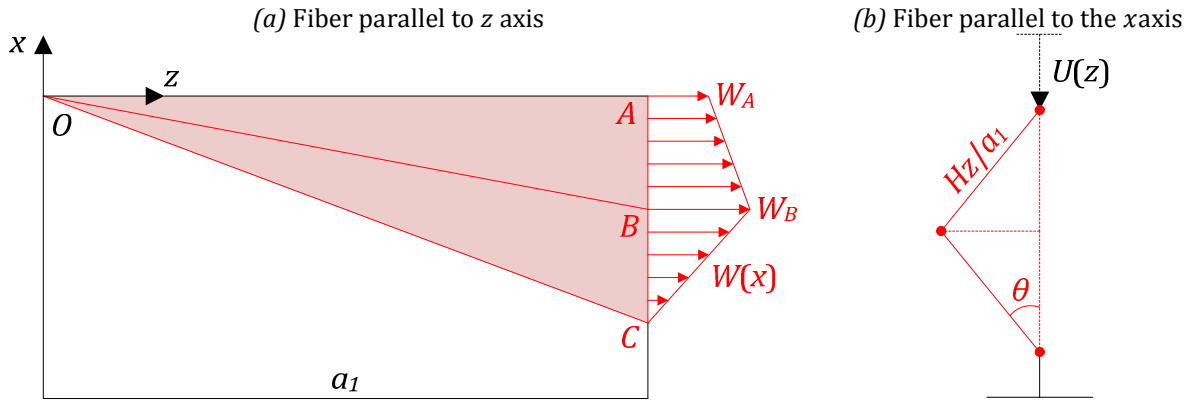


Figure 3.28. Displacement field for a fiber parallel to the x or z axis

Regarding a vertical fiber parallel to the x axis (Figure 3.28b) and located at any position $z \in [0 ; a_1]$, it is submitted to an indentation $U(z) = \delta z / a_1$ (Figure 3.28b) and is folded by rotating around three plastic hinges located along OA , OB and OC . If the initial length $2Hz/a_1$ of the fiber is kept unchanged, then the rotation angle θ is given by:

$$\frac{2Hz}{a_1} \cos \theta = \frac{2Hz}{a_1} - U(z) \Leftrightarrow \theta = \arccos \left(1 - \frac{\delta}{2H} \right) \quad (3.42)$$

In the optic of applying the upper-bound theorem, the next step is to evaluate the internal energy rate \dot{E}_{int} . This one may be obtained by summing up the dissipation due the fibers that are parallel to x and z axis. According to the plate strip model, these ones are supposed to deform without shearing, so according to (3.17), their contributions to \dot{E}_{int} are as follows:

$$d\dot{E}_{int}^{(x)} = dz \int_{-2H}^0 (m_0 \dot{K}_{zz} + n_0 \dot{E}_{xx}) dx \quad dE_{int}^{(z)} = dx \int_0^{a_1} (m_0 \dot{K}_{xx} + n_0 \dot{E}_{zz}) dz \quad (3.43)$$

where \dot{K}_{xx} and \dot{K}_{zz} are the curvature rates. Nevertheless, as the axial straining along the z axis is predominant, the bending energy rate $m_0 \dot{K}_{xx}$ may be neglected with respect to $n_0 \dot{E}_{zz}$, which means that the rotations of the horizontal fibers along the plastic hinges OB , OC , AB and BC are disregarded. Furthermore, as there is no modification of the length along the x axis, it is obvious that $\dot{E}_{xx} = 0$. Consequently, accounting for all these observations and integrating (3.43) over the deforming surface OAC leads to:

$$\dot{E}_{int} = \int_{-2H}^0 dx \int_0^{a_1} (m_0 \dot{K}_{zz} + n_0 \dot{E}_{zz}) dz = \dot{E}_b + \dot{E}_m \quad (3.44)$$

which may be seen as the sum of a bending and a membrane energy rate denoted by \dot{E}_b and \dot{E}_m respectively. The first contribution \dot{E}_b is only due to the rotation θ along the plastic hinges OA , OB and OC . Consequently, if $H \ll a_1$, then the length of these segments is more or less equal to a_1 , so for the two wings of the fold, \dot{E}_b is given by:

$$\dot{E}_b = 4m_0(a_1 + a_2)\dot{\theta} \quad ; \quad \dot{\theta} = \frac{\dot{\delta}/2H}{\sqrt{1 - (\delta/2H)^2}} \quad (3.45)$$

where $\dot{\theta}$ is found by deriving (3.42) and $m_0 = \sigma_0 t_w^2/4$. From this last equation, it is clear that \dot{E}_b tends to infinity when $\delta = 0$. On a theoretical level, this may be simply assimilated to the buckling phenomenon that takes place before the activation of the plastic folding mechanism. The usual way to overcome this particularity is to approximate \dot{E}_b by an average value calculated over one fold, i.e.:

$$\frac{1}{2H} \int_0^{2H} \dot{E}_b(\delta) d\delta = \frac{m_0(a_1 + a_2)\pi}{H} \dot{\delta} \quad (3.46)$$

Regarding the evaluation of the membrane energy rate \dot{E}_m , it first requires to get the strain rate component \dot{E}_{zz} . According to (2.7), it can be shown that:

$$\dot{E}_{zz} = \frac{\partial \dot{w}}{\partial z} = \frac{\dot{W}(x)}{a_1(1 + x/2H)} \quad \Rightarrow \quad \dot{E}_m = \frac{n_0 H a_1 + a_2}{2 a_1 a_2} (\delta + 2H) \dot{\delta} \quad (3.47)$$

where $\dot{W}(x)$ is obtained by deriving (3.40) and $n_0 = \sigma_0 t_w$. Finally, applying the upper-bound theorem with an external power given by $\dot{W} = P_f \dot{\delta}$ leads to:

$$P_f(\delta) = \frac{\dot{E}_b + \dot{E}_m}{\dot{\delta}} = \frac{m_0(a_1 + a_2)\pi}{H} + \frac{n_0 H a_1 + a_2}{2 a_1 a_2} (\delta + 2H) \quad (3.48)$$

It is important to bear in mind that the approach exposed here above is only consistent under the hypotheses $H \ll a_1$ and $H \ll a_2$, but H is still unknown so far. As suggested by many authors such as Simonsen [140], this parameter can be derived by minimizing the mean crushing force P calculated over one fold, i.e.:

$$\bar{P}_f = \frac{1}{2H} \int_0^{2H} P_f(\delta) d\delta \quad \Rightarrow \quad \frac{\partial \bar{P}_f}{\partial H} = 0 \Leftrightarrow H = \sqrt[3]{\frac{\pi}{12} a_1 a_2 t_w} \quad (3.49)$$

but this theoretical value is sometimes corrected to have a better modeling of the physical process. Indeed, instead of considering that the closure of one fold occurs when $\delta = 2H$, an effective crushing distance of $2\lambda H$ (with $\lambda \leq 1$) may be considered. This correction should be done to account for the radius and the thickness of the folded parts which do not allow the actual plate to be entirely compressed. In a quite detailed literature review, it is mentioned by Hong and Amdahl [71] that the values suggested for λ range from $2/3$ to 1 . Nevertheless, by considering different λ , it was found that this parameter has little influence on the resistance $P(\delta)$, so it is decided here to keep $\lambda = 1$.

It is worth noting that formula (3.48) is valid as long as $0 \leq \delta \leq 2H$. For $\delta > 2H$, a new fold is created (Figure 3.29), with the same pattern than the one depicted on Figure 3.26. In this case, (3.48) may be generalized by following the procedure described in Appendix B.2. As

long as the web is not completely crushed, if k is the current fold number, it can be shown that the resistance is given by:

$$P_f(\delta) = \frac{m_0(a_1 + a_2)\pi}{H} + n_0H \frac{a_1 + a_2}{a_1a_2} \left(\delta \left(2k - \frac{3}{2} \right) + 2kH \left(\frac{3}{2} - k \right) \right) \quad (3.50)$$

However, if n is the maximal number of folds that can be created over the web height, for $\delta > 2nH$, equation (3.50) is no longer valid and has to be corrected in the following way:

$$P_f(\delta) = \frac{m_0(a_1 + a_2)\pi}{H} + \frac{a_1 + a_2}{a_1a_2} (2n_0n^2H^2 + \sigma_0A_n(\delta - 2nH)) \quad (3.51)$$

where $A_n = (h_w - 2nH)t_w + h_f t_f$ is the area of the cross-section that has not been crushed. Of course, the two previous formulae are only valid as long as there is no rupture. Two different failure modes are possible when the super-element is impacted in its plane. The first one is the plate tearing (Figure 3.29b) phenomenon, which usually occurs from the very beginning of the impact. In this case, the folding process described here above does not take place. This rupture mechanism has been theoretically and experimentally studied by Simonsen [140], Zhang [179] or Ohtsubo and Wang [117] amongst others. These authors developed an upper-bound solution to the problem of plate tearing and validated their developments by comparison with numerical and experimental results. These studies point out that this phenomenon mainly occurs with sharp indenters, so it is not really relevant in case of an impact by a ship bow.

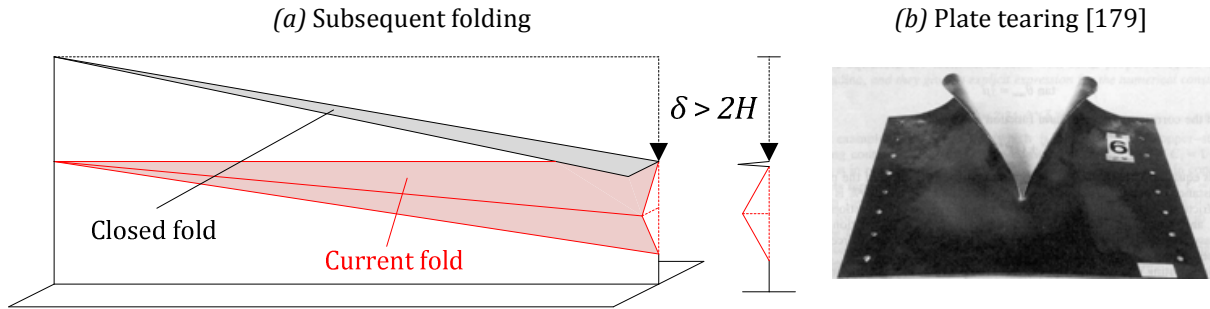


Figure 3.29. Subsequent folding and plate tearing in case of a large penetration

Apart from this failure mode, another one that is more likely to appear is the concertina tearing (Figure 3.25b). This latter has been theoretically studied by Wierzbicki [167], who found the following constant resistance:

$$P = 4.33\sigma_0 t_w^{5/3} (a_1 + a_2)^{1/3} + \frac{8}{3} R_m t_w \quad (3.52)$$

where R_m is the tearing resistance of steel, usually ranging from 300 to 1000 N/mm . Once again, the initiation of rupture will be detected by the strain failure criteria, i.e. when the maximal value of E_{zz} calculated by (3.47) reaches a critical limit ϵ_c that will be fixed later (section 3.4.3). Consequently, the local resistance for this super-element will be given by (3.50) or (3.51) as long as there is no concertina tearing, and by (3.52) if this mechanism has been activated.

3.4.2.2. Bending mechanism

In the case of a deep plate, it is sufficient to consider only the folding mechanism briefly detailed here above, but doing so is not relevant for shallower structures like web girders. In

fact, these latter have an impact response that may be divided into two different phases. At the beginning of the collision, the folding process is activated and the resistance formulae derived in section 3.4.2.1 are still valid. Nevertheless, when the penetration is getting larger, it is more difficult for the ship to progress by crushing the plate. A beam-like behavior is then activated, such as depicted on Figure 3.30.

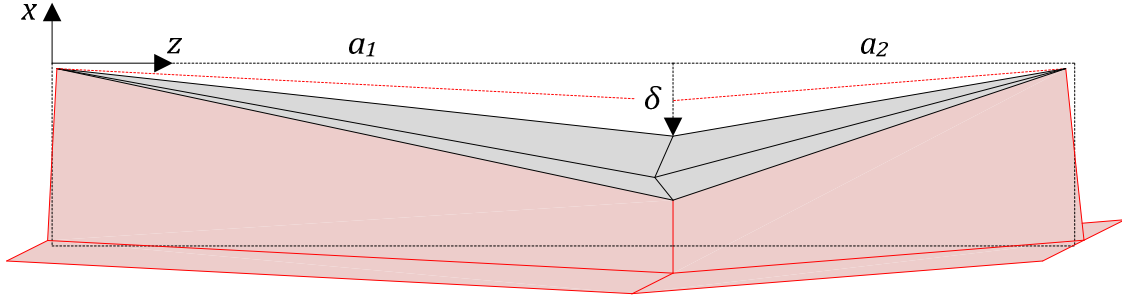


Figure 3.30. Three dimensional view of the bending mechanism

During this phase, the super-element is submitted to a plastic bending and may no longer be assimilated to a plate. Three hinges are required for initiating this new collapse mechanism (Figure 3.31), but it is worth noting that the full plastic bending moment M_0 of the initial T-shape cross-section (Figure 3.3) is not necessarily reached at these locations.

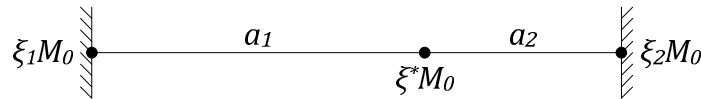


Figure 3.31. Three-hinge mechanism for a plastic beam

Indeed, at the left support, as the beam is not perfectly clamped, only a reduced value $\xi_1 M_0$ (with $\xi_1 \leq 1$) has to be considered. The parameter ξ_1 is quite difficult to evaluate and is influenced by the stiffness of the other structural elements connected to the impacted one. It has to be chosen to reflect the actual rotational restraint. A conservative approach is to take $\xi_1 = 0$ (simple supports) because this leads to the minimal energy dissipation. The same considerations are also valid for the right support, where a reduced bending capacity $\xi_2 M_0$ is used (with $\xi_2 \leq 1$).

For the cross-section immediately located under the initial contact point, the folding process has of course an incidence on its ability to develop the full plastic moment M_0 . Indeed, if the beam has been crushed over a distance δ during the primary denting mechanism, only a reduced bending capacity $\xi^*(\delta) M_0$ can be reached. Deriving $\xi^*(\delta)$ is not straightforward but may be done by a simplified procedure detailed in section B.2.2 of Appendix B.2.

If an indentation δ is reached during the initial folding phase, by following a similar procedure than for the global deforming mode (see section 3.6), it can be shown that the force $P_b^*(\delta)$ required to activate the beam collapse mechanism of Figure 3.31 is given by:

$$P^*(\delta) = M_0 \frac{a_1(\xi_2 + \xi^*(\delta)) + a_2(\xi_1 + \xi^*(\delta))}{a_1 a_2} \quad (3.53)$$

which is a piecewise linear function of δ (Figure 3.32a) because of the approximation made on $\xi^*(\delta)$ described in Appendix B.2. Consequently, the first folding process will be activated as long as the resistance $P_f(\delta)$ calculated by (3.50) or (3.51) is not equal to $P^*(\delta)$. When $\delta = \delta^*$ (Figure 3.32a), the force developed during the first folding phase is sufficient to

initiate the collapse mode of Figure 3.31, which means that there is a theoretical change in the structural behavior.

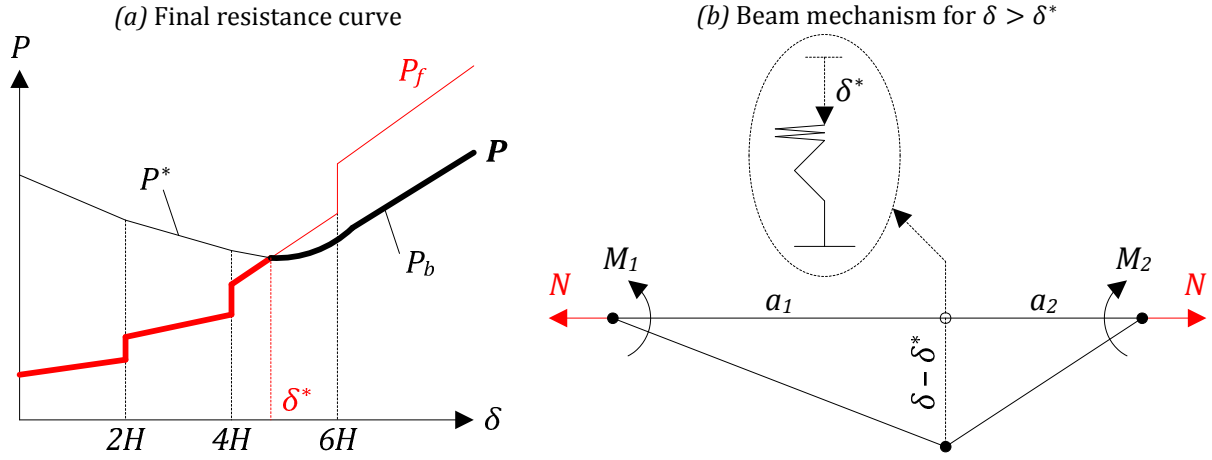


Figure 3.32. Three-hinge mechanism and resistance curves for a SE2

For $\delta > \delta^*$, the super-element is resisting through the three-hinge mechanism of Figure 3.32b, where the central cross-section is characterized by a reduction coefficient ξ^* evaluated for $\delta = \delta^*$ as there is no more folding in this second phase. During the plastic collapse, the beam is of course submitted to bending, but also to a tensile membrane force N (Figure 3.32a) that can be largely influenced by the actual restraints of the supports (see Jones [80] for more details). As detailed Appendix B.2 (section B.2.2), it is assumed that the folding process has no effect on the structure ability to develop membrane forces, which means that N could theoretically reach a maximal value N_0 calculated for the initial T-shape cross-section (Figure 3.3).

With the model presented here above and considering the developments of Appendix B.2, the resistance $P_b(\delta)$ associated to the bending mechanism may be evaluated by following a similar procedure than for the global deforming mode (see section 3.6). It can be shown that:

$$P_b(\delta) = M_0 \frac{a_2(\xi_1 + \xi^*) + a_1(\xi_2 + \xi^*)}{a_1 a_2} \left(1 - \frac{N^2}{N_0^2} \right) + N \frac{a_1 + a_2}{a_1 a_2} (\delta - \delta^*) \quad (3.54)$$

$$\text{with: } N = \min \left(\frac{N_0^2}{2M_0} \frac{(a_1 + a_2)(\delta - \delta^*)}{a_2(\xi_1 + \xi^*) + a_1(\xi_2 + \xi^*)}; N_0 \right)$$

Of course, for $\delta = \delta^*$, it is obvious that $P_b = P^*$ in these equations. The evolution of the resistance $P_b(\delta)$ for the bending mechanism is depicted on Figure 3.32a.

3.4.2.3. Final resistance of the super-element

Finally, the super-element resistance $P(\delta)$ is found by combining $P_f(\delta)$ and $P_b(\delta)$. As long as $\delta < \delta^*$, then $P_f(\delta) < P^*(\delta)$, which means that the force applied by the vessel during the folding process is not yet sufficient to activate a beam mechanism. Consequently, the resistance is governed by $P_f(\delta)$ during this first phase. Nevertheless, when the penetration increases, creating new folds becomes more and more difficult for the ship. At this moment, the super-element is forced to deform like a beam and a three hinge mechanism if formed. The theoretical transition between the two modes occurs when $\delta = \delta^*$ and obviously, the resistance when $\delta > \delta^*$ is ruled by $P_b(\delta)$. In other words, the resistance is given by:

$$P(\delta) = P_f(\delta) \text{ if } \delta \leq \delta^* \quad \text{or} \quad P(\delta) = P_b(\delta) \text{ if } \delta > \delta^* \quad (3.55)$$

which is depicted on Figure 3.32a. As a final remark, it should be recalled that if the failure criteria is satisfied, then $P(\delta)$ has to be calculated by (3.52). Furthermore, all the previous developments are only valid as long as there is no contact between the striking vessel and one of the supports of the super-element. In this case, the resistance is no longer given by (3.55) but is set to zero because a super-element of type 3 is now involved in the analytical derivation. The corresponding formulae are therefore presented in section 3.5.

3.4.3. Numerical validation

In order to corroborate the analytical formulae derived here above, some finite element simulations were performed using LS-DYNA. As an example, the case of the horizontal girder with the properties reported in Table 3.5 is considered in this section. The impact scenario is non-symmetric, as $a_1 \neq a_2$. The material properties used for the numerical simulations are those previously listed in Table 3.2.

| | |
|-------|--------|
| h_w | 0.9 m |
| t_w | 0.02 m |
| h_f | 0.4 m |
| t_f | 0.02 m |
| a_1 | 1.5 m |
| a_2 | 2.5 m |

Table 3.5. Geometrical properties of the impacted element

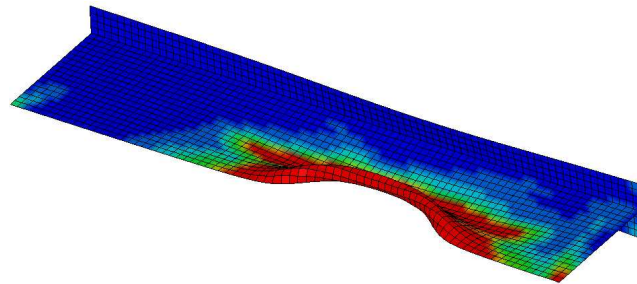


Figure 3.33. Equivalent plastic strain in the folded element

In an attempt to give a general insight on the deformed configuration obtained with LS-DYNA, the equivalent plastic strains have been reported on Figure 3.33. The purpose of this picture is only to show the agreement with the theoretical crushing process. Obviously, the folding pattern is not really similar to the one postulated on Figure 3.26, but it is worth bearing in mind that a ship with quite large dimensions is used for the numerical simulations, which is not exactly similar to a point load. Therefore, it is not surprising to have some differences with the analytical model.

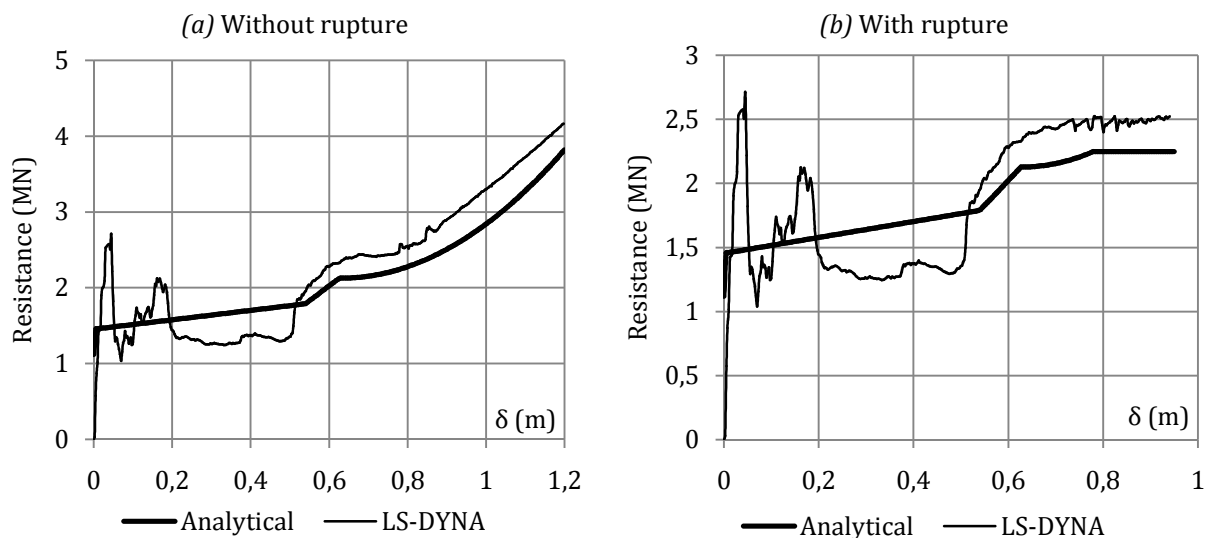


Figure 3.34. Comparison between the analytical and numerical results

The resistance curves are compared on Figure 3.34. In order to illustrate the need of accounting for the two mechanisms detailed in sections 3.4.2.1 and 3.4.2.2, a first simulation is run in which rupture is disregarded. The LS-DYNA curve reported on Figure 3.34a clearly shows that there is a modification of the girder behavior when δ is more or less equal to 0.7 m . In fact, the slope modification can be explained by the important membrane straining that takes place if failure is not considered. In the analytical model, this precisely corresponds to the transition from the folding to the bending mechanism, which is theoretically predicted to occur for $\delta^* = 0.63\text{ m}$. This value is quite close to the 0.7 m found by LS-DYNA.

The influence of rupture is investigated in a second simulation. The failure strain ϵ_r is calculated in accordance with (3.37). As the element length and thickness are respectively $l_e = 0.05\text{ m}$ and $t_e = 0.02\text{ m}$, a value of 27 % is used for ϵ_r . The critical strain ϵ_c to be considered in the theoretical model is found to be more or less equal to 12 %. Of course, this value is not only based on the results presented on Figure 3.34b. It is derived by adjusting the analytical and numerical curves for many other simulations with different mesh sizes. $\epsilon_c = 12\%$ corresponds to a mean value that allows for a reasonable failure prediction in almost all the cases.

Furthermore, when rupture is taken into account, it appears from Figure 3.34b that the membrane straining depicted on Figure 3.34a does not appear. This is not surprising, as the concertina tearing prohibits the development of axial forces in the bending mechanism, which is also reflected by the theoretical curve.

As a final remark, it can be concluded that the good agreement between the results of Figure 3.34 corroborates the analytical model presented in section 3.4.2 for the second type of super-element.

3.5. Local resistance for super-elements of type 3

The third type of super-element to consider is directly related to collisions occurring on intersections between a horizontal girder and a vertical frame (Figure 3.11c). This situation may appear in the case of a direct impact (Figure 3.35a) or because of a subsequent contact with one of the supports of a SE2 (Figure 3.35b). According to their location on the gate, these intersections may have three or four wings and are respectively designated by T or X-shaped elements. In the local deforming mode, these latter are known to be crushed axially through a folding process (see section 3.5.2).

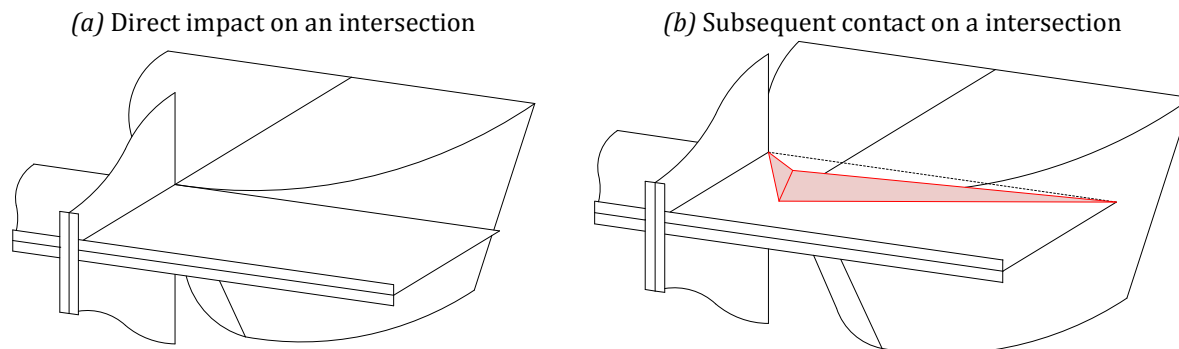


Figure 3.35. Impact on the intersection between a frame and a girder

3.5.1. Literature review

In the literature, many authors investigated the axial crushing resistance of plated structure by applying the upper-bound method. Since the primary developments of Alexander [5], this problem has been revisited by Wierzbicki and Abramowicz [168], Amdahl [8] or Yang and Caldwell [174] amongst others. They developed simplified formulae to estimate the resistance of L, T or X-shaped elements by postulating various crushing mechanisms.

Abramowicz [1] also derived theoretical formulae for T-shaped sections by assuming symmetric and asymmetric deformation patterns. Based on these researches, Paik and Wierzbicki [123] proposed generalized equations by combining various kinematically admissible collapse modes. Additional developments on this topic were also performed by Wang and Ohtsubo [165], who slightly modified the crushing mechanisms of Yang and Caldwell [174] for L, T and X elements.

In the purpose of evaluating the resistance of offshore platforms to vessel impacts, Amdahl [8] suggested to use a straight edge crushing mechanism combined to a folding process. This pioneer work was later used by Paik and Pedersen [119] to estimate the ultimate strength of plated structures. Zhang [180] also extended these results to evaluate the crushing resistance of intersections during ship-ship collisions.

To conclude this brief literature review, it is worth mentioning that an extensive summary of many existing methods was performed by Yamada and Pedersen [173] in the optic of analyzing the axial crushing of bulbous bows.

3.5.2. Analytical derivation

The first part of the analytical derivation of the local resistance for this third type of super-element concerns an impact occurring directly on an intersection (Figure 3.35a). For

conciseness, the case of a subsequent contact on the support of a SE2 (Figure 3.35b) is treated in Appendix B.3, but the developments are quite similar to those presented here.

3.5.2.1. Folding mechanism

As illustrated on Figure 3.36, experimental investigations of impacts on intersections have shown that these latter were crushed axially during the collision process [8]. The deformation pattern depicted on Figure 3.37a is therefore postulated in the optic of applying the upper-bound theorem. It is worth mentioning that for convenience, only two wings are represented on Figure 3.37a, but three or four wings may be involved in the crushing process for T or X-shaped intersections respectively.

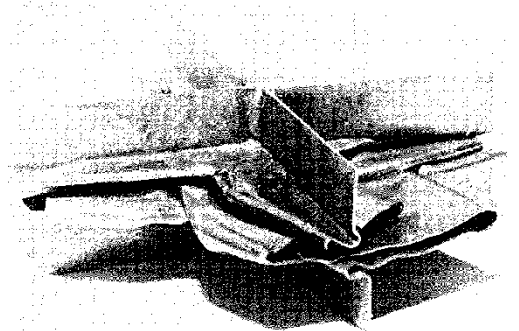


Figure 3.36. Complete axial crushing of a X-shaped intersection [8]

The purpose of this section is to derive the local resistance for such a plastic mechanism. As the analytical developments are strictly similar for all the wings involved in the deformation pattern, only a horizontal one will be considered so far (Figure 3.37a). This latter has a length denoted by a and is decomposed into two different parts numbered ① and ② respectively.

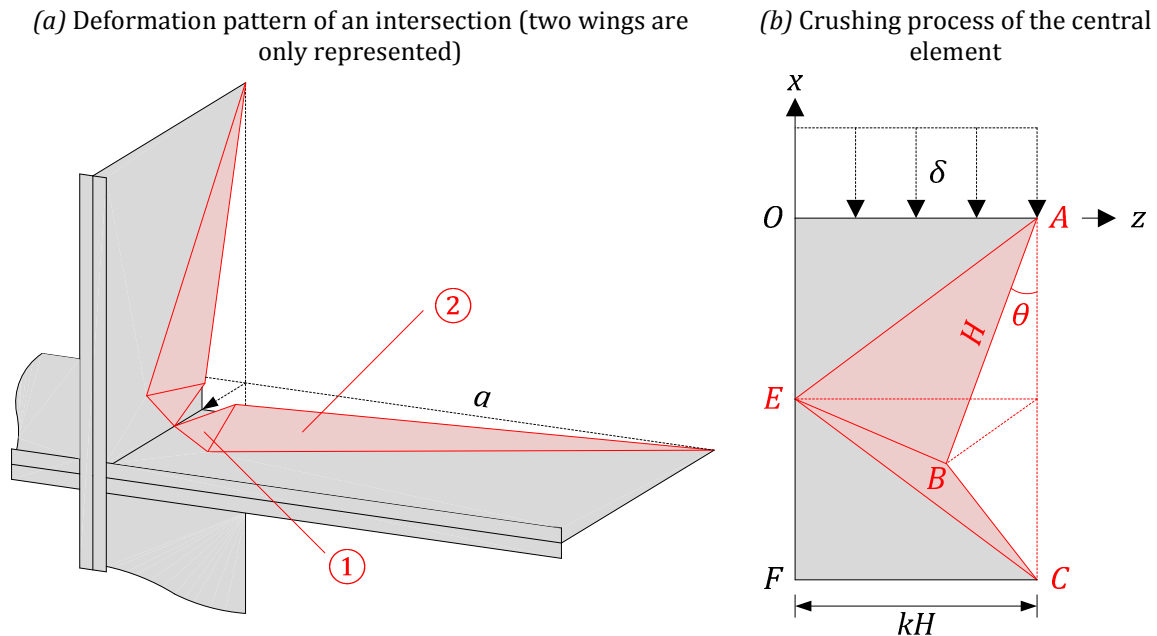


Figure 3.37. Folding mechanism in the case of an impact occurring directly on an intersection

The resistance $P_w(\delta)$ opposed by the wing during the crushing process can be obtained by summing up the individual contributions $P_1(\delta)$ and $P_2(\delta)$ associated to part ① and ②. As $P_2(\delta)$ may be obtained by using the developments of section 3.4.2.1, only $P_1(\delta)$ still needs to be evaluated. To do so, the deformation pattern depicted on Figure 3.37b can be considered for part ①. It is made of two triangles ABE and BCE that are submitted to a membrane

extension and rotate around the plastic hinges AB , BC , EB , AE and EC . During this movement, the distances \overline{AB} and \overline{BC} are constant and equal to their initial value denoted by H , while the two remaining surfaces OAE and EFC simply follow an axial compressive motion. The horizontal length of part ① is assumed to be proportional to the folding height $2H$ and is designated by αH , where α is a coefficient determined hereafter.

The resistance opposed by this plastic mechanism has been evaluated by Amdahl [8]. Nevertheless, combining these results with those obtained in 3.4.2.1 for the remaining part of the wing is not straightforward on a theoretical point of view. Indeed, in order to evaluate $P_2(\delta)$, the displacement field of Figure 3.28 is postulated, from which it is evident that the main part of the membrane dissipation is produced in the area near the edges AB and BC . However, in the derivation performed by Amdahl [8], these latter are precisely supposed to move rigidly during the plastic rotations around the hinges, which is in apparent contradiction with the developments of section 3.4.2.1. Consequently, in order to be consistent with Figure 3.28, it is required to consider another displacement field than the one used in [8]. Doing so is not conflicting with the upper-bound method, provided that the compatibility requirements and the kinematic conditions are respected. Of course, this leads a formula for $P_1(\delta)$ that is different from the one given in [8].

As the derivation of the contribution $P_1(\delta)$ opposed by part ① during the plastic collapse is similar to the procedure followed in 3.4.2.1, it is not detailed here but is reported in Appendix B.3 (section B.3.1). It is found that:

$$P_1(\delta) = \frac{n_0 H}{\sqrt{6}} \hat{G}(\theta) + m_0 \pi \left(\sqrt{\alpha^2 + 1} + \frac{\alpha}{6} + \frac{2}{5} \right) \quad (3.56)$$

where $\hat{G}(\theta)$ is a function defined by (B.37), $\alpha = 0.8601$ and θ is the opening angle (Figure 3.37b) related to the indentation δ by (3.42). This result can be compared to the solution proposed by Amdahl [8]:

$$P_1(\delta) = \frac{n_0 \alpha H}{\sqrt{3}} \left(1 + \frac{\cos \theta}{\alpha} \sqrt{\frac{4\alpha^2 + 1}{4\alpha^2 + \sin^2 2\theta}} \right) + \frac{m_0 \pi}{2} (2\alpha + 1) \quad (3.57)$$

in which α is this time equal to 0.573. In the two previous formulae, the optimal value of H is determined by minimizing the mean value of $P_w(\delta)$. This achieved in Appendix B.3 (section B.3.1.2), where it is found that:

$$H = \sqrt{3\pi/8at_w} \quad (3.58)$$

In this last equation, t_w is the web thickness of the horizontal wing. It can be shown that (3.58) is very close to the expression proposed by Amdahl [8]. Therefore, it could be interesting to have an idea of the difference on $P_1(\delta)$ when using (3.56) or (3.57). As an example, it is proposed to consider the following values for the parameters involved in these formulae: $\sigma_0 = 240 \text{ MPa}$, $t_p = 0.01 \text{ m}$ and $a = 2 \text{ m}$. The corresponding curves are plotted on Figure 3.38, from which it can be seen that the difference of the present approach with the one followed by Amdahl [8] is very small.

Regarding the resistance $P_2(\delta)$ opposed by part ② during the plastic collapse, the developments performed in section 3.4.2.1 are still valid but some adaptations need to be done. As explained in section B.3.1.2 of Appendix B.3, $P_2(\delta)$ can be evaluated by:

$$P_2(\delta) = \frac{m_0(a - \alpha H)\pi}{H} + \frac{n_0 H}{2(a - \alpha H)}(\delta + 2H) \quad (3.59)$$

The resistance $P_w(\delta)$ of one wing is then obtained by summing up $P_1(\delta)$ and $P_2(\delta)$. Therefore, gathering (3.56) and (3.59) leads to:

$$P_w(\delta) = m_0\pi \left(\sqrt{\alpha^2 + 1} + \frac{\alpha}{6} + \frac{2}{5} + \frac{a - \alpha H}{H} \right) + n_0 H \left(\frac{\hat{G}(\theta)}{\sqrt{6}} + \frac{\delta + 2H}{2(a - \alpha H)} \right) \quad (3.60)$$

where $\alpha = 0.8601$, $\hat{G}(\theta)$ is a function defined by (B.37) and H is calculated in accordance with (3.58).

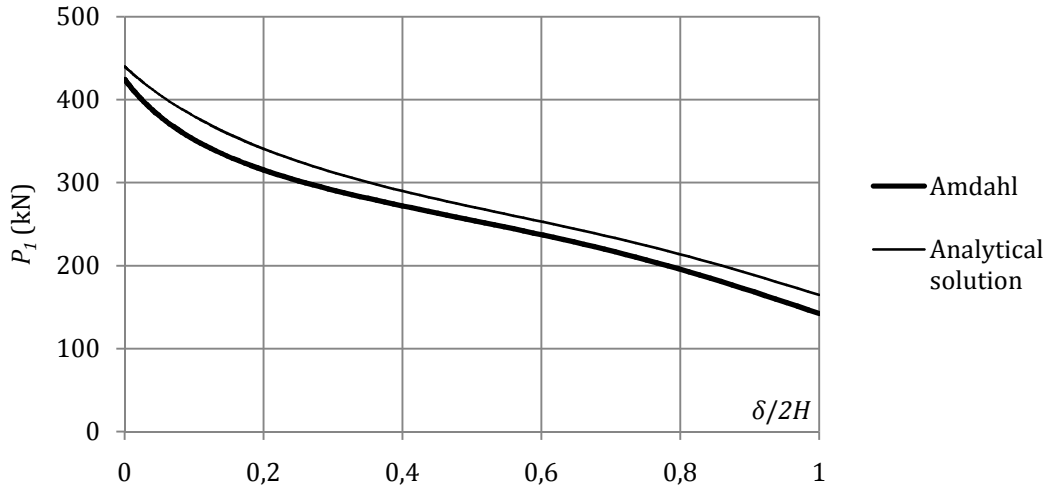


Figure 3.38. Crushing resistance of an intersection according to Amdahl and the present solution

It is important to mention that formula (3.60) is valid as long as $0 \leq \delta \leq 2H$. As in section 3.4.2.1, for $\delta > 2H$, (3.60) can be generalized by assuming that a new fold is created with the same pattern than the one represented on Figure 3.37b. As soon as part ① is completely crushed, it is clear that it does not provide any contribution to the resistance. Therefore, if k is the current fold number, $P_1(\delta)$ is still given by (3.56), but (3.42) is no more valid to evaluate θ as δ should be replaced by $\delta - 2(k - 1)H$ in this relation, i.e.:

$$\theta = \arccos \left(k - \frac{\delta}{2H} \right) \quad (3.61)$$

The situation is not the same for part ② because it should be accounted for the additional contributions coming from the $k - 1$ folds already completely closed. This can be achieved simply by adapting the developments performed in Appendix B.2. Doing so leads to:

$$P_w(\delta) = m_0\pi \left(\sqrt{\alpha^2 + 1} + \frac{\alpha}{6} + \frac{2}{5} + \frac{a - \alpha H}{H} \right) + n_0 H \left(\frac{\hat{G}(\theta)}{\sqrt{6}} + \frac{\delta(4k - 3) + 2kH(3 - 2k)}{2(a - \alpha H)} \right) \quad (3.62)$$

Of course, the previous formula is valid as long as the wing is not completely crushed. In this case, the maximal fold number n is reached and for $\delta > 2nH$ and equation (3.62) becomes:

$$P_w(\delta) = m_0\pi \left(\sqrt{\alpha^2 + 1} + \frac{\alpha}{6} + \frac{2}{5} + \frac{a - \alpha H}{H} \right) + n_0 H \frac{\hat{G}(\theta)}{\sqrt{6}} + \frac{2n_0 n^2 H^2 + \sigma_0 A_n (\delta - 2nH)}{2(a - \alpha H)} \quad (3.63)$$

where A_n has the same meaning than in section B.2.1. Finally, the total resistance $P_f(\delta)$ for the crushing of T or X-shaped intersections is simply found by adding the individual

contributions (3.62) or (3.63) coming from the three or four wings. It is worth noticing that if these latter do not have the same length a and web thickness t_w , the value of H calculated by (3.58) will not be the same for each of them. However, in order to respect the compatibility along the super-element axis, a unique value is strictly required.

On a theoretical point of view, this one has to be derived by minimizing the mean total resistance \bar{P}_f , but doing so is not very practical. Consequently, a most convenient way is to take H as the average of all the folding heights calculated individually for each wing. By so doing, the parameter k involved in (3.61) and (3.62) is still obtained by (B.23), in which H is actually this mean value. Similarly, (B.23) is also valid to evaluate the maximal number of folds n , but the meaning of h_w is different. Indeed, if the web heights are not the same for each wing⁴, then h_w has to be taken as the minimum value between all of them.

3.5.2.2. Bending mechanism

Apart from the folding mechanism described here above, it is not reasonable to suppose that there is no other way for the super-element to oppose a local resistance. Indeed, this could only be the case for very deep intersections, such as those between the decks and the transverse bulkhead of a ship. In the present situation, as the web heights are quite short, a beam-like behavior is recovered after an indentation δ^* for which the whole intersection starts moving backward (Figure 3.39).

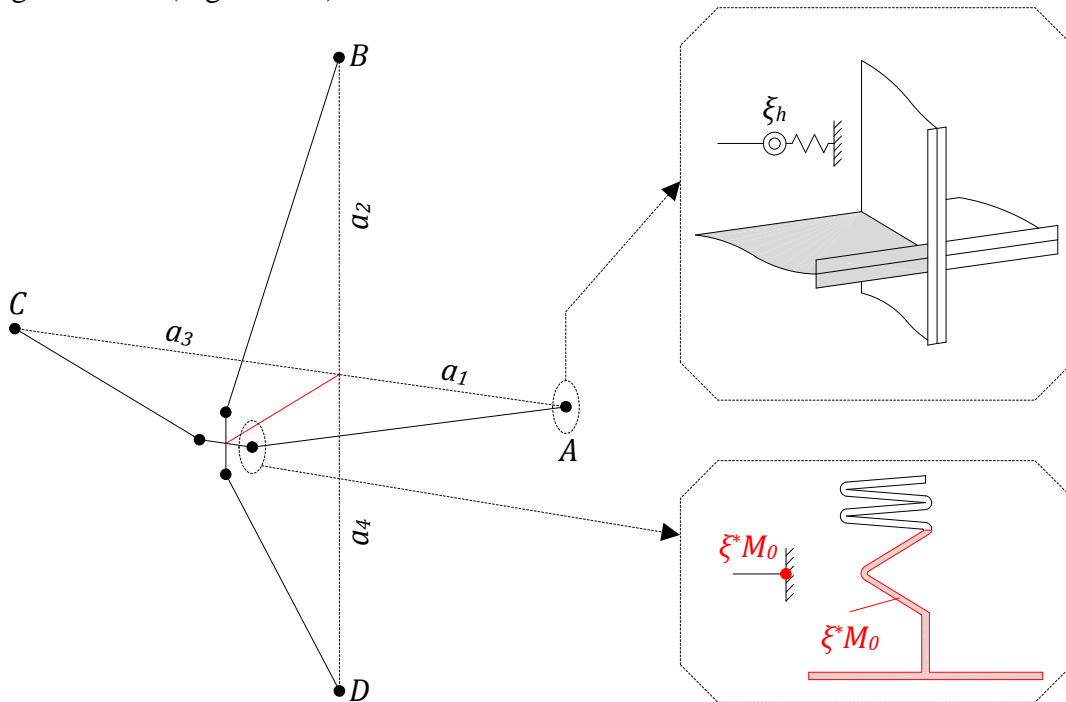


Figure 3.39. Bending mechanism in the case of an impact occurring directly on an intersection

As an example, the cruciform intersection between a horizontal girder and a vertical frame is considered in this section. As depicted on Figure 3.39, eight plastic hinges are required to activate the mechanism. Four of them are located at the center of the super-element, while the remaining ones simply lie at the boundaries. Denoting by M_h and M_v the respective plastic bending capacities of the girder and the frame, for similar reasons than the ones detailed in section 3.4.2.2, only the reduced values $\xi_h M_h$ and $\xi_v M_v$ can be reached at the supports A, B, C, D (Figure 3.39). Similarly, regarding the four central plastic hinges, the maximal bending

⁴ This situation may appear at the junction between a horizontal girder and a vertical frame for example.

moments at these locations are only equal to $\xi_h^*(\delta)M_h$ and $\xi_v^*(\delta)M_v$ because the sections have already been indented over a distance δ^* during the folding phase. More details on this topic can be found in Appendix B.3 (section B.3.1.3).

By applying the plastic theory of beams, it is possible to evaluate the force $P^*(\delta)$ that is required to activate the bending phase. Its derivation is partly reported in Appendix B.3, where it is shown that:

$$P^*(\delta) = M_h \left(\frac{\xi_h + \xi_h^*(\delta)}{a_1 - \alpha H} + \frac{\xi_h + \xi_h^*(\delta)}{a_2 - \alpha H} \right) + M_v \left(\frac{\xi_v + \xi_v^*(\delta)}{b_1 - \alpha H} + \frac{\xi_v + \xi_v^*(\delta)}{b_2 - \alpha H} \right) \quad (3.64)$$

Here again, the transition from the folding to the bending process takes place at a particular value δ^* of the penetration for which $P_f(\delta)$ is equal to $P^*(\delta)$, as depicted on Figure 3.32a.

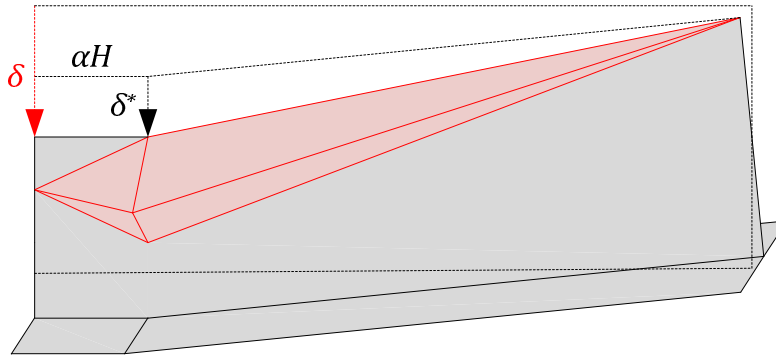


Figure 3.40. Beam-like behavior of one wing

For $\delta > \delta^*$, each of the four wings represented on Figure 3.39 is submitted to a plastic rotation in the central and support hinges, but also to an axial straining (Figure 3.40). As detailed in Appendix B.3, the resistance $P_b(\delta)$ for the bending mechanism is given by:

$$P_b(\delta) = \left(M_h(\xi_h + \xi_h^*) \left(1 - \frac{N_1^2}{N_h^2} \right) + N_1(\delta - \delta^*) \right) \frac{a_1 + a_2 - 2\alpha H}{(a_1 - \alpha H)(a_2 - \alpha H)} + \left(M_v(\xi_v + \xi_v^*) \left(1 - \frac{N_2^2}{N_v^2} \right) + N_2(\delta - \delta^*) \right) \frac{b_1 + b_2 - 2\alpha H}{(b_1 - \alpha H)(b_2 - \alpha H)} \quad (3.65)$$

$$\text{with: } N_1 = \min \left(\frac{N_h^2(\delta - \delta^*)}{2M_h(\xi_h + \xi_h^*)}; N_h \right) ; N_2 = \min \left(\frac{N_v^2(\delta - \delta^*)}{2M_v(\xi_v + \xi_v^*)}; N_v \right)$$

where N_1 and N_2 are the normal forces in the horizontal and vertical wings respectively. In the previous formulae, it is worth noticing that the parameters ξ_h^* and ξ_v^* are evaluated for $\delta = \delta^*$, i.e. when the transition from the folding to the bending mechanism occurs. Furthermore, as discussed in Appendix B.3, it should be noted that (3.65) is only applicable to cruciforms and is not strictly valid for T-shaped intersections.

3.5.2.3. Final resistance of the super-element

The final resistance $P(\delta)$ for this third type of super-element can be obtained by combining $P_f(\delta)$ and $P_b(\delta)$ in accordance with (3.55). Doing so is only valid as long as there is no failure in the material. From numerical simulations, it transpires that rupture (Figure 3.41) mainly occurs because of an important tensile tearing which appears along the supports. As

postulated for the analytical derivation of section 3.5.2.2, this is simply due to the membrane straining developing in the wings for large penetrations.

As it was done for the two previous types of super-elements, failure is included in this simplified approach by defining a critical strain ϵ_c . In the present case, for most of the numerical simulations, a value of 12 % is found to be quite convenient but it should be mentioned that a convergence on the failure criteria was rather difficult to obtain. This is mainly due to the fact that the elements located near the intersection axis are strongly deformed during the impact. Therefore, the rupture modeling is highly sensitive to the mesh size and quite small elements are required to reach a more or less satisfactory convergence. Of course, for all the simulations, the rupture strain is chosen by applying (3.37), which leads to quite important values.

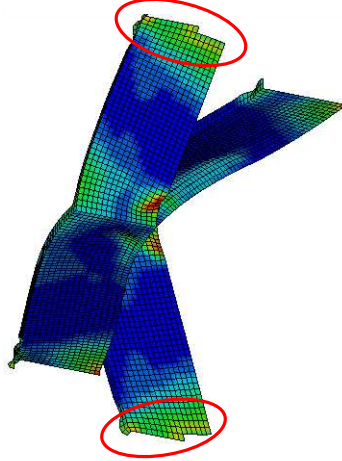


Figure 3.41. Failure mode during the denting or bending process

The post-failure resistance may be evaluated as follows. If the critical strain ϵ_c is reached during the crushing phase, then the contribution of the wing is restricted to the bending part of (3.62) or (3.63) because it is postulated that there are no membrane effects anymore, i.e.:

$$P_w(\delta) = m_0\pi \left(\sqrt{\alpha^2 + 1} + \frac{\alpha}{6} + \frac{2}{5} + \frac{a - \alpha H}{H} \right) \quad (3.66)$$

On the other hand, if rupture develops during the bending mechanism, then the contributions of the wings where failure takes place have to be ignored in (3.65). Nevertheless, adapting this equation is not straightforward, as it should be accounted for some particularities regarding the normal forces. As an example, let us assume that a tensile tearing appears at point *A* on Figure 3.39. N_1 has then to be set to zero as there are no more membrane effects in the horizontal wings. There is only a bending dissipation at point *C* and rupture may now occur at this support because of an excessive rotation, so we have:

$$P_b(\delta) = \frac{M_h(\xi_h + \xi_h^*)}{a_1 - \alpha H} + \left(M_v(\xi_v + \xi_v^*) \left(1 - \frac{N_2^2}{N_v^2} \right) + N_2(\delta - \delta^*) \right) \frac{b_1 + b_2 - 2\alpha H}{(b_1 - \alpha H)(b_2 - \alpha H)} \quad (3.67)$$

3.5.3. Numerical validation

3.5.3.1. Impact on a X-shaped intersection

In the optic of checking if the results obtained from the analytical developments detailed here above are more or less realistic, numerical simulations were performed with LS-DYNA. As an example, the impact on a cruciform is considered here. The geometrical dimensions of the

horizontal and vertical wings are listed in Table 3.6, from which it can be seen that the intersection is doubly symmetric, as $a_1 = a_2$ and $b_1 = b_2$. The frame and the girder have nearly the same cross-section, the only difference is coming from the flange width.

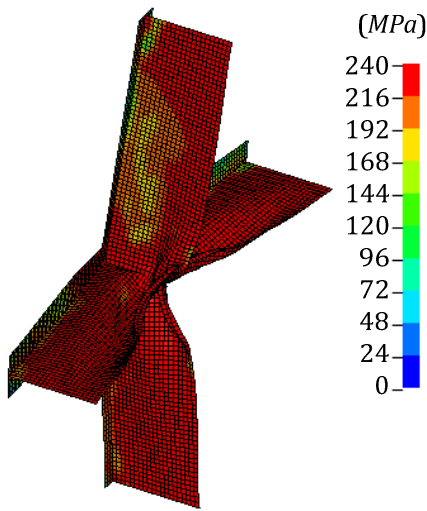


Figure 3.42. Von Mises stresses in the impacted cruciform (for $\delta = 0.9\text{ m}$)

| Horizontal wings | | |
|------------------|------------------------|------------------------|
| Length | $a_1 = 2.6\text{ m}$ | $a_2 = 2.6\text{ m}$ |
| Web height | $h_w = 1\text{ m}$ | $h_w = 1\text{ m}$ |
| Web thickness | $t_w = 0.015\text{ m}$ | $t_w = 0.015\text{ m}$ |
| Flange width | $h_f = 0.5\text{ m}$ | $h_f = 0.5\text{ m}$ |
| Flange thickness | $t_f = 0.015\text{ m}$ | $t_f = 0.015\text{ m}$ |
| Vertical wings | | |
| Length | $b_1 = 3\text{ m}$ | $b_2 = 3\text{ m}$ |
| Web height | $h_w = 1\text{ m}$ | $h_w = 1\text{ m}$ |
| Web thickness | $t_w = 0.015\text{ m}$ | $t_w = 0.015\text{ m}$ |
| Flange width | $h_f = 0.3\text{ m}$ | $h_f = 0.3\text{ m}$ |
| Flange thickness | $t_f = 0.015\text{ m}$ | $t_f = 0.015\text{ m}$ |

Table 3.6. Geometrical properties characterizing the horizontal and vertical wings of the cruciform

The material properties used for the present finite element analysis are those listed in Table 3.2. However, failure having already been discussed above, ϵ_r is not considered for this simulation. Doing so, the major advantage is to clearly point out the developments of membrane effects for large penetrations. This is already visible on Figure 3.42 showing the equivalent Von Mises stresses in the impacted structure. It transpires from this picture that the stress field is nearly uniform and equal to $\sigma_0 = 240\text{ MPa}$, which simply means that due to membrane straining, the axial tensile capacities N_v and N_h are reached in the vertical and horizontal wings. Furthermore, it also appears from Figure 3.42 that the folding and bending collapse mechanisms respectively presented in sections 3.5.2.1 and 3.5.2.2 are indeed activated during the collision process.

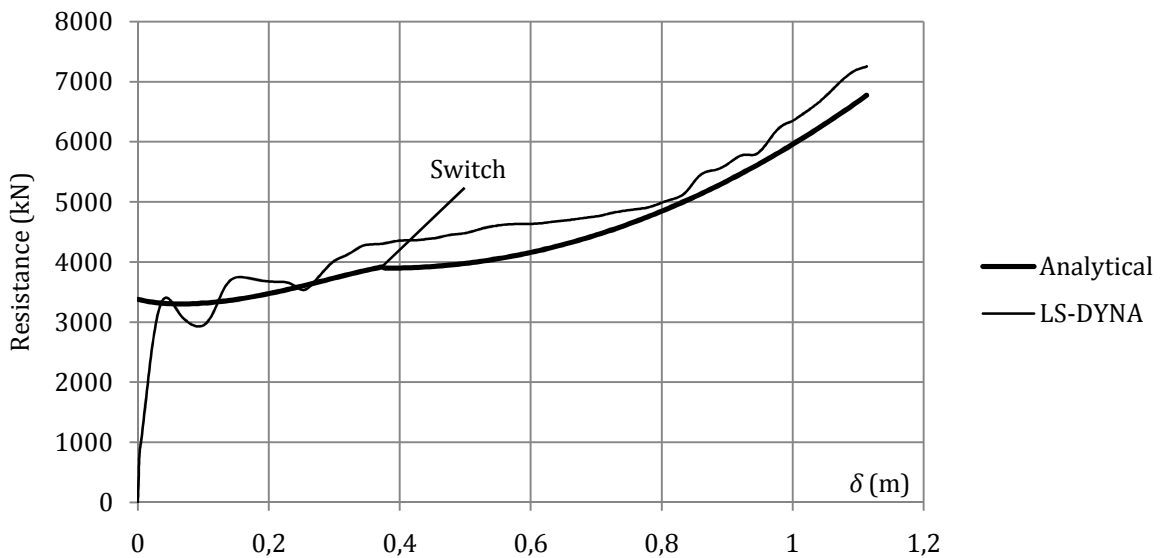


Figure 3.43. Comparison between the analytical and numerical results for a X-shaped intersection

The numerical and analytical resistances are compared on Figure 3.43. Considering the results obtained with LS-DYNA, it can be observed that the curve is made of three different parts. For

$\delta \leq 0.3 \text{ m}$, the resistance is more or less constant because this phase is associated to the plastic folding of the four wings. For $0.3 < \delta \leq 0.8 \text{ m}$, the beam-like deforming mode is activated and the cruciform starts moving as a whole. During this phase, the small increase can be imputed to predominant bending effects. For $\delta > 0.8 \text{ m}$, the curve grows more rapidly because strong the membrane forces are now developing in the structure. Obviously, if rupture had been considered in the model, this would not be the case.

The analytical resistance also reflects this three-phase behavior. In this simplified approach, the switch from the folding to the bending mechanism is found to take place for $\delta^* = 0.37 \text{ m}$, which explains why a slope discontinuity occurs for this particular value of the penetration. This is more or less in agreement with what is observed from the finite element simulation.

3.5.3.2. Impact on a T-shaped intersection

As detailed in Appendix B.3 (section B.3.1.3), in the case of a T-shaped intersection, the development of large membrane forces in the vertical wing is prohibited because the horizontal girders usually do not have sufficient shear stiffness. In the purpose of validating the analytical resistance predicted by (B.62) for these particular intersections, it could be interesting to perform comparisons with numerical solutions given by LS-DYNA.

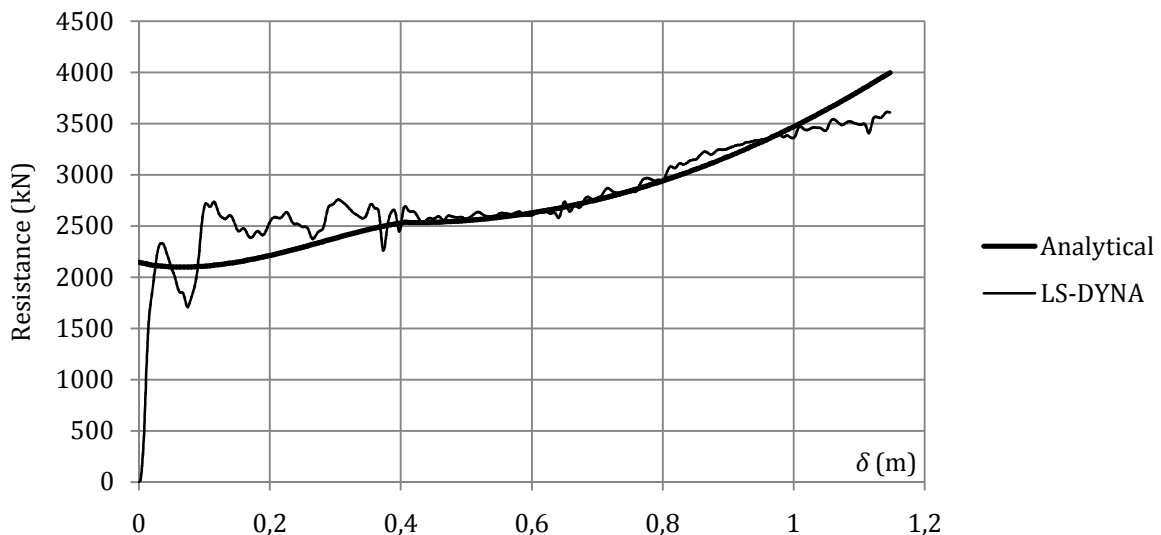


Figure 3.44. Comparison between the analytical and numerical results for a T-shaped intersection

To do so, the upper wing of the cruciform considered here above (Figure 3.42) has been removed in order to transform it into a T-shaped intersection. The material and geometrical properties respectively listed in Table 3.2 and in Table 3.6 are kept unchanged. Here again, the simulation is run without considering rupture.

The results are reported on Figure 3.44, from which it can be seen that the agreement is satisfactory. In comparison with Figure 3.43, it can be stated that the three-phase behavior discussed previously is also valid in the present case, but it can be noted that the development of the membrane forces is not as important than for a cruciform. Of course, this can be explained by the fact that one wing is missing, but also because the axial straining is reduced in the vertical part.

3.6. Resistance in the global deforming mode

When the gate exhibits an overall bending motion (Figure 3.9), the main difference with the developments performed so far for the local deforming mode is coming from the elastic phase that is not necessarily negligible. Indeed, when developing super-elements, it is reasonable to postulate a rigid-plastic material because the deformations are localized and increase therefore rapidly. Nevertheless, in the present case, this assumption is not valid anymore, so the derivation of the global resistance has to be done in two steps, by distinguishing between the elastoplastic and rigid-plastic regimes.

3.6.1. General procedure

Before starting the analytical evaluation of the global resistance, it is necessary to give more precisions about the procedure that will be followed. This is particularly true for the definition of the equivalent mechanical model of the gate, but it is also required to provide some details on the way to combine the local and global components to get the total resistance $P(\delta)$.

3.6.1.1. Mechanical model

The mechanical model for the global deforming mode has already been discussed in section 3.2.2.2. As this topic is not really reported in the literature, it is mainly based on observations coming from numerical simulations. The only paper providing some information is the one written by Le Sourne et al. [99], where the global dissipation is treated by dividing the gate into a set of horizontal beams and postulating an overall plastic mechanism. The same procedure is followed in the present section and therefore, in accordance with Figure 3.12, the structure is divided into a set of horizontal beams obtained by combining the gross cross-section of the girders with a collaborating portion of the plating. According to Paik and Thayamballi [121], this latter has to be derived by accounting for the following phenomena:

- The shear-lag effect occurring at the junction between the plating and the web of the horizontal girders. This is mainly due to the action of lateral loads and out-of-plane bending that are responsible for a non-uniform stress distribution in wide flanged beams.
- The buckling of plate elements under predominantly axial compressive forces that also results in a non-uniform stress distribution. As depicted on Figure 3.45, two different situations may be of interest: (a) an overall buckling of the stiffened panel located between two girders or (b) a local instability of the plating between two stiffeners.

Paik [121] suggested some practical formulae to evaluate the effective widths $b_{\text{eff},1}$ and $b_{\text{eff},2}$ (Figure 3.45) on both sides of each horizontal girders. According to Eurocode 3 [52], the procedure is much more difficult because there are many others instabilities to consider. For example, one should also account for a column type buckling of the plating together with the stiffeners, which leads to a very cumbersome method. On a practical point of view, it is not of prior importance to have a precise calculation of the effective width because the present approach dealing with the global deforming mode of the gate is already quite approximate.

Another simplification is also introduced here, as the derivation of $b_{\text{eff},1}$ and $b_{\text{eff},2}$ does not lead to the same values if the stiffening configurations are not the same on both sides of the girders. This causes the resulting cross-section to be asymmetric, which is not convenient for the beam plastic theory. Consequently, to work with a conventional symmetric I-shaped

cross-section (Figure 3.45), the collaborating portion of the plating is characterized by an equivalent height given by:

$$h_{eq} = 2 \min(b_{eff,1}; b_{eff,2}) \quad (3.68)$$

which is conservative. On the contrary, it should be mentioned that the hypothesis made by Le Sourne et al. [99] of a fully effective cross-section may be too optimistic, in particular if there is a large distance between two successive girders.

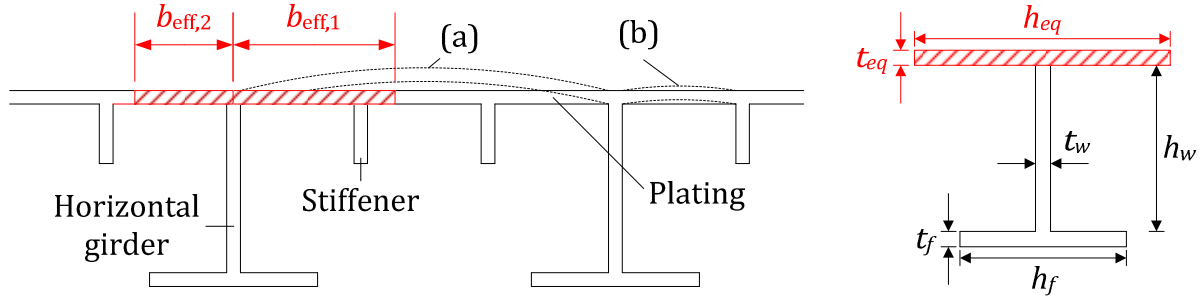


Figure 3.45. Calculation of the effective width

As a final result, accounting for the hypotheses presented in section 3.2.2.2, the beam located at a level Y_i with the above-mentioned properties can be modeled as depicted on Figure 3.46. It is assumed to be simply supported at its two extremities, which means that the rotational restraint provided by the torsional stiffness of the vertical frames is neglected. Furthermore, if these latter are weaker than the girders, it can be postulated that they simply follow the overall out-of-plane displacements $u(Y_i, Z)$ imposed by the beams. The only roles of the frames are then to prevent the lateral torsional buckling and limit the in-plane displacements $w_1(Y_i)$ and $w_2(Y_i)$.

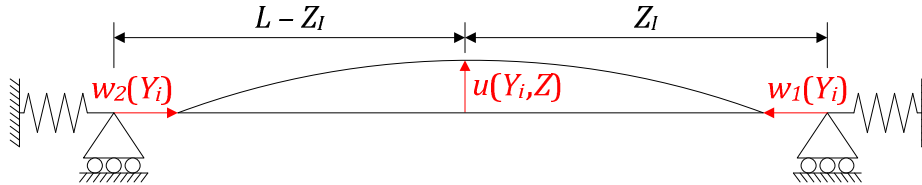


Figure 3.46. Equivalent mechanical model of a beam

The model depicted on Figure 3.46 will be used to evaluate the individual resistance $P_i(\delta)$ characterizing each of the beam constituting the gate in the global deforming mode.

3.6.1.2. Combination of the local and global resistances

A first idea to calculate the penetration δ_t for which there is a switch from the local to the global deforming mode occurs when $P_L(\delta)$ reaches a sufficient value $P_t(\delta)$ that is required to activate an overall collapse mechanism over the gate (Figure 3.9). For consistency, as $P_L(\delta)$ is derived in the plastic regime, this should also be the case for $P_t(\delta)$. Therefore, similarly to what has been done for the transition between the folding and bending mechanisms in SE2 or SE3, one could simply derive the total resistance $P(\delta)$ in the following manner:

- If $\delta \leq \delta_t$: $P(\delta) = P_L(\delta) \rightarrow$ Local deforming mode
- If $\delta > \delta_t$: $P(\delta) = P_G(\delta) \rightarrow$ Global deforming mode

$$(3.69)$$

which may be illustrated by the curves depicted on Figure 3.47a. Nevertheless, this approach is not really appropriate because it transpires from numerical simulations that before reaching a full plastic state and activating the global deforming mode (i.e. for $\delta \leq \delta_t$), the local

crushing process develops concomitantly with a limited elastoplastic overall bending motion of the gate. In other words, accounting only for $P_L(\delta)$ when $\delta < \delta_t$ could lead to an unsafe evaluation of the resistance. For this reason, (3.69) must be adapted by performing a rigid-plastic derivation of $P_G(\delta)$ when $\delta > \delta_t$, but also an elastoplastic evaluation of $P_G(\delta)$ when $\delta \leq \delta_t$. Doing so, instead of using (3.69) to obtain the gate resistance, the subsequent formula is suggested:

- If $\delta \leq \delta_t$: $P(\delta) = \min(P_L(\delta) ; P_G(\delta)) \rightarrow$ Local deforming mode
 - If $\delta > \delta_t$: $P(\delta) = P_G(\delta) \rightarrow$ Global deforming mode
- (3.70)

which corresponds to the situation of Figure 3.47b. For clarity, the procedure to combine the local resistance $P_L(\delta)$ with the global one $P_G(\delta)$ is also summarized on Figure 3.48.

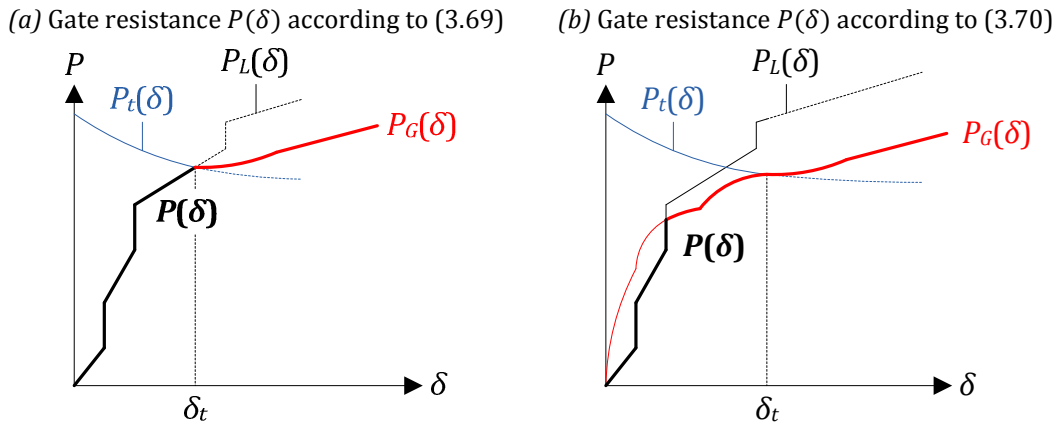


Figure 3.47. Calculation of the gate resistance

The only parameters that are still unknown to apply (3.70) are the global resistance $P_G(\delta)$ and the force $P_t(\delta)$ required to activate an overall plastic mechanism over the gate. As mentioned earlier, the derivation of $P_G(\delta)$ has to be done in both the elastoplastic (if $\delta \leq \delta_t$) and rigid-plastic (if $\delta > \delta_t$) domains.

Finding an elastoplastic solution for $P_G(\delta)$ is however not straightforward, the main difficulty being to account for the influence of the crushing process during this phase. To solve this problem, it is proposed to evaluate $P_G(\delta)$ by applying equation (3.5), where the individual resistances $P_i(\delta)$ are calculated by following the subsequent steps:

- 1) For a given kinematically admissible displacement field (Figure 3.49b), the elastic bending theory of beams is first used to evaluate $P_i(\delta)$, as detailed in section 3.6.2.
- 2) This solution is only valid as long as there is no plastic collapse of beam i , which occurs when $P_i(\delta)$ reaches a certain level $P_{t,i}(\delta)$.
- 3) An elastoplastic solution for beam i is then simply found by taking the minimum value between $P_i(\delta)$ and $P_{t,i}(\delta)$.
- 4) Of course, if there is a simultaneous indentation of beam i due to the local crushing process, $P_i(\delta)$ and $P_{t,i}(\delta)$ have to be derived by considering that the cross-section is not fully efficient.

Applying the following procedure leads to a coupled elastoplastic evaluation of $P_G(\delta)$ for $\delta \leq \delta_t$. Regarding the rigid-plastic solution, there is no real difficulty because a lot of theoretical results are already available on this topic (see section 3.6.3).

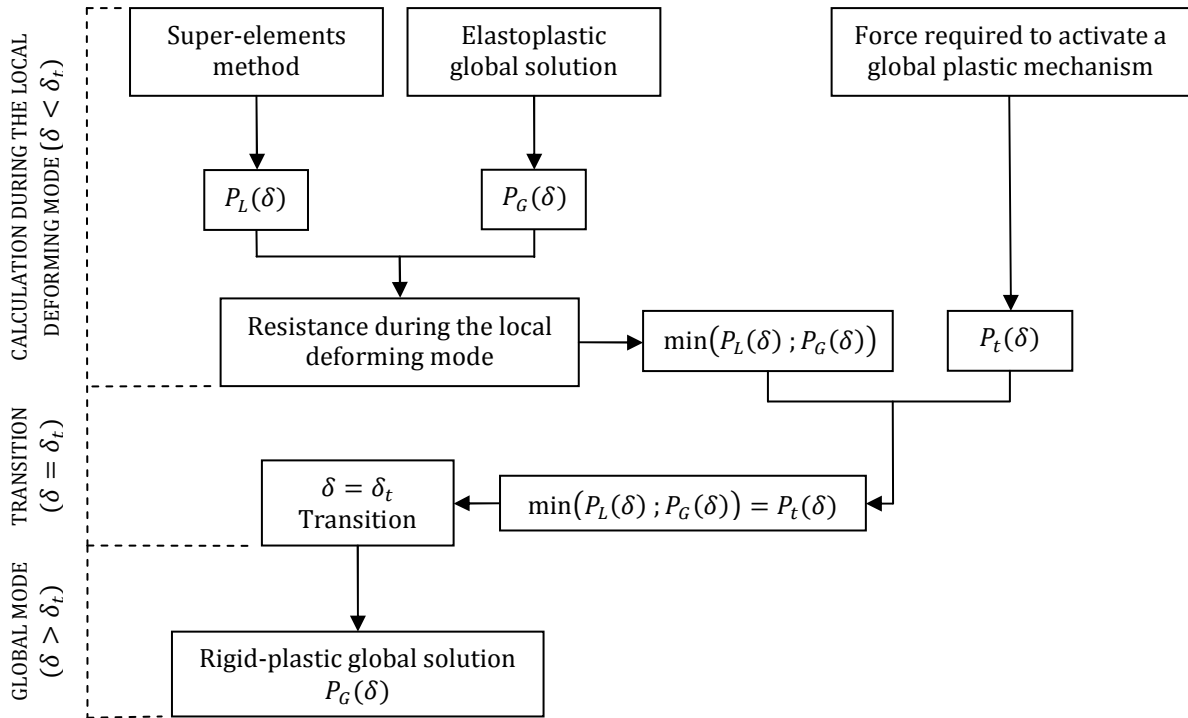


Figure 3.48. Procedure to combine the local and global resistances

From the procedure exposed here above, it is clear that an overall plastic mechanism will be activated as soon as $P_i(\delta)$ is equal to $P_{t,i}(\delta)$ for all the beams. Consequently, $P_t(\delta)$ may be simply found by summing up all the threshold values $P_{t,i}(\delta)$. The derivations of $P_i(\delta)$, $P_G(\delta)$, $P_{t,i}(\delta)$ and $P_t(\delta)$ are discussed in more details in the following sections.

3.6.2. Elastoplastic solution

As explained here above, for $\delta \leq \delta_t$, the beam depicted on Figure 3.46 may be first studied in the elastic range. This phase is assumed to end when the applied force is equal to a limit value $P_{t,i}(\delta)$ for which a plastic mechanism is initiated. At this moment, the bending resistance of the beam is reached, so the first step in the analysis is now to provide some formulae allowing for its derivation.

3.6.2.1. Derivation of the resistant bending moment

The resistant bending moment depends on the cross-section classification and is not necessarily the same in all the cases. Indeed, according to Eurocode 3 [52], the distinction should be made between the following situations:

- Class 1 cross-sections that are characterized by a full plastic bending resistance $M_{p,i}$. They are able to develop a plastic hinge and have the required rotation capacities for a plastic analysis.
- Class 2 cross-sections, for which $M_{p,i}$ can also be reached but the rotation capacities are limited due to local buckling.
- Class 3 cross-sections, where the elastic bending resistance $M_{e,i}$ should be considered because the local buckling prevents important yielding.

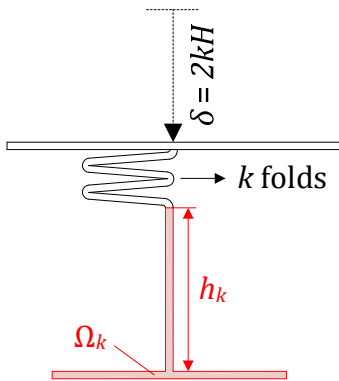
- Class 4 cross-sections, in which buckling takes place before the occurrence of any plastic deformation. Only an effective elastic bending moment $\bar{M}_{e,i}$ can be reached. This latter is obtained by assuming that the cross-section is not entirely efficient.

From this brief recall, it appears that developing a collapse mechanism involving plastic hinges is not relevant for all the girders because of a too early local buckling. This is an important restriction that has not been considered so far, in particular when establishing the resistance of SE2 and SE3 during the beam-like behavior⁵. Another conclusion that can be drawn from the previous considerations is that the force $P_{t,i}(\delta)$ causing a plastic mechanism is such that the maximal bending moment over the beam is equal to the resistance $M_{p,i}$, $M_{e,i}$ or $\bar{M}_{e,i}$ according to the cross-section class.

As explained in section 3.6.1.2, one of the crucial point is now to evaluate the reduced bending capacities $\xi_{p,i}(\delta)M_{p,i}$, $\xi_{e,i}(\delta)M_{e,i}$ or $\bar{\xi}_{e,i}(\delta)\bar{M}_{e,i}$ by accounting for the coupling with the local mode. The reduction coefficients have to represent the effect of the crushing and a very simple way to achieve this goal is to generalize what has already been proposed in Appendix B.2.

To do so, let us consider the particular situation for which the initial I-shaped cross-section has been indented over a distance $\delta = 2kH$. In this case, k folds are already completely closed (Figure 3.49a) and the uncrushed web height is equal to h_k . In order to evaluate the bending resistance for such a configuration, it is proposed to focus only on the intact area Ω_k (Figure 3.49a). Associating the collaborative part of the plating to Ω_k is questionable, because this region also suffers important plastic disorders coming from the simultaneous folding process, so this will be conservatively omitted here. The derivation of the bending resistance M_k of Ω_k then leads to a plastic, elastic or effective elastic solution according to the initial cross-section classification. It is worth noticing that this latter is based on the uncrushed web height h_0 and is not recalculated for each value of h_k , which implies that the coefficients $\xi_{p,i}(\delta)$, $\xi_{e,i}(\delta)$ and $\bar{\xi}_{e,i}(\delta)$ are monotonically decreasing functions of the penetration.

(a) Bending resistance of a crushed beam



(b) Compatible displacement field of an horizontal beam

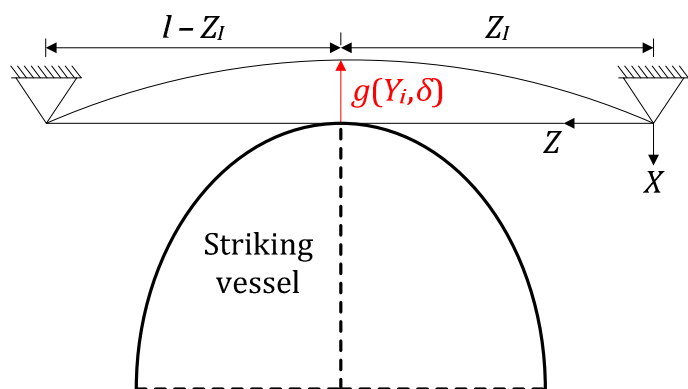


Figure 3.49. Geometrical data for the elastic solution

Finally, to get the bending resistance $\xi_{p,i}(\delta)M_{p,i}$, $\xi_{e,i}(\delta)M_{e,i}$ or $\bar{\xi}_{e,i}(\delta)\bar{M}_{e,i}$ for any value of the local indentation δ , the linear interpolation (B.26) suggested in Appendix B.2 can be used.

⁵ See sections 3.4.2.2, 3.5.2.2, B.2.2, B.3.1.3 and B.3.2.2. For conciseness, it was voluntarily omitted to precise that these developments were only valid for class 1. Of course, if the T-shaped cross-section of a SE2 or a SE3 does not satisfy this requirement, the procedure exposed here is applicable.

Of course, for a given value of the local penetration δ , as long as the beam has not been impacted by the vessel, the derivation has to be done for the initial undamaged cross-section obtained by combining the girder and the collaborating part of the plating, which leads to $M_{p,i}$, $M_{e,i}$ or $\bar{M}_{e,i}$.

The method proposed here above is arguable because it has no real theoretical basis. It is simply an approximate, practical and conservative approach that is only corroborated by finite element analyses of entire lock gates (see section 3.7). This way of doing allows for a better agreement between the analytical and numerical curves, in particular at the beginning of the collision, when the local deforming mode sometimes overestimates the resistance.

3.6.2.2. Derivation of the global resistance

The derivation of the global resistance in the elastic regime (i.e. for $\delta \leq \delta_t$) can be achieved by postulating kinematically admissible expressions for u_i and w_i (Figure 3.46). In fact, before the transition, there is no need to account for the in-plane component w_i because this one is very small. Consequently, for a beam located at a level Y_i along the vertical axis, the following cubic functions may be used to define an acceptable deformation profile:

$$\begin{aligned}
 \bullet \text{ For } 0 \leq Z \leq Z_I : \quad u(Y_i, Z) &= \frac{1}{2} \frac{Z}{Z_I} \frac{2lZ_I - Z_I^2 - Z^2}{Z_I(l - Z_I)} g(Y_i, \delta) \\
 \bullet \text{ For } Z_I < Z \leq l : \quad u(Y_i, Z) &= \frac{1}{2} \frac{l - Z}{l - Z_I} \frac{2lZ - Z_I^2 - Z^2}{Z_I(l - Z_I)} g(Y_i, \delta)
 \end{aligned} \tag{3.71}$$

where Z_I is the horizontal coordinate of the impact point I (Figure 3.6) and l is the total width of the gate (Figure 3.3). The function $g(Y_i, \delta)$ gives the maximal displacement of the beam (Figure 3.49b). It is supposed to occur in the vertical plane $Z = Z_I$ passing through the first contact point I . In order to have a quite realistic global deformation pattern, the definition of the function $g(Y, \delta)$ has to be done by accounting for the shape of the striking vessel. In particular, the presence of a bulb may have a great influence on the overall bending motion exhibited by the gate. Furthermore, in order to be compatible, $g(Y, \delta)$ has also to respect the boundary conditions of the structure. For conciseness, only the case of a gate free at the bottom and impacted by a raked bow is considered here. The other situations are presented in Appendix B.4 (section B.4.1).

As explained previously, for $\delta \leq \delta_t$, the plastic mechanism is not yet activated. The gate suffers a local plastic indentation (Figure 3.50c) coupled with a global elastoplastic movement (Figure 3.50a). In the vertical plane $Z = Z_I$, this latter is described by a bilinear function $g(Y, \delta)$ such that $g(Y_I, \delta) = \delta$. The only difficulty lies in having reasonable estimations for the displacements $g(h, \delta)$ and $g(0, \delta)$ of the uppermost and lowermost beams. To achieve this goal, one can consider the situation where the impact point I is progressively nearing the top of the gate. In this case, it may be thought that $g(h, \delta) \rightarrow \delta$ and $g(0, \delta) \rightarrow 0$. It seems therefore interesting to use the coefficients Y_I/h and $1 - Y_I/h$ in their definitions, but this is not sufficient. Indeed, because of the concomitant local indentation, the vertical distance between the lowermost beam and the vessel is progressively reduced by $\delta \tan \phi$ (Figure 3.50c), which means that $g(0, \delta)$ becomes more and more sensitive to the penetration of the ship. When the ship is completely in contact with the gate, $\delta \tan \phi = h_b$ and it seems consistent to use the ratio $\delta \tan \phi / h_b$ as a second coefficient for $g(0, \delta)$. Gathering all the previous considerations leads to the following results:

$$g(0, \delta) = \delta \left(1 - \frac{Y_I}{h}\right) \min\left(\frac{\delta \tan \phi}{h_b}; 1\right) ; \quad g(h, \delta) = \frac{Y_I}{h} \delta \quad (3.72)$$

Using these definitions, it is now possible to extend the definition of $g(Y, \delta)$ by interpolating linearly between $g(0, \delta)$, $g(Y_I, \delta)$ and $g(h, \delta)$, which leads to:

- For $0 \leq Y \leq Y_I$:
$$g(Y, \delta) = \delta \frac{Y}{Y_I} + \delta \left(1 - \frac{Y}{Y_I}\right) \left(1 - \frac{Y_I}{h}\right) \min\left(\frac{\delta \tan \phi}{h_b}; 1\right) \quad (3.73)$$
- For $Y_I < Y \leq h$:
$$g(Y, \delta) = \delta \left(1 - \frac{Y - Y_I}{h}\right)$$

Of course, in (3.73), only the discrete locations $Y = Y_i$ of the horizontal girders are of interest to evaluate $u(Y_i, Z)$ by (3.71). This latter being completely defined, the resistance $P_i(\delta)$ can be found by applying the elastic beam theory.

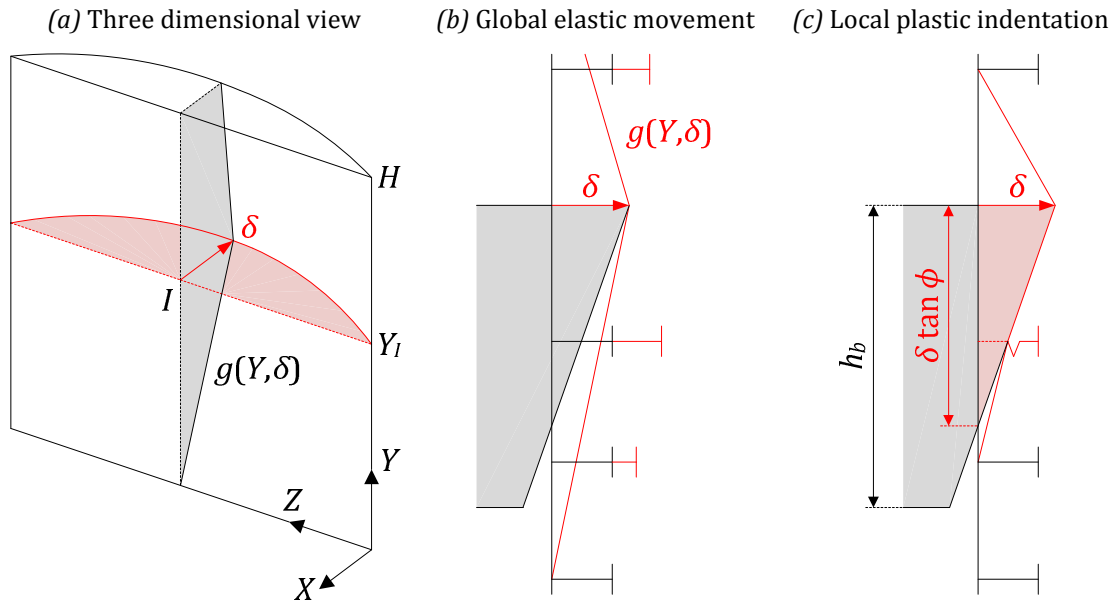


Figure 3.50. Global and local displacements before the activation of the plastic mechanism

As long as the overall motion of the gate remains small, it can be shown that the bending moments $M_i(Z, \delta)$ in the beam and the equilibrium equation are simply as follows:

$$M_i(Z, \delta) = -EI_i \frac{\partial^2 u}{\partial Z^2} ; \quad M_i(\delta) = P_i(\delta) \frac{(l - Z_I)Z_I}{l} \quad (3.74)$$

where $M_i(\delta) = M_i(Z_I, \delta)$ is the maximal bending moment located in the central cross-section and I_i is the relevant inertia. It is worth noting that this latter has to be calculated by accounting for the crushing process if the beam is also indented by the vessel. This can be achieved by applying the same technique than the one presented in Appendix B.2 for the bending capacities of a beam. Substituting (3.71) in (3.74) leads to:

$$P_i(\delta) = \min \left\{ \frac{3lEI_i}{Z_I^2(l - Z_I)^2} g(Y_i, \delta); P_{t,i}(\delta) \right\} ; \quad P_{t,i}(\delta) = \frac{l}{(l - Z_I)Z_I} \begin{cases} \xi_{p,i}(\delta) M_{p,i} \\ \xi_{e,i}(\delta) M_{e,i} \\ \bar{\xi}_{e,i}(\delta) \bar{M}_{e,i} \end{cases} \quad (3.75)$$

where it is worth noting that $P_i(\delta)$ is a piecewise non-linear function of δ due to the definitions of I_i and $g(Y_i, \delta)$. In this last equation, it may be worth recalling that according to

section 3.6.2.1, $P_{t,i}(\delta)$ is the force required to activate a plastic mechanism on the beam. This happens when the maximal bending moment $M_i(\delta)$ reaches the plastic, elastic or effective elastic resistance of the cross-section. The coefficients $\xi_{p,i}(\delta)$, $\xi_{e,i}(\delta)$ and $\bar{\xi}_{e,i}(\delta)$ are only useful if the beam is simultaneously indented during the crushing process, otherwise they are equal to unity.

The evolution of the individual resistance $P_i(\delta)$ given by (3.75) during the local deforming mode is depicted on Figure 3.51a for an impacted beam. From this picture, it can be seen that $P_i(\delta)$ is not increasing continuously with δ because discontinuities are noticeable at the initiation of each new fold, which is simply due to the change of inertia.

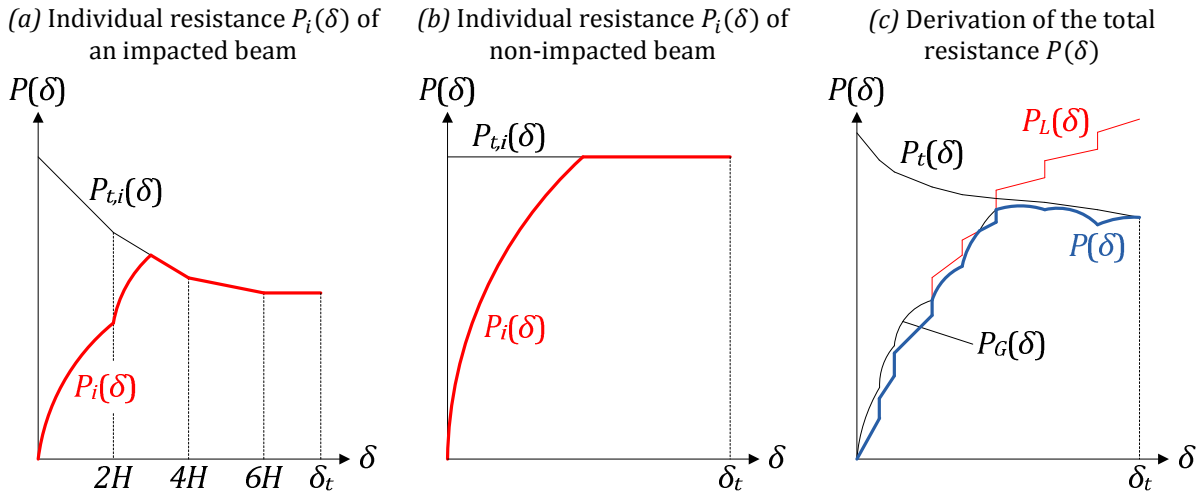


Figure 3.51. Individual and total resistances during the local deforming mode

As soon as the force $P_{t,i}(\delta)$ required to activate a global mechanism on the beam is reached, then $P_i(\delta)$ simply follows $P_{t,i}(\delta)$, which is a discontinuously decreasing function of δ because of the coefficients $\xi_{p,i}(\delta)$, $\xi_{e,i}(\delta)$ or $\bar{\xi}_{e,i}(\delta)$. On the contrary, if the beam is not impacted, its individual contribution $P_i(\delta)$ is monotonically growing with the penetration, until $P_{t,i}(\delta)$ is reached (Figure 3.51b). This latter is constant, as there is no need to reduce the resistant bending moment $M_{p,i}$, $M_{e,i}$ or $\bar{M}_{e,i}$ of the beam. As a final result, the elastoplastic global resistance $P_G(\delta)$ in the local deforming mode is obtained with help of equation (3.5), i.e. by summing-up the contributions $P_i(\delta)$ coming from all the horizontal beams.

3.6.3. Perfectly plastic solution

The threshold value $P_t(\delta)$ that is required to activate a global plastic mechanism on the entire gate is simply obtained by adding the forces $P_{t,i}(\delta)$ that are necessary to initiate a plastic behavior for each individual beam. As soon as the resistance $P(\delta)$ calculated by (3.70) in the elastoplastic local deforming mode reaches $P_t(\delta)$, then $\delta = \delta_t$ and the transition occurs. Consequently, in accordance with section 3.6.1.2, there will be a switch from the local to the global deforming mode when the two following expressions are equal:

$$P(\delta) = \min(P_L(\delta) ; P_G(\delta)) \quad ; \quad P_t(\delta) = \sum_{i=1}^{N_h} P_{t,i}(\delta) \quad (3.76)$$

such as depicted on Figure 3.51c. In accordance with (3.70), for $\delta > \delta_t$, the gate resistance $P(\delta)$ is derived by considering this time only a global plastic solution $P_G(\delta)$. As usual, this

latter is obtained by applying (3.5), where the individual contributions $P_i(\delta)$ coming from each beam are now calculated under the hypothesis of a perfectly plastic material.

3.6.3.1. Derivation of the displacement field

Before deriving the resistance, it is first necessary to define the displacement field for $\delta > \delta_t$. As in the previous section, the case of a raked bow impacting a gate free at the bottom is investigated (other situations are reported in section B.4.2 of Appendix B.4). In this configuration, all the beams are assumed to collapse individually through a plastic mechanism (Figure 3.52a) where the out-of-plane displacements are given by $g(Y, \delta)$ while the in-plane ones are characterized by the functions $w_1(Y)$ and $w_2(Y)$ at the two ends.

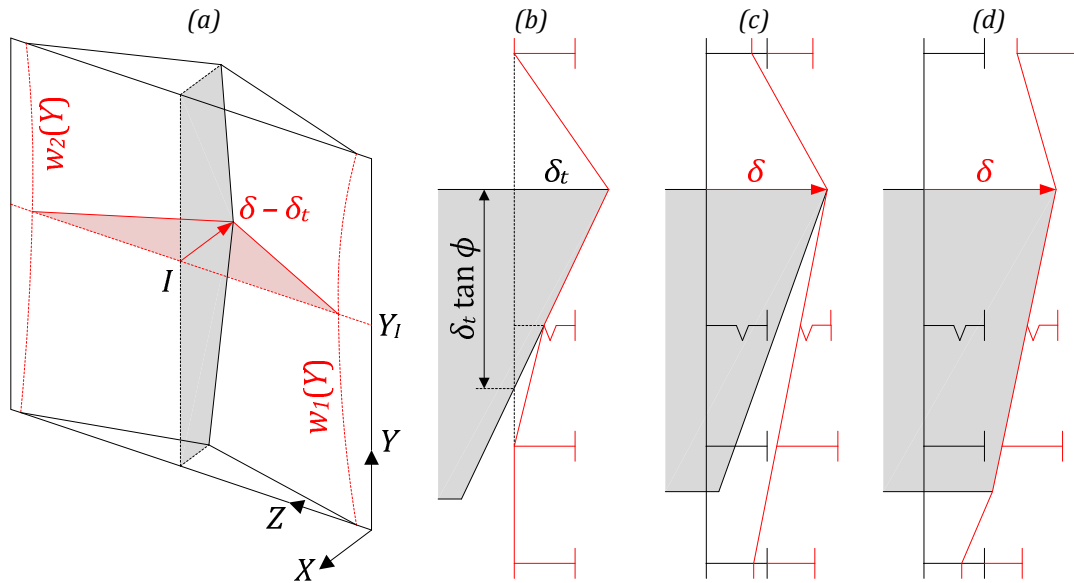


Figure 3.52. Displacement field after the activation of the plastic mechanism

In order to have a reasonable evaluation of $g(Y, \delta)$, one can consider the local penetration of the striking vessel when the transition occurs. For $\delta = \delta_t$, it can be seen from Figure 3.52b that the vertical distance between the lowermost beam and the impact point I is reduced to $Y_I - \delta_t \tan \phi$. Consequently, by using similar arguments than those exposed in section 3.6.2.2, it seems reasonable to postulate that the coefficients $1 - Y_I/h$ and $\delta_t \tan \phi / h_b$ should be involved in the definition of $g(0, \delta)$. Here again, assuming that $g(0, \delta)$ and $g(h, \delta)$ are proportional to the displacement $\delta - \delta_t$ of the contact point leads to:

$$g(0, \delta) = (\delta - \delta_t) \left(1 - \frac{Y_I}{h}\right) \min\left(\frac{\delta_t \tan \phi}{h_b}; 1\right) ; \quad g(h, \delta) = \frac{Y_I}{h} (\delta - \delta_t) \quad (3.77)$$

A linear interpolation can then be used to get the vertical profile of Figure 3.52c. However, if $\delta_t \tan \phi \leq h_b$, then (3.77) is not always valid. Indeed, if the stem angle is close to 90° , then a subsequent contact may appear between the stem and the deforming gate (Figure 3.52d). This occurs for a given penetration δ_1 that can be calculated from simple geometrical considerations. From this point onwards, $g(0, \delta)$ grows more rapidly as the distance between the bottom of the ship and the lowermost beam is now only equal to $Y_I - h_b$. Consequently, the coefficient $1 - Y_I/h$ should be replaced by $1 - (Y_I - h_b)/h$ in (3.77) to get:

$$g(0, \delta) = (\delta_1 - \delta_t) \left(1 - \frac{Y_I}{h}\right) \min\left(\frac{\delta_t \tan \phi}{h_b}; 1\right) + (\delta - \delta_1) \left(1 - \frac{Y_I - h_b}{h}\right) \quad (3.78)$$

in which the first term is simply the displacement reached by the gate when the subsequent contact happens. Of course, the definition of $g(h, \delta)$ remains unaffected for $\delta > \delta_1$. To achieve the derivation of the displacement field, it is still required to precise the functions $w_1(Y)$ and $w_2(Y)$ for the in-plane movements. Ideally, these latter should be calculated by accounting for the true flexibility of the structure in the plastic regime.

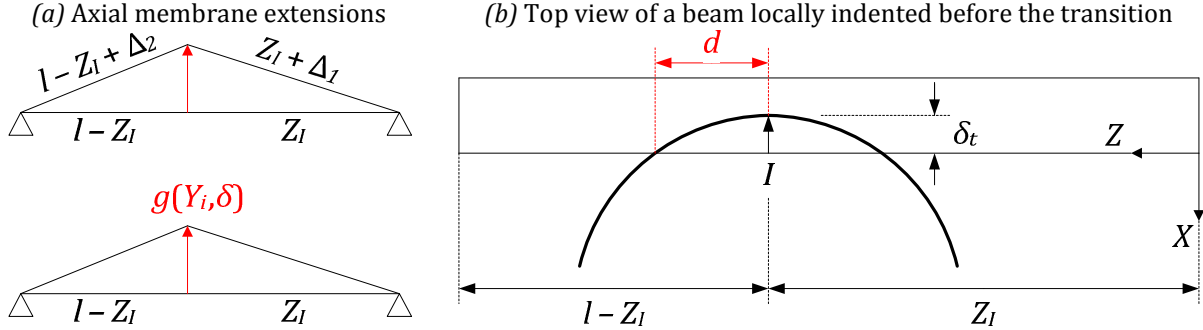


Figure 3.53. Definition of the in-plane displacement field

However, in this simplified procedure, as the vertical frames are considered to have little influence in the global deforming mode, it seems reasonable to follow the hypothesis formulated by Jones [80] and postulate that the in-plane displacements $w_1(Y)$ and $w_2(Y)$ are proportional to the axial extensions Δ_1 and Δ_2 of each part of the beam in the case of fixed supports (Figure 3.53a). These latter are given by:

$$\Delta_1 = \sqrt{Z_l^2 + g^2(Y_i, \delta)} - Z_l \approx \frac{g^2(Y_i, \delta)}{2Z_l} ; \quad \Delta_2 = \sqrt{(l - Z_l)^2 + g^2(Y_i, \delta)} \approx \frac{g^2(Y_i, \delta)}{2(l - Z_l)} \quad (3.79)$$

in which the approximations are valid within the frame of moderately large displacements, i.e. for $g(Y_i, \delta) \ll \min(Z_l ; l - Z_l)$. In addition to (3.79), another hypothesis is made to account for the actual distance separating the bow from the lateral supports. To do so, one can consider the situation depicted on Figure 3.53b showing the indentation of a beam during the local deforming mode. When the transition occurs, it appears that the left and right horizontal distances are reduced to $l - Z_l - d$ and $Z_l - d$ respectively, d being calculated by considering the intersection of the stem with the vertical plane $X = 0$. As the maximal value for d is p (Figure 3.7a), it is suggested here to use the coefficient d/p when defining $w_1(Y)$ and $w_2(Y)$. Finally, interpolating linearly leads to:

- For $0 \leq Y \leq Y_l$: $w_1(Y) = \frac{1}{2} \frac{g^2(Y_i, \delta)}{Z_l} \left(1 - \frac{Z_l}{l}\right) \left(1 + \frac{Y - Y_l}{h}\right) \min\left(\frac{d}{p} ; 1\right)$
- For $Y_l < Y \leq h$: $w_1(Y) = \frac{1}{2} \frac{g^2(Y_i, \delta)}{Z_l} \left(1 - \frac{Z_l}{l}\right) \left(1 - \frac{Y - Y_l}{h}\right) \min\left(\frac{d}{p} ; 1\right)$

(3.80)

in which $d = p\sqrt{\delta_t/q}$. Of course, the definition of $w_2(Y)$ is similar, except that Z_l has to be replaced by $l - Z_l$ in (3.80).

3.6.3.2. Derivation of the resistance

Once a kinematically admissible displacement field is postulated for $\delta > \delta_t$, the individual resistance $P_i(\delta)$ provided by each horizontal beam can be calculated by applying the equilibrium method (see section 2.3.2.2). As briefly discussed here above, the calculation of $P_i(\delta)$ has to be done by accounting carefully for the classification. Indeed, from Eurocode 3

[52], only class 1 cross-sections have the required rotation capacities for a plastic analysis. In this single case, the mechanism depicted on Figure 3.54 can be postulated, where a central plastic hinge is formed. This kind of situation has already been quickly analyzed when dealing with the beam behavior of folded super-elements in sections 3.4.2.2 and 3.5.2.2. Therefore, it could be of interest to perform a quite more detailed theoretical investigation in the present situation.

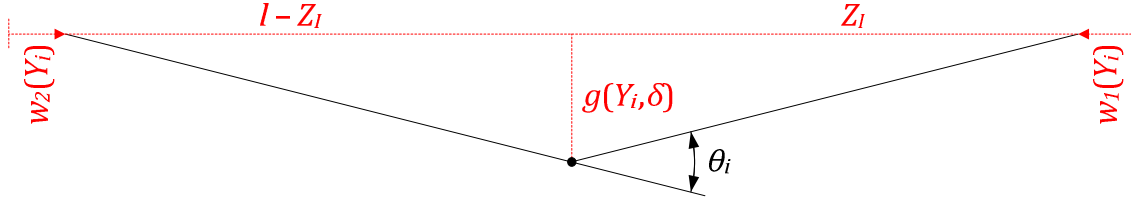


Figure 3.54. Plastic collapse in case of a class 1 cross-section

In fact, when the transition occurs ($\delta = \delta_t$), the cross-section located in $Z = Z_l$ is only submitted to a bending moment $M_i(\delta)$ equal to $\xi_{p,i}M_{p,i}$, where $\xi_{p,i}$ corresponds to the particular value of $\xi_{p,i}(\delta)$ when $\delta = \delta_t$, which is only relevant if the beam has been previously impacted during the local mode. Nevertheless, because of the moderately large out-of-plane displacements, some additional membrane effects develop because the structure is also submitted to an axial straining. Consequently, a normal force $N_i(\delta)$ and a bending moment $M_i(\delta)$ simultaneously act on the central cross-section. These two internal forces are not independent from each other because they are related by a yield criterion. In the present case, the interaction formula should be the one characterizing an I-shape cross-section. Ueda and Rashed [150] have elaborated a very refined and cumbersome description of this yield locus, but as suggested by Paik and Thayamballi [121], another easier and conservative approach is to adopt the following parabolic formula:

$$\frac{M_i}{\xi_{p,i}M_{p,i}} + \left(\frac{N_i}{N_{p,i}}\right)^2 = 1 \Leftrightarrow M_i(\delta) = \xi_{p,i}M_{p,i} \left(1 - \frac{N_i^2(\delta)}{N_{p,i}^2}\right) \quad (3.81)$$

which was already encountered in Appendix B.2. and where $M_{p,i}$ and $N_{p,i}$ are respectively the bending and axial capacities of the I-shaped cross-section depicted on Figure 3.45. Because of the combination of both membrane and bending effects, the central hinge is simultaneously submitted to a rotation θ_i and an extension Δ_i (Figure 3.54). These latter are related by the normality rule:

$$\frac{\partial M_i}{\partial N_i} = -\frac{\dot{\Delta}_i}{\dot{\theta}_i} \Leftrightarrow N_i(\delta) = \frac{N_{p,i}^2}{2\xi_{p,i}M_{p,i}} \frac{\dot{\Delta}_i}{\dot{\theta}_i} \quad (3.82)$$

which, as explained by Jones [81], simply states that there is no acceptable combination of $M_i(\delta)$ and $N_i(\delta)$ outside the yield locus with non-hardening materials. This relation is quite important, as it allows for the evaluation of the internal normal force if Δ_i and θ_i are known. These two parameters can be easily obtained from the displacement field defined in 3.6.3.1. Indeed, under the assumption that $g(Y_i, \delta)$ is small in comparison with Z_l and $L - Z_l$, from Figure 3.54, it can be shown that:

$$\theta_i = \frac{l}{Z_l(l - Z_l)} g(Y_i, \delta) \quad ; \quad \Delta_i = \frac{g^2(Y_i, \delta)}{2} \frac{l}{Z_l(l - Z_l)} - w_1(Y_i) - w_2(Y_i) \quad (3.83)$$

Deriving (3.83) with respect to time and substituting the ratio $\dot{\Delta}_i/\dot{\theta}_i$ in (3.82) leads to $N_i(\delta)$. As $N_i(\delta) \leq N_{p,i}$ to have a statically admissible solution, the following result is found:

$$N_i(\delta) = \min \left\{ \frac{N_{p,i}^2}{2\xi_{p,i}M_{p,i}} \left(g(Y_i, \delta) - \frac{Z_I(l - Z_I)}{l} \left(\frac{\partial w_1}{\partial \delta} + \frac{\partial w_2}{\partial \delta} \right) \right); N_{p,i} \right\} \quad (3.84)$$

which can be introduced in (3.81) to get the bending moment $M_i(\delta)$. Once $M_i(\delta)$ and $N_i(\delta)$ are known, the equilibrium of the gate can be expressed in a similar manner than Tin-Loi [149], which finally leads to:

$$P_i(\delta) = \frac{l}{Z_I(l - Z_I)} (M_i(\delta) + N_i(\delta)g(Y_i, \delta)) \quad (3.85)$$

Of course, when the transition occurs in $\delta = \delta_t$, this equation is exactly the same as (3.75) and leads to $P_{t,i}(\delta)$. However, the analytical developments performed here above are based on a plastic analysis, which is only possible if the central cross-section of is class 1. As explained in section 3.6.2.1, if this is not the case, the web will be submitted to an early buckling, so the model of Figure 3.54 is irrelevant for these situations.

In order to evaluate $P_i(\delta)$ for class 2, 3 or 4 cross-sections, the beam can be treated as a thin-walled structure. In this approach, the web is seen a classical plate that is likely to buckle because of the compressive stresses induced by the bending moment. As detailed by Kotelko [88], during this phenomena, the structural behavior may be divided into the four phases depicted on Figure 3.55a. In the present analysis, the elastic and elastoplastic post-buckling stages (denoted by ② and ③ on Figure 3.55a) are disregarded and the evolution of the beam resistance curve is only divided into three successive parts. As presented on Figure 3.55b, the elastic solution derived in section 3.6.2.2 is first considered, until the maximal value $P_{t,i}(\delta)$ is reached. The second portion is then assimilated to an elastoplastic phase that ends when the transition occurs, i.e. for $\delta = \delta_t$. From this point onwards, the beam collapses by following a mechanism that still needs to be investigated.

The plastic collapse of a thin-walled structure can be studied by the upper-bound method. To do so, a given deformation pattern has first to be postulated. Of course, this choice is arbitrary and has to be done in accordance with some numerical or physical observations. In the present case, the buckling model that is commonly observed when performing LS-DYNA finite element simulations is the one depicted on Figure 3.56. It is made of a unique asymmetric fold created over the total web height⁶ and allows for a relative rotation of the two arms of the beam as it is progressively closed. The horizontal extension 2ℓ of the folded area may be expressed as a fraction of the web height and will be derived later.

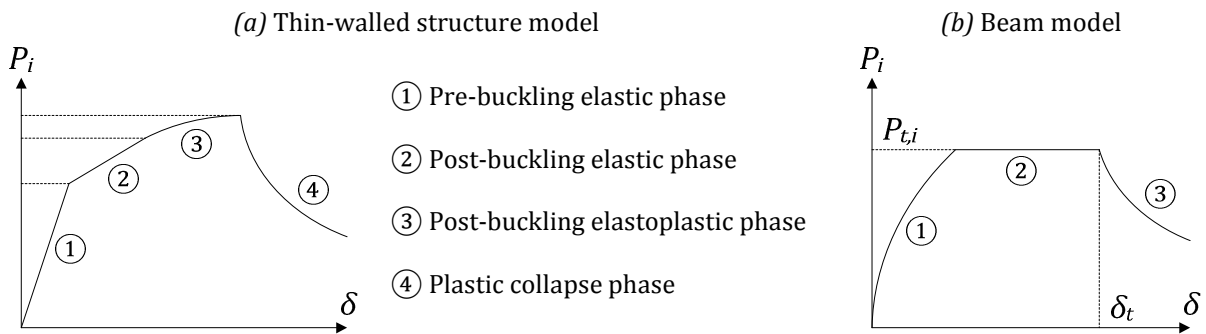


Figure 3.55. Evolution of the resistance with the penetration

⁶ If necessary, instead of working with the initial total web height h_w , the uncrushed portion h_k should be considered. This is particularly the case when the plastic mechanism of Figure 3.56 has to be used for modeling the beam behavior of SE2 and SE3, as explained in sections 3.4.2.2 and 3.5.2.2.

Of course, besides the mechanism represented on Figure 3.56, many others can be postulated such as all those collected in the database of Ungureanu et al. [151]. Choosing the most appropriate one depends on the web slenderness, the stress state and the imperfections. Selecting a proper folding geometry is therefore not easy and has to be done carefully to get a true characterization of the post-buckling behavior. Nevertheless, from all the numerical simulations realized on entire lock gates (see section 3.7), it results that the one considered here is quite convenient as the total collision force is more or less correctly approximated, so only this particular collapse model will be used.

In an attempt to derive the plastic resistance $P_i(\delta)$, it is required to evaluate the energy rate \dot{E}_f associated to the folding process. Unfortunately, the buckling pattern suggested here is not listed in the database of Ungureanu et al. [151] and very little information are given by Kotelko [88] about the analytical derivation \dot{E}_f . Consequently, as for super-elements, the derivation has to be achieved by applying the upper-bound method, but this will be done in Chapter 4, when dealing with mitre gates.

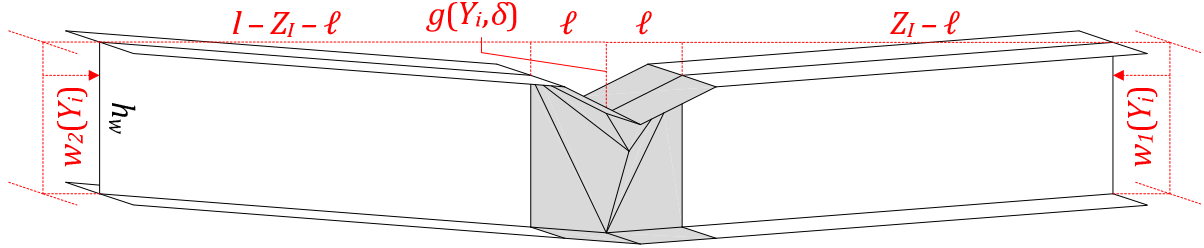


Figure 3.56. Collapse mechanism in case of a class 2, 3 or 4 cross-section

In addition to \dot{E}_f , there is also an energy dissipation that is coming from the membrane effects in the two arms of the beam. These latter have initial lengths equal to $Z_l - \ell$ and $l - Z_l - \ell$ and are submitted to a total axial straining also given by (3.83), except that Z_l has to be replaced by $Z_l - \ell$. Consequently, the total internal energy \dot{E}_{int} dissipated by the plastic collapse of the beam is equal to:

$$\dot{E}_{int} = N_{p,i} \left(\frac{(l - 2\ell)g(Y_i, \delta)}{(Z_l - \ell)(l - Z_l - \ell)} - \frac{\partial w_1}{\partial g} - \frac{\partial w_2}{\partial g} \right) \frac{\partial g}{\partial \delta} \dot{\delta} + \frac{\partial E_f}{\partial g} \frac{\partial g}{\partial \delta} \dot{\delta} \quad (3.86)$$

On the other hand, the work rate \dot{W} coming from the external forces has to be calculated by accounting for the contribution of $P_i(\delta)$, but also for the one coming from the reaction forces because of the displacements $w_1(Y_i)$ and $w_2(Y_i)$ at the supports, i.e.:

$$\dot{W} = P_i(\delta) \frac{\partial g}{\partial \delta} \dot{\delta} - N_{p,i} \left(\frac{\partial w_1}{\partial g} + \frac{\partial w_2}{\partial g} \right) \frac{\partial g}{\partial \delta} \dot{\delta} \quad (3.87)$$

According to the upper-bound method, (3.86) and (3.87) can be equated to get $P_i(\delta)$. Doing so leads to:

$$P_i(\delta) = N_{p,i} \frac{(l - 2\ell)g(Y_i, \delta)}{(Z_l - \ell)(l - Z_l - \ell)} + \frac{\partial E_f}{\partial g} \quad (3.88)$$

As a conclusion, the global plastic resistance after the transition can be obtained by applying (3.5), where $P_i(\delta)$ is given by (3.85) in the case of a class 1 cross-section, or by (3.88) in the other cases. Furthermore, the curves of Figure 3.51a and b can now be completed to get the final evolution of $P_i(\delta)$ with the penetration. Doing so leads to the diagrams presented on Figure 3.57a and b for an impacted or non-impacted beam respectively.

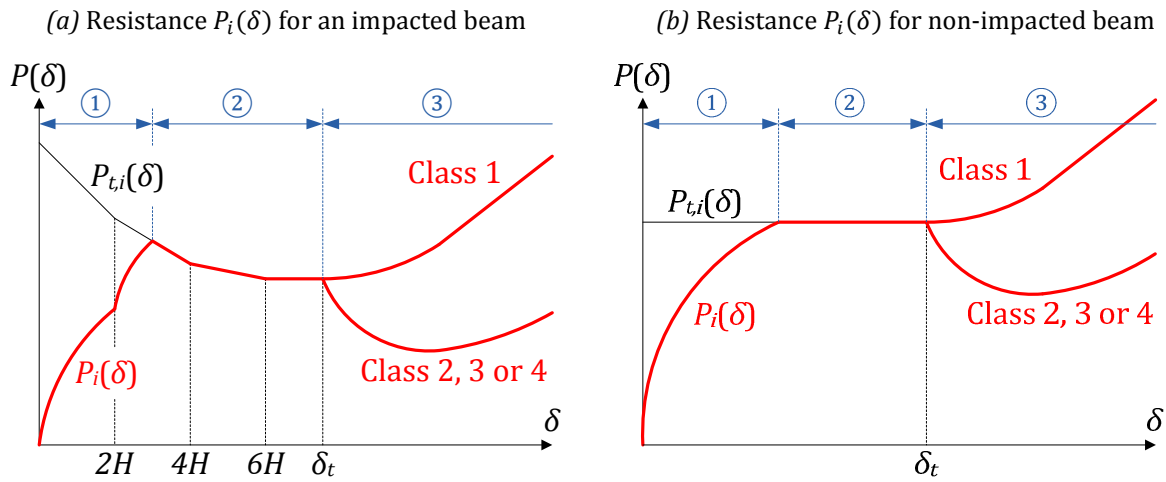


Figure 3.57. Individual resistances during the local deforming mode

On these two pictures, it is worth noticing that even though there is an unstable plastic collapse during the global deforming mode (i.e. for $\delta > \delta_t$), the resistance keeps growing because of the membrane effects. If these effects were not present after the transition, then $P_i(\delta)$ would be a constant or decreasing function of δ according to the cross-section class. As a final remark, it should be noted that the three successive elastic, elastoplastic and plastic phases discussed here above are also represented on Figure 3.57. They are affected with the numbers ①, ② and ③ respectively.

3.7. Numerical validations

The aim of this section is to check if the analytical developments performed for the local and the global deforming modes provide a realistic estimation of the collision resistance. To do so, numerical simulations were run using the finite element software LS-DYNA that is capable of solving dynamic non linear problems [66].

3.7.1. Preliminary considerations

Before exposing the results, it is of interest to give some information about the numerical models and about the collision scenarios used for the simulations.

3.7.1.1. Finite element model

For all the simulations of the validation process, both the striking vessel and the impacted gate are entirely modeled using Belytschko-Tsay shell elements, based on a combined co-rotational and velocity strain formulation. This means that a coordinate system is embedded in the element while the Rivlin-Eriksen rate of the Almansi strain tensor $[\dot{\mathbf{a}}]$ is used in conjunction with Cauchy stresses⁷. For the structure, five integration points are placed over the thickness, but only two are required for the ship as it is assumed to be perfectly rigid.

Concerning the mesh size, many attempts were made before reaching an acceptable configuration. Starting from an initial size, the element dimensions are progressively reduced until the numerical results stabilize. From this convergence process, the following conclusions may be drawn:

- In the area near the first impact point, the mesh size has to be quite refined in order to have a proper modeling of the deformation mechanisms involved during the collision. This is particularly true for the folding of horizontal and vertical members but is not of prior importance to represent tensile effects in the plating. Furthermore, it is worth bearing in mind that the contact zone between the structure and the ship is progressively extending when the penetration increases, which implies that the mesh size has to be sufficiently small in a large area around the impact point. Consequently, the case of a vessel with a more or less rectangular hull form is quite unfavorable regarding the meshing effort.
- Similarly, in the regions near the boundaries, it is advisable to avoid a too coarse mesh because the deformations involved during the global mode may also be non-negligible along these places. This observation was already made by many authors who worked with finite element during ship-ship collisions, such as Lützen [103], Simonsen [141] or Zhang [180].
- In the remaining parts of the gate, there is no real need to have a very refined mesh as the bending deformations due to the global mode are moderate enough. This allows for a reduction of the total time needed to simulate the impact.

In the present situation, it was finally found that the element dimensions should be of about 10 *cm* in order to preserve an acceptable precision on the numerical results without requiring an excessive calculation time.

⁷ See the LS-DYNA theory manual [66], section 2.3.1 and Appendix A.2 for more details.

The boundary conditions applied on the gate are those mentioned in section 3.1.1.3. They are briefly recalled on Figure 3.58 and in Table 3.7. For edges ② and ④, there is only a translational constraint along the horizontal X axis, which conservatively supposes that the structure remains free to move in its plane without friction. At the bottom of the lock chamber, the X -displacements are also prohibited if a sill is present. Finally, for the uppermost girder ③, if some cables are supporting the gate (Figure 3.2), this can be taken into account by imposing a vertical restraint along the Y axis. Nevertheless, finite element simulations have shown that imposing this additional constraint has very little influence on the impact resistance, so the suspension cables can be disregarded during the collision process.

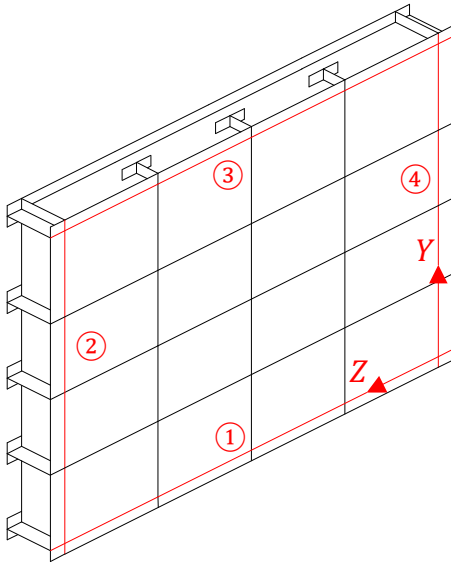


Figure 3.58. Definition of the edges

| Edge | DOF | Boundary condition |
|------|-----|--|
| ① | X | Constrained with a sill and free otherwise |
| | Y | Constrained |
| | Z | Constrained along the impact line |
| ② | X | Constrained because of the lock walls |
| | Y | Free |
| | Z | Free |
| ③ | X | Free |
| | Y | Constrained with cables and free otherwise |
| | Z | Free |
| ④ | X | Constrained because of the lock walls |
| | Y | Free |
| | Z | Free |

Remark: on Figure 3.58, the horizontal X axis is defined perpendicularly to the initial plane of the gate.

Table 3.7. Summary of the boundary conditions

The contact between the vessel and the structure is modeled by using the general surface-to-surface penalty contact algorithm of LS-DYNA. In the optic of providing ideal conditions, the elements dimensions of striking vessel are closed to 10 cm in the regions near the impact point. A coarser mesh is used outside these areas. As a conservative hypothesis, the ship is assumed to be perfectly rigid, while the gate still has the properties listed in Table 3.2.

3.7.1.2. Collision scenarios

In order to define the collision scenarios useful for the validation process, it may be interesting to stress the following points:

- Regarding the impact velocity, the finite element simulations have shown that the resistance curves were nearly identical for an initial speed V_0 equal to 0.5, 1 or 2 m/s. This means that the inertia effects do not have a significant influence on the collision process, so it is sufficient to only consider the maximal value of 2 m/s. Furthermore, it is also worth noting that the previous conclusion tends to corroborate the quasi-static approach used in the previous sections for developing the analytical model.
- Finally, regarding the mass M_s of the striking vessel, as barges are not considered here, it appears from Table A.1 that choosing a value of 4000 t should be consistent enough.

In conclusion, from the previous considerations, it transpires that performing finite element simulations with a vessel of 4000 t and travelling at an initial speed of 2 m/s should lead to a

reasonably unfavorable situation. Only the impact location needs to be varied to get different collision scenarios. As explained in section 3.2.1, the simulation is stopped when the initial kinetic energy has been entirely absorbed by the gate.

3.7.2. Impact on a gate supported by a sill

Different gates were considered for the validation. For conciseness, this section only focuses on the one represented on Figure 3.59, but other results are available in Appendix B.5. The geometrical properties of the structure are listed in Table 3.8, from which it can be seen that the total length l and height h are both equal to 13.1 m for this first gate. The cases of a raked or bulbous striking bow are considered separately.

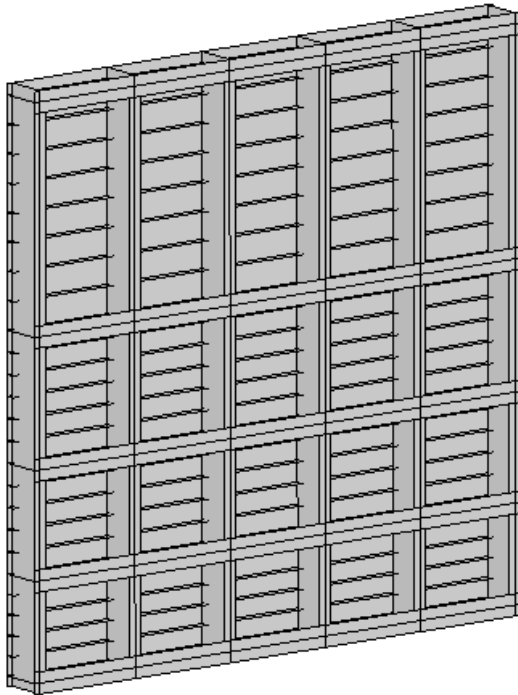


Figure 3.59. Three dimensional view of gate 1

| <i>Horizontal girders</i> | | | | |
|------------------------------|-----------|----------------|-----------|-----------|
| Y (m) | h_w (m) | t_w (m) | h_f (m) | t_f (m) |
| 0 | 1 | 0.02 | 0.6 | 0.025 |
| 2.3 | 1 | 0.02 | 0.5 | 0.025 |
| 4.8 | 1 | 0.02 | 0.5 | 0.025 |
| 7.8 | 1 | 0.02 | 0.6 | 0.035 |
| 13.1 | 1 | 0.025 | 0.4 | 0.025 |
| <i>Vertical frames</i> | | | | |
| Z (m) | h_w (m) | t_w (m) | h_f (m) | t_f (m) |
| 0 | 1 | 0.02 | 0.3 | 0.025 |
| 2.62 | 1 | 0.02 | 0.3 | 0.025 |
| 5.24 | 1 | 0.02 | 0.3 | 0.025 |
| 7.86 | 1 | 0.02 | 0.3 | 0.025 |
| 10.48 | 1 | 0.02 | 0.3 | 0.025 |
| 13.1 | 1 | 0.02 | 0.3 | 0.025 |
| <i>Horizontal stiffeners</i> | | <i>Plating</i> | | |
| h_w (m) | t_w (m) | t_p (m) | | |
| 0.021 | 0.009 | 0.01 | | |

Table 3.8. Geometrical properties of gate 1

In order to corroborate the analytical model presented here above, the comparison is made between the numerical and analytical curves showing the evolution of the total collision force with the penetration. The same is done for the internal energy dissipated by the structure.

3.7.2.1. Impact by a raked bow

The case on an impact by a raked bow was treated by using two different vessels (Figure 3.60). The first one has a stem angle ϕ that is close to 90° , while the second one is much sharper. For each of them, the initial contact point is such that $Y_l = 8$ m and $Z_l = 6.5$ m (Figure 3.6). Considering two different ships principally aims to check that the transition from the local to the global deforming mode is more or less correctly assessed. Indeed, for vessel 1, as ϕ is quite important, the contact area between the bow and the gate grows rapidly, which means that the transition should occur earlier than for vessel 2.

The numerical and analytical curves showing the evolution of the resistance with the penetration are represented on Figure 3.61. From these results, it can be concluded that the simplified approach leads to a reasonably conservative estimation of the impact force and of the total penetration.

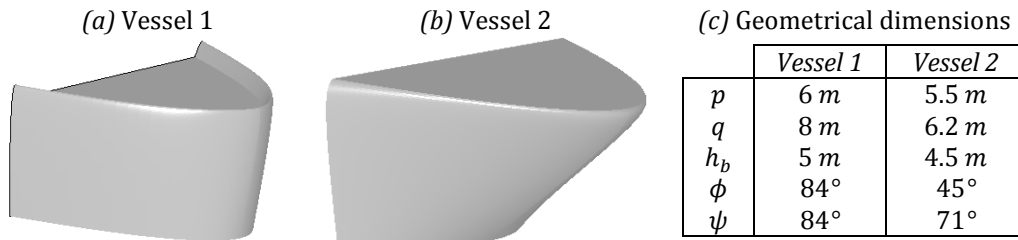


Figure 3.60. Three dimensional views of the raked bows

The only unsafe approximation appears for large values of δ , where the curves given by LS-DYNA tend to stabilize while the analytical ones keep growing. This is particularly visible on Figure 3.61b and can be explained by the fact that the membrane effects in the beams during the global mode are too generously calculated by the present approach. In fact, the postulated in-plane displacements $w_1(Y)$ and $w_2(Y)$ given by (3.80) are only based on geometrical considerations, but do not account for any mechanical properties of the gate. As claimed in section 3.6, doing so is only consistent under the assumption that the frames are weaker than the girders, which is not exactly the case in the light of the values listed in Table 3.8. Consequently, (3.80) is only acceptable as long as the values of δ are not too large, but the influence of the frames is increasing with the penetration and they finally force $w_1(Y)$ and $w_2(Y)$ to become more or less linear over the gate height. This is not totally reproduced by the analytical model, which leads to an underestimation of $w_1(Y)$ and $w_2(Y)$ and to increased membrane forces.

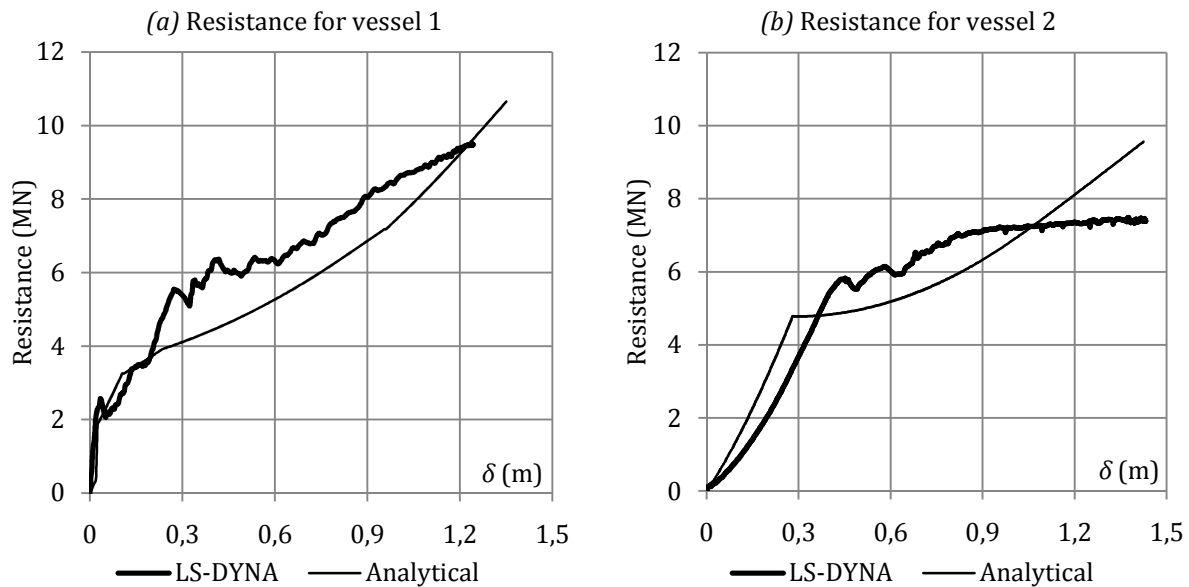


Figure 3.61. Comparison of the analytical and numerical resistance curves

Nevertheless, an overestimation of the resistance for important values of δ is not really problematic because in this case, the geometrical disorders on the gate are such that they are definitely not acceptable. In other words, in this situation, the crashworthiness is much more influenced by a serviceability limit state than by ultimate strength.

The curves showing the internal energy dissipated by the structure are depicted on Figure 3.62. As there is no other dissipative effect, the value reached at the end of the penetration is equal to the initial kinetic energy of 8 MJ. Furthermore, as these curves are obtained by integrating the resistance, it seems logical that they also reflect the conclusions detailed above.

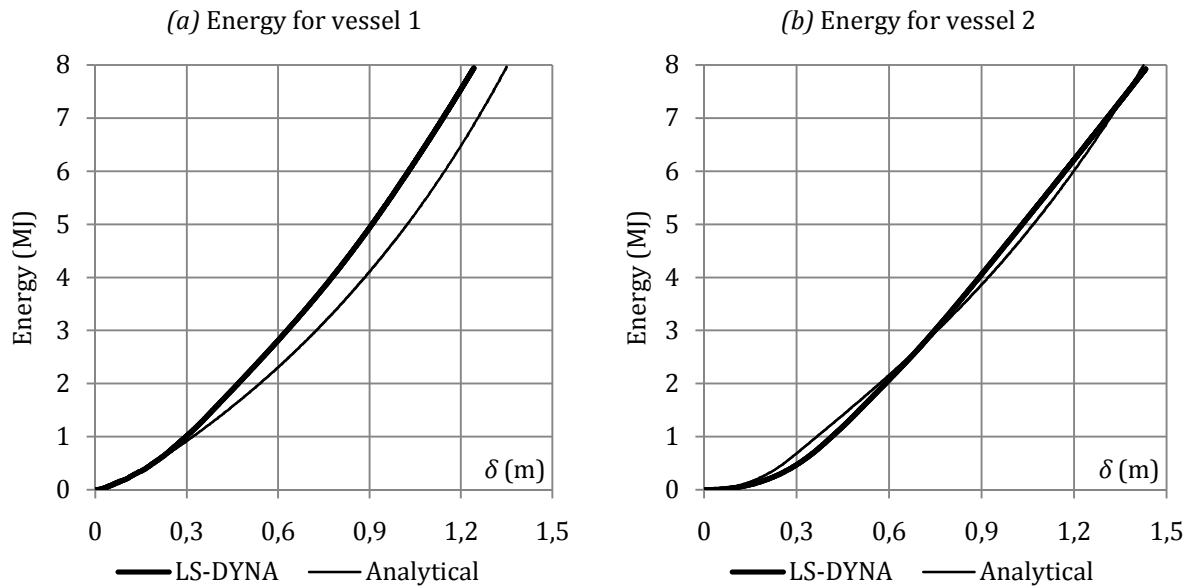


Figure 3.62. Comparison of the analytical and numerical energy curves

As a final comment, it can be seen from Figure 3.61 that the analytical model gives an acceptable prediction of the transition in the two cases. The switch from the local to the global mode occurs more or less around $\delta \approx 0.25 \text{ m}$ for both vessel 1 and 2.

3.7.2.2. Impact by a bulbous bow

The bulbous bow that is used here for the simulations is depicted on Figure 3.63. The geometrical dimensions are such that the contact first occurs between the bulb and the gate, with $Y_l = 5 \text{ m}$ and $Z_l = 6.5 \text{ m}$. The numerical and analytical curves showing the evolution of the resistance and of the internal energy with the penetration are reported on Figure 3.64. It can be seen that the overall agreement is quite satisfactory. As expected, the observations made in section 3.7.2.1 regarding the membrane effects still hold as the resistance is overestimated for large values of δ .

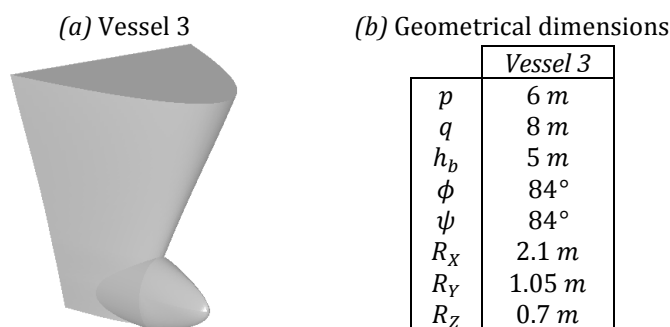


Figure 3.63. Three dimensional view of the bulbous bow

However, from Figure 3.64a, another divergence may also be pointed out during the local deforming mode and can be explained in the following way. At the beginning of the simulation, only the bulb is involved in the collision process but when the penetration is more or less equal to 0.15 m , a subsequent contact develops between the gate and the stem. Numerically, this is assimilated to a slight shock and explains why the resistance computed by LS-DYNA is suddenly increasing. However, in the analytical approach, as the subsequent contact only implies local deformations of plating super-elements, there is no theoretical reason for having an abrupt increment.

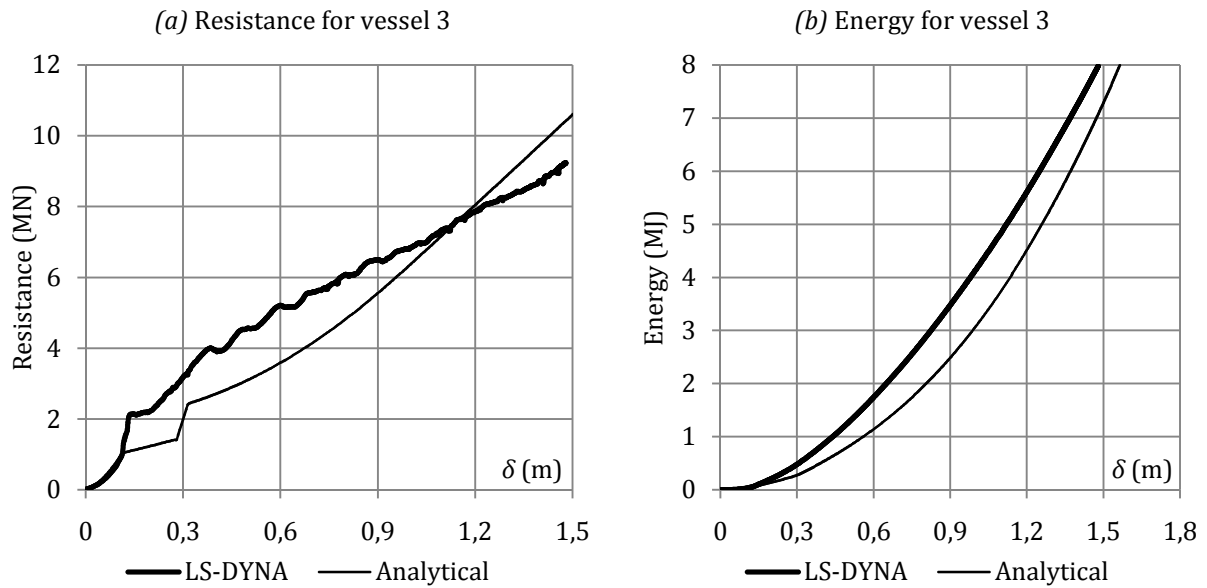


Figure 3.64. Comparison of the analytical and numerical resistance and energy curves

In conclusion, there is no physical shortcoming in the simplified approach that may justify the divergence in the local mode. Furthermore, neglecting the shock caused by the stem leads to a conservative estimation of the resistance. This is particularly visible on Figure 3.64b, from which it can be observed that the energy dissipation is always safely predicted.

3.7.3. Impact on a gate free at the bottom

In order to investigate a gate that is free at the bottom, the same impact situations than those considered in section 3.7.2 can be relevant. For conciseness however, only two vessels will be used and the energy curves will not be presented.

The evolution of the collision force with the penetration is depicted on Figure 3.65 for an impact by a raked or a bulbous bow. By comparing these results with those of Figure 3.62 and Figure 3.64, it is clear that the resistance is strongly reduced if the gate is not supported by a sill. After reaching a maximal value that is more or less equal to 6000 kN in both cases, the curves start decreasing slowly with the penetration, which is quite typical of an unstable behavior. This phenomenon is also reported by the analytical approach and can be explained in the following manner. During the global mode, when the plastic mechanism is activated, some membrane effects tends to develop in the horizontal beams (see section 3.6.3) and each of them is submitted to an extension rate $\dot{\Delta}_i$ that is given by (3.83). At the beginning of the penetration, the lateral displacements $w_1(Y)$ and $w_2(Y)$ are still sufficiently small, so $\dot{\Delta}_i$ is positive and the resistance is growing. Nevertheless, this is not the case anymore with larger values of δ and for some of the beams, the axial straining increment is negative, which implies that their contribution $P_i(\delta)$ calculated by (3.85) or (3.88) decreases.

On a physical point of view, having $\dot{\Delta}_i < 0$ can be justified as follows. In fact, the in-plane displacements are more important for the beams located near the impact point than for the other ones because they are strongly influenced by striking bow. Ideally, each beam tends to keep a constant axial length ($\dot{\Delta}_i \simeq 0$) in order to minimize its internal dissipation. However, this is practically impossible because they are connected to each other by the frames and submitted to the out-of-plane displacement field $g(Y, \delta)$ imposed by the vessel (Figure 3.52a). As a consequence, the beams located near the impact point are put into tension by the

others because these latter have a smaller axial reduction. This explains why the resistance still increases at the beginning of the collision. When the penetration gets larger, the mechanism simply works the other way round: the beams located near the impact point force the others to follow them, which finally leads to an unstable configuration.

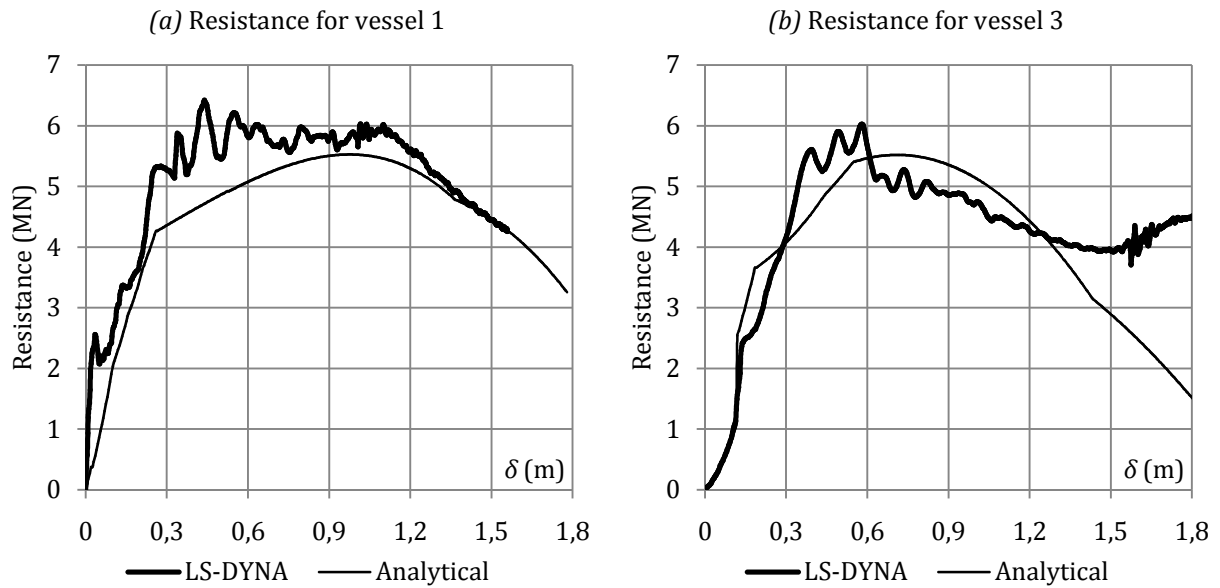


Figure 3.65. Numerical and analytical resistance curves

The phenomenon explained here above is of course influenced by the stiffness of the frames because they transfer the displacement field to all the beams. If these latter are slightly connected to each other, then it is probable that this kind of instability will only happens for very large indentations. Another factor that also plays an important role is the distance between the contact point and the supports. If the impact is located near the lock walls, then it is also to fear that the in-plane displacements will be quite important. These observations are confirmed by the results reported in Appendix B.5.

As a final remark, it can be noted from Figure 3.65b that the analytical resistance leads to a drastic underestimation when $\delta > 1.5 \text{ m}$. In fact, this is exactly the same problem than the one already noticed in section 3.7.2 regarding the membrane forces that are also too generously estimated, but in the negative range this time.

3.8. Conclusions

The purpose of this chapter was to develop an analytical model to predict the collision resistance of a plane lock gate with a single plating. The mathematical procedure followed is briefly summarized hereafter.

As a first step, the gate behavior was studied in the local deforming mode, by supposing that the deformations were essentially located in a confined area near the impact point. The super-elements method was used to evaluate the collision resistance under this hypothesis and three different types of structural entities were considered. For each of them, the upper-bound method was applied to get an analytical estimation of their individual contribution to the local resistance (sections 3.3, 3.4 and 3.5).

As a second step, to account for the coupling that occurs between all the super-elements, another analytical solution was derived by assuming that the structure was submitted to an overall bending motion. During this global deforming mode, the gate was modeled as a set of horizontal beams weakly connected to each other by the frames. The resistance was evaluated by applying the equilibrium method in both the elastoplastic and rigid-plastic regimes (section 3.6).

Finally, a method was proposed to combine the local and the global calculations in order to approximate the resulting gate resistance. As matter of validation, the results of this simplified method were directly compared to those obtained by simulating numerically ship collisions on lock gates (section 3.7).

In addition to the mathematical and numerical efforts listed here above, it is also important to stress the following points:

- Applying the upper-bound method to get the local resistance for each type of super-element leads to analytical solutions that reasonably match the numerical results. This assertion is confirmed by the numerical validations presented in sections 3.3.4, 3.4.3 and 3.5.3. Nevertheless, one of the major difference with similar developments performed to study ship-ship collisions is the need to include the beam-like behavior when working with SE2 or SE3.
- Similarly, applying the equilibrium method to get the global resistance also provides a quite acceptable approximation of the resistance when the gate is submitted to an overall bending motion. However, the agreement with finite element results is conditioned to a realistic evaluation of the lateral displacements occurring at the lock walls. If this requirement is not fulfilled, the simplified approach could lead to an overestimation of the resistance. The same observation is also valid regarding the stiffness of the vertical frames, as the analytical solution is found to be more satisfactory if these latter are quite weak.
- As expected, when studying numerically and analytically collisions on lock gates, it was found that the impact resistance was higher if the structure is supported by a sill. Moreover, it was also pointed out that an unstable behavior is possible for quite large penetrations. This is roughly illustrated on Figure 3.66 for the gate studied in section 3.7. The equivalent Von Mises stresses during the overall bending mechanism are plotted when the bulbous bow penetration is equal to $1.6 m$ (the red portions indicate where the flow stress is reached). From these pictures, if the gate is not supported at the bottom (Figure

3.66a), it appears that the structure simply slides on the lateral supports and rotates at the same time around a generalized plastic hinge, which explains the instability. On Figure 3.66b, this phenomenon is much less pronounced because of the additional support provided by the sill.

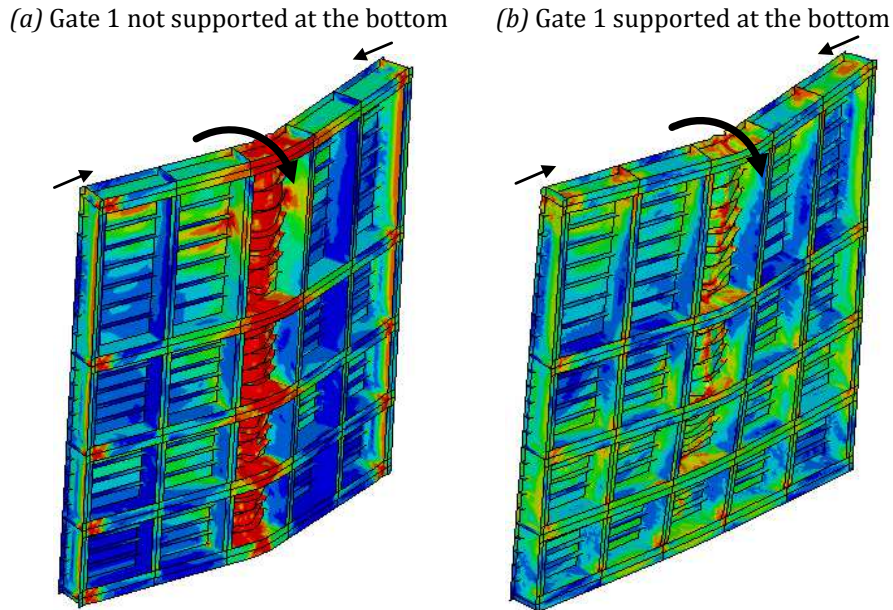


Figure 3.66. Comparison of the plastic mechanisms for gate 1 ($\delta = 1.6 \text{ m}$)

As a conclusion, it can be said that an analytical tool has been developed to evaluate the impact resistance of plane lock gates with a single plating. Both the situations of a structure supported or free at the bottom have been treated under the assumption that the frames are weaker than the girders. The results given by this simplified tool are essentially the evolutions of the total collision force and internal energy with the penetration and the internal energy curve. Nevertheless, one of the main limitation is due to the method used. Indeed, as the main theoretical basis is the virtual work principle, only the overall equilibrium is satisfied. Consequently, trying to evaluate local fields such as stresses, strains or reaction forces is illusory with the present energy approach.

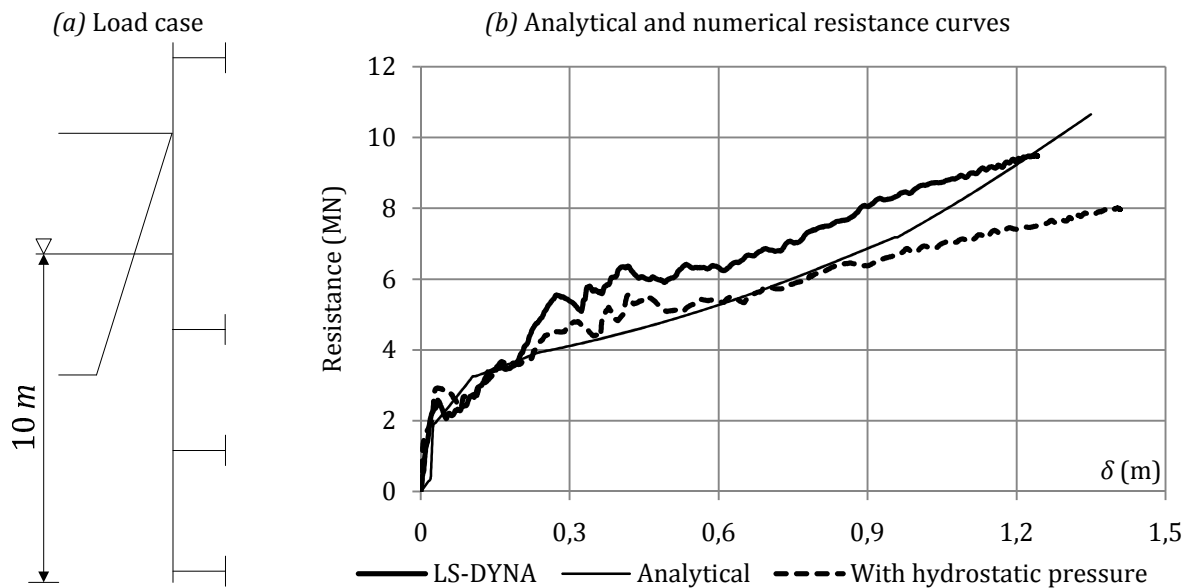


Figure 3.67. Influence of the hydrostatic pressure

Finally, it is worth recalling that the impact on a lock gate has to be studied in parallel with other load cases, which can be done by applying the combination methods of Eurocode 0 [50]. Accounting for this remark is of prior importance to evaluate the final resistance. As a matter of illustration, if the lock gate studied in section 3.7.2.1 is simultaneously submitted to an impact by a raked bow and a 10 m hydrostatic pressure (Figure 3.67a), the resistance curves depicted on Figure 3.67b are obtained. This picture shows that the collision force is approximately reduced by 25 % if the action of water is retained. By the same time, the final penetration reached by the vessel is increased by 4 %, which is not really significant.

CHAPTER 4. Analytical derivation of the collision resistance of mitre gates

This chapter presents an analytical method to derive the collision opposed by mitre lock gates during a collision involving a vessel of given shape. The structure properties postulated for this study are presented in section 4.1.

The resistance is first derived under the assumption of a local deforming mode by applying the super-elements method. Three types of structural components are studied separately. The analytical developments are performed by accounting for the inclination due to the mitre angle. The upper-bound method is applied to derive kinematically admissible formulae that are each time validated by numerical comparisons in section 4.2.

In section 4.3, the calculation is made for the global deforming mode by dividing each leaf into a set of horizontal beams supported at their extremities by the lateral and central studs. The derivation is done for both an elastoplastic and a perfectly plastic material.

The analytical results of the simplified method are validated in section 4.4 by comparing them to those obtained numerically.

Finally, the main steps and achievements presented in this chapter are summarized in the conclusion.

The developments presented in this chapter have been partly published by Buldgen et al. [24] and presented in the 32nd International Conference on Ocean, Offshore and Arctic Engineering [23].

4.1. Introduction

This chapter is devoted to the analytical study of ship collisions with mitre gates (Figure 4.1). They are one of the oldest gate type encountered in lock structures but are still commonly used today, especially for modest locks but also for larger ones (up to a width of 25 to 35 m). In an attempt to develop a simplified tool to evaluate their impact resistance, the first step is probably to have a proper description of the structure considered here.

4.1.1. Description of the impacted gate

4.1.1.1. Structural properties

The structure of a mitre gate is represented on Figure 4.2 (in order to have a better insight, some additional pictures are also reported in Appendix C.1). As shown by the top view of Figure 4.2a, such gates are made of two leafs that are usually symmetric and maneuvered by hydraulic jacks. At the middle of the gate, they are simply resting against each other through the action of central blocks, while the contact with the lock walls is provided by some lateral blocks that may be seen on Figure 4.1b. The link between the leaf and its supports is made by rigid vertical studs.

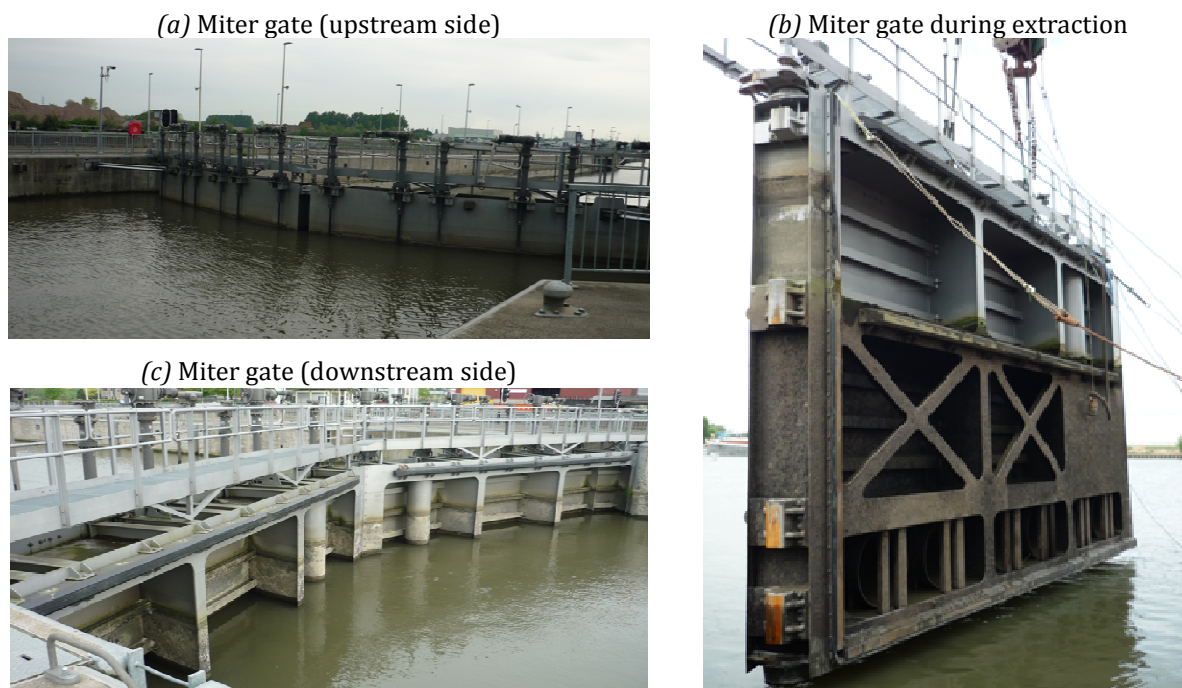


Figure 4.1. Mitre gate of the Evergem lock (Belgium)

The plane view of one leaf is depicted on Figure 4.2b. It is only a simplification of the real structure because it does not account for the various other reinforcing components that may be placed on the downstream face (Figure 4.1b). These latter are disregarded in the present study to keep only the regular structure made of the plating and reinforced by horizontal girders and vertical frames, which constitute the principal stiffening system of the gate. These elements are of prior importance when dealing with collisions, as they provide the major contribution to the crashworthiness of the struck structure. As for plane lock gates, they also have a T-shaped cross-section (Figure 3.3). In some cases, transverse and/or vertical stiffeners are added to prevent the plating from buckling, but they do not play an important role in the capacity of the gate to withstand collisions.

At the bottom of the lock chamber, the gate is placed on a pivot that allows for its rotation during the opening. This motion is also possible because one or several ties are placed at the top of the lock walls and prevent the leaf from falling into water. Sometimes, one or two additional diagonal diaphragms link the upper left and lower right corners (Figure 4.2b) in order to reduce the in-plane deformations and bending of the leaf under its dead weight during the opening movement. However, as these latter do not play a crucial role for the crashworthiness of the structure, they will not be considered here.

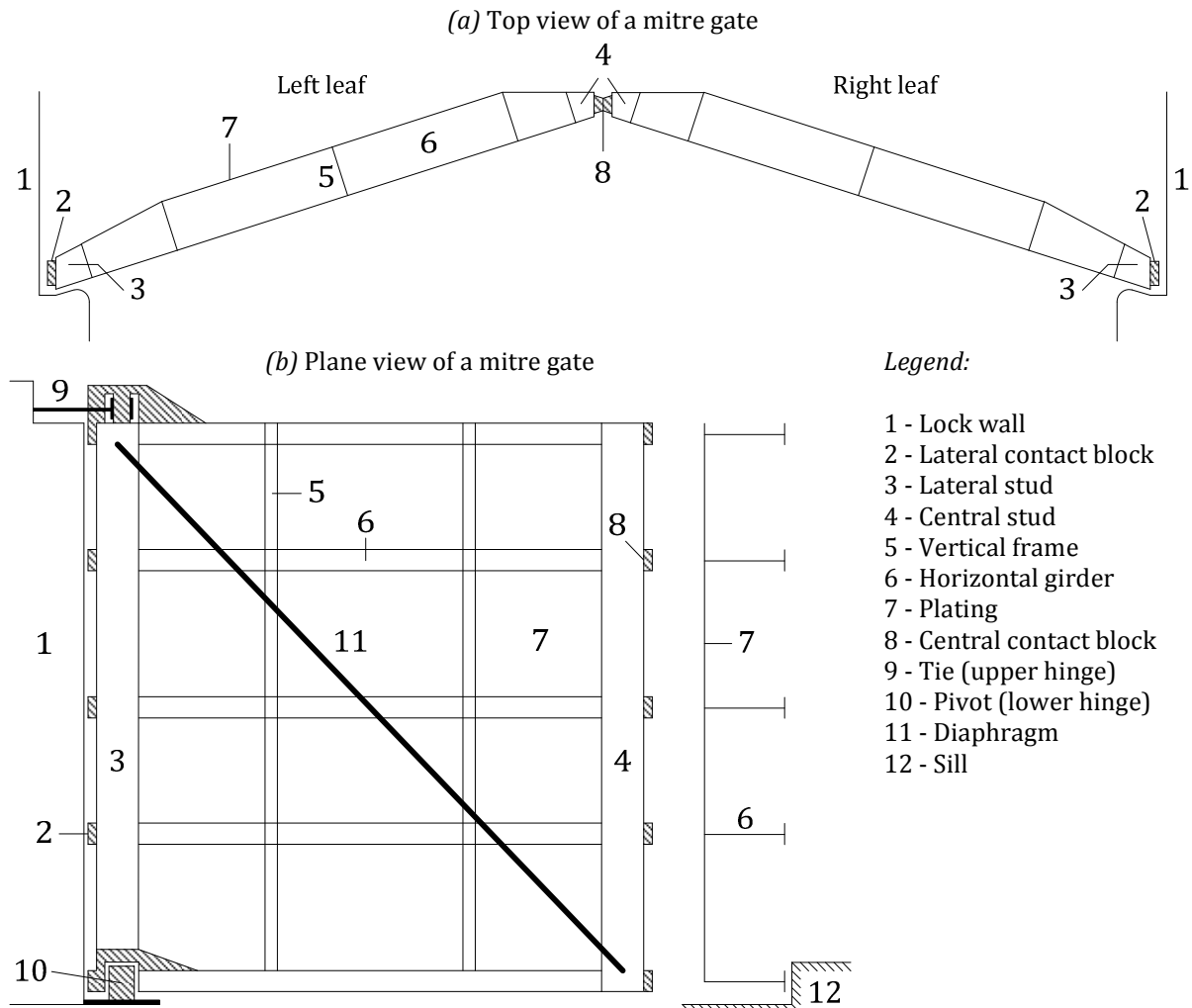


Figure 4.2. Top and plane views of the structure of a miter lock gate

Finally, it should be mentioned that the gate is usually supported by a sill whose primary functions are to ensure watertightness and provide a supplementary support to structure in some cases. As additional contacts are likely to develop in this region during the collision, the sill may constitute an indirect restraint to the motion of the gate.

4.1.1.2. Geometrical properties

In order to derive analytically the collision resistance, all the previous structural data need to be formalized mathematically. To do so, two different global reference frames are introduced (Figure 4.3). The first one (X, Y, Z) is the same as for plane gates and is such that the axes X and Z are respectively parallel to the longitudinal and transversal directions of the lock chamber. The second one (X', Y', Z') is placed in the plane of the gate and is simply obtained by rotating (X, Y, Z) around the vertical axis.

As for plane gates, the horizontal girders and the vertical frames are placed in some discrete positions that are defined to properly characterize the structure. This time, instead of working in the (X, Y, Z) coordinate system, it is probably more convenient to use directly the rotated frame (X', Y', Z') . Doing so, the reinforcing elements are located along the Y' and Z' axes by introducing their respective positions Y'_i and Z'_i .

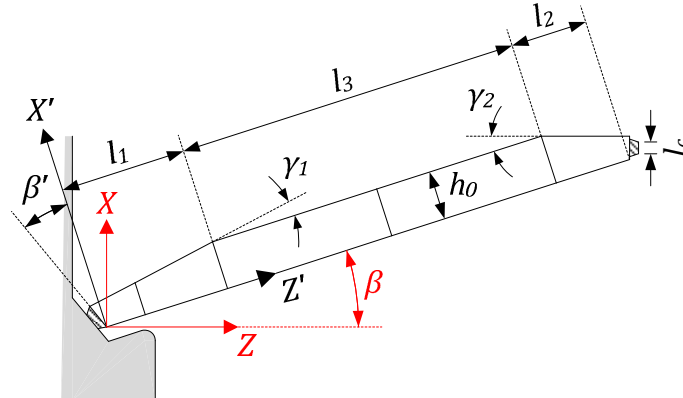


Figure 4.3. Geometrical data characterizing one leaf

Regarding the orientation of each leaf, two different angles are required to have a proper positioning. The first one is called the mitre angle denoted by β and measured between the Z and Z' axes (Figure 4.3). Usually, for classical gates, it is more or less equal to 20° . The second one is the support angle designated by β' and introduced to precise the inclination of the leaf with respect to the lock wall. Most of the time, it is of current practice to choose $\beta' = \beta$.

In order to define more specifically the shape of the upstream side, many other geometrical parameters are still required, such as the lengths l_1 , l_2 , l_3 and the angles γ_1 and γ_2 . They are mainly useful to locate the initial contact point between the stem and the gate, but also to detect the super-elements that are activated for a given penetration. As they will be extensively used in this chapter, length l_c of the central contact block and the maximal web height h_0 of the girders (Figure 4.3) are also introduced.

4.1.1.3. Boundary conditions

The boundary conditions of a mitre gate are essential to ensure its overall stability. As mentioned previously, the contact between the leaves and the lock walls is provided by lateral contact blocks that are placed at the same discrete levels Y'_i than the girders. Ideally, these latter may be assimilated to hinges, as they allow for rotational movements. Their role is mainly to transmit compressive forces, even though some shearing components may develop because of friction. Of course, it is obvious that no tensile forces are likely to appear at these locations.

Similarly, at the center of the gate, the two leaves rest against each other through the central blocks. Consequently, neither bending moment nor tensile forces are expected at these locations. In the case of an off-centered impact however, the friction forces are of prior importance to define a non-sliding condition but this will be discussed later.

Finally, at the bottom of the lock chamber, the downstream displacements along the X' axis are prohibited by the sill. Of course, in practice, short displacements are required before having a contact due to the rubber seal.

4.1.2. Description of the collision scenario

The striking vessel that is considered here is the same as the one described in section 3.1.2.1 for plane lock gates. On a mathematical point of view, it is still made of a stem \mathcal{S} and eventually of a bulb \mathcal{B} whose summits are respectively denoted by S and B (Figure 3.7a). In the local reference frames (x_s, y_s, z_s) and (x_b, y_b, z_b) attached to \mathcal{S} and \mathcal{B} , the mathematical equations describing the stem and the bulb are strictly identical to (3.1) and (3.2). They can be used to derive the position (X_I, Z_I) of the first impact point simply by imposing a tangency condition between the bow and gate. Finding the initial position of the striking vessel is thus a bit more complicated than with a plane situation.

Another difference with Chapter 3 is that two distinct situations have to be considered regarding the collision scenario:

- If the ship dimensions are sufficiently small in comparison with those of the lock chamber, then an off-centered collision is possible (Figure 4.4a). In this case, only one leaf is impacted, the other one remaining undamaged.
- On the other hand, it is also possible to have a configuration such that the two leaves are both simultaneously impacted. This situation is called a "centered collision" and is represented on Figure 4.4b.

Of course, because of their particular design, mitre lock gates are not able to withstand severe collisions if the ship moves upstream. In such a case, the impact force can be only compensated by the action of the hydraulic jacks and by the hydrostatic pressure if the downstream and upstream water levels are not the same. Consequently, only the two collisions configurations of Figure 4.4 will be treated in this chapter.

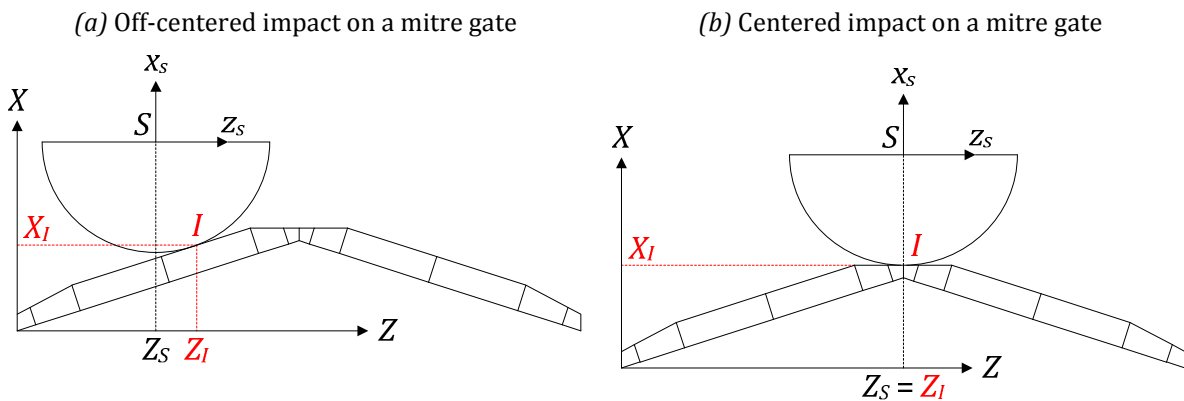


Figure 4.4. Collision scenario

Predicting the worst scenario for mitre gates is an arduous task. Obviously, it can be argued that off-centered impacts are only possible with quite small vessels that may only induce minor collisions. However, if the initial kinetic energy of the striking ship is such that the contact between the two leaves is lost, then the integrity and the watertightness of the lock gate is no longer preserved. Such a situation may have severe consequences, such as a progressive individual collapse of the leaves because of the water pressure or an emptying of the upstream reach. Moreover, it is also to fear that important potential damages will be caused to the striking bow. On the contrary, a centered impact is more likely to lead to a stable deformed configuration. Consequently, it cannot systematically be claimed that the

most severe damages to the structure appear when it is impacted by a large vessel. Of course, the recommendations given in 2.2 regarding the choice of the mass and of the initial velocity are still valid for mitre gates.

4.1.3. General methodology

Under the conservative hypothesis that the ship is perfectly rigid, all its initial kinetic energy E_0 calculated by (2.3) has to be entirely absorbed by the deforming impacted structure. To achieve this goal, the deformation sequence for the two collision scenarios of Figure 4.4 is exactly the same as for plane gates. The local mode is first activated, in combination with an overall elastoplastic bending motion of the gate. Three different calculations are done during this phase:

- The first one is performed by decomposing the structure into large uncoupled entities made of a rigid-plastic material (Figure 4.6a). In accordance with (3.3), it is possible to derive the local resistance $P_L(\delta)$ by summing up the individual contributions $P_i(\delta)$ coming from the activated super-elements. Three different types are also required here. They are strictly identical to those presented in section 3.2.2.1, but unlike plane gates, it is important to stress that a careful distinction has to be made between an impact involving a girder or a frame (SE2). The definitions are briefly recalled in Table 4.1.
- The second one is based on the assumption that each leaf may be idealized as a set of horizontal elastoplastic beams that are simply bent between the central and the lateral studs (Figure 4.6b). Doing so provides the global resistance $P_G(\delta)$ given by (3.5), where $P_i(\delta)$ is the elastoplastic contribution of each individual beam.
- The third one is also carried out by considering the mechanical model of Figure 4.6b, in which the beams are this time assumed to be made of a rigid-plastic material. Using this model, it is possible to evaluate the force $P_t(\delta)$ that is required to activate an overall plastic mechanism over the gate.

The resistance during the local mode is then found by combining the results of the aforementioned calculations. Here again, it is proposed to use the same formula than for plane gates and to take the minimum value between $P_L(\delta)$ and $P_G(\delta)$ as an approximation of the resistance. This is roughly depicted on Figure 4.5 for $\delta < \delta_t$.

| | |
|-----|---|
| SE1 | Plating elements limited by two horizontal girders and two vertical frames. |
| SE2 | Portion of a horizontal girder limited by two vertical frames. |
| | Portion of a vertical frame limited by two horizontal girders. |
| SE3 | Intersection between a vertical frame and a horizontal girder. |

Table 4.1. Definition of the super-element types for mitre gates

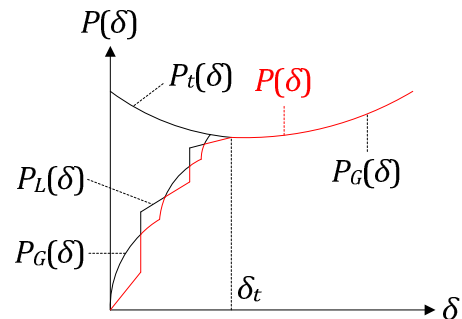


Figure 4.5. Combination of the local and global resistances

As soon as the collision force applied during the local mode reaches $P_t(\delta)$, it is sufficient to activate an overall plastic mechanism, so there is a switch to the global deforming mode. This

transition occurs for a given particular value δ_t of the penetration that may be found by resolving the following equation:

$$\min(P_L(\delta) ; P_G(\delta)) = P_t(\delta) \quad (4.1)$$

where $P_G(\delta)$ is the global elastoplastic solution mentioned here above. Consequently, all the beams depicted on Figure 4.6b are in a perfectly plastic state if $\delta > \delta_t$. In this situation, it is possible to perform a new rigid-plastic calculation of the resistance $P_G(\delta)$ and to consider this solution for the global deforming mode. To do so, equation (3.5) is still valid, but $P_i(\delta)$ is this time the rigid-plastic contribution of each individual beam.

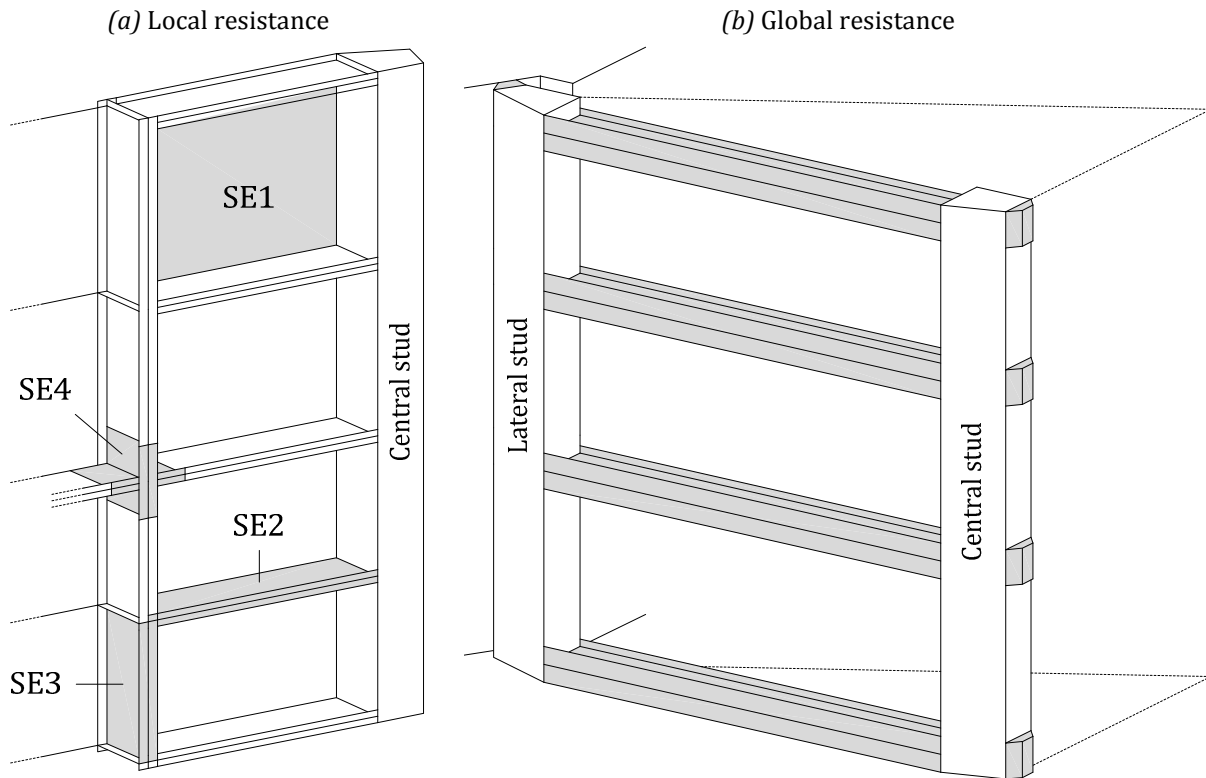


Figure 4.6. Mechanical models to derive the local and global resistances

From the procedure detailed here above, it appears that the methodology to evaluate the collision resistance of a mitre gate is strictly identical to what has been done in Chapter 3 for plane configurations. Nevertheless, the mathematical expressions of $P_L(\delta)$ and $P_G(\delta)$ are somewhat different because there is now a relative inclination between the vessel and the structure, due to the mitre angle β .

4.2. Resistance in the local deforming mode

The analytical derivation of $P_L(\delta)$ in the case of a mitre gate is similar to what has been done in Chapter 3. The main difficulty is to account for the relative inclination between the gate and the impacted leaf. In fact, the developments of this section can be seen as a generalization of those already performed for plane gates, so there is probably no need to have an extensive presentation of all the mathematical calculations leading to the local resistance. The various super-elements of Table 4.1 will be considered in sections 4.2.1, 4.2.2 and 4.2.3 respectively.

4.2.1. Super-elements of type 1

4.2.1.1. Analytical derivation of the resistance

For conciseness, only an impact implying the stem \mathcal{S} will be treated in this section, the case of a collision by the bulb \mathcal{B} being strictly similar. The mathematical equation of \mathcal{S} in the global reference frame (X, Y, Z) is still given by (3.9), in which the coordinates Y_S and Z_S of the summit S are two parameters specifying the collision scenario. The position X_S along the horizontal X axis is calculated by imposing a tangency condition between the gate and the vessel.

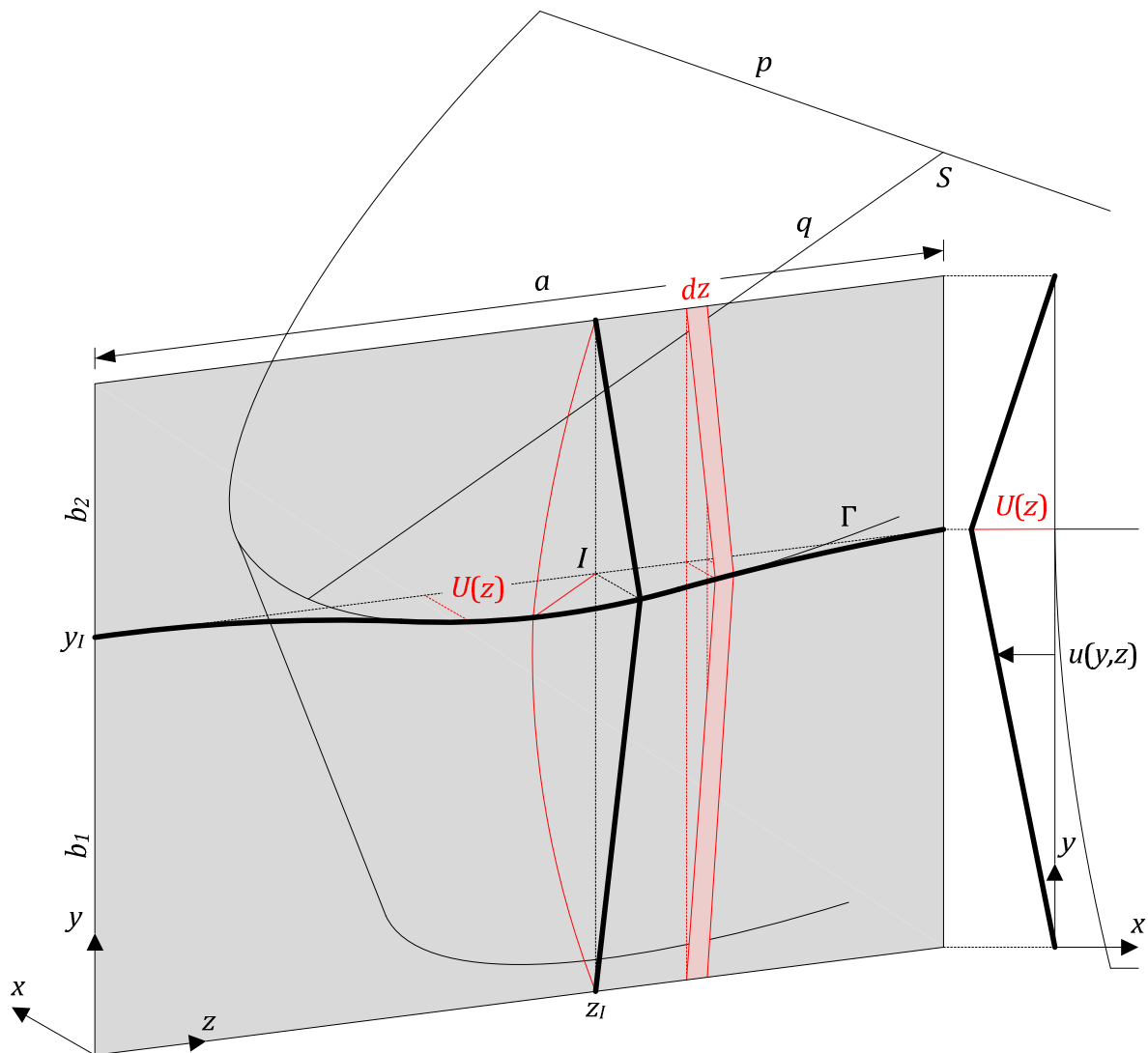


Figure 4.7. Deformation pattern and displacement field $u(y,z)$

In order to derive mathematically the resistance opposed by plating elements, let us start by introducing a local reference frame (x, y, z) such that the y and z axes are in the plane of the super-element, while the x axis is perpendicular to the (y, z) plane (Figure 4.7). This new frame is not parallel to the global one, but makes a certain angle with it. On Figure 4.8, for convenience, this latter is denoted by β , but from Figure 4.3, it is clear that it could also be equal to $\beta + \gamma_1$ or $\beta - \gamma_2$ according to the position of the impacted gate element along the Z' axis.

Under the hypothesis that the out-of-plane motions are predominant, the evaluation of the internal energy rate can be done by considering only a kinematically admissible displacement field $u(y, z)$ that is parallel to the local x axis. This remark is of prior importance: even though the ship is travelling along the global X axis, the displacements imposed to the plate remains perpendicular to its initial plane, which means that a free sliding condition is supposed between the bow and the plating. Of course, this would not be the case if friction was implied during the contact.

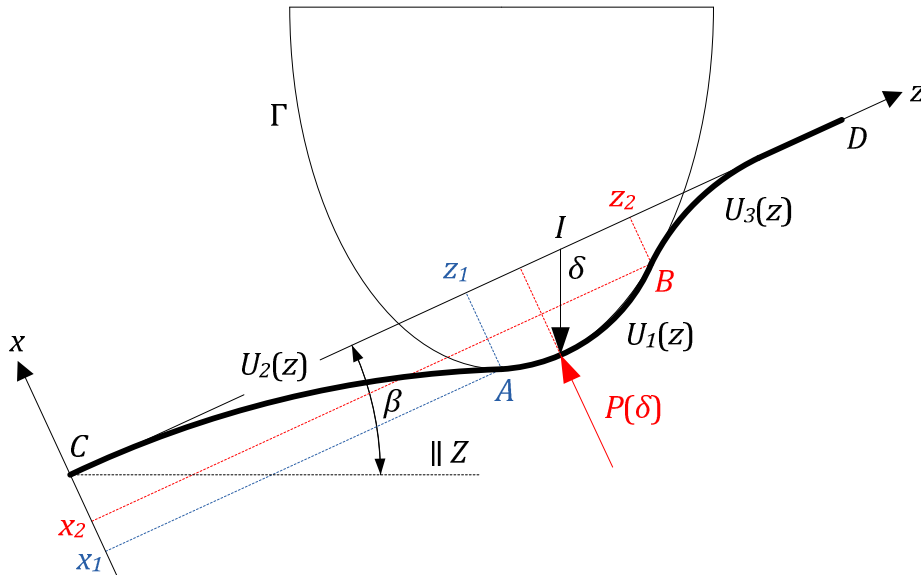


Figure 4.8. Plane view of the out-of-plane displacements imposed by the uppermost deck

The particular profile of $u(y, z)$ in the plane of the uppermost deck is denoted by $U(z)$. The displacement pattern is depicted on Figure 4.8 and is made of two parts. The first one is restricted on the portion bounded by points A and B , placed in z_1 and z_2 along the local z axis respectively. It is worth noting that z_1 decreases with the penetration, while z_2 is an increasing function of δ , which means that there is an extension of AB when the vessel moves forward. The derivation of z_1 and z_2 is not straightforward as it has to be achieved by imposing continuity conditions at points A and B . The analytical derivation is detailed in Appendix C.2.

From Figure 4.8, it can be seen that there is a continuous contact between the bow and the plate along the portion AB , which means that $U_1(z)$ has to follow the shape of the stem. Consequently, the displacements have to be defined in accordance with the curve Γ that models the elliptic profile of the uppermost deck. To do so, it is first required to express equation (3.9) in the local reference frame, which can be achieved by considering the following formulae:

$$X = X_C + x \cos \beta + z \sin \beta \quad ; \quad Z = Z_C - x \sin \beta + z \cos \beta \quad (4.2)$$

where X_C and Z_C are the coordinates of point C in the global axes. These two coordinates are not unknown because they have to be specified while defining the gate geometry. Introducing (4.2) in (3.9) and solving with respect to x leads to the following result for $U_1(z)$:

$$U_1(z) = K_1 + z \cot \beta - K_2 \sqrt{K_3 + z \sin \beta + \delta \sin^2 \beta} \quad (4.3)$$

where K_1 , K_2 and K_3 are constant parameters that may be expressed with help of the position (X_S, Z_S) of the summit S in the global reference frame. It can be shown that:

$$K_1 = \frac{p^2 \cot \beta}{2q \sin \beta} - \frac{X_S - X_C}{\sin \beta}; \quad K_2 = \frac{p}{\sqrt{q} \sin^2 \beta}; \quad K_3 = \frac{p^2}{q} (1 - \tan^2 \beta) - (X_S - X_C) \tan \beta \quad (4.4)$$

Once $U_1(z)$ is completely defined, the next step is to perform the same work for the two remaining portions AC and BD . For compatibility reasons, $U_2(z)$ and $U_3(z)$ are defined as parabolic functions of z that are adjusted to fulfill the following requirements:

$$\begin{aligned} \bullet \text{ If } z = 0: \quad U_2 = 0; \quad \frac{\partial U_2}{\partial z} = 0 & \quad \bullet \text{ If } z = a: \quad U_3 = 0; \quad \frac{\partial U_3}{\partial z} = 0 \\ \bullet \text{ If } z = z_1: \quad U_2 = U_1(z_1) = x_1 & \quad \bullet \text{ If } z = z_2: \quad U_3 = U_1(z_2) = x_2 \end{aligned} \quad (4.5)$$

where x_1 and x_2 can be easily found with help of equation (4.3). These considerations leads to:

$$U_2(z) = -x_1 \left(\frac{z}{z_1} \right)^2; \quad U_3(z) = -x_2 \left(\frac{z - a}{z_2 - a} \right)^2 \quad (4.6)$$

where (x_1, z_1) and (x_2, z_2) are calculated in Appendix C.2. Finally, the displacement field over the entire element is found by interpolating linearly over the heights b_1 and b_2 (Figure 4.7), with the particular conditions that $u(y, z) = 0$ if $y = 0$ and $y = b_1 + b_2$. With this assumption, equation (3.15) remains valid, in which $f(y)$ may still be found by applying (3.14). Unlike plane gates, it is worth noting that this linearity is only effective in a plane that is perpendicular to plate, but not in the direction followed by the striking vessel. This deformation pattern correctly reflects numerical simulations (see section 4.2.1.2 hereafter).

Once the displacement field $u(y, z)$ is properly defined, the resistance provided by the plate may be calculated. This can be achieved by considering the same theoretical basis as the one postulated in sections 2.3.2 and 3.3.2.2 for a rigid-plastic material (Figure 2.6). According to the plate strip model of Wierzbicki and Simonsen in [154], the internal energy rate associated to a fiber of length $b_1 + b_2$ and width dz (Figure 4.7) can be evaluated by (3.16), while (3.17) is also still relevant for a horizontal strip. Furthermore, assuming that the out-of-plane displacements parallel to the x axis are predominant and that the bending effects are negligible, formula (3.18) allows for a consistent derivation of the internal energy rate \dot{E}_{int} . The analytical calculation of \dot{E}_{int} is a quite fastidious task that has been performed by Buldgen et al. [21] for an inclined plate. Even though the present problem is quite similar, the formulae presented in [21] may not be directly extended to mitre gates. For conciseness, the detailed formulae to determine \dot{E}_{int} are reported in Appendix C.2.

In accordance with the upper-bound method, the external power \dot{W} is equated to \dot{E}_{int} to find the resistance. Under the assumption that there is no friction between the striking vessel and the plate, $P(\delta)$ may be assumed to remain always perpendicular to the initial plane of the plate (Figure 4.8). Consequently, if the velocity of the striking vessel is equal to δ , the impact

point I is only moving with a speed of $\dot{\delta} \cos \beta$ along the x axis. The external power \dot{W} is then calculated in the following manner:

$$\dot{W} = P(\delta)\dot{\delta} \cos \beta \Rightarrow P(\delta) = \frac{\dot{E}_{int}}{\dot{\delta} \cos \beta} \quad (4.7)$$

However, equation (4.7) is only valid as long as there is no rupture of the super-element. As in Chapter 3, this is assumed to occur when the deformations exceed a critical value ϵ_c that may be set to 7 % to have a satisfactory agreement with finite element simulations. As a final remark, it is also worth mentioning that all the formulae exposed here above degenerate into the ones developed for a plane gate when β tends to 0.

4.2.1.2. Numerical validation

As a matter of validation, the results given by the analytical developments performed here above were compared with numerical ones obtained using LS-DYNA. In most of the cases, the agreement was found to be quite satisfactory. This can be illustrated by the example presented hereafter. The impacted plate is characterized by a length a of 5.89 m, a total height $b_1 + b_2$ of 4 m and a mitre angle β equal to 17°. Its material properties are those of Table 3.2. The rigid striking vessel involved in the collision is the one depicted on Figure 3.60b. It is placed such that the first contact point I is located in $y_I = 2.9$ m and $z_I = 3.3$ m (Figure 4.7).

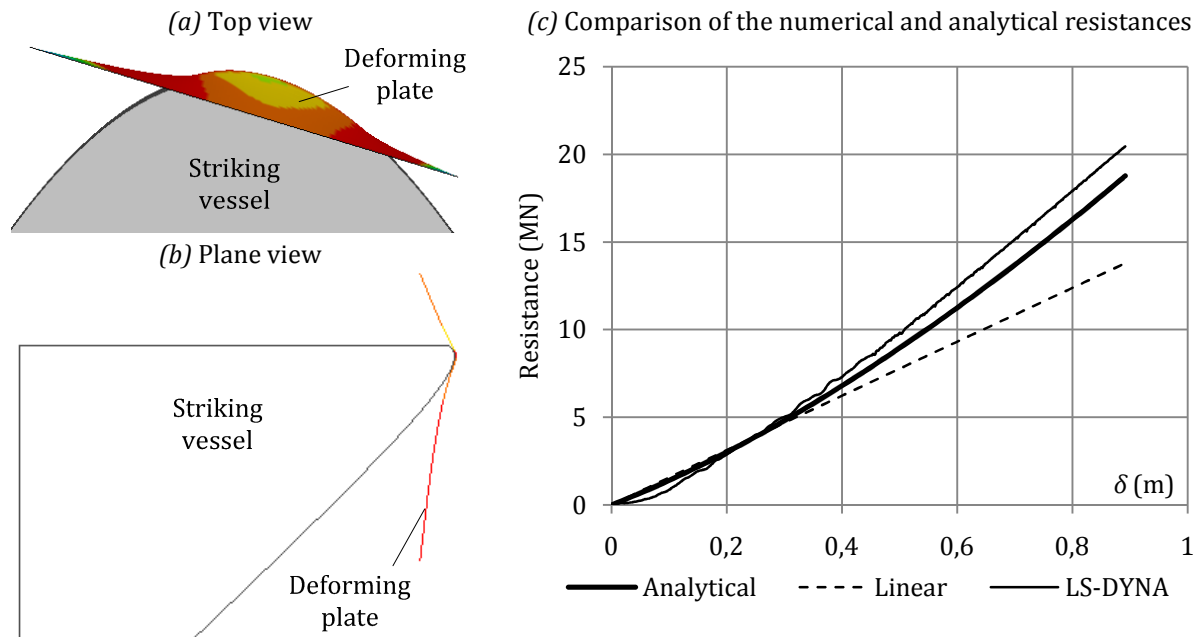


Figure 4.9. Comparison of the numerical and analytical results

In an illustrative purpose, the equivalent Von Mises stresses calculated by LS-DYNA are represented on Figure 4.9a. This top view of the collision process shows that the plate more or less truly follows the shape of the stem in the central part, which tends to corroborate the deformation pattern postulated on Figure 4.8. Similarly, from Figure 4.9b, it can be seen that the displacement profile in a plane perpendicular to plate is roughly made of two straight lines, which also justifies the linear interpolation suggested in section 4.2.1.1.

The comparison of the analytical and numerical resistances is presented on Figure 4.9c, from which the agreement is shown to be satisfactory. In order to point out the need of accounting for the true shape of the stem, the curve obtained by using the formulae suggested by Zhang

[180] is also plotted on this graph. This latter is obtained by assuming a punctual impact, which leads to the following equation:

$$P(\delta) = \frac{n_0}{3} a(b_1 + b_2) \delta \cos \beta \left(\frac{z_I(a - z_I) + \delta^2 \sin^2 \beta}{(z_I - \delta \sin \beta)^2 (a - z_I - \delta \sin \beta)^2} + \frac{1}{b_1 b_2} \right) \quad (4.8)$$

where z_I is the position of the initial contact point along the z axis and a is the length of the plate (Figure 4.7). It is obvious from Figure 4.9c that (4.8) tends to underestimate the resistance, in particular at the end of the impact. Such a conclusion was already noticed in section 3.3.4, where it was pointed out that postulating a linear displacement field leads to smaller values for the resistance and the internal energy. Once again, these results show that regarding plating elements, it is quite important to account for the shape of the bow if this latter has more or less the same dimensions than the plate.

4.2.2. Super-elements of type 2

The second type of super-element is introduced to treat the impact on the portion of longitudinal girders limited by two vertical frames (Figure 4.10a). Here again, two deformation modes need to be investigated: a folding and a bending mechanism.

4.2.2.1. Folding mechanism

Regarding the folding mechanism, the situation is nearly the same as the one investigated in section 3.4, except that the collision occurs obliquely because of the mitre angle β (Figure 4.10b).

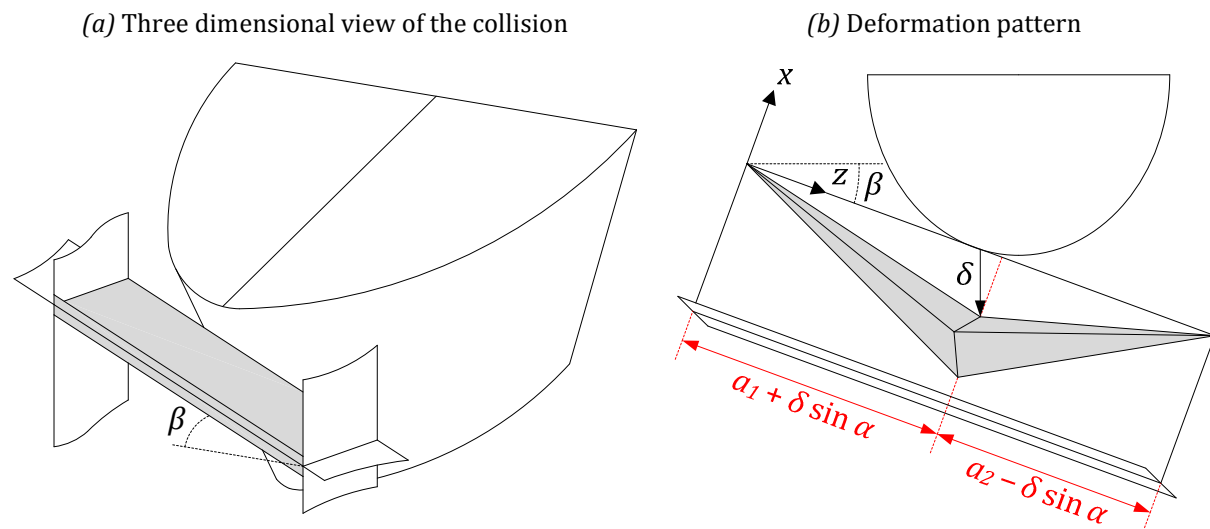


Figure 4.10. Impact on a horizontal girder

The deformation pattern is also a fold made of two wings of height H , but in comparison with the situation depicted on Figure 3.26, two main differences can be pointed out:

- Instead of considering an indentation equal to δ , the folding process has now to be derived for a local penetration of $\delta \cos \beta$.
- The lengths of each wing are no longer constant: they are equal to $a_1 + \delta \sin \beta$ and $a_2 - \delta \sin \beta$, which means that one wing increases, while the other decreases.

From the previous observations, it transpires that the connection between the two wings is nothing else than a moving plastic hinge line that is travelling with a velocity $\dot{w} = \dot{\delta} \sin \beta$ along the local z axis (Figure 4.10b). On a theoretical point of view, this particularity should have some implications on the deformation pattern in the central region. However, as the folding height H is supposed to be quite small, the bending effects at the junction can be neglected, so the questioning issue of having a moving hinge will be discussed later (see section 4.2.2.2).

In order to develop the formulae leading to the collision resistance, one can consider the generalized crushing process of Figure 4.11 for which the height and length of the current wing are respectively equal to $2H$ and $a_1 + \delta \sin \beta$. From this picture, it appears that (3.38) and (3.39) are no more valid and have to be corrected in the subsequent manner:

$$\begin{aligned} \bullet \quad \overline{OA} &= \sqrt{(a_1 + \delta \sin \beta)^2 + \delta^2 \cos^2 \beta} & \rightarrow W_A &= \frac{\delta^2 \cos^2 \beta}{2(a_1 + \delta \sin \beta)} \\ \bullet \quad \overline{BD} &= \sqrt{\frac{(a_1 + \delta \sin \beta)^2}{4} + H\delta \cos \beta} & \rightarrow W_B &= \frac{H\delta \cos \beta}{a_1 + \delta \sin \beta} \end{aligned} \quad (4.9)$$

where W_A and W_B are the displacements of points A and B along the z axis. Using these new definitions, the same linear interpolation than (3.40) is applied to get the function $W(x)$ characterizing the horizontal motion of any point located along the junction ABC of the two wings (Figure 4.11). Doing so, the following displacement field can be postulated:

$$w(x, z) = W(x) \frac{z + (a_1 + \delta \sin \beta)x/2H}{(a_1 + \delta \sin \beta)(1 + x/2H)} \quad (4.10)$$

which is coherent with the assumption already made in section 3.4.2.1 that only the portion of the horizontal fibers located beyond the straight line OC is submitted to an axial straining. This latter is responsible for a membrane dissipation that can be quantified by calculating the energy rate \dot{E}_m , which can be achieved by applying (3.47). The procedure is similar to the one followed in section 3.4.2.1 but leads to quite cumbersome equations because of the more complex definition of $w(x, z)$.

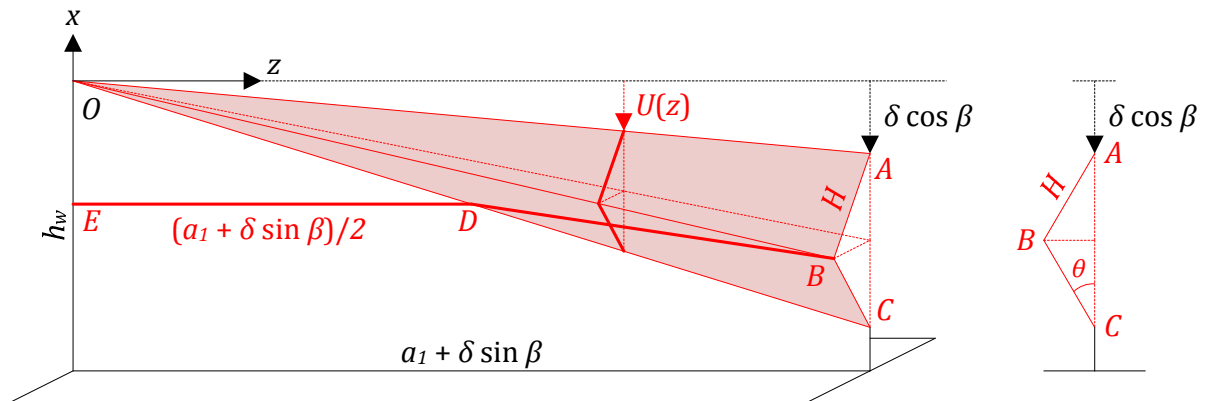


Figure 4.11. Deformation pattern for one wing

Apart from the axial straining, there is also an energy dissipation due to the plastic rotations along the segments OA , OB , OC , AB and BC . Under the hypothesis that H is small with respect to the lengths a_1 and a_2 , the contributions of the central hinges can be neglected, which leads to a simplified evaluation of the bending energy rate \dot{E}_b . The detailed analytical

developments leading to \dot{E}_m and \dot{E}_b are not reported here but some additional information can be found in Appendix C.2 (section C.2.2.1). It can be shown that:

$$\dot{E}_m = n_0 H \left(\frac{a_1(\delta + 2H) + \delta^2 \sin 2\beta / 4}{(a_1 + \delta \sin \beta)^2} - \frac{a_2(\delta + 2H) - \delta^2 \sin 2\beta / 4}{(a_2 - \delta \sin \beta)^2} \right) \delta \cos \beta \quad (4.11)$$

$$\dot{E}_b = \frac{\pi m_0 (a_1 + a_2)}{H} \delta \cos \beta$$

where, as a reminder, $n_0 = \sigma_0 t_w$ and $m_0 = \sigma_0 t_w^2 / 4$ are respectively the linear axial and bending capacities of a plate with a thickness t_w . Finally, in the optic of applying the upper-bound theorem, the last step consists in calculating the external work \dot{W} . Here again, if the collision force is supposed to act perpendicularly to the element orientation, \dot{W} can still be obtained using (4.7). Equating \dot{W} to the internal energy rate \dot{E}_{int} leads to:

$$P_f(\delta) = \frac{\dot{E}_b + \dot{E}_m}{\dot{\delta} \cos \beta} \quad (4.12)$$

where \dot{E}_b and \dot{E}_m are given by (4.11). In order to derive the crushing resistance, the folding height H needs to be determined. This can be done by minimizing the mean crushing force over one fold, but doing so leads to very cumbersome equations (see section C.2.2.1 of Appendix C.2). As the mitre angle is usually quite small ($\beta \simeq 20^\circ$), a good approximation is to keep using (3.49), which is also justified by the fact that all the formulae presented here above degenerate into those developed for plane gates when β tends to 0. Another possibility is to work with the following approximate relation (see section C.2.2.1 of Appendix C.2 for more details):

$$H = \sqrt[3]{\frac{\pi}{12} a_1 a_2 t_w / \cos \beta} \quad (4.13)$$

Of course, the analytical derivation of $P_f(\delta)$ is only valid as long as the fold is not completely closed, which occurs when $\delta = 2H / \cos \beta$. When indentation is reached, a new fold is simply supposed to be created immediately after. In this case, the resistance can be easily generalized by applying a similar procedure than the one discussed in section B.2.1 of Appendix B.2 to get formulae that are very close to (3.50) and (3.51).

Apart from the resistance $P_f(\delta)$, it is also required to calculate the one associated to a beam-like behavior of the super-element, which is the topic of the next section.

4.2.2.2. Bending mechanism

For a given indentation δ^* , the collision force reached during the folding process is sufficient to activate the bending of the super-element. At this moment, if the web is of class 1, the three-hinge mechanism of Figure 4.12a is activated. It can be shown (see section C.2.2.2 of Appendix C.2) that the resulting force $P^*(\delta)$ required to initiate this transition is equal to:

$$P^*(\delta) = M_0 \left(\frac{\xi_1 + \xi^*(\delta)}{a_1 + \delta \sin \beta} + \frac{\xi_2 + \xi^*(\delta)}{a_2 - \delta \sin \beta} \right) \quad (4.14)$$

where ξ_1 and ξ_2 have the same meaning than in section 3.4.2.2. The derivation of $\xi^*(\delta)$ is also based on the method detailed in section B.2.2 of Appendix B.2, except that δ has to be replaced by $\delta \cos \beta$ in all the expressions.

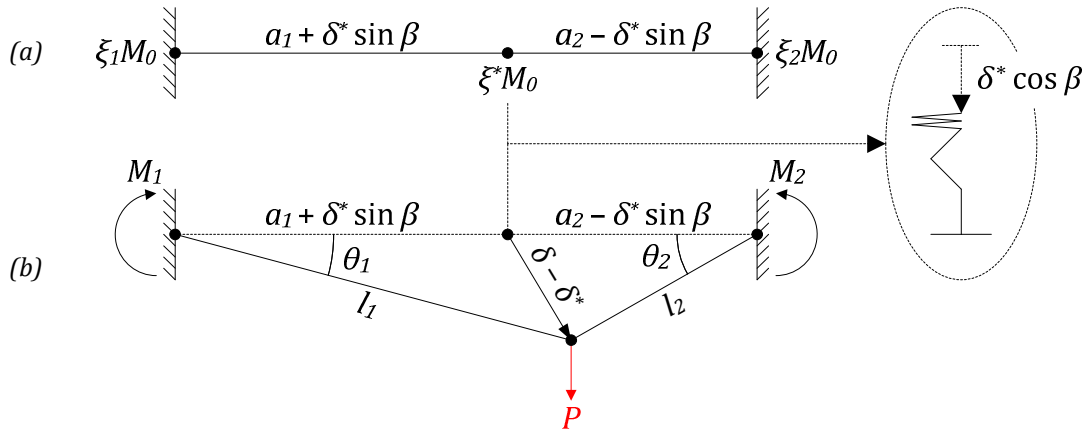


Figure 4.12. Initiation and development of the bending mechanism

When $\delta > \delta^*$, the resistance has to be derived according to the plastic collapse of Figure 4.12b. As shown in section C.2.2.2 of Appendix C.2, if ξ^* is the particular value of $\xi^*(\delta)$ when $\delta = \delta^*$, the impact force P is given by:

$$P_b(\delta) = M_0 \left(1 - \frac{N^2}{N_0^2} \right) \left(\frac{\xi_1 + \xi^*}{a_1 + \delta \sin \beta} + \frac{\xi_2 + \xi^*}{a_2 - \delta \sin \beta} \right) + N \frac{(a_1 + a_2)(\delta - \delta^*) \cos \beta}{(a_1 + \delta \sin \beta)(a_2 - \delta \sin \beta)} \quad (4.15)$$

where the normal force N can be calculated by using the formulae listed in Appendix C.2. Before closing this section, a final remark regarding the theoretical model still needs to be done. In the present simplified approach, the moving plastic hinge is not treated in a rigorous way. According to Hopkins [73], only stationary plastic hinges allow for a slope discontinuity. If moving hinges are used in the model, there must be a continuous change of slope between the collapsing arms. This can be achieved by considering two distinct hinges A and B , moving at the same velocity $\dot{w} = \dot{\delta} \sin \beta$ and connected together by a smooth line of constant curvature AB (Figure 4.13a). The total rotation is still $\theta = \theta_1 + \theta_2$ but is imposed this time without any discontinuity.

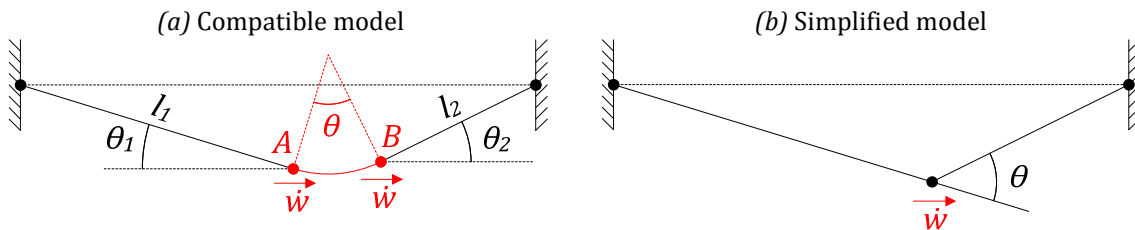


Figure 4.13. Discontinuity at moving plastic hinges

However, in the present simplified approach, the central connection AB is neglected and it is assumed that there is only one plastic hinge, moving at the velocity \dot{w} and imposing an abrupt rotation θ (Figure 4.13b). This is not theoretically exact but may be justified by the fact that AB is usually quite small with respect to l_1 and l_2 . Furthermore, if this simplification was not introduced, deriving a consistent collision resistance is rather impossible to do analytically (see section C.2.2.2 of Appendix C.2 for more details).

4.2.2.3. Extension to vertical super-elements

All the previous developments are in fact only valid for impacts occurring on girders and the goal is now to extend them to frames. Unlike plane gates, it is of importance to distinguish between horizontal girders and vertical frames because of the inclination due to the mitre

angle β . Indeed, in sections 4.2.2.1 and 4.2.2.2, the impact could be assimilated to an oblique collision (Figure 4.10b), but this is not true in the present situation.

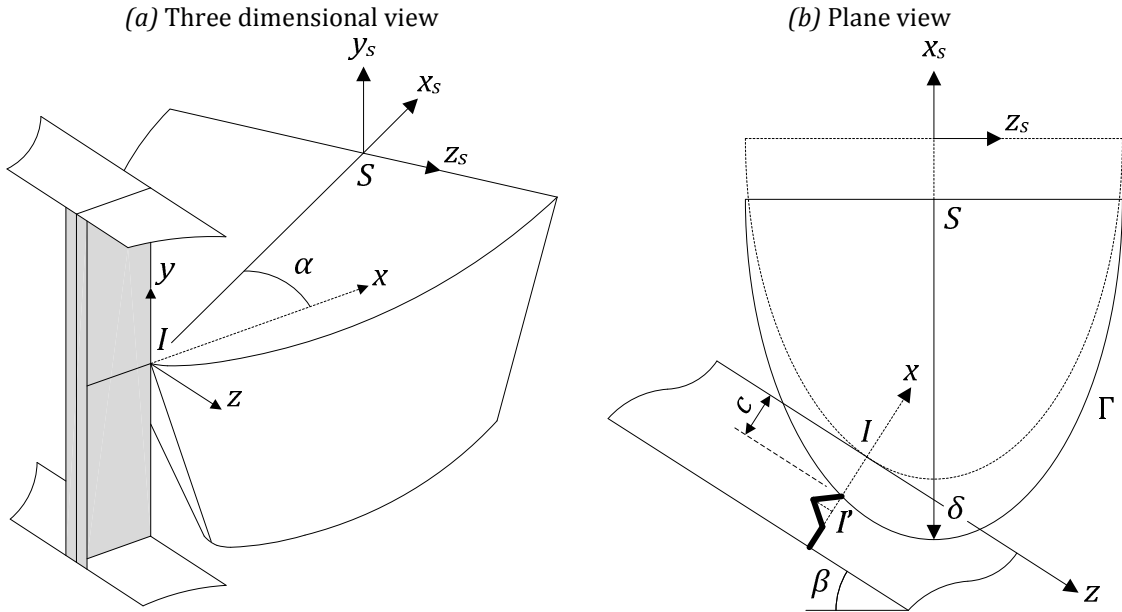


Figure 4.14. Impact on a vertical frame

This last assertion can be understood by considering the three dimensional view of Figure 4.14a. Initially, the first contact point between the deck of the striking vessel and the super-element occurs at point I , where a tangent condition is imposed in case of a direct impact. When the ship moves forward, it simply follows the direction of the longitudinal axis x_s , but the frame is folded or bent in its plane, i.e. along the local x axis (Figure 4.14b). Consequently, for a given penetration δ , the indentation to consider for the super-element is given by a function $c(\delta)$ that may be found by calculating the current intersection I' of the uppermost deck with the super-element.

In order to derive $c(\delta)$, let us denote by C the lower node of the super-element (Figure 4.14a) that is characterized by its coordinates (X_C, Y_C, Z_C) in the global axes. In the local reference frame (x_s, y_s, z_s) placed at the initial location of point S but not moving with (Figure 4.14b), the position of C is given by:

$$x_{s,C} = X_C - X_S \quad ; \quad y_{s,C} = Y_C - Y_S \quad ; \quad z_{s,C} = Z_C - Z_S \quad (4.16)$$

where (X_S, Y_S, Z_S) is known because the ship has to be tangent to the gate at point I for a given collision scenario (Figure 4.4). Using these new parameters, it may be shown that:

$$c(\delta) = \sqrt{\left(\frac{p^2 \cot \beta}{2q \sin \beta} + \frac{z_{s,C}}{\sin \beta}\right)^2 + \frac{p^2 \delta}{q \sin^2 \beta}} - \left(\frac{p^2 \cot \beta}{2q \sin \beta} + \frac{z_{s,C}}{\sin \beta}\right) \quad (4.17)$$

in which, as a reminder, p and q are the two radii describing the shape Γ of the uppermost deck. Apart from this modification, the situation is strictly similar to the one studied in sections 4.2.2.1 and 4.2.2.2 with $\beta = 0$, except that δ has to be replaced by $c(\delta)$. Doing so, the following formula is found for the folding mechanism:

$$P_f(\delta) = \frac{m_0(a_1 + a_2)\pi}{H} + \frac{n_0 H a_1 + a_2}{2 a_1 a_2} (c(\delta) + 2H) \quad (4.18)$$

where H is still given by (3.49). Of course, equation (4.18) is only valid as long as the current fold is not complete closed, which occurs when $c(\delta) = 2H$. For larger values of the penetration, an identical deformation pattern is assumed to be immediately repeated. In this case, applying the same procedure than the one followed in Appendix B.2 leads to generalized formulae similar to (3.50) and (3.51).

Regarding the force $P^*(\delta)$ required to activate the bending mechanism, for an indentation $c(\delta)$, adapting (4.14) provides the subsequent result:

$$P^*(\delta) = M_0 \left(\frac{\xi_1 + \xi^*(c)}{a_1} + \frac{\xi_2 + \xi^*(c)}{a_2} \right) \quad (4.19)$$

in which (B.26) can be used to get $\xi^*(c)$, provided that δ is replaced by $c(\delta)$. As usual, when the folding resistance is equal to $P^*(\delta)$, then the penetration δ^* is reached and the transition takes place. Denoting by ξ^* and c^* the particular values of $\xi^*(\delta)$ and $c(\delta)$ at this moment, one may write:

$$P(\delta) = M_0 \left(1 - \frac{N^2}{N_0^2} \right) \left(\frac{\xi^* + \xi_1}{a_1} + \frac{\xi^* + \xi_2}{a_2} \right) + N(c - c^*) \frac{a_1 + a_2}{a_1 a_2} \quad (4.20)$$

In this last relation, N is the normal force due to the membrane effects calculated by using (C.35), provided that β is set to zero, δ is replaced by $c(\delta)$ and c^* is substituted to δ^* . As a closing remark, it should be recalled that all the formulae derived in sections 4.2.2 and 4.2.3 are only valid if there is no subsequent contact between the stem and one of the boundaries of the super-element. If this is the case, the resistance is set to zero because a super-element of type 3 is activated, as detailed hereafter (section 4.2.3).

4.2.2.4. Numerical validation

In an attempt to check the formulae established here above, many numerical simulations were performed using the LS-DYNA software. For all of them, a mesh size smaller than 5 cm was used to correctly represent the folding process. As usual, Belytschko-Tsay shells [66] were used for the finite element models of both the rigid striking vessel and the deformable oblique girder.

The local failure of the super-element was also investigated in this validation process. To do so, the threshold strain value was calculated by equation (3.37) and it was found that choosing ϵ_c of 11 % leads to a safe approximation of the rupture initiation. Furthermore, it was also pointed out that formula (3.52) proposed by Wierzbicki [167] for the concertina tearing also provides an adequate evaluation of the resistance when ϵ_c is exceeded. The results presented here aim to focus on the two possible behaviors mentioned in sections 4.2.2.1 and 4.2.2.2. Two different impact configurations are therefore considered.

The first one is a collision occurring on a quite deep girder with a moderate span. The geometrical data are those listed in Table 4.2, while the material properties are the same as in section 3.3.4. In an illustrative purpose, the equivalent Von Mises stress in the deforming girder is plotted on Figure 4.15, from which it is clear that only a folding process is initiated in the case of a deep girder. The disorders are mainly located in the web, the flange remaining nearly unaffected. Moreover, it can be observed that the folding process develops along the inclined direction followed by the vessel, which tends to confirm the presence of moving central plastic lines.

| | | | |
|-------|--------|--------------|-------|
| h_w | 1 m | a_1 | 1.6 m |
| t_w | 0.02 m | a_2 | 1 m |
| h_f | 0.5 m | β | 20° |
| t_f | 0.02 m | ϵ_c | 11 % |

Table 4.2. Geometrical data for the first simulation

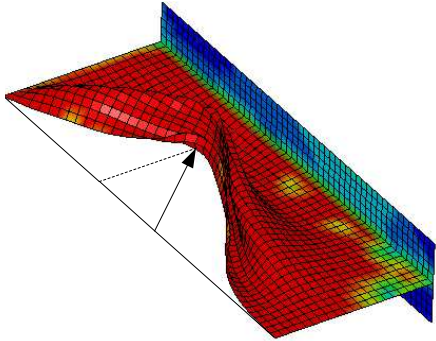


Figure 4.15. Folding process in the case of a deep girder

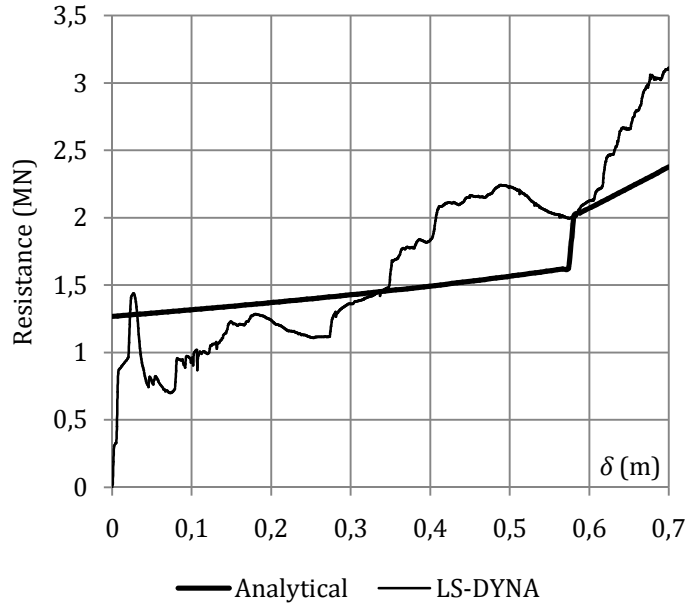


Figure 4.16. Comparison of the numerical and analytical resistances for the first simulation

The comparison of the analytical and numerical resistances for this first case is plotted on Figure 4.16. At the beginning, the simplified approach tends to overestimate the solution found by LS-DYNA. This is essentially due to the fact that the theoretical model is based on a rigid-plastic material, while an elastoplastic behavior is first observed at the initiation of the finite element simulation. On the contrary, when the penetration is getting larger, the analytical solution turns out to be conservative because an overall plastic state develops almost everywhere on the impacted structure. This may be observed on Figure 4.15, where it can be seen that the flow stress is nearly reached over the entire web height.

| | | | |
|-------|--------|--------------|--------|
| h_w | 0.63 m | a_1 | 2.45 m |
| t_w | 0.06 m | a_2 | 3.55 m |
| h_f | 0.3 m | β | 20° |
| t_f | 0.06 m | ϵ_c | 11 % |

Table 4.3. Geometrical data for the first simulation

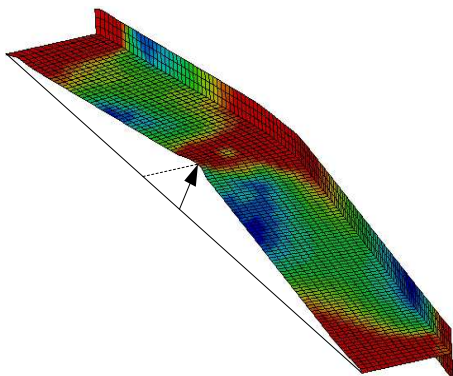


Figure 4.17. Folding process in the case of a slender girder

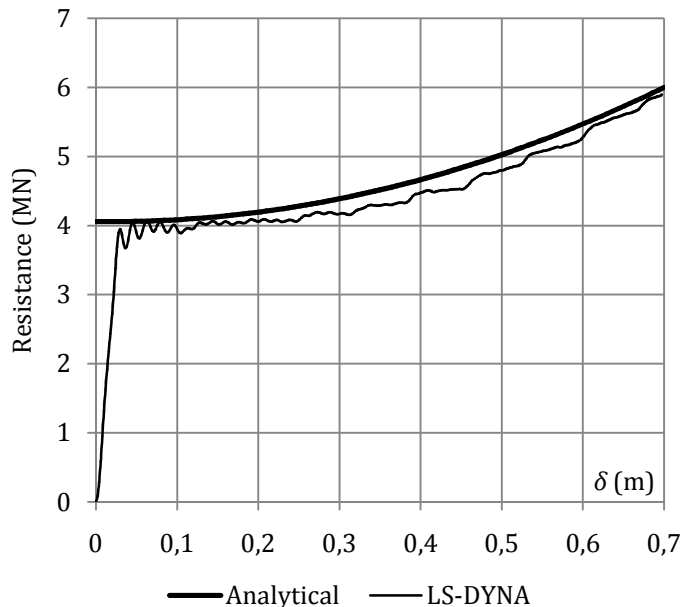


Figure 4.18. Comparison of the numerical and analytical resistances for the second simulation

The second configuration presented here aims to investigate a collision occurring on a slender girder having a smaller web height and a larger span than in previous case (see Table 4.3).

From the equivalent Von Mises stresses plotted on Figure 4.17, it transpires that only a beam-like behavior is activated this time. Furthermore, it can also be seen that the flow stress is reached near the supports and in the central cross-section immediately located under the impact point, which tends to corroborate the three-hinge mechanism of Figure 4.13b.

The resistance curves of Figure 4.18 show that the agreement is quite satisfactory and is an additional validation for the theoretical model discussed in section C.2.2.2 of Appendix C.2.

Nevertheless, one can argue that this good concordance is only due to the fact that the mitre angle is quite small ($\beta = 20^\circ$), so that the collision situation is not too far from a perpendicular impact. Therefore, in order to check this assumption, other simulations were run with a more important inclination ($\beta = 60^\circ$). Even though these configurations are not realistic for mitre gates, the purpose here is only to verify if the theoretical model could also provide satisfactory results when β is increased.

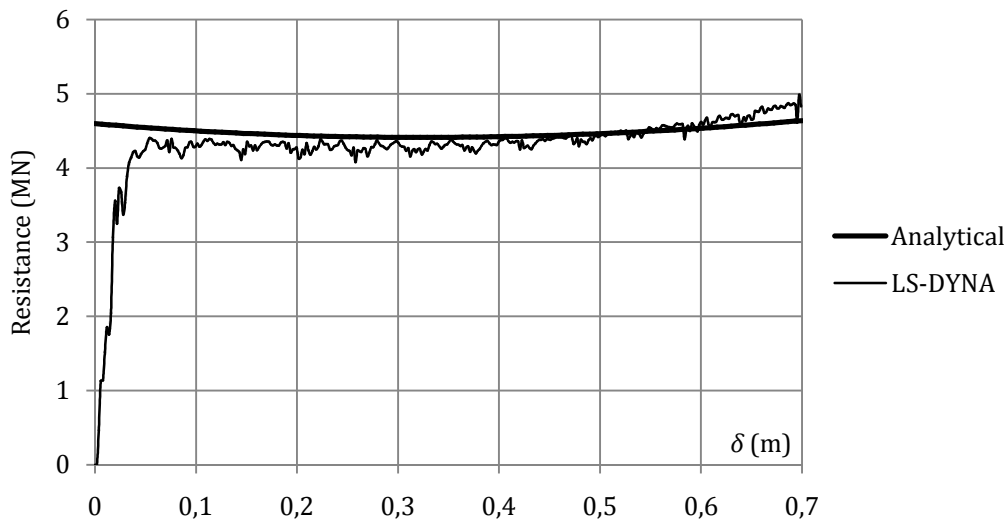


Figure 4.19. Numerical and analytical resistances for a mitre angle of 60°

The numerical and analytical results for an angle of 60° are reported on Figure 4.19. On this picture, it can be observed that the resistance curve obtained by the simplified approach is first slightly decreasing. This can be explained by the fact that the additional energy dissipated by the membrane straining is not sufficient to balance the reduction of the bending effects coming from the diminution of the moments in accordance with the interaction criteria. This phenomenon is also reflected by the finite element simulation, which tends to corroborate the theoretical solution proposed for the beam-like behavior.

4.2.3. Super-elements of type 3

Super-elements of type 3 are introduced to deal with collisions occurring on the intersection between horizontal girders and vertical frames (Figure 4.6). As in Chapter 3, they may be activated in case of a direct impact or if there is a subsequent contact between the stem and the support of a SE2 or a SE3 (Figure 3.35).

4.2.3.1. Analytical derivation

When the vessel immediately collides the gate on one of its intersections, the deformation pattern associated to the folding process is still the one depicted on Figure 3.37, but instead of considering an indentation equal to δ , one should account for the current intersection I'

between the uppermost deck and the super-element axis (Figure 4.20). In this case, the true penetration of the striking stem $c(\delta)$ is given by a formula very similar to (4.17).

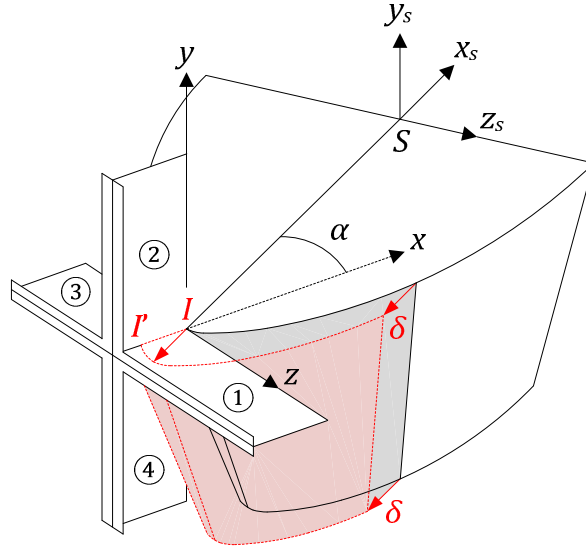


Figure 4.20. Three dimensional view of an impact on an intersection

From this observation, it transpires that all the formulae developed in section 3.5.2.1 are also valid for the present situation, provided that δ is replaced by $c(\delta)$. In particular, equations (3.62) and (3.63) are still relevant to get the contribution of each wing, but the following modifications must be noted for the opening angle θ (Figure 3.37b) and the fold number k :

$$\theta = \arccos\left(k - \frac{c(\delta)}{2H}\right) ; \quad k = \left\lceil \frac{c(\delta)}{2H} \right\rceil \quad (4.21)$$

Similarly, regarding the bending process, the eight-hinge mechanism of Figure 3.39 can be easily extended to an oblique impact by considering that the out-of-plane displacement of the central node is not equal to δ but to $c(\delta)$. Doing so, if the transition from the folding to the bending process takes place when $\delta = \delta^*$, the resistance can be calculated by applying equation (3.65) with the subsequent corrections:

$$\delta \mapsto c(\delta) ; \quad \delta^* \mapsto c^* ; \quad c^* = c(\delta^*) ; \quad \xi_v^* = \xi_v^*(c^*) ; \quad \xi_h^* = \xi_h^*(c^*) \quad (4.22)$$

Furthermore, in the case of an impact arising near the top of the gate, it is likely that T-shaped intersections may be involved during the collision process. Of course, if this is the case, the bending resistance can still be obtained with help of equation (3.67), but the modifications introduced in (4.22) have to be taken into account.

On the other hand, when a super-element of type 3 is activated because of a subsequent contact, the corresponding resistance formulae have to be derived by generalizing the developments performed in section B.3.2 of Appendix B.3. The approach is very similar to what has been done so far, the major difficulty being the fact the lengths a_1 and a_2 are now continuously varying with the penetration. Here again, the analytical derivation has to be done for both a bending and a folding mechanism. The mathematical procedures are not particularly arduous but require cumbersome developments. For the sake of conciseness, these ones have been partly reported in sections C.2.3.1 and C.2.3.2 of Appendix C.2. Even though these calculations are not always rigorous on a theoretical point of view, they are at least consistent with those performed for plane gates as taking the limit for $\beta \rightarrow 0$ leads to the formulae established in Chapter 3.

4.2.3.2. Numerical validation

In order to illustrate the numerical validation process, the cruciform having the geometrical properties of Table 4.4 is used here (the notations corresponds to those of Figure 3.39). It is made of more or less 6000 Belytschko-Tsay shells [66] elements having a regular size of 5 cm. The material properties are the same as in section 3.3.4 for the impacted elements, while the striking vessel is still assumed to be perfectly rigid. In order to account for rupture in the numerical model, the failure strain is calculated in accordance with equation (3.37) and it is found that a critical strain ϵ_c of 10 % in the analytical approach is quite adequate to reproduce the numerical observations.

| | Length | Web height | Web thickness | Flange height | Flange thickness |
|------------------|-----------------------|---------------------|-------------------------|-----------------------|-------------------------|
| Horizontal wings | $a_1 = 2.5 \text{ m}$ | $h_w = 1 \text{ m}$ | $t_w = 0.02 \text{ m}$ | $h_f = 0.5 \text{ m}$ | $t_f = 0.02 \text{ m}$ |
| | $a_2 = 3 \text{ m}$ | $h_w = 1 \text{ m}$ | $t_w = 0.02 \text{ m}$ | $h_f = 0.5 \text{ m}$ | $t_f = 0.02 \text{ m}$ |
| Vertical wings | $b_1 = 2.5 \text{ m}$ | $h_w = 1 \text{ m}$ | $t_w = 0.015 \text{ m}$ | $h_f = 0.3 \text{ m}$ | $t_f = 0.015 \text{ m}$ |
| | $b_2 = 2.6 \text{ m}$ | $h_w = 1 \text{ m}$ | $t_w = 0.015 \text{ m}$ | $h_f = 0.3 \text{ m}$ | $t_f = 0.015 \text{ m}$ |

Table 4.4. Geometrical properties of the impacted cruciform

The validation has been performed for eleven different cruciforms having various geometrical properties. The mesh size was selected after a convergence study and was progressively reduced from a value of 0.2 m to 0.05 m for which there is a stabilization of the collision resistance.

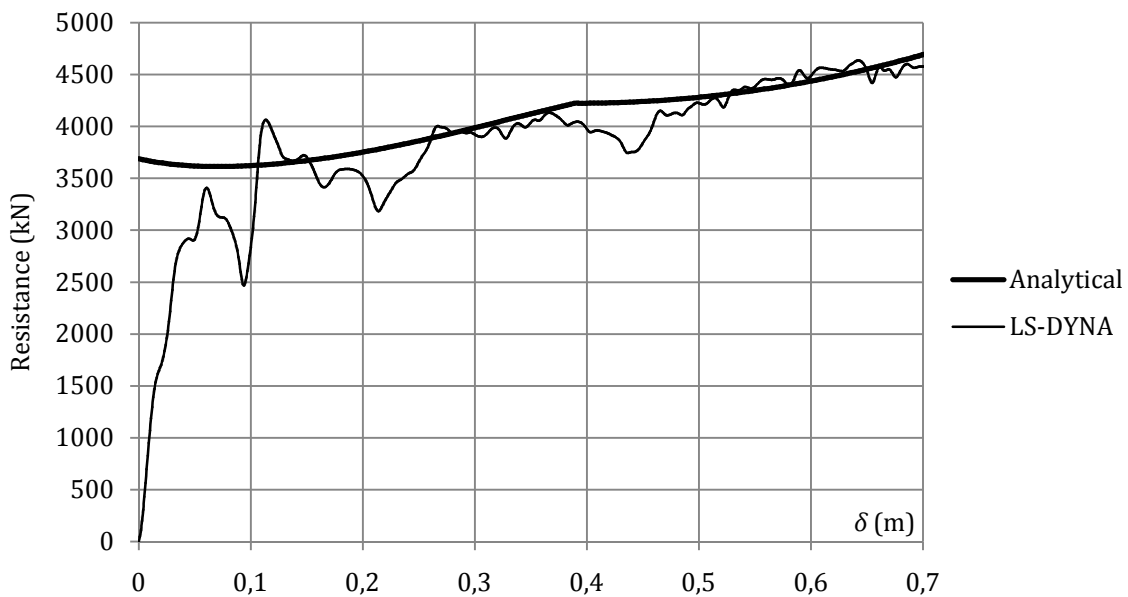
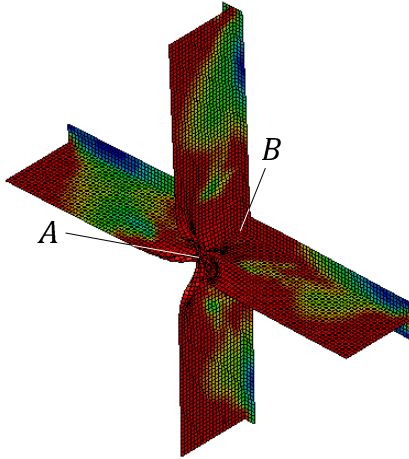


Figure 4.21. Comparison between the analytical and numerical results

The results that are presented in this section corresponds to a direct impact with a mitre angle β of 20° . The curves showing the analytical and numerical resistances are plotted on Figure 4.21. From this picture, the agreement is found to be quite satisfactory, even though there is a slight overestimation at the beginning of the indentation. Once again, this may be explained by the fact that the theoretical model is based on a rigid-plastic material, while the simulations are run for an elastoplastic behavior. Therefore, when the collision starts, the force opposed by the cruciform is lower than the one predicted analytically as the plastic deformations are predominant.

Another point that is also interesting to investigate is the transition from the folding to the bending mechanism. From Figure 4.21, it can be seen that this one takes place for $\delta^* \approx 0.4 m$ because there is a discontinuity in the curve of the analytical resistance. To check if this prediction is more or less realistic, one can investigate the out-of-plane displacement of the central rear node (Figure 4.22a).

(a) Folding process for a cruciform



A: front node ; B : rear node

(b) Rear and front node displacements

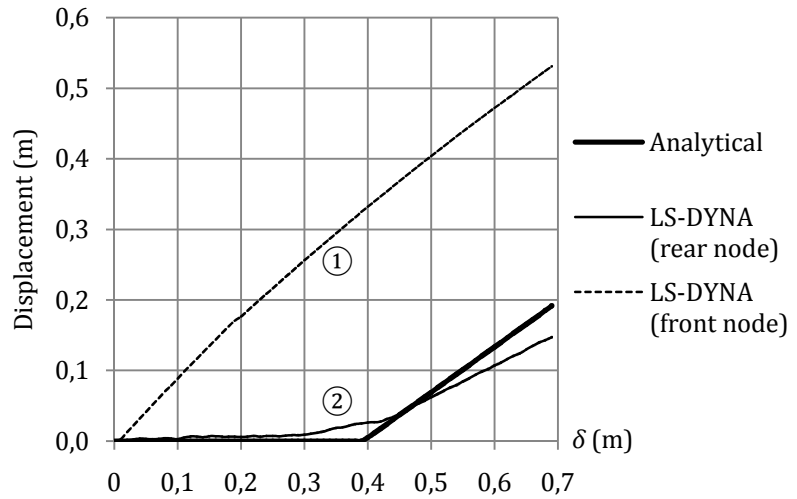


Figure 4.22. Comparison of the displacements due to the beam-like behavior

According to the present simplified approach, the motion due to the beam-like behavior of the cruciform is given by $c(\delta) - c^*$, so there is no activation of the bending phase as long as $\delta < \delta^*$. Of course, this approach is only an idealization as it transpires from numerical simulations that there is a coupling between the crushing and bending mechanisms. This is particularly true at the beginning of the penetration, where both of them develop concomitantly.

A simple way to verify the previous assertion is to consider the numerical curve ② of Figure 4.22b showing that the central rear node is submitted to an out-of-plane displacement since the beginning of the collision. As far as $\delta < 0.4 m$, this latter remains quite negligible with respect to the one of the central front node, which tends to confirm the predominance of the crushing process during this first phase. Nevertheless, when $\delta > 0.4 m$, the data provided by LS-DYNA leads to the conclusion that the beam-like behavior is activated, as curves ① and ② are now nearly parallel.

Regarding the analytical prediction, it appears that the transition penetration δ^* is more or less realistic. As expected, the displacements associated to the beam-like behavior are slightly overestimated, but this does not lead to a noticeable divergence of the resistance.

4.3. Resistance in the global deforming mode

The previous analytical developments are only valid under the hypothesis that the structural elements located near the impact point are locally crushed. Nevertheless, this situation is not relevant for larger values of the penetration when an overall motion is activated. In comparison with plane gates (Chapter 3), the global deforming mode is not so strongly marked for mitre gates because the connection between the two leafs does not usually allow for an efficient bending. This particular point is quite important to correctly assess the resistance of such structures and is deeply investigated in this section.

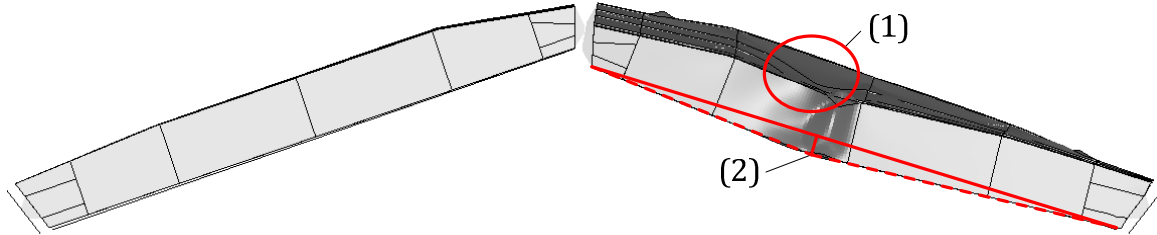


Figure 4.23. Local (1) and global (2) deforming mode for a mitre gate

In an illustrative purpose, the deformed configuration of an impacted mitre gate is depicted on Figure 4.23, from which a clear distinction can be made between the local and global deforming modes. As in Chapter 3, both an elastoplastic and a rigid-plastic calculation of the global resistance $P_G(\delta)$ have to be performed. Nevertheless, the situation is a bit more complicated than for plane gates as the distinction should also be made between a centered or an off-centered impact (Figure 4.4).

4.3.1. Preliminary considerations

4.3.1.1. Mechanical model

As mentioned in section 4.1.3, during the global mode, each leaf of the gate is seen as a set of horizontal beams weakly connected by the frames (Figure 4.6b). Along the vertical Y axis, they are placed at the same discrete locations Y_i as the horizontal girders but they do not have an exactly identical shape. Indeed, as shown on Figure 4.3, the girders have a variable web height that is smaller at their extremities. Consequently, an equivalent model (Figure 4.24a) is considered in order to avoid working with a non-uniform beam⁸. In fact, the web height is simply supposed to be the same as the one characterizing the cross-section placed at the level of the first contact point I (Figure 4.24a). By using the notations of Figure 4.3, if Z'_I is the position of point I along the horizontal Z' axis, one can write:

$$\begin{aligned}
 h_w &= h_0 + (Z' - l_1) \tan \gamma_1 & \text{if } 0 \leq Z'_I \leq l_1 \\
 h_w &= h_0 & \text{if } l_1 \leq Z'_I \leq l_1 + l_3 \\
 h_w &= h_0 - (Z' - l_1 - l_3) \tan \gamma_2 & \text{if } l_1 + l_3 \leq Z'_I \leq l_1 + l_2 + l_3
 \end{aligned} \tag{4.23}$$

From the previous equations, it is clear that the web height is unchanged if the impact is initially located on the central part of the leaf. In practice however, having an off-centered collision such that Z'_I is outside the area $[l_1 ; l_1 + l_3]$ is rather unlikely because the lengths l_1

⁸ Apart from an important reduction of the mathematical complexity, working with a uniform cross-section also allows the use of Eurocode 3 [52].

and l_2 are usually quite small with respect to the dimensions of the striking vessel. This is particularly visible on the two pictures of Figure 4.24b showing l_1 and l_2 .

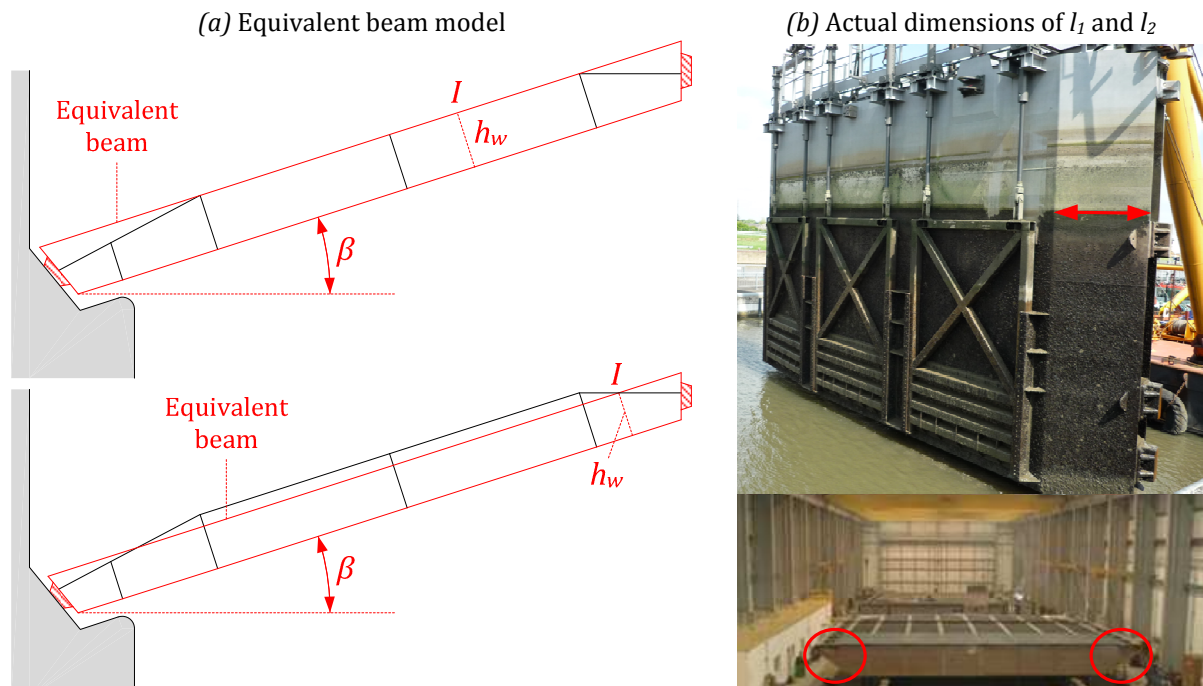


Figure 4.24. Calculation of the equivalent web height

From (4.23), it can be argued that the approach suggested here is not necessarily conservative as it tends to overestimate the resistance of the beam in the inclined portions. In practice however, this argument is not always valid. Indeed, because of the important local forces due to the contacts at the central or lateral blocks (Figure 4.2), the gate is often reinforced there. Its resistance may therefore be thought to be higher at these locations than at the center of the leaf, so increasing the web height is in fact a way to account for this particularity.

Apart from the equivalent web, the remaining parts of the cross-section are the girder flange and the collaborating portion coming from the plating. As for plane gates, this latter is found by applying the recommendations of Eurocode 3 [52]. A conservative symmetric shape is obtained by working with the minimum effective length in accordance with equation (3.68).

4.3.1.2. Effect of the hydrostatic pressure

Regarding the hydrostatic pressure, this one has little influence on the resistance opposed by the various super-elements analyzed in section 4.2, but the action of water should be carefully accounted for when developing the mathematical formulae for the global deforming mode. This is a major difference with the approach followed in Chapter 3. The justification lies in the very particular functioning conditions of mitre gates. Indeed, apart from additional bending moments in the structure, another effect of the hydrostatic pressure is to generate compressive normal forces that are crucial to insure the overall stability of each leaf (see Dehousse [38] for a more detailed study). Of course, this is likely to have a relative influence on the global resistance and it is of prior importance to account for this phenomenon. To do so, one can consider the simplified model of Figure 4.25b showing the situation of a horizontal beam before the impact. This one is assumed to be submitted to a uniformly distributed load p_i that is the resulting force associated to the trapezoidal hydrostatic pressure

of Figure 4.25a. In order to provide the overall equilibrium, it can be shown that the following reactions forces are required (Figure 4.25c):

$$n_i = \frac{p_i l}{2 \sin \beta} \quad ; \quad f_i = 0 \quad ; \quad R_i = \frac{p_i l}{2 \sin \beta} \quad (4.24)$$

where n_i and f_i are the horizontal and vertical components at the central block respectively, while R_i is the reaction at the lock wall. Ideally, this latter is only acting with an inclination β .

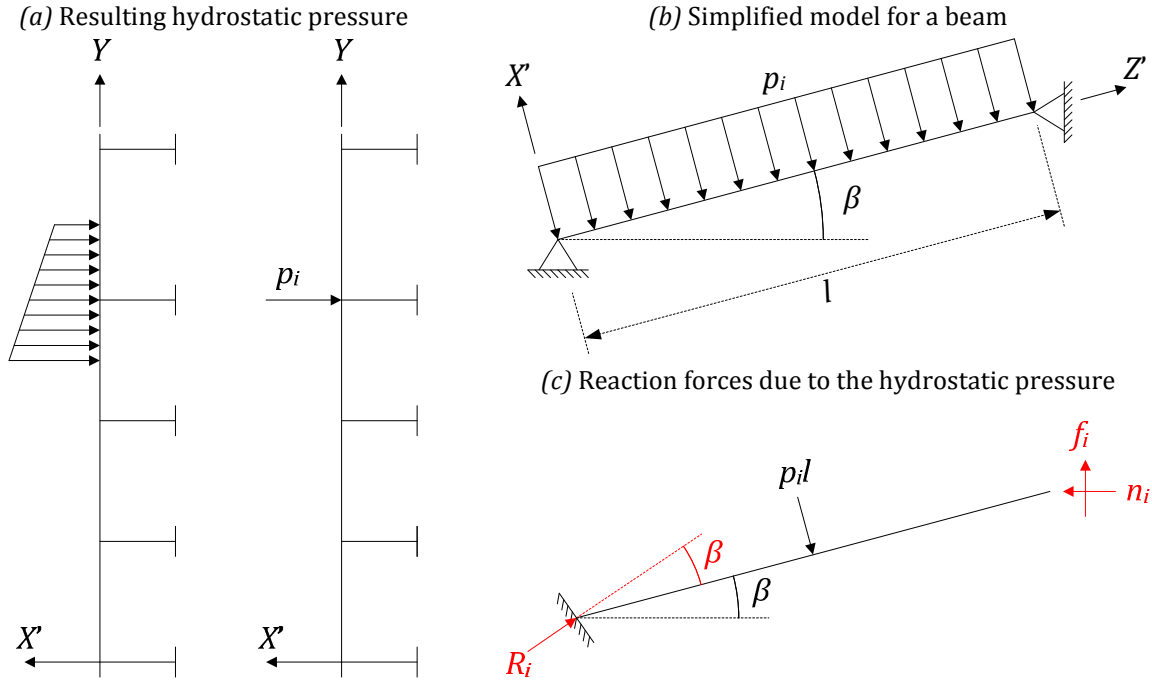


Figure 4.25. Hydrostatic pressure and reaction forces acting on an equivalent beam

By using (4.24), it is easy to derive the normal compressive force N_i and the bending moments $M_i(Z')$ acting on each beam. It is found that:

$$N_i = \frac{p_i l}{2} \cot \beta \quad ; \quad M_i(Z') = \frac{p_i Z'}{2} (l - Z') \quad (4.25)$$

where Z' is the horizontal coordinate measured in the plane of the gate. From (4.25), it can be concluded that the gate is initially bent and compressed before the collision, which has an influence on the global resistance.

4.3.2. Off-centered impact

As in Chapter 3, the derivation of the global resistance $P_G(\delta)$ has to be done for both an elastoplastic or rigid-plastic material. The method applied in this section is nearly similar than the one followed for plane gates, except that the inclination due to the mitre angle β and the effects of the hydrostatic pressure have now to be considered.

4.3.2.1. Elastoplastic solution

In order to derive an elastic solution, the cubic displacement field $u(Y_i, Z')$ of Figure 4.26 is assumed, where the maximal out-of-plane displacement $g(Y_i, \delta)$ is reached at the first contact point I . If Z'_I denotes the position of I along the Z' axis, it can be shown that the analytical

expression of $u(Y_i, Z')$ is the same as (3.71), provided that Z and Z_I are replaced by Z' and Z'_I respectively. On Figure 4.26, it is worth noticing that only the impacted gate leaf is submitted to a displacement field, the other one remaining unaffected. In reality, when the portion AB is bent, there is a short motion of point B such that the length of AB remains more or less unchanged, which implies that BC rotates as a rigid body. Nevertheless, these phenomena are negligible during the elastic phase.

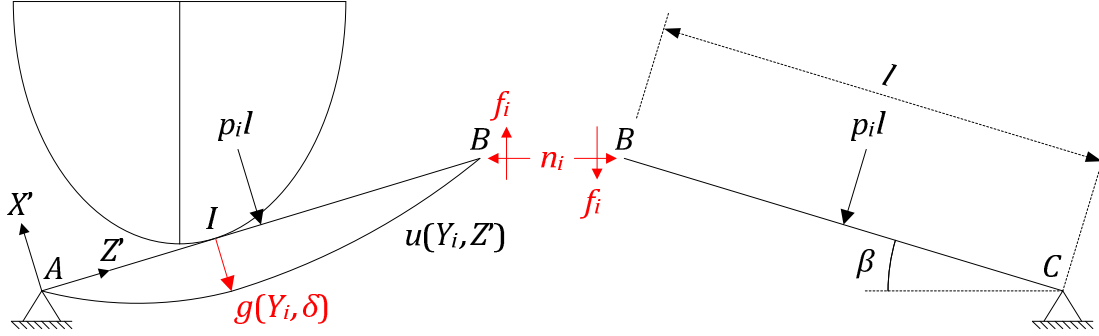


Figure 4.26. Displacement field for an off-centered impact

The bending moments $M_i(Z', \delta)$ due to $u(Y_i, Z')$ can be found by applying the fundamental equation for elastic beams recalled by (3.74). With this result, the reaction forces n_i , f_i and R_i (Figure 4.25c) may be easily derived by writing the translational and rotational equilibrium for each leaf individually. Accounting also for the effects of the hydrostatic pressure calculated in (4.24), it can be shown that the maximal bending moment $M_i(\delta)$ and the normal force $N_i(\delta)$ acting in the beam are given by:

$$N_i(\delta) = \frac{p_i l}{2} \cot \beta + \frac{3EI_i \cot 2\beta}{Z'_I(l - Z'_I)^2} g(Y_i, \delta) ; \quad M_i(\delta) = \frac{p_i Z'_I}{2} (l - Z'_I) + \frac{3EI_i g(Y_i, \delta)}{Z'_I(l - Z'_I)} \quad (4.26)$$

where E is the Young modulus and I_i the inertia of the cross-section. A rapid comparison of equations (4.24) and (4.26) when $g(Y_i, \delta) = 0$ shows that there is a continuity in the definition of the normal force and the bending moment.

Regarding the reaction forces, it is worth noting that initially, when only the hydrostatic pressure is acting on the structure, the situation is ideally symmetric (Figure 4.27a), so the reaction forces on the left and right lateral contact blocks are perfectly the same. However, for an off-centered impact, the symmetry is lost and the reaction forces R_i and Q_i (Figure 4.27a) on the lateral blocks do not necessarily have the same magnitude and orientation (R_i is usually greater than Q_i). In particular, the inclination of R_i is no longer equal to β (Figure 4.27b), which means that there are additional components $R_i \cos \Delta\beta$ and $R_i \sin \Delta\beta$ that have to be balanced at the lock wall. Therefore, one should always take care that the compensation is not made by unexpected contacts between the gate and some other weaker parts, such as the pivot for example.

Once the bending moments $M_i(Z', \delta)$ and the normal force $N_i(\delta)$ are known, let us calculate the contribution $P_i(\delta)$ to the global resistance. Applying the equilibrium method leads to:

$$P_i(\delta) = \frac{3EI_i l}{Z'_I{}^2 (l - Z'_I)^2} g(Y_i, \delta) \quad (4.27)$$

in which the last unknown is the maximal displacement $g(Y_i, \delta)$ of the first contact point I (Figure 4.26). In fact, this function can be obtained by holding the same reasoning as in

Appendix B.4 for a gate supported by a sill (Figure B.17a and c). Therefore, (B.69) and (B.70) are still valid in the present case.

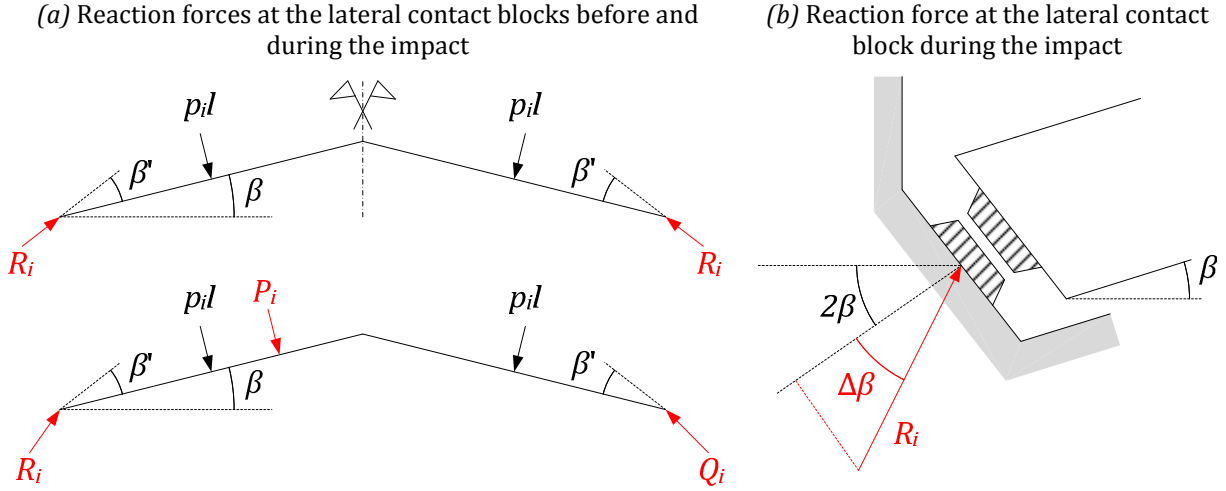


Figure 4.27. Reaction forces at the lock walls

Of course, (4.27) is only valid as long as the beam resistance $P_{t,i}(\delta)$ is not reached. In order to calculate $P_{t,i}(\delta)$, the following definitions are recalled (in order to clarify all these notations, a summary is provided at the end of Table C.1 in Appendix C.3):

- As detailed in section 3.6.2.1, the maximal allowable bending moment is equal to $M_{p,i}$, $M_{e,i}$ or $\bar{M}_{e,i}$ according to the classification. Furthermore, in order to account for the coupling with the local deforming mode, these values have to be reduced if the horizontal girder is simultaneously crushed. To do so, the coefficients $\xi_{p,i}(\delta)$, $\xi_{e,i}(\delta)$ and $\bar{\xi}_{e,i}(\delta)$ may be introduced. They are calculated by applying the linear interpolation suggested in Appendix B.2.
- Regarding the normal force, whatever the classification, the tensile resistance is always equal to the plastic limit $N_{p,i}$ even though there is a simultaneous crushing due to the local mode. However, this is not true in compression. For classes 1, 2 and 3, the compression resistance is also equal to $N_{p,i}$, but this is not valid if buckling is likely to occur. In this case, one may only consider the contribution $\bar{N}_{p,i}$ of the efficient portion.

The evaluation of the beam resistance $P_{t,i}(\delta)$ can now be achieved with help of the previous definitions. To do so, the philosophy is the same as in section 3.6.2.2, but the situation is a bit more complicated here because the structure is simultaneously bent and compressed. Therefore, a combination formula has to be used in accordance with the classification. By adapting the recommendations of Eurocode 3 [53], the resistance for class 1 and 2, 3 or 4 cross-sections is reached when the following criteria are respectively met:

$$\frac{M_i(\delta)}{\xi_{p,i}(\delta)M_{p,i}} + \left(\frac{N_i(\delta)}{N_{p,i}}\right)^2 = 1 ; \quad \frac{M_i(\delta)}{\xi_{e,i}(\delta)M_{e,i}} + \frac{N_i(\delta)}{N_{p,i}} = 1 ; \quad \frac{M_i(\delta)}{\bar{\xi}_{e,i}(\delta)\bar{M}_{e,i}} + \frac{N_i(\delta)}{\bar{N}_{p,i}} = 1 \quad (4.28)$$

where $N_i(\delta)$ and $M_i(\delta)$ are the maximal normal force and bending moment given by (4.26). Consequently, introducing (4.26) in (4.28) allows to determine the value of $g(Y_i, \delta)$ for which the resistance is reached. This result may then be introduced in (4.27) to get the resistance $P_{t,i}(\delta)$. Finally, the contribution of beam i during the elastoplastic phase is found by

admitting that once $P_{t,i}(\delta)$ is reached, the resistance remains equal to $P_{t,i}(\delta)$ until the transition to the global plastic mechanism is activated ($\delta = \delta_t$). In other words, for $\delta < \delta_t$, the contribution of beam i to the global resistance may be obtained by adapting (4.27) in the following manner:

$$P_i(\delta) = \min \left\{ \frac{3EI_i l}{Z_i'^2 (L - Z_i')^2} g(Y_i, \delta); P_{t,i}(\delta) \right\} \quad (4.29)$$

which is strictly similar to the procedure applied in section 3.6.2.2. The curves depicted on Figure 3.51 are therefore also applicable to the present case. With (4.29), the global elastoplastic resistance $P_G(\delta)$ can be calculated by (3.5).

4.3.2.2. Perfectly plastic solution

As for plane gates (Chapter 3), when the resistance during the local deforming mode reaches a sufficient value $P_t(\delta)$, an overall plastic mechanism is activated over the entire structure. This second phase starts when the transition penetration δ_t is reached, i.e. when the two terms of equation (3.76) are equal. In order to evaluate the global resistance $P_G(\delta)$ when $\delta > \delta_t$, it is assumed that all the beams of the equivalent mechanical model are made of a rigid-plastic material and collapse according to a predefined scheme.

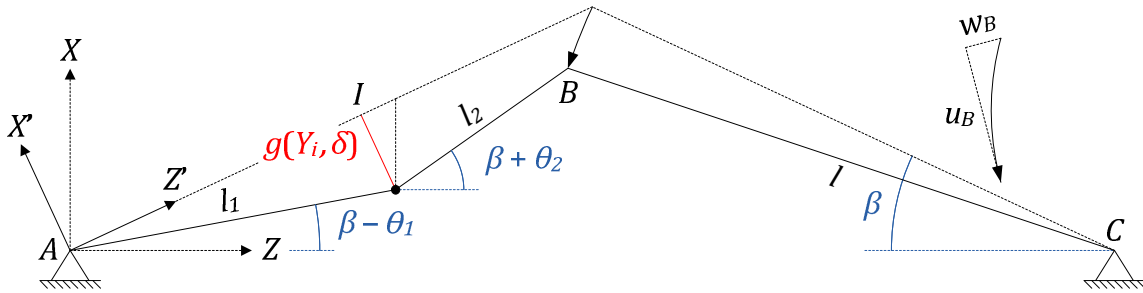


Figure 4.28. Plastic mechanism for a class 1 cross-section in the case of an off-centered impact

For a class 1 cross-section, the mechanism considered here is depicted on Figure 4.28 and only involves one moving plastic hinge. This one is initially placed at point I , but travels with a velocity $\dot{g}(Y_i, \delta) \tan \beta$ along the Z' axis. During the collapse procedure, the non-impacted leaf is assumed to rotate as a rigid body, which implies that the $\overline{BC} = l$. On the other hand, it is further postulated that the total length of AB remains unchanged, with the consequence that $l_1 + l_2 = l$. This last assumption is also used by Paik and Thayamballi [121] when deriving the post-ultimate behavior of a column under pure compression. Nevertheless, such a way of doing is arguable because it does not respect the normality rule. Indeed, when a structural element is submitted to a normal compressive force N_i (Figure 4.29), according to (3.82), the axial reduction rate $\dot{\Delta}$ should not be equal to zero, but this requirement is not verified if $l_1 + l_2 = l$.

As a consequence, applying the equilibrium method to find the resistance $P_i(\delta)$ leads to a solution that is not entirely statically admissible because it violates the normality criterion. Of course, this approach is not really satisfactory but finding a totally consistent solution leads to equations that are impossible to solve analytically. More details about the exact application of the equilibrium method to the present problem can be found in section C.3.2 of Appendix C.3.

Under the hypothesis that there is no axial shortening of AB , it is possible to find the current lengths l_1 and l_2 characterizing the two parts of the impacted leaf. It may be shown that:

$$l_1 = Z'_I - g(Y_i, \delta) \tan \beta + \frac{g^2(Y_i, \delta)}{2(Z'_I - g(Y_i, \delta) \tan \beta)} ; \quad l_2 = l - l_1 \quad (4.30)$$

where Z'_I is the coordinate along the Z' axis of the initial contact point I (Figure 4.28). Furthermore, if \overline{BC} only suffers a rigid rotation, the current coordinates (X_B, Z_B) of point B in the (X, Z) axis can be obtained by solving simultaneously the subsequent set of equations:

$$\left(X_B - Z'_I \sin \beta - \frac{g(Y_i, \delta)}{\cos \beta} \right)^2 + (Z_B - Z'_I \cos \beta)^2 = l_2^2 ; \quad X_B^2 + (Z_B - 2l \cos \beta)^2 = l^2 \quad (4.31)$$

which allows to calculate the components u_B and w_B along the X' and Z' axes of the displacement imposed to point B . From these results, it can be shown that the rotation angles θ_1 , and θ_2 at the plastic hinge (Figure 4.28) are given by:

$$\theta_1 = \frac{g(Y_i, \delta)}{Z'_I - g(Y_i, \delta) \tan \beta} ; \quad \theta_2 = \frac{g(Y_i, \delta) - u_B}{l - Z'_I - w_B + g(Y_i, \delta) \tan \beta} \quad (4.32)$$

In the attempt of applying the equilibrium method, one can consider the internal forces N_i and T_i acting at the central contact block (Figure 4.29). For moderately large displacements, they may be supposed to act along the X' and Z' axes and equation (3.81) can still be used as an interaction criteria with the bending moment M_i . Furthermore, if H_i and V_i are respectively the horizontal and vertical components of the reaction at the lateral block, expressing the overall equilibrium of the gate allows to determine them as a function of the resistance $P_i(\delta)$. Similarly, if only the impacted leaf is considered, the stability requirements impose that:

$$N_i = H_i \cos \beta - p_i l_1 \sin \theta_1 + p_i l_2 \sin \theta_2 + V_i \sin \beta \leq N_0$$

$$T_i = H_i \sin \beta + p_i l_2 \cos \theta_1 + p_i l_2 \cos \theta_2 - V_i \cos \beta + P_i \quad (4.33)$$

$$M_i = N_i(g(Y_i, \delta) - u_B) + T_i(l - Z'_I - w_B + g(Y_i, \delta) \tan \beta) - p_i l_2^2 / 2$$

where θ_1 and θ_2 are given by (4.32). As suggested by Paik and Thayamballi [121], the contribution $P_i(\delta)$ of the beam to the global resistance $P_G(\delta)$ may then be obtained by using the yield criterion (3.81), in which N_i and M_i are replaced by their expressions given in (4.33). Doing so, it is worth noting that the approach allows for a continuous transition between the solutions obtained during the elastoplastic phase and the present ones.

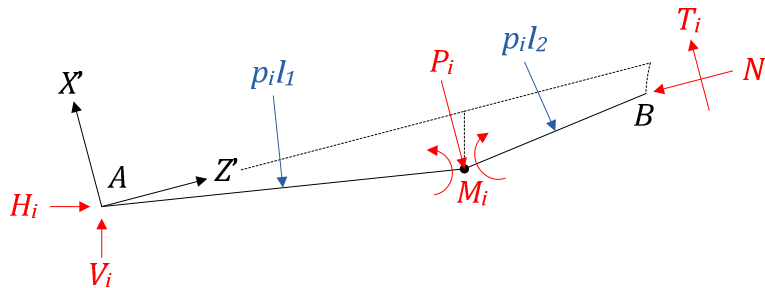


Figure 4.29. Definition of the internal and reaction forces for an off-centered impact

As a final comment, it should be mentioned that the displacement function $g(Y_i, \delta)$ is unknown so far. In fact, this latter may still be evaluated with help of the formulae listed in Table B.1 of Appendix B.4 for a gate with a sill.

Of course, all the previous developments are only valid for class 1 cross-sections. If this condition is not fulfilled, then the plastic mechanism of Figure 4.28 cannot be used because

the beam is submitted to an early buckling. In this case, another plastic solution involving a folding process has to be derived (Figure 3.56). For conciseness, the details are reported in section C.3.3 of Appendix C.3.

Finally, the individual resistance $P_i(\delta)$ provided by the beam is obtained by combining the elastoplastic and perfectly plastic solutions as discussed in section 3.6.3.2 (Figure 3.57).

4.3.2.3. Sliding condition

The elastoplastic and perfectly plastic solutions that were derived here above are in fact only valid as long as there is a sufficient collaboration between the two parts of the gate. Indeed, the shearing force f_i should be transmitted from one leaf to the other in order to insure the overall stability of the structure.

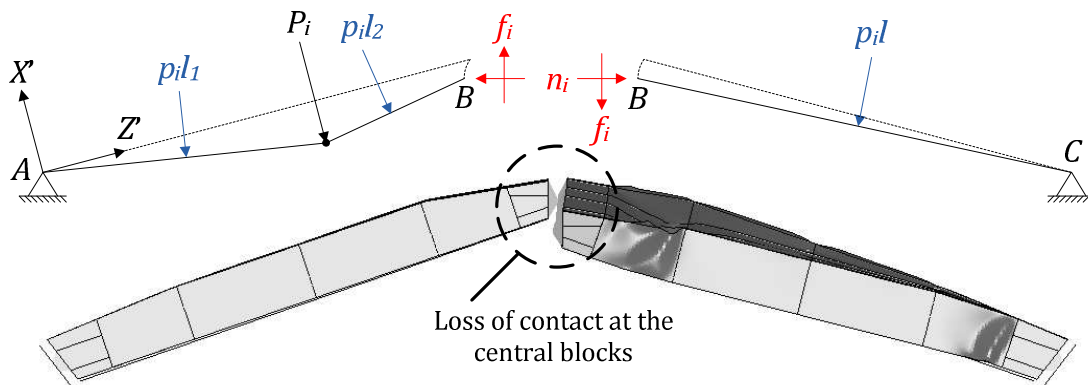


Figure 4.30. Internal forces at the central contact block

If the contact blocks are not physically connected, friction is the only phenomenon that may put the non-impacted leaf into motion. Consequently, for a beam located at the level Y_i along the vertical axis, only a shearing force f_i can develop at the central junction as long as no sliding occurs (Figure 4.30). If the two contact blocks are pushed against each other by a normal force n_i , according to the Coulomb criterion, sliding takes place as soon as the following condition is fulfilled:

$$|f_i| > \mu n_i \quad (4.34)$$

in which μ is a friction coefficient (usually ranging from 0.3 to 0.6) and where the components n_i and f_i can be simply obtained from equivalence considerations:

$$n_i = N_i \cos \beta + T_i \sin \beta \quad ; \quad f_i = T_i \cos \beta - N_i \sin \beta \quad (4.35)$$

where N_i and T_i are given by (4.33) for a class 1 cross-section. Of course, the duration of the sliding phase is limited because the contact between the two parts of the structure is lost when the central displacement is equal to the length l_c of the blocks (Figure 4.3). At this moment, the contribution $P_i(\delta)$ is set to zero, which means that the beam does not contribute anymore to the global resistance of the gate.

4.3.3. Centered impact

In the case of a centered impact, the collision scenario is symmetric (Figure 4.4b) and this should be also the case for the global deformation pattern. In order to derive $P_C(\delta)$, the mechanical model introduced in section 4.3.1.1 is also used, so the gate is represented as a set

of horizontal beams having a uniform web height that is calculated in accordance with Figure 4.24a and equation (4.23).

4.3.3.1. Elastoplastic solution

In the elastic regime, the beam located at a level Y_i along the vertical axis is submitted to an out-of-plane displacement $g(Y_i, \delta)$ at the central contact blocks (Figure 4.31). On a theoretical point of view, this can be assimilated to a support settlement and it is assumed that this motion is only responsible for an axial reduction Δ of the two segments AB and BC given by:

$$\Delta_i = l - \sqrt{l^2 + g^2(Y_i, \delta) - 2lg(Y_i, \delta) \sin \beta} \quad (4.36)$$

where l is the initial length of each leaf. In order to generate this shortening, AB and BC should be submitted to a total compressive force $N_i(\delta)$ parallel to Z' and having the following magnitude:

$$N_i(\delta) = EA_i \frac{\Delta_i}{l} + \frac{p_i l}{2} \cot \beta \quad (4.37)$$

where E is the Young modulus and A_i is the cross-section area. In (4.37), it is worth noting that the first term only is due to the axial reduction, the second one coming from the hydrostatic pressure. Another effect of the surrounding water is to produce bending moments that are also given by (4.25) with a maximal value $M_i(\delta) = p_i l^2 / 8$ obtained when $Z' = l/2$.

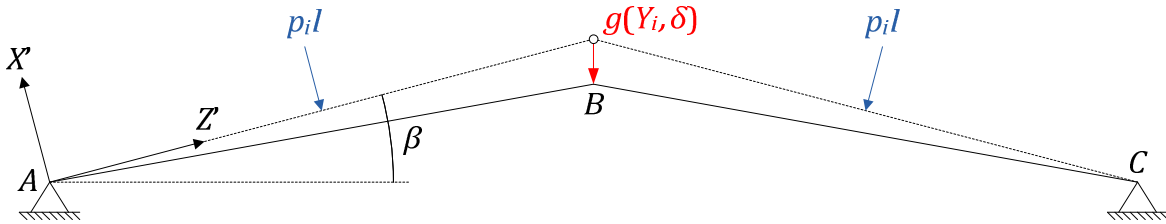


Figure 4.31. Displacement field for a centered impact

Under the assumption that the elastic regime only involves small displacements, the equilibrium can be expressed in the initial configuration and it can be shown that the individual contribution $P_i(\delta)$ to the global resistance writes:

$$P_i(\delta) = 2N_i(\delta) \sin \beta = 2 \frac{EA_i}{l} \left(l - \sqrt{l^2 + g^2(Y_i, \delta) - 2lg(Y_i, \delta) \sin \beta} \right) \sin \beta \quad (4.38)$$

In fact, (4.38) is only valid as long as the beam resistance $P_{t,i}(\delta)$ has not been reached. This arises when the appropriate interaction criterion given by (4.28) is satisfied. At this moment, it is assumed that the contribution to the total resistance is simply given by $P_{t,i}(\delta)$ until the transition penetration δ_t is reached. So instead (4.38), one should write:

$$P_i(\delta) = \min \left\{ 2 \frac{EA_i}{l} \left(l - \sqrt{l^2 + g^2(Y_i, \delta) - 2lg(Y_i, \delta) \sin \beta} \right) \sin \beta ; P_{t,i}(\delta) \right\} \quad (4.39)$$

where $g(Y_i, \delta)$ can still be calculated with help of the formulae provided in section B.4.1 of Appendix B.4 for a gate with a sill.

4.3.3.2. Perfectly plastic solution

For $\delta > \delta_t$, the global resistance $P_G(\delta)$ is calculated by assuming that an overall mechanism is activated over the whole gate. The contribution $P_i(\delta)$ of a beam located at the level Y_i along

the vertical axis is obtained by assuming a perfectly plastic material and a given collapse scheme. For a centered impact, this latter is symmetric, as depicted on Figure 4.32. Each leaf is made of two rigid arms AI and IB separated by a stationary plastic hinge at point I such that their initial lengths remain unchanged, i.e. $\overline{AI} = \overline{IB} = l/2$. As mentioned in section 4.3.2.2, doing so is not theoretically acceptable because the normality rule is not satisfied, which implies that the present solution is not statically admissible. However, unlike the off-centered configuration, all the compatibility requirements are respected here as no moving hinge is involved in the plastic mechanism, so the solution is at least kinematically admissible.

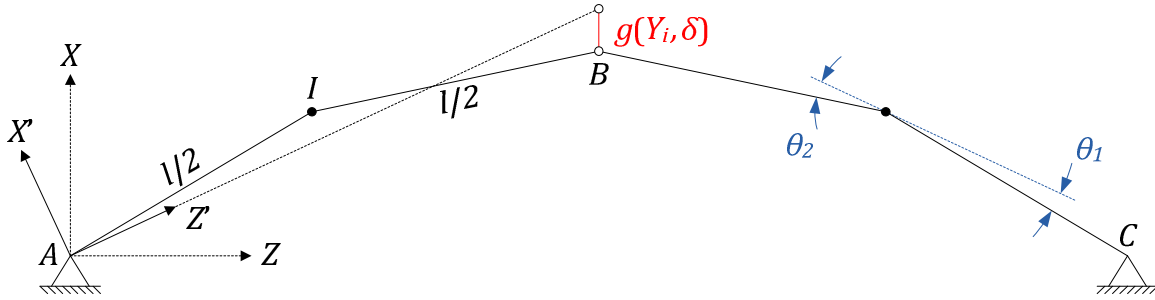


Figure 4.32. Plastic mechanism for a class 1 cross-section in the case of a centered impact

In the optic of using the equilibrium method, let us denote by (X_I, Z_I) the current coordinates of point I in the (X, Z) axes (Figure 4.32). From geometrical considerations, it can be shown that these parameters are obtained by solving simultaneously the two subsequent equations:

$$X_I^2 + Z_I^2 = l^2/4 \quad ; \quad (l \sin \beta - g(Y_i, \delta) - X_I)^2 + (l \cos \beta - Z_I)^2 = l^2/4 \quad (4.40)$$

where the displacement function $g(Y_i, \delta)$ is still given by the formulae listed in Table B.1 of Appendix B.4 for a gate with a sill. With these results, the rotation angles θ_1 and θ_2 at the plastic hinge (Figure 4.32) are found to be as follows:

$$\theta_1 = \arctan\left(\frac{X_I}{Z_I}\right) - \beta \quad ; \quad \theta_2 = \beta - \arctan\left(\frac{l \sin \beta - g(Y_i, \delta) - X_I}{l \cos \beta - Z_I}\right) \quad (4.41)$$

Once all the required geometrical properties are calculated, the next step consists in writing the overall equilibrium of the structure. This allows to express the reaction forces H_i and V_i at the lateral contact blocks (Figure 4.33) as functions of the resistance $P_i(\delta)$. From these relations, one can calculate the internal forces T_i and N_i respectively acting along the X' and Z' axes at point B as well as the bending moment M_i at point I . These latter are found to be:

$$\begin{aligned} N_i &= H_i \cos \beta + \frac{p_i l}{2} \sin \theta_1 - \frac{p_i l}{2} \sin \theta_2 + V_i \sin \beta \leq N_0 \\ T_i &= H_i \sin \beta + \frac{p_i l}{2} \cos \theta_1 + \frac{p_i l}{2} \cos \theta_2 - V_i \cos \beta + P_i \\ M_i &= \frac{N_i l}{2} \sin \theta_2 + \frac{p_i l^2}{2} - \frac{T_i l}{2} \cos \theta_2 \end{aligned} \quad (4.42)$$

in which the angles θ_1 and θ_2 are given by (4.41). Once again, the contribution $P_i(\delta)$ of the beam to the global resistance $P_G(\delta)$ can be calculated by introducing (4.42) in the yield criterion (3.81). Of course, doing so is only valid for a class 1 cross-section. For the other cases, the mechanism of Figure 4.32 can still be used, but instead of having a plastic hinge at point I , the folding pattern of Figure C.12 can be used. Doing so, the resistance $P_i(\delta)$ is evaluated by following a procedure very similar to the one exposed in section C.3.3 of

Appendix C.3, except that θ_i is this time obtained by summing up the rotations θ_1 and θ_2 given in (4.41).

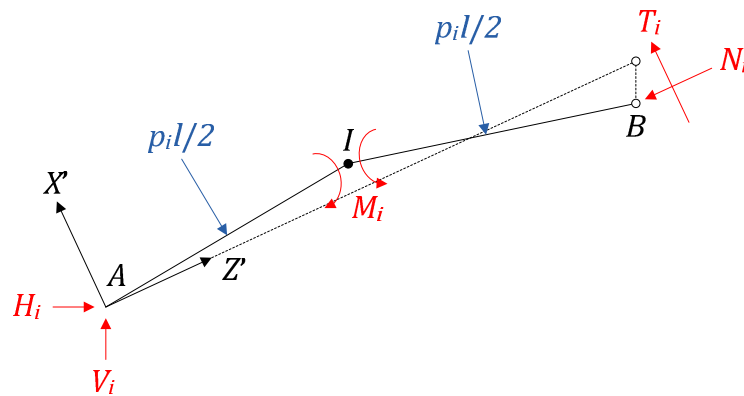


Figure 4.33. Definition of the internal and reaction forces for a centered impact

Finally, the individual resistance $P_i(\delta)$ is calculated by combining the elastoplastic and perfectly plastic solutions derived here above.

4.4. Numerical validations

The goal of this section is to present comparisons between the resistance curves obtained numerically and analytically. To do so, the finite element software LS-DYNA is used to simulate collisions on mitre lock gates.

4.4.1. Description of the finite element model

Building a realistic finite element model for a mitre lock gate is not straightforward because the boundary conditions are quite particular. In an attempt to properly represent the supports of the structure, the lock walls and the sill are also modeled (Figure 4.34) but considered as rigid. The contact between the leaves and the sill is provided by the lowermost horizontal girder, while the support at the lock walls is made through lateral blocks. At the middle of the gate, the central blocks are also modeled to insure the contact between the two leaves. All these components are meshed with Belytschko-Tsai shell elements [66] and the general surface to surface penalty contact algorithm of LS-DYNA is used to avoid any relative penetration. In order to model friction, the static and dynamic coefficients are set to 0.3.

When the gate is pushed against the lock walls, the forces are transmitted through the lateral blocks. On the contrary, when the structure tends to separate from the walls, this motion is prohibited by the tension in the ties and the shearing of the pivots. Therefore, these two components are modeled with cable elements that are infinitely stiff in tension but do not have any stiffness in compression. Such a representation has the advantage of being quite easy to implement, but it also avoids introducing rotational restraints on the lateral studs.

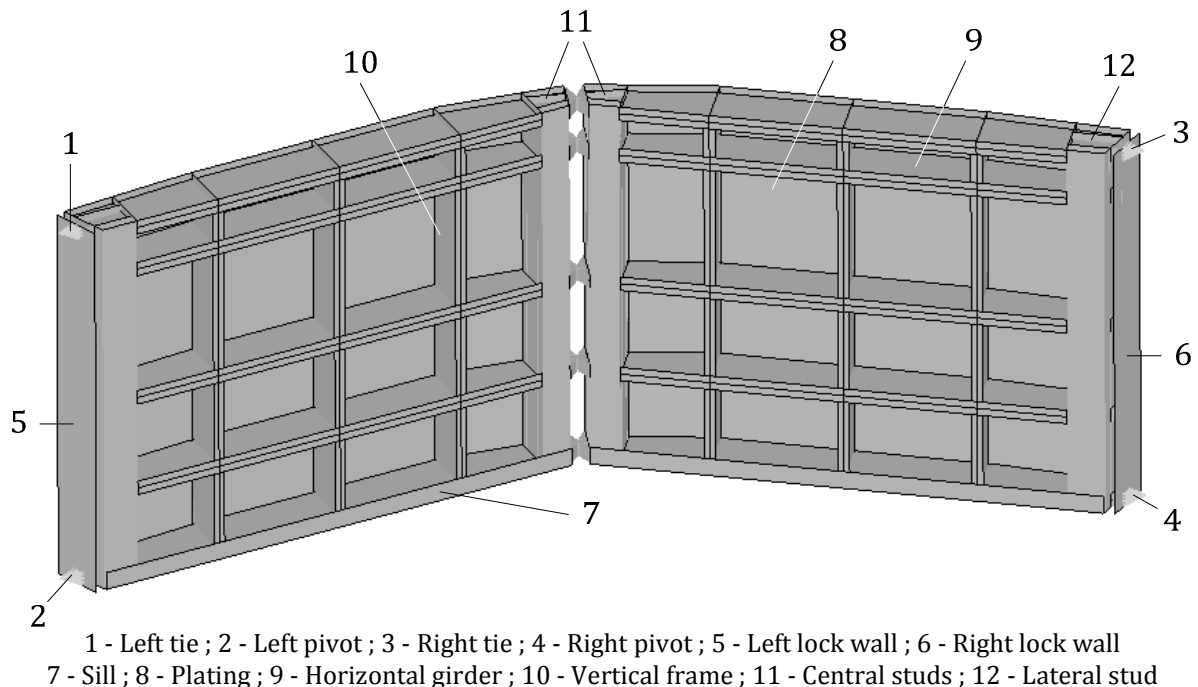


Figure 4.34. Finite element model of a mitre gate

Regarding the material properties, except for the lock walls and the sill that are perfectly stiff, all the remaining parts are affected with the mild steel properties listed in Table 3.2, the stress-strain relation being still the one depicted on Figure 3.21. The strain-rate effect is not taken into account because the striking velocities are quite low. Concerning the mesh size, the

same remarks than those mentioned in section 3.7.1.1 are applicable. In particular, the refinement should be sufficient near the central and lateral blocks because these areas are very sensitive due to large contact forces. Typically, the elements dimensions vary between 5 and 10 *cm* to keep a sufficient precision on the results provided by LS-DYNA.

As a final remark, it should be mentioned that the hydrostatic water was applied on the lock gate by loading the immersed shell elements with an appropriate distributed pressure.

4.4.2. Off-centered impact

It is focused here on an off-centered impact (Figure 4.4a) occurring on the gate of Figure 4.34. The corresponding geometrical data are listed in Table 4.5, using the notations introduced on Figure 4.3. For this scenario, the first striking vessel shown on Figure 3.60 is used for the simulation and its geometrical dimensions are listed in the associated table. It has a total mass of 4000 *t* and an initial velocity of 2 *m/s*. The simulation is stopped when the total initial kinetic energy of 8 *MJ* is completely dissipated or when the contact between the two leafs is lost. In the (*X, Y, Z*) axes of Figure 4.4, the position of the summit *S* of the stem is such that $Y_S = 8.2\text{ m}$ and $Z_S = 7.15\text{ m}$.

| General data | | | | | | | | | Plating |
|--------------------|------------------|------------------|------------------|------------------|-----------------|------------------|------------------|------------------|------------------|
| $l_1\text{ (m)}$ | $l_2\text{ (m)}$ | $l_3\text{ (m)}$ | β | β' | γ_1 | γ_2 | $h_0\text{ (m)}$ | $l_c\text{ (m)}$ | $t_p\text{ (m)}$ |
| 3.35 | 3.15 | 7 | 19° | 19° | 6° | 10° | 1.5 | 0.1 | 0.022 |
| Horizontal girders | | | | | Vertical frames | | | | |
| $Y\text{ (m)}$ | $h_w\text{ (m)}$ | $t_w\text{ (m)}$ | $h_f\text{ (m)}$ | $t_f\text{ (m)}$ | $Z'\text{ (m)}$ | $h_w\text{ (m)}$ | $t_w\text{ (m)}$ | $h_f\text{ (m)}$ | $t_f\text{ (m)}$ |
| 0 | 1.5 | 0.016 | 0.4 | 0.012 | 1 | 1.5 | 0.012 | 0.3 | 0.012 |
| 2.53 | 1.5 | 0.016 | 0.4 | 0.012 | 3.35 | 1.5 | 0.012 | 0.3 | 0.012 |
| 5.23 | 1.5 | 0.016 | 0.4 | 0.012 | 6.85 | 1.5 | 0.012 | 0.3 | 0.012 |
| 9.06 | 1.5 | 0.016 | 0.4 | 0.012 | 10.35 | 1.5 | 0.012 | 0.3 | 0.012 |
| 10.3 | 1.5 | 0.016 | 0.4 | 0.012 | 12.7 | 1.5 | 0.012 | 0.3 | 0.012 |

Table 4.5. Geometrical properties of the gate

The numerical and analytical curves showing the evolution of the resistance are depicted on Figure 4.35. From this comparison, it can be observed that the simplified approach provides a reasonable approximation of the collision force in the present case.

According to the analytical solution, the gate resistance is first provided through the local deforming mode until the transition penetration of 0.6 *m* is reached. This is particularly visible on Figure 4.35, where the abrupt discontinuities for $\delta \leq 0.6\text{ m}$ correspond to the successive activations of various super-elements. For $\delta > 0.6\text{ m}$, the global mode is initiated and the resistance becomes more or less constant. Such a situation is not really surprising and is due to the plastic mechanism detailed in section 4.3.2.2. After that, when $\delta > 0.9\text{ m}$, the theoretical sliding condition (4.34) is satisfied, which allows for a progressive relative motion of the leafs. Each time the contact between two central blocks is lost, there is a sudden decrease in the resistance, as depicted on Figure 4.35.

From the numerical simulation, it appears that sliding is initiated when δ is close to 0.8 *m*, which means that the theoretical prediction is a bit unsafe. This is due to the difficulty to get a refined analytical prediction of internal forces n_i and f_i involved in equation (4.34). Nevertheless, it can be concluded from Figure 4.35 that the agreement on the resistance is quite satisfactory for a pre-design stage. Even though they have not been reported here, this

conclusion is also valid for the curves showing the evolution of the internal energy with the penetration.

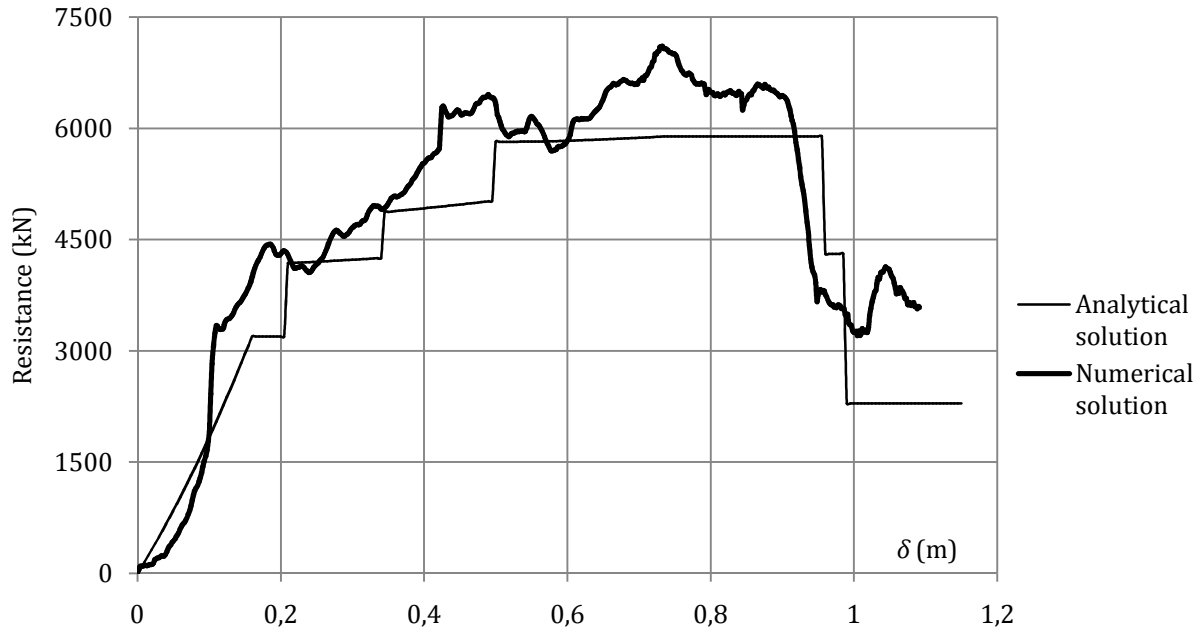


Figure 4.35. Comparison of the analytical and numerical resistance curves for an off-centered impact

As a closing remark about off-centered collisions, it is worth mentioning that all the simulations performed with LS-DYNA systematically lead to a loss of contact between the two leafs for an initial kinetic energy of 8 MJ (i.e. for a vessel of 4000 t with an initial velocity of 2 m/s). In practice, this situation is of course not acceptable because it produces a loss of watertightness and the potential emptying of the upstream reach to the downstream one. In addition, apart from the important damages caused to the gate, the vessel itself could be severely damaged. One should therefore carefully account for such a dangerous situation.

4.4.3. Centered impact

The case of a centered impact (Figure 4.4b) is now investigated. The initial position of the striking vessel in the (X, Y, Z) axes of Figure 4.4 is such that $Y_S = 7.7 \text{ m}$ and $Z_S = 12.8 \text{ m}$. The gate used for the simulation is the same as the one presented in the previous section. The corresponding analytical and numerical resistance curves are shown on Figure 4.36.

From this picture, it can be seen that initially, there is a sudden increase of the resistance that is simply due to the local deforming mode. After that, when δ is close to 0.18 m , there is another discontinuity in the curve because other super-elements are impacted. At this moment, the local resistance is sufficient to activate the overall plastic mechanism of Figure 4.32 and consequently, for the subsequent values of δ , the analytical impact force is calculated in accordance with the formulae detailed in section 4.3.3.2. As this collapse process is unstable, it is not surprising to have a decreasing curve.

Once again, the agreement of the simplified approach with the finite element solution is satisfactory. Nevertheless, for $\delta > 0.7 \text{ m}$, the curve given by LS-DYNA starts growing again and stabilizes around 0.82 m . This is simply due to the fact that for large values of the penetration, as the stem angle ϕ is close to 90° , there is a second contact between the stem and the gate, which is assimilated as a shock and explains the divergence. On a mathematical

point of view, this situation is also considered by modifying the definition of the displacement function $g(Y_i, \delta)$ such as discussed in section B.4.2 of Appendix B.4. However, doing so only produces a small slope modification of the analytical curve but finally leads to a conservative estimation.

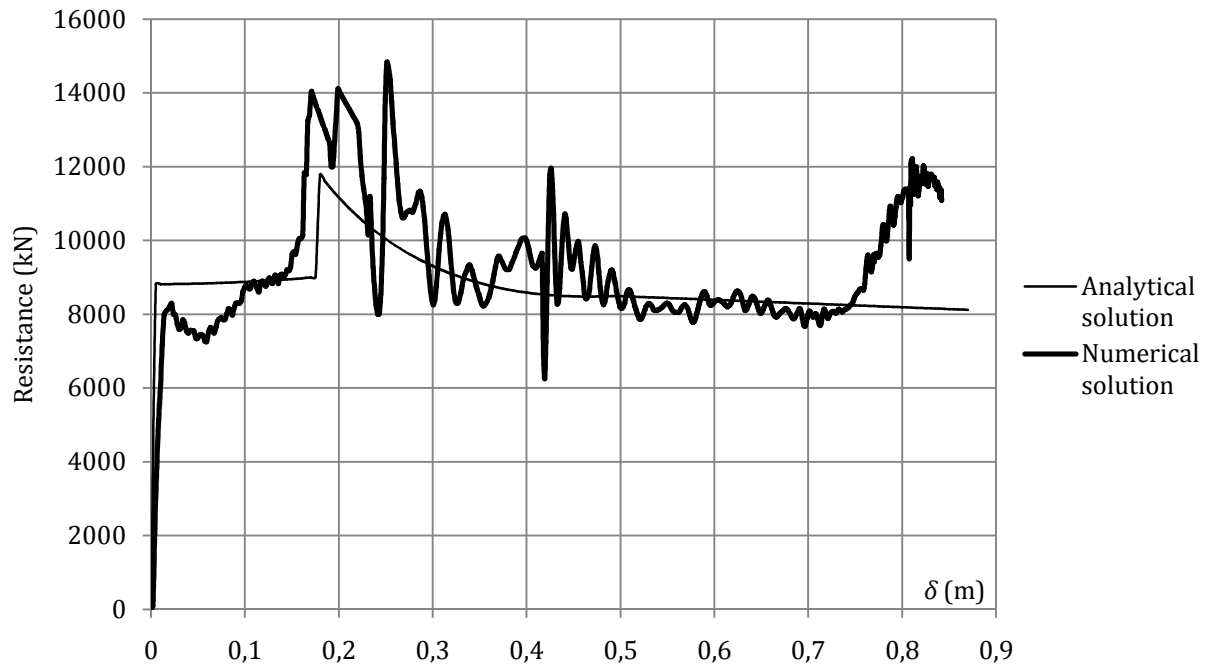


Figure 4.36. Comparison of the analytical and numerical resistance curves for an off-centered impact

For $\delta = 0.82$ m, the simulation is stopped because the initial kinetic energy of 8 MJ has been entirely converted into internal one. Consequently, one may argue that a centered collision is a less critical impact configuration than an off-centered one.

The influence of various parameters such as the impact point, the stiffening system... on the collision resistance are briefly investigated in Appendix B.4. Some other comparisons between the analytical and numerical results are also available in this section.

4.5. Conclusions

The purpose of this chapter was to develop an analytical model to predict the resistance of a mitre lock gate. To achieve this goal, the structural behavior was first studied in a local deforming mode, which required to develop the three super-elements introduced in section 4.2. These ones are mainly similar to those already introduced in Chapter 3 for plane lock gates, except that the mathematical derivation had to be performed by accounting for the mitre angle β . The developments realized here may be seen as a generalization of the former ones. Furthermore, for $\beta \rightarrow 0$, the results of sections 3.3, 3.4 and 3.5 can be recovered. This explains why the presentation was a bit more succinct in this chapter.

As a second step, the gate was studied in the global deforming mode by assuming that each leaf may be decomposed into a set of horizontal beams weakly connected by the vertical frames. The equilibrium method was applied to derive analytical solutions for an elastoplastic and a perfectly plastic material. These ones were detailed in section 4.3.

In order to validate these mathematical developments, numerical simulations were performed with the finite element software LS-DYNA. The agreement was found to be satisfactory and the simplified approach tends to be conservative. From this validation procedure, the following important remarks may be stressed:

- The analysis of the numerical and analytical results shows that a major difference as compared to plane gates (Chapter 3) appears during the global deforming mode. Indeed, from the figures presented in section 4.4 and in Appendix C.4, it transpires that the impact force tends to decrease (or at least to stabilize) when an overall mechanism is activated. Such an observation can be theoretically explained by the fact that the solutions characterizing the plastic collapse are unstable. This was not necessarily the case for plane structures, where tensile membrane effects may cause an increase of the global resistance. For mitre gates however, as compressive forces dominate, such a situation is not possible.
- For a striking vessel with an initial kinetic energy of $8 MJ$ (i.e. a mass of $4000 t$ and a velocity of $2 m/s$), all the simulations have shown that in case of an off-centered impact, the contact between the two leafs was systematically lost before having an entire internal dissipation. Of course, if the two parts of the gate separate, the watertightness is not preserved and severe damages may be caused to both the gate and the striking vessel, which is not acceptable.
- The direct implication of the previous observations is that unlike plane gates, the most dangerous impact configurations are not necessarily those with huge vessels. Indeed, if the ships are quite large, a centered collision is more likely to occur than an off-centered one. In such a case, the contact between the two leafs will never be lost as they are forced to move in unison. Consequently, in this situation, the striking ship may be stopped by the structure if this latter is capable of absorbing the initial kinetic energy.
- Another reason for arguing that a centered impact is less dangerous is due to the fact that the two legs are deformed under the impact, which allows for a better internal absorption and a higher resistance. On the contrary, for an off-centered collision, only the impacted leaf is mobilized to stop the penetration of the striking vessel, which is much less efficient. This reasoning can be corroborated by comparing the results presented in section 4.4.2 and 4.4.3, from which it appears that the maximal resistance reached for a centered impact

(Figure 4.36) is approximately two times higher than the one observed (Figure 4.35) for an off-centered configuration.

From the last three previous points, it can be concluded that an off-centered impact involving a vessel with a reasonable initial kinetic energy may be the most dangerous scenario to consider when designing lock gates.

As a final remark, it should be mentioned that all the previous mathematical and numerical efforts were performed by accounting explicitly for the hydrostatic pressure. Unlike plane gates, the effect of the surrounding water is quite important in the present case, in particular for off-centered impacts. Indeed, the pressure exerted on the non-impacted leaf contributes to its rotational stability and prevents a too early separation of the two parts of the gate⁹. In order to illustrate this last comment, a finite element simulation was run without modeling the action of water. By so doing, the separation arises at the very beginning of the impact and the non-impacted leaf starts rotating as a rigid body (Figure 4.37), which causes the immediate collapse of the other one.

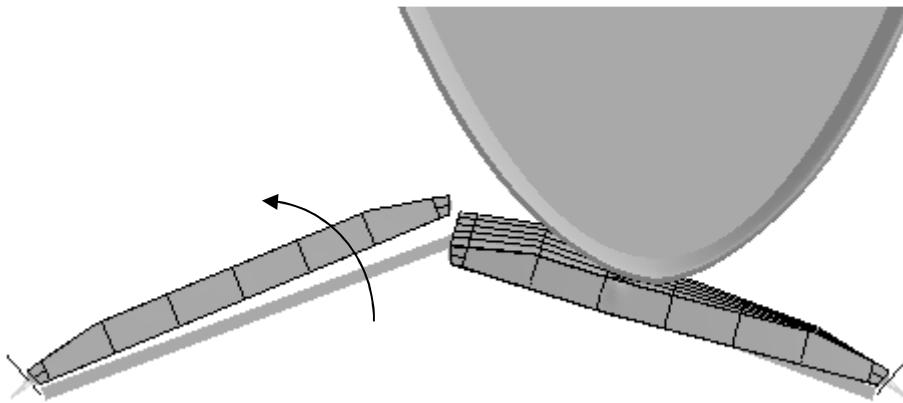


Figure 4.37. Opening of the non-impacted leaf if the hydrostatic pressure is not modeled

Apart from insuring the rotational stability, the hydrostatic pressure is also quite important for the collaboration between the two leafs because it tends to push them against each other. As a direct implication, the criterion (4.34) requiring that $f_i > \mu n_i$ is more difficult to satisfy, which delays the initiation of sliding. Consequently, one should always account for the hydrostatic pressure when analyzing the crashworthiness of mitre lock gates.

⁹ This assertion may be easily understood by considering the resulting hydrostatic force $p_i l$ acting on the non-impacted leaf of Figure C.8.

CHAPTER 5. Conclusions about ship impacts on lock
gates

5.1. Scientific developments

The purpose of this first part was to develop an analytical method to evaluate the collision resistance of plane and mitre lock gates. In addition to the particular conclusions already presented in sections 3.8 and 4.5, we would like to insist on the main innovative scientific developments that have been required to achieve this goal.

The fundamental assumption is that there are two possible ways for a lock gate to withstand ship impacts. The first one is known as the local deforming mode and only involves a localized crushing of structural components, while the second one is called the global deforming mode and implies an overall bending of the structure (Figure 3.9a).

The resistance during the *local deforming mode* is evaluated by using the super-elements method. In this approach, the gate is divided into large structural entities. Each of them is characterized by some geometrical and mechanical properties and is assumed to be decoupled from the others. Three different types of super-element are introduced. Their individual resistance is derived by applying the energy theorems. In addition to the results already available in the literature, the following original developments are performed in the framework of this thesis:

- The resistance of impacted plating elements (Figure 3.11a) is derived to account for the true elliptic shape of the stem (Figure 3.14) and of the bulb (Figure 3.18). Doing so is highly required, as the classical developments corresponding to a punctual impact are found to lead to prohibitively conservative results. Using these new formulae, the local resistance is evaluated in a more realistic way.
- The theoretical approach to derive the collision resistance of horizontal girders and vertical frames (Figure 3.11b) is unified to be consistent with the plate strip formulation. Furthermore, it is shown that considering only a folding process (Figure 3.26) is not sufficient for slender elements because they are likely to bend during the impact (Figure 3.30). Considering an abrupt transition between the two mechanisms is found to be quite realistic.
- Another original contribution concerning girders and frames is that the resistance provided during the above-mentioned bending mechanism is calculated by accounting for the preliminary crushing of the cross-section occurring during the first folding phase (Figure 3.32b). To do so, it is proposed to evaluate the plastic bending moment by neglecting the portion of the web that is completely crushed and by interpolating linearly for the intermediate configurations.
- For a direct impact occurring on the intersection between horizontal and vertical stiffening elements (Figure 3.35a), the resistance is theoretically developed with a consistent assumption on the displacement field. In addition, it is also shown that considering only a folding process (Figure 3.37) is not conservative as an overall bending of the super-element is also likely to occur (Figure 3.39). Consequently, new formulae are developed to include this particularity. They also account for the influence of the crushing process.
- The same work is done in the case of an impact occurring on an intersection because of a subsequent contact (Figure 3.35b). Such a situation has never been treated in the literature, which means that the suggested folding and bending mechanisms are totally original.

- In the case of mitre lock gates (Figure 4.1), all the previous developments have been extended to account for the inclination angle β of the leafs (Figure 4.3). On a mathematical point of view, this is equivalent to an oblique impact, so the corresponding formulae are in fact a generalization of the previous ones, these latter being recovered when β tends to 0.
- Apart from the mathematical efforts mentioned previously, the case of a collision on a mitre lock gate also requires to treat the particular case of a beam impacted obliquely (Figure 4.12). Such a situation has never been treated in the literature and finding a theoretical solution that is entirely satisfactory is not yet achieved. The resistance proposed in this thesis is not strictly admissible but is found to be sufficient for the present purpose.

However, the previous derivation of the local resistance cannot account for the coupling between the super-elements, so considering only a localized impact leads to a drastic overestimation of the collision force. To solve this problem, a second calculation is performed in the *global deforming mode* by assuming that the gate is forced into an overall motion. In this case, the resistance is calculated by assuming that the gate is seen as a set of independent beams (Figure 3.12). Each of them corresponds to a horizontal girder, to which is attached a collaborating part of the plating. The innovative achievements of this thesis related to the global mode may be summarized as follows:

- An elastoplastic evaluation of the bending resistance is performed for each beam. Even though this is not theoretically exact, this is simply achieved by combining an elastic and a rigid-plastic calculation. The elastic derivation is carried out without difficulty but regarding the plastic solution, the Eurocode cross-section classification is considered.
- In the case of class 1 cross-sections, the resistance is calculated by assuming a collapse mechanism involving a sufficient number of hinges. For each of them, the plastic capacity is calculated by accounting for the potential web folding that may take place during the local mode. A simplified formula is proposed in this purpose.
- For other cross-sections that do not have a sufficient rotation capacity, the post-buckling resistance is evaluated by supposing that a localized folding mechanism occurs over the uncrushed web height (Figure 3.56).
- In the particular case of mitre lock gates, the calculations are done with due consideration for the inclination angle β of the two leafs (Figure 4.3). In addition, a sliding criterion is proposed to detect the penetration for which there is a separation of the two parts of the gate (Figure 4.30).

Finally, in order to have a more realistic evaluation of the final lock gate resistance, a method is suggested to *combine the local and global calculations*. This approximate procedure allows for a better assessment of the coupling between the two deforming modes.

5.2. Perspectives

The results provided by the simplified analytical procedure described in chapters 3 and 4 are the curves showing the resistance and the internal energy as functions of the vessel penetration. If a new lock has to be designed, these results can be used in the following purposes:

- One of the main concerns regarding collision is the definition of the worst collision scenario, but this problem can be circumvented with help of the present tool. Indeed, the position of the impact point and the striking vessel properties can be varied within a certain range of values. In each case, the final resistance can be quickly evaluated and the configurations leading to the lowest values may then be retained as the most critical ones.
- During the pre-design phase of lock gate, the precision of the simplified method may be thought to be sufficient and the collision resistance can be assessed in this way. Therefore, this approach is quite convenient if an optimization is performed. Indeed, if the geometrical and mechanical properties of the gate are varied in order to reduce the construction cost for example, the consequences on the ability of the new structure to withstand an impact can be quickly reevaluated.
- If a more refined design is required at the final stage, believing that the simplified approach is sufficient would be too presumptuous. It is evident that local fields (such as stresses and strains for example) cannot be correctly evaluated without resorting to other software. In fact, numerical and analytical tools are complementary in the framework of ship collisions. Indeed, the simplified method can be seen as a good way to isolate the most critical impact scenarios, these latter being investigated later into more details by using finite element.

From the previous points, it can be concluded that some applications may be found in design offices where engineers are dealing with the conception of new lock gates. However, the approach may also be interesting to realize a rapid strength assessment of existing structures, which can be useful for the administrations managing the inland waterways. Such a tool may help them to decide whether a gate should be reinforced or if protection devices (such as cables) are needed for example.

Regarding the future potential developments, it is probably valuable to draw a non exhaustive list of the subjects that may be investigated in future research:

- Derivation of simplified criteria to account for rupture during the global deforming mode. So far, only the failure localized on super-elements has been considered during the derivation, which means that rupture is only integrated in the local resistance. Nevertheless, it is desirable to extend these developments to the global one. Doing so is a quite sensitive problem, particularly because of the difficulty to perform realistic numerical simulations as a validation.
- Investigation of the real support conditions of the gate. The hypotheses made for the analytical derivation of the global resistance do not necessarily reflect the real boundary conditions. Therefore, it could be valuable to perform numerical simulations in which the contact between the gate and its supports would be explicitly modeled. Of course, doing so is a quite fastidious and arduous procedure that requires a lot of skill with finite element software.

- Extension of the simplified method to other lock gates. So far, only plane and mitre gates have been treated, but many other configurations could be considered, such as radial sector gates (Figure 5.1a) or double side gates (Figure 5.1b) that are quite currently encountered in maritime conditions. Adapting the analytical developments to this last case should not be too challenging, but facing with curves elements is maybe a more arduous task.

From the three subjects mentioned here above, it is clear that there is still a lot of work to be done in the field of collisions on lock gates, leading to various industrial applications.

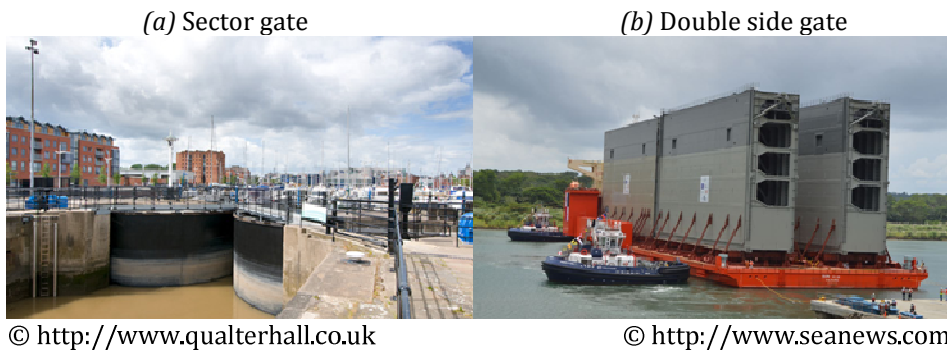


Figure 5.1. Other lock gates configurations

- PART II -

Seismic analysis of lock gates

CHAPTER 6. Literature review on the seismic design of lock gates

The purpose of this chapter is to provide a general overview of what has already been done for the seismic design of lock gates. In order to perform this literature review, it is first proposed to focus on dams and on liquid storage tanks. Even though they are not really similar to lock gates, gathering information about the seismic design of these two structures is appreciable because they are typical examples on the way fluid-structure interaction can be treated. Therefore, some valuable indications about the methodology may be extracted from the references published on these topics.

Consequently, the present chapter will be divided into three main parts. Section 6.1. proposes a non-exhaustive summary of what is currently available in the literature regarding the dam-reservoir interaction.

In section 6.2, the fluid-structure interaction in liquid storage tanks is briefly reviewed. The case of perfectly rigid structures is first considered, but after that, it is proposed to focus on cylindrical and rectangular configurations. For each situation, some indications are given on some analytical and numerical methods available.

Finally, section 6.3 focuses on the seismic design of lock gates. Two different examples are presented to give an insight of what is done in practice.

6.1. Dam-reservoir interaction

The analytical evaluation of hydrodynamic pressure induced during a seism is a quite difficult topic that has been investigated first by Westergaard [166] who treated the case of a rigid dam with a vertical upstream face and an infinite reservoir. Denoting by g the acceleration due to gravity, the structure was supposed to be submitted to a sinusoidal acceleration along the x axis (Figure 6.1) with an amplitude equal to αg . Under the hypothesis of small water motions, the Laplace equation was solved with the appropriate boundary conditions, which led to the following formula for the pressure acting on the dam:

$$p(y) = \frac{7}{8} \alpha g \rho_f \sqrt{h_s(h_s - y)} \quad (6.1)$$

where ρ_f is the fluid mass density, h_s is the water level and y is the vertical coordinate measured from the bottom of the lock (Figure 6.1).

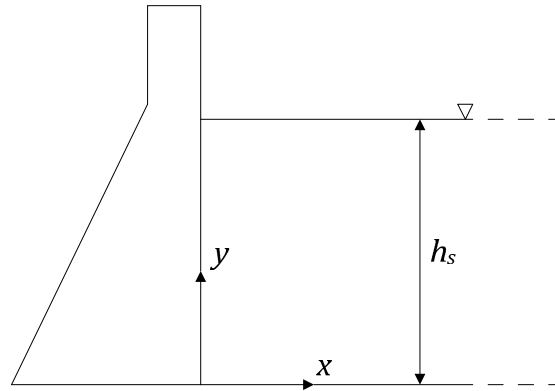


Figure 6.1. Geometry of the flexible reservoir

The results of Westergaard were later extended by Chopra [34] to the case of a similar dam submitted to a horizontal or a vertical arbitrary ground acceleration. An impulse response was first derived in both situations. The convolution integral was then used to get the final hydrodynamic pressure. One of the main achievement in this paper is to propose an analytical solution for the case of a vertical acceleration that also integrates the sloshing at the free surface. Indeed, due to analytical complexities, many authors such as Haroun [67] or Kim et al. [85] considered only a horizontal free surface for the derivation. In fact, it can be shown [17] that this hypothesis is only valid if the water level h_s is sufficient, which is almost always the case for dams. Nevertheless, the work performed by Chopra has the advantage of completeness. It was applied in another paper [35] to assess the safety of concrete dams during earthquake where some practical applications were detailed.

One of the main hypothesis in the work performed by Chopra [34] or Westergaard [166] is that the dam is assumed to be perfectly rigid. With such an approach, the pressures are the same as if a body of water was forced to move in unison with the dam, which means that the fluid-structure interaction is neglected. In order to investigate the influence of the dam vibrations, an analytical approach was suggested by Rashed and Iwan [134] for short-length gravity dams. In this study, the structure was modeled as a thick plate. The eigenfrequencies and mode shapes of the coupled system were first derived by applying the Rayleigh-Ritz method, in which four eigenmodes of a dry plate were used as admissible functions. After that, a forced vibration analysis was performed by solving the local equilibrium equations.

Some application examples were then proposed, but without performing any comparison with other approaches.

Apart from the previous analytical approaches, some numerical studies are also available in the literature. Amongst them, Pani and Bhattacharyya [127] investigated the case of a flexible plate attached to a rigid dam and subjected to a horizontal sinusoidal ground acceleration. A finite element technique was developed, in which the pressure in the fluid and the displacements of the plate are treated as independent nodal variables, but the interaction was provided through an iterative procedure such that the equilibrium and compatibility equations were respected at the interface. A far boundary condition was developed in order to use a truncated domain to simulate an infinite one. No sloshing was considered in the solution and the plate was supposed to have only one dominant mode. With all these hypotheses, a finite element formulation was developed and implemented to treat some examples. It was shown that the plate flexibility increases the pressure and that the fluid compressibility may have some important effects, particularly for high frequencies of the ground excitation. A bit later, Pani and Bhattacharyya [128] extended their previous developments to include sloshing.

Instead of developing finite element techniques, another way to perform seismic analyses is to resort to commercial software. As an example, this was done by Muto et al. [115] who used ABAQUS to study the dam-reservoir interactions. They modeled the fluid domain with acoustic elements that only track the pressure but not the displacements. Such an approach is of course only valid under the assumption that the fluid motions remain sufficiently small. A non-reflecting boundary was used to model an infinite reservoir. Two different simulations were run with a sinusoidal excitation. In the first one, the dam was modeled with rigid shell elements. The pressures obtained in this situation were then compared to the theoretical solutions of Housner [74] in order to validate the finite element model. In the second simulation, deformable solid elements were used for the structure, which led to a pressure 15 % higher than the one predicted by Housner [74]. This conclusion tends to refute the commonly accepted hypothesis that dams may be considered as rigid structures.

6.2. Fluid-structure interaction in containers

The hydrodynamic pressures induce in containers during an earthquake is an important practical case because it allows for the design of storage tanks, which are quite commonly encountered in civil engineering. For this reason, the subject has been treated by various authors in the literature. As a lot of references deal with rigid reservoirs, a short review of the existing solutions is first proposed. After that, a summary of the main achievements for flexible cylindrical and rectangular containers is performed.

6.2.1. Hydrodynamic pressure in rigid containers

Under the hypothesis of a perfectly rigid reservoir, the fluid-structure interaction can be disregarded and it is possible to solve the Laplace equation with simplified appropriate boundary conditions. The corresponding theoretical bases of such an approach are extensively described in the book of Currie [37] or Ibrahim [76], amongst others.

Cylindrical and rectangular storage tanks submitted to a horizontal ground acceleration were both treated by Epstein [49]. The pressure was derived under the assumption of a rigid structure. The sloshing of the free surface was considered by writing the boundary condition in the deformed configuration, which led to simplified expressions that can be used to check if an overtopping was likely or not. The same work was performed by Housner [74] in a more physical approach, while a very refined analytical method was proposed by Graham and Rodriguez [63].

The previous developments were later extended by Haroun [67] to a rectangular concrete container submitted to simultaneous horizontal and vertical seismic accelerations. Here again, the classical potential flow theory was used to estimate the pressure, but the sloshing was neglected. As a matter of application, some formulae were presented to calculate the internal bending moments in the tank due to the earthquake.

In addition to the previous references, it is worth mentioning that some formulae are also available in international standards. This is the case for example in Eurocode 8 [54], where both cylindrical and rectangular containers are considered.

6.2.2. Hydrodynamic pressure in flexible cylindrical containers

In practice however, liquid storage tanks may not necessarily be assimilated to perfectly rigid structures. For this reason, some investigations were performed to account for their flexibility when deriving the hydrodynamic pressure. On an analytical point of view, due to their axisymmetric configuration, flexible cylindrical reservoirs have been more extensively treated in the literature than rectangular ones. Even though they are not particularly similar to lock gates, it may be useful however to quickly review some examples to have a better understanding of the methodology.

An extensive analytical derivation was performed by Fischer [57], who treated the case of a flexible cylinder with due consideration for the free surface displacements. The boundary condition at the fluid-structure interface was expressed by postulating three different given shapes for the radial displacements of the tank wall. With this hypothesis, the Helmholtz equation was solved by applying the Galerkin method, which led to an approximate solution for the hydrodynamic pressure. In an attempt to provide a more practical procedure for the

seismic analysis, the author suggested to replace the actual coupled system by a dry cylinder with a modified mass density. This latter was iteratively calculated such that the total shearing force and overturning moment at the base of the structure were preserved. Such an approach is also suggested in Eurocode 8 [54].

The same procedure was followed by Fujita and Shiraki [60], except that they considered separately the vibration of the couple-system and the sloshing. In order to validate these developments, a reduced-scale model of a cylindrical tank was placed on a shaking table and submitted to a seismic acceleration. The experiment values were found to be in good agreement with the analytical prediction. They were also used by Fischer [57] to corroborate its own calculations.

The idea of working with a fictitious equivalent mass density was later used by Rammerstorfer et al. [133] within an engineering approach that also includes the vertical ground acceleration. As a first step, it was first suggested to perform a numerical modal analysis of the cylinder with the modified mass density to get the fundamental eigenfrequencies of the coupled system. These ones were then used in response spectra to get the relevant horizontal and vertical accelerations. Finally, the pressure obtained in this way were combined with the SRSS formula to derive a design value. Another application example of this method was also proposed by Fischer and Rammerstorfer [58] to check the stability of shell under dynamic load.

In addition to the previous references, it is also quite interesting to mention the developments performed by Yang [172], in which the dynamic response of the cylinder was derived analytically by postulating three different eigenmodes for the coupled system. The Laplace equation was analytically solved to get the pressure and the virtual work principle was used to derive the cylinder displacements. This approach is more or less the same as the one followed here (see Chapter 7) for rectangular reservoirs.

In order to close this short review on flexible cylinders, a final remark can be made on numerical approaches. Some references dealing with this topic are available in the literature, the oldest being probably the one published by Haroun and Housner [68]. However, this paper is still quite interesting because it provides a clear summary of the method. In addition to that, some applications are presented that clearly stress the real need to account for the structural flexibility when evaluating the seismic pressure.

6.2.3. Hydrodynamic pressure in flexible rectangular containers

In comparison with cylindrical reservoirs, the case of rectangular ones is more difficult to treat because the situation is not axisymmetric anymore. This may explain why there are very few references available in the literature. One of them is due to Kim et al. [85] for both horizontal and vertical ground motions. The solutions were obtained by applying the Rayleigh-Ritz method, where the vibration modes of simply supported or cantilever beams were used as admissible functions. The developments were validated by comparison with numerical results and it was clearly pointed out that the hydrodynamic pressure tends to be amplified and that its distribution largely differs from the one obtained for a rigid configuration.

Regarding numerical solutions, Chen and Kianoush [29] focused on the total hydrodynamic pressure in a flexible rectangular tank submitted to a horizontal earthquake excitation. To do

so, the sequential technique was applied. This approach may be summarized as described on Figure 6.2, where the hydrodynamic pressure $p(t)$ is seen as an external force. Instead of solving simultaneously the equations for the solid and fluid domains, each of them is treated separately. Let us imagine that the flexible tank response $u(t)$ is known at time t for a given seismic acceleration $\ddot{X}(t)$. With $u(t)$, it is possible to evaluate analytically the hydrodynamic pressure $p(t)$ acting on the reservoir. At the next time step $t + \Delta t$, this latter may be used for a numerical evaluation of $u(t + \Delta t)$, which means that the pressure and the displacements considered for the analysis are not concomitant.

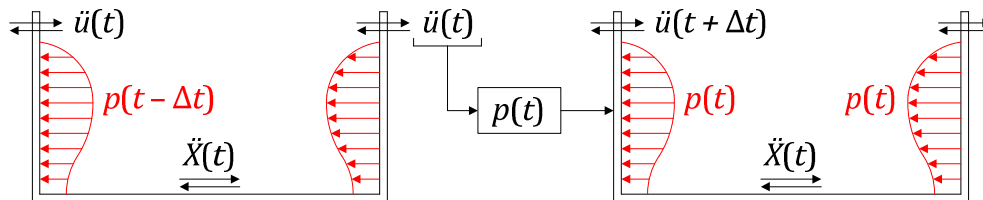


Figure 6.2. Sequential technique

This method was implemented in the finite element code SAP IV developed at the Berkeley University and two reservoirs were investigated with the north-south component of the El-Centro accelerogram. From the time-history analyses performed, it was concluded that the effects of the tank wall flexibility should be considered in the calculation of hydrodynamic pressures. This procedure was later extended by Kianoush and Chen [83] to the case of a vertical ground acceleration.

In all the previous references, the sloshing of the free surface was neglected. In order to account for this phenomenon, Kianoush et al. [84] proposed a new approach to account for the motion of the free surface in the 2D analysis of rectangular flexible tanks. A more detailed study on this topic was proposed by Ghaemmaghami and Kianoush [61], who gave an extensive presentation of the finite element formulation used to model the fluid domain. These developments were first validated by comparing the results with theoretical solutions known for rigid walls conditions. From these investigations, it was concluded that the structural vibrations have practically no influence on the convective response. Only a slight increase in the pressure was observed, which tends to corroborate that the free surface motions can be evaluated under a rigid assumption. Similar conclusions were also addressed by Mitra and Sinhamahapatra [113].

Finally, regarding the numerical investigations of the fluid-structure interaction, it is worth mentioning that this topic can be also investigated by using various commercial software such as LS-DYNA, ABAQUS, MSC NASTRAN, ADINA, ANSYS... Most of them proposes various refined techniques, such as the arbitrary Lagrangian-Eulerian approach. In the literature however, most of the scientific papers are based on finite element codes directly developed by the authors, which renders real industrial examples rather hard to find.

6.3. Seismic analysis of locks

There are very few papers in the literature dealing with the seismic design of lock gates. Some recommendations are however provided by the World Association for Waterborne Transport Infrastructure [170] that suggests to use the equivalent static method. The idea is to apply a static force on the structure to model the action of the fluid for a particular ground acceleration. This latter can be read on a response spectrum at the frequency corresponding to the fundamental mode of the coupled system. Therefore, the method is only applicable if the dynamic response is driven by one unique mode.

This last assumption is an important limitation of the method because an immersed lock gate is not necessarily characterized by a dominant mode. Furthermore, the derivation of the pseudo-static force is not a priori easy to achieve and very few recommendations are available in the literature. In [170], it is proposed to use the Westergaard formula (6.1) to evaluate the hydrodynamic pressure. The parameter α should be chosen as follows:

$$\alpha = a/g \quad \text{if} \quad a > 0.2g \qquad \alpha = \frac{1}{3} \sqrt[3]{a/g} \quad \text{if} \quad a < 0.2g \quad (6.2)$$

where a is the peak ground acceleration of an earthquake with a return period of 5000 years. Of course, such an approach is arguable because it is based on the Westergaard formula, which is only valid for perfectly rigid structures (see section 6.1) and therefore does not account for any interaction with the surrounding fluid. Furthermore, the choice of the non-dimensional acceleration α is done without considering the frequency of the coupled system, which is also questionable. For these reasons, as mentioned in [170], it is suggested to use equations (6.1) and (6.2) only in the very early pre-design stage.

Another approach that is sometimes cited in the literature is known as the added mass method and was used by Forsyth and Porteous [59] for the seismic design of the entrance lock at the Rosyth Royal Dockyard in the United Kingdom (Figure 6.3). For this application, a finite element model of the gate was build and the action of the surrounding water during the earthquake was modeled by attaching some lumped masses to the immersed nodes. These latter were calculated with help of the Zangar formula [176], which is a generalization of the Westergaard equation (6.1) to a dam with a non-vertical upstream face. The seismic analysis was then carried out with acceleration response spectra.



Figure 6.3. Rosyth Royal Dockyard [59]

Nevertheless, regarding the methodology, the previous way of doing is questionable because the lumped masses are calculated as if the gate was perfectly rigid, which means that the

fluid-structure interaction is not taken into account when deriving them. Furthermore, the use of response spectra is also arguable because it is not established that the eigenfrequencies of the gate with the added mass are the same as those of the real coupled system. On a practical point of view however, as the structure is quite stiff (the total width is equal to 6 m, as shown on Figure 6.3), this procedure may be more or less consistent in the present case. As a final observation anyway, the damping coefficient used to calibrate the response spectra is not clearly identified in the paper of Forsyth and Porteous [59]. As discussed in [17], this has to be done carefully because the added mass of water should not interfere in this process.

As another example of good practice, it is also interesting to focus on the new set of locks at the Panama canal [125]. The seismic design was performed as described hereafter.

As a first step, a finite element model of the gate alone was considered, the superstructure being disregarded so far. The action of the hydrodynamic pressure was taken into account by the added mass method, for which the Westergaard formula (6.1) was used. This approach is therefore strictly similar to the one followed by Forsyth and Porteous [59], with the same restrictions. A response spectrum analysis was performed with ANSYS for both the horizontal and vertical excitations, which allows for a structural optimization.

These calculations were performed by using a damping coefficient of 5 % to calibrate the spectra, but this value has been extensively discussed during the design process. Indeed, it was first argued that the added mass of water attached to the structure does not provide any additional damping and should therefore be disregarded when evaluating the coefficient. To account for this observation, it was suggested to choose a much lower value but this idea has not finally been retained for the final design. More details about this topic can be found in [17].

Once a quite optimized model was obtained, a more refined seismic analysis was performed to account for the interaction between the lock gate and the surrounding superstructure. To do so, the initial finite element model was enhanced to include also the lock head and the foundation. Seven time-history analyses were then performed, which allows to account for the soil-structure interaction and to model the real contacts between the gate and its supports. However, the fluid domain was not explicitly represented and the fluid-structure was still considered through the added mass method. As this new finite element model was quite huge, the purpose of these analyses was not to improve the design of the gate but only to check if the response spectrum analysis performed previously was conservative or not.

From the literature review briefly exposed here above, it appears that modeling the fluid-structure interaction during the seismic design of lock gates is still questioning so far. Indeed, using lumped mass with flexible structures is not entirely satisfactory and representing the fluid with finite element leads to very huge models that are too prohibitive for a standard design process. Consequently, deriving an approximate simplified technique could be highly valuable.

CHAPTER 7. Seismic analysis of large flexible reservoirs

In this chapter, the seismic behavior of large reservoirs is considered. These structures are made of two parallel flexible plates connected by two rigid walls. They are submitted to a longitudinal earthquake acceleration and it is the aim of this chapter to find a simplified analytical evaluation of the hydrodynamic pressures appearing in such a situation.

To solve this fluid-structure interaction problem, it is proposed to work in three different steps. The first part of the chapter is devoted to the modal analysis of a dry plate. This section indicates how to derive the vibration frequencies and mode shapes of an unstiffened dry plate that is simply supported on three edges.

In the second part of the chapter, the presence of water is investigated. The flexible plate is this time assumed to be in contact with a liquid on one side. The goal is then to evaluate the wet modal properties in this case. To do so, the Rayleigh-Ritz method is applied, in which the dry mode shapes obtained in the previous section are taken as admissible functions. This leads to an analytical evaluation of the vibration characteristics of the immersed structure. In order to have a kind of validation, comparisons are made with some numerical results obtained by using the finite element software NASTRAN. Finally, some closure remarks on the fluid-structure interaction in flexible reservoirs are presented.

As a last step, the third part of the chapter is devoted to the dynamic analysis of containers. This time, the effect a longitudinal seismic acceleration is investigated. An analytical method is developed to get the hydrodynamic pressures acting on the flexible plate during such an event. To achieve this goal, the virtual work principle is used in conjunction with the Newmark integration scheme, which quickly provides the time evolution of the pressure. Once again, as a validation process, the simplified analytical results are compared with those obtained by simulating numerically the earthquake with LS-DYNA. As a conclusion, the end of the section contains some considerations about the fluid-structure interaction and the added mass method.

The developments presented in this chapter have been partly exposed in the 9th International Conference on Structure Dynamics [18].

7.1. Introduction

In this chapter, the case of a lock gate is not immediately considered. It is first proposed to work on a simple flexible reservoir. The goal here is to draw some general conclusions on the fluid-structure interaction characterizing such kind of structures, which can be useful for investigating further the dynamic behavior of stiffened gates.

7.1.1. Description of the structure

The rectangular reservoir depicted on Figure 7.1 is considered. It has a total length L (along the longitudinal x direction), a total width l (along the transversal z direction) and is filled with water at a level h_s . The reservoir is made of two longitudinal rigid walls located in $z = 0$ and $z = l$, while two identical transverse flexible walls are positioned in $x = 0$ and $x = L$. In the plane $y = 0$, the floor is also supposed to be rigid.

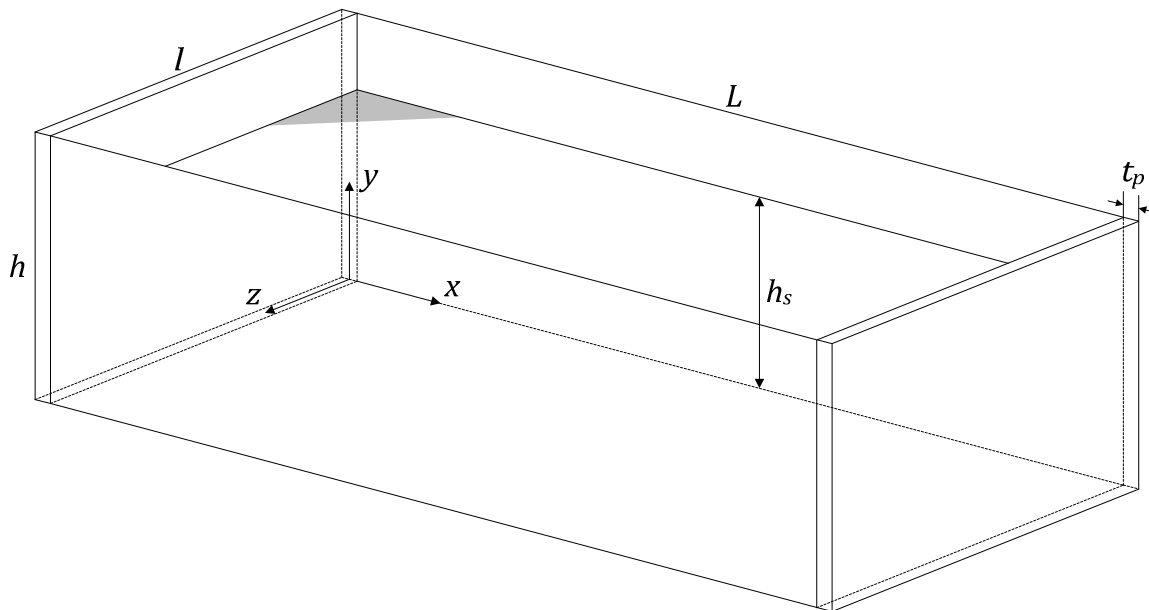


Figure 7.1. Geometry of the flexible reservoir

The flexible walls are assumed to be simply connected to the rigid ones, which means that rotations around the y axis are free along the vertical edges in $z = 0$ and $z = l$. In addition, free rotations around the z axis are also permitted along the horizontal edges in $x = 0$ and $x = L$. In other words, the flexible plates are considered having three simply supported edges, while the upper one is free. In this situation, if the plate were submitted to an out-of-plane loading, it would typically exhibit the displacements pattern depicted on Figure 7.2.

The total height of the flexible walls is denoted by h and the thickness is designated by t_p . In an attempt to analyze flexible reservoirs to draw some conclusions on the seismic behavior of lock gates, it is required to choose more or less realistic values for h and l . As an order of magnitude, these parameters will be close to 10 m . However, as it is quite common for simply-reinforced lock gates to exhibit a bending behavior, the thickness t_p of the plate has to be chosen so that it will work in a similar way. Consequently, if h and l are not far away from 10 m , then it is required to select quite large values of t_p in order to avoid dominant membrane effects. Currently, one should have $t_p \geq 10\text{ cm}$.

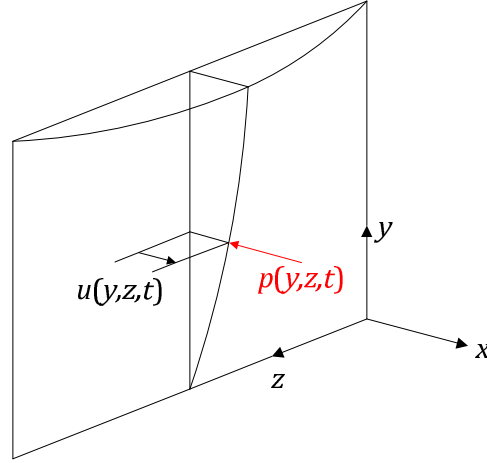


Figure 7.2. Typical deformation of the plate due to an out-of-plane loading

This reservoir is then submitted to an earthquake and the component of the seismic acceleration along the horizontal x axis is denoted by $\ddot{X}(t)$. As the water is forced to move, some additional hydrodynamic pressures $p(y, z, t)$ are induced on the structure (Figure 7.2). The goal is now to provide some analytical formulae to evaluate these actions.

7.1.2. Evaluation of the hydrodynamic pressure

It is well known that the total pressure $p(y, z, t)$ acting on the structure during the earthquake is due to both static and dynamic forces and may be written as:

$$p(y, z, t) = p_h(y) + p_r(y, t) + p_f(y, z, t) \quad (7.1)$$

In this expression, $p_h(y)$ represents the hydrostatic action, while $p_r(y, t) + p_f(y, z, t)$ is the impulsive pressure induced by the seism. This one is obtained by summing up the rigid and flexible contributions, respectively denoted by $p_r(y, t)$ and $p_f(y, z, t)$. An additional term may eventually be added in (7.1) to account for the convective pressure. This last one is coming from the sloshing corresponding to the motion of the free surface. Nevertheless, in the present case, this contribution will be disregarded as it is known to be insignificant for reservoirs where both L and l are quite large [17]. Moreover, according to Eurocode 8 [54], this convective term is reputed to have very little effect on the vibrations characterizing the structure, which is an additional reason for neglecting its contribution.

The analytical derivation of the hydrodynamic pressure may be conducted by assuming that the fluid is irrotational, incompressible and has no viscosity. With these hypotheses, it can be demonstrated (see [17] or [37] for example) that the total hydrodynamic pressure is given by the following relation:

$$p = -\rho_f \frac{\partial \mathcal{H}}{\partial t} \quad (7.2)$$

where ρ_f denotes the fluid mass density and $\mathcal{H}(x, y, z, t)$ is the potential function. This last one may be shown to satisfy the Laplace equation [17]:

$$\Delta \mathcal{H} = 0 \Leftrightarrow \frac{\partial^2 \mathcal{H}}{\partial x^2} + \frac{\partial^2 \mathcal{H}}{\partial y^2} + \frac{\partial^2 \mathcal{H}}{\partial z^2} = 0 \quad (7.3)$$

over the fluid domain. In order to have a unique solution, the following boundary conditions are assorted with (7.3):

- (a) $\frac{\partial \mathcal{H}}{\partial y} = 0$ for $y = 0$ The vertical component of the fluid velocity has to be set to zero at the bottom of the reservoir.
- (b) $\frac{\partial \mathcal{H}}{\partial t} = 0$ for $y = h_s$ The hydrodynamic pressure has to be set to zero at the free surface, as it is equal to the atmospheric pressure.
- (c) $\frac{\partial \mathcal{H}}{\partial z} = 0$ for $z = 0$ The horizontal z component of the fluid velocity has to be set to zero at left wall as this one is perfectly rigid.
- (d) $\frac{\partial \mathcal{H}}{\partial z} = 0$ for $z = l$ The horizontal z component of the fluid velocity has to be set to zero at right wall as this one is perfectly rigid.
- (e) $\frac{\partial \mathcal{H}}{\partial x} = \dot{X}(t) + \frac{\partial u}{\partial t}$ for $x = 0$ The horizontal x component of the fluid velocity has to be equal to the one of the upstream wall.
- (f) $\frac{\partial \mathcal{H}}{\partial x} = \dot{X}(t) + \frac{\partial u}{\partial t}$ for $x = L$ The horizontal x component of the fluid velocity has to be equal to the one of the downstream wall.

where $u(y, z, t)$ denotes the proper displacements of the flexible walls, as it was already depicted on Figure 7.2. The problem defined by (7.3) may be solved by dividing the boundary conditions (e) and (f) in two different parts. As a first step, it can be assumed that each wall of the reservoir is perfectly rigid, which means that (e) and (f) have to be replaced by:

$$\frac{\partial \mathcal{H}}{\partial x} = \dot{X}(t) \quad \text{for } x = 0 \text{ and } x = L \quad (7.4)$$

If (7.3) is solved together with (7.4) and conditions (a) to (d), the so-called rigid impulsive contribution $p_r(y, t)$ introduced in (7.1) is obtained. As the analytical derivation of this pressure is quite extensively documented in the literature, it is not our purpose here to report all the corresponding mathematical developments. More information about this topic has been reported by Abramson [2], Buldgen [17], Curie [37], Epstein [49], Graham and Rodriguez [63], Haroun [67], Housner [74], Ibrahim [76] or Kianoush et al. [84] amongst others (see also section 6.2.1). Practical formulae are also available in Eurocode 8 [54].

As a second step, it is now assumed that the reservoir is no longer submitted to the earthquake event, but that the proper displacements $u(y, z, t)$ exhibited by the flexible walls are this time not equal to zero. Consequently, the following condition has to be substituted to (e) and (f):

$$\frac{\partial \mathcal{H}}{\partial x} = \frac{\partial u}{\partial t} \quad \text{for } x = 0 \text{ and } x = L \quad (7.5)$$

Solving (7.3) together with (7.5) and conditions (a) to (d) leads to the flexible impulsive contribution $p_f(y, z, t)$ in (7.1). It is not difficult to find a closed-form solution to this problem, but once again, all the detailed developments will not be provided here. Further information is provided by Chen et al. [27], Chen and Kianoush [29], Ghaemmaghami and Kianoush [61], Kim et al. [85], Malhotra [105], Meskouris et al. [109] or Veletsos [155] amongst others (see also section 6.2.3).

Following the two steps described here above, it is possible to find analytical expressions for both the rigid and flexible pressures. As a final result, one can establish that the three terms introduced in (7.1) are given by the subsequent relations:

$$p_h(y) = \rho_f g (h_s - y) \quad (7.6)$$

$$p_r(y, t) = -\rho_f \left(\sum_{n=1}^{+\infty} \frac{4}{\beta_n^2 L} \frac{\cosh(\beta_n y)}{\cosh(\beta_n h_s)} - \frac{L}{2} \right) \ddot{X}(t) \quad (7.7)$$

$$p_f(y, z, t) = - \sum_{n=1}^{+\infty} \sum_{m=0}^{+\infty} c_{mn} \cos(\alpha_n y) \cos(\bar{\gamma}_m z) \int_0^{h_s} \int_0^l \ddot{u}(y, z, t) \cos(\alpha_n y) \cos(\bar{\gamma}_m z) dy dz \quad (7.8)$$

in which $\beta_n = (2n - 1)\pi/L$. The other parameters involved in the previous equations are defined as follows:

$$c_{mn} = 2\rho_f \frac{1 - \cosh(\xi_{mn}L)}{h_s l_m \xi_{mn} \sinh(\xi_{mn}L)} \quad \bar{\gamma}_m = \frac{m\pi}{l} \quad \alpha_n = \frac{(2n - 1)\pi}{2h_s} \quad \xi_{mn} = \sqrt{\alpha_n^2 + \bar{\gamma}_m^2} \quad (7.9)$$

where $l_m = l$ if $m = 0$ and $l_m = l/2$ if $m > 0$. With the formulae given in (7.6) to (7.8), it is possible to evaluate the total pressure acting on the flexible walls. It is worth noting that these results are not just valid for a flexible plate, but are still holding for the case of a stiffened structure like a plane lock gate.

It is also important to mention that equation (7.8) has been derived under the assumption that the proper displacements $u(y, z, t)$ in $x = 0$ are the same as those in $x = L$. In other words, the reservoir is supposed to be perfectly symmetric, with two flexible walls that are strictly identical. Asymmetric configurations will not be considered for the moment.

7.2. Free vibration analysis of a dry plate

The vibrations of a plate are quite different if it is surrounded by a fluid or not. The goal of this section is to derive the natural frequencies and mode shapes of a plate that is not in contact with water. Before considering the wet case, some information will first be given on free vibrations of dry plates.

7.2.1. Characteristic equation

In this section, the free vibrations of the isotropic and homogenous plate depicted on Figure 7.2 are considered. It is simply supported along the edges $y = 0$, $z = 0$ and $z = l$, while the last edge in $y = h$ is free. The plate is made of a material with a mass density ρ , exhibiting a linear elastic behavior characterized by a Young modulus E and a Poisson ratio ν . The out-of-plane displacements along the x axis are denoted by $u(y, z, t)$, while the in-plane components along the y and z axes are designated by $v(y, z, t)$ and $w(y, z, t)$ respectively. The structure might be submitted to a transverse pressure $p(y, z, t)$, but this is not the case for a dry situation.

The plate is expected to follow the classical bending theory developed by Kirchhoff. Under the assumption that there is no extension of the mid-surface of the plate, the in-plane displacements $v(y, z, t)$ and $w(y, z, t)$ are simply given by:

$$v(y, z, t) = -x \frac{\partial u}{\partial y} \quad ; \quad w(y, z, t) = -x \frac{\partial u}{\partial z} \quad (7.10)$$

Furthermore, if the out-of-plane displacements are not too large, then small deformations may be assumed. As stated by Shames and Dym [137], it is commonly accepted that this hypothesis is holding, provided that the maximal deflection is less than $t_p/10$. In such a case, one may resort to the Cauchy tensor and derive the following relations:

$$\epsilon_{yy} = -x \frac{\partial^2 u}{\partial y^2} \quad \epsilon_{zz} = -x \frac{\partial^2 u}{\partial z^2} \quad \epsilon_{yz} = -x \frac{\partial^2 u}{\partial y \partial z} \quad (7.11)$$

where ϵ_{yy} , ϵ_{zz} and ϵ_{yz} are the strain components. Additionally, admitting that the material is elastic and linear, the stresses may be related to the strains by using Hooke's law by the following equations:

$$\begin{aligned} \sigma_{yy} &= \frac{E}{1-\nu^2} (\epsilon_{yy} + \nu \epsilon_{zz}) = -x \frac{E}{1-\nu^2} \left(\frac{\partial^2 u}{\partial y^2} + \nu \frac{\partial^2 u}{\partial z^2} \right) \\ \sigma_{zz} &= \frac{E}{1-\nu^2} (\epsilon_{zz} + \nu \epsilon_{yy}) = -x \frac{E}{1-\nu^2} \left(\frac{\partial^2 u}{\partial z^2} + \nu \frac{\partial^2 u}{\partial y^2} \right) \\ \sigma_{yz} &= \frac{E}{1+\nu} \epsilon_{yz} = -x \frac{E}{1+\nu} \frac{\partial^2 u}{\partial y \partial z} \end{aligned} \quad (7.12)$$

where σ_{yy} , σ_{zz} and σ_{yz} are the stress components. Equations (7.10) to (7.12) are the basis of the Kirchhoff bending theory that is mainly applicable to the case of thin plates in small deformations. Nevertheless, as mentioned previously, the value of the thickness t_p may be expected to be quite large. Therefore, it is first necessary to carefully examine the validity of applying such an approach in the present case. The most sensitive point to discuss is the effect

of the shearing forces. Indeed, if the plate is quite thick, these latter may be expected to play an important role in the deformation of the plate. Applying the Kirchhoff theory to such a situation may then be irrelevant. However, one has to bear in mind that the value of t_p has always to be compared to the extensions h and l . According to Shames and Dym [137], if the following condition on the ratios h/t_p and l/t_p is fulfilled:

$$\min\{h/t_p ; l/t_p\} \geq 10 \quad (7.13)$$

then the transverse shears τ_{xy} and τ_{xz} are negligible in comparison with the midplane shear τ_{yz} . This is also the case for the transverse normal stress σ_{xx} which may be disregarded in comparison with the midplane normal stresses σ_{yy} and σ_{zz} . As condition (7.13) is respected in the present study, the dynamic equilibrium of the plate depicted on Figure 7.2 is simply given by the classical equation (in N/m^2):

$$\rho t_p \frac{\partial^2 u}{\partial t^2} + D \left(\frac{\partial^4 u}{\partial y^4} + 2 \frac{\partial^4 u}{\partial y^2 \partial z^2} + \frac{\partial^4 u}{\partial z^4} \right) = -p(y, z, t) \quad (7.14)$$

where $D = Et_p^3/12(1 - \nu^2)$ is the flexural rigidity of the plate and $p(y, z, t)$ is the external pressure acting on the structure. It is worth noting that (7.14) supposes that there is no stretching of the middle surface along the y and z axes. In other words, there is no action of in-plane membrane forces. This last assumption seems reasonable, as the out-of-plane displacements $u(y, z, t)$ may be thought to be kept sufficiently small in comparison with t_p .

To the equilibrium equation (7.14) are associated various boundary conditions. According to Bazant and Cedolin [13], the corresponding mathematical expressions are as follows:

- As the plate is simply supported along the vertical edges $z = 0$ and $z = l$, the first requirement is to prohibit any displacement along the x axis. The second restriction is that the bending moments around the y axis have to be set to zero. Mathematically, one has:

$$u(y) = 0 \quad \text{and} \quad \frac{\partial^2 u}{\partial z^2} + \nu \frac{\partial^2 u}{\partial y^2} = 0 \quad (7.15)$$

- Similarly, as simple supports are also assumed along the horizontal edge $y = 0$, the following conditions have to be respected:

$$u(z) = 0 \quad \text{and} \quad \frac{\partial^2 u}{\partial y^2} + \nu \frac{\partial^2 u}{\partial z^2} = 0 \quad (7.16)$$

- Finally, as the last horizontal edge in $y = h$ is free, the bending moments and the effective shear forces have both to be set to zero, i.e.:

$$\frac{\partial^2 u}{\partial y^2} + \nu \frac{\partial^2 u}{\partial z^2} = 0 \quad \text{and} \quad \frac{\partial^3 u}{\partial y^3} + (2 - \nu) \frac{\partial^3 u}{\partial y \partial z^2} = 0 \quad (7.17)$$

In order to obtain the free vibrations characteristics of a dry plate, we further postulate that the out-of-plane displacement field has the following form:

$$u(y, z, t) = \delta_i(y, z) \sin(\omega_i t) \quad (7.18)$$

where $\delta_i(y, z)$ is the mode shape associated to the pulsation ω_i . This result and the equilibrium equation (7.14) may now be used to derive the characteristic equation. In (7.14),

as the plate is not in contact with water, it is evident that $p(y, z, t) = 0$ and consequently, inserting relation (7.18) into (7.14) leads to:

$$\rho t_p \omega_i^2 - D \left(\frac{\partial^4 \delta_i}{\partial y^4} + 2 \frac{\partial^4 \delta_i}{\partial y^2 \partial z^2} + \frac{\partial^4 \delta_i}{\partial z^4} \right) = 0 \quad (7.19)$$

which, together with the boundary conditions (7.15) to (7.17), constitutes the characteristic equation for a dry plate.

7.2.2. Vibration properties

The vibrations of a dry plate are entirely characterized by determining the eigenvalues ω_i^2 and the eigenfunctions δ_i . The admissible values of ω_i are those leading to a singular solution for the set of equations (7.15), (7.16), (7.17) and (7.19). As shown by Leissa [95], ω_i has to be found by solving a transcendental equation:

$$\left(\frac{\gamma_i^2(1-\nu) - c_i^2}{\gamma_i^2(1-\nu) + c_i^2} \right)^2 \bar{\lambda}_i \tan(\lambda_i H) - \lambda_i \tanh(\bar{\lambda}_i H) = 0 \quad (7.20)$$

where c_i^2 is the unknown related to ω_i by (7.21). The other different parameters also present in (7.20) are defined by the following expressions:

$$\lambda_i = \sqrt{c_i^2 - \gamma_i^2} \quad \bar{\lambda}_i = \sqrt{c_i^2 + \gamma_i^2} \quad \gamma_i = \frac{n_i \pi}{l} \quad c_i^2 = \omega_i \sqrt{\frac{12\rho(1-\nu^2)}{Et_p^2}} \quad (7.21)$$

with $n_i \in \mathbb{N}_0$. For a given value of ω_i , it may be shown [95] that the corresponding dry mode shape $\delta_i(y, z)$ is given by:

$$\delta_i(y, z) = A_i \left(\sin\left(\frac{\lambda_i y}{l}\right) - B_i \sinh\left(\frac{\bar{\lambda}_i y}{l}\right) \right) \sin\left(\frac{n_i \pi z}{l}\right) \quad (7.22)$$

where A_i is the modal amplitude used to normalize the vibration mode $\delta_i(y, z)$. In (7.22), the coefficient B_i is related to the other parameters by:

$$B_i = \frac{\gamma_i^2(1-\nu) - c_i^2 \sin(\lambda_i h)}{\gamma_i^2(1-\nu) + c_i^2 \sinh(\bar{\lambda}_i h)} \quad (7.23)$$

The physical meaning of n_i appears now more clearly. In fact, this parameter corresponds to the number of half-waves along the horizontal z axis. Equation (7.20) clearly shows that it is possible to find an infinite number of solutions ω_i for each value of $n_i \in \{1, 2, \dots\}$. Of course, ω_i is rapidly increasing with n_i , which means that the activation of corresponding mode of vibration becomes more and more unlikely. As an example, Figure 7.3 gives a broad approximation of the first mode shapes associated to $n_i = 1$ and $n_i = 2$.

It also is worth noting that equations (7.20) to (7.23) are only valid for eigenvalues c_i greater than $\gamma_i = n_i \pi / l$. If this is not the case, other analytical solutions are available [95]. However, for the reservoirs considered here, the relation $c_i < \gamma_i$ is always satisfied and there is no need to resort to additional analytical developments.

As a final remark, it should also be mentioned that the dry modes are orthogonal to each others. This result is quite important and will be used later to simplify the mathematical

calculations. Considering two different modes (i.e. if $i \neq j$), this property allows to write the following result:

$$\int_0^h \int_0^l \delta_i(y, z) \delta_j(y, z) dy dz = 0 \quad (7.24)$$

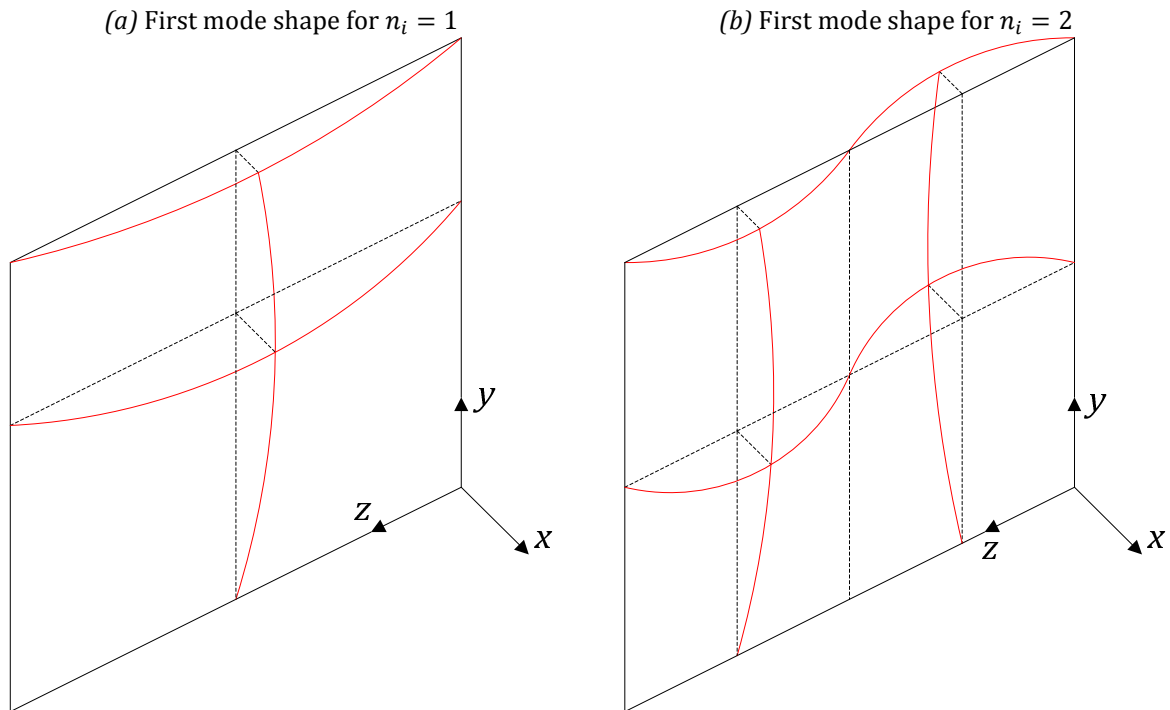


Figure 7.3. First vibration mode shapes for two different values of n_j

7.3. Free vibration analysis of an immersed plate

7.3.1. Characteristic equation

The vibration properties of a plate immersed in water are quite different from those previously derived for the dry situation. The surrounding liquid has an effect on both the natural frequencies and modes of vibration. Indeed, one may intuitively predict that the frequencies will be lowered in the case of a wet plate, but also that the mode shapes will be influenced by the pressure acting on the vibrating structure. Therefore, it is quite important to account for these phenomena while performing the seismic analysis of flexible reservoirs. Evaluating the natural frequencies and mode shapes of a wetted plate is precisely the goal of this section.

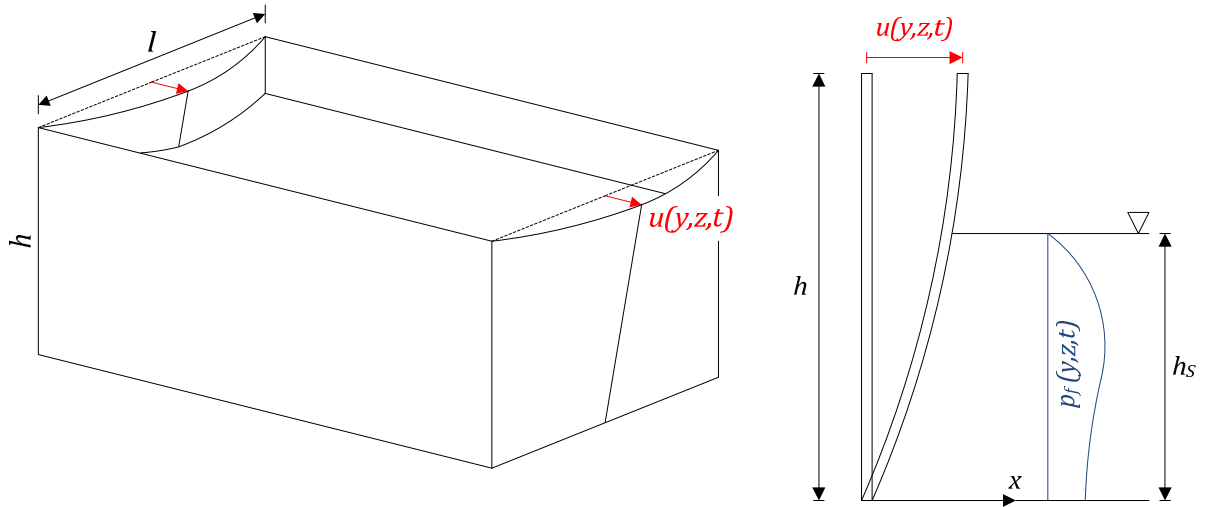


Figure 7.4. Hydrodynamic pressure on a plate vibrating in a fluid

It is more difficult to derive the characteristic equation for a wet plate than for a dry one. The main reason is that the accelerations of the flexible walls of the reservoir produce an additional hydrodynamic pressure. This phenomenon was already mentioned previously, and it was found that this pressure could be evaluated by using equation (7.8). This last expression is recalled hereafter:

$$p_f(y, z, t) = - \sum_{n=1}^{+\infty} \sum_{m=0}^{+\infty} c_{mn} \cos(\alpha_n y) \cos(\bar{\gamma}_m z) \int_0^{h_s} \int_0^l \ddot{u}(y, z, t) \cos(\alpha_n y) \cos(\bar{\gamma}_m z) dy dz \quad (7.25)$$

where the coefficients c_{mn} , $\bar{\gamma}_m$ and α_n are defined in (7.9). When the plate exhibits free vibrations (Figure 7.4), the acceleration term $\ddot{u}(y, z, t)$ appearing in (7.25) may be derived from the classical expression:

$$u(y, z, t) = \Delta_i(y, z) \sin(\Omega_i t) \quad (7.26)$$

where Ω_i and $\Delta_i(y, z)$ are respectively the pulsations and mode shapes characterizing the free vibrations of the immersed plate. With this relation, one may write:

$$p_f(y, z, t) = \Omega_i^2 \sin(\Omega_i t) \sum_{n=1}^{+\infty} \sum_{m=0}^{+\infty} I_{mn}^{(i)} c_{mn} \cos(\alpha_n y) \cos(\bar{\gamma}_m z) \quad (7.27)$$

In this last expression, $I_{mn}^{(i)}$ is a coefficient that is only related to the mode shape $\Delta_i(y, z)$ of the wet plate. It is simply given by:

$$I_{mn}^{(i)} = \int_0^{h_s} \int_0^l \Delta_i(y, z) \cos(\alpha_n y) \cos(\bar{\gamma}_m z) dydz \quad (7.28)$$

As the plate is now subjected to $p_f(y, z, t)$, referring to the equilibrium equation of the structure, (7.14) has to be completed to account for this external force. Introducing (7.26) and (7.27) in (7.14) leads to:

$$\Omega_i^2 \left(\rho t_p \Delta_i - \sum_{n=1}^{+\infty} \sum_{m=0}^{+\infty} I_{mn}^{(i)} c_{mn} \cos(\alpha_n y) \cos(\bar{\gamma}_m z) \right) - D \left(\frac{\partial^4 \Delta_i}{\partial y^4} + \frac{\partial^4 \Delta_i}{\partial y^2 \partial z^2} + \frac{\partial^4 \Delta_i}{\partial z^4} \right) = 0 \quad (7.29)$$

which, together with the boundary conditions expressed in (7.15) to (7.17), constitutes the characteristic equation for a wet plate. However, finding an exact solution to a such problem is not easy. For this reason, the Rayleigh-Ritz method will be used.

7.3.2. Rayleigh-Ritz solution

7.3.2.1. Mathematical approach

The characteristic equation of a wet plate (7.29) may be rewritten in a more compact form. To do so, let us denote by \mathcal{L}_1 and \mathcal{L}_2 the two linear differential operators associated with (7.29). These ones are such that this equation simply becomes:

$$\Omega_i^2 \mathcal{L}_1(\Delta_i) - \mathcal{L}_2(\Delta_i) = 0 \quad (7.30)$$

which is the classical form of a generalized eigenvalue problem. In this last expression, it is obvious that \mathcal{L}_1 and \mathcal{L}_2 are defined by:

$$\mathcal{L}_1(\cdot) = \rho t_p (\cdot) - \sum_{n=1}^{+\infty} \sum_{m=0}^{+\infty} c_{mn} \cos(\alpha_n y) \cos(\bar{\gamma}_m z) \int_0^{h_s} \int_0^l (\cdot) \cos(\alpha_n y) \cos(\bar{\gamma}_m z) dydz \quad (7.31)$$

$$\mathcal{L}_2(\cdot) = D \left(\frac{\partial^4 (\cdot)}{\partial y^4} + 2 \frac{\partial^4 (\cdot)}{\partial y^2 \partial z^2} + \frac{\partial^4 (\cdot)}{\partial z^4} \right) \quad (7.32)$$

Let now $\Delta_1(y, z)$ and $\Delta_2(y, z)$ be two arbitrary functions satisfying the boundary conditions (7.15) to (7.17) associated to (7.29). For each of them, it may be shown [137] that the operators \mathcal{L}_1 and \mathcal{L}_2 are self-adjoint [40] over the surface A of the plate, i.e.:

$$\begin{aligned} \langle \mathcal{L}_1(\Delta_1) | \Delta_2 \rangle &= \langle \Delta_1 | \mathcal{L}_1(\Delta_2) \rangle \\ \langle \mathcal{L}_2(\Delta_1) | \Delta_2 \rangle &= \langle \Delta_1 | \mathcal{L}_2(\Delta_2) \rangle \end{aligned} \quad (7.33)$$

where $\langle \cdot | \cdot \rangle$ denotes the inner product¹⁰ of two functions. This property is fundamental to apply the Rayleigh-Ritz method. Indeed, if \mathcal{L}_1 and \mathcal{L}_2 are self-adjoint, it may be

¹⁰ The inner product (or scalar product) of two functions $f(x, y, z)$ and $g(x, y, z)$ over a domain V of the space is written as:

$$\langle f | g \rangle = \iiint_V f(x, y, z) g(x, y, z) dx dy dz$$

mathematically stated [137] that the admissible eigenvalues Ω_i^2 in (7.30) are the stationary values of the so-called Rayleigh quotient:

$$R = \frac{\langle \Delta | \mathcal{L}_2(\Delta) \rangle}{\langle \Delta | \mathcal{L}_1(\Delta) \rangle} \quad (7.34)$$

which means that the only admissible eigenfunctions Δ_i in (7.30) are those who minimize (7.34). However, it is not easy to find particular expressions of Δ for which the Rayleigh quotient is stationary. A brief literature review shows that a classical approach to overcome this problem is to express $\Delta_i(y, z)$ as a linear combination of admissible predefined functions. For example, this procedure was followed by Rajalingham et al. [132] to get the vibration modes of a dry rectangular plate with clamped edges¹¹. Another application was made by Liew and Wang [101], who studied the vibrations of plates with curved boundaries or reentrant corners. Lam and Liew [90] used the Gram-Schmidt recurrence algorithm to derive orthogonal functions, which were then employed in the Rayleigh-Ritz method to study free vibrations of elliptical plates. Finally, a particularly interesting application was made by Lamb [91] and Liang et al. [100], who also applied this method to get the frequencies and modes of submerged plates.

Following the ideas suggested in the literature, it is proposed here to express the wet modes Δ_i as a linear combination of M dry ones:

$$\Delta_i(y, z) = \sum_{j=1}^M v_{ji} \delta_j(y, z) \quad (7.35)$$

where the analytical expression of the dry modes is given by (7.22). The functions $\delta_j(y, z)$ are reputed to be admissible, as they satisfy the boundary conditions (7.15) to (7.17) and linearly independent (as they are orthogonal to each others). Consequently, this is also the case for $\Delta_i(y, z)$. The next step is then to evaluate the Rayleigh quotient R with help of (7.35):

$$\langle \Delta_i | \mathcal{L}_1(\Delta_i) \rangle = \sum_{j=1}^M \sum_{k=1}^M v_{ji} v_{ki} \iint_A \delta_j(y, z) \mathcal{L}_1(\delta_k(y, z)) dydz = \sum_{j=1}^M \sum_{k=1}^M v_{ji} (\hat{T}_{jk} - \hat{W}_{jk}) v_{ki} \quad (7.36)$$

$$\langle \Delta_i | \mathcal{L}_2(\Delta_i) \rangle = \sum_{j=1}^M \sum_{k=1}^M v_{ji} v_{ki} \iint_A \delta_j(y, z) \mathcal{L}_2(\delta_k(y, z)) dydz = \sum_{j=1}^M \sum_{k=1}^M v_{ji} \hat{U}_{jk} v_{ki} \quad (7.37)$$

where A is the surface of the plate. \hat{T}_{jk} , \hat{W}_{jk} and \hat{U}_{jk} are to be found by considering the expressions (7.31) and (7.32) of the operators \mathcal{L}_1 and \mathcal{L}_2 :

$$\hat{T}_{jk} = \rho t_p \int_0^l \int_0^H \delta_j(y, z) \delta_k(y, z) dydz \quad \hat{W}_{jk} = \sum_{n=1}^{+\infty} \sum_{m=0}^{+\infty} c_{mn} \hat{I}_{mn}^{(j)} \hat{I}_{mn}^{(k)} \quad (7.38)$$

$$\hat{U}_{jk} = D \int_0^l \int_0^H \delta_j(y, z) \left(\frac{\partial^4 \delta_k}{\partial y^4} + 2 \frac{\partial^4 \delta_k}{\partial y^2 \partial z^2} + \frac{\partial^4 \delta_k}{\partial z^4} \right) dydz \quad (7.39)$$

¹¹ It is mentioned by Blevins [14] and Leissa [95] that it is possible to find exact solutions to the characteristic dry equation (7.19) only for plates having at least two simply supported edges. This is rather impossible for other boundary conditions.

where $\hat{\Gamma}_{mn}^{(j)}$ and $\hat{\Gamma}_{mn}^{(k)}$ are given equation (7.28), in which $\Delta_i(y, z)$ is replaced by $\delta_j(y, z)$ and $\delta_k(y, z)$ respectively. The detailed expressions of \hat{T}_{jk} , \hat{W}_{jk} and \hat{U}_{jk} are not reported here but may be consulted in section D.1.1 of Appendix D.1. The Rayleigh quotient may now be rewritten as:

$$R = \left(\sum_{j=1}^M \sum_{k=1}^M v_{ji} (\hat{T}_{jk} - \hat{W}_{jk}) v_{ki} \right) \div \left(\sum_{j=1}^M \sum_{k=1}^M v_{ji} \hat{U}_{jk} v_{ki} \right) = \frac{\mathbf{v}_i^T ([\hat{T}] - [\hat{W}]) \mathbf{v}_i}{\mathbf{v}_i^T [\hat{U}] \mathbf{v}_i} \quad (7.40)$$

where $[\hat{T}]$, $[\hat{W}]$ and $[\hat{U}]$ are the $(M \times M)$ matrices associated to \hat{T}_{jk} , \hat{W}_{jk} and \hat{U}_{jk} . \mathbf{v}_i is a $(M \times 1)$ vector containing the coefficients v_{ji} and \mathbf{v}_i^T is the corresponding transpose. In order to get the stationary values of R , the particular vectors \mathbf{v}_i minimizing (7.40) have to be found. As \mathcal{L}_1 and \mathcal{L}_2 are self-adjoint, these stationary values of R are reputed to be the eigenvalues Ω_i^2 . It may be demonstrated [137] that these ones are found by solving the classical equation:

$$\det([\hat{U}] - \Omega_i^2([\hat{T}] - [\hat{W}])) = 0 \quad (7.41)$$

As $\Delta_i(y, z)$ is expressed as linear combination of M dry modes, it is possible to find only M particular values Ω_i verifying (7.41). The associated M eigenvector \mathbf{v}_i are then derived by:

$$([\hat{U}] - \Omega_i^2([\hat{T}] - [\hat{W}])) \mathbf{v}_i = \mathbf{0} \quad (7.42)$$

Finally, it appears that solving (7.41) provides an estimation of the vibration frequencies of an immersed plate. As stated by Shames and Dym [137], these approximations always tend to overestimate the real frequencies of the structure, but it is possible to get better values by increasing the number M of admissible functions considered in (7.35). Additionally, the solutions of (7.42) lead to the coefficients v_{ji} that may be introduced in (7.35) to get the wet mode shapes.

It is worth noting that the dry modes $\delta_j(y, z)$ are orthogonal. As a consequence, matrices $[\hat{U}]$ and $[\hat{T}]$ are diagonal, but this is unfortunately not the case for the matrix $[\hat{W}]$ which is simply symmetric.

7.3.2.2. Energy approach

In section 7.3.2.1, the Rayleigh-Ritz method was introduced in a purely mathematical way, but it is also possible to consider this approach in a energy manner. Doing so is more common and will be useful for further developments on stiffened plates. Let us start by recalling some basic results for elastic plates in plane-stress state. By definition, the potential energy \mathcal{U} (or the strain energy) of a such structure is given by:

$$\mathcal{U} = \frac{1}{2} \iint_A (\sigma_{yy} \epsilon_{yy} + \sigma_{zz} \epsilon_{zz} + 2\sigma_{yz} \epsilon_{yz}) dydz \quad (7.43)$$

Considering equations (7.11) and (7.12) relating σ_{ij} and ϵ_{ij} to the out-of-plane displacements $u(y, z, t)$, developing (7.43) leads to the following classical expression:

$$\mathcal{U} = \frac{D}{2} \iint_A \left(\left(\frac{\partial^2 u}{\partial y^2} \right)^2 + \left(\frac{\partial^2 u}{\partial z^2} \right)^2 + 2\nu \frac{\partial^2 u}{\partial y^2} \frac{\partial^2 u}{\partial z^2} + 2(1 - \nu) \left(\frac{\partial^2 u}{\partial y \partial z} \right)^2 \right) dydz \quad (7.44)$$

which is widely used in the literature (see references [90], [100], [101] and [132], amongst others). For the particular case of modal displacements, since $\Delta_i(y, z)$ is an eigenfunction minimizing the Rayleigh quotient and $u(y, z, t) = \Delta_i(y, z) \sin(\Omega_i t)$, introducing this relation in (7.44) gives:

$$u = \frac{D}{2} \sin^2(\Omega_i t) \iint_A \left(\left(\frac{\partial^2 \Delta_i}{\partial y^2} \right)^2 + \left(\frac{\partial^2 \Delta_i}{\partial z^2} \right)^2 + 2\nu \frac{\partial^2 \Delta_i}{\partial y^2} \frac{\partial^2 \Delta_i}{\partial z^2} + 2(1-\nu) \left(\frac{\partial^2 \Delta_i}{\partial y \partial z} \right)^2 \right) dydz \quad (7.45)$$

As a second step, a similar procedure can now be followed to get the total kinetic energy \mathcal{T} of the plate. Doing so, it can be established that \mathcal{T} is given by:

$$\mathcal{T} = \frac{1}{2} \iint_A \rho t_p \dot{u}^2(y, z, t) dydz = \frac{\rho t_p}{2} \Omega_i^2 \cos^2(\Omega_i t) \iint_A \Delta_i^2(y, z) dydz \quad (7.46)$$

Finally, as the plate is in contact with a fluid, a last step is to evaluate the potential \mathcal{W} of the hydrodynamic pressure (7.25) acting on the vibrating structure. As no rational development of this potential has been found in the literature, more details about its derivation are given in section D.1.3 of Appendix D.1. It is found that:

$$\mathcal{W} = \sum_{n=1}^{+\infty} \sum_{m=0}^{+\infty} \frac{c_{mn}}{2} \left(\int_0^{h_s} \int_0^l \dot{u}(y, z, t) \cos(\alpha_n y) \cos(\bar{\gamma}_m z) dydz \right)^2 \quad (7.47)$$

which is very similar to the definition of a kinetic energy. For this reason, \mathcal{W} may be seen as a kind of energy associated to the water put in motion by the own vibrations of the plate [137]. Once again, for modal displacements, one gets:

$$\mathcal{W} = \frac{\Omega_i^2 \cos^2(\Omega_i t)}{2} \sum_{n=1}^{+\infty} \sum_{m=0}^{+\infty} c_{mn} I_{mn}^{(i)} I_{mn}^{(i)} \quad (7.48)$$

Considering now the amplitudes of total kinetic and strain energies, equations (7.45), (7.46) and (7.48) show that:

$$\max_t \{\mathcal{T} - \mathcal{W}\} = \frac{\Omega_i^2}{2} \left(\rho t_p \iint_A \Delta_i^2(y, z) dydz - \sum_{n=1}^{+\infty} \sum_{m=0}^{+\infty} c_{mn} I_{mn}^{(i)} I_{mn}^{(i)} \right) = \frac{\Omega_i^2}{2} \langle \Delta_i | \mathcal{L}_1(\Delta_i) \rangle \quad (7.49)$$

$$\max_t \{\mathcal{U}\} = \frac{D}{2} \iint_A \left(\left(\frac{\partial^2 \Delta_i}{\partial y^2} \right)^2 + \left(\frac{\partial^2 \Delta_i}{\partial z^2} \right)^2 + 2\nu \frac{\partial^2 \Delta_i}{\partial y^2} \frac{\partial^2 \Delta_i}{\partial z^2} + 2(1-\nu) \left(\frac{\partial^2 \Delta_i}{\partial y \partial z} \right)^2 \right) dydz \quad (7.50)$$

If $\Delta_i(y, z)$ satisfies the boundary conditions of the plate (which is the case in the present situation), it may be shown that expression (7.50) can be simplified to get:

$$\max_t \{\mathcal{U}\} = \frac{\langle \Delta_i | \mathcal{L}_2(\Delta_i) \rangle}{2} \quad (7.51)$$

Unfortunately, a complete mathematical proof of (7.51) has not been in the literature. Since the entire demonstration of this statement is quite fastidious, it will not be provided as an appendix and the result will be simply admitted. As there is no dissipation in the system, the

maximum kinetic energy may be equated to the maximum strain energy, which leads to the following relations:

$$\max_t \{\mathcal{U}\} = \max_t \{\mathcal{T} - \mathcal{W}\} \Leftrightarrow \frac{\Omega_i^2}{2} \langle \Delta_i | \mathcal{L}_1(\Delta_i) \rangle = \frac{\langle \Delta_i | \mathcal{L}_2(\Delta_i) \rangle}{2} \Leftrightarrow \Omega_i^2 = \frac{\langle \Delta_i | \mathcal{L}_2(\Delta_i) \rangle}{\langle \Delta_i | \mathcal{L}_1(\Delta_i) \rangle} \quad (7.52)$$

As a conclusion, the energy approach detailed here above shows that if $\Delta_i(y, z)$ is an eigenfunction which minimizes the Rayleigh quotient, this latter is nothing else than the eigenvalue Ω_i^2 associated to $\Delta_i(y, z)$.

The mathematical procedure detailed in section 7.3.2.1 to get the eigenvalues and eigenfunctions may now be revisited in terms of energy parameters. Indeed, for a given function $\Delta_i(y, z)$ satisfying the boundary conditions, one may first evaluate the associated maximal kinetic and strain energies. These ones will be denoted by \mathcal{T} , \mathcal{W} and \mathcal{U} , even if their expressions bellow are not formally similar to those introduced previously. From (7.49) and (7.50), let us now rewrite:

$$\mathcal{T} - \mathcal{W} = \frac{\rho t_p}{2} \iint_A \Delta_i^2(y, z) dydz - \sum_{n=1}^{+\infty} \sum_{m=0}^{+\infty} \frac{c_{mn}}{2} I_{mn}^{(i)} I_{mn}^{(i)} \quad (7.53)$$

$$\mathcal{U} = \frac{D}{2} \iint_A \left(\left(\frac{\partial^2 \Delta_i}{\partial y^2} \right)^2 + \left(\frac{\partial^2 \Delta_i}{\partial z^2} \right)^2 + 2\nu \frac{\partial^2 \Delta_i}{\partial y^2} \frac{\partial^2 \Delta_i}{\partial z^2} + 2(1 - \nu) \left(\frac{\partial^2 \Delta_i}{\partial y \partial z} \right)^2 \right) dydz \quad (7.54)$$

With these new definitions of \mathcal{T} , \mathcal{W} and \mathcal{U} , the Rayleigh quotient may now be expressed as the ratio between the maximal kinetic and potential energies:

$$R = \frac{\mathcal{T} - \mathcal{W}}{\mathcal{U}} \quad (7.55)$$

and the next step is then to find the particular expressions $\Delta_i(y, z)$ for which R is minimized. This can be achieved by following a procedure similar to the one given by equations (7.35), (7.41) and (7.42). Doing so, it is worth noting that:

$$\mathcal{T} - \mathcal{W} = \frac{1}{2} \sum_{j=1}^M \sum_{k=1}^M v_{ji} (\hat{T}_{jk} - \hat{W}_{jk}) v_{ki} \quad \mathcal{U} = \frac{1}{2} \sum_{j=1}^M \sum_{k=1}^M v_{ji} \hat{U}_{jk} v_{ki} \quad (7.56)$$

where \hat{T}_{jk} , \hat{W}_{jk} and \hat{U}_{jk} are still given by (7.38) and (7.39). Alternatively, one may also resort to the following expression:

$$D \int_A \left(\frac{\partial^2 \delta_j}{\partial y^2} \frac{\partial^2 \delta_k}{\partial y^2} + \frac{\partial^2 \delta_j}{\partial z^2} \frac{\partial^2 \delta_k}{\partial z^2} + \nu \frac{\partial^2 \delta_j}{\partial y^2} \frac{\partial^2 \delta_k}{\partial z^2} + \nu \frac{\partial^2 \delta_k}{\partial y^2} \frac{\partial^2 \delta_j}{\partial z^2} + 2(1 - \nu) \frac{\partial^2 \delta_j}{\partial y \partial z} \frac{\partial^2 \delta_k}{\partial y \partial z} \right) dA \quad (7.57)$$

to evaluate \hat{U}_{jk} . This latter is directly obtained by developing equation (7.54). It is shown to be strictly similar to (7.39) because of the equality stated in (7.51), but this is only true as long as the functions $\delta_j(y, z)$ satisfy the boundary conditions. The approach mentioned here above is commonly encountered in the literature and will be extensively used later when dealing with lock gates. Nevertheless, before going any further in the analysis of immersed plates, it is probably useful to perform a numerical validation of all the previous analytical developments.

7.3.3. Numerical validation

In order to check the validity of the present procedure, the analytical solutions can be compared to those obtained numerically. To do so, it is proposed here to consider the reservoir depicted on Figure 7.5. The flexible walls are slightly rectangular, with a width l of 7 m and a height h of 6 m. The thickness t_p may take three different values, as depicted on Figure 7.5. The reservoir has a total length L of 15 m and is filled up to a level of 3.5 or 5 m. Other reservoirs with different geometrical properties were also used for the validation process, but the obtained results are not presented here to avoid any redundancy. The conclusions found for these other cases are similar to the ones summarized here.

As it was already discussed before, the thicknesses chosen for the flexible walls may appear to be quite large. Nevertheless, one should always bear in mind that the ratios l/t_p and h/t_p have to be kept sufficiently high to limit the effect of shearing forces. Moreover, if the plates were too thin, it is to fear that the out-of-plane displacements would be such that the structure would exhibit a membrane behavior. The classical Kirchhoff bending theory used in the analytical approach would be irrelevant for this situation.

Additionally, some comments need to be done about the dimensions considered for this reservoir, which are definitely not similar to those of a real lock chamber. Nevertheless, the geometrical properties have been restricted due to computational limitations when performing finite element simulations. Indeed, modeling the fluid with solid elements quickly leads to large models, for which a modal analysis requires unfortunately a lot of numerical capacities.

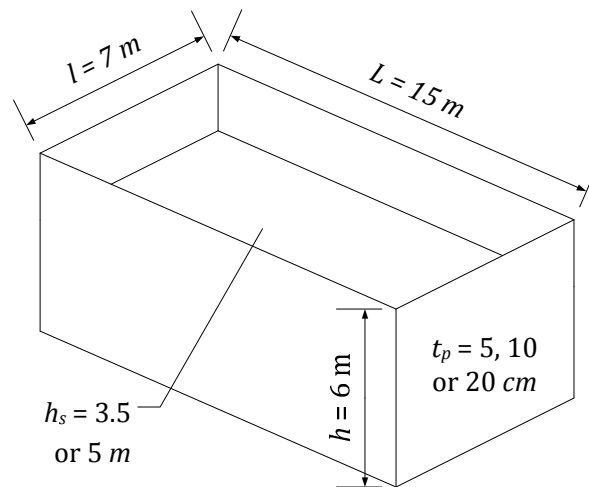


Figure 7.5. Main characteristics of the reservoir used for validation

The pre-processor PATRAN is first used to realize a finite element model of the reservoir. The flexible walls are modeled by using isoparametric quadrilateral CQUAD shell elements with four grid points, while hexahedral CHEXA solid elements with eight grid points are used for the fluid¹². The material parameters are given in Table 7.1. Steel properties are taken for the structure, which is assumed to have a linear elastic behavior defined by a Young modulus E and a Poisson coefficient ν . The fluid has the characteristics of water. Its mass density is denoted by ρ_f , while the bulk modulus and speed of sound are respectively identified by K_f and c_f .

¹² See the Nastran reference manual [114] for additional information on these elements.

The finite element software NASTRAN is then used to perform a modal analysis of the reservoir. Doing so provides a numerical estimation of the wet frequencies and mode shapes characterizing the flexible walls. In order to check the validity of the present analytical developments, it is the aim of this section to compare the solutions obtained by the Rayleigh-Ritz method to those given by NASTRAN.

| Material properties of the walls | | | Material properties of the fluid | | |
|----------------------------------|--------|------------------------|----------------------------------|----------|------------------------|
| Young modulus | E | 210 GPa | Bulk modulus | K_f | 2.25 GPa |
| Poisson coefficient | ν | 0.3 | Speed of sound | c_f | 1500 m/s |
| Mass density | ρ | 7850 kg/m ³ | Mass density | ρ_f | 1000 kg/m ³ |

Table 7.1. Material properties for the flexible walls and for the fluid

7.3.3.1. Comparison of the frequencies

As a first validation step, comparisons are first performed for the wet frequencies obtained for the reservoir. The results for the first seven modes are reported in Table 7.2 and Table 7.3, considering a water level of 3.5 m or 5 m respectively. For the different thickness values (5, 10 or 20 cm), the dry frequencies are first given, then the theoretical wet frequencies are compared to the ones obtained by NASTRAN. For each mode, the relative error is computed from the formula:

$$\frac{|f_T - f_N|}{f_N} (\%) \tag{7.58}$$

where f_T and f_N are respectively the theoretical and NASTRAN wet frequencies. The agreement between the numerical and theoretical results is found to be satisfactory, as the maximal discrepancy does not exceed 6 %. For the first mode, the agreement is even better, with a maximal error of 1 %.

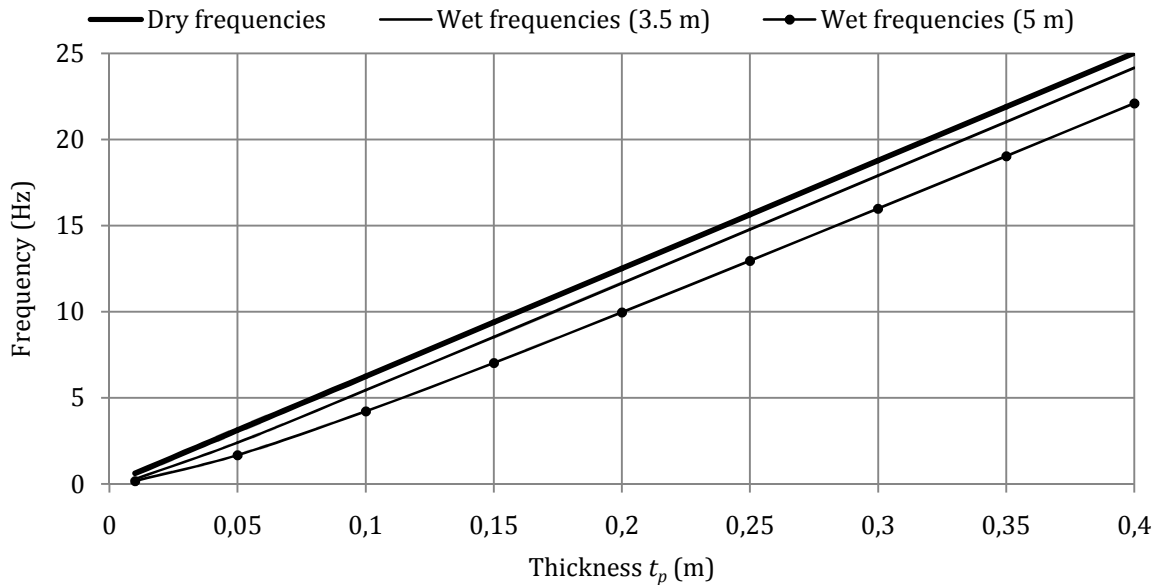


Figure 7.6. Evolution of the theoretical dry and wet frequencies (first mode) with the thickness for reservoir 1

Figure 7.6 shows the evolution of the fundamental dry and wet eigenfrequencies for different values of the thickness t_p . For the dry solutions, it may be analytically shown that the curve is linear, but this is not true for the wet solutions. For large values of t_p , the wet curves tends to increase linearly with the thickness, but this is not the case if t_p is becoming smaller.

| Water level: $h_s = 3.5\text{ m}$ | | | | | | | | | | | | | | |
|-----------------------------------|--------------------------------|----------|--------------|-----------|---------------------------------|----------|--------------|-----------|---------------------------------|----------|--------------|-----------|--|------|
| Mode number | Thickness: $t_p = 5\text{ cm}$ | | | | Thickness: $t_p = 10\text{ cm}$ | | | | Thickness: $t_p = 20\text{ cm}$ | | | | | |
| | Dry (Hz) | Wet (Hz) | NASTRAN (Hz) | Error (%) | Dry (Hz) | Wet (Hz) | NASTRAN (Hz) | Error (%) | Dry (Hz) | Wet (Hz) | NASTRAN (Hz) | Error (%) | | |
| 1 | 3.13 | 2.40 | 2.41 | 0.23 | 6.25 | 5.44 | 5.43 | 0.22 | 12.51 | 11.66 | 11.55 | 0.94 | | |
| 2 | 8.56 | 5.55 | 5.52 | 0.61 | 17.11 | 12.50 | 12.36 | 1.12 | 34.22 | 27.96 | 27.30 | 2.43 | | |
| 3 | 10.65 | 7.76 | 7.80 | 0.60 | 21.30 | 18.27 | 18.27 | 0.01 | 42.59 | 39.78 | 39.42 | 0.92 | | |
| 4 | 16.70 | 12.44 | 12.35 | 0.76 | 33.41 | 26.52 | 26.12 | 1.53 | 66.82 | 57.25 | 55.37 | 3.40 | | |
| 5 | 20.34 | 14.63 | 14.65 | 0.14 | 40.68 | 32.79 | 32.37 | 1.28 | 81.36 | 70.92 | 68.08 | 4.17 | | |
| 6 | 23.13 | 16.63 | 16.80 | 1.03 | 46.25 | 39.44 | 39.44 | 0.01 | 92.51 | 86.62 | 85.15 | 1.73 | | |
| 7 | 28.80 | 21.68 | 21.52 | 0.74 | 57.61 | 48.37 | 47.20 | 2.49 | 115.22 | 103.81 | 100.85 | 2.94 | | |
| | | | | 1.03 | | | | | 2.49 | | | | | 4.17 |

Table 7.2. Comparison between the dry frequencies and the wet frequencies calculated theoretically or by nastran for reservoir 1, with a water height of 3.5 m

| Water level: $h_s = 5\text{ m}$ | | | | | | | | | | | | | | |
|---------------------------------|--------------------------------|----------|--------------|-----------|---------------------------------|----------|--------------|-----------|---------------------------------|----------|--------------|-----------|--|------|
| Mode number | Thickness: $t_p = 5\text{ cm}$ | | | | Thickness: $t_p = 10\text{ cm}$ | | | | Thickness: $t_p = 20\text{ cm}$ | | | | | |
| | Dry (Hz) | Wet (Hz) | NASTRAN (Hz) | Error (%) | Dry (Hz) | Wet (Hz) | NASTRAN (Hz) | Error (%) | Dry (Hz) | Wet (Hz) | NASTRAN (Hz) | Error (%) | | |
| 1 | 3.13 | 1.69 | 1.68 | 0.18 | 6.25 | 4.23 | 4.21 | 0.41 | 12.51 | 9.96 | 9.86 | 1.05 | | |
| 2 | 8.56 | 5.13 | 5.13 | 0.06 | 17.11 | 11.78 | 11.65 | 1.09 | 34.22 | 26.41 | 25.65 | 2.95 | | |
| 3 | 10.65 | 6.18 | 6.22 | 0.70 | 21.30 | 15.33 | 15.36 | 0.19 | 42.59 | 35.59 | 35.28 | 0.90 | | |
| 4 | 16.70 | 11.24 | 11.27 | 0.24 | 33.41 | 25.57 | 25.30 | 1.06 | 66.82 | 56.05 | 54.23 | 3.37 | | |
| 5 | 20.34 | 12.71 | 12.65 | 0.49 | 40.68 | 29.60 | 29.12 | 1.65 | 81.36 | 66.74 | 63.60 | 4.93 | | |
| 6 | 23.13 | 14.39 | 14.58 | 1.31 | 46.25 | 35.02 | 35.12 | 0.31 | 92.51 | 79.83 | 79.71 | 0.15 | | |
| 7 | 28.80 | 19.39 | 19.16 | 1.19 | 57.61 | 44.19 | 43.00 | 2.76 | 115.22 | 98.04 | 92.56 | 5.92 | | |
| | | | | 1.31 | | | | | 2.76 | | | | | 5.92 |

Table 7.3. Comparison between the dry frequencies and the wet frequencies calculated theoretically or by nastran for reservoir 1, with a water height of 5 m

7.3.3.2. Comparison of the mode shapes

As a second validation step, comparisons are now performed for the wet mode shapes. It is commonly accepted that the approximated solutions derived by the Rayleigh-Ritz method are better for the eigenfrequencies than for the eigenmodes. As a consequence, the present agreement between the theoretical and numerical solutions is not expected to be as good as for the frequencies.

The two first mode shapes are plotted on Figure 7.9 and Figure 7.10 for a water level h_s of 3.5 or 5 m respectively. These figures correspond to a thickness of 10 cm. For each mode, two different illustrations are proposed. The first one is a plot of the profile in the vertical plane $z = l/2$ (plane π_1 on Figure 7.8), while the second one corresponds to the profile in the horizontal plane $y = h$ (plane π_2 on Figure 7.8). For the horizontal profile, it is clear that a sine half-wave seems to be a good approximation. Concerning the vertical one, the agreement appears to be satisfactory, even if some discrepancy may be observed near the top of the gate where water is not present.

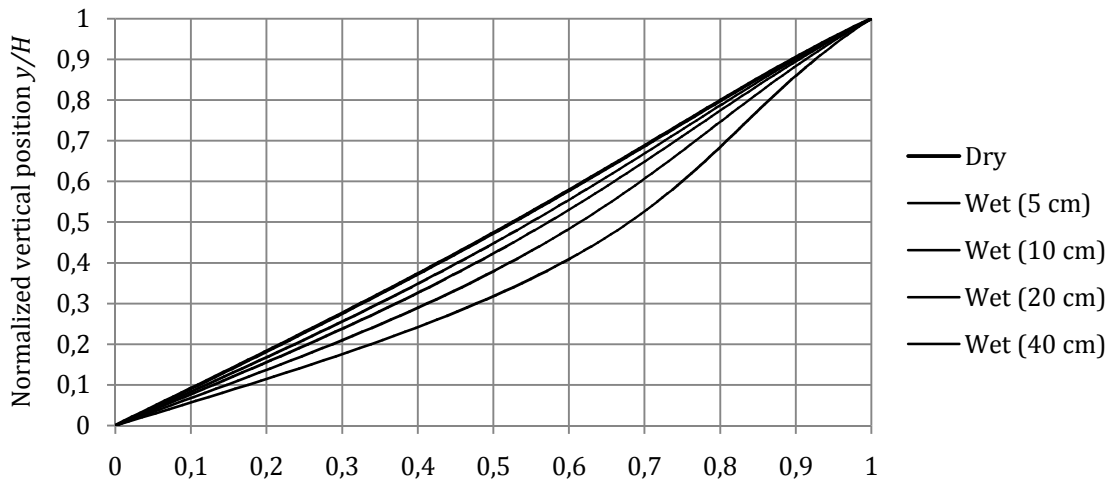


Figure 7.7. Evolution of the vertical profile in $z = l/2$ (first mode shape) with the thickness of reservoir 1 for $h_s = 3.5$ m; the wet curves are coming closer to the dry one as the thickness is increasing

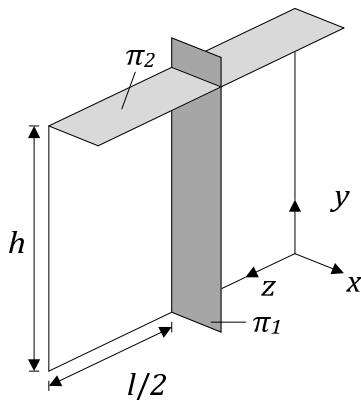


Figure 7.8. Horizontal and vertical profile locations

| $h_s = 3.5$ m | | |
|---------------|-------------|--------------|
| Thickness | Maximal gap | Location |
| 5 cm | 0.164 | $y/h = 0.4$ |
| 10 cm | 0.094 | $y/h = 0.4$ |
| 20 cm | 0.049 | $y/h = 0.4$ |
| 30 cm | 0.034 | $y/h = 0.4$ |
| $h_s = 5$ m | | |
| Thickness | Maximal gap | Location |
| 5 cm | 0.169 | $y/h = 0.44$ |
| 10 cm | 0.127 | $y/h = 0.44$ |
| 20 cm | 0.084 | $y/h = 0.44$ |
| 30 cm | 0.063 | $y/h = 0.44$ |

Table 7.4. Maximal amplification and corresponding location for the first mode shape of reservoir 1

Figure 7.7 shows the evolution of the vertical profile of the first mode shape for different values of the thickness. For increasing values of t_p , the wet curves are coming closer to the dry one, which shows that the fluid-structure interaction is progressively reduced.

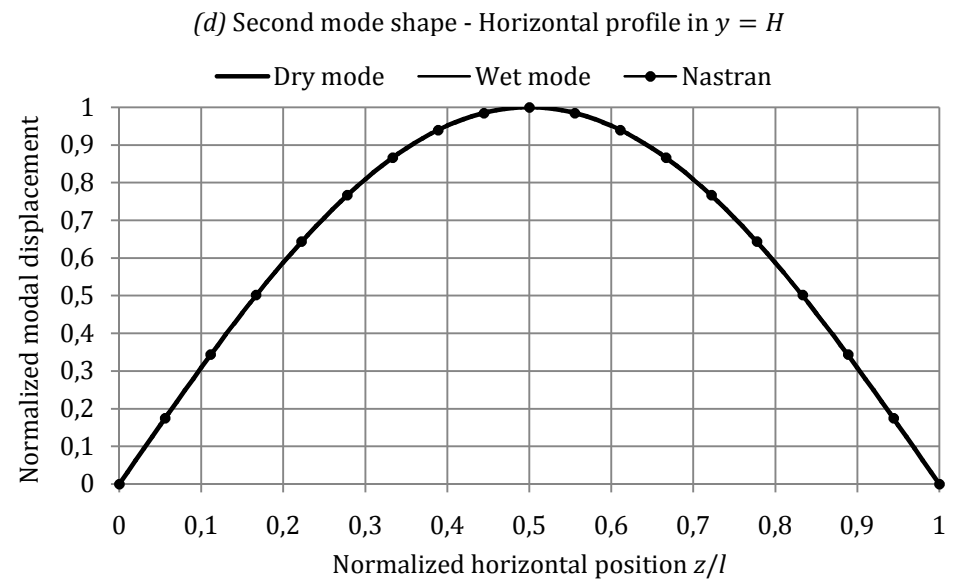
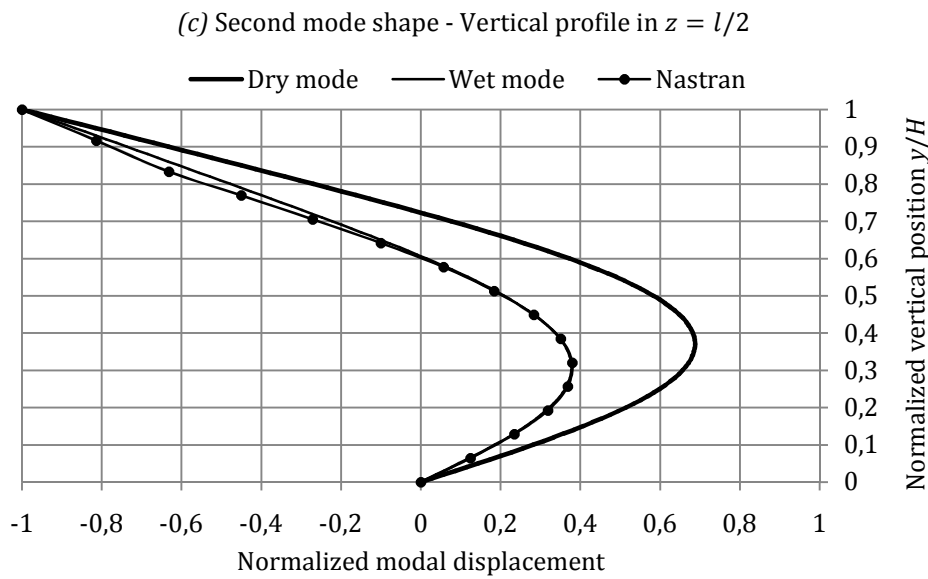
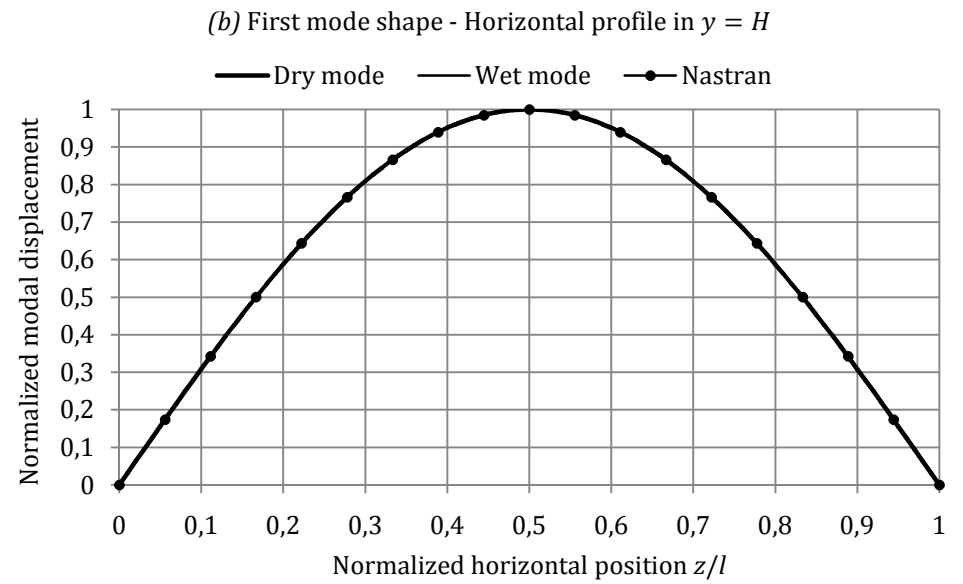
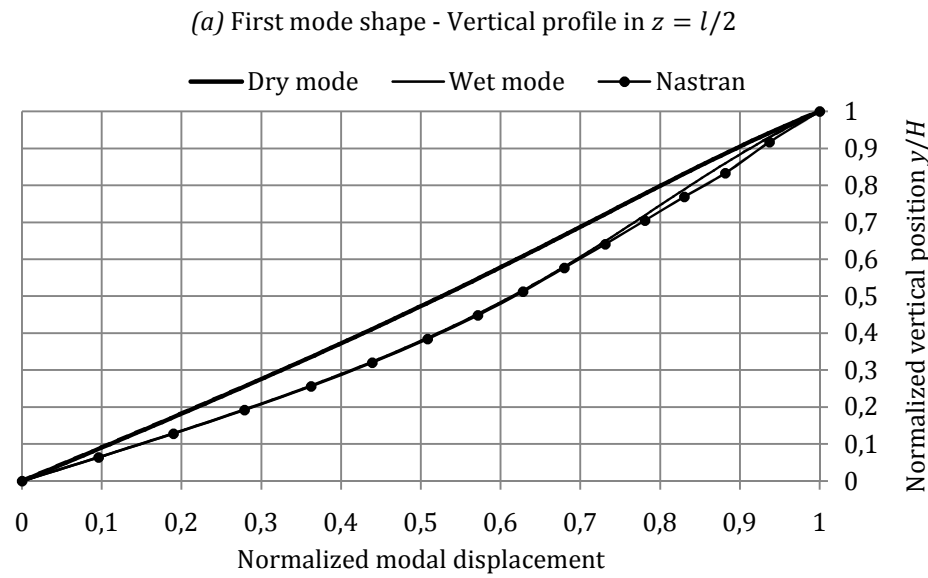


Figure 7.9. Comparison between the dry and wet mode shapes (calculated theoretically or by NASTRAN) for reservoir 1, with a water height of 3.5 m

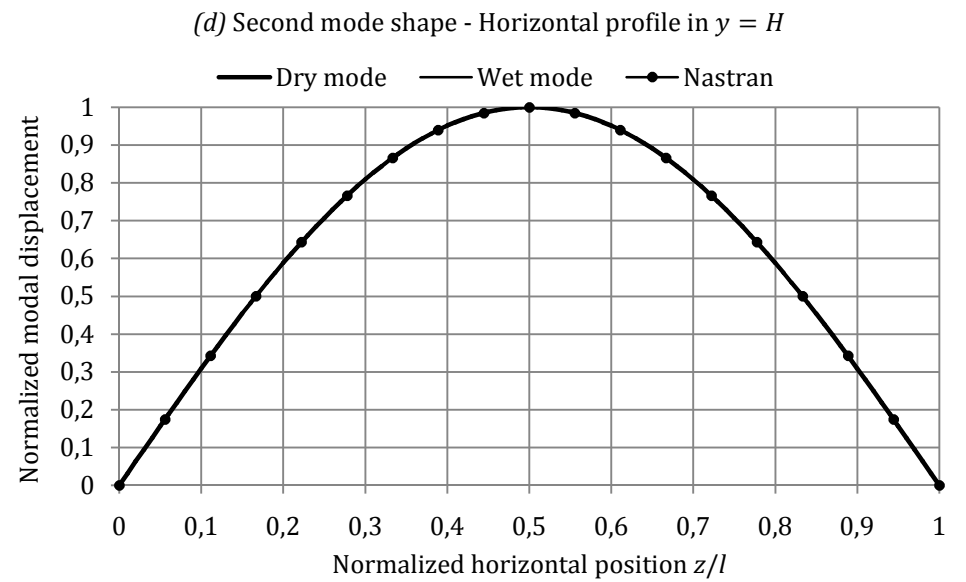
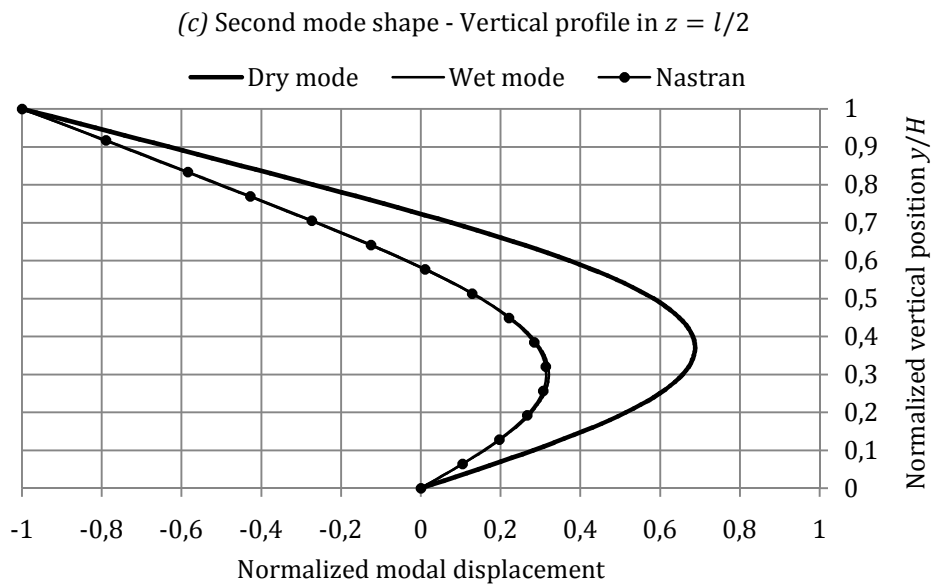
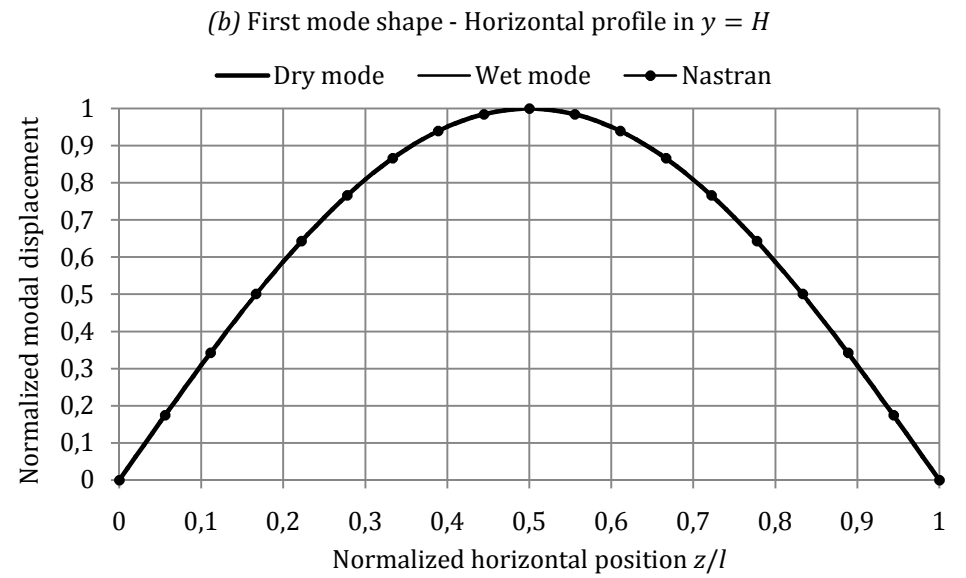
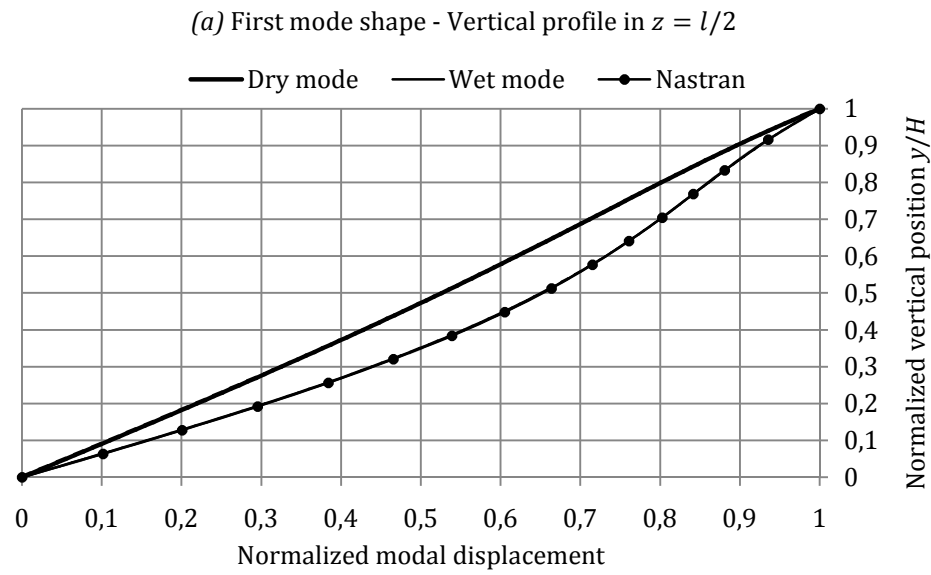


Figure 7.10. Comparison between the dry and wet mode shapes (calculated theoretically or by NASTRAN) for reservoir 1, with a water height of 5 m

Table 7.4 also provides additional information on the first wet mode shape. This table shows the maximal absolute gap between the dry and wet vertical profiles, denoted by $\delta(y, l/2)$ and $\Delta(y, l/2)$ respectively. This gap is defined as follows:

$$\max\{\delta(y, l/2) - \Delta(y, l/2)\} \quad ; \quad 0 \leq y \leq h \quad (7.59)$$

It is evident from Table 7.4 that the deviation is also progressively reduced as the thickness increases. On the contrary, it can be seen that the vertical location y where this maximal gap may be measured does not change with t_p . For $h_s = 3.5 \text{ m}$, it is equal to $0.4h$, while it is equal to $0.44h$ for $h_s = 5 \text{ m}$. As expected, this shows that the point of the vertical profile where the fluid-structure interaction is maximum is progressively elevating as the water level is also getting higher.

7.3.3.3. Additional investigations

The comparisons performed here above for this reservoir show that the agreement between the analytical and numerical results is satisfactory. This tends to validate the theoretical derivation of the vibration properties for an immersed plate by using the Rayleigh-Ritz method. The present analytical approach is also corroborated by other comparisons made with different reservoirs. From this validation process, some additional results can be emphasized. They are briefly summarized hereafter but a more detailed parametric study is available in section D.1.2 of Appendix D.1. Regarding the plate thickness, the two following particular points may be highlighted:

- If the structure is not in contact with water, the corresponding natural dry frequencies of vibration are directly proportional to the thickness t_p of the plate. However, this statement is not exact while considering an immersed structure. This is particularly true for small values of the thickness, for which a strong non-linearity may appear. On the contrary, the relation becomes nearly linear if t_p is growing.
- The relative difference between the dry and wet eigenfrequencies tends to reduce if the thickness of the plate increases. This simply means that the fluid-structure interaction is more important for thin plate, as it could be expected.

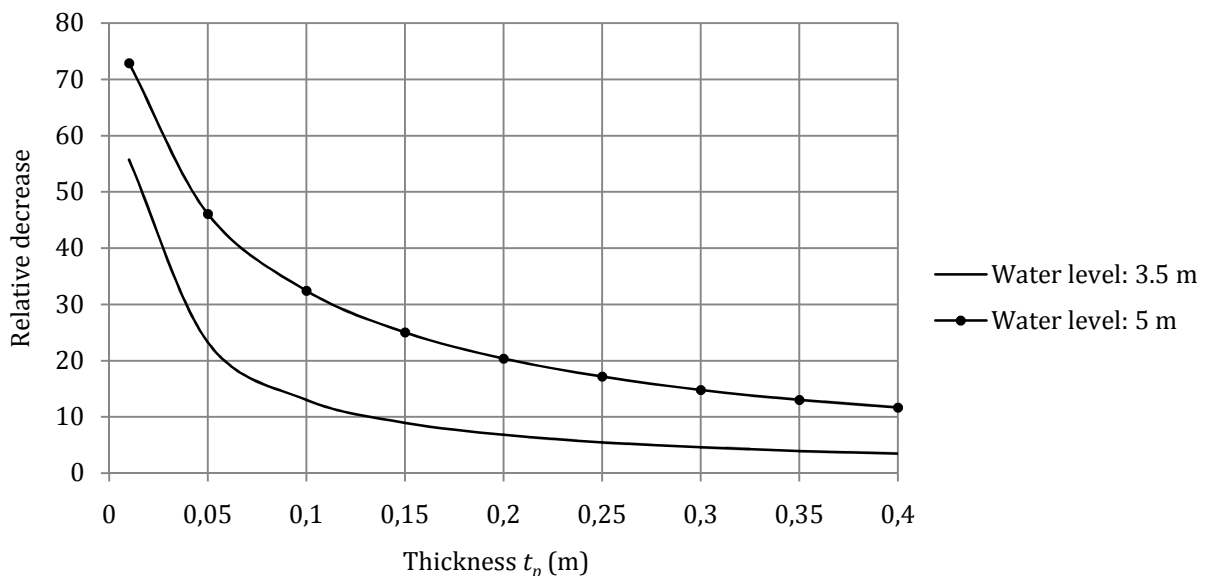


Figure 7.11. Evolution of the relative difference between the dry and wet frequencies with the thickness

This last assertion may be illustrated by considering the relative difference between the dry and wet fundamental frequencies for the two water levels considered here above. This one is simply defined by the classical relation:

$$\frac{f_D - f_I}{f_D} (\%) \quad (7.60)$$

where f_D and f_I denote the fundamental frequencies of vibration for the dry and immersed configurations respectively. The results are plotted on Figure 7.11, from which it is evident that the reduction becomes more and more important as the thickness is getting smaller. On the contrary, this picture also shows that the effect of the surrounding water tends to disappear if the plate is thicker. This is particularly true for the lowest value of the water level ($h_s = 3.5 \text{ m}$).

Apart from the influence of the plate thickness, it is also interesting to know how the other geometrical parameters act on the fluid-structure interaction. For a given plate thickness, the main conclusions of the detailed investigation presented in section D.1.2 of Appendix D.1 can be summarized as follows:

- As expected, the fluid-structure interaction is always more important if the water level h_s is close to the reservoir height h . On the contrary, neglecting the surrounding water in a modal analysis is therefore only valid if h_s is very small.
- If the ratio l/L does not exceed 0.1 (which is usually the case for classical lock chambers), then it can be stated that the fluid-structure interaction is more important if the h/l ratio is large (i.e. for high reservoirs).
- If the ratio l/L does not exceed 0.1, this latter is found to have very little influence on the modal properties of an immersed plate.
- Finally, if the length L of the reservoir is at least equal to $3h_s$, it is observed that the eigenvalues and the mode shapes do not depend on this parameter anymore.

All the previous conclusions are quite interesting to get a quantitative overview of the results expected during a modal analysis. Furthermore, they may also have some practical consequences, particularly for numerical simulations, but this last point will be discussed in more details in section 7.4.

7.4. Dynamic analysis of flexible reservoirs

The modal analysis of flexible walls immersed in water performed in the previous chapter provides a global insight on the way such structures respond to a seismic excitation. The next step is now to consider the situation described in section 7.1, where a reservoir is submitted to an earthquake having a longitudinal acceleration component denoted by $\ddot{X}(t)$. The two remaining vertical and transversal components $\ddot{Y}(t)$ and $\ddot{Z}(t)$ acting along the axes y and z of Figure 7.1 respectively will not be considered so far. Of course, all the hypotheses listed in 7.2 regarding the plate properties are still holding here.

7.4.1. Equilibrium equation

The direct form of the equilibrium equation given in (7.14) and the boundary conditions (7.15), (7.16) and (7.17) may also be used to study the forced vibrations of an immersed plate, but two modifications are now required. The first one concerns the inertial forces: in addition to the proper displacements of the structure $u(y, z, t)$, one should also account for the motion $X(t)$ of the support, which results in supplementary inertial forces $\rho t_p \ddot{X}(t)$. The second one is introduced to avoid reasoning phenomena, by considering that damping forces $f_d(y, z, t)$ are also present in the model. With these two corrections, (7.14) becomes:

$$\rho t_p (\ddot{u}(y, z, t) + \ddot{X}(t)) + f_d(y, z, t) + D \left(\frac{\partial^4 u}{\partial y^4} + 2 \frac{\partial^4 u}{\partial y^2 \partial z^2} + \frac{\partial^4 u}{\partial z^4} \right) = -p(y, z, t) \quad (7.61)$$

In order to characterize a bit further the term $f_d(y, z, t)$, these additional forces will be assumed to be directly related to the velocity $\dot{u}(y, z, t)$. They may be seen as having two different contributions: a first one coming from the mass of the structure and a second one coming from its stiffness. The mass-proportional damping force is simply written as:

$$\alpha \rho t_p \dot{u}(y, z, t) \quad (7.62)$$

where ρt_p is the surface mass of the plate and α is a constant. On the other hand, stiffness proportional damping is known to produce additional internal stresses that are related to the velocity $\dot{u}(y, z, t)$ by the classical formulae:

$$\begin{aligned} \sigma_{yy}^d &= \frac{\beta E}{1 - \nu^2} (\dot{\epsilon}_{yy} + \nu \dot{\epsilon}_{zz}) = -\frac{\beta E x}{1 - \nu^2} \left(\frac{\partial^2 \dot{u}}{\partial y^2} + \nu \frac{\partial^2 \dot{u}}{\partial z^2} \right) \\ \sigma_{zz}^d &= \frac{\beta E}{1 - \nu^2} (\dot{\epsilon}_{zz} + \nu \dot{\epsilon}_{yy}) = -\frac{\beta E x}{1 - \nu^2} \left(\frac{\partial^2 \dot{u}}{\partial z^2} + \nu \frac{\partial^2 \dot{u}}{\partial y^2} \right) \\ \sigma_{yz}^d &= \frac{\beta E}{1 + \nu} \dot{\epsilon}_{yz} = -\frac{\beta E x}{1 - \nu^2} \frac{\partial^2 \dot{u}}{\partial y \partial z} \end{aligned} \quad (7.63)$$

where $\dot{\epsilon}_{yy}$, $\dot{\epsilon}_{zz}$ and $\dot{\epsilon}_{yz}$ are the strain rates, E is the Young modulus and β is a constant. By applying a development similar to the one leading to the classical Kirchhoff equilibrium equation (7.14), the stresses given in (7.63) can be easily transformed into the following stiffness-proportional internal damping force:

$$\beta D \left(\frac{\partial^4 \dot{u}}{\partial y^4} + 2 \frac{\partial^4 \dot{u}}{\partial y^2 \partial z^2} + \frac{\partial^4 \dot{u}}{\partial z^4} \right) \quad (7.64)$$

where D is still the plate flexional rigidity. Finally, gathering (7.62) and (7.64) in (7.61) leads to the dynamic equation characterizing the forced vibrations of an immersed plate:

$$\rho t_p (\ddot{u} + \ddot{X}) + \alpha \rho t_p \dot{u} + \beta D \left(\frac{\partial^4 \dot{u}}{\partial y^4} + \frac{2\partial^4 \dot{u}}{\partial y^2 \partial z^2} + \frac{\partial^4 \dot{u}}{\partial z^4} \right) + D \left(\frac{\partial^4 u}{\partial y^4} + \frac{2\partial^4 u}{\partial y^2 \partial z^2} + \frac{\partial^4 u}{\partial z^4} \right) = -p \quad (7.65)$$

where it is worth remembering that the total hydrodynamic pressure $p(y, z, t)$ is the sum of the rigid and flexible impulsive contributions respectively given by (7.7) and (7.8). So far, the two parameters α and β are still undetermined, but they will be fixed later on. They are known as the Rayleigh damping coefficients.

7.4.2. Virtual work principle

An analytical way to study the forced vibrations of an immersed plate is to apply the virtual work principle, which simply states that a necessary and sufficient condition for equilibrium is to equate the external and internal virtual works for any kinematically compatible displacement field. Consequently, to express the equilibrium of the plate, it is first required to consider a compatible virtual field $\delta u(y, z, t)$, $\delta v(y, z, t)$ and $\delta w(y, z, t)$ acting on the plate. Under the hypothesis of preponderant out-of-plane displacements, one can write:

$$\delta v(y, z, t) = -x \frac{\partial \delta u}{\partial y} \quad ; \quad \delta w(y, z, t) = -x \frac{\partial \delta u}{\partial z} \quad (7.66)$$

which is consistent with (7.10). Furthermore, because of the developments performed in section 7.2, it seems reasonable to express that the motions $u(y, z, t)$ exhibited by the immersed structure during the seismic excitation are based on the wet mode shapes. In other words, it is postulated that:

$$u(y, z, t) = \sum_{j=1}^N q_j(t) \Delta_j(y, z) \quad ; \quad \delta u(y, z, t) = \sum_{k=1}^N \delta q_k(t) \Delta_k(y, z) \quad (7.67)$$

where N is the number of wet modes $\Delta_j(y, z)$ that are used for developing $u(y, z, t)$. At this stage, the modal amplitudes $q_j(t)$ and $\delta q_k(t)$ are still unknown but will be determined by applying the virtual work principle. To do so, let us start by developing the mathematical expressions of the virtual work performed by each of the different forces involved in the present problem. Rearranging (7.65) leads to:

$$D \left(\frac{\partial^4 u}{\partial y^4} + \frac{2\partial^4 u}{\partial y^2 \partial z^2} + \frac{\partial^4 u}{\partial z^4} \right) = - \left(\rho t_p (\ddot{u} + \ddot{X}) + \alpha \rho t_p \dot{u} + \beta \left(\frac{\partial^4 \dot{u}}{\partial y^4} + \frac{2\partial^4 \dot{u}}{\partial y^2 \partial z^2} + \frac{\partial^4 \dot{u}}{\partial z^4} \right) + p \right) \quad (7.68)$$

which may be identified as the equilibrium equation of a plate submitted to an external resulting horizontal action $f_{ext}(y, z, t)$ given by the right hand side:

$$f_{ext}(y, z, t) = \rho t_p (\ddot{u} + \ddot{X}) + \alpha \rho t_p \dot{u} + \beta \left(\frac{\partial^4 \dot{u}}{\partial y^4} + \frac{2\partial^4 \dot{u}}{\partial y^2 \partial z^2} + \frac{\partial^4 \dot{u}}{\partial z^4} \right) + p \quad (7.69)$$

This expression is the sum of the pressure, damping and inertial forces. It is important to bear in mind that, by essence, these forces are always opposed to the displacements $u(y, z, t)$, as recalled on Figure 7.12. Therefore, it is not surprising that the work performed by these actions will always be affected by a minus sign.

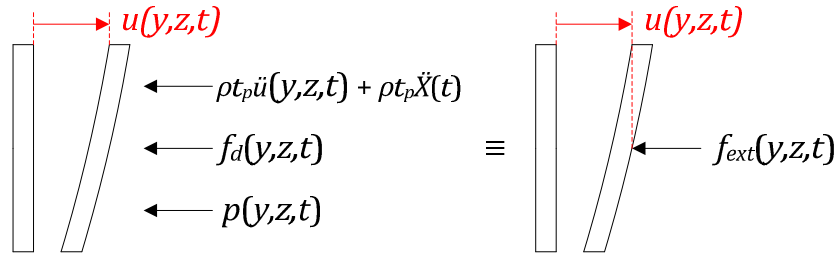


Figure 7.12. Orientation of the resulting external force acting on the plate

The left hand side of equation (7.68) corresponds to the internal forces $f_{int}(y, z, t)$. They always produce a positive work, that is sometimes referred to as an internal energy.

7.4.2.1. Internal virtual work

In a more conventional approach of the virtual work principle, the contribution of the internal forces are seen as a virtual energy. For a given virtual displacement field, it is possible to derive the associated virtual strain tensor $\delta\epsilon_{ij}$ and the subsequent internal energy:

$$\delta W_{int} = \int_0^h \int_0^l (\sigma_{yy}\delta\epsilon_{yy} + \sigma_{zz}\delta\epsilon_{zz} + 2\sigma_{yz}\delta\epsilon_{yz}) dydz \quad (7.70)$$

where σ_{ij} is the stress tensor. If we account for (7.11) and (7.12), it is shown by Shames and Dym [137] that developing (7.70) leads to the widely used expression for δW_{int} :

$$D \int_A \left(\frac{\partial^2 u}{\partial y^2} \frac{\partial^2 \delta u}{\partial y^2} + \frac{\partial^2 u}{\partial z^2} \frac{\partial^2 \delta u}{\partial z^2} + \nu \frac{\partial^2 u}{\partial y^2} \frac{\partial^2 \delta u}{\partial z^2} + \nu \frac{\partial^2 \delta u}{\partial y^2} \frac{\partial^2 u}{\partial z^2} + 2(1-\nu) \frac{\partial^2 u}{\partial y \partial z} \frac{\partial^2 \delta u}{\partial y \partial z} \right) dA \quad (7.71)$$

Nevertheless, another way will be adopted here to evaluate the contribution of the internal forces. Indeed, it can be stated that the virtual work performed by $f_{int}(y, z, t)$ during any virtual displacement $\delta u(y, z, t)$ is simply:

$$\delta W_{int} = \int_0^h \int_0^l f_{int}(y, z, t) \delta u(y, z, t) dydz \quad (7.72)$$

The left hand side of (7.68) shows that this last equation can be developed in the following more explicit (but quite unusual) form:

$$\delta W_{int} = D \int_0^h \int_0^l \left(\frac{\partial^4 u}{\partial y^4} + \frac{2\partial^4 u}{\partial y^2 \partial z^2} + \frac{\partial^4 u}{\partial z^4} \right) \delta u(y, z, t) dydz \quad (7.73)$$

In fact, it may be demonstrated that (7.71) and (7.72) are strictly identical, provided that the functions $u(y, z, t)$ and $\delta u(y, z, t)$ both satisfies the plate boundary conditions expressed in (7.15) to (7.17), which should be the case as these displacement fields are kinematically admissible. As a last step, introducing the modal decomposition (7.67) in (7.73) leads to:

$$\delta W_{int} = \sum_{k=1}^N \delta q_k \left(\sum_{j=1}^N q_j \int_0^h \int_0^l D \left(\frac{\partial^4 \Delta_j}{\partial y^4} + \frac{2\partial^4 \Delta_j}{\partial y^2 \partial z^2} + \frac{\partial^4 \Delta_j}{\partial z^4} \right) \Delta_k dydz \right) = \sum_{k=1}^N \delta q_k \sum_{j=1}^N q_j U_{jk} \quad (7.74)$$

where U_{jk} is directly constructed by using the wet mode shapes. As it will be detailed later, U_{jk} may also be expressed as a function of the dry modes of vibration.

7.4.2.2. External virtual work

Developing the second part of the virtual work theorem, the work associated to the external forces during an horizontal virtual displacement $\delta u(y, z, t)$ has now to be evaluated. This one is simply written as:

$$\delta W_{ext} = - \int_0^h \int_0^l f_{ext}(y, z, t) \delta u(y, z, t) dy dz \quad (7.75)$$

and subsequently, the contributions coming from all the terms involved in the expression of $f_{ext}(y, z, t)$ given in (7.69) have to be examined. This task is quite fastidious, so we will only provide here a short summary of the final results, obtained after incorporating the modal form (7.67) in (7.75). It can be proved that:

- For the inertial forces corresponding to the first term of (7.69), the associated virtual work is as follows:

$$- \sum_{k=1}^N \delta q_k \left(\sum_{j=1}^N \ddot{q}_j \int_0^h \int_0^l \rho t_p \Delta_j \Delta_k dy dz + \ddot{X} \int_0^h \int_0^l \rho t_p \Delta_k dy dz \right) \quad (7.76)$$

- For the damping forces given by the second and third terms in equation (7.69), the virtual work is written as:

$$- \sum_{k=1}^N \delta q_k \left(\sum_{j=1}^N \dot{q}_j \int_0^h \int_0^l \left(\alpha \rho t_p \Delta_j + \beta D \left(\frac{\partial^4 \Delta_j}{\partial y^4} + \frac{2 \partial^4 \Delta_j}{\partial y^2 \partial z^2} + \frac{\partial^4 \Delta_j}{\partial z^4} \right) \right) \Delta_k dy dz \right) \quad (7.77)$$

Concerning the total hydrodynamic pressure force, which is the last term in (7.69), both the rigid and flexible contributions denoted by $p_r(y, t)$ and $p_f(y, z, t)$ respectively have to be considered. Their mathematical expressions are given in section 7.2 by equations (7.7) and (7.8). During any kinematically admissible displacement $\delta u(y, z, t)$, these forces are always opposed to the motion of the plate and will therefore produce a negative virtual work. Moreover, it is worth noting that the pressure is not acting on the whole surface of the plate, so the integration has only to be conducted on the wet area of the structure. Accounting for these remarks, the virtual work associated to $p_r(y, t)$ and $p_f(y, z, t)$ is given by:

$$- \int_0^{h_s} \int_0^l (p_r(y, t) + p_f(y, z, t)) \delta u(y, z, t) dy dz \quad (7.78)$$

Introducing the modal decomposition in the mathematical expressions of $p_r(y, t)$ and $p_f(y, z, t)$ given in (7.7) and (7.8), one can develop (7.78) in the following form:

$$\sum_{k=1}^N \delta q_k \left(\ddot{X} \int_0^{h_s} \int_0^l \left(\sum_{n=1}^{+\infty} \frac{4 \rho_f \cosh(\beta_n y)}{\beta_n^2 L \cosh(\beta_n h_s)} - \frac{L}{2} \right) \Delta_k dy dz + \sum_{j=1}^N \ddot{q}_j \sum_{n=1}^{+\infty} \sum_{m=0}^{+\infty} c_{mn} I_{mn}^{(j)} I_{mn}^{(k)} \right) \quad (7.79)$$

where the coefficient β_n , c_{mn} , α_n and $\bar{\gamma}_m$ have the definitions listed in section 7.2. The functions $I_{mn}^{(j)}$ and $I_{mn}^{(k)}$ were already encountered in (7.28). Finally, gathering (7.76), (7.77) and (7.79), the external virtual work associated to $f_{ext}(y, z, t)$ can be expressed in a more compact form:

$$\delta W_{ext} = - \sum_{k=1}^N \delta q_k \left(\sum_{j=1}^N \ddot{q}_j (T_{jk} - W_{jk}) + \sum_{j=1}^N \dot{q}_j (\alpha T_{jk} + \beta U_{jk}) - V_k \ddot{X} \right) \quad (7.80)$$

where U_{jk} has the same definition than in section 7.4.2.1. T_{jk} , W_{jk} and V_k are directly extracted from (7.76), (7.77) and (7.79):

$$T_{jk} = \rho t_p \int_0^h \int_0^l \Delta_j(y, z) \Delta_k(y, z) dy dz \quad W_{jk} = \sum_{n=1}^{+\infty} \sum_{m=0}^{+\infty} c_{mn} I_{mn}^{(j)} I_{mn}^{(k)} \quad (7.81)$$

$$V_k = \int_0^{h_s} \int_0^l \left(\sum_{n=1}^{+\infty} \frac{4\rho_f \cosh(\beta_n y)}{\beta_n^2 L \cosh(\beta_n h_s)} - \frac{L}{2} \right) \Delta_k dy dz - \rho t_p \int_0^h \int_0^l \Delta_k(y, z) dy dz \quad (7.82)$$

7.4.2.3. Global equilibrium equation

After having briefly developed the analytical expressions of the internal and external virtual works δW_{int} and δW_{ext} , in accordance with the theorem, (7.74) and (7.80) can be equated to get the global equilibrium equation:

$$\sum_{k=1}^N \delta q_k \left(\sum_{j=1}^N \ddot{q}_j (T_{jk} - W_{jk}) + \sum_{j=1}^N \dot{q}_j (\alpha T_{jk} + \beta U_{jk}) + \sum_{j=1}^N q_j U_{jk} - V_k \ddot{X} \right) = 0 \quad (7.83)$$

As the displacement field $\delta u(y, z, t)$ is arbitrary, this equation has to be satisfied for any particular values of the N coefficients δq_k . Consequently, the only way to satisfy (7.83) is to verify the following equation for $k = 1, \dots, N$:

$$\sum_{j=1}^N \ddot{q}_j (T_{jk} - W_{jk}) + \sum_{j=1}^N \dot{q}_j (\alpha T_{jk} + \beta U_{jk}) + \sum_{j=1}^N q_j U_{jk} = V_k \ddot{X} \quad (7.84)$$

Denoting by $[T]$, $[W]$, $[U]$ and \mathbf{V} the matrices and vector associated to T_{jk} , W_{jk} , U_{jk} and V_k respectively, (7.84) can be rewritten as:

$$([T] - [W])\ddot{\mathbf{q}}(t) + (\alpha[T] + \beta[U])\dot{\mathbf{q}}(t) + [U]\mathbf{q}(t) = \mathbf{V}\ddot{X}(t) \quad (7.85)$$

where $\alpha[T] + \beta[U]$ can be recognized as the classical Rayleigh damping matrix. Let us now give some particular comments on the matrices involved in (7.85). By carefully examining equations (7.76) to (7.79), it is possible to identify the differential operators \mathcal{L}_1 and \mathcal{L}_2 already mentioned in (7.31) and (7.32). In fact:

$$T_{jk} - W_{jk} = \langle \Delta_j | \mathcal{L}_1(\Delta_k) \rangle \quad ; \quad U_{jk} = \langle \Delta_j | \mathcal{L}_2(\Delta_k) \rangle \quad (7.86)$$

Even if this is quite fastidious, it can be shown that the wet modes are orthogonal to the operators \mathcal{L}_1 and \mathcal{L}_2 . In other words, the internal products between these modes and the

corresponding differential operator \mathcal{L}_1 or \mathcal{L}_2 have to satisfy the following traditional perpendicularity property:

$$\langle \Delta_j | \mathcal{L}_1(\Delta_k) \rangle = \langle \Delta_j | \mathcal{L}_2(\Delta_k) \rangle = 0 \quad \text{if } j \neq k \quad (7.87)$$

which means that the wet mode shapes are orthogonal to the matrices $[T] - [W]$ and $[U]$, as it could be expected. Consequently, these matrices are diagonal. Nevertheless, this is not the case for the damping matrix, because the mass proportional damping term $\alpha[T]$ is not reputed to have the same property. This due to the fact that the wet mode shapes are not perpendicular to each others¹³, and are not orthogonal to the matrix $[T]$ as they verify this property with $[T] - [W]$. Therefore, the N equations given in (7.85) may not be decoupled and have to be solved as a whole, by applying the Newmark method for example. After having determined the modal amplitudes \mathbf{q} , it is possible to rebuild the displacement by (7.67) and also the hydrodynamic pressure with (7.7) and (7.8).

As a final remark, it is worth mentioning that the matrices $[T]$, $[W]$ and $[U]$ can be directly calculated with help of $[\hat{T}]$, $[\hat{W}]$ and $[\hat{U}]$ introduced during the modal analysis:

$$T_{jk} = \mathbf{v}_j^T [\hat{T}] \mathbf{v}_k \quad W_{jk} = \mathbf{v}_j^T [\hat{W}] \mathbf{v}_k \quad U_{jk} = \mathbf{v}_j^T [\hat{U}] \mathbf{v}_k \quad (7.88)$$

These last formulae may be directly justified by using equation (7.35) relating the dry and wet modes.

7.4.3. Numerical validation

To corroborate the procedure exposed previously, the analytical solutions obtained by applying the virtual work principle can be compared to those provided by finite element simulations. It is proposed here to focus again on the same reservoir than the one considered in section 7.3.3 (Figure 7.5). The material and fluid properties are still those listed in Table 7.1. This reservoir is submitted to a seism having the longitudinal acceleration component $\ddot{X}(t)$ depicted on Figure 7.13 (synthetic accelerogram).

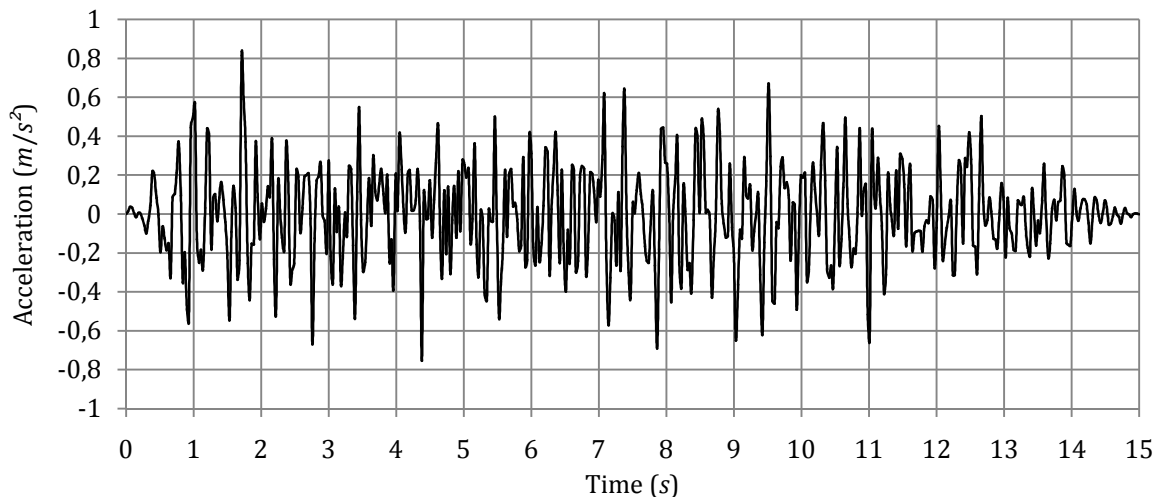


Figure 7.13. Longitudinal component of the seismic acceleration

¹³ It is recalled that, as mentioned by Delhez [40], the eigenmodes found by solving a generalized eigenvalues problem are linearly independent, but not necessarily orthogonal to each others. They are only orthogonal to the matrices defining the eigenvalues problem.

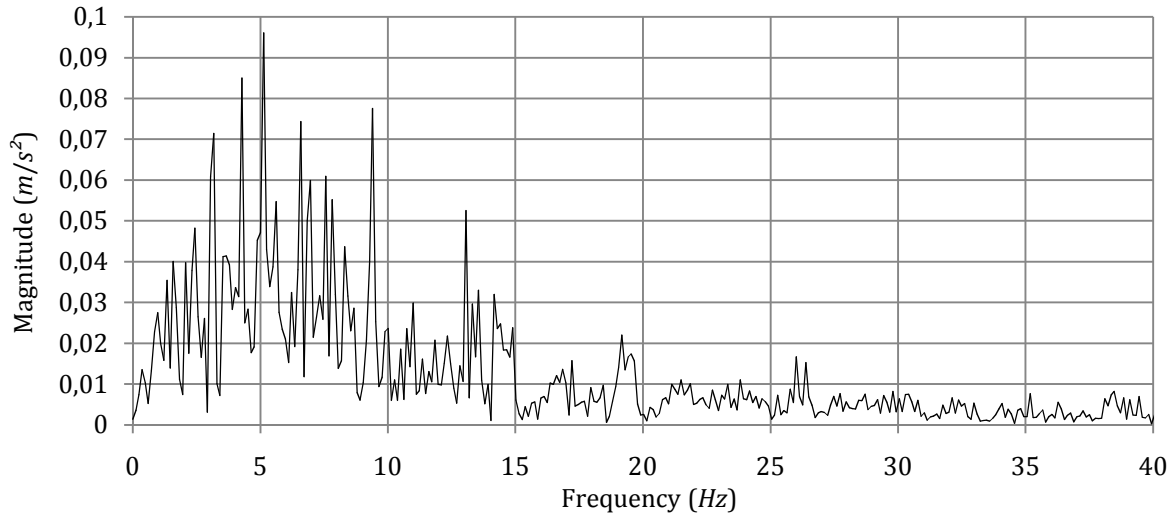


Figure 7.14. Fourier transform of the longitudinal seismic acceleration

The Fourier transform of this signal is represented on Figure 7.14. It shows that the main part of the seismic excitation is located in the frequency range going approximately from 1 Hz to 15 Hz.

7.4.3.1. Numerical model

The numerical analysis is performed with the finite element software LS-DYNA. Before presenting the results, some indications are first given on the model itself. To account for the fluid-structure interaction, it is required to represent these two entities separately, as detailed hereafter:

- The flexible walls are modeled with Belytschko-Tsay shell elements [66] of uniform thickness t_p . They have a linear elastic behavior, characterized by a mass density ρ , a Young modulus E and a Poisson ratio ν . The stress and strain tensors are related according to the classical Hooke's law.

The mesh of the solid domain is quite coarse, with a more or less regular size of 20×20 cm for the shell elements. This choice is due to the necessity of limiting the size of the model. Nevertheless, simulations on more refined models with a meshing of 5×5 cm or 10×10 cm were also performed, and the results do not show important discrepancies with the present ones.

- The fluid is modeled with constant stress solid elements [66] affected by a particular material law (MAT_ELASTIC_FLUID). The liquid is seen as an elastic medium with a mass density ρ_f and a bulk modulus K_f , for which the stress and strain rates are related by:

$$\begin{aligned} \dot{p} = \dot{\sigma}_{xx} = \dot{\sigma}_{yy} = \dot{\sigma}_{zz} &= K_f (\dot{\epsilon}_{xx} + \dot{\epsilon}_{yy} + \dot{\epsilon}_{zz}) \\ \dot{\sigma}_{xy} = \dot{\sigma}_{xz} = \dot{\sigma}_{yz} &= 0 \end{aligned} \quad (7.89)$$

where p is the pressure inside the solid elements. As shown by (7.89), there is no shearing with this material. This is coherent with the behavior of water.

The mesh of the fluid domain is also regular, with an approximate size of $19 \times 19 \times 19$ cm for the solid elements (as it will be discussed later, it is necessary to avoid having

similar mesh sizes on both the solid and fluid domains). Here again, using more refined meshes do not provide any additional interest.

The two previous separated entities representing the water and the structure do not share any node in common, which means that the fluid nodes are distinct from the solid ones at the boundary between the two domains. The LS-DYNA penalty contact algorithm [66] is then used to simulate the interaction between the plate and the surrounding liquid. This allows the fluid to slide on the flexible walls without friction, but prevents it from passing through the structure.

Nevertheless, in order to provide good contact conditions, it is necessary to avoid having fluid nodes exactly facing the solid ones, as represented on Figure 7.15b (this condition may be easily fulfilled by imposing different mesh sizes on the two domains). Moreover, to prohibit any initial penetration, it is also needed to account for the plating thickness t_p by imposing an initial gap of $t_p/2 + \epsilon$, where ϵ is a very small distance of 1 mm for example. All these geometrical dispositions are summarized on Figure 7.15. If they are not carefully followed, then it is to fear that leakage may appear during the simulation.

Let us now give some comments on the boundary conditions. Concerning the fluid domain, these ones are as follows:

- In the horizontal plane $y = 0$, the water is always in contact with the bottom of the reservoir. To account for this situation, it is required to prohibit the vertical motions along the y axis for all the fluid nodes located in this plane. However, the displacements along the x and z axes remain free, which corresponds to the possibility for the liquid to slide (without friction) on the bottom.
- In the vertical planes $z = 0$ and $z = l$, the contact with the rigid walls may be modeled similarly, by preventing any horizontal motion along the z axis. Nevertheless, all the nodes positioned there may slide (without friction) on the walls and are therefore free to move along the x and y axes.
- In the vertical planes $x = 0$ and $x = L$, there is no need to impose particular boundary conditions as the interaction with the plate is covered by the contact algorithm.
- In the horizontal plane $y = h_s$, it is not necessary to provide any kind of special restriction as this plane corresponds to the free surface. Provided that the numerical calculation runs correctly, the pressure there should always be close to zero without having to impose any constraint.

All the previous conditions are kept constant throughout the entire simulation. This is not the case for the ones affecting the structure, because it is first necessary to impose the gravity forces before considering the seismic input. This has to be done to consistently model the action of the hydrostatic pressure.

Consequently, during this first phase of loading, all the nodes located on the three supported edges of the plates (see the thick lines on Figure 7.15) are prevented from translating along the x , y and z axes. Nevertheless, once the hydrostatic pressure is established, the seismic acceleration may be applied to these nodes, which requires to release the constraint imposed on their x translational degree of freedom.

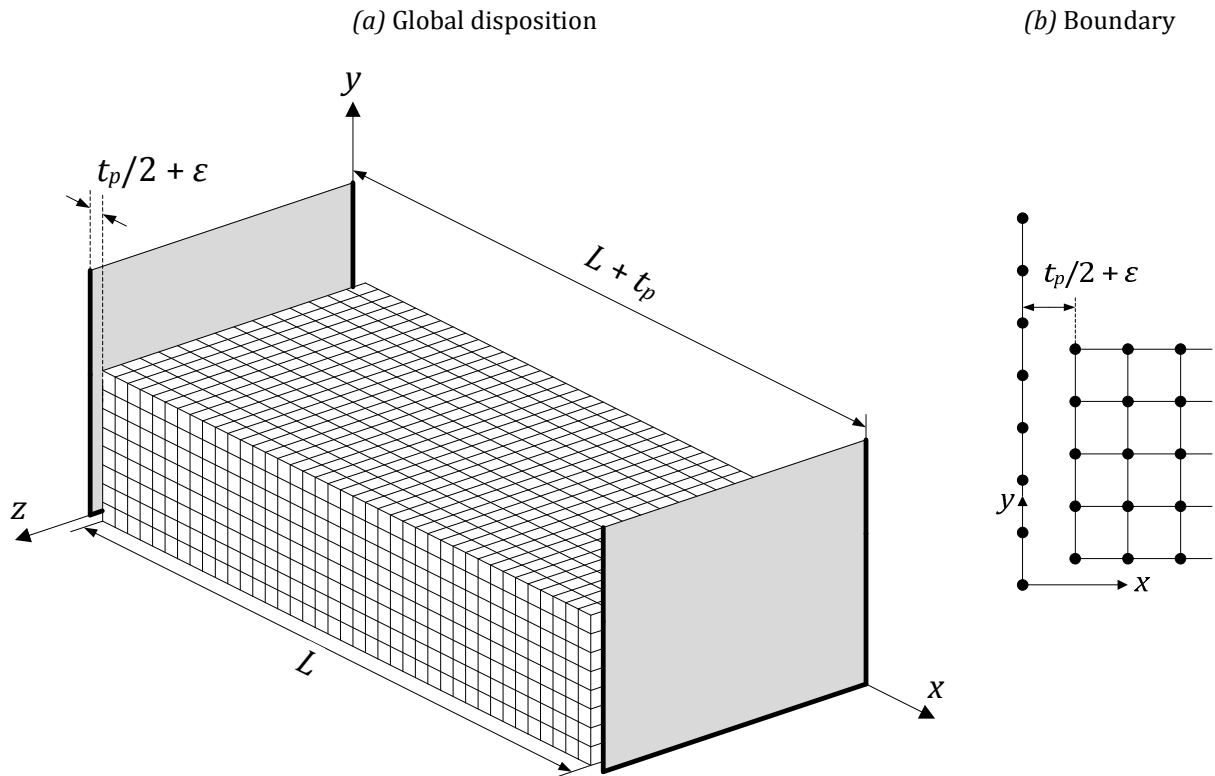


Figure 7.15. Geometrical requirements of the finite element model

After having briefly described the model that will be used to perform the numerical validations, particular results will now be presented for the reservoir depicted on Figure 7.5 and having the properties listed in Table 7.1.

7.4.3.2. Dynamic analysis

Even though it is not of primary concern, the case of a rigid reservoir has first been investigated. For such a situation, some well-known analytical solutions are available, such as the Westergaard formula [166]. The goal of such an approach is to consolidate the finite element model detailed above by making sure that the numerical solutions are sticking to the theoretical predictions for this simple example. The detailed results are reported in section D.2.1 of Appendix D.2, from which it transpires that the agreement is quite satisfactory.

The analytical predictions derived from the virtual work principle will now be confronted to the numerical ones. In this section, the presentation will be limited to the case of the reservoir depicted on Figure 7.5, for a thickness t_p of 20 cm and a water level h_s of 3.5 m or 5 m. Of course, many other additional simulations were performed, using different geometrical configurations than the one of Figure 7.5. The conclusions found in all cases were very similar to those presented here, so there is no need to consider them extensively in this section.

Regarding the structural damping, it is applied on LS-DYNA through the classical Rayleigh formulation. The mass and stiffness coefficient are calibrated to have a 4 % damping on the two first modes of vibration. This value of 4 % has been chosen arbitrarily for this example, but this question needs to be carefully discussed when working on a new project. Some considerations about this problem are given by Buldgen [17] and summarize the discussions related to the seismic design of the new locks in the Panama canal [125].

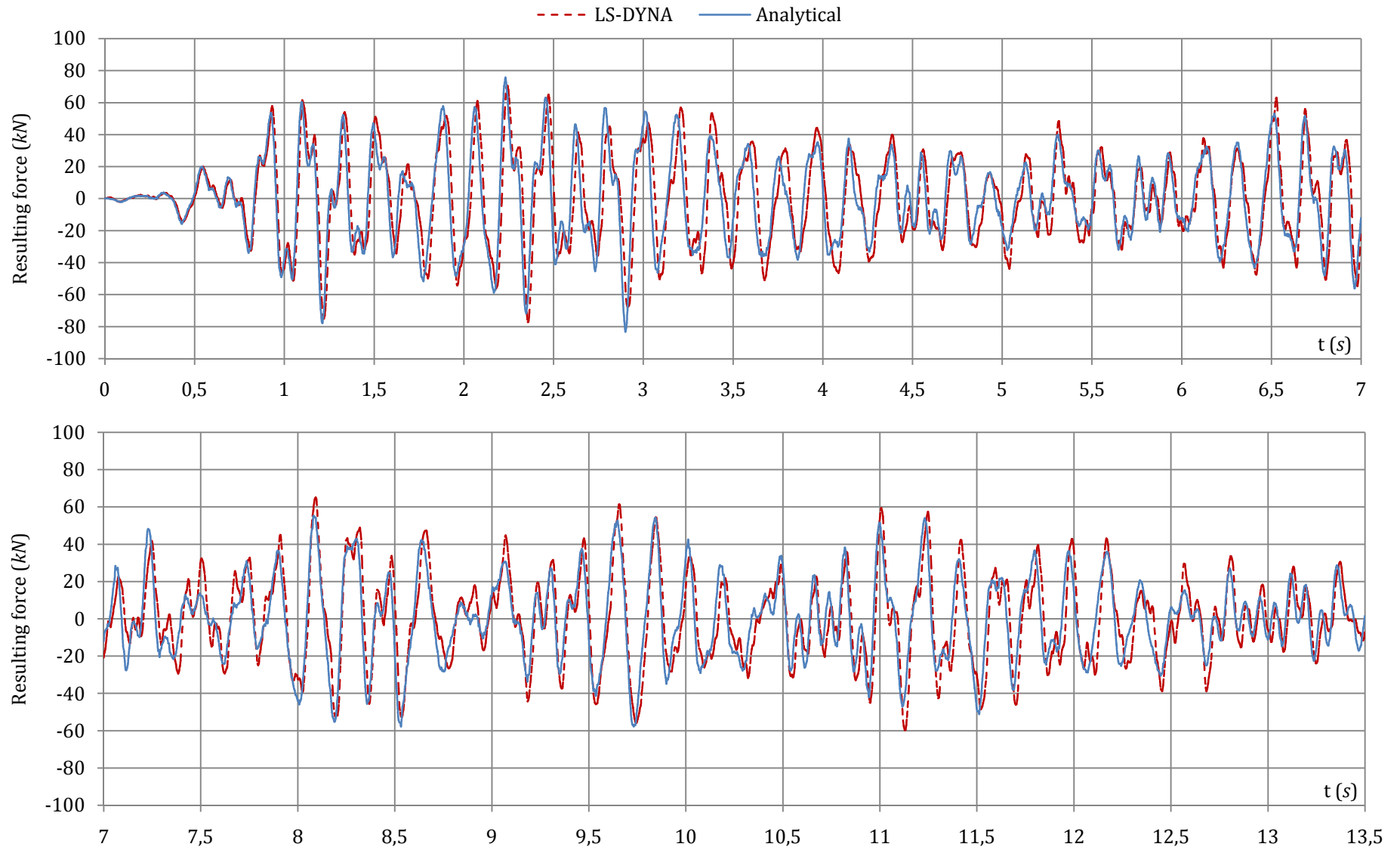


Figure 7.16. Analytical and numerical evolution of the resulting force applied on the flexible wall ($h_s = 3.5 \text{ m}$)

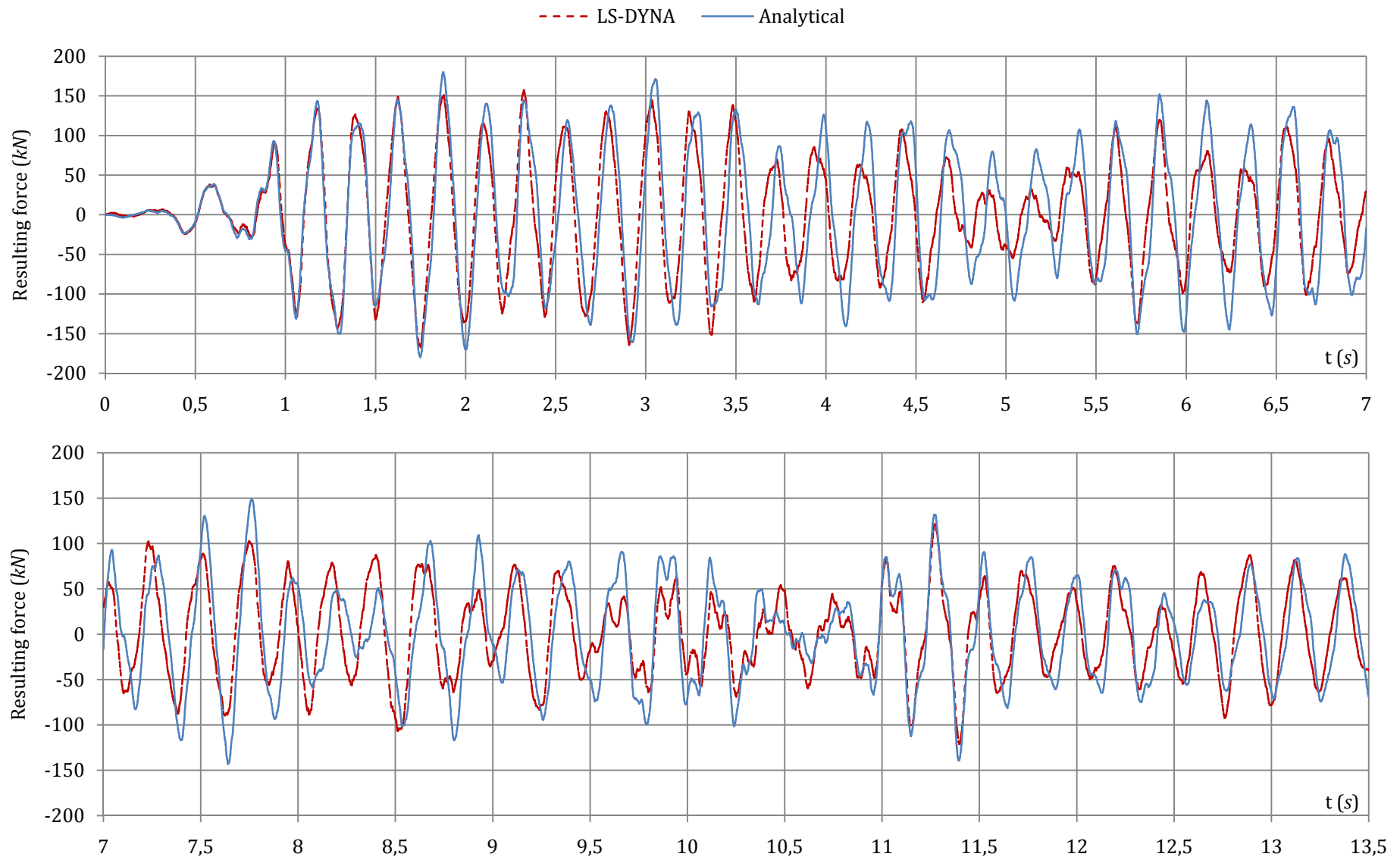


Figure 7.17. Analytical and numerical evolution of the resulting force applied on the flexible wall ($h_s = 5\text{ m}$)

As a matter of validation, the comparison is made on the total hydrodynamic force $F(t)$ applied on the flexible wall, in excess to the hydrostatic pressure. This one is obtained by summing the contributions $F_r(t)$ and $F_f(t)$ respectively coming from the rigid and flexible impulsive pressures given in (7.7) and (7.8):

$$F(t) = F_r(t) + F_f(t) = l \int_0^{h_s} p_r(y, t) dy + \int_0^{h_s} \int_0^l p_f(y, z, t) dydz \quad (7.90)$$

The evolution of $F(t)$ is represented on Figure 7.16 for $h_s = 3.5 m$ and on Figure 7.17 for $h_s = 5 m$. For the first case, it can be seen that the analytical curve sticks quite closely to the numerical one. However, the agreement is not as good for the second case. This discrepancy may be explained because of the assumptions underlying the theoretical model. The developments performed in section 7.4.2 are based on the bending theory of thin plates, which is valid if the out-of-plane motions are kept sufficiently small. More precisely, it is recommended by Shames and Dym [137] that the maximal displacement should not exceed $t_p/10$. For the present reservoir, $t_p = 10 cm$, so the restriction is around $1 cm$.

| | $h_s = 3.5 m$ | $h_s = 5 m$ |
|---------------------------|---------------|-------------|
| Hydrostatic pressure only | 0.48 cm | 1.4 cm |
| Total pressure | 1.1 cm | 2.1 cm |

Table 7.5. Maximal out-of-plane displacements

The maximal out-of-plane components calculated by LS-DYNA are reported in Table 7.5 for $h_s = 3.5 m$ and $h_s = 5 m$. In the first case, it appears that the previous limitation is more or less respected, but for a higher water level, this is not true anymore. Indeed, applying only the hydrostatic pressure on the model already leads to a displacement of $1.4 cm$, and a value of $2.1 cm$ is even reached during the seism. Consequently, it is to fear that membrane effects are not negligible in such a situation, and this explains the discrepancy observed on Figure 7.17. Moreover, numerical simulations performed with $t_p = 15 cm$ and $h_s = 5 m$ show a better agreement, which tends to confirm that the problem is actually coming from too large out-of-plane motions.

| $h_s = 3.5 m$ | | | |
|---------------|---------------------|--------------------|---------------------|
| Result | Analytical solution | Numerical solution | Relative difference |
| Maximal value | 75.67 kN | 70.67 kN | 7.1 % |
| Minimal value | -83.31 kN | -77.18 kN | 7.9 % |
| $h_s = 5 m$ | | | |
| Result | Analytical solution | Numerical solution | Relative difference |
| Maximal value | 180.09 kN | 157.36 kN | 14.4 % |
| Minimal value | -179.88 kN | -167.29 kN | 7.5 % |

Table 7.6. Comparison between the extreme values of the analytical and numerical flexible solutions

To have a better comparison between the numerical and analytical results, let us now analyze Table 7.6. This one gives the maximal and minimal values of the resulting force $F(t)$ acting on the wall during the seism. It is clear that the theoretical model tends to be more conservative than the solutions provided by the finite element simulations, which is a quite safe observation for the pre-design process. Moreover, the maximal overestimation does not exceed 15 %, which is still acceptable. Similar conclusions are also valid for the simulations performed with other reservoirs.

7.4.3.3. Additional investigations

In order to illustrate the real need of accounting for the fluid-structure interaction during the dynamic analysis, some comparisons have been made between the theoretical solutions for a rigid and a flexible wall. An example is proposed in section D.2.2.1 of Appendix D.2, from which it transpires that neglecting the wall flexibility could lead to a drastic underestimation of the hydrodynamic pressure (more than 50 % in the present case). Consequently, one should always be careful before applying classical solutions such as the one of Westergaard [166] because they are only valid for very stiff structures¹⁴.

Regarding the influence of the reservoir length L , it is shown in section D.2.2.2 of Appendix D.2 that the conclusion exposed in 7.3.3.3 during the modal analysis are still valid in the present case. Indeed, for $L \geq 3h_s$, one can consider that the rigid and flexible contributions do not depend on L anymore. Consequently, this means that for a given value of h_s , performing the seismic analysis of a reservoir with a length L greater than $3h_s$ is equivalent to realizing the same analysis on a "fictitious" reservoir with a length of $3h_s$ (see Figure 7.18).

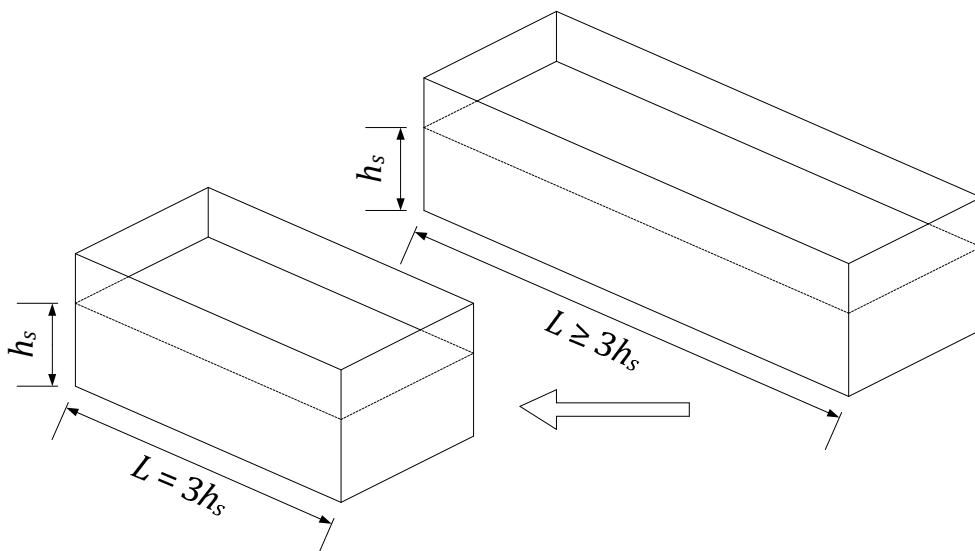


Figure 7.18. Definition of a fictitious reservoir for a seismic analysis

The direct practical implication of the previous conclusion is to simplify numerical seismic analyses of reservoirs. Indeed, to account for the fluid-structure interaction, it is necessary to represent both the gate and the fluid with finite element. In this process, the main effort is mostly on modeling the fluid part, as lock chambers are often quite long. So if $L \geq 3h_s$, performing simulations on a fictitious model with a length of $3h_s$ could drastically reduce the time and the capacities needed to realize numerical analyses. This last assertion is discussed in section D.2.2.2 of Appendix D.2 where an application example is also proposed.

7.4.4. Added mass method

7.4.4.1. Theoretical overview

The added mass method is based on the fact that the surrounding water reduces the vibration frequencies of the immersed plate. As it is clear that the stiffness of the dry structure is the

¹⁴ It is worth remembering that the Westergaard formula [166] was initially derived for gravity dams, which are usually quite rigid structures (see section 6.1).

same as for the wet one, this phenomenon may be modeled by increasing fictitiously the mass of the flexible walls. In other words, the consequence of the liquid is to make the structure heavier.

Instead of working with a plate having a mass density ρ and immersed in water, the added mass approach proposes to work directly on a dry structure having a modified mass density $\rho + \rho^*$. When such a flexible wall is submitted to a longitudinal seismic acceleration, the dynamic equilibrium equation (7.61) simply becomes:

$$(\rho + \rho^*)t_p(\ddot{u} + \ddot{X}) + f_d + D \left(\frac{\partial^4 u}{\partial y^4} + 2 \frac{\partial^4 u}{\partial y^2 \partial z^2} + \frac{\partial^4 u}{\partial z^4} \right) = 0 \quad (7.91)$$

$$\Leftrightarrow \rho t_p(\ddot{u} + \ddot{X}) + f_d + D \left(\frac{\partial^4 u}{\partial y^4} + 2 \frac{\partial^4 u}{\partial y^2 \partial z^2} + \frac{\partial^4 u}{\partial z^4} \right) = -\rho^* t_p \ddot{u} - \rho^* t_p \ddot{X}$$

Comparing (7.61) and (7.91), it transpires that the pressure in this last expression is given by $p = \rho^* t_p \ddot{X} + \rho^* t_p \ddot{u}$. The first term $\rho^* t_p \ddot{X}$ may be identified as the rigid impulsive part $p_r(y, t)$, while the second one $\rho^* t_p \ddot{u}$ is clearly the contribution coming from the vibrations of the plate. To have a strict equivalence between (7.61) and (7.91), the fictitious mass density ρ^* should be calibrated in accordance with (7.7) and (7.8) to have:

$$\rho^* t_p \ddot{X} = -\rho_f \left(\sum_{n=1}^{+\infty} \frac{4}{\beta_n^2 L} \frac{\cosh(\beta_n y)}{\cosh(\beta_n h_s)} - \frac{L}{2} \right) \ddot{X} \quad (7.92)$$

$$\rho^* t_p \ddot{u} = - \sum_{n=1}^{+\infty} \sum_{m=0}^{+\infty} c_{mn} \cos(\alpha_n y) \cos(\bar{\gamma}_m z) \int_0^{h_s} \int_0^l \ddot{u} \cos(\alpha_n y) \cos(\bar{\gamma}_m z) dy dz \quad (7.93)$$

However, it is impossible to find an expression of ρ^* satisfying (7.93). Therefore, the equivalence is only performed on the rigid contribution, which means that:

$$\rho^*(y) = \frac{\rho_f}{t_p} \left(\frac{L}{2} - \sum_{n=1}^{+\infty} \frac{4}{\beta_n^2 L} \frac{\cosh(\beta_n y)}{\cosh(\beta_n h_s)} \right) \quad (7.94)$$

Using (7.94) leads to the exact expression for $p_r(y, t)$, but this is not the case for $p_f(y, z, t)$, which implies that the fluid-structure interaction is not correctly assessed. So the added mass method is only an approximate approach, that is not based on theoretical or physical developments. Increasing fictitiously the mass density by resorting to (7.94) is only valid for perfectly rigid structures, but not for flexible ones. In other words, the additional density calibrated with (7.94) does not lead to the correct vibration frequencies and mode shapes. Nevertheless, this way of doing may be more or less suited for moderately flexible structures and for situations where the interaction with the fluid is quite low (i.e. for the intermediate values of the FSI quotient introduced in section D.1.2 of Appendix D.1).

7.4.4.2. Numerical application

The main practical interest of working with added masses is that the finite element model is much easier to build. Indeed, there is no need to represent the fluid part, which also means that the simulations will be shorter and less demanding in terms of computational resources. Moreover, if the structure has an elastic behavior and if the boundary conditions are linear,

one may resort to response spectra instead of having to perform multiple time history analyses. So it is quite easy to work with added masses, but one has always to bear in mind that the solution is only approximate and not strictly valid.

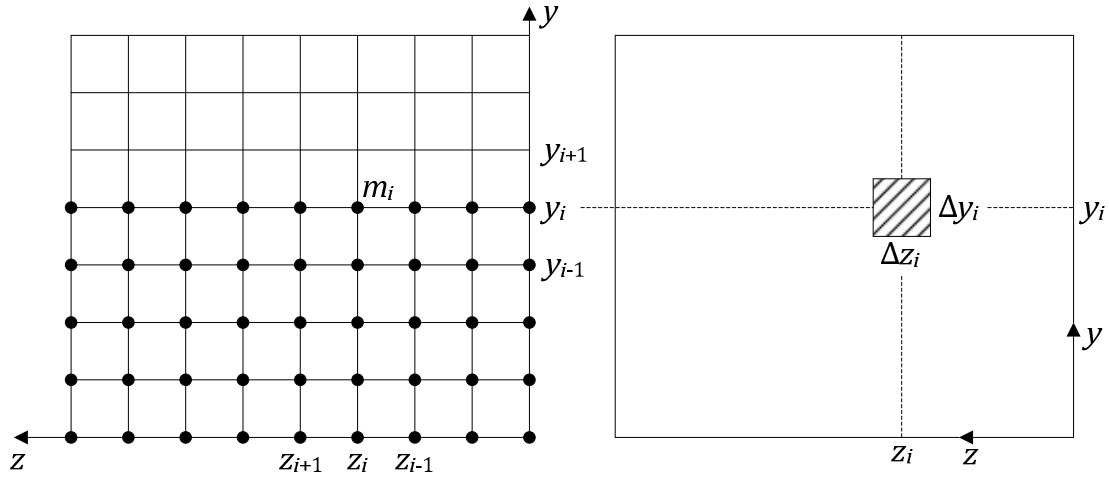


Figure 7.19. Derivation of the numerical added masses

The aim is now to compare the pressure obtained by modeling the fluid domain (as it has been done in section 7.4.3.1) with the one given by the added mass method. In this last approach, the plate is first modeled by shell elements having a uniform thickness t_p with a mass density ρ , and the appropriate boundary conditions are applied to the supports in $y = 0$, $z = 0$ and $z = l$. To represent the effect of the fluid, concentrated mass elements are then attached to the nodes located in the wet area of the structure. The lumped mass m_i affected in (y_i, z_i) is simply given by (Figure 7.19):

$$m_i = \rho^*(y_i) t_p \Delta y_i \Delta z_i ; \quad \Delta y_i = \frac{y_{i+1} - y_{i-1}}{2} ; \quad \Delta z_i = \frac{z_{i+1} - z_{i-1}}{2} \quad (7.95)$$

where $\rho^*(y_i)$ is directly obtained from (7.94). As a next step, the supported edges of the plate are submitted to the seismic acceleration $\ddot{X}(t)$, and it is possible with LS-DYNA to compute the time evolution of the total accelerations $\ddot{u}(y, z, t) + \ddot{X}(t)$ at each nodes of the model. Using these values in conjunction with (7.94) leads to the total hydrodynamic pressure in a set of discrete locations (y_i, z_i) . According to the added mass theory, the total pressure is given by:

$$p_r(y, t) + p_f(y, z, t) = \rho^* t_p (\ddot{u}(y, z, t) + \ddot{X}(t)) \quad (7.96)$$

As a matter of comparison, it is proposed here to focus on the resulting pressure force acting in the middle of the gate, i.e. in $z = l/2$. Analytically, this one is simply given by:

$$\left[\int_0^{h_s} p(y, z, t) dy \right]_{z=l/2} = \int_0^{h_s} p_r(y, t) dy + \left[\int_0^{h_s} p_f(y, z, t) dy \right]_{z=l/2} \quad (7.97)$$

Once again, the reservoir depicted on Figure 7.5 is used to have an application example. The numerical and theoretical results related to this configuration have already been presented on Figure 7.16 and Figure 7.17 for $h_s = 3.5 \text{ m}$ and $h_s = 5 \text{ m}$ respectively. The purpose is now to compare them with those obtained by applying the added mass method. The evolution of the resulting pressure force in $z = l/2$ as defined in (7.97) has been calculated by LS-DYNA for the signal depicted on Figure 7.13. The curves are plotted on Figure 7.20 for $h_s = 3.5 \text{ m}$ and on Figure 7.21 for $h_s = 5 \text{ m}$.

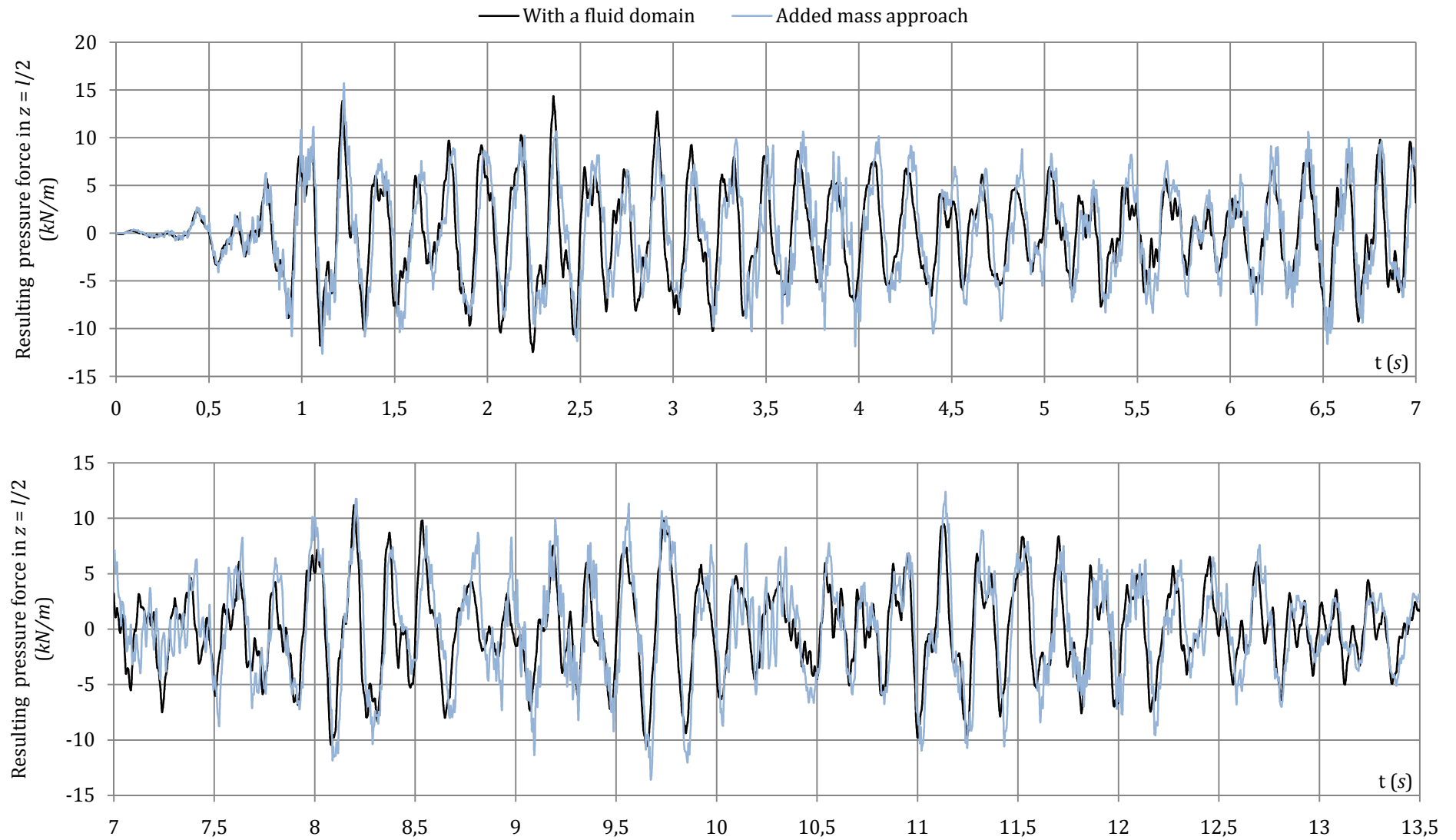


Figure 7.20. Comparison between the numerical results obtained by modeling the fluid or by using the added mass method ($h_s = 3.5$ m)

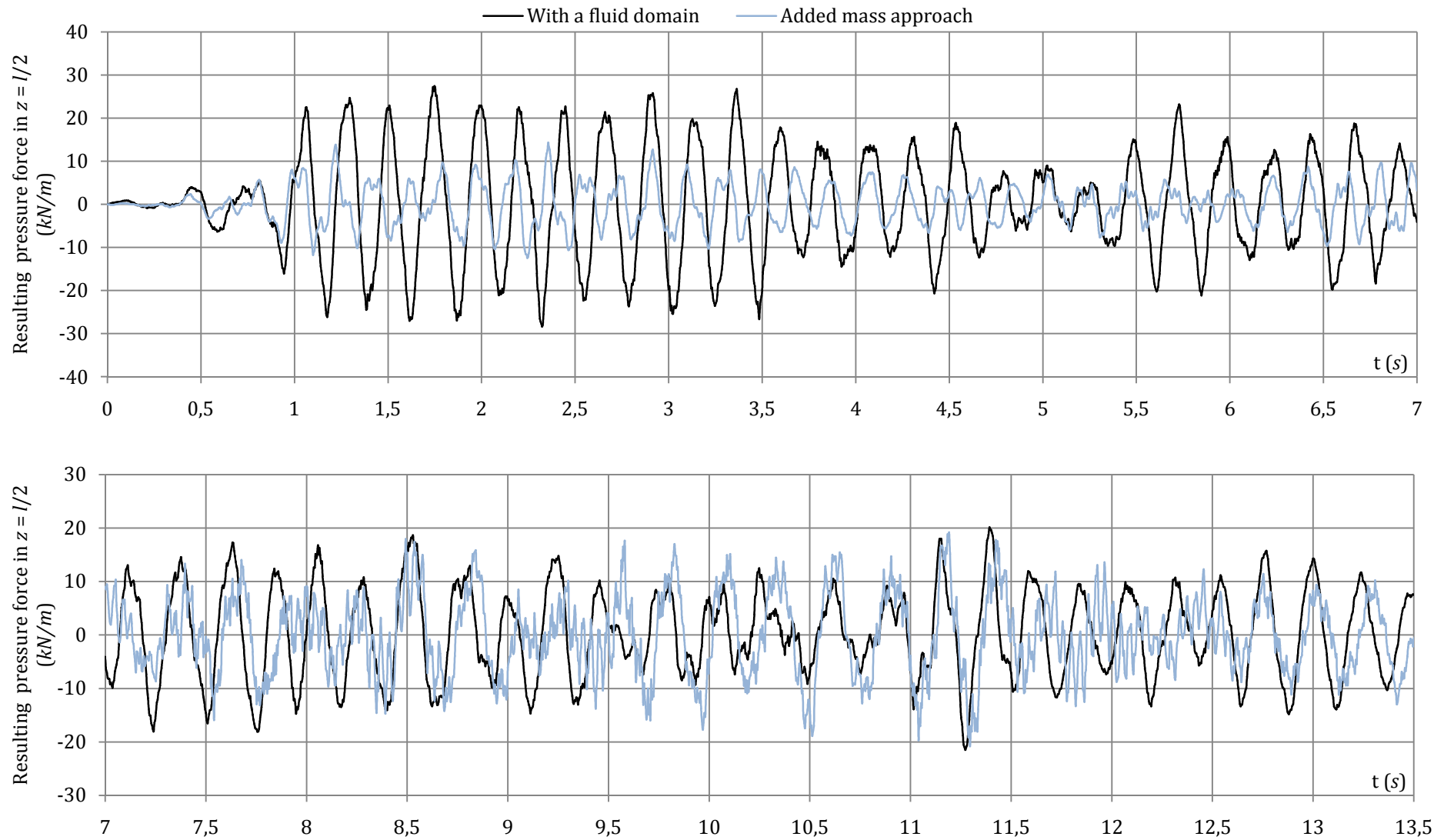


Figure 7.21. Comparison between the numerical results obtained by modeling the fluid or by using the added mass method ($h_s = 5$ m)

In the first case, it appears that modeling entirely the fluid domain or using added masses is equivalent, as there is a very good agreement between the results given by the two techniques. However, if the water level is raised up to 5 m , the discrepancy becomes much more important and working with lumped masses is not relevant.

This application example confirms what was already suggested in the theoretical overview of section 7.4.4.1: the added mass method is only applicable to situations where the fluid-structure interaction is limited, which is the case if the water level is not too high. As detailed in section D.1.2 of Appendix D.1, this may be corroborated by checking the values of the FSI quotient for this example (as a reminder, it is recalled if $\text{FSI} \ll 1$, the liquid has practically no influence on the plate vibrations). For $h_s = 3.5\text{ m}$, $\text{FSI} = 0.37$, which is quite an intermediate value with respect to unity. Therefore, using concentrated mass is still adequate in this case. Nevertheless, for $h_s = 5\text{ m}$, the interaction is much more severe as $\text{FSI} = 1.31$, and this is why the added mass method fails to correctly represent the action of the fluid.

7.5. Conclusions

The goal of this chapter was to develop an analytical method to evaluate the hydrodynamic pressure on flexible reservoirs during a seism. To do so, the dry modal properties were first briefly derived in section 7.2 and then extended to account for the presence of water. This was achieved by applying the Rayleigh-Ritz method. The corresponding wet eigenfrequencies and modes shapes were validated by comparison with numerical solutions. In section 7.4.3.3, these latter were completed by further investigations to analyze the effects of some geometrical parameters.

Once the wet modal properties were obtained, the dynamic analysis of a flexible reservoir was investigated in section 7.4. The analytical solutions were derived by applying the virtual work principle and validated by comparisons with finite element simulations. The agreement was found to be quite satisfactory for a pre-design stage.

Apart from these developments, additional investigations were made on some other particular points. The main conclusions are summarized hereafter:

- Regarding the fluid-structure interaction, it can be shown that the length L of the reservoir does not have any influence on the modal properties and on the hydrodynamic pressure provided that $L \geq 3h_s$. On a practical point of view, this observation means that there is no need to consider the whole reservoir when performing numerical simulations. It is sufficient to model it only over a length of $3h_s$, which could lead to an important reduction of the computation effort.
- Evaluating the hydrodynamic pressure by considering only the rigid contribution may result in an unsafe design. Indeed, as claimed in section 7.4.3.3, such an approach tends to drastically underestimate the forces acting on the flexible walls. This is particularly true if the fluid-structure interaction is important.
- In the same optic, for the well-known added mass method presented in section 7.4.4, it is also found that the hydrodynamic pressure obtained in this way was not correctly assessed.

From the previous points, it can be concluded that performing the seismic analysis of a flexible reservoir is not straightforward. Except for very rigid configurations, this has to be achieved by considering the fluid-structure interaction, otherwise the hydrodynamic pressure could be underestimated. Consequently, the classical Westergaard formula [166] or the added mass methods should be carefully used.

CHAPTER 8. Seismic analysis of plane lock gates

This chapter is this time devoted to study the seismic behavior of lock gates. The structures considered here are made of a plating bearing an orthogonal reinforcing system. Once again, the objective is to establish a simplified procedure leading to the evaluation of the resulting hydrodynamic pressures induced by an earthquake. The procedure followed to achieve this goal is quite similar to the one exposed in Chapter 7 and is divided in two main parts.

The first section is concerned with the determination of the modal properties of a stiffened plate. The vibration characteristics are derived by using the Rayleigh-Ritz method, in which the mode shapes of beams with various support conditions are used as admissible functions. The validity of such an approach is then briefly discussed, and the section is closed by presenting some comparisons between the analytical results and those obtained numerically with the software NASTRAN and LS-DYNA.

The second part of the chapter presents a simplified method for performing the dynamic analysis of a lock gate. The virtual work principle is used as a basis and its applicability to the present situation is discussed in detail. As a validation step, the analytical curves showing the time evolution of the hydrodynamic pressure are compared to those given by the finite element software LS-DYNA. After that, some more investigations are made about the use of the added mass method.

The developments exposed in this chapter have been partly presented in the 33rd PIANC World Congress [19] and to the 7th International Conference on Thin-Walled Structures [20].

8.1. Introduction

8.1.1. Preliminary considerations

The developments on unstiffened plates performed in the previous chapter give a global insight on the process that will now be followed to investigate lock gates.

As suggested by some authors, the vibrations of a stiffened plate may be studied by considering an equivalent orthotropic structure characterized by the material parameters listed in Table 8.1. The main advantage of such an approach is that it allows to use all the results already available in the literature. For example, Aksu [4], Grace [62] and Vijayakumar [156] provide very interesting results by deriving approximate solutions for the characteristic equation of orthotropic plates. In addition, the work performed by Greenspon [65] also constitutes an interesting extension to account for the presence of water. To do so, the equilibrium equations proposed in references [4], [62] and [156] are corrected to account for the hydrodynamic pressure induced by the plate vibrations. The wet modal properties are then derived and a closed-form solution is proposed for the dynamic analysis of a plate submitted to an impulsive load.

| | |
|----------------------|--|
| E_y, E_z | Young modulus in the y and z direction |
| ν_{yz}, ν_{zy} | Poisson ratios |
| G_{yz} | Shear modulus |

Table 8.1. Material parameters of an orthotropic plate

To work this way, the parameters $E_y, E_z, \nu_{yz}, \nu_{zy}$ and G_{yz} should be derived to have the same vibration properties for the orthotropic plate and for the lock gate. Huffington [75] and Lekhnitskii [96], amongst others, proposed some formulae to evaluate these parameters in function of the properties characterizing the reinforcing system. Nevertheless, their recommendations are based on the hypothesis that the plate is regularly stiffened, which is not the case for a lock gate. Moreover, the approach proposed by these authors is based on a static equivalence, which is not really coherent to treat vibrating structures. Another suggestion was also made by Iyengar [78], who derived the orthotropic parameters to have the same fundamental frequency of vibration for both the plate and the gate. However, the method is not really interesting as it first requires to know the eigenfrequencies of the lock gate, which is precisely what is sought.

Consequently, even if the method appears to be quite interesting, it seems that an equivalent orthotropic plate fails to properly represent the vibration properties of a non-regularly stiffened lock gate. Furthermore, the equivalence should be based on the modal properties characterizing the stiffened structure, which are usually unknown at the early design stage. For these reasons, it is decided to avoid using such an approach to analyze the seismic behavior of lock gates. Nevertheless, the developments performed in Chapter 7 are still a good basis and will be extensively used in the next sections.

8.1.2. Description of the structure

As a first step, it is probably necessary to proceed to a better description of the structure to analyze. In this chapter, the case of a lock gate with a single plating and an orthogonal stiffening system is investigated. It is similar to the one consider in Chapter 3, except that

water is now present. The notations are very similar to those introduced in section 3.1.1 and are recalled on Figure 8.1. Nevertheless, one of the major difference with Chapter 3 is that the present methodology is exclusively developed for a uniform plating thickness denoted by t_p . Unfortunately, this is not really realistic because the plates are usually thicker at the bottom of the lock. In this case, t_p may be taken as a mean value calculated over the entire gate (Figure 8.2a):

$$t_p = \sum_n \frac{h_n}{h} t_n \quad ; \quad h = \sum_n h_n \quad (8.1)$$

where t_n is the plating thickness over a portion h_n of the total height h . Having a unique value for t_p is required so far to develop an analytical approach.

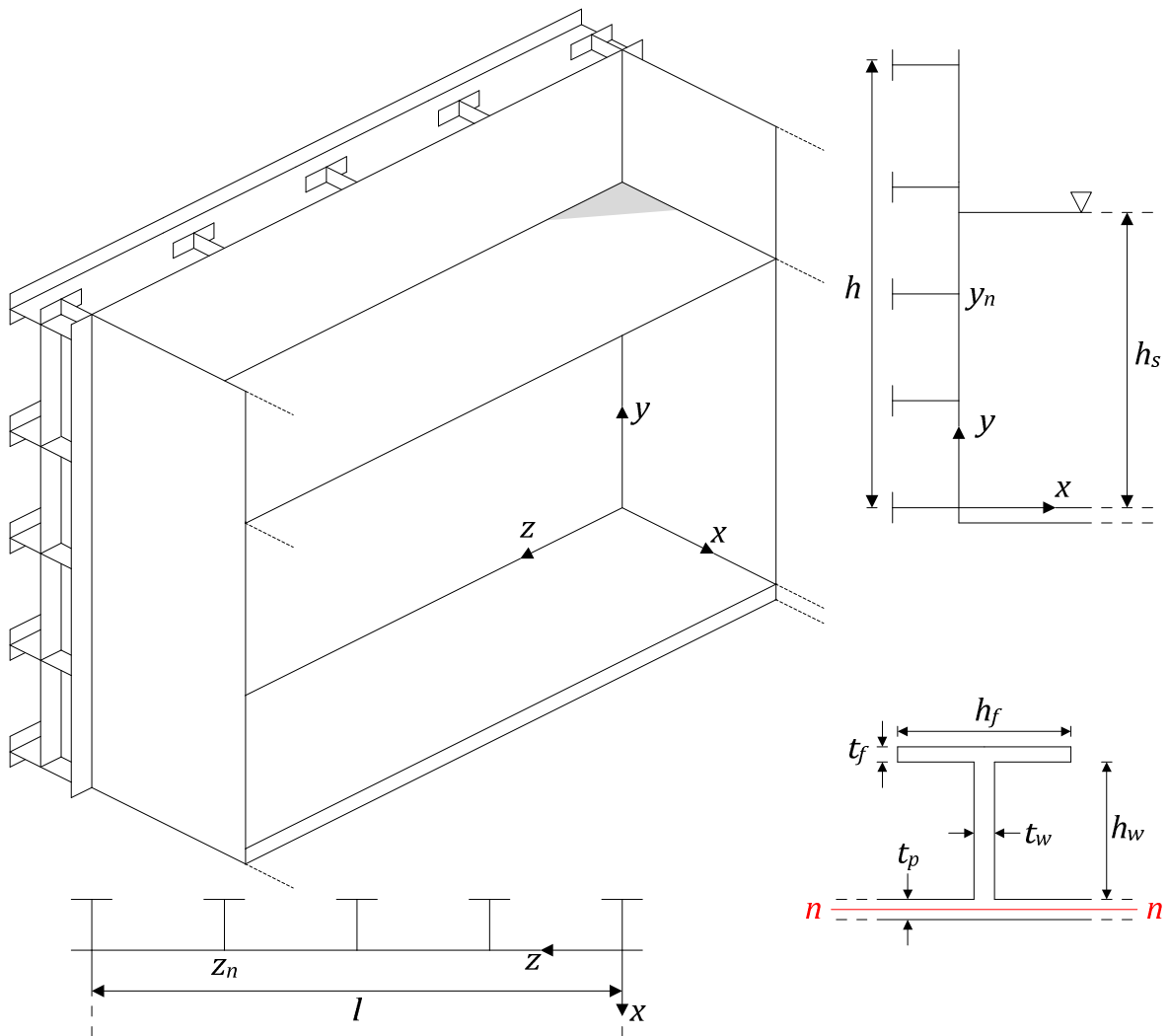


Figure 8.1. General geometry of the reinforced gate

It is further assumed that the lock chamber is separated from the upstream and downstream reaches by two identical gates (the situation of a non-symmetric disposition will be discussed later). It is submitted to an earthquake having a longitudinal acceleration denoted by $\ddot{X}(t)$, as depicted on Figure 8.2b. In this study, the two other components $\ddot{Y}(t)$ and $\ddot{Z}(t)$ oriented along the y and z axes respectively are disregarded for the moment (Figure 8.2b).

In order to evaluate the hydrodynamic pressure induced on the structure by $\ddot{X}(t)$, it is still valid to use (7.7) for the rigid contribution and (7.8) for the flexible one. Indeed, the lock gate

is in fact nothing more than a stiffened plate. Therefore, by neglecting the local disturbance that may be caused by the reinforcing elements on the pressure field, the developments leading to these formulae are still perfectly valid. The only modification is that the term $\ddot{u}(y, z, t)$ appearing in (7.8) denotes this time the acceleration of the gate.

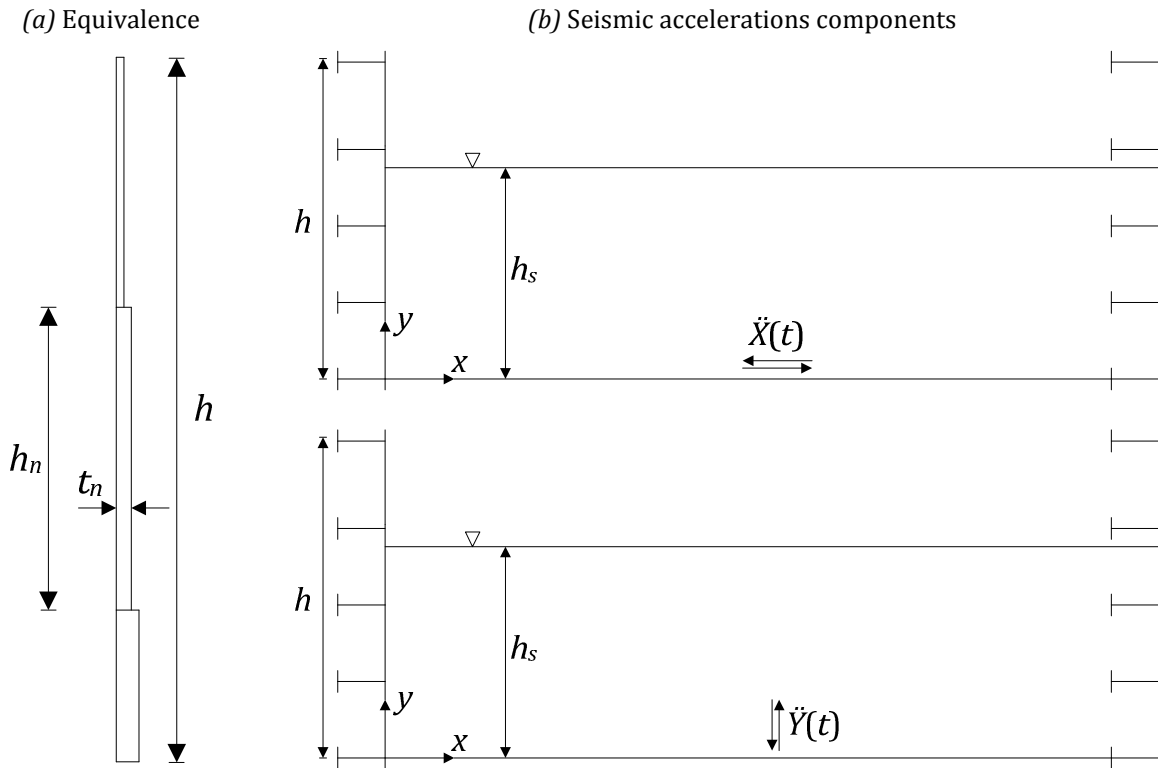


Figure 8.2. Equivalent plating thickness and seismic accelerations in two directions

Regarding the boundary conditions, they are the same as for the impact analysis performed in Chapter 3 (see section 3.1.1.3). Two different situations are also considered here, as the gate may be supported or free at the bottom. This distinction is important because the presence or the absence of a sill may have some incidence on the vibration properties of the structure.

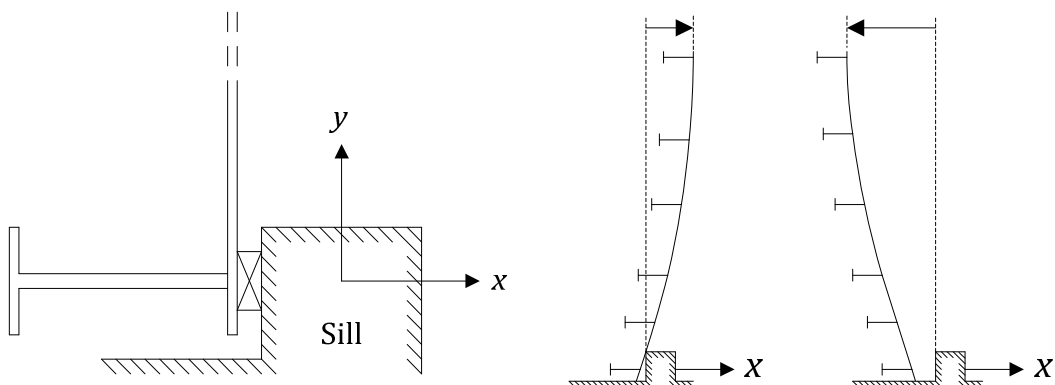


Figure 8.3. Boundary conditions at the bottom

Nevertheless, it is worth noting that such a support implies very particular boundary conditions. Indeed, if we examine the situation depicted on Figure 8.3, it transpires that if the gate is submitted to a positive acceleration along the x axis, it can be seen as being supported at the bottom. However, this is not true if the acceleration occurs in the opposite direction. It is unfortunately not possible to develop an analytical solution that includes such

particularities. Therefore, when a sill is present, it is assumed that a complete support is provided at the bottom, which means that both the positive and negative displacements in the x direction are forbidden. Doing so, one has to bear in mind that the boundary conditions applied to the structure do not truly represent the real configuration of the gate.

8.2. Free vibration analysis of a dry gate

The goal of this section is to derive the natural frequencies and mode shapes of a gate with a single plating and reinforced by a simple stiffening system, as described on Figure 8.1. The presence of water in the lock chamber is disregarded so far. So the purpose is now only to evaluate the dry mode shapes $\delta_i(y, z)$ and natural frequencies ω_i of the structure. The two situations of the gate is resting against a sill or not will be considered separately in this section.

To achieve this goal, one may resort to the Rayleigh-Ritz method and follow the energy approach described in section 7.3.2.2. As it was done in 7.3 for an immersed plate, it is first required to define a set of M admissible functions $\psi_j(y, z)$ to have:

$$\delta_i(y, z) = \sum_{j=1}^M v_{ji} \psi_j(y, z) \quad (8.2)$$

The coefficients v_{ij} are to be found by using the Rayleigh-Ritz method. For the analytical expressions of $\psi_j(y, z)$, it is decided to use a combination of beam eigenmodes, as detailed hereafter.

8.2.1. Free vibration analysis of beams

In order to find consistent equations for $\psi_j(y, z)$, it is suggested to derive the eigenfunctions $f_j(y)$ and $g_j(z)$ characterizing the free vibrations of the vertical and horizontal reinforcing elements respectively. With these functions, it is postulated that:

$$\psi_j(y, z) = f_j(y)g_j(z) \quad (8.3)$$

As the gate is always supported by the lock walls along the edges $z = 0$ and $z = l$, it seems reasonable to choose $g_j(z)$ as being the eigenmodes of a doubly supported beam with a span l , as depicted on Figure 8.4a. Similarly, for the case where the gate is resting against a sill, $f_j(y)$ may characterize the vibrations of the supported-free beam of Figure 8.4b. On the contrary, if there is no particular support condition in $y = 0$, then $f_j(y)$ this time corresponds to the mode shapes of a free-free beam, as shown on Figure 8.4c.

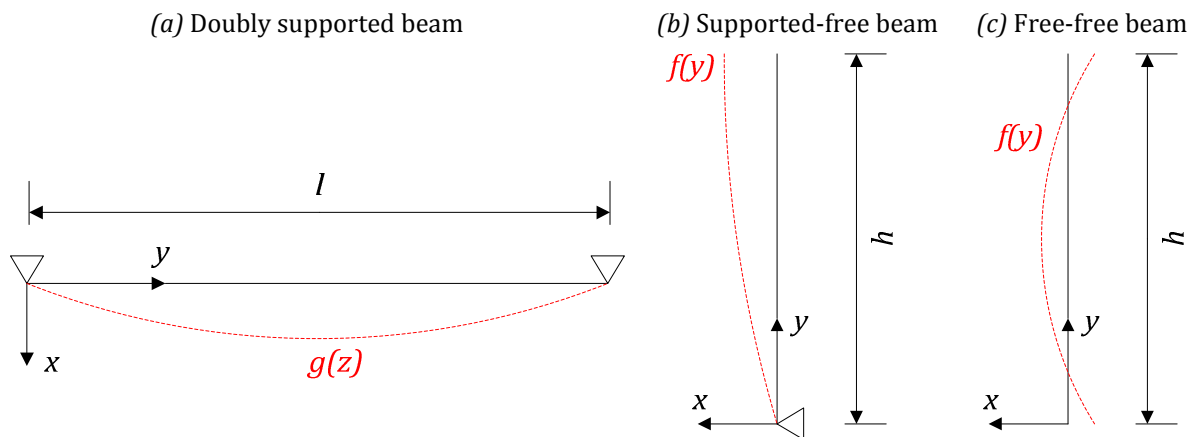


Figure 8.4. Support conditions for the horizontal and vertical reinforcing elements

8.2.1.1. Solution for a gate supported at the bottom

As many references may be easily found in the literature, the purpose is not to perform a complete derivation leading to the vibration properties of beams. Therefore, some very useful fundamental results will be recalled here. Let us start by considering the horizontal reinforcing elements represented on Figure 8.4a. If they have a cross-section A_h and an inertia I_h , it may be shown that they obey to the following characteristic equation:

$$\frac{\partial^4 g_j}{\partial z^4} - \frac{\rho A_h \omega_j^2}{EI_h} g_j(z) = 0 \quad (8.4)$$

where ρ and E are respectively the mass density and Young modulus associated to the beam material. This expression is completed by imposing that the displacement and the bending moment have to be set to zero at the two supports (for $z = 0$ and $z = l$), i.e.:

$$g_j(z) = 0 \quad \text{and} \quad \frac{\partial^2 g_j}{\partial z^2} = 0 \quad (8.5)$$

It is obvious that a solution of (8.4) satisfying the boundary conditions (8.5) is simply a sinusoid having as many half-waves as required. In other words:

$$g_j(z) = \sin(\gamma_j z) \quad (8.6)$$

where $\gamma_j = n_j \pi / l$, with $n_j \in \mathbb{N}_0$ being the number of half-waves along the horizontal z axis. Regarding the situation for the vertical beams, denoting this time by A_v and I_v the cross-sectional properties, one may easily adapt (8.4) to get the characteristic equation:

$$\frac{\partial^4 f_j}{\partial y^4} - \frac{\rho A_v \omega_j^2}{EI_v} f_j(z) = 0 \quad (8.7)$$

In the case of the supported-free beam depicted on Figure 8.4b, the displacement and the bending moment are both prohibited at the support, so for $y = 0$, one should have:

$$f_j(y) = 0 \quad \text{and} \quad \frac{\partial^2 f_j}{\partial y^2} = 0 \quad (8.8)$$

Additionally, to simulate a free boundary condition in $y = H$, the shearing force and the bending moment have to be set to zero at this location. So the following boundary conditions are holding for $y = h$:

$$\frac{\partial^2 f_j}{\partial y^2} = 0 \quad \text{and} \quad \frac{\partial^3 f_j}{\partial y^3} = 0 \quad (8.9)$$

It may be shown that (8.7), (8.8) and (8.9) are satisfied for the closed-form solutions given in (8.10). It is worth noting that the particular rigid mode $f_j(y) = y$ is associated to a null eigenvalue. When this mode is activated, it means that the beam is simply rotating around its support without suffering any deformation. So finally, one gets:

- If $\lambda_j = 0$: $f_j(y) = y/h$
 - If $\lambda_j \neq 0$: $f_j(y) = A_j(\sin(\lambda_j y) - B_j \sinh(\lambda_j y))$
- (8.10)

where A_j is the modal amplitude, calculated in such a way that the maximal value of $f_j(y)$ is equal to unity for $0 \leq y \leq h$. The parameters B_j and λ_j only depend on the total height h of the gate. It may be shown that they have the following definitions, in which it can be seen that the eigenvalues λ_j may only be determined numerically by solving an implicit equation:

$$B_j = -\frac{\sin(\lambda_j h)}{\sinh(\lambda_j h)} \quad \cos(\lambda_j h) \sinh(\lambda_j h) - \sin(\lambda_j h) \cosh(\lambda_j h) = 0 \quad (8.11)$$

So finally, gathering all the results listed before leads to the conclusion that for a gate supported at the bottom of the lock chamber and for $\lambda_j \neq 0$, the functions $\psi_j(y, z)$ defined in (8.3) have the subsequent analytical expressions:

$$\psi_j(y, z) = A_j(\sin(\lambda_j y) - B_j \sinh(\lambda_j y)) \sin(\gamma_j z) \quad (8.12)$$

where B_j and λ_j are given in (8.11).

8.2.1.2. Solution for a gate free at the bottom

All the previous developments are only valid for the situation where a support is present in $y = 0$. If this is not the case, then the vibrations of the free-free beam depicted on Figure 8.4c have to be considered and the solutions obtained in (8.10) are no longer valid. Of course, the characteristic equation (8.7) is still the same, but the boundary conditions are now different. As the beam is free at the two extremities, the conditions listed in (8.9) have this time to be satisfied for $y = 0$ and $y = h$. The following solutions may be shown to satisfy all these requirements:

- If $\lambda_j = 0$: $f_j(y) = 1$ or $f_j(y) = y/h$
- If $\lambda_j \neq 0$: $f_j(y) = A_j(\sin(\lambda_j y) + \sinh(\lambda_j y) - B_j \cos(\lambda_j y) - B_j \cosh(\lambda_j y))$

(8.13)

where A_j is still the modal amplitude. For $\lambda_j = 0$, it is possible to find an infinite number of rigid modes, but only the ones given in (8.13) are linearly independent. It is worth noting that B_j and λ_j are defined in a somewhat different way, as these parameters satisfy:

$$B_j = \frac{\sinh(\lambda_j h) - \sin(\lambda_j h)}{\cosh(\lambda_j h) - \cos(\lambda_j h)} \quad \cos(\lambda_j h) \cosh(\lambda_j h) = 1 \quad (8.14)$$

Considering all the previous developments, it can be concluded that for a gate free at the bottom of the lock chamber and for $\lambda_j \neq 0$, the functions $\psi_j(y, z)$ defined in (8.3) are given by:

$$\psi_j(y, z) = A_j(\sin(\lambda_j y) + \sinh(\lambda_j y) - B_j \cos(\lambda_j y) - B_j \cosh(\lambda_j y)) \sin(\gamma_j z) \quad (8.15)$$

where B_j and λ_j correspond this time to the expressions in (8.14).

8.2.1.3. Discussion on the boundary conditions

With these definitions, the functions $\psi_j(y, z)$ are reputed to be linearly independent, as this property is already valid for the eigenmodes of beams. Nevertheless, they are not strictly admissible for the Rayleigh-Ritz procedure. This is due to the fact that we have to deal with a continuous plate bearing a discrete reinforcement. Therefore, in some locations, the boundary conditions are those of a plate, while in other places they have to be derived from the beam

theory (see also the work of Laura and Smith [92] for more details). Such a requirement may first be explained by considering the cross-section of the gate in a vertical plane (x, y) , as depicted on Figure 8.5b, where only two horizontal girders and a portion of the plating have been represented. Along the vertical simple supports in $z = 0$ and $z = l$, the boundary conditions that have to be respected by $\psi_j(y, z)$ along the plating are as follows:

$$\psi_j(y) = 0 \quad ; \quad \frac{\partial^2 \psi_j}{\partial z^2} + \nu \frac{\partial^2 \psi_j}{\partial y^2} = 0 \quad z \in \bigcup_{n=1}^{n_h-1} \left[y_n + \frac{t_w}{2} ; y_{n+1} - \frac{t_w}{2} \right] \quad (8.16)$$

where n_h is the total number of horizontal stiffeners distributed over the height of the gate. Because of (8.5) and (8.6), it is obvious that (8.16) is always satisfied in $z = 0$ and $z = l$. Regarding now the boundary conditions that have to be fulfilled by $\psi_j(y, z)$ around the discrete locations occupied by the stiffeners, one may write:

$$\psi_j(y) = 0 \quad ; \quad \frac{\partial^2 \psi_j}{\partial z^2} = 0 \quad z \in \bigcup_{n=1}^{n_h-1} \left[y_n - \frac{t_w}{2} ; y_n + \frac{t_w}{2} \right] \quad (8.17)$$

Once again, these two relations are always satisfied because of (8.5). Therefore, along the lock walls in $z = 0$ and $z = l$, it can be concluded that both the boundary conditions coming from the beam and from the plate theory are respected. This particularity is only due to the presence of simple supports at these locations. By a similar procedure, it can be shown that this conclusion is also valid along the sill.

The situation is however different for the free edge. The cross-section in a horizontal plane (x, z) is depicted on Figure 8.5a, where only two vertical frames and a portion of the plating have been represented. For the plate segment located between the two frames, the boundary conditions that have to be respected there are given by:

$$\frac{\partial^2 \psi_j}{\partial y^2} + \nu \frac{\partial^2 \psi_j}{\partial z^2} = 0 \quad ; \quad \frac{\partial^3 \psi_j}{\partial y^3} + (2 - \nu) \frac{\partial^3 \psi_j}{\partial y \partial z^2} = 0 \quad z \in \bigcup_{n=1}^{n_v-1} \left[z_n + \frac{t_w}{2} ; z_{n+1} - \frac{t_w}{2} \right] \quad (8.18)$$

where, as a reminder, n_v is the total number of vertical reinforcing elements positioned on the gate. On the other hand, near the frames, one may write the following boundary conditions coming from the theory of beams:

$$\frac{\partial^2 \psi_j}{\partial y^2} = 0 \quad ; \quad \frac{\partial^3 \psi_j}{\partial y^3} = 0 \quad z \in \bigcup_{n=1}^{n_v} \left[z_n - \frac{t_w}{2} ; z_n + \frac{t_w}{2} \right] \quad (8.19)$$

Unfortunately, from (8.18) and (8.19), it seems rather impossible to find a continuous analytical expression for $\psi_j(y, z)$ satisfying all these requirements. As a consequence, if $\psi_j(y)$ is derived from the beam theory detailed in sections 8.2.1.1 and 8.2.1.2, then only the equations given by (8.19) are fulfilled. In other words, along an horizontal free edge, some unbalanced forces are still applied as the plate boundary conditions (8.18) are not satisfied by the chosen closed-form solution of $\psi_j(y, z)$. This will be investigated in more details when dealing with the dynamic analysis of lock gates.

From all the previous considerations, it transpires that the functions $\psi_j(y, z)$ defined by (8.12) or (8.15) are not strictly admissible for the Rayleigh-Ritz method. Nevertheless, if the

stiffened plate is mainly behaving as a beam structure (which is almost the case for lock gates), then using such analytical expressions for $\psi_j(y,z)$ should lead to a good approximation of the modal properties. For this reason, they are sometimes said to be pseudo-admissible. Additionally, it is worth mentioning that this approach has been widely used in the literature, which also corroborates the applicability of the method. Some theoretical studies related to the vibrations of stiffened structures are available in references [10], [16], [43], [77], [78], [87], [92], [110], [112], [139], [177], and [178].

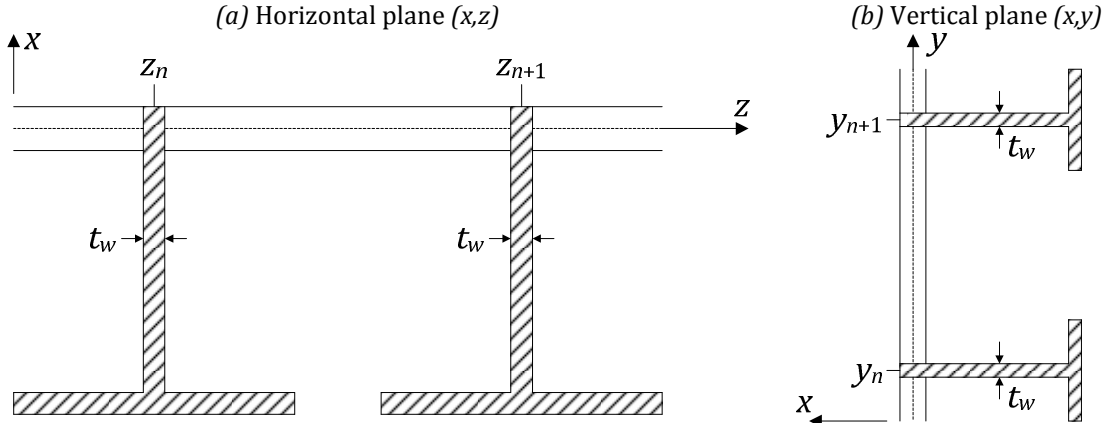


Figure 8.5. Boundary conditions along the support in $y = 0$

8.2.2. Rayleigh-Ritz solution

The problem that is analyzed now is to derive analytically the dry frequencies ω_i and mode shapes $\delta_i(y,z)$ characterizing the free vibrations of a stiffened plate. As mentioned here above, an approximate solution may be found by resorting to the Rayleigh-Ritz procedure, which was already encountered while deriving the modal properties of an immersed plate (see 7.3). Nevertheless, as discussed in section 8.2.1.3, the set of functions $\psi_j(y,z)$ chosen so far is not strictly admissible. As a consequence, the method that will now be followed is not purely rigorous, and it is probably more convenient to work with the energy approach (see 7.3.2.2) instead of using the exact mathematical developments performed in 7.3.2.1.

8.2.2.1. Modal formulation

As a beginning, let us start by expressing the Rayleigh quotient R as a function of the dry mode shapes $\delta_i(y,z)$. According to the theory of section 7.3.2.2, R is simply obtained by dividing the maximal kinetic energy \mathcal{T} by the maximal internal one \mathcal{U} :

$$R = \mathcal{T}/\mathcal{U} \tag{8.20}$$

which is similar to (7.55) with $\mathcal{W} = 0$, as water has not been considered so far. In this last equation, one may get the mathematical forms of \mathcal{T} and \mathcal{U} by considering successively the various elements constituting the gate, i.e.:

$$\mathcal{T} = \mathcal{T}_p + \mathcal{T}_h + \mathcal{T}_v \quad ; \quad \mathcal{U} = \mathcal{U}_p + \mathcal{U}_h + \mathcal{U}_v \tag{8.21}$$

where \mathcal{T}_p , \mathcal{T}_h and \mathcal{T}_v respectively denote the individual kinetic energy coming from the plating, the n_h horizontal reinforcing elements and the n_v vertical ones (similar notations are used for the internal energy \mathcal{U}). In order to analytically derive all the previous terms, it is first required to make an important assumption on the deformation pattern exhibited by the gate. In Chapter 7, it is postulated that the free vibrations of the unstiffened plate simply occur by

bending around its neutral axis. For a stiffened structure as the one depicted on Figure 8.1, this is not necessarily the case, but it is supposed here that this hypothesis is still holding. Consequently, at the discrete locations y_n and z_n where some reinforcing elements are positioned, the deformation pattern leading to the evaluation of \mathcal{T} and \mathcal{U} should be the one of Figure 8.6.

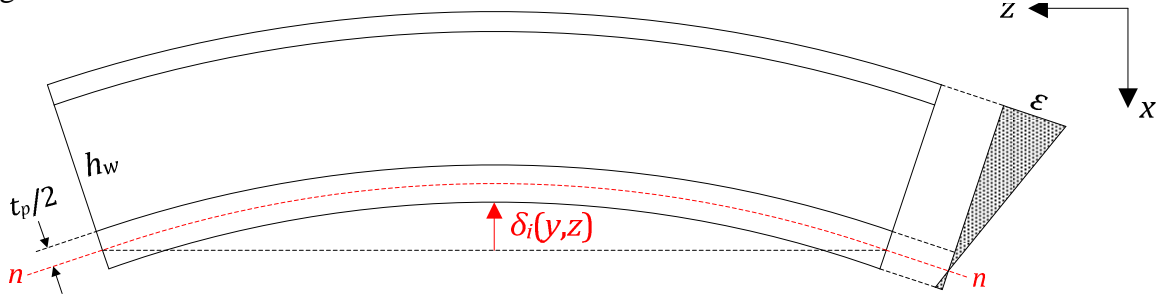


Figure 8.6. Deformation of the plating and the attached reinforcing element

It is clear that such an assumption is questionable, in particular for structures where the reinforcement is predominant. An interesting discussion about this topic was conducted by Wah [161], who showed that considering bending around the neutral fiber of the plate could lead to an overestimation of the stiffness. Nevertheless, this approach is widely encountered in the literature as it allows for some simplifications in the analytical process. Indeed, considering first the plating, as it is still supposed to be bent around its neutral fiber, it is possible to keep the previous definition of the flexural rigidity $D = Et_p^3/12(1 - \nu^2)$ and directly calculate \mathcal{T}_p and \mathcal{U}_p by performing an analogy with (7.53) and (7.54). This leads to:

$$\mathcal{T}_p = \frac{\rho t_p}{2} \iint_A \delta_i^2(y, z) dy dz \quad (8.22)$$

$$\mathcal{U}_p = \frac{D}{2} \iint_A \left(\left(\frac{\partial^2 \delta_i}{\partial y^2} \right)^2 + \left(\frac{\partial^2 \delta_i}{\partial z^2} \right)^2 + 2\nu \frac{\partial^2 \delta_i}{\partial y^2} \frac{\partial^2 \delta_i}{\partial z^2} + 2(1 - \nu) \left(\frac{\partial^2 \delta_i}{\partial y \partial z} \right)^2 \right) dy dz \quad (8.23)$$

Regarding now the situation for the horizontal stiffening elements., under the bending hypothesis made here above, they will be submitted to the deformation diagram depicted on Figure 8.6, which directly shows that the cross-sectional inertia has to be calculated with respect to the neutral fiber $n-n$. In other words, the inertia I_h of the T-shaped beam represented on Figure 8.1 has to be calculated by:

$$I_h = \frac{t_w}{3} \left[\left(h_w + \frac{t_p}{2} \right)^3 - \frac{t_p^3}{8} \right] + \frac{h_f}{3} \left[\left(h_w + \frac{t_p}{2} + t_f \right)^3 - \left(h_w + \frac{t_p}{2} \right)^3 \right] \quad (8.24)$$

If it is further assumed that the stiffening elements are mainly submitted to an in-plane bending, then the contributions to the internal energy \mathcal{U}_h coming from the torsional, axial and shear rigidities of the beam can be neglected. So if the structure is made of n_h horizontal reinforcing components positioned at the discrete locations y_n , it may be shown [106] that:

$$\mathcal{T}_h = \sum_{n=1}^{n_h} \frac{\rho A_{h,n}}{2} \int_0^l \delta_i^2(y_n, z) dz \quad ; \quad \mathcal{U}_h = \sum_{n=1}^{n_h} \frac{E I_{h,n}}{2} \int_0^l \left[\frac{\partial^2 \delta_i}{\partial z^2}(y_n, z) \right]^2 dz \quad (8.25)$$

where $A_{h,n}$ and $I_{h,n}$ respectively denote the area and inertia of the cross-section characterizing the horizontal stiffening element in $y = y_n$. By following a similar procedure, the kinetic and

internal energies \mathcal{T}_v and \mathcal{U}_v related to the n_v vertical stiffening components positioned at the discrete locations z_n are given by:

$$\mathcal{T}_v = \sum_{n=1}^{n_v} \frac{\rho A_{v,n}}{2} \int_0^h \delta_i^2(y, z_n) dy \quad ; \quad \mathcal{U}_v = \sum_{n=1}^{n_v} \frac{EI_{v,n}}{2} \int_0^h \left[\frac{\partial^2 \delta_i}{\partial y^2}(y, z_n) \right]^2 dy \quad (8.26)$$

where $A_{v,n}$ and $I_{v,n}$ have the same meaning as for the horizontal elements. It is worth noting that, for simplicity, in equations (8.22), (8.23), (8.25) and (8.26) uniform values are assumed for E , ν and ρ , but it is clear that the formulae could be easily adapted to treat gates made of different steel grades.

8.2.2.2. Matrix formulation

All the theoretical results listed before have been developed with respect to the dry mode shapes $\delta_i(y, z)$. Nevertheless, according to (8.2), these ones are themselves related to the pseudo-admissible functions $\psi_j(y, z)$, and it is therefore required to go one step further to apply the Rayleigh-Ritz method. As it was done in section 7.3.2.2, a similar expression (7.56) can be found here by writing:

$$\mathcal{T} = \frac{1}{2} \sum_{j=1}^M \sum_{k=1}^M v_{ji} \hat{T}_{jk} v_{ki} \quad \mathcal{U} = \frac{1}{2} \sum_{j=1}^M \sum_{k=1}^M v_{ji} \hat{U}_{jk} v_{ki} \quad (8.27)$$

where M is the number of pseudo-admissible functions considered in (8.2). The kinetic energy term \hat{T}_{jk} has to be calculated by introducing (8.2) successively in (8.22), (8.25) and (8.26). Summing up all these contributions, it is easy to show that:

$$\hat{T}_{jk} = \rho t_p \int_0^l dz \int_0^h f_{jk}(y, z) dy + \sum_{n=1}^{n_h} \rho A_{h,n} \int_0^l f_{jk}(y_n, z) dz + \sum_{n=1}^{n_v} \rho A_{v,n} \int_0^h f_{jk}(y, z_n) dy \quad (8.28)$$

where $f_{jk}(y, z) = \psi_j \psi_k$. On the other hand, performing the same operations for the internal energy term \hat{U}_{jk} finally leads to:

$$\hat{U}_{jk} = D \int_0^l dz \int_0^h f_{jk}(y, z) dy + \sum_{n=1}^{n_h} EI_{h,n} \int_0^l g_{jk}(y_n, z) dz + \sum_{n=1}^{n_v} EI_{v,n} \int_0^h h_{jk}(y, z_n) dy \quad (8.29)$$

but this time, as reported by Shames and Dym [137], the parameters f_{jk} , g_{jk} and h_{jk} are found to satisfy the following mathematical expressions:

$$\begin{aligned} f_{jk}(y, z) &= \frac{\partial^2 \psi_j}{\partial y^2} \left(\frac{\partial^2 \psi_k}{\partial y^2} + \nu \frac{\partial^2 \psi_k}{\partial z^2} \right) + \frac{\partial^2 \psi_j}{\partial z^2} \left(\frac{\partial^2 \psi_j}{\partial y^2} + \nu \frac{\partial^2 \psi_j}{\partial z^2} \right) + 2(1 - \nu) \frac{\partial^2 \psi_j}{\partial y \partial z} \frac{\partial^2 \psi_k}{\partial y \partial z} \\ g_{jk}(y, z) &= \frac{\partial^2 \psi_j}{\partial z^2} \frac{\partial^2 \psi_k}{\partial z^2} \\ h_{jk}(y, z) &= \frac{\partial^2 \psi_j}{\partial y^2} \frac{\partial^2 \psi_k}{\partial y^2} \end{aligned} \quad (8.30)$$

In (8.28) and (8.29), the functions $\psi_j(y, z)$ are defined by (8.12) or (8.15) according to the support conditions of the gate. The detailed expressions of \hat{T}_{jk} and \hat{U}_{jk} are not listed here but

are given in section E.1.1 of Appendix E.1. Finally, if we denote by $[\hat{T}]$ and $[\hat{U}]$ the $(M \times M)$ matrices associated respectively to \hat{T}_{jk} and \hat{U}_{jk} , the Rayleigh quotient (8.20) can be rewritten in the more classical way:

$$R = \frac{\mathcal{U}}{\mathcal{J}} = \left(\sum_{j=1}^M \sum_{k=1}^M v_{ji} \hat{T}_{jk} v_{ki} \right) \div \left(\sum_{j=1}^M \sum_{k=1}^M v_{ji} \hat{U}_{jk} v_{ki} \right) = \frac{\mathbf{v}_i^T [\hat{T}] \mathbf{v}_i}{\mathbf{v}_i^T [\hat{U}] \mathbf{v}_i} \quad (8.31)$$

where \mathbf{v}_i is a $(M \times 1)$ vector containing the coefficients v_{ji} . As it was already stated in section 7.3.2.2, these ones are found by minimizing R , which can be achieved by solving a classical generalized eigenvalues problem:

$$\det([\hat{U}] - \omega_i^2 [\hat{T}]) = 0 \quad ; \quad ([\hat{U}] - \omega_i^2 [\hat{T}]) \mathbf{v}_i = \mathbf{0} \quad (8.32)$$

It is worth noting that the functions f_{jk} , g_{jk} and h_{jk} defining \hat{T}_{jk} and \hat{U}_{jk} are symmetric with respect to j and k . Consequently, this is also the case for the matrices $[\hat{T}]$ and $[\hat{U}]$. However, these ones are not necessarily diagonal and solving analytically (8.32) remains quite complex (but this may be achieved by using a dedicated software like MATLAB for example).

As a conclusion, it appears that the procedure described here above gives an estimation of the vibration frequencies ω_i^2 for the dry stiffened structure. Additionally, (8.32) also provides the coefficients v_{ji} , which, together with (8.12) or (8.15), may be used in (8.2) to estimate the mode shapes $\delta_i(y, z)$. The Rayleigh-Ritz method seems therefore to be a quite appropriate way to derive the modal properties of the dry structure. Nevertheless, as the gate is in contact with water, the next step should be to find the wet vibration frequencies and modes shapes. Even if this would be useful to have a better characterization of the gate behavior during a seism, this operation is not mathematically required for applying the virtual work principle, but this point will be discussed later on.

8.2.3. Numerical validation

In order to corroborate the analytical developments carried out in the previous sections, they can be compared to the solutions obtained through finite element analyses. As the ratio h/l is approximately ranging from 0.5 to 2 for lock gates with a single plating, the validation process has been performed by considering various structures characterized by a h/l ratio varying within this interval. Nevertheless, the results obtained for all cases will not be presented here. To have a quite representative panel, three different structures will be analyzed to more or less cover the extreme and intermediate configurations. These ones are characterized by a h/l ratio of 1, 0.5 and 2 respectively. They are briefly described hereafter:

- Gate 1: this structure has a square plating, with $h = l = 13.1 \text{ m}$ and a thickness t_p of 1.2 cm . It is reinforced by six vertical frames and five horizontal girders. The first ones are regularly placed over the width l , with a spacing of 2.62 m . The disposition of the girders is not regular, as the reinforcement is more important near the bottom of the gate. Some smaller horizontal stiffeners are also present, mainly to avoid buckling of the panel (see Figure 8.7).
- Gate 2: this structure has a rectangular plating, with $h = 8 \text{ m}$, $l = 22.5 \text{ m}$ and $t_p = 1.8 \text{ cm}$. Such dimensions are typically encountered for maritime locks, for which the water level fluctuations are low, but where the width l has to be quite large to allow the travel of

important vessels. The width is regularly divided by ten vertical frames, while only five girders are disposed over the height. In addition, the structure is also reinforced by horizontal flat stiffeners, as depicted on Figure E.1 in section E.1.2 of Appendix E.1.

- Gate 3: this structure has a rectangular shape as well, but the height is this time largely preponderant, as $h = 21\text{ m}$ and $l = 10.5\text{ m}$ only. The plating has a thickness t_p of 1.5 cm . Four vertical frames are placed each 3.5 m , while eight horizontal girders and various smaller stiffeners are distributed over the height (see Figure E.3 in section E.1.3 of Appendix E.1). Such lock configurations may appear on inland waterways, where the difference between the upstream and downstream levels is important.

For each of these three gates, two different situations have to be treated, as they may be supported at the bottom or not. However, in all cases, the material properties listed in Table 8.2 will be used, which more or less corresponds to the characteristics of a mild steel.

| | | |
|---------------------|--------|----------------------|
| Young modulus | E | 265 GPa |
| Poisson coefficient | ν | 0.3 |
| Mass density | ρ | 7850 kg/m^3 |

Table 8.2. Material properties for each lock gate

Of course, apart from the three gates described above, the validation was also performed by using other intermediate configurations that are not reported here. Furthermore, to avoid a too fastidious presentation, only the first gate will be considered in the remaining parts of this section. The results related to the second and third configurations may be consulted in sections E.1.2 and E.1.3 of Appendix E.1 respectively.

8.2.3.1. Case of a gate supported at the bottom

The situation where the gate is supported at the bottom of the lock is first considered. It is worth recalling that in such a case, the displacements in the x direction are forbidden at the bottom even if they are negative. As already discussed in section 8.1.2, doing so is not strictly realistic because a sill does not impose this kind of restraint (this point will be investigated later on, in section E.3.1). The other boundary conditions are those listed in section 8.1, but it should also be mentioned that the displacements in the z direction are not simultaneously forbidden along the edges $z = 0$ and $z = l$ (see Figure 8.1) because the gate is considered as being free to bent without suffering any transverse restrain.

| | $h_w\text{ (m)}$ | $t_w\text{ (m)}$ | $h_f\text{ (m)}$ | $t_f\text{ (m)}$ |
|-----------------------|------------------|------------------|------------------|------------------|
| Horizontal girders | 0.98 | 0.02 | 0.4 | 0.025 |
| Vertical frames | 0.98 | 0.02 | 0.5 | 0.025 |
| Horizontal stiffeners | 0.21 | 0.006 | 0 | 0 |

Table 8.3. Geometrical parameters for gate 1

To obtain numerically the modal properties of gate 1, the pre-processor PATRAN is first used to realize a finite element model of the structure. The plating is modeled by using isoparametric quadrilateral CQUAD shell elements with four grid points, while classical linear CBAR beam elements are used for the reinforcing system¹⁵. The dimensions characterizing the cross-sections are listed in Table 8.3, with the notations introduced on Figure 8.1. The material is assumed to have a linear elastic behavior defined by the parameters given in Table 8.2.

¹⁵ See the Nastran reference manual [114] for additional information on these elements.

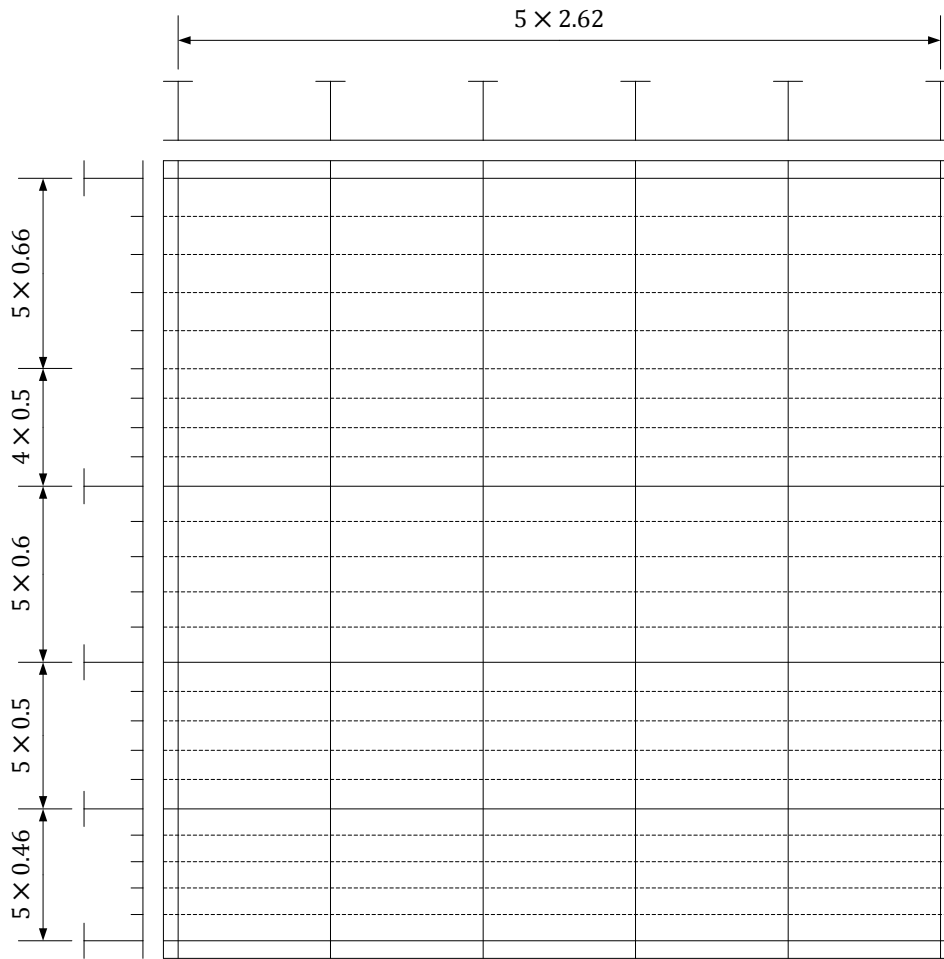


Figure 8.7. Structural configuration and main dimensions (*m*) of gate 1

The finite element software NASTRAN is then used to perform a modal analysis of the gate. This leads to a numerical estimation of its dry frequencies and mode shapes. In order to check the validity of the present analytical developments, the solutions obtained by the Rayleigh-Ritz method will be compared to those given by NASTRAN.

The modal analysis realized with NASTRAN shows that the gate has only two dominant global modes and a great number of local ones, which is a quite typical result for this kind of stiffened structures. The natural frequencies derived by the simplified procedure of section 8.2.2 and the values given by NASTRAN are listed in Table 8.4 for these two first modes of vibration. An estimation made by LS-DYNA is also provided in this table. It can be seen that the agreement is quite satisfactory. This is particularly true if the results of LS-DYNA are considered, as the maximal relative error calculated according to (7.58) does not exceed 3 %. The discrepancy with NASTRAN is a bit more important, as an error of 12 % may be reached this time.

| Mode | Frequency (Hz) | | | Error (%) | |
|------|----------------|---------|------------|-----------|---------|
| | NASTRAN | LS-DYNA | Analytical | NASTRAN | LS-DYNA |
| 1 | 19.22 | 20.27 | 20.84 | 8.41 | 2.81 |
| 2 | 37.78 | 40.91 | 42.26 | 11.87 | 3.33 |

Table 8.4. Comparison of the natural frequencies obtained numerically and analytically

From Table 8.4, it transpires that the analytical approach tends to overestimate the natural frequencies. This observation was already made when dealing with unstiffened plates in Chapter 7 and may be justified mathematically. Indeed, as demonstrated by Shames and Dym

[137], the Rayleigh-Ritz method always gives an upper estimation of the eigenvalues ω_i^2 , which partially justifies the results of Table 8.4. Some other reasons may also explain why the analytical values are too high. This will be discussed later, in section 8.2.3.3.

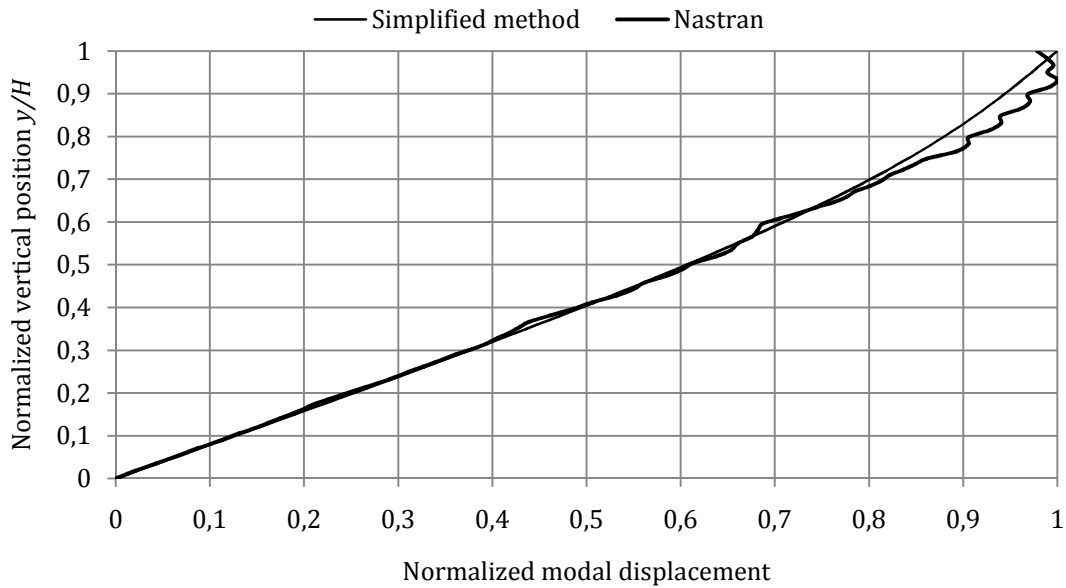


Figure 8.8. Comparison of the first mode shapes obtained numerically and analytically

In order to compare the numerical and analytical eigenmodes of vibration, it is suggested to look at the displacements in the plane $z = l/2$ (called π_1 on Figure 7.8). The results are plotted on Figure 8.8 and on Figure 8.9 (the meaning of the red point placed on this picture will be explained later), from which it can be concluded that the agreement is rather good. In the horizontal plane $y = h$ (called π_2 on Figure 7.8), the shape is very closed to a sinusoid with only one half-wave, such as the one reported on Figure 7.9b.

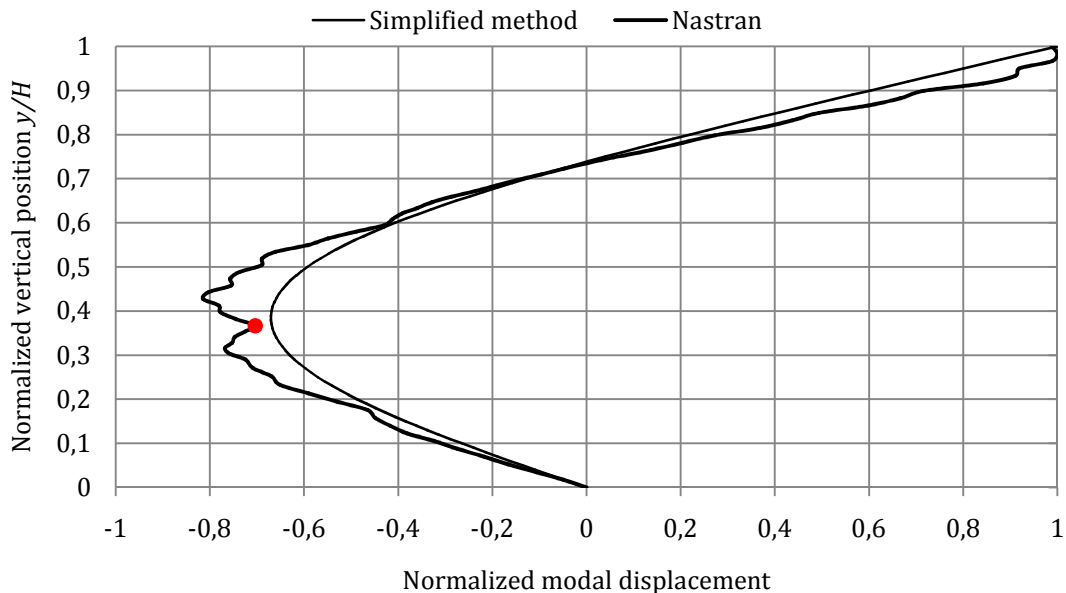


Figure 8.9. Comparison of the second mode shapes obtained numerically and analytically

8.2.3.2. Case of a gate free at the bottom

Let us now analyze the situation if the structure is not resting against a sill. The boundary conditions are the same as in section 8.2.3.1, except that no restraints have to be applied along

the line $x = 0$ (Figure 8.1), where the displacements in the x direction are totally free. Such boundary conditions are more realistic than in the previous case, as many gates do not have any support near the bottom of the lock.

The main dimensions of the structure are still those depicted on Figure 8.7 and it is assumed that the cross-sectional properties of Table 8.3 are still valid. This choice is mainly motivated for practical reasons, but in reality, the stiffening system of a gate resting against a sill will probably be lighter than the one characterizing a structure with no support at the bottom. However, for this validation process, it seems sufficient to keep the same geometrical and mechanical characteristics as in the previous case. Consequently, the modal analysis will be performed with the same finite element model as before (after having changed the boundary conditions).

| Mode | Frequency (Hz) | | | Error (%) | |
|------|----------------|---------|------------|-----------|---------|
| | NASTRAN | LS-DYNA | Analytical | NASTRAN | LS-DYNA |
| 1 | 19.17 | 19.99 | 21.3 | 11.11 | 6.54 |
| 2 | 23.33 | 25.27 | 26 | 11.43 | 2.89 |

Table 8.5. Comparison of the natural frequencies obtained numerically and analytically

Here again, the modal analysis leads to the conclusion that the gate has only two main global modes, which are characterized by the frequencies of Table 8.5. The conclusions drawn in section 8.2.3.1 are still holding for the present case: the analytical procedure tends to overestimate the stiffness of the structure, but the agreement with the numerical values is kept satisfactory. Indeed, the relative errors with respect to the solutions of NASTRAN and LS-DYNA do not exceed 11 % and 3 %, which seems to be sufficient for a first estimation. Moreover, by comparing the values of Table 8.4 and Table 8.5, it appears that the frequencies are lower in the second case, which seems to be coherent as the structure is more flexible if it is not supported at the bottom.

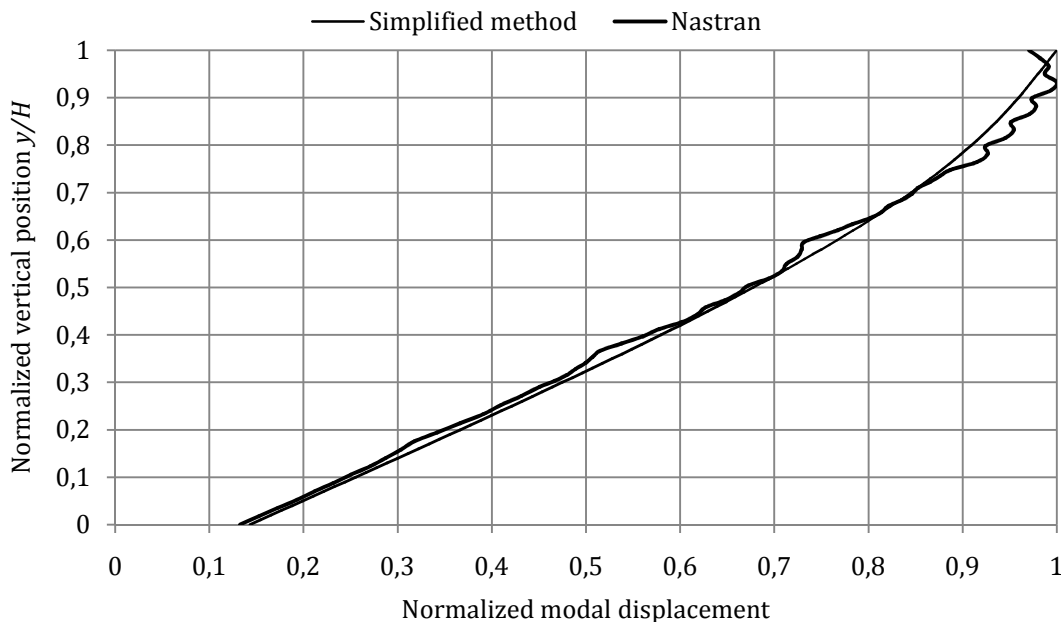


Figure 8.10. Comparison of the first mode shapes obtained numerically and analytically

The first mode shape calculated by NASTRAN is compared to the analytical solutions on Figure 8.10. The same is done for the second eigenmode on Figure 8.11. It can be seen that the agreement on the deformation patterns in the plane π_1 is quite good. In the horizontal plane

π_2 (see Figure 7.8), the numerical profile is very close to the sinusoid predicted by the analytical approach.

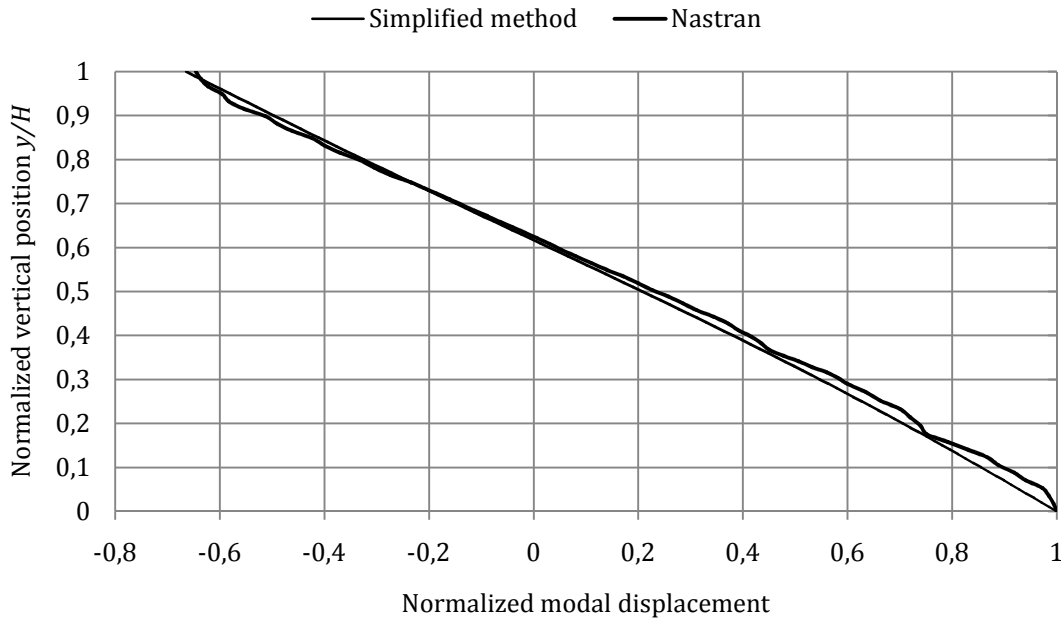


Figure 8.11. Comparison of the second mode shapes obtained numerically and analytically

Even if the analytical calculation of the dry frequencies appears to be sufficiently reasonable, it seems however important to provide some more indications to explain why it tends to overestimate the numerical values. Doing so may be useful for an eventual future improvement of the present simplified method. This is precisely the goal of the next section.

8.2.3.3. Discussion of the results

From all the results presented here above, it can be concluded that the Rayleigh-Ritz method provides a satisfactory evaluation of the modal properties characterizing the stiffened gate. Nevertheless, one can first argue that the agreement with the numerical simulations largely depends on the choice of the pseudo-admissible functions $\psi_j(y, z)$ in (8.2), which do not satisfy all the boundary conditions. In the present case, this is only partially true, because the global mode shapes are quite correctly estimated if $\psi_j(y, z)$ is given by (8.12) or (8.15). Moreover, derived an analytical solution was also derived by considering for $\psi_j(y, z)$ the eigenmodes of an unstiffened plate defined in (7.22), but this led to results that were very close to the ones presented before.

So a poor choice of $\psi_j(y, z)$ does not seem to justify the observed discrepancies. Another explanation may lie in the evaluation of the inertia affected to the stiffening elements. Indeed, according to (8.24), it is assumed that the beams are bent around the neutral fiber $n-n$ of the plating, but this is not necessarily true. One can also imagine that bending occurs around the gravity center G of the T-shaped cross-section depicted on Figure 8.1. With such a situation, the inertia is no longer given by (8.24) but has to be corrected to account for the eccentricity e , as shown on Figure 8.12. The bending rigidities characterizing the beams and the plating are this time given by:

$$EI_h^* = E(I_h - e^2 A_h) \quad ; \quad D^* = D + e^2 \frac{Et_p}{1 - \nu^2} \quad (8.33)$$

where E is the Young modulus, A_h is the cross-sectional area and $D = Et_p^3/12(1 - \nu^2)$ is the flexional rigidity of the plate around its neutral fiber. In comparison with the situation of Figure 8.6, it clear from (8.33) that the beam rigidity is reduced while the plating stiffness is increased. Nevertheless, as t_p is quite small, there is no compensation, which means that the model of Figure 8.6 is stiffer than the one of Figure 8.12. As a consequence, the vibration frequencies calculated by assuming that bending takes place around G will be lower in this last case.

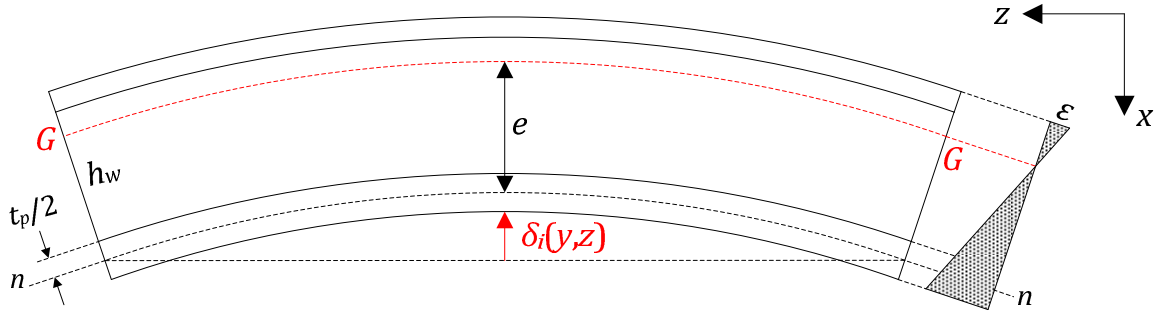


Figure 8.12. Deformation if bending occurs around the gravity center

As a conclusion, a more probable reason to justify the higher values found analytically for the frequencies is that bending does not exactly take place around the $n-n$ axis. In fact, each cross-section appears to rotate around an undetermined point located somewhere between $n-n$ and G , which seems to be confirmed if by looking at the mode shapes. Indeed, for the case of bending around the $n-n$ line, the dominant mode shape in the plane π_1 should be the one depicted on Figure 8.13a, with a quite regular deformation of the plating. On the contrary, if G is the rotation point, then each reinforcing element will deform in its plane, as is the plating was simply clamped along the connection lines. In this case, it is more likely to adopt the pattern represented on Figure 8.13b.

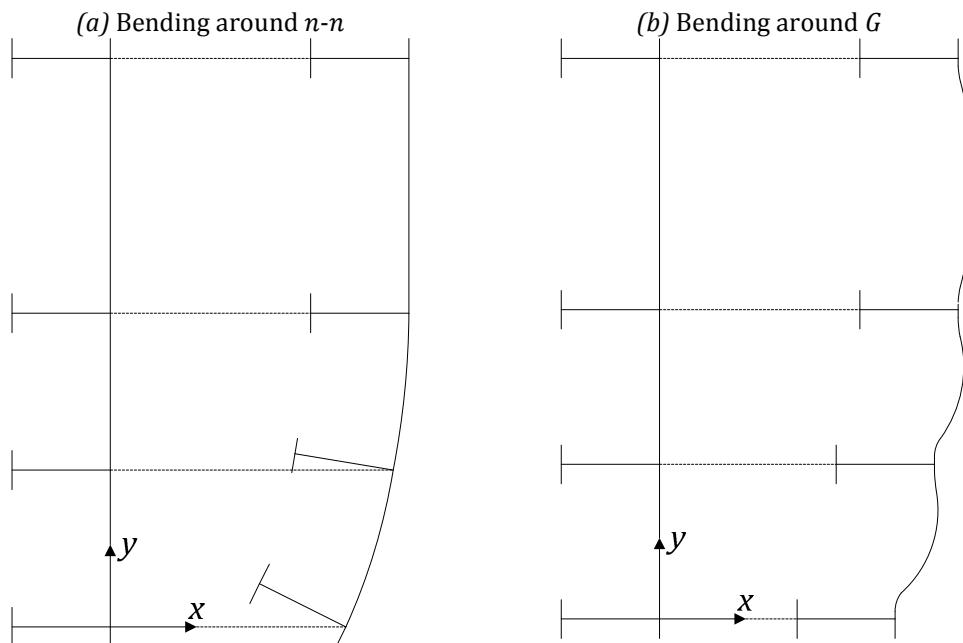


Figure 8.13. Bending situations

The small oscillations visible on Figure 8.8 to Figure 8.11 confirm that the reinforcing elements have a local influence on the deformation profile characterizing the plating. This is particular true from Figure 8.9, where the strong indentation occurring near the red point

shows that the behavior of the horizontal girder positioned there is preponderant. As a consequence, the mode shape seems to take an intermediate profile between the ones depicted on Figure 8.13a and b.

From all the previous indications, it can be concluded that it is not easy to find a rational definition for the bending rigidity affecting the reinforcing elements. In the present simplified approach, this latter is calculated it by considering the neutral axis $n-n$. This has the main advantage of simplifying a little bit the analytical calculations, but such an assumption is not necessarily realistic as it tends to overestimate the global stiffness of the structure. Nevertheless, as the agreement with the numerical results is quite satisfactory, we this hypothesis is kept in the next section to perform the dynamic analysis of lock gates.

8.3. Dynamic analysis of lock gates

The modal analysis performed previously allows to know the vibration properties of lock gates with a single plating reinforced by an orthogonal stiffening system. The next step is now to analyze the problem depicted on Figure 8.2b, where a lock chamber is submitted to an earthquake having a longitudinal acceleration component denoted by $\ddot{X}(t)$. The goal is here to estimate the hydrodynamic pressure acting on the structure in such a situation.

Before starting the dynamic analysis, one should first try to derive the vibration properties of the immersed gate, as it was done in Chapter 7 for an unstiffened plate. However, as detailed in section E.2.1 of Appendix E.2, this is not really useful in the present case. In fact, using the wet or the dry modes is equivalent. Consequently, in order to simplify the dynamic analysis of a lock gate, one can avoid to calculate its wet modal properties. Nevertheless, this operation remains useful to have a more complete insight on the seismic behavior characterizing the immersed structure, as it allows for an extensive study of the fluid-structure interaction (see section 7.3.3.3 and Appendix D.1). This is the main reason why they were introduced in Chapter 7.

8.3.1. Equilibrium equation

For the isolated plating elements that are far away from the reinforcing elements, it is clear that the equilibrium equation (7.65) may still be applied without any restriction. However, this is not true near the stiffeners, where the plating may be seen as being locally submitted to some additional forces. Adopting the same philosophy as the one followed in 7.4.1, one can simply express the translational equilibrium of the plating along the horizontal x axis by adapting (7.65) to account for the supplementary actions of the beams.

Let us try first to apply this methodology to the vertical stiffeners occupying the discrete positions z_n . The aim is to evaluate the total resulting force $f_{v,n}(y, z, t)$ that they exert on the plating (see Figure 8.14) in the x direction when the gate is submitted to the earthquake. In the present simplified procedure, it is sufficient to consider the action of the inertial, shearing and damping forces. From the classical theory of beams, it comes immediately that the two first contributions are given by:

$$\rho A_{v,n}(\ddot{u} + \ddot{X}) + EI_{v,n} \frac{\partial^4 u}{\partial y^4} \quad (8.34)$$

where, as already mentioned before, $A_{v,n}$ et $I_{v,n}$ respectively denote the area and inertia of the cross-section characterizing the vertical frame located in $z = z_n$. Furthermore, proceeding in a similar manner as in section 7.4.1, the damping forces may be seen as being proportional to the mass and to the stiffness of the vertical frames. With such an assumption, it is easy to show that they are simply given by:

$$\alpha \rho A_{v,n} \dot{u} + \beta EI_{v,n} \frac{\partial^4 u}{\partial y^4} \quad (8.35)$$

where α and β are the mass and stiffness damping coefficients. For convenience, it is assumed here that these two parameters are the same as those previously encountered in 7.4.1, but this has not necessarily to be the case. The formulae can be easily adapted to work with coefficients that are different for the reinforcing elements than for the plating.

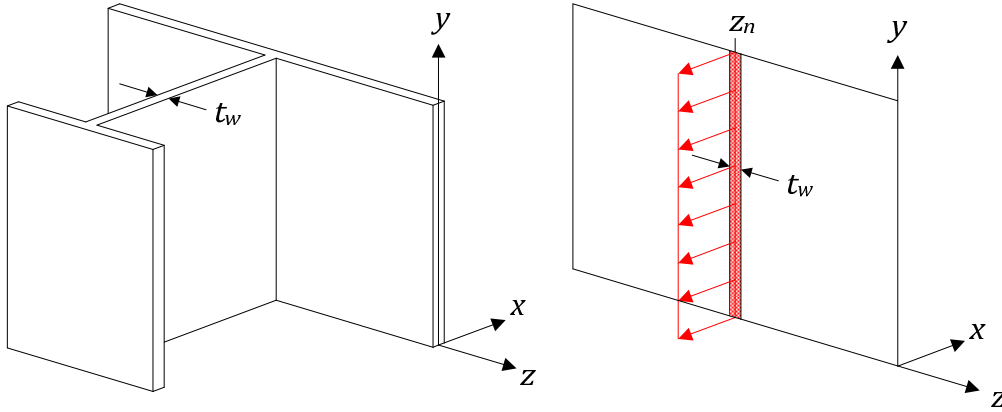


Figure 8.14. Substitution of a vertical stiffener by an equivalent force

It is obvious that (8.34) and (8.35) correspond to line loads, which is not really convenient for writing the plate equilibrium. For this reason, one may try to convert them into pressures. To do so, these forces are assumed to be uniformly distributed over the web thickness t_w , but this hypothesis is purely arbitrary. Another choice could be to spread these line loads over a certain collaborating length (which, according to Dehousse and Deprez [39], can be chosen as the flange length h_f), but one may also resort to the use of Dirac functions, as explained by Laura [92] for example. Nevertheless, it seems that there is no real satisfactory way for integrating rigorously (8.34) and (8.35) into the equilibrium equation of the plate. So pursuing the hypothesis of smearing (8.34) and (8.35) over t_w , then it is finally found that $f_{v,n}(y, z, t)$ has the following expression:

$$f_{v,n}(y, z, t) = \mathbb{H}_n(z) \left[\rho A_{v,n} (\ddot{u} + \ddot{X}) + EI_{v,n} \frac{\partial^4 u}{\partial y^4} + \alpha \rho A_{v,n} \dot{u} + \beta EI_{v,n} \frac{\partial^4 \dot{u}}{\partial y^4} \right]_{z=z_n} \quad (8.36)$$

in which the displacements, speeds and accelerations have to be evaluated at the particular location $z = z_n$. The term $\mathbb{H}_n(z)$ is nothing else than a truncated form of the Heaviside function:

$$\begin{aligned} \mathbb{H}_n(z) &= 1/t_w & \text{if } z \in [z_n - t_n/2; z_n + t_n/2] \\ \mathbb{H}_n(z) &= 0 & \text{if } z \notin [z_n - t_n/2; z_n + t_n/2] \end{aligned} \quad (8.37)$$

The previous developments can be extended to the horizontal stiffeners without any difficulty. For an element located in $y = y_n$, this leads to a total resulting force denoted by $f_{h,n}(y, z, t)$ and acting on the plating in horizontal x direction:

$$f_{h,n}(y, z, t) = \mathbb{H}_n(y) \left[\rho A_{h,n} (\ddot{u} + \ddot{X}) + EI_{h,n} \frac{\partial^4 u}{\partial z^4} + \alpha \rho A_{h,n} \dot{u} + \beta EI_{h,n} \frac{\partial^4 \dot{u}}{\partial z^4} \right]_{y=y_n} \quad (8.38)$$

As a last step, (8.36) and (8.38) may be inserted in equation (7.61) expressing the equilibrium of the plating. Gathering the contributions $f_{h,n}(y, z, t)$ and $f_{v,n}(y, z, t)$ coming from all the n_h and n_v horizontal and vertical stiffeners, the following result is obtained:

$$\rho t_p (\ddot{u} + \ddot{X}) + f_d + D \left(\frac{\partial^4 u}{\partial y^4} + 2 \frac{\partial^4 u}{\partial y^2 \partial z^2} + \frac{\partial^4 u}{\partial z^4} \right) + \sum_{n=1}^{n_h} f_{h,n} + \sum_{n=1}^{n_v} f_{v,n} = -p \quad (8.39)$$

in which $f_d(y, z, t)$ denotes the damping forces acting on the plating and already detailed in 7.4.1. This last expression may be seen as the dynamic equilibrium equation of a stiffened

plate. From the definition (8.37) of the Heaviside function, it is obvious that it degenerates into (7.61) in the regions far enough from the reinforcing stiffeners.

8.3.2. Virtual work principle

The philosophy that will now be followed to study the dynamic behavior of a lock gate is formally similar to what has already been done in section 7.4.2. Once again, it is postulated that the displacements $v(y, z, t)$ and $w(y, z, t)$ occurring in the plane of the gate are related to the transverse ones by (7.66). Furthermore, due to the analytical results detailed in 8.2, the out-of-plane component may be decomposed by using the dry modes shapes $\delta_i(y, z)$ given by (8.2):

$$u(y, z, t) = \sum_{j=1}^N q_j(t) \delta_j(y, z) \quad (8.40)$$

where N is the number of dry modes considered in the summation process. By comparing (8.40) with (7.67), it can be noticed that these two equations are dissimilar, as the wet modes $\Delta_i(y, z)$ are not used this time. This choice is justified in the section E.2.1 of Appendix E.2, where it is shown that working with the dry or wet properties is equivalent. Moreover, by looking at (8.2) and (8.40), it is clear that working with $\Delta_i(y, z)$ would add a new summation term, which turns out to be very fastidious.

According to the virtual work principle, equilibrium is guaranteed by equating the internal and external virtual works performed during any kinematically admissible displacement $\delta u(y, z, t)$. In the present case, this theorem has to be applied carefully because the functions $\psi_j(y, z)$ used in (8.2) are only pseudo-admissible. As discussed in section E.2.2 of Appendix E.2, this may have some consequences on the exactness of the solution and keeping this particularity in mind is quite important. In such a situation, the classical way to proceed is to choose a virtual field $\delta u(y, z, t)$ that is homothetic to the sought approximate solution $u(y, z, t)$. So according to (8.40), one should have the following definition:

$$\delta u(y, z, t) = \sum_{k=1}^N \delta q_k(t) \delta_k(y, z) \quad (8.41)$$

As the dry modes are reputed to be kinematically compatible, this is also the case for $\delta u(y, z, t)$ and (8.41) may therefore be used in conjunction with (8.40) in the virtual work principle. These operations are detailed hereafter.

8.3.2.1. Internal virtual work

The total virtual amount of internal energy dissipated by the gate has three different contributions. The first one is of course coming from the plating, while the second and third ones are respectively due to the horizontal and vertical reinforcing elements, i.e.:

$$\delta W_{int} = \delta W_p + \delta W_h + \delta W_v \quad (8.42)$$

As the plating is bent around its mean surface, it is obvious that (7.71) is still holding, so this formula can be directly reused to evaluate δW_p . Concerning the stiffeners, it is easy to show that the deformation energies associated to these beams are simply given by:

$$\delta W_h = \sum_{n=1}^{n_h} EI_{h,n} \left[\int_0^l \frac{\partial^2 u}{\partial z^2} \frac{\partial^2 \delta u}{\partial z^2} dz \right]_{y=y_n} ; \quad \delta W_v = \sum_{n=1}^{n_v} EI_{v,n} \left[\int_0^h \frac{\partial^2 u}{\partial y^2} \frac{\partial^2 \delta u}{\partial y^2} dy \right]_{z=z_n} \quad (8.43)$$

Furthermore, considering N mode shapes in (8.40) and M pseudo-admissible functions in (8.2), one may write:

$$u(y, z, t) = \sum_{j=1}^N q_j(t) \sum_{r=1}^M v_{rj} \psi_r(y, z) ; \quad \delta u(y, z, t) = \sum_{k=1}^N \delta q_k(t) \sum_{s=1}^M v_{sk} \psi_s(y, z) \quad (8.44)$$

If (8.44) is introduced in (7.71) and (8.43), then it is possible to express δW_{int} under a more formal decomposition:

$$\delta W_{int} = \sum_{k=1}^N \delta q_k \sum_{j=1}^N q_j U_{jk} ; \quad U_{jk} = \sum_{r=1}^M \sum_{s=1}^M v_{rj} \hat{U}_{rs} v_{sk} \quad (8.45)$$

where the matrix $[\hat{U}]$ was already encountered in (8.29). It is worth noting that the dominant terms in (8.42) are δW_h and δW_v , which means that the main contribution to the internal energy is coming from the reinforcing elements. This can be easily understood with help of the comments made in section 8.2.3.3, where it was pointed out that the inertias $I_{h,n}$ and $I_{v,n}$ characterizing the beam cross-sections were slightly overestimated. Due to the relation given in (8.43), this may also be the case for δW_h and δW_v , so it is to fear that the internal energy tends to be overestimated while applying the virtual work principle. Concerning the contribution δW_p provided by the plating, this one is attempted to be relatively modest, particularly because of the small values of the thickness t_p .

8.3.2.2. External virtual work

The external dissipation δW_{ext} is due to the work performed by several actions during the virtual displacement $\delta u(y, z, t)$ and can be evaluated by proceeding in a very similar manner than in section 7.4.2.2, so the all derivation process will not be described here. In fact, referring to (8.39), it can be seen that various terms have to be dealt with:

- The external work performed by the inertial forces acting on the plating: these forces correspond to the first term in (8.39) and have the following contribution to δW_{ext} :

$$- \int_0^h \int_0^l \rho t_p (\ddot{u} + \ddot{X}) \delta u(y, z, t) dy dz \quad (8.46)$$

- The external work associated to the damping forces that are proportional to the mass and to the stiffness of the plating. These forces are designated by $f_d(y, z, t)$ in (8.39) and it is obvious that they have the subsequent contribution to δW_{ext} :

$$- \int_0^h \int_0^l f_d(y, z, t) \delta u(y, z, t) dy dz \quad (8.47)$$

- The external work of the forces modeling the action of the horizontal reinforcing elements on the plating, which only corresponds to a part of $f_{h,n}$ in (8.39). In fact, going back to the

definition (8.38) of $f_{h,n}$, it appears that it was already accounted for the stiffness term $EI_{h,n}\partial^4 u/\partial z^4$ while dealing with the internal energy δW_h in equation (8.43). Consequently, the contribution to δW_{ext} is simply:

$$-\sum_{n=1}^{n_h} \left[\int_0^l \left(\rho A_{h,n}(\ddot{u} + \ddot{X} + \alpha\dot{u})\delta u + \beta EI_{h,n} \frac{\partial^2 \dot{u}}{\partial z^2} \frac{\partial^2 \delta \dot{u}}{\partial z^2} \right) dz \right]_{y=y_n} \quad (8.48)$$

- The external work of the forces coming from the vertical stiffeners, which is only a part of $f_{v,n}$ in (8.36). As it was already accounted for the term $EI_{v,n}\partial^4 u/\partial y^4$ in (8.36) through δW_v , the contribution is as follows:

$$-\sum_{n=1}^{n_v} \left[\int_0^h \left(\rho A_{v,n}(\ddot{u} + \ddot{X} + \alpha\dot{u})\delta u + \beta EI_{v,n} \frac{\partial^2 \dot{u}}{\partial y^2} \frac{\partial^2 \delta \dot{u}}{\partial y^2} \right) dy \right]_{y=y_n} \quad (8.49)$$

The last term to consider in (8.39) is the total hydrodynamic pressure $p(y, z, t)$. As mentioned earlier, the analytical formulae giving the flexible and rigid parts of $p(y, z, t)$ are exactly the same as those encountered for a unstiffened plate. Equations (7.7) and (7.8) are therefore still valid when dealing with a lock gate, which implies that the external work associated to the pressure may still be derived by applying (7.78).

So finally, the total virtual work performed by all the external forces acting on the structure has to be found by summing up equations (8.46) to (8.49) with (7.78). As soon as this operation is completed, it is still required to develop explicitly δW_{ext} as a function of the unknown coefficient $q_j(t)$ by introducing (8.44) in all of the above-mentioned contributions. Doing so is quite fastidious but once all the calculations are done, δW_{ext} can be written in the same condensed form than (7.80) in which T_{jk} , W_{jk} and V_k are evaluated by applying the following results:

$$T_{jk} = \sum_{r=1}^M \sum_{s=1}^M v_{rj} \hat{T}_{rs} v_{sk} \quad ; \quad W_{jk} = \sum_{r=1}^M \sum_{s=1}^M v_{rj} \hat{W}_{rs} v_{sk} \quad ; \quad V_k = \sum_{s=1}^M v_{sk} \hat{V}_k \quad (8.50)$$

where the matrix $[\hat{T}]$ was introduced previously in the Rayleigh-Ritz method. As for the dynamic analysis of an unstiffened plate performed in section 7.4, the term W_{jk} represents the fluid-structure coupling and has an expression that is formally similar to (7.81). The matrix $[\hat{W}]$ has not been encountered yet but is defined by (see section E.2.3 of Appendix E.2):

$$\hat{W}_{rs} = \sum_{n=1}^{+\infty} \sum_{m=0}^{+\infty} c_{mn} \hat{I}_{mn}^{(r)} \hat{I}_{mn}^{(s)} \quad ; \quad \hat{I}_{mn}^{(r)} = \int_0^{h_s} \int_0^l \psi_r(y, z) \cos(\alpha_n y) \cos(\bar{\gamma}_m z) dy dz \quad (8.51)$$

The last term V_k in (8.50) gather some contributions of the external forces. The vector \hat{V} may be derived by adding the following result:

$$-\sum_{n=1}^{n_h} \rho A_{h,n} \int_0^l \psi_s(y_n, z) dz - \sum_{n=1}^{n_v} \rho A_{v,n} \int_0^h \psi_s(y, z_n) dy \quad (8.52)$$

to equation (7.82), in which $\Delta_k(y, z)$ has of course to be replaced by $\psi_s(y, z)$. Even if the derivation is rather fastidious, all the previous results provide an analytical way to evaluate

the external virtual work δW_{ext} . Here again, the main contribution comes from the inertial forces acting on the stiffening system.

8.3.2.3. Global equilibrium equation

With the developments presented in the two previous sections, δW_{ext} and δW_{int} can finally be equated, which reflects the global equilibrium of the gate during the seismic event. Doing so, one gets an equation that is strictly similar to (7.85):

$$([T] - [W])\ddot{\mathbf{q}}(t) + (\alpha[T] + \beta[U])\dot{\mathbf{q}}(t) + [U]\mathbf{q}(t) = \mathbf{V}\ddot{\mathbf{X}}(t) \quad (8.53)$$

but where $[U]$, $[T]$, $[W]$ and \mathbf{V} have the definitions proposed in (8.45) and (8.50) respectively. For a given time evolution of $\ddot{\mathbf{X}}(t)$, (8.53) may be solved by applying the Newmark integration method. This leads to the coefficients $\mathbf{q}(t)$, which allows to rebuild the displacement $u(y, z, t)$ with help of (8.40) and provides a complete solution to the problem.

It is worth bearing in mind that the solution obtained by the previous approach is not theoretically satisfying, as it does not verify the local equilibrium equation and violates the static boundary conditions along the free edges. Moreover, as discussed in section 8.2.3.3, the method tends to overestimate the stiffness of the gate. These restrictions are important, as they may have some implications on the exactness of the results.

8.3.3. Numerical validation

The goal is now to check if the analytical procedure detailed here above may lead to a reasonable approximation of the total hydrodynamic pressure induced on a lock gate during a seism. In order to have a practical example, it is proposed here to work again with the first gate presented in 8.2.3 and depicted on Figure 8.7, with the sectional properties of Table 8.3 and the material characteristics of Table 8.2. Of course, many other configurations were also tested, but for conciseness, all the results are not reported here. The parameters defining the fluid are still those listed in Table 7.1.

The finite element model has the same particularities as the ones detailed in section 7.4.3.1. The two gates delimiting the lock chamber are represented together with the fluid enclosed between them. Here again, the liquid is modeled as an elastic medium and the fluid-structure interaction is provided through the contact algorithm of LS-DYNA.

Concerning the gate, the plating is modeled with Belytschko-Tsay shell elements [66]. To reduce a little bit the size of the model, the reinforcing system is not explicitly represented with shell elements, but rather with Hughes-Liu beams [66]. The structure is stabilized by the boundary conditions described in 8.1.2 and its supports are submitted to the longitudinal acceleration of Figure 7.13. Two different numerical simulations have to be performed to account for the presence or the absence of a sill.

The lock chamber is assumed to have a total length L of 50 m and is filled with water at a level h_s of 8 m. Of course, a length of 50 m does not seem realistic for a traditional lock configuration, but it is worth recalling that the conclusions of sections D.1.2.3 and D.2.2.2 are still valid here. Consequently, as $L \geq 3h_s$, all the results presented hereafter are also perfectly valid for any lock chamber with a more important longitudinal extension than the one considered here.

8.3.3.1. Case of a gate supported at the bottom

To corroborate the analytical results derived by using the virtual work principle, they will be confronted to those obtained numerically. As a matter of validation, the idea is to compare the total resulting hydrodynamic force $F(t)$ applied on the wall during the seism, in excess to the hydrostatic pressure. The definition of $F(t)$ is given in (7.90) and the results are plotted on Figure 8.15 for the situation where gate 1 is resting against a sill. These curves are obtained with LS-DYNA by imposing a 4 % damping on the two first modes of vibration.

| | Analytical solution F_T | Numerical solution F_N | Rigid solution F_R | Relative difference $ 1 - F_T/F_N $ | Ratio F_T/F_R |
|---------------|---------------------------|--------------------------|----------------------|-------------------------------------|-----------------|
| Maximal value | 1114.6 kN | 1382.8 kN | 375.2 kN | 19.4 % | 2.9 |
| Minimal value | -1259.9 kN | -1417.6 kN | -517.1 kN | 11.1 % | 2.5 |

Table 8.6. Comparison between the extreme values for gate 1 supported by a sill

It is worth recalling that if a sill is present, the boundary conditions imposed at the bottom of the lock chamber are such that both the positive and negative displacements along the x axis are prohibited at the support. As discussed in section 8.1.2, this is not necessarily coherent as only the positive translations should be blocked.

Nevertheless, as the analytical solutions have been developed under the hypothesis of a full translational restraint, it is probably interesting to check their validity for such a boundary condition. The case of more realistic restrictions will be investigated later on.

As shown by Figure 8.15, there is a quite good agreement between the numerical and analytical results. Unfortunately, from this analysis, it transpires that the simplified approach tends to underestimate the hydrodynamic pressure. A reason could lie in a wrong evaluation of the structural stiffness (as explained in 8.2.3.3), which can lead to a poor approximation of the proper accelerations $\ddot{u}(y, z, t)$. Because of (7.8), this will also be the case for the flexible hydrodynamic pressure.

This tendency is confirmed by the extreme values reported in Table 8.6, where it is shown that the analytical prediction of the maximal resulting pressure is more or less 20 % lower than the numerical one. The agreement is better for the minimal values, with a relative difference of 11 %. Such discrepancies seem however to remain quite acceptable for a pre-design stage.

Another interesting comparison made in Table 8.6 is related to the flexibility of the gate. If the structure were considered as being perfectly rigid, then the total maximal resulting pressure derived in this case would be more or less 3 times lower than the one obtained by accounting for the flexibility. This points out the necessity of considering the real stiffness of lock gates to perform the seismic design.

8.3.3.2. Case of a gate free at the bottom

Let us now investigate the situation where no sill is present. In this case, the gate is free at the bottom and no restriction is made on the positive or negative translations along the x axis.

The analytical and numerical curves showing the evolution of the total hydrodynamic force $F(t)$ are represented on Figure 8.16, from which the agreement appears to be quite satisfactory, even if discrepancies are sometimes noticeable.

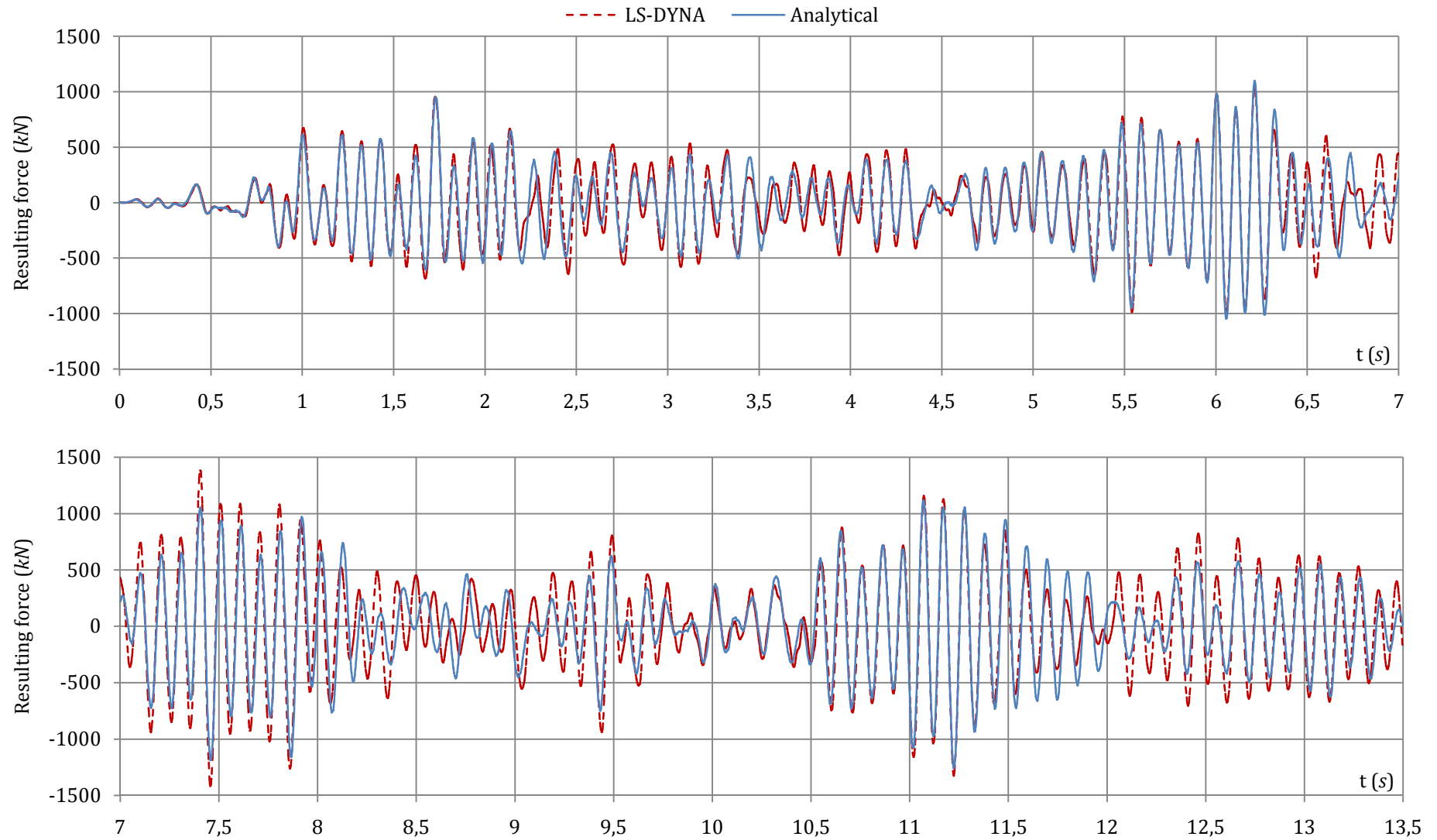


Figure 8.15. Analytical and numerical evolution of the resulting hydrodynamic pressure on gate 1 supported by a sill

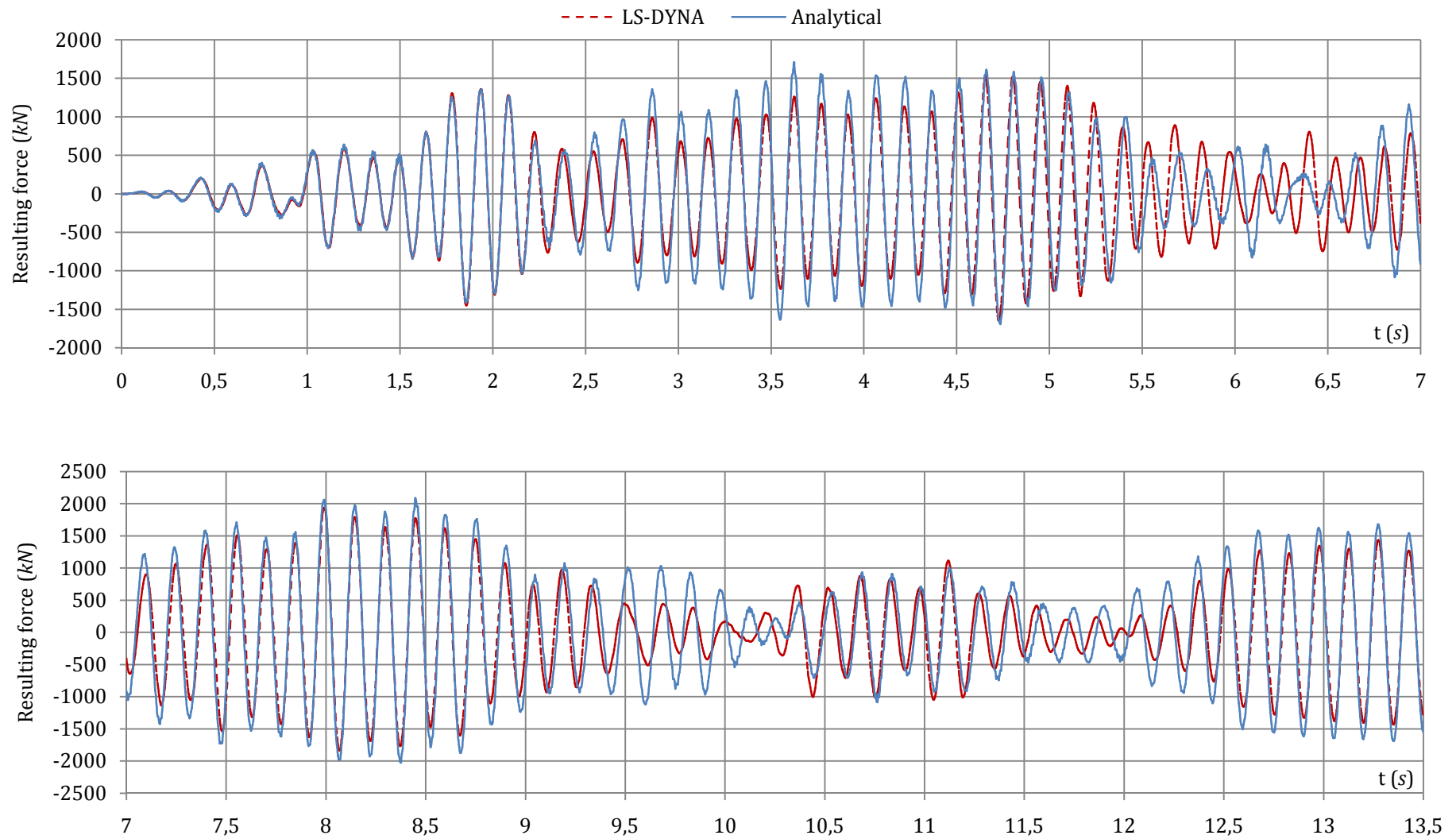


Figure 8.16. Analytical and numerical evolution of the resulting hydrodynamic pressure on gate 1 free at the bottom

Another observation from Figure 8.16 is that the simplified approach tends this time to be conservative, which is confirmed by the values of Table 8.7. Indeed, it can be seen from this table that the analytical prediction of the maximal pressure is more or less 8 % higher than the one given by LS-DYNA.

| | Analytical solution F_T | Numerical solution F_N | Rigid solution F_R | Relative difference $ 1 - F_T/F_N $ | Ratio F_T/F_R |
|---------------|---------------------------|--------------------------|----------------------|-------------------------------------|-----------------|
| Maximal value | 2085.4 kN | 1936.1 kN | 375.2 kN | 7.7 % | 5.6 |
| Minimal value | -2020.8 kN | -1834.2 kN | -517.1 kN | 10.2 % | 3.9 |

Table 8.7. Comparison between the extreme values for gate 1 free at the bottom

Furthermore, comparing the results of Table 8.6 and Table 8.7, it can immediately concluded that the pressure is higher when no sill is present. This is probably due to the fact that the structure is more flexible in this last situation, which can lead to increased proper accelerations $\ddot{u}(y, z, t)$. Due to (7.8), the flexible hydrodynamic pressure follows the same tendency. The direct consequence of this last observation is that considering the gate as being perfectly rigid is not realistic at all. This is corroborated by Table 8.7, where it is shown that the pressure derived under such an assumption would be at least 5 times lower than the true one.

8.3.3.3. Discussion of the results

The results presented on Figure 8.15 (if a sill is present) and on Figure 8.16 (if the gate is free at the bottom) show a quite good agreement with those obtained from finite element simulations. Nevertheless, in order to be sure that the analytical approach is entirely satisfactory, as claimed in 8.3.2, it is worth remembering that this solution is arguable on a theoretical point of view. Therefore, to check the consistency of this approximate method, some additional verifications still need to be conducted. These ones are presented in section E.2.2 of Appendix E.2 and show that the analytical approach is quite satisfactory.

As a final remark concerning gate 1, it should be mentioned that finite element simulations were also realized for a lock chamber with a length L of 150 m. The total hydrodynamic pressures obtained for this configuration were very closed to those presented here above. The only difference lies in an important increase of the time needed by LS-DYNA to perform the calculation. Once again, this tends to corroborate the conclusions of section D.2.2.2 and shows that is sufficient to work with a truncated part of the fluid domain.

8.3.4. Added mass method

The added mass method was previously introduced in 7.4.4, where its limitations were already stressed. However, in this previous section, only the case of unstiffened plates was investigated. Even if these ones were already quite thick, they do not have the same stiffness as real lock gates, which are attempted to be less flexible. As the fluid-structure interaction was found to be decreasing with the rigidity (see section D.2.2 of Appendix D.2), one may believe that the added mass method is still relevant to treat this kind of stiffened plates. Once again, thinking this way is only valid under the hypothesis of having a sufficient stiffness. For example, in the paper of Forsyth and Porteous [59], the added mass approach was applied to a lock gate with a double plating and a quite imposing reinforcing system. The total width of the structure (along the x direction on Figure 8.1) was of about 6 m. With a such rigidity, it is clear that the methodology could be adequate, but it is not always the case. The purpose here is to illustrate this observation with an example.

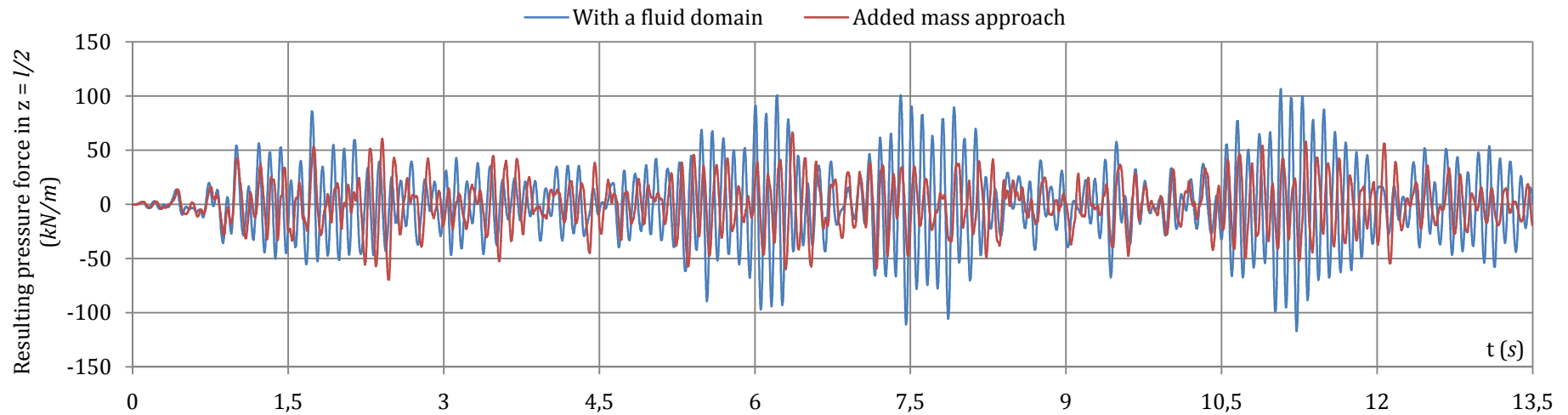


Figure 8.17. Comparison between the numerical results obtained by modeling the fluid or by using the added mass method for gate 1 supported by a sill

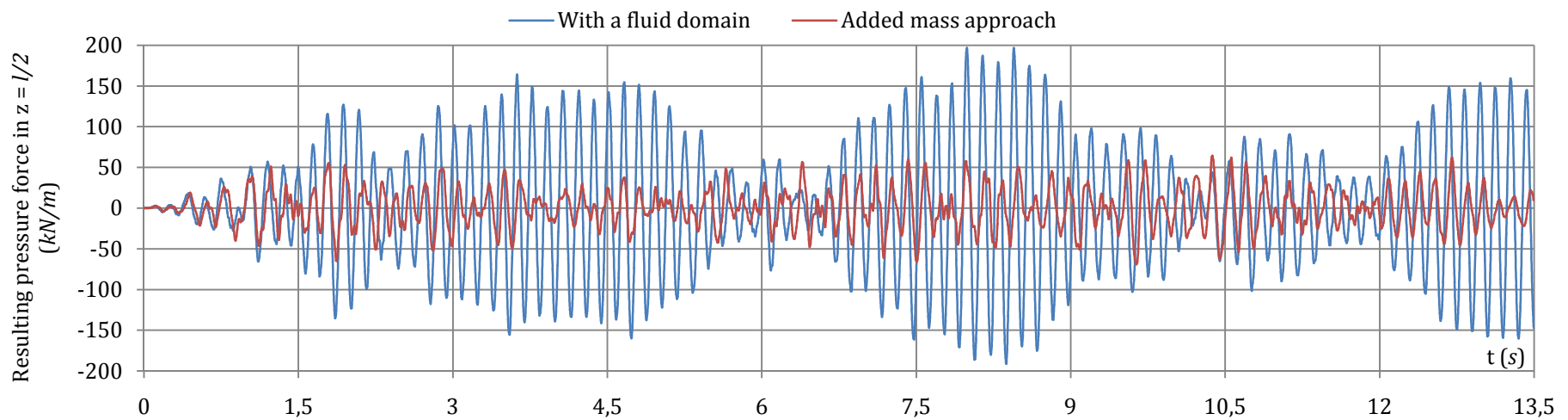


Figure 8.18. Comparison between the numerical results obtained by modeling the fluid or by using the added mass method for gate 1 free at the bottom

To do so, the first gate introduced in 8.2.3 (Figure 8.7) is considered. As a matter of comparison, it is focused here on the total pressure acting in the middle of the gate (i.e. in $z = l/2$) given by (7.97). The corresponding results are plotted on Figure 8.17 for the case of a gate supported by a sill. It can be seen that the two curves are quite dissimilar, but the convergence may still be eventually satisfactory for a very early design stage. This is also confirmed by the values listed in Table 8.8, where it appears that the maximal relative difference is around 40 %.

| | Gate 1 supported by a sill | | | Gate 1 free at the bottom | | |
|---------------|----------------------------|---------------------|---------------------|---------------------------|---------------------|---------------------|
| | With a fluid domain | Added mass approach | Relative difference | With a fluid domain | Added mass approach | Relative difference |
| Maximal value | 106.59 kN | 67.13 kN | 37.1 % | 196.86 kN | 67.03 kN | 67.1 % |
| Minimal value | -116.69 kN | 70.48 kN | 39.6 % | -192.36 kN | 64.07 kN | 64.1 % |

Table 8.8. Comparison of the extreme values for the added mass approach

When starting the design of the gate, it is probably sufficient to have a good order of magnitude for all the forces acting on the structure. Even if an error of 40 % seems to be rather problematic, one may argue that it is still acceptable if the seismic action is not predominant regarding all the other forces applied on the structure. In fact, the main advantage of working with lumped masses is that the approach allows for a drastic reduction of the time needed to perform finite element simulations. In the present case, by comparison with the simulations where the fluid domain is extensively modeled, the time required to get the results with the added mass method was approximately divided by one hundred. But one has also to consider the time needed to build the model, which is much more difficult to do if the water has to be represented. This explains why using lumped masses is sometimes quite popular.

Let us now consider the situation where the gate is totally free to move at the bottom of the lock. In this case, the curves showing the time evolution of the resulting pressure force in $z = l/2$ are depicted on Figure 8.18. This time, it is clear that the added mass approach fails to correctly stand for the fluid-structure interaction. This is also corroborated by the values listed in Table 8.8, where it can be seen that the relative error may reach 65 %. Such an underestimation of the seismic pressure does not seem to be acceptable (even at the early design stage), which is not surprising. Indeed, if the gate is no longer supported by a sill, it is therefore more flexible. As stated in 7.3.3.3, this leads to an increased fluid-structure interaction that cannot be correctly captured by the lumped masses.

As a conclusion, it is worth recalling that the added mass method was initially developed to analyze the seismic behavior of dams, which are much more rigid than lock gates. Even if the approach is computationally seducing, one has to bear in mind that its validity is directly related to the stiffness of the structure. If the flexibility is too important, working with lumped masses may lead to drastically underestimated water pressures. As an alternative, the results given by the simplified approach (see Figure 8.15 and Figure 8.16) provides a quite good approximation in a very short time and without having to build a finite element model.

8.4. Conclusions

In this chapter, a simplified method was proposed to evaluate the hydrodynamic pressures acting on a flexible lock gate. To achieve this goal, the dry modal properties were first derived by applying the Rayleigh-Ritz method to a structure made of a single plating and reinforced by an orthogonal stiffening system. The analytical results were validated for different gate configurations by comparing them with those given by the finite element software NASTRAN. In all the cases, the agreement on the dry eigenfrequencies and eigenmodes was found to be sufficient for a pre-design stage.

As a second step, the total hydrodynamic pressure acting on lock gates during a seism was evaluated in section 8.3. To do so, the virtual work principle was applied to perform the dynamic analysis and numerical validations were provided for a gate free or supported at the bottom. Here again, the discrepancies with the results obtained with the software LS-DYNA were found to remain quite satisfactory.

In addition to these analytical and numerical developments, further investigations were conducted to provide more practical information about the seismic design of lock gates. The conclusions can be summarized as follows:

- As for rectangular flexible reservoirs, the length L does not have any influence on the fluid-structure interaction, provided that $L \geq 3h_s$. Consequently, for the numerical simulations, there is no need to have a complete modeling of the whole lock chamber.
- Even if applying the added mass method is quite straightforward, such an approach should be avoided when dealing with the seismic design of lock gates. Indeed, as pointed out in section 8.3.4, this method could lead to a drastic underestimation of the hydrodynamic pressure.

All the developments performed in sections 8.2 and 8.3 are strictly valid for an ideal situation, in which the upstream and downstream gates are perfectly identical. Furthermore, if a sill is present, the boundary conditions applied at the bottom of the lock may be arguable. In addition, it is worth noting that the simplified method do not account for the surrounding water present in the reaches and that the other components of the seismic action have not been considered so far. In fact, for conciseness, all these particular points have been discussed in Appendix E.3, where some indications are given about the way to include them within an analytical approach.

The different considerations detailed here above show that performing the seismic design of a lock gate is a quite arduous task, even on a numerical point of view. The results presented in this chapter aim to provide some information on the way this operation should be achieved. The analytical method suggested here can be used as a pre-design tool, but it is likely that numerical simulations are still needed if more refined solutions are desirable.

CHAPTER 9. Conclusions about the seismic design of
lock gates

9.1. Scientific developments

The purpose of this second part is to provide an analytical evaluation of the hydrodynamic pressures induced on a plane lock gate reinforced by an orthogonal stiffening system. As a complementary information to the conclusions detailed in sections 7.5 and 8.4 of chapters 7 and 8 respectively, we would like to emphasize some particular achievements related to the seismic analysis of lock gates. The main developments performed in the framework of this thesis may be summarized as follows:

- The analytical procedure starts by the evaluation of the modal properties, which is achieved by applying the Rayleigh-Ritz method. The eigenmodes of horizontal and vertical beams are chosen as generating functions, but doing so is not entirely satisfactory on a theoretical point of view because the boundary conditions are not fully respected (Figure 8.5). Furthermore, having an accurate evaluation of the vibration properties also depends on the inertia affected to the stiffening system (Figure 8.13).
- Besides the previous theoretical difficulties, by comparisons with finite element solutions, it is found that the simplified approach leads to slightly overestimated eigenfrequencies, but the discrepancies remain acceptable. Similarly, some divergences are also observed on the mode shapes (Figure 8.11) because of the local action of the reinforcing system.
- On an analytical point of view, the dynamic analysis is performed by applying the virtual work principle in which the external forces are obtained by summing the pressure, damping and inertial forces. The equations are then developed to get a matrix formulation of the structural equilibrium. This one is solved by the Newmark integration scheme (section 8.3.2), which leads to the time evolution of the hydrodynamic pressure.
- On a numerical point of view, finite element models are developed with the software LS-DYNA. It is suggested to model the water with constant stress solid elements affected by a particular elastic material law with no shearing (section 7.4.3.1). Classical beam and shell elements may still be used for the gate and the fluid-structure interaction is simulated by the penalty contact algorithm of LS-DYNA. The consistency of this approach is checked by comparing the numerical results with the well-known theoretical predictions for rigid reservoirs (section D.2.1 of Appendix D.2).
- In order to simplify the finite element simulations, it is suggested that the fluid domain does not need to be entirely modeled. Indeed, if $L \geq 3h_s$ (L being the length of the lock and h_s the water level), it is demonstrated analytically that L does not have any influence on the hydrodynamic pressure induced on the gate. Consequently, for the numerical simulations, the fluid domain can be truncated after a length of $3h_s$ (Figure 7.18), which is particularly interesting to reduce the modeling and calculation efforts.
- Comparisons between the simplified method and finite element simulations show that the agreement is quite satisfactory (see Figure 8.15 for example). Of course, this tends to validate the present analytical developments, but this also corroborates the numerical models used with LS-DYNA.
- The classical added mass method based on the Westergaard formula [166] is investigated in details. Comparisons with analytical and numerical solutions show that this approach is

not conservative and should be avoided for flexible structures. The main reason is that the fluid-structure interaction is not correctly assessed by adding lumped mass on the gate. As an example, it is observed (Figure 8.18 and Table 8.8) that the maximal resulting hydrodynamic force may be underestimated by 65 % if this procedure is followed.

In addition to all the previous points, some indications are also given on the way the vertical and transversal seismic accelerations should be treated analytically. Similarly, some numerical and analytical considerations are presented to account for the water present in the upstream and downstream reaches, but this topic is not treated in details.

9.2. Perspectives

The results obtained through the analytical approach described in this second part of the thesis are the modal properties of a lock gate and the time evolution of the hydrodynamic pressure. The purpose is now to indicate how they can be used for the seismic design of a lock gate.

The principal concern for the seismic numerical study of a lock gate leads in the modeling of the surrounding water. Various techniques are available, such as those relying on acoustic elements, arbitrary Lagrangian-Eulerian methods... Unfortunately, building these models may be sometimes arduous. For example, if corners or sharp angles are located on the fluid-structure boundary, this may cause problems related to fluid leakage. If this is the case, the water can penetrate into the solid domain, which is of course not acceptable. Typically, such difficulties may arise at the corners of a reservoir. So building a consistent finite element model is not necessarily straightforward. In addition, it is also worth mentioning that due to the dimensions of the lock chamber, the numerical model may be quite heavy and therefore prohibitive regarding the computation and calculation efforts.

The previous reasons explain why simplified meshless methods may be quite successful, as they do not need the fluid domain to be represented and therefore circumvent the difficulties mentioned above. One of these techniques is of course the classical added mass approach, but it is not conservative for flexible structures. Consequently, the simplified method developed in chapters 7 and 8 may appear to be a more reliable alternative. Indeed, going back to equation (8.39) expressing the dynamic equilibrium, it appears that the situation is strictly similar to the one of a lock gate submitted to the following external force:

$$f_{ext}(y, z, t) = -\rho \left(t_p + \sum_{n=1}^{n_h} A_{v,n} \mathbb{H}_n(z) + \sum_{n=1}^{n_v} A_{h,n} \mathbb{H}_n(y) \right) \ddot{X}(t) - p(y, z, t) \quad (9.1)$$

which is nothing else than the sum of the hydrodynamic pressure $p(y, z, t)$ with the inertia terms coming from the ground acceleration $\ddot{X}(t)$. In other words, as depicted on Figure 9.1, the seismic analysis where both the structure and the water are represented can simply be replaced by a dynamic one, in which the lock gate is only submitted to $f_{ext}(y, z, t)$.

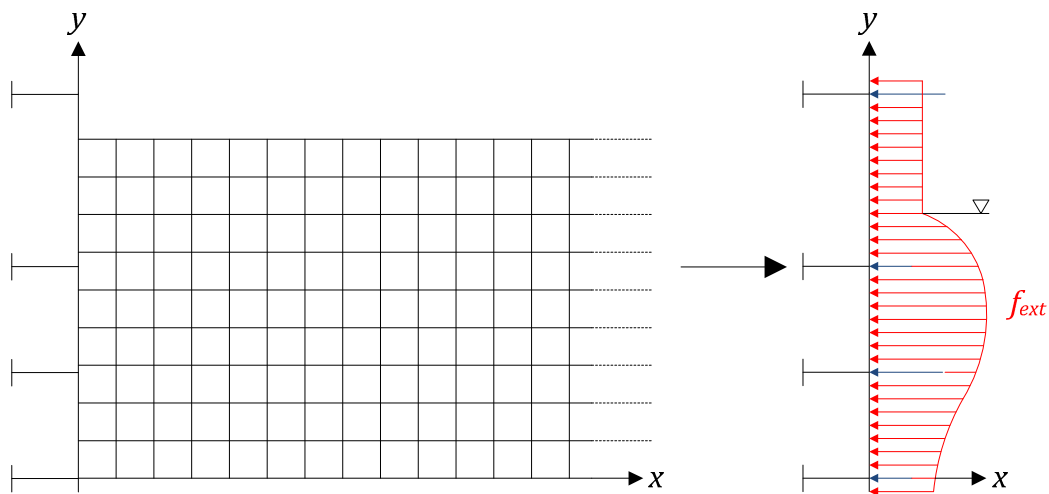


Figure 9.1. Simplified seismic analysis of a lock gate

This way of doing should drastically reduce the calculation and modeling efforts, allowing for a more efficient integration of the seismic action during the pre-design phase. On a more

practical point of view, it is reasonable to believe that some applications can be found in design offices dealing with hydraulic constructions.

Regarding the extension of the simplified analytical approach, it may be of interest to present some possible developments that could be achieved through further research:

- Derivation of the mathematical formulae to account for the hydrodynamic pressures in the downstream and upstream reaches. Some indications about this topic are already presented in sections E.3.3.1 and E.3.3.2 of Appendix E.3, where the remaining task is to apply the virtual work principle to get a matrix formulation of the equilibrium equation. Although this operation is still quite fastidious, it should lead to a more complete analytical method that could be validated by applying the recommendations suggested in section E.3.3.3 of Appendix E.3.
- Extension of the analytical procedure to the other components of the seismic acceleration. So far, only the longitudinal one is considered, but for the sake of completeness, the transversal and vertical motions should also be treated. Although the gate is quite rigid in these two directions, these latter may be however expected to have an influence on the resulting flexible pressures. Some indications about this topic are already given in section E.3.4 of Appendix E.3.
- Investigations on the influence of the real supports of the gate. Of course, the boundary conditions used for the analytical derivation do not exactly reflect the real situation. This topic is briefly discussed in section E.3.1 of Appendix E.3 for the particular case of the sill. However, it is clear that a similar questioning may be hold for the lock walls. Consequently, having a deeper numerical investigation that accounts for the real contact conditions could be of interest.
- Extension of the simplified method to other lock gates. So far, only the case of a plane lock gate with an orthogonal stiffening system is treated. A challenging goal could be to perform similar developments for mitre or sector gates (Figure 5.1a), but this is probably too ambitious. Indeed, having a consistent evaluation of the modal properties for such structures seems to be quite illusory as the Rayleigh-Ritz method requires realistic admissible functions. However, a more reasonable objective could be to adapt the method to lock gates with a double plating (Figure 5.1b).

The subjects mentioned here above show that some developments are still required to have a complete assessment of the seismic pressure acting on plane lock gates. Furthermore, some other possibilities could be examined to extend the procedure to other simple configurations.

- PART III -
Appendices

APPENDIX A. Addendum to Chapter 2

In this short addendum to Chapter 2, additional information is presented to complete the theoretical background related to the analytical derivation of the collision resistance.

Appendix A.1 presents the European classification of the inland waterways, which provides some practical information about the choice of reasonable values for the mass of the striking vessel.

In Appendix A.2, the total and actualized lagrangian formulations are briefly discussed in the optic of establishing consistent formulae to evaluate the internal energy rate in the upper-bound method. A simplified approach is also presented for the plastic regime.

A.1. Appendix A.1

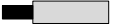







| Type of inland waterways | | Class | Motor vessels and barges | | | | Pushed convoys | | | | |
|-----------------------------|-----------------|----------|--------------------------|------------------|-------------|---|---|--------------------|------------------|--------------|---------------|
| | | | Maximum length (m) | Maximum beam (m) | Draught (m) | Tonnage (t) | Arrangement | Maximum length (m) | Maximum beam (m) | Draught (m) | Tonnage (t) |
| Of regional importance | To West of Elbe | I | 38.5 | 5.05 | 1.8 - 2.2 | 250 - 400 | | | | | |
| | | II | 50 - 55 | 6.6 | 2.5 | 400 - 650 | | | | | |
| | | III | 67 - 80 | 8.2 | 2.5 | 650 - 1000 | | | | | |
| | To East of Elbe | I | 41 | 4.7 | 1.4 | 180 | | | | | |
| | | II | 57 | 7.5 - 9 | 1.6 | 500 - 630 | | | | | |
| | | III | 67 - 70 | 8.2 - 9 | 1.6 - 2 | 470 - 700 | | | | | |
| Of international importance | IV | 80 - 85 | 9.5 | 2.5 | 1000 - 1500 |  | 85 | 9.5 | 2.5 - 2.8 | 1250 - 1450 | |
| | Va | 95 - 110 | 11.4 | 2.5 - 2.8 | 1500 - 3000 |  | 95 - 110 | 11.4 | 2.5 - 4.5 | 1600 - 3000 | |
| | Vb | | | | |  | 172 - 185 | 11.4 | 2.5 - 4.5 | 3200 - 6000 | |
| | VIa | | | | |  | 95 - 110 | 22.8 | 2.5 - 4.5 | 3200 - 6000 | |
| | VIb | | | | |  | 185 - 195 | 22.8 | 2.5 - 4.5 | 6400 - 12000 | |
| | VIc | | | | | |  | 270 - 280 | 22.8 | 2.5 - 4.5 | 9600 - 18000 |
| | | | | | | |  | 195 - 200 | 33 - 34.2 | 2.5 - 4.5 | 9600 - 18000 |
| | VII | | | | | |  | 285 | 33 - 34.2 | 2.5 - 4.5 | 14500 - 27000 |

Table A.1. Classification of the European waterways [55]

A.2. Appendix A.2

This appendix recalls some expressions that are useful to evaluate the internal energy E_{int} and energy rate \dot{E}_{int} . As in section 2.3, it is assumed that a solid is deformed from its initial configuration Ω_0 to the current one Ω (Figure A.1). The displacement and velocity fields are measured from Ω_0 and are respectively designated by \mathbf{u} and $\dot{\mathbf{u}}$. It is worth noting that no hypothesis is made so far on their magnitudes, which means that the developments performed here are also valid for finite displacements.

A.2.1. Definition of the strains

Denoting by (X_1, X_2, X_3) and (x_1, x_2, x_3) the coordinates of each point in Ω_0 and Ω respectively, the transformation of the solid can be characterized by the following relation:

$$x_i(X_1, X_2, X_3) = X_i + u_i(X_1, X_2, X_3) \quad (\text{A.1})$$

where u_i are the components of the displacement vector \mathbf{u} . With these notations, it is now possible to define consistent equations to derive the deformations. Within the frame of large displacements, these latter may be evaluated by different manners, but only the Almansi and Green-Lagrange strain tensors will be invoked here.

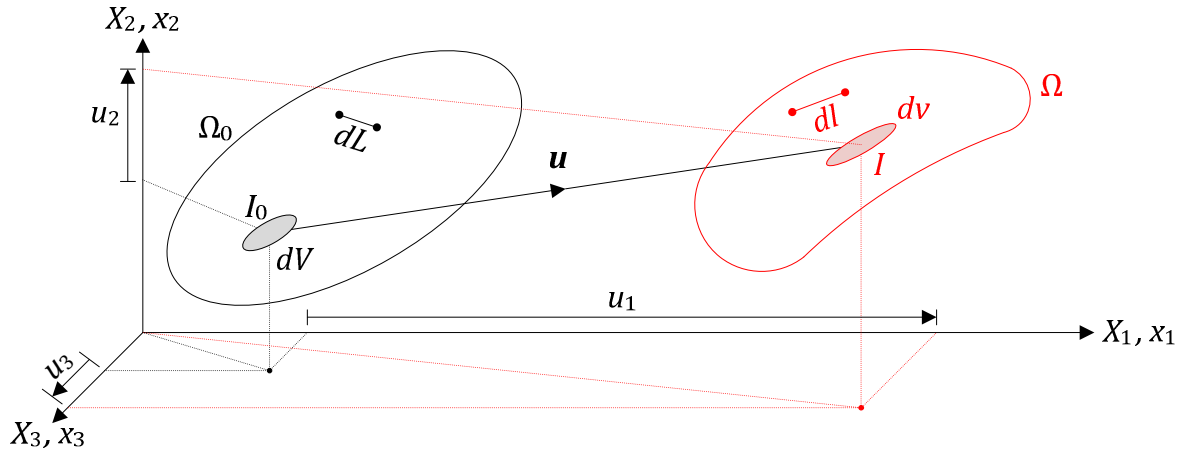


Figure A.1. Transformation of a solid from its initial configuration to the current one

Let us consider a small element having initially a length dL (Figure A.1). In the current configuration, this one is changed to dl . The transformation can be characterized by the two following strain definitions:

- The Green-Lagrange strain tensor $[\mathbf{E}]$ is a way of measuring the deformations with respect to the reference configuration. If this latter is chosen as being Ω_0 , then the components E_{ij} of $[\mathbf{E}]$ are defined as follows:

$$dl^2 - dL^2 = 2E_{ij}dX_i dX_j \Leftrightarrow E_{ij} = \frac{dx_k dx_k - dX_k dX_k}{dX_i dX_j} \quad (\text{A.2})$$

- The Almansi strain tensor $[\mathbf{a}]$ is a way of measuring the deformations with respect to the current configuration Ω . The components a_{ij} of $[\mathbf{a}]$ have the following definition:

$$dl^2 - dL^2 = 2a_{ij}dx_i dx_j \Leftrightarrow a_{ij} = \frac{dx_k dx_k - dX_k dX_k}{dx_i dx_j} \quad (\text{A.3})$$

By introducing (A.1) in (A.2) and (A.3), it is possible to express the strains as a function of the displacements u_i . Doing so leads to:

$$E_{ij} = \frac{1}{2} \left(\frac{\partial u_i}{\partial X_j} + \frac{\partial u_j}{\partial X_i} + \frac{\partial u_k}{\partial X_i} \frac{\partial u_k}{\partial X_j} \right) \quad a_{ij} = \frac{1}{2} \left(\frac{\partial u_i}{\partial x_j} + \frac{\partial u_j}{\partial x_i} - \frac{\partial u_k}{\partial x_i} \frac{\partial u_k}{\partial x_j} \right) \quad (\text{A.4})$$

where it is important to bear in mind that \mathbf{u} is defined from the reference configuration (chosen here as being Ω_0) to the current one Ω . In the optic of establishing a relation between $[E]$ and $[a]$, the jacobian matrix $[F]$ can be introduced:

$$[F] = \begin{bmatrix} \frac{\partial x_1}{\partial X_1} & \frac{\partial x_1}{\partial X_2} & \frac{\partial x_1}{\partial X_3} \\ \frac{\partial x_2}{\partial X_1} & \frac{\partial x_2}{\partial X_2} & \frac{\partial x_2}{\partial X_3} \\ \frac{\partial x_3}{\partial X_1} & \frac{\partial x_3}{\partial X_2} & \frac{\partial x_3}{\partial X_3} \end{bmatrix} \Leftrightarrow F_{ij} = \frac{\partial x_i}{\partial X_j} = \delta_{ij} + \frac{\partial u_i}{\partial X_j} \quad (\text{A.5})$$

in which δ_{ij} is the Kronecker symbol. Similarly, denoting by $[F]^{-1}$ the inverse matrix of $[F]$, it can be shown that:

$$[F]^{-1} = \begin{bmatrix} \frac{\partial X_1}{\partial x_1} & \frac{\partial X_1}{\partial x_2} & \frac{\partial X_1}{\partial x_3} \\ \frac{\partial X_2}{\partial x_1} & \frac{\partial X_2}{\partial x_2} & \frac{\partial X_2}{\partial x_3} \\ \frac{\partial X_3}{\partial x_1} & \frac{\partial X_3}{\partial x_2} & \frac{\partial X_3}{\partial x_3} \end{bmatrix} \Leftrightarrow F_{ij}^{-1} = \frac{\partial X_i}{\partial x_j} = \delta_{ij} - \frac{\partial u_i}{\partial x_j} \quad (\text{A.6})$$

In fact, $[F]$ links the initial coordinates to the actual ones and can therefore be used to relate E_{ij} and e_{ij} . It is possible to show that:

$$[E] = [F]^T [a] [F] \Leftrightarrow E_{ij} = F_{ki} a_{kl} F_{lj} \quad (\text{A.7})$$

where $[F]^T$ is the transpose of the jacobian matrix. This last equation can be easily demonstrated by introducing (A.4) and (A.5) into (A.7).

A.2.2. Definition of the stresses

The internal forces acting inside the deformed solid may also be characterized by various stress tensors, but only two of them will be introduced here. Let us consider a small tetrahedron of Ω_0 (Figure A.2) constructed on three vectors $(\mathbf{e}_1, \mathbf{e}_2, \mathbf{e}_3)$ that are unitary, orthogonal and parallel to the reference basis (X_1, X_2, X_3) . These latter are engraved on the solid and therefore follow its deformations. When moving from Ω_0 to Ω , they are transformed into the vectors $(\mathbf{g}_1, \mathbf{g}_2, \mathbf{g}_3)$ that are not necessarily unitary and orthogonal anymore.

The components of the internal forces acting on each face of this small tetrahedron may be expressed either by using $(\mathbf{e}_1, \mathbf{e}_2, \mathbf{e}_3)$ or $(\mathbf{g}_1, \mathbf{g}_2, \mathbf{g}_3)$. Furthermore, to get the corresponding stresses, one can choose to divide these components by the initial or deformed area of each face of the tetrahedron. This allows for the following definitions [157]:

- The Cauchy stress tensor $[\sigma]$ is a way of defining the stresses along the reference axes $(\mathbf{e}_1, \mathbf{e}_2, \mathbf{e}_3)$, but with respect to the actual area of the current configuration Ω .

- The second Piola-Kirchhoff stress tensor $[S]$ is a way of defining the stresses along the actual axes $(\mathbf{g}_1, \mathbf{g}_2, \mathbf{g}_3)$, but with respect to initial area of the reference configuration Ω_0 .

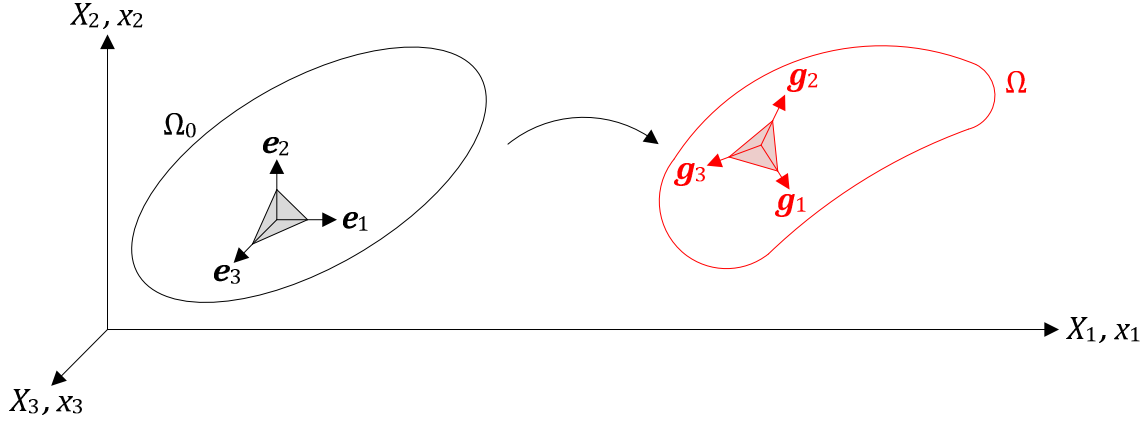


Figure A.2. Stress tensor definition

As for the strains, it also possible to use the jacobian matrix $[F]$ to get a relation between these two tensors. It can be shown [157] that:

$$[\sigma] = \frac{1}{F} [F][S][F]^T \Leftrightarrow \sigma_{ij} = \frac{1}{F} F_{ik} S_{kl} F_{jl} \quad (\text{A.8})$$

where $F = \det[F]$. Now that the relations defining the stresses and the strains are available, the next step is to evaluate E_{int} and \dot{E}_{int} .

A.2.3. Derivation of the internal energy

The internal energy E_{int} associated to the deforming solid of Figure A.1 may be expressed either in the reference configuration Ω_0 or in the current one. Let us start by first considering Ω_0 and try to derive the corresponding equation in Ω . Referring to Ω_0 , the internal energy is defined as follows:

$$E_{int} = \iiint_V [S][E]dV = \iiint_V S_{ij}E_{ij}dV \quad (\text{A.9})$$

where V is the initial volume. In order to develop (A.9) with respect to Ω this time, S_{ij} and E_{ij} can be transformed by making use of (A.7) and (A.8). Doing so leads to:

$$\begin{aligned} E_{int} &= \iiint_V F(F_{ik}^{-1}\sigma_{kl}F_{jl}^{-1})(F_{mi}a_{mn}F_{nj})dV \\ \Leftrightarrow E_{int} &= \iiint_v \sigma_{kl}a_{mn}(F_{mi}F_{ik}^{-1})(F_{nj}F_{jl}^{-1})dv \end{aligned} \quad (\text{A.10})$$

where v is the volume of the actual configuration. The last step in (A.10) is due to the definition of the determinant of the jacobian matrix, as $dv = FdV$. This property allows to integrate over the actual volume, so (A.10) is indeed an expression of E_{int} in the current configuration. But this last equation can still be simplify by noticing that:

$$F_{mi} = \frac{\partial x_m}{\partial X_i} ; F_{ik}^{-1} = \frac{\partial X_i}{\partial x_k} \Rightarrow F_{mi}F_{ik}^{-1} = \frac{\partial x_m}{\partial X_i} \frac{\partial X_i}{\partial x_k} = \frac{\partial x_m}{\partial x_k} = \delta_{mk} \quad (\text{A.11})$$

and the same development can be done for $F_{nj}F_{jl}^{-1} = \delta_{nl}$. Consequently, substituting these two results in (A.10) leads to:

$$E_{int} = \iiint_{\mathcal{V}} \sigma_{kl} a_{mn} \delta_{mk} \delta_{nl} dv = \iiint_{\mathcal{V}} \sigma_{ij} a_{ij} dv = \iiint_{\mathcal{V}} [\sigma][a] dv \quad (\text{A.12})$$

As a conclusion, it can be said that regarding the evaluation of the internal energy E_{int} , the second Piola-Kirchhoff stress tensor $[S]$ is conjugated to the Green-Lagrange strain tensor $[E]$, while the Cauchy stress tensor $[\sigma]$ is conjugated to the Almansi strain tensor $[a]$.

A.2.4. Derivation of the internal energy rate

As for E_{int} , it is also possible to define the internal energy rate \dot{E}_{int} in the reference and actual configurations. Considering Ω_0 first, the evaluation of \dot{E}_{int} can be performed by using the Green-Lagrange strain rate tensor $[\dot{E}]$ that is simply found by taking the time derivative of (A.4):

$$\dot{E}_{ij} = \frac{1}{2} \left(\frac{\partial \dot{u}_i}{\partial X_j} + \frac{\partial \dot{u}_j}{\partial X_i} + \frac{\partial \dot{u}_k}{\partial X_i} \frac{\partial u_k}{\partial X_j} + \frac{\partial u_k}{\partial X_i} \frac{\partial \dot{u}_k}{\partial X_j} \right) \quad (\text{A.13})$$

It is worth noting that it is correct to permute the time and the spatial derivatives in (A.13) as the initial coordinates (X_1, X_2, X_3) do not vary with time. The internal energy rate in the reference configuration Ω_0 is then found by multiplying the second Piola-Kirchhoff stress tensor with the one introduced here above:

$$\dot{E}_{int} = \iiint_{\mathcal{V}} [S][\dot{E}] dV = \iiint_{\mathcal{V}} S_{ij} \dot{E}_{ij} dV \quad (\text{A.14})$$

The transformation of (A.14) to get the expression of \dot{E}_{int} with respect to Ω is not straightforward. In this optic, (A.8) can first be introduced in (A.14) and \dot{E}_{ij} replaced in accordance with equation (A.13). Doing so provides the following results:

$$\begin{aligned} \dot{E}_{int} &= \frac{1}{2} \iiint_{\mathcal{V}} F(F_{ik}^{-1} \sigma_{kl} F_{jl}^{-1}) \left(\frac{\partial \dot{u}_i}{\partial X_j} + \frac{\partial \dot{u}_j}{\partial X_i} + \frac{\partial \dot{u}_r}{\partial X_i} \frac{\partial u_r}{\partial X_j} + \frac{\partial u_r}{\partial X_i} \frac{\partial \dot{u}_r}{\partial X_j} \right) dV \\ \Leftrightarrow \dot{E}_{int} &= \frac{1}{2} \iiint_{\mathcal{V}} \sigma_{kl} \left(\frac{\partial \dot{u}_i}{\partial X_j} + \frac{\partial \dot{u}_j}{\partial X_i} + \frac{\partial \dot{u}_r}{\partial X_i} \frac{\partial u_r}{\partial X_j} + \frac{\partial u_r}{\partial X_i} \frac{\partial \dot{u}_r}{\partial X_j} \right) F_{jl}^{-1} F_{ik}^{-1} dv \end{aligned} \quad (\text{A.15})$$

In order to simplify this last relation, one can consider the definition of the inverse jacobian matrix given by (A.6) to get:

- $F_{ik}^{-1} F_{jl}^{-1} \frac{\partial \dot{u}_i}{\partial X_j} = F_{ik}^{-1} \frac{\partial X_j}{\partial x_l} \frac{\partial \dot{u}_i}{\partial X_j} = F_{ik}^{-1} \frac{\partial \dot{u}_i}{\partial x_l} = \left(\delta_{ik} - \frac{\partial u_i}{\partial x_k} \right) \frac{\partial \dot{u}_i}{\partial x_l} = \frac{\partial \dot{u}_k}{\partial x_l} - \frac{\partial u_i}{\partial x_k} \frac{\partial \dot{u}_i}{\partial x_l}$
- $F_{ik}^{-1} F_{jl}^{-1} \frac{\partial \dot{u}_j}{\partial X_i} = F_{jl}^{-1} \frac{\partial X_i}{\partial x_k} \frac{\partial \dot{u}_j}{\partial X_i} = F_{jl}^{-1} \frac{\partial \dot{u}_j}{\partial x_k} = \left(\delta_{jl} - \frac{\partial u_j}{\partial x_l} \right) \frac{\partial \dot{u}_j}{\partial x_k} = \frac{\partial \dot{u}_l}{\partial x_k} - \frac{\partial u_j}{\partial x_l} \frac{\partial \dot{u}_j}{\partial x_k}$
- $F_{ik}^{-1} F_{jl}^{-1} \frac{\partial \dot{u}_r}{\partial X_i} \frac{\partial u_r}{\partial X_j} = F_{ik}^{-1} \frac{\partial \dot{u}_r}{\partial X_i} \frac{\partial u_r}{\partial X_j} F_{jl}^{-1} = \frac{\partial X_i}{\partial x_k} \frac{\partial \dot{u}_r}{\partial X_i} \frac{\partial u_r}{\partial X_j} \frac{\partial X_j}{\partial x_l} = \frac{\partial u_r}{\partial x_l} \frac{\partial \dot{u}_r}{\partial x_k}$
- $F_{ik}^{-1} F_{jl}^{-1} \frac{\partial u_r}{\partial X_i} \frac{\partial \dot{u}_r}{\partial X_j} = F_{ik}^{-1} \frac{\partial u_r}{\partial X_i} \frac{\partial \dot{u}_r}{\partial X_j} F_{jl}^{-1} = \frac{\partial X_i}{\partial x_k} \frac{\partial u_r}{\partial X_i} \frac{\partial \dot{u}_r}{\partial X_j} \frac{\partial X_j}{\partial x_l} = \frac{\partial u_r}{\partial x_k} \frac{\partial \dot{u}_r}{\partial x_l}$

$$(\text{A.16})$$

Substituting all these results in (A.15), many terms of (A.16) cancel each others, which leads to the following result:

$$\dot{E}_{int} = \frac{1}{2} \iiint_v \sigma_{kl} \left(\frac{\partial \dot{u}_k}{\partial x_l} + \frac{\partial \dot{u}_l}{\partial x_k} \right) dv \Leftrightarrow \dot{E}_{int} = \iiint_v [\sigma][\dot{a}] dv \quad (\text{A.17})$$

where $[\dot{a}]$ is called the Rivlin-Eriksen rate of the Almansi strain tensor [12]. It is worth noting that (A.17) is derived without making any assumption on the magnitude of \mathbf{u} and $\dot{\mathbf{u}}$ and is therefore also valid for finite displacements.

Another point that is important to stress is that, unlike $[\dot{E}]$ which was obtained by taking the rate of $[E]$, $[\dot{a}]$ is not the time derivative of $[a]$. Indeed, going back to equation (A.4) shows that deriving $[a]$ is a quite complex operation. This is mainly due to the fact that the current coordinates (x_1, x_2, x_3) are varying with time, which implies that the time derivative may not be permuted with the spatial ones. In fact, it can be shown that [36]:

$$\dot{a}_{ij} = \frac{1}{2} \left(\frac{\partial \dot{u}_i}{\partial x_j} + \frac{\partial \dot{u}_j}{\partial x_i} \right) - \left(a_{ki} \frac{\partial \dot{u}_k}{\partial x_j} + \frac{\partial \dot{u}_k}{\partial x_i} a_{kj} \right) \quad (\text{A.18})$$

which is definitely not the same as the deformation rate involved in (A.17). Similarly, it can also be concluded that $[\dot{a}]$ is not obtained by taking the time derivative of the Cauchy strain tensor $[\epsilon]$ defined by:

$$\epsilon_{ij} = \frac{1}{2} \left(\frac{\partial u_i}{\partial x_j} + \frac{\partial u_j}{\partial x_i} \right) \quad (\text{A.19})$$

because permuting the time and spatial derivatives is not allowed. Of course, under the hypothesis of small strains and displacements, the aforementioned equations may be linearized to get $[\dot{a}] = [\dot{\epsilon}] = [\dot{\epsilon}]$. As a conclusion, it can be said that regarding the evaluation of the internal energy rate \dot{E}_{int} , the second Piola-Kirchhoff stress tensor $[S]$ is conjugated to the Green-Lagrange strain rate tensor $[\dot{E}]$, while the Cauchy stress tensor $[\sigma]$ is conjugated to Rivlin-Eriksen rate $[\dot{a}]$ of the Almansi strain tensor.

A.2.5. Derivation of the internal energy rate in the plastic regime

Before trying to evaluate the internal energy rate for large deformations, it is probably of interest to present a non-exhaustive recall of some basic results of the plasticity theory for metals (see [28] or [102] for more details). In the case of a material having a perfectly plastic behavior (i.e. exhibiting no strain-hardening), it can be assumed that plastic deformations occur under a constant flow stress σ_0 . On a mathematical point of view, this property is translated by the definition of a convex yield surface \mathcal{F} such that:

$$\mathcal{F}(\sigma_{ij}) - \sigma_0 = 0 \quad (\text{A.20})$$

where σ_0 is a constant as there is no strain-hardening and $[\sigma]$ is the Cauchy stress tensor. Furthermore, within the frame of small deformations, it is usually assumed that the Cauchy strain rate tensor $[\dot{\epsilon}]$ can be decomposed into the sum of an elastic and a plastic part, which can be expressed as follows:

$$\dot{\epsilon}_{ij} = \dot{\epsilon}_{ij}^e + \dot{\epsilon}_{ij}^p \quad (\text{A.21})$$

and in the case of an associated plasticity, the theory also states that the plastic part has to be perpendicular to the yield surface. In other words, one should have:

$$\dot{\epsilon}_{ij}^p = \dot{\lambda} \frac{\partial \mathcal{F}}{\partial \sigma_{ij}} \Leftrightarrow \dot{\epsilon}_{ij} = \dot{\lambda} \frac{\partial \mathcal{F}}{\partial \sigma_{ij}} \quad (\text{A.22})$$

where $\dot{\lambda}$ is a positive scalar multiplier. In the particular case of metals, it is quite common to work with the Von Mises plasticity criteria and it is therefore quite interesting to adapt all the previous relations. Under the assumption of a non-hardening material with a flow stress equal to σ_0 , the equation of the Von Mises yield locus is as follows:

$$\mathcal{F} \equiv \frac{1}{2} \hat{\sigma}_{ij} \hat{\sigma}_{ij} - \frac{1}{3} \sigma_0^2 = 0 \quad \hat{\sigma}_{ij} = \sigma_{ij} - \frac{\sigma_{kk}}{3} \delta_{ij} \quad (\text{A.23})$$

where $[\hat{\sigma}]$ is the deviatoric stress tensor. With this definition, the application (A.22) allows to determine the different components of the plastic strain rate tensor:

$$\dot{\epsilon}_{ij} = \dot{\lambda} \frac{\partial \mathcal{F}}{\partial \sigma_{ij}} = \frac{3\dot{\lambda}}{2} \frac{\hat{\sigma}_{ij}}{\sigma_0} \quad ; \quad \dot{\lambda} = \sqrt{2\dot{\epsilon}_{ij}\dot{\epsilon}_{ij}/3} \quad (\text{A.24})$$

in which the definition of $\dot{\lambda}$ may be easily demonstrated with help of (A.23). The internal dissipation rate \dot{E}_{int} is then given by particularizing (A.17) to the special case of small strains, for which $[\hat{\mathbf{a}}] = [\dot{\epsilon}]$, i.e.:

$$\dot{E}_{int} = \iiint_v \sigma_{ij} \dot{\epsilon}_{ij} dv = \iiint_v \sigma_0 \dot{\epsilon}_p dv \quad ; \quad \dot{\epsilon}_p = \sqrt{2\dot{\epsilon}_{ij}\dot{\epsilon}_{ij}/3} \quad (\text{A.25})$$

The previous relation may be easily demonstrated with help of (A.24) and (A.25). This leads to the definition of the equivalent plastic strain rate $\dot{\epsilon}_p$. It is worth bearing in mind that the developments exposed here above are only valid for small strains. Unfortunately, the theories of elastoplasticity with large deformations are still a topic under discussion and even for metals, there are many approaches currently available. Without entering in too many details, the plastic rules in the case of finite strains are usually developed by following one of these two hypotheses:

$$\hat{\mathbf{a}}_{ij} = \hat{\mathbf{a}}_{ij}^e + \hat{\mathbf{a}}_{ij}^p \quad \text{or} \quad F_{ij} = F_{ik}^e F_{kj}^p \quad (\text{A.26})$$

In the first case, it is simply assumed that the results exposed here above for small strains may be directly extended to treat large deformations by assuming that the Rivlin-Eriksen rate of the Almansi strain tensor is obtained by the addition of an elastic and a plastic contribution. In the second case, it is postulated that every material point undergoes two successive transformations associated to the elastic and plastic deformations. These transformations are respectively characterized by the tensors $[F^e]$ and $[F^p]$.

Unfortunately, none of these two models is able to satisfactorily represent the behavior of metal in large deformations. Another attempt was made by Green and Naghdi [64], who assumed a summative decomposition of the Green-Lagrange strain rate tensor in the form of $\dot{E}_{ij} = \dot{E}_{ij}^e + \dot{E}_{ij}^p$, in which \dot{E}_{ij} is calculated with help of (A.13) but not \dot{E}_{ij}^e and \dot{E}_{ij}^p . With this hypothesis, they develop a mathematical consistent plastic theory with respect to the initial configuration. Nevertheless, on the physical point of view, this approach is criticized by some authors such as Volokh [158], who argues that materials only have a perfect remembrance of their initial reference configuration within the range of elastic deformations. Consequently, in the case of a plastic flow, the constitutive equations should be developed for the current configuration and not for the initial one.

From the brief previous discussion, it transpires that selecting an appropriate plastic theory is a quite arduous task. Nevertheless, under the assumption that the collision process only implies moderate strains and displacements in which the plastic deformations are predominant, then according to Volokh [158], it is relevant to work under the first hypothesis mentioned in (A.26). Doing so, the internal energy rate may be simply evaluated by adapting (A.25) in the following way [158]:

$$\dot{E}_{int} = \iiint_v \sigma_{ij} \dot{a}_{ij} dv = \iiint_v \sigma_0 \dot{a}_p dv \quad ; \quad \dot{a}_p = \sqrt{2\dot{a}_{ij}\dot{a}_{ij}/3} \quad (\text{A.27})$$

in which the matrix components \dot{a}_{ij} are still given by (2.6). In this last formula, it is worth noticing that the integration has to be performed over the deformed configuration, which is not always convenient. According to (A.7), remembering that $dv = FdV$ and $\dot{a}_{ij} = F_{ki}^{-1} \dot{E}_{kl} F_{lj}^{-1}$, it is possible to transform (A.27) in a more practical form:

$$\dot{E}_{int} = \iiint_V \sigma_0 \dot{E}_p dV \quad ; \quad \dot{E}_p = F \sqrt{2(F_{ki}^{-1} \dot{E}_{kl} F_{lj}^{-1})(F_{mi}^{-1} \dot{E}_{mn} F_{mj}^{-1})/3} \quad (\text{A.28})$$

This last equation provides a way to evaluate the internal energy in the case of finite strains and displacements. It is quite close to the theoretical reasoning hold by Voyiadjis and Kiouisis [159] for a hardening material.

APPENDIX B. Additional developments for ship impacts on plane lock gates

In this addendum to Chapter 3, additional developments are presented in order to complete the analytical evaluation of the impact resistance for plane lock gates. Each appendix always refers to one section of Chapter 3.

In Appendix B.1, additional mathematical developments are presented as a complement to the analytical derivations related to the first type of super-elements. The formulae detailed in section 3.3 are also extended to the case of a subsequent contact.

Appendix B.2 and Appendix B.3 give more details on the way the resistance should be calculated for the second and third types of super-elements respectively. In particular, they focus on the beam mechanism that may also appear during the impact.

Finally, complementary information is provided in Appendix B.4 about the displacement field postulated during the global deforming mode and an additional validation case is presented in Appendix B.5.

B.1. Appendix B.1

B.1.1. Internal energy rate for stiffened plates

The theoretical derivation of the internal energy rate performed in section 3.3.2 and 3.3.3 are only valid for non-stiffened plates. Nevertheless, it is of current practice to reinforce the plating of lock gates by smaller horizontal and vertical elements. Of course, doing so has a consequence on the crashworthiness. Numerical investigations show that during an impact, these stiffeners are mainly submitted to membrane straining, the bending effects being negligible. In other words, they follow the deformation of the plating. Consequently, as suggested by Paik and Thayamballi [120], it is sufficient to smear them over the surface of the plate, as explained hereafter.

Considering the portion between the two girders located in Y_{n-1} and Y_n (Figure B.1), the plating thickness t_p can be replaced by an equivalent value t_z to account for the additional membrane energy that is also dissipated by the horizontal smaller components during the collision. Denoting by A_i each individual section area and by N the total number of stiffeners present between the two girders, one should simply have:

$$t_y = t_p + \sum_{i=1}^N \frac{A_i}{Z_n - Z_{n-1}} \quad ; \quad t_z = t_p + \sum_{i=1}^N \frac{A_i}{Y_n - Y_{n-1}} \quad (\text{B.1})$$

Similarly, to account for the membrane energy that is also dissipated by the N vertical stiffeners located between the two frames Z_{n-1} and Z_n , it is also possible to work with an equivalent thickness t_y calculated as mentioned in (B.1). As a final result, the plate is replaced by a fictitious one, having two different thicknesses along the y and z axis.

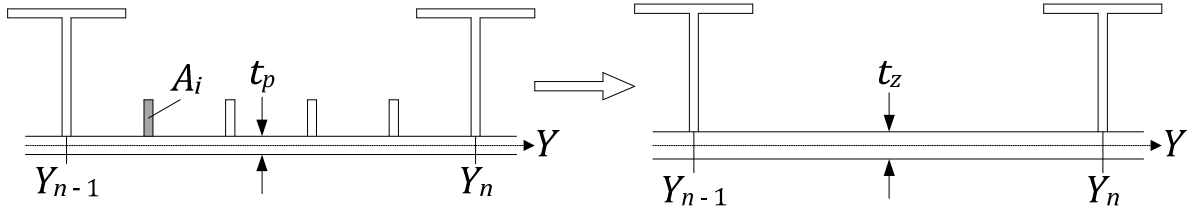


Figure B.1. Calculation of the equivalent plating thickness

The evaluation of the internal energy rate is therefore no longer given by (3.18) because $n_0 = \sigma_0 t_p$ is now different for the horizontal and vertical fibers. Instead of (3.18), the following formula should be used:

$$\dot{E}_{int} = \iint_A \sigma_0 (t_y \dot{E}_{yy} + t_z \dot{E}_{zz}) dy dz \quad ; \quad \dot{E}_{yy} = \frac{\partial u}{\partial y} \frac{\partial \dot{u}}{\partial y} \quad \dot{E}_{zz} = \frac{\partial u}{\partial z} \frac{\partial \dot{u}}{\partial z} \quad (\text{B.2})$$

However, it is quite interesting to note that these smaller reinforcing components usually do not increase to a large extent the collision resistance of the impacted plate. For this reason, they could be neglected, which is a conservative approach.

B.1.2. Resistance after contact with a lateral support

The formulae developed in section 3.3.2 are only valid if one of the boundary of the super-element has not been impacted by the stem. Nevertheless, when the penetration is equal to δ_1

or δ_2 (Figure B.2), this is no longer the case as a contact develops with the right or the left lateral support respectively. This causes the activation of two additional super-elements: a vertical SE2 and the adjacent SE1.

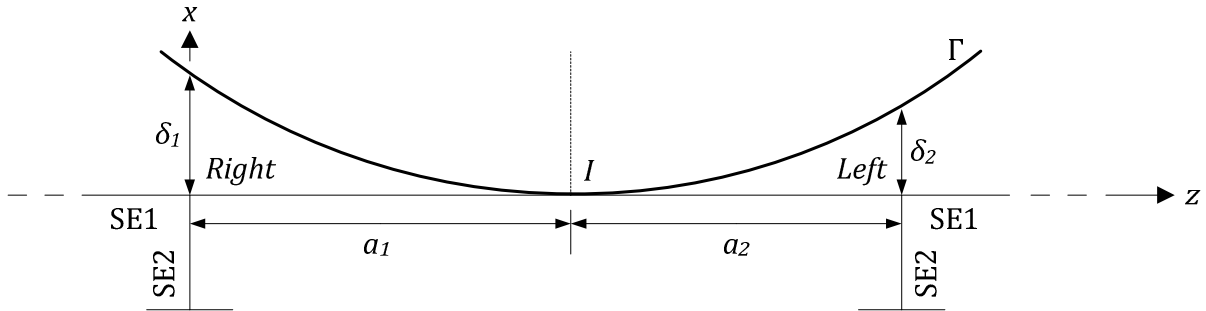


Figure B.2. Contact between the stem and the lateral supports

The penetrations δ_1 and δ_2 for which a subsequent contact occurs may be found by geometrical considerations. Indeed, they are simply given by the initial distance between the corresponding support and the curve Γ materializing the stem at the super-element level. From equation (3.11), it is easy to show that:

$$\delta_1 = X_S + q \left(\frac{a_1^2}{p^2} - 1 \right) \quad ; \quad \delta_2 = X_S + q \left(\frac{a_2^2}{p^2} - 1 \right) \quad (\text{B.3})$$

from which it can be concluded that the subsequent contact may first concern the right or the left support, according to the respective values of a_1 and a_2 .

B.1.2.1. Impact on the right support

Let us first consider the case where $\delta_1 < \delta_2$. In this situation, for $\delta_1 \leq \delta < \delta_2$, only the right lateral support has been impacted.

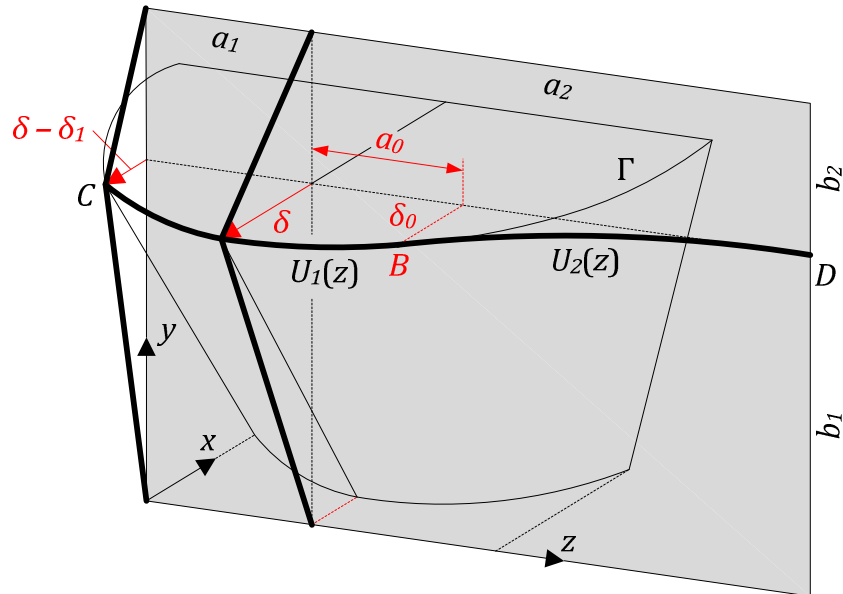


Figure B.3. Definition of the deformation pattern in the case of a contact with a lateral support

It seems therefore reasonable to postulate the deformation pattern of Figure B.3. As in section 3.3.2.1, the displacement field $U(z)$ in the plane of the uppermost deck is still made of two parts:

- For $0 \leq z \leq a_1 + a_0$, the displacements are characterized by $U_1(z)$ and such that the plate is simply sticking to the shape Γ of the striking vessel.
- For $a_1 + a_0 \leq z \leq a_1 + a_2$, the displacements are described by $U_2(z)$ and such that the compatibility conditions along the vertical support in $z = a_1 + a_2$ are respected.

The junction between $U_1(z)$ and $U_2(z)$ is made at point B , which is characterized by the two parameters a_0 and δ_0 . In fact, comparing Figure 3.14 and Figure B.3 clearly shows that the situation on the sub-areas $a_2 \times b_1$ and $a_2 \times b_2$ is strictly similar. Consequently, it is obvious that the two parameters a_0 and δ_0 may be directly found by adapting equations (3.13) as follows:

$$a_0 = \frac{p^2}{a_2 q} (q - X_S + \delta) \quad ; \quad \delta_0 = \frac{q}{p^2} a_0 (a_2 - a_0) \quad (\text{B.4})$$

For similar reasons, the formulae (3.21) and (3.22) giving the resistances $P_3(\delta)$ and $P_4(\delta)$ provided by the two aforementioned sub-areas are also still relevant in the present case. However, this is not true for $P_1(\delta)$ and $P_2(\delta)$, as the displacement field $u(y, z)$ arising on $a_1 \times b_1$ and $a_1 \times b_2$ is not the same as in section 3.3.2.1. Indeed, applying (3.11) and (3.15) leads to the following result:

$$u(y, z) = U_1(z) f(y) = \left(q - X_S + \delta - \frac{(z - a_1)^2}{R} \right) f(y) \quad (\text{B.5})$$

in which $R = p^2/q$ and $f(y)$ is given by (3.14). With this definition, the derivation of $P_1(\delta)$ and $P_2(\delta)$ may be achieved by evaluating the internal energy rate with help of (3.18). Doing so, it can be shown that $P(\delta)$ is obtained by summing up the four following contributions:

$$\bullet \quad P_1(\delta) = \sigma_0 t_p \frac{a_1}{b_1} \left(\delta + q - X_S - \frac{a_1^2}{3R} \right) \quad (\text{B.6})$$

$$\bullet \quad P_2(\delta) = \sigma_0 t_p \frac{a_1}{b_1} \left(\delta + q - X_S - \frac{a_1^2}{3R} \right) \quad (\text{B.7})$$

$$\bullet \quad P_3(\delta) = \sigma_0 t_p \left(\delta + q - X_S - \frac{a_0^2}{3R} + \frac{4b_1^2}{9R} + \frac{(a_2 - a_0)^2}{5R} \right) \quad ; \quad a_0 = \frac{R}{a_2} (q - X_S + \delta) \quad (\text{B.8})$$

$$\bullet \quad P_4(\delta) = \sigma_0 t_p \left(\delta + q - X_S - \frac{a_0^2}{3R} + \frac{4b_2^2}{9R} + \frac{(a_2 - a_0)^2}{5R} \right) \quad ; \quad a_0 = \frac{R}{a_2} (q - X_S + \delta) \quad (\text{B.9})$$

Of course, these formulae remains valid as long as the maximal strain arising in the plate is lower than the critical value ϵ_c for which rupture occurs. At this moment, the resistance $P(\delta)$ is set to zero.

B.1.2.2. Impact on the left support

It is now focused on the case where $\delta_2 < \delta_1$. In this situation, if $\delta_2 \leq \delta < \delta_1$, only the left lateral support has been impacted and it is obvious that the impact situation is symmetric with respect to the one depicted on Figure B.3. In particular, this means that the contributions $P_1(\delta)$ and $P_2(\delta)$ are still given by (3.19) and (3.20), while (3.21) and (3.22) are no longer valid to evaluate $P_3(\delta)$ and $P_4(\delta)$. Indeed, these latter have to be corrected, as the sub-areas $a_2 \times b_1$ and $a_2 \times b_2$ are now entirely submitted to the displacement field $u(y, z) =$

$U_1(z)f(y)$ imposed by the striking vessel. Accounting for all these considerations leads this time to the subsequent results:

$$\bullet P_1(\delta) = \sigma_0 t_p \left(\delta + q - X_S - \frac{a_0^2}{3R} + \frac{4b_1^2}{9R} + \frac{(a_1 - a_0)^2}{5R} \right) ; \quad a_0 = \frac{R}{a_1}(q - X_S + \delta) \quad (\text{B.10})$$

$$\bullet P_2(\delta) = \sigma_0 t_p \left(\delta + q - X_S - \frac{a_0^2}{3R} + \frac{4b_2^2}{9R} + \frac{(a_1 - a_0)^2}{5R} \right) ; \quad a_0 = \frac{R}{a_1}(q - X_S + \delta) \quad (\text{B.11})$$

$$\bullet P_3(\delta) = \sigma_0 t_p \frac{a_2}{b_1} \left(\delta + q - X_S - \frac{a_2^2}{3R} \right) \quad (\text{B.12})$$

$$\bullet P_4(\delta) = \sigma_0 t_p \frac{a_2}{b_2} \left(\delta + q - X_S - \frac{a_2^2}{3R} \right) \quad (\text{B.13})$$

which are only valid as long as there is no rupture, otherwise $P(\delta)$ has to be set to zero. As a final remark, it is worth noting that equations (B.6) to (B.13) are derived under the assumption that only one of the two vertical boundaries has been impacted. Nevertheless, if $\delta > \max(\delta_1, \delta_2)$, then the two lateral supports are simultaneously in contact with stem. In this case, $P(\delta)$ is simply obtained by summing up (B.6), (B.7) (B.12) and (B.13).

B.1.3. Resistance after contact with the lower support

For a given value δ_3 of the penetration, the stem is assumed to enter in contact with the lower support of the plate, which causes the activation of two super-elements: an additional SE1 and a horizontal SE2 (Figure B.4a). The formulae developed in section 3.3.2 are of course no more valid, as the displacement field $u(y, z)$ is now affecting one of the boundaries (Figure B.4b). The restriction of $u(y, z)$ to the horizontal planes $y = 0$ and $y = b_1$ are denoted by $\hat{U}(z)$ and $U(z)$ respectively.

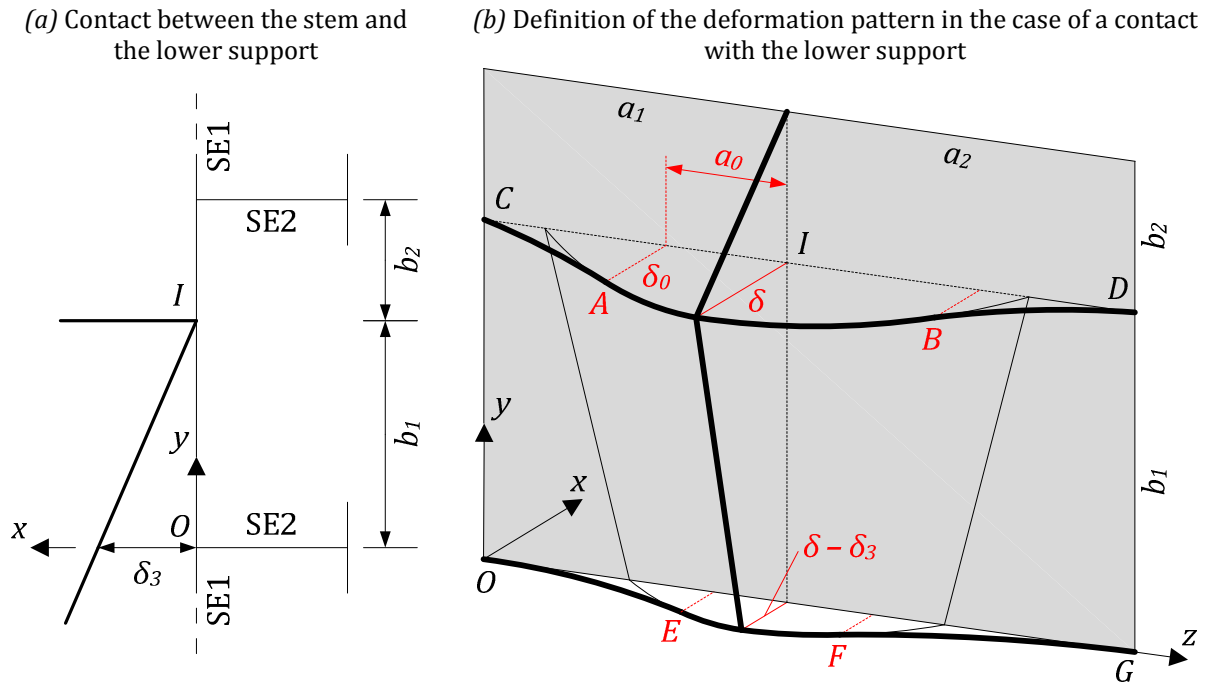


Figure B.4. Parameters for the contact between the stem and the lower support

The mathematical expression of $U(z)$ is still given by formulae (3.13) to (3.15) and the derivation of $\hat{U}(z)$ is straightforward, as it may be found simply by extrapolating the developments performed in section 3.3.2. It is still made of two different parts $\hat{U}_1(z)$ and $\hat{U}_2(z)$, the first being imposed by the shape of the stem in the plane $y = 0$, while the second is defined to respect the compatibility with the supports (Figure B.5). For the sub-area $a_1 \times b_1$, going back to (3.9) and extrapolating (3.12) leads to:

$$\bullet \quad \hat{U}_1(z) = \hat{q} \left(1 - \frac{(z - a_1)^2}{\hat{p}^2} \right) - X_S + \delta \quad \text{if} \quad a_1 - \hat{a}_0 \leq z \leq a_1 \quad (\text{B.14})$$

$$\bullet \quad \hat{U}_2(z) = \frac{\hat{\delta}_0}{(a_1 - \hat{a}_0)^2} z^2 \quad \text{if} \quad 0 \leq z \leq a_1 - \hat{a}_0 \quad (\text{B.15})$$

where $\hat{q} = q - b_1 \cot \phi$ and $\hat{p} = p - b_1 \cot \psi$ are the radii of the stem at the level of the lower support. Similarly, in the two previous equations, the parameters \hat{a}_0 and $\hat{\delta}_0$ describing the current position of the junction point E (Figure B.4b and Figure B.5) are simply obtained by extending the results of section 3.3.2. Considering (3.13), one should get:

$$\hat{a}_0 = \frac{\hat{p}^2}{a_1 \hat{q}} (\hat{q} - X_S + \delta) \quad \hat{\delta}_0 = \frac{\hat{q}}{\hat{p}^2} \hat{a}_0 (a_1 - \hat{a}_0) \quad (\text{B.16})$$

With all the previous definitions, it is now possible to postulate a reasonable displacement field $u(y, z)$ for the sub-area $a_1 \times b_1$. The most convenient way is to perform a linear interpolation between $U(z)$ and $\hat{U}(z)$, which leads to:

$$u(y, z) = U(z) \frac{y}{b_1} + \hat{U}(z) \frac{b_1 - y}{b_1} = U(z) f(y) + \hat{U}(z) \hat{f}(y) \quad (\text{B.17})$$

It is obvious that all the developments exposed here above may be easily adapted to the sub-area $a_2 \times b_1$. Moreover, as $u(y, z)$ is strictly identical to the displacement fields defined in 3.3.2 for the regions $a_1 \times b_2$ and $a_2 \times b_2$, there is no need to reevaluate the contributions $P_2(\delta)$ and $P_4(\delta)$ to the local resistance opposed by the plate.

To calculate the internal energy rate \dot{E}_{int} , (B.17) may be introduced in (3.18). Then, equating \dot{E}_{int} to the external energy rate gives $P_1(\delta) = \sigma_0 t_p (I_1 + I_2)$, where I_1 and I_2 have the following definitions:

$$\begin{aligned} I_1 &= \frac{(a_0 - a_1)^5 + (a_1 - \hat{a}_0)^5}{5b_1(a_1 - \hat{a}_0)^2} \left(\frac{\hat{a}_0}{\hat{R}(a_1 - \hat{a}_0)} + \frac{1}{6R} \right) - \frac{a_0^3 - \hat{a}_0^3}{3b_1 R} + \frac{\delta - X_S + q}{b_1} (a_0 - \hat{a}_0) \\ &+ \frac{(a_1 - a_0)^3 - (a_1 - \hat{a}_0)^3}{3(a_1 - \hat{a}_0)^2} \left(\frac{4b_1}{3\hat{R}} \frac{\hat{a}_0}{a_1 - \hat{a}_0} + \frac{\hat{a}_0(a_1 - \hat{a}_0)}{b_1 \hat{R}} + \frac{\delta - X_S + q}{b_1} - \frac{b_1}{3R} \right) \\ &+ \frac{\hat{a}_0}{3R} \left(b_1 + \frac{a_1^2 - \hat{a}_0^2}{2b_1} \right) - \frac{a_0(a_1 - a_0)^2}{3R(a_1 - \hat{a}_0)^2} \left(b_1 + \frac{a_1^2 - a_0^2}{2b_1} \right) \end{aligned} \quad (\text{B.18})$$

$$\begin{aligned} I_2 &= \left(\frac{4b_1}{9} + \frac{(a_1 - a_0)^2}{5b_1} \right) \left(\frac{a_0}{R} + \frac{\hat{a}_0}{\hat{R}} \left(\frac{a_1 - a_0}{a_1 - \hat{a}_0} \right)^3 \right) + \frac{a_0}{R} \left(\frac{a_1 - a_0}{a_1 - \hat{a}_0} \right)^2 \left(\frac{2b_1}{9} - \frac{(a_1 - \hat{a}_0)^2}{5b_1} \right) \\ &+ \frac{a_0}{R} \left(\frac{a_1 - a_0}{a_1 - \hat{a}_0} \right) \left(\frac{2b_1}{9} - \frac{(a_1 - \hat{a}_0)^2}{5b_1} \right) \end{aligned} \quad (\text{B.19})$$

in which $R = p^2/q$ and $R = \hat{p}^2/\hat{q}$. Of course, the previous results are still valid for the sub-area $a_2 \times b_1$, provided that a_1 is replaced by a_2 in (B.18). Doing so leads to $P_3(\delta)$, while $P_2(\delta)$ and $P_4(\delta)$ are still given by (3.20) and (3.22). Summing up all these contributions finally leads to the total local resistance $P(\delta)$ opposed by the plate if its lower edge has been impacted by the stem.

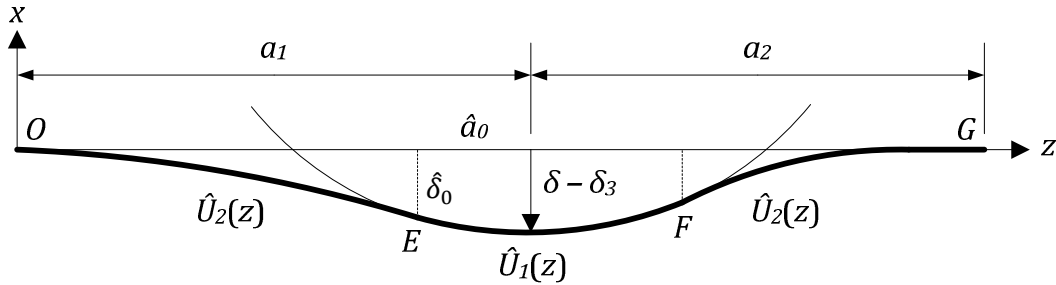


Figure B.5. Definition of the displacement field in the horizontal plane $y = 0$

B.2. Appendix B.2

B.2.1. Subsequent folding

As depicted on Figure 3.29, as soon as one fold is completely crushed, it is assumed that a new one is immediately created. Doing so is possible as long as the web has not been entirely crushed. For a fold number j that is completely closed, its contribution to the super-element resistance is only coming from a membrane straining and it can be shown [180] that the corresponding energy rate \dot{E}_j is given by:

$$\dot{E}_j = 2n_0H \frac{a_1 + a_2}{a_1 a_2} (H + \delta - 2jH)\delta \quad (\text{B.20})$$

Consequently, if k is the current fold number, the total internal dissipation is obtained by summing up the bending and membrane energy rates \dot{E}_b and \dot{E}_m with the individual contributions \dot{E}_j coming from all the $k - 1$ folds that have already been totally crushed (Figure B.6a), i.e.:

$$\dot{E}_{int} = \dot{E}_b + \dot{E}_m + \sum_{j=1}^{k-1} \dot{E}_j \quad (\text{B.21})$$

In this last formula, it is worth noting that \dot{E}_b is the same as in section 3.4.2.1 because it is not a function of δ . Nevertheless, regarding \dot{E}_m , equation (3.47) has to be corrected because the relative indentation for the current fold is only equal to $\delta - 2(k - 1)H$. In other words, (3.47) is still valid to get \dot{E}_m , provided that δ is replaced by $\delta - 2(k - 1)H$. Developing (B.21) leads to the following relation:

$$\dot{E}_{int} = (a_1 + a_2)\delta \left(\frac{m_0\pi}{H} + \frac{n_0H}{2} \frac{(\delta - 2(k - 2)H)}{a_1 a_2} + \sum_{j=1}^{k-1} 2n_0H \frac{(\delta - (2j - 1)H)}{a_1 a_2} \right) \quad (\text{B.22})$$

By rearranging the terms in (B.22) and applying the upper-bound theorem, it is easy to derive equation (3.50) giving the resistance.

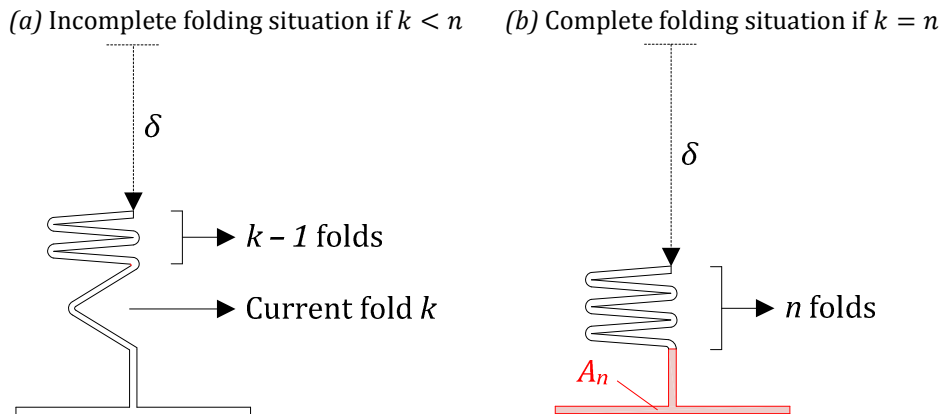


Figure B.6. Folding situations if $k < n$ and $k = n$

Nevertheless, all the calculations performed here above are only valid as long as the web is not totally crushed. If n is the maximal number of folds, then (B.22) and (3.50) are only valid as long as $k \leq n$, with:

$$k = \left\lceil \frac{\delta}{2H} \right\rceil \quad ; \quad n = \left\lfloor \frac{h_w}{2H} \right\rfloor \quad (\text{B.23})$$

If $k = n$, the super-element resistance is calculated as the level reached for $\delta = 2nH$, to which is added the membrane extension of the uncrushed part of the cross-section. Noticing that this latter has an area A_n equal to $(h_w - 2nH)t_w + h_f t_f$, the corresponding internal dissipation is given by:

$$\dot{E}_{int} = A_n \sigma_0 (\delta - 2nH) \frac{a_1 + a_2}{a_1 a_2} \quad (\text{B.24})$$

Adding (B.24) to (B.22) in which $\delta = 2nH$, rearranging the terms and applying the virtual work principle finally leads to equation (3.51).

B.2.2. Plastic capacities of a crushed beam

The derivation of the plastic moment for a folded cross-section is a quite arduous task. Considering first the particular situation in which the web has been crushed over the distance $2kH$ (Figure B.7a), the main difficulty consists in evaluating the contribution of the k folds to the bending capacity. A conservative hypothesis is to assume that the efficient cross-section is made of the flange and the unfolded height h_k of the web, which leads to the plastic capacity denoted by M_k . This latter is an irregularly decreasing function of k (Figure B.7c) and with $h_k = h_w - 2kH$, it may be shown that:

- If $h_k t_w \geq h_f t_f$:
$$M_k = \sigma_0 \frac{h_k}{2} \left(\frac{h_k t_w}{2} + h_f t_f \right) + \sigma_0 \frac{h_f t_f}{2} \left(1 - \frac{h_f}{2t_w} \right) \quad (\text{B.25})$$
- If $h_k t_w < h_f t_f$:
$$M_k = \sigma_0 \frac{h_k t_w}{2} \left(h_w + t_f - \frac{h_w t_w}{2h_f} \right) + \sigma_0 \frac{h_f t_f^2}{4}$$

Of course, when no additional fold can be created over the web height (i.e. for $k = n$), then M_k remains constant: $M_k = M_n$.

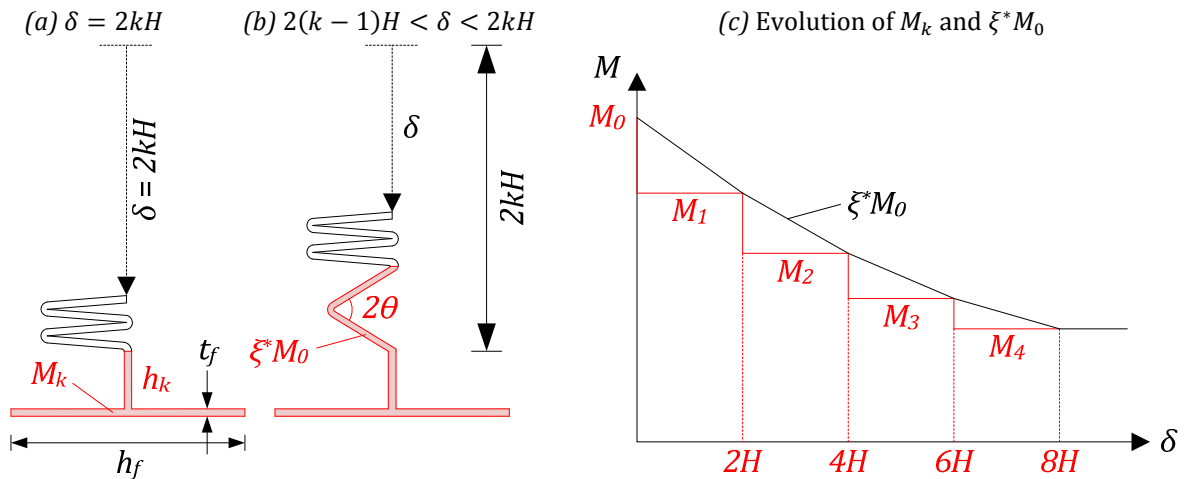


Figure B.7. Plastic bending capacity of a folded cross-section

Let us now consider the situation where the fold number k is not completely closed (Figure B.7b), which means that $2(k-1)H < \delta < 2kH$. In this case, it is too conservative to consider only the efficient portion of Figure B.7a. The derivation of the plastic bending moment $\xi^* M_0$ for the surface depicted on Figure B.7b can be achieved by working with the

opening angle 2θ , but doing so leads to very cumbersome equations that may be reasonably approximated by interpolating linearly between M_{k-1} and M_k . With such an approach, ξ^*M_0 is a piecewise linear function of δ , as depicted on Figure B.7c and given by:

- If $k < n$: $\xi^*M_0 = M_k + \frac{M_k - M_{k-1}}{2H}(\delta - 2kH)$ with $2(k-1)H \leq \delta \leq 2kH$
- If $k = n$: $\xi^*M_0 = M_n$ with $\delta \geq 2nH$

Regarding now the axial resistance of a crushed beam, it is assumed that the folded part is still capable of developing its full tensile resistance. Consequently, there is no difference with the initial T-shape cross-section of Figure 3.3, i.e.:

$$N_0 = \sigma_0(h_w t_w + h_f t_f) \quad (\text{B.27})$$

Finally, the last step to characterize the plastic capacities of the folded cross-section is to define an interaction criteria between the bending moment M and the normal force N . The derivation for the section depicted on Figure B.7b is not tractable within an analytical approach. As a matter of simplification, it is proposed here to used the following parabolic formula:

$$\frac{M}{\xi^*M_0} = 1 - \left(\frac{N}{N_0}\right)^2 \quad (\text{B.28})$$

in which ξ^*M_0 is a function of δ given by (B.26). Consequently, the interaction criteria (B.28) changes with the value of the indentation reached during the folding mechanism and is progressively flattened as long as ξ^*M_0 decreases.

B.3. Appendix B.3

B.3.1. Derivation of the resistance for a direct impact

In this appendix, the resistance is first established for the situation where the intersection is directly impacted by the stem (Figure 3.35a). The case of a subsequent contact is treated later.

B.3.1.1. Folding mechanism

In order to derive the local resistance $P_f(\delta)$ for the third type of super-element during the folding process, it is first required to postulate a compatible displacement field. To do so, it is probably more intuitive to start by considering the deformed configuration and imagine a restoring motion that takes it back to its primary position. Of course, by symmetry, it is sufficient to work only on one half of the mechanism of Figure 3.37b by considering the two triangles OAE and AEB . For convenience, these latter will be respectively denoted by I and II in this section (Figure B.8a). The initial locations of points A , B , E and O are denoted by A_0 , B_0 , E_0 and O_0 respectively.

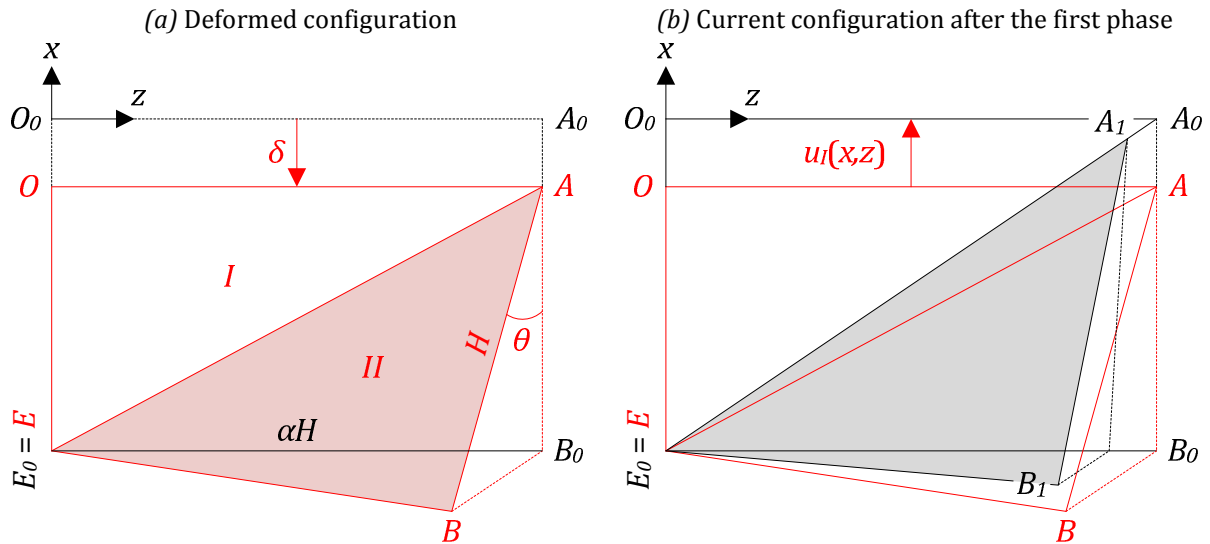


Figure B.8. First phase of the restoring motion

During the first phase of the restoring movement, surface I is submitted to a displacement $u_I(x, z)$ that brings O and A back to O_0 and A_0 respectively (obviously, point E is not moving as $E = E_0$). If θ is the opening angle (Figure B.8a), it can be shown that:

$$u_I(x, z) = (1 - \cos \theta)(x + H) \quad (\text{B.29})$$

with $-H \leq x \leq 0$ and $0 \leq z \leq \alpha(x + H)$. According to Amdahl [8], the derivation of the membrane energy rate can be conducted under the assumption of small strains. Consequently, applying (A.19) and (A.25) leads to:

$$\dot{\epsilon}_{xx} = \frac{\partial \dot{u}_I}{\partial x} \Rightarrow \dot{\epsilon}_I = \sqrt{2/3} \dot{\epsilon}_{xx} = \dot{\theta} \sqrt{2/3} \cos \theta \quad (\text{B.30})$$

where $\dot{\epsilon}_I$ is the equivalent plastic strain rate associated to surface I . During this first phase of the motion, there should be no plastic dissipation over AEB , which means that this triangle moves like a rigid body. This is possible by postulating that OAE and AEB are weakly

connected along the line AE , where no shearing may take place. Therefore, when OAE is brought back to its initial configuration, point A simply slides along AE until it reaches an intermediate position A_1 (Figure B.8b) such that $\overline{EA_1} = \overline{EA} \leq \overline{EA_0}$. Similarly, by symmetry and for compatibility reasons, point B is displaced in the horizontal plane EBB_0 until B_1 such that $\overline{EB} = \overline{EB_1}$ and $\overline{AB} = \overline{AB_1} = H$. So at the end of this first phase, after applying $u_I(x, z)$, OAE is moved back to $O_0A_0E_0$ and AEB is rigidly transformed into A_1EB_1 .

Nevertheless, it is obvious that the material fibers of surfaces I and II are not independent, which means that point A is not allowed to move freely along AE without violating the continuity requirement. Therefore, the next step is now to define a restoring motion to project A_1EB_1 onto $A_0E_0B_0$. To do so, A_1EB_1 may first be rotated around the plastic hinge A_0E until it reaches the (x, z) plane. By imposing this movement, B_1 is transformed into B_2 (Figure B.9) but A_1EB_2 is kept isometric to A_1EB_1 and the initial situation is still not yet recovered.

Consequently, in order to reestablish the compatibility, it appears from Figure B.9 that A_1 has to follow a displacement u_A along the x axis and w_A along the z axis. Of course, a similar conclusion is valid for B_2 .

From simple geometrical considerations, it can be shown that the components of the displacements imposed to points A and B are as follows:

$$\begin{aligned}
 \bullet \quad u_A &= H \left(1 - \sqrt{\frac{\alpha^2 + \cos^2 \theta}{\alpha^2 + 1}} \right) & w_A &= \alpha H \left(1 - \sqrt{\frac{\alpha^2 + \cos^2 \theta}{\alpha^2 + 1}} \right) \\
 \bullet \quad u_B &= \alpha H \frac{\sqrt{4\alpha^2 + \sin^2 2\theta} - 2\alpha}{2\sqrt{\alpha^2 + 1}\sqrt{\alpha^2 + \cos^2 \theta}} & w_B &= H \left(\alpha - \frac{2\alpha^3 + \sqrt{4\alpha^2 + \sin^2 2\theta}}{2\sqrt{\alpha^2 + 1}\sqrt{\alpha^2 + \cos^2 \theta}} \right)
 \end{aligned} \tag{B.31}$$

The velocities of points A_1 and B_2 are found by differentiating (B.31) with respect to time. Doing so leads to:

$$\begin{aligned}
 \dot{u}_A &= \frac{H \sin 2\theta}{2\sqrt{\alpha^2 + 1}\sqrt{\alpha^2 + \cos^2 \theta}} \dot{\theta} = H \sin 2\theta \hat{u}_A(\theta) \dot{\theta} \\
 \dot{u}_B &= \frac{\alpha H \sin 2\theta}{2\sqrt{\alpha^2 + 1}} \frac{2 \cos^2 \theta (2\alpha^2 + \cos^2 \theta) - \alpha^3 \sqrt{4\alpha^2 + \sin^2 2\theta}}{\sqrt{4\alpha^2 + \sin^2 2\theta} (\alpha^2 + \cos^2 \theta)^{3/2}} \dot{\theta} = H \sin 2\theta \hat{u}_B(\theta) \dot{\theta} \\
 \dot{w}_A &= \frac{\alpha H \sin 2\theta}{2\sqrt{\alpha^2 + 1}\sqrt{\alpha^2 + \cos^2 \theta}} \dot{\theta} = H \sin 2\theta \hat{w}_A(\theta) \dot{\theta} \\
 \dot{w}_B &= \frac{H \sin 2\theta}{2\sqrt{\alpha^2 + 1}} \frac{2 \cos^2 \theta (2\alpha^2 + \cos^2 \theta) + \alpha^3 \sqrt{4\alpha^2 + \sin^2 2\theta}}{\sqrt{4\alpha^2 + \sin^2 2\theta} (\alpha^2 + \cos^2 \theta)^{3/2}} \dot{\theta} = H \sin 2\theta \hat{w}_B(\theta) \dot{\theta}
 \end{aligned} \tag{B.32}$$

With these results, it is now possible to define the velocity fields $\dot{u}_{II}(x, z)$ and $\dot{w}_{II}(x, z)$ that are applied on surface II . These ones are obtained by interpolating linearly between (\dot{u}_A, \dot{w}_A) and (\dot{u}_B, \dot{w}_B) , i.e.:

$$\begin{aligned}
 \bullet \quad \dot{u}(x, z) &= \left(1 + \frac{x}{H} \right) \dot{u}_A + \left(\frac{z}{\alpha H} - \frac{x}{H} - 1 \right) \dot{u}_B \\
 \bullet \quad \dot{w}(x, z) &= \left(1 + \frac{x}{H} \right) \dot{w}_A + \left(\frac{z}{\alpha H} - \frac{x}{H} - 1 \right) \dot{w}_B
 \end{aligned} \quad \text{with:} \quad \begin{aligned} & -H \leq x \leq 0 \\ & \alpha(x + H) \leq z \leq \alpha H \end{aligned} \tag{B.33}$$

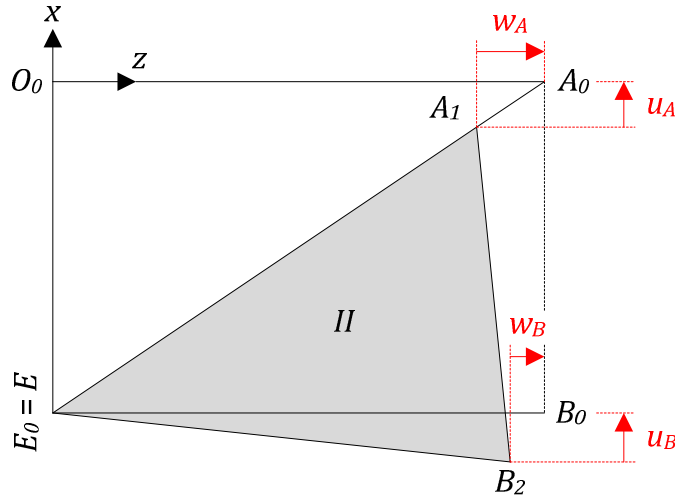


Figure B.9. Second phase of the restoring motion

Once again, under the hypothesis that (u_A, w_A) and (u_B, w_B) are reasonably small, then (B.33) can be introduced in (A.19) to get the strain rates:

$$\dot{\epsilon}_{xx} = \frac{\dot{u}_A - \dot{u}_B}{H} ; \quad \dot{\epsilon}_{zz} = \frac{\dot{w}_B}{\alpha H} ; \quad \dot{\epsilon}_{xz} = \frac{\dot{u}_B}{2\alpha H} + \frac{\dot{w}_A - \dot{w}_B}{2H} \quad (\text{B.34})$$

In accordance with the plastic flow theory, (A.25) allows for the derivation of the equivalent plastic strain rate $\dot{\epsilon}_{II}$ for surface *II*. By substituting (B.34) in (A.25), this latter is found to be:

$$\dot{\epsilon}_{II} = \sqrt{2/3} \sqrt{\dot{\epsilon}_{xx}^2 + \dot{\epsilon}_{zz}^2 + 2\dot{\epsilon}_{xz}^2} = \dot{\theta} \sqrt{2/3} \hat{g}(\theta) \sin \theta \quad (\text{B.35})$$

where $\hat{g}(\theta)$ is a function that may be evaluated with help of the \hat{u}_A , \hat{u}_B , \hat{w}_A and \hat{w}_B defined in (B.32). It can be shown that:

$$\hat{g}(\theta) = 2 \cos \theta \sqrt{(\hat{u}_A - \hat{u}_B)^2 + \hat{w}_B^2/\alpha^2 + 1/2 (\hat{u}_B/\alpha + \hat{w}_A - \hat{w}_B)^2} \quad (\text{B.36})$$

Once the equivalent plastic strain rates have been defined over the surfaces *I* and *II*, the total membrane energy dissipation \dot{E}_m associated to the plastic mechanism of Figure 3.37b can be calculated by integrating $\dot{\epsilon}_I$ and $\dot{\epsilon}_{II}$ over the triangles $O_0A_0E_0$ and $E_0A_0B_0$ respectively. Doing so leads to:

$$\dot{E}_m = \sqrt{2/3} \frac{n_0 H^2 \sin \theta}{2} \hat{G}(\theta) \dot{\theta} ; \quad \hat{G}(\theta) = \alpha (\hat{g}(\theta) + 1) \quad (\text{B.37})$$

The determination of α can be achieved in order to minimize (B.37). Deriving this last relation with respect to α implies that $\partial \hat{G}(\theta) / \partial \alpha = 0$. Nevertheless, solving this equation leads to an expression of α that is a function of θ , which means that the length of part ① (Figure 3.37a) is continuously changing with the opening angle. According to Amdahl [8], doing so is physically not acceptable, as it is natural to assume that the collapse pattern is defined in the early stages of collapse and is kept constant throughout the indentation process. Therefore, $\partial \hat{G}(\theta) / \partial \alpha = 0$ has to be solved for $\theta = 0$ and it can be shown that doing so is equivalent to minimizing:

$$\hat{G}(0) = \alpha + \sqrt{\frac{1}{\alpha^2} + \frac{1}{2} \left(\frac{2\alpha^2 + 2\alpha + 3}{\alpha^2 + 1} \right)^2} \quad (\text{B.38})$$

The optimal value of α is numerically found equal to 0.8601, which is a bit higher than the solution proposed by Amdahl [8].

The second step in deriving the resistance of the folding mechanism consists in evaluating the bending energy dissipation \dot{E}_b produced by the plastic hinges AE , AB and EB (Figure B.8a). If the rotations angles around AE , AB and EB are respectively denoted by θ_1 , θ_2 and θ_3 , from geometric considerations, the following results can be established:

$$\bullet \theta_1 = \arccos\left(\frac{2\alpha \cos \theta}{\sqrt{4\alpha^2 + \sin^2 2\theta}}\right) \Leftrightarrow \dot{\theta}_1 = \frac{4\alpha (\alpha^2 + \cos^4 \theta)}{(4\alpha^2 + \sin^2 2\theta)\sqrt{\alpha^2 + \cos^2 \theta}} \dot{\theta} \quad (\text{B.39})$$

$$\bullet \theta_2 = \arccos\left(\frac{4\alpha^3 \sin \alpha}{\sqrt{4\alpha^2 + \sin^2 2\theta} \sqrt{4\alpha^2(\alpha^2 + 1) + \sin^2 2\theta}}\right) \Leftrightarrow \dot{\theta}_2 \simeq \dot{\theta} \quad (\text{B.40})$$

$$\bullet \theta_3 = \arcsin\left(\frac{\sin 2\theta}{\sqrt{4\alpha^2 + \sin^2 2\theta}}\right) \Leftrightarrow \dot{\theta}_3 = \frac{|4\alpha^2 - \sin^2 2\theta| |\cos 2\theta|}{\alpha(4\alpha^2 + \sin^2 2\theta)} \dot{\theta} \quad (\text{B.41})$$

Multiplying the lengths \overline{AE} , \overline{AB} and \overline{EB} of the plastic hinges with the rotation rates given here above leads to the following result for the bending dissipation:

$$\dot{E}_b = m_0 H \left(\frac{4\alpha (\alpha^2 + \cos^4 \theta)}{4\alpha^2 + \sin^2 2\theta} + \sqrt{\alpha^2 + \sin^2 \theta} + \frac{|4\alpha^2 - \sin^2 2\theta| |\cos 2\theta|}{\alpha(4\alpha^2 + \sin^2 2\theta)} \right) \dot{\theta} \quad (\text{B.42})$$

According to the upper-bound theorem, equating the external work $P_1 \dot{\delta}$ to the total energy rate $2(\dot{E}_b + \dot{E}_m)$ allows to determine the resistance P_1 coming from part ① during the folding mechanism. As δ and θ are still related by (3.42), one should have $\dot{\delta} = 2H\dot{\theta} \sin \theta$ and:

$$P_1(\delta) = \frac{2(\dot{E}_m + \dot{E}_b)/\dot{\theta}}{2H \sin \theta} = \frac{n_0 H}{\sqrt{6}} \hat{G}(\theta) + \frac{\dot{E}_b/\dot{\theta}}{H \sin \theta} \quad (\text{B.43})$$

From (B.43), it appears that the limit for $\theta \rightarrow 0$ does not converge because of the bending energy rate, which is exactly the same problem than in section 3.4.2.1. In order to overcome this difficulty, \dot{E}_b can be averaged over one fold using (3.46) to get:

$$P_1(\delta) = \frac{n_0 H}{\sqrt{6}} \hat{G}(\theta) + m_0 \pi \left(\sqrt{\alpha^2 + 1} + \frac{\alpha}{6} + \frac{2}{5} \right) \quad (\text{B.44})$$

Finally, the total resistance $P_w(\delta)$ associated to one wing of the intersection is obtained by adding the contributions $P_1(\delta)$ and $P_2(\delta)$ respectively associated to parts ① and ② (Figure 3.37a). Of course, $P_2(\delta)$ may still be found by (3.48), in which a_1 is replaced by $a - \alpha H$ and all the terms involving a_2 are deleted:

$$P_2(\delta) = \frac{m_0(a - \alpha H)\pi}{H} + \frac{n_0 H}{2(a - \alpha H)} (\delta + 2H) \quad (\text{B.45})$$

Summing up (B.44) and (B.45) gives the following formula for the resistance $P_w(\delta)$ coming from one wing:

$$P_w(\delta) = n_0 H \left(\frac{\hat{G}(\theta)}{\sqrt{6}} + \frac{\delta + 2H}{2(a - \alpha H)} \right) + m_0 \pi \left(\sqrt{\alpha^2 + 1} + \frac{\alpha}{6} + \frac{2}{5} + \frac{a - \alpha H}{H} \right) \quad (\text{B.46})$$

where $\hat{G}(\theta)$ is given by (B.37) and $\alpha = 0.8601$. The opening angle θ is related to the indentation δ by (3.42), but H is still unknown so far. As it was done for the second super-

element type, this latter can be calculated by minimizing the mean crushing resistance \bar{P}_w of the wing, as detailed hereafter.

B.3.1.2. Folding height

As in section 3.4.2.1, the optimal folding height H is such that the average value \bar{P}_w of the wing resistance is minimum. Consequently, the following problem has to be solved:

$$\frac{\partial \bar{P}_w}{\partial H} = 0 \Leftrightarrow \frac{\partial}{\partial H} \left(\frac{1}{2H} \int_0^{2H} P_w(\delta) d\delta \right) = 0 \quad (\text{B.47})$$

in which $P_w(\delta)$ is given by (B.46). A first step to get \bar{P}_w is to calculate the mean value \bar{P}_2 of the resistance opposed by part ②. By integrating (B.45), this latter is found to be:

$$\bar{P}_2 = \frac{3n_0H^2}{2(a - \alpha H)} + \frac{m_0(a - \alpha H)\pi}{H} \simeq \frac{3n_0H^2}{2a} + \frac{m_0a\pi}{H} \quad (\text{B.48})$$

where the approximate solution is obtained by assuming that $a \gg H$. Regarding the average resistance \bar{P}_1 for part ①, integrating (B.44) may be achieved as follows:

$$\bar{P}_1 = \frac{1}{2H} \int_0^{2H} P_1(\delta) d\delta = \int_0^{\pi/2} P_1(\theta) \sin \theta d\theta \quad (\text{B.49})$$

because $d\delta = 2H \sin \theta d\theta$ according to (3.42). Furthermore, substituting equation (B.44) in the previous relation leads to:

$$\bar{P}_1 = \frac{n_0H}{\sqrt{6}} \int_0^{\pi/2} \hat{G}(\theta) \sin \theta d\theta + m_0\pi \left(\sqrt{\alpha^2 + 1} + \frac{\alpha}{6} + \frac{2}{5} \right) \quad (\text{B.50})$$

Unfortunately, it is not possible to realize an analytical integration of (B.50) because $\hat{G}(\theta)$ is a complex function of θ . Nevertheless, this can be achieved numerically and it is concluded that a reasonable approximation for the first term in (B.50) is $2n_0H/3$. Finally, gathering all the developments detailed previously provides the subsequent result:

$$\bar{P}_w = \frac{2n_0H}{3} + m_0\pi \left(\sqrt{\alpha^2 + 1} + \frac{\alpha}{6} + \frac{2}{5} \right) + \frac{3n_0H^2}{2a} + \frac{m_0a\pi}{H} \quad (\text{B.51})$$

In order to minimize \bar{P}_w , (B.51) has to be derived with respect to H . The optimal folding height is such that the following equation is satisfied:

$$\frac{2n_0}{3} + \frac{3n_0H}{a} - \frac{m_0a\pi}{H^2} = 0 \Leftrightarrow \frac{3n_0H^3}{a} + \frac{2n_0H^2}{3} = m_0a\pi \quad (\text{B.52})$$

Of course, (B.52) can be solved numerically for given values of σ_0 , t_w and a . However, doing so is not really satisfactory. Indeed, under the assumption that $H \ll a$, the first term of (B.52) can be neglected, which leads to a more systematic evaluation of the folding height:

$$H = \sqrt{3\pi/8at_w} \simeq 1.085\sqrt{at_w} \quad (\text{B.53})$$

This solution can be compared with the one obtained while considering the displacement field suggested by Amdahl [8]. In this case, following the same procedure than the one exposed

here above, the mean crushing force for one wing and the optimal folding height are as follows:

$$\bar{P}_w = \frac{2.58n_0}{4}H + \frac{m_0\pi}{4} + \frac{3n_0H^2}{2a} + \frac{m_0a\pi}{H} ; H \approx 1.103\sqrt{at_w} \quad (\text{B.54})$$

which is very close to the expressions given in (B.51) and (B.53). Nevertheless, in order to have a better idea of the error made by solving (B.52) instead of the exact minimization equation, it could be of interest to compare (B.53) with the value obtained by considering all the terms in \bar{P}_w , i.e:

$$\bar{P}_w = \frac{2n_0H}{3} + m_0\pi \left(\sqrt{\alpha^2 + 1} + \frac{\alpha}{6} + \frac{2}{5} \right) + \frac{3n_0H^2}{2(a - \alpha H)} + \frac{m_0(a - \alpha H)\pi}{H} \quad (\text{B.55})$$

Deriving (B.55) with respect to H , it is found that the optimal value for the ratio H/a has to satisfy the following equation:

$$3(H/a)^3 \frac{2 - \alpha(H/a)}{2(1 - \alpha(H/a))^2} + \frac{2(H/a)^2}{3} - \frac{\pi t_w}{4a} = 0 \quad (\text{B.56})$$

which can be solved numerically for different values of t_w/a . The corresponding curve is plotted on Figure B.10 with the one obtained by considering (B.53). From this picture, it appears that the folding height is overestimated when using (B.53). As expected, the difference between the results is increasing with the ratio t_w/a .

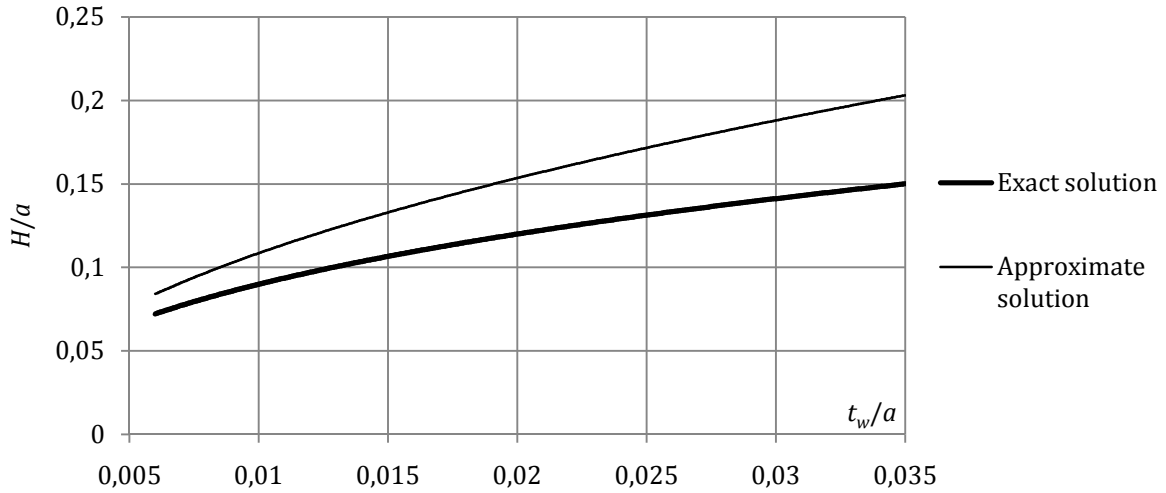


Figure B.10. Comparison of the exact and approximate folding height

Of course, using a too high value of H is not necessarily conservative. Nevertheless, even though the discrepancy on Figure B.10 may be quite important, it is worth noting that working with (B.53) is not really a problem, as the influence of H on the crushing resistance is moderate.

B.3.1.3. Derivation of the resistance for the bending mechanism

The derivation of the local resistance during the bending mechanism is first performed for a cruciform, the case of a T-shaped intersection being treated later. The collapse mode involves four plastic hinges at the center and four other ones at the connection points A, B, C, D (Figure B.11a). In this configuration, for a given penetration δ of the striking vessel, each of the four wings is submitted to both a rotation in the hinges and a membrane straining.

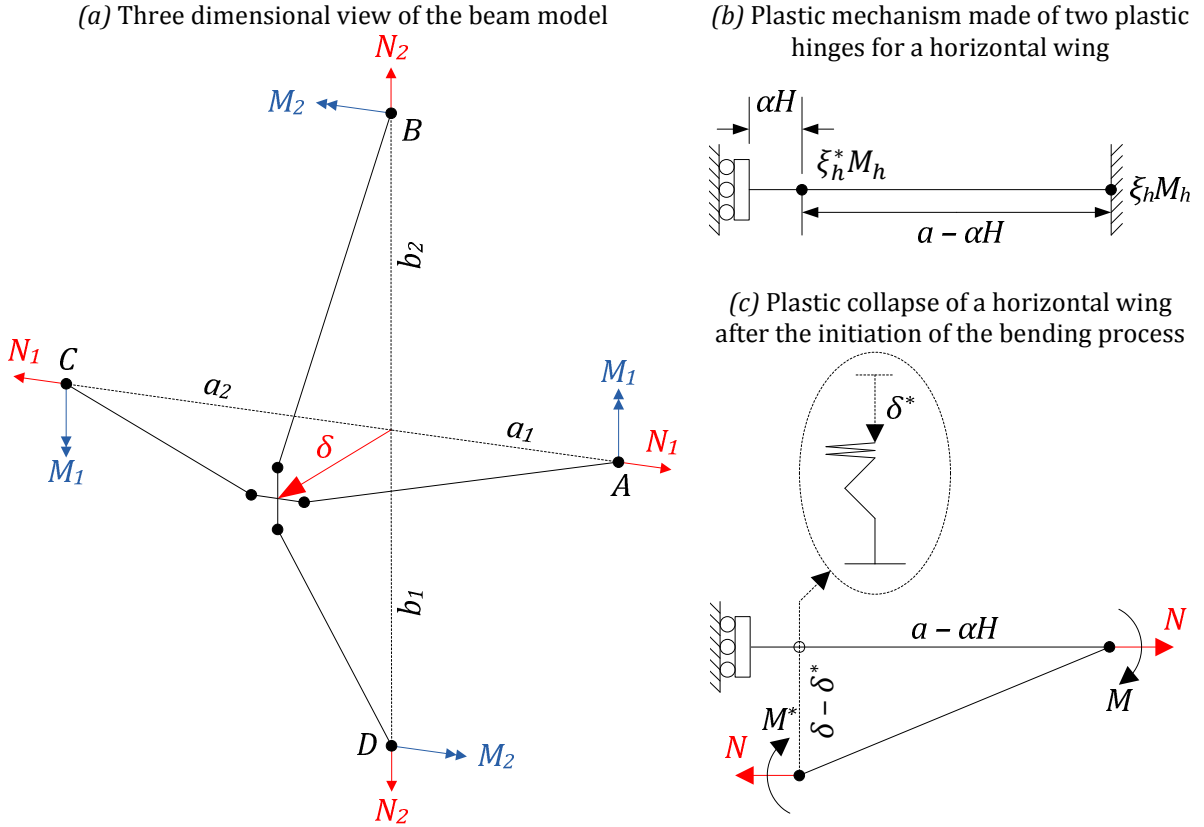


Figure B.11. Backward motion of an intersection during the bending process

In the purpose of evaluating the resistance, the axial and bending plastic capacities of the horizontal girder are respectively denoted by N_h and M_h , while the corresponding ones for the vertical frame are N_v and M_v . These latter may be evaluated with help of equations (B.25) and (B.27), in which the fold number k is set to 0. In the present model, it assumed that the full values of M_h and M_v cannot be reached for the following reasons:

- In the four plastic hinges located at the supports A , B , C , D , the bending moment could only be equal to M_h or M_v if the wings were perfectly clamped at these locations. As shown on Figure 3.39, this is not the case because the junction is made with other structural elements that are not infinitely rigid. Consequently, the rotational restraint should be modeled by a torsion spring characterized by a reduction coefficient (Figure 3.39). This latter is denoted by ξ_h for the horizontal girder and is assumed to be the same for the two connections A and C . Similarly, regarding the vertical frame, the supports B and D are also affected with an identical coefficient ξ_v . The corresponding maximal bending moments are therefore only equal to $\xi_h M_h$ or $\xi_v M_v$.
- In the four central hinges, as the sections have already been submitted to a primary indentation δ^* during the folding process, M_h and M_v may also not be reached at these locations. As the parameters H , k and n are uniquely defined for the four wings¹⁶, it is obvious that the two hinges located on the horizontal girder may be characterized by the same coefficient ξ_h^* . This is also the case for the vertical frame, where a unique reduction

¹⁶ Let us recall that H is obtained by taking the average value of the individual folding heights calculated by (B.53) for each wing. k and n are respectively the current and final fold number. They are calculated by (B.23), in which h_w denotes the smallest web height of the four wings. Consequently, because of these definitions, it is clear that H , k and n have a unique value.

factor ξ_v^* may be used. Consequently, only the reduced bending capacities $\xi_h^* M_h$ and $\xi_v^* M_v$ have to be considered there. Of course, these coefficients may still be found with the formulae detailed in section B.2.2.

As usual, the derivation of the resistance $P_b(\delta)$ for the bending phase is performed by applying the upper-bound method. Focusing on a horizontal wing for example, it can be seen from Figure B.11b that the beam-like behavior involves two plastic hinges. At the initiation of the plastic mechanism, the maximal admissible capacities $\xi_h^*(\delta) M_h$ and $\xi_h M_h$ are reached at these locations. By following a procedure that is very similar to the one described in section 3.6, it is possible to show that the required collapse force $P^*(\delta)$ is as follows:

$$P^*(\delta) = M_h \left(\frac{\xi_h + \xi_h^*(\delta)}{a_1 - \alpha H} + \frac{\xi_h + \xi_h^*(\delta)}{a_2 - \alpha H} \right) + M_v \left(\frac{\xi_v + \xi_v^*(\delta)}{b_1 - \alpha H} + \frac{\xi_v + \xi_v^*(\delta)}{b_2 - \alpha H} \right) \quad (\text{B.57})$$

in which it is worth recalling that $\xi_h^*(\delta)$ and $\xi_v^*(\delta)$ are piecewise linearly decreasing functions of the indentation δ . As soon as the force $P_f(\delta)$ applied during the denting phase is equal to $P^*(\delta)$, then $\delta = \delta^*$ and the crushing of the central cross-section is stopped. At this moment, the value of $\xi_h^*(\delta)$ is stabilized to ξ_h^* .

For $\delta > \delta^*$, the two-hinge mechanism of Figure B.11c is activated and the portion $a - \alpha H$ of the beam is submitted to an axial straining responsible for the development of a membrane force N . Consequently, the bending moments M^* and N are no longer equal to $\xi_h^* M_h$ and $\xi_h M_h$ but have to be calculated in accordance with an interaction criterion (see section B.2.2):

$$\frac{M}{\xi_h M_h} + \left(\frac{N}{N_h} \right)^2 = 1 \quad ; \quad \frac{M^*}{\xi_h^* M_h} + \left(\frac{N}{N_h} \right)^2 = 1 \quad (\text{B.58})$$

According to the plastic theory of beams detailed in section 3.6, the normality rule can be applied to get the tensile force, which leads to:

$$N = \frac{N_h^2 (\delta - \delta^*)}{2 M_h (\xi_h + \xi_h^*)} \quad ; \quad N \leq N_h \quad (\text{B.59})$$

As expected, it can be seen from (B.59) that the membrane force increases linearly with the penetration, until the axial capacity of the beam is reached. In the present case, this latter is still calculated by applying (B.27), but it is worth bearing in mind that the intensity of the axial straining remains questionable. Indeed, (B.59) is derived under the assumption of having a perfectly fixed support, but this is not necessarily the case, as represented on Figure 3.39. Nevertheless, accounting for the real flexibility of the boundaries is not feasible with the super-elements method but can be achieved through other techniques such as the ISUM approach (see section 3.2.2).

The derivation of the contribution $P_w(\delta)$ of the wing to the total local resistance $P_b(\delta)$ is simply found by expressing the rotational equilibrium of the structure shown on Figure B.11c. Accounting for (B.58) at the same time, the following result can be established:

$$P_w(\delta) = \frac{M_h (\xi_h + \xi_h^*)}{a - \alpha H} \left(1 - \frac{N^2}{N_h^2} \right) + \frac{N (\delta - \delta^*)}{a - \alpha H} \quad (\text{B.60})$$

where N is given by (B.59). Of course, the developments for the vertical wings are very similar, provided that the corresponding geometrical and mechanical properties are used.

Finally, the total resistance for the cruciform is obtained by summing up the four individual contributions $P_w(\delta)$, which leads to equation (3.65).

In the case of an impact occurring at the top of the door, the resistance of T-shaped cross section is also a matter of concern (Figure B.12). Of course, the considerations exposed here above are still relevant, but some adaptations need to be done. Regarding the force $P^*(\delta)$ required to activate the bending mechanism, it is obvious that it is simply given by deleting one term in (B.57), i.e.:

$$P^*(\delta) = M_h \left(\frac{\xi_h + \xi_h^*(\delta)}{a_1 - \alpha H} + \frac{\xi_h + \xi_h^*(\delta)}{a_2 - \alpha H} \right) + M_v \frac{\xi_v + \xi_v^*(\delta)}{b - \alpha H} \quad (\text{B.61})$$

Nevertheless, for $\delta > \delta^*$, additional corrections are required. Indeed, from Figure B.12, it appears that the membrane force N_2 in the vertical wing can only be balanced by the shearing of the horizontal girder, which is not realistic. In fact, instead of being only submitted to a horizontal displacement δ , the intersection also suffers a vertical one. Point E is therefore simply sliding along the bow, such that the length $\overline{EC} = b$ is kept constant. Consequently, in accordance with the normality rule, $N_2 = 0$ and there is no axial straining.

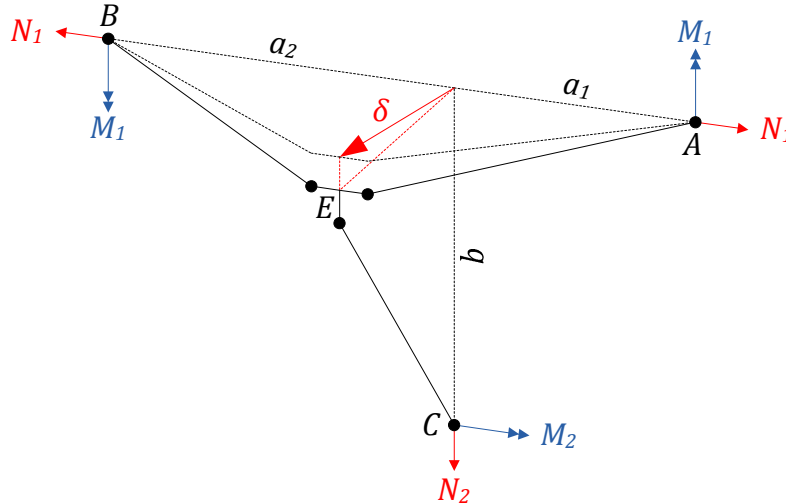


Figure B.12. Bending mechanism for a T-shaped cross-section

Considering only bending effects in the third wing, it is easy to show that the resistance is as follows:

$$P_b(\delta) = \left(M_h(\xi_h + \xi_h^*) \left(1 - \frac{N^2}{N_h^2} \right) + N(\delta - \delta^*) \right) \frac{a_1 + a_2 - 2\alpha H}{(a_1 - \alpha H)(a_2 - \alpha H)} + \frac{M_v(\xi_v + \xi_v^*)}{b - \alpha H} \quad (\text{B.62})$$

with N given by (B.59). As a closing remark on T-shaped intersections, it is interesting to note that having a membrane force in the vertical wing is however possible in the case of lifting gates, as the cables could allow for the development of an axial straining. $P^*(\delta)$ is then still obtained by (B.61) and $P_b(\delta)$ can be calculated by deleting the adequate term in (3.65).

B.3.2. Derivation of the resistance for a subsequent contact

This second part of the appendix is devoted to the derivation of the resistance when one of the supports of a SE2 is impacted by the striking vessel. Here again, two mechanisms are considered.

B.3.2.1. Folding mechanism

In section 3.4.2.1, it was postulated that the deformation pattern for a super-element of type 2 during the folding process was made of two wings, each of them being characterized by a length a_1 and a_2 (Figure 3.26). Of course, this assumption is only reasonable as long one of the supports is not impacted by the vessel. If this is the case, the crushing mechanism is modified and the one depicted on Figure 3.26 is no longer valid.

The particular value for which a subsequent contact occurs is denoted by δ_1 and can be easily calculated by accounting for the bow geometry. At this moment (Figure B.13), the development of the current fold¹⁷ is stopped and a new mechanism is initiated immediately after it. This latter is characterized by a height $2H_1$ that is not necessarily the same as the previous one. It is made of three different parts respectively numbered *I*, *II* and *III* on Figure B.13.

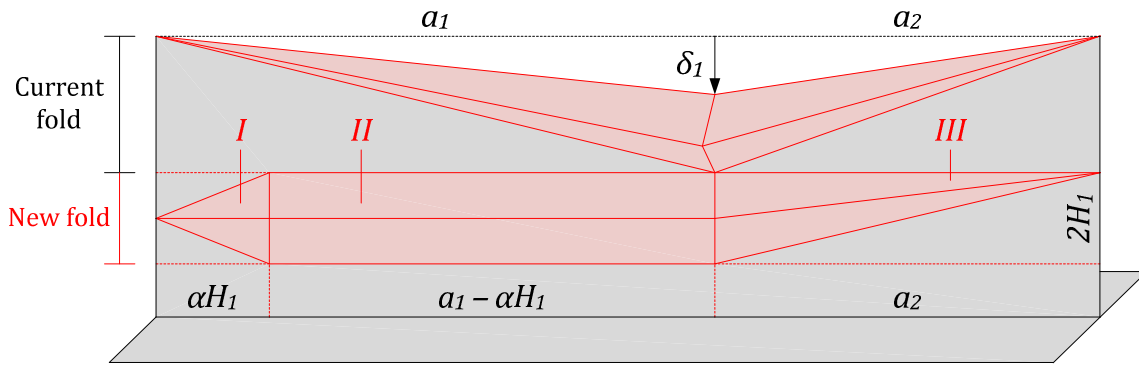


Figure B.13. Initiation of a new fold for $\delta = \delta_1$

For $\delta > \delta_1$, it is assumed that the ship is only moving forward because of the crushing of the new fold (Figure B.14), the first one keeping a constant opening. From numerical simulations, it appears that this is not exactly the case because there is a progressive closure of the first fold concomitant to the plastic collapse of the new one. As this transitory phase is not of primary importance in the crushing process, it will not be considered here. Therefore, the hypothesis is made that only the new mechanism is involved for $\delta > \delta_1$.

Of course, the total resistance is obtained by summing up the individual contributions coming from the surfaces *I*, *II* and *III* (Figure B.13), but it should be also accounted for the effect of the first fold. From Figure B.14, it can be stated that the left wing (i.e. connected to the impacted support) is simply moving as a rigid body and therefore remains totally unaffected for $\delta > \delta_1$, but this is not true for the right wing. Indeed, as there is not displacement of the non-impacted support, the fibers of part *IV* (Figure B.14) are submitted to an axial straining that is responsible for a membrane energy dissipation. The contributions $P_I(\delta)$ and $P_{III}(\delta)$ of parts *I* and *III* have already been derived in section 3.5.2.1. The first one is still given by (3.56), while the second one may be obtained by (3.59) in which $a - \alpha H$ is replaced by a_2 . Obviously, in these two equations, $\delta - \delta_1$ has to be substituted to δ . On the other hand, it can be shown that the resistances $P_{II}(\delta)$ and $P_{IV}(\delta)$ of surfaces *II* and *IV* are simply given by the following equations:

$$P_{II}(\delta) = \frac{m_0 \pi (a_1 - \alpha H_1)}{H_1} \quad ; \quad P_{IV}(\delta) = 2Hn_0 \frac{\delta - \delta_1}{a_2} \left[\frac{\delta_1}{2H} \right] \quad (\text{B.63})$$

¹⁷ On Figure B.13, for convenience, the contact with the left support is assumed to occur during the development of the first fold. Of course, many other folds could be already totally crushed before subsequent contact.

in which $P_{II}(\delta)$ is derived under the assumption that only bending effects in the horizontal plastic hinges are induced during the collapse of part *II*. The parameters used in (B.63) have the same meanings as in the previous section, except for H_1 that will be derived hereafter.

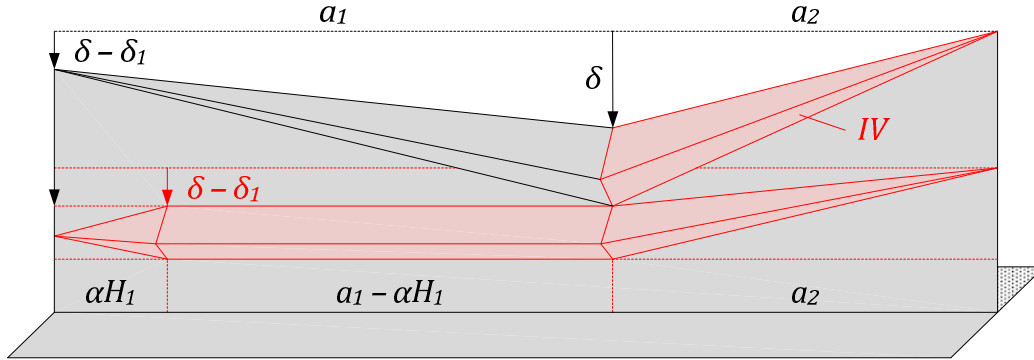


Figure B.14. Folding process for $\delta > \delta_1$

Accounting for all these results, by adding $P_I(\delta)$, $P_{II}(\delta)$, $P_{III}(\delta)$ and $P_{IV}(\delta)$, the resistance after subsequent contact is found to be as follows:

$$\begin{aligned}
 P_{w,1}(\delta) = & n_0 \left(\frac{H_1}{\sqrt{6}} \hat{G}(\theta) + H_1 \frac{\delta - \delta_1 + 2H_1}{2a_2} \right) + m_0 \pi \left(\sqrt{\alpha^2 + 1} - \frac{5\alpha}{6} + \frac{2}{5} + \frac{a_1 + a_2}{H_1} \right) \\
 & + 2n_0 H \frac{\delta - \delta_1}{a_2} \left[\frac{\delta_1}{2H} \right]
 \end{aligned} \tag{B.64}$$

where the opening angle θ is given by equation (3.42), in which δ and H are respectively replaced by $\delta - \delta_1$ and H_1 . The last parameter to determine is precisely the folding height H_1 . This one can be found by minimizing the average value of $P_{w,1}(\delta)$. Following a similar procedure than the one described in section B.3.1.2, it can be shown that (3.58) is still holding to evaluate H_1 , provided that a is replaced by $a_1 + a_2$.

It is worth noting that (B.64) is not the total resistance $P_f(\delta)$ associated to the crushing process. Indeed, when there is a contact with one the supports of a SE2, two or three other adjacent elements are simultaneously impacted, implying that a SE3 is activated. This can be illustrated by considering the cruciform of Figure B.15a that is made of four wings respectively numbered from ① to ④. Initially, only the horizontal part ① is concerned by the collision and therefore deforms like a SE2 (Figure 3.26). However, when the striking bow reaches the support at point O (i.e. when $\delta = \delta_1$), the remaining parts ②, ③ and ④ also contribute to the total resistance $P_f(\delta)$, which means that the intersection is now behaving like a SE3.

The individual contributions $P_{w,2}(\delta)$, $P_{w,3}(\delta)$ and $P_{w,4}(\delta)$ of the adjacent wings ②, ③ and ④ are supposed to be given by the formulae established in section 3.5.2.1. Consequently, the deformation pattern at the initiation of the folding process is the one depicted on Figure B.15a. From this picture, it is apparent that the compatibility along the intersection line is not respected, as the folds generated on the wings ②, ③ and ④ are not consistent with those developing on part ①. Furthermore, it is worth noting that the folding height H obtained by averaging (3.58) is not necessarily equal to H_1 . Consequently, the approach proposed here is not strictly rigorous regarding the upper-bound method. Nevertheless, as the displacement fields are compatible for each wing separately, the derivation of the corresponding individual resistances respects the basic theorems.

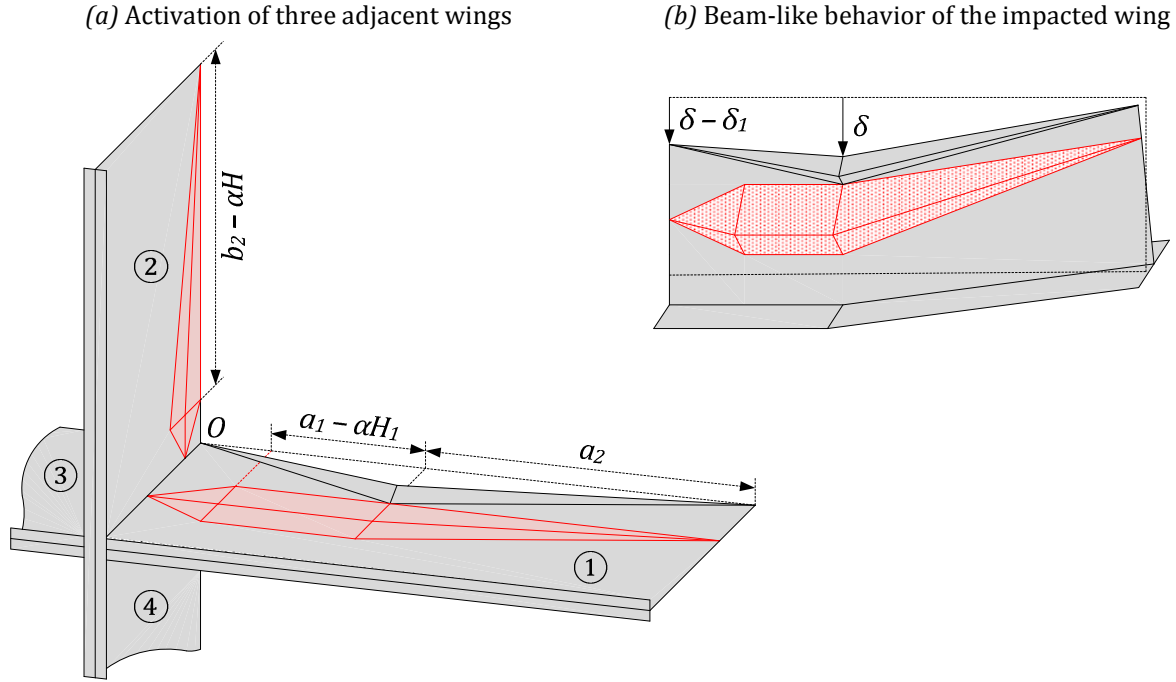


Figure B.15. Crushing and denting mechanism after subsequent contact

Consequently, completing (B.64) leads to the following result for the total resistance associated to the crushing process:

$$\begin{aligned}
 P_f(\delta) = & n_0 \left(\frac{H_1}{\sqrt{6}} \hat{G}(\theta) + H_1 \frac{\delta - \delta_1 + 2H_1}{2a_2} \right) + m_0 \pi \left(\sqrt{\alpha^2 + 1} - \frac{5\alpha}{6} + \frac{2}{5} + \frac{a_1 + a_2}{H_1} \right) \\
 & + 2n_0 H \frac{\delta - \delta_1}{a_2} \left[\frac{\delta_1}{2H} \right] + \sum_{i=2}^{\{3;4\}} P_{w,i}(\delta)
 \end{aligned} \tag{B.65}$$

where the summation involves two or three terms in case of a T or X-shape intersection respectively. Of course, $P_{w,i}(\delta)$ may still be obtained by applying (3.60), in which θ is given by substituting $\delta - \delta_1$ to δ in equation (3.42).

Finally, it should be mentioned that (B.65) can be extended to account for subsequent folding. As usual, this can be achieved by supposing that the same deformation pattern is immediately reproduced as soon as the current fold is completely closed. Doing so leads to formulae that are similar to (3.62) and (3.63).

B.3.2.2. Bending mechanism

Considering the cruciform of Figure B.15a, it is likely that the crushing process is not always relevant because the super-element starts moving as whole for large values of $\delta - \delta_1$. Each wing adopts a beam-like behavior, such as depicted on Figure B.15b for the one where the subsequent contact occurs. This transition is assumed to occur abruptly, when the folding resistance $P_f(\delta)$ is equal to the force $P^*(\delta)$ required to activate the bending mechanism. The particular value of δ for which the behavior changes is denoted by δ^* and has to be carefully determined because two different situations are possible:

- If $\delta^* < \delta_1$, then the switch from the denting to the bending phase happens before the contact with one of the support. In this case, it is assumed that the super-element keeps

moving as a whole for $\delta > \delta_1$. In other words, the crushing process does not take place and the mechanism of Figure B.16a is immediately activated when $\delta = \delta_1$.

- If $\delta^* \geq \delta_1$, there is only a denting phase before the impact with one of the supports. As no transition occurs for $\delta < \delta_1$, the crushing process can continue after the subsequent contact and the developments of section B.3.2.1 are applicable. In this case, the bending mechanism of Figure B.16b is activated when $\delta = \delta^*$.

Consequently, the derivation of δ^* has to be done in accordance with the situation existing before a subsequent contact.

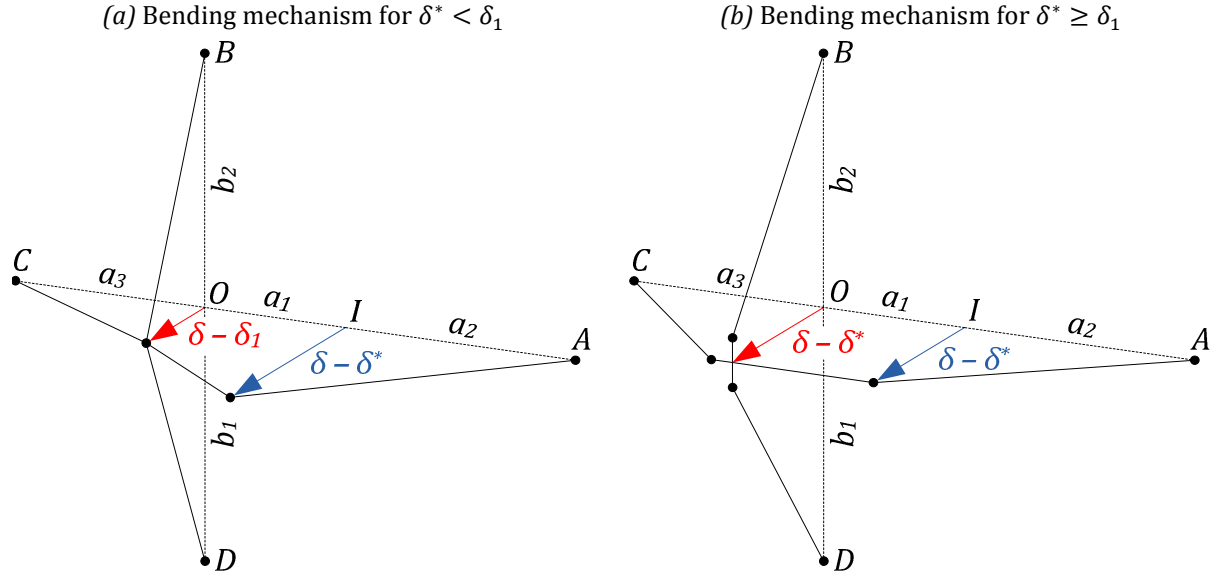


Figure B.16. Bending process in case a subsequent contact

In the first case, when $\delta^* < \delta_1$, the developments performed for a super-element of type 2 are still relevant, so formulae (3.50), (3.51) and (3.53) leading to $P_f(\delta)$ and $P^*(\delta)$ can therefore be used to evaluate δ^* . Furthermore, as long as $\delta < \delta_1$, the resistance during the bending phase $P_b(\delta)$ given by (3.54) is also valid.

Nevertheless, applying (3.54) is only consistent as long as one of the supports has not been impacted (i.e. for $\delta^* < \delta < \delta_1$). If $\delta > \delta_1$, a super-element of type three is activated and (3.54) is not valid anymore. The bending resistance has then to be derived in accordance with the collapse mechanism of Figure B.16a.

Regarding the individual resistances of the vertical wings ② and ④, it is clear that the situation is totally similar to the one studied previously in section 3.5.2.2, except that their central cross-sections at point O (Figure B.16a) have not been impacted. Consequently, the contributions of these two wings is still the same as in equation (3.65), provided that ξ_v^* has to be replaced by ξ_v .

Focusing now on the horizontal elements, the analysis of the third wing is the same as in section B.3.1.3 (Figure B.11), except that the sections have not been crushed. Therefore, the membrane tensile force \tilde{N}_1 and the contribution to the total resistance can be found with help of (B.59) and (B.60), where $\alpha = 0$, $\xi_h^* = \xi_h$ and $\delta^* = \delta_1$. Finally, concerning the first wing, a comparison with the developments of section 3.5.2.2 does not show any major difference,

except that there is no rotation in the plastic hinges over the segment of length a_1 . Consequently, modifying (3.65) and gathering all the previous remarks leads to the following result, where N_1 is still obtained by (3.65):

$$\begin{aligned}
 P_b(\delta) &= M_h \left(\frac{\xi_h + \xi_h^*}{a_2} \left(1 - \frac{N_1^2}{N_h^2} \right) + \frac{2\xi_h}{a_3} \left(1 - \frac{\tilde{N}_1^2}{N_h^2} \right) \right) + \frac{N_1}{a_2} (\delta - \delta^*) + \frac{\tilde{N}_1}{a_3} (\delta - \delta_1) \\
 &+ \frac{b_1 + b_2}{b_1 b_2} \left(2\xi_v M_v \left(1 - \frac{\tilde{N}_2^2}{N_v^2} \right) + \tilde{N}_2 (\delta - \delta_1) \right) \quad (\text{B.66})
 \end{aligned}$$

$$\text{with: } \tilde{N}_1 = \min \left\{ \frac{N_h^2 (\delta - \delta_1)}{4M_h \xi_h} ; N_h \right\} ; \tilde{N}_2 = \min \left\{ \frac{N_v^2 (\delta - \delta_1)}{4M_v \xi_v} ; N_v \right\}$$

In the second case, when $\delta^* > \delta_1$, the wings ②, ③ and ④ are preliminary damaged before the activation of the bending mechanism. Nevertheless, for a given penetration δ of the striking vessel, the indentation at point O is only equal to $\delta - \delta_1$, which means that the plastic moments of their central sections have to be evaluated by accounting for the reduction factors $\xi_h^*(\delta - \delta_1)$ and $\xi_v^*(\delta - \delta_1)$. This can be done in accordance with the linearized procedure detailed in section B.2.2 of Appendix B.2. Consequently, it is worth noting that these cross-sections are not so crushed than the one directly located under the first impact point I (Figure B.16b) because the indentation reached at point O is only $\delta - \delta_1$, while it is equal to δ at point I .

Accounting for the previous remark, it appears that the force $P^*(\delta)$ required to activate the plastic mechanism of Figure B.16b may simply be found by modifying (3.64). Doing so provides the following equation:

$$P^*(\delta) = M_h \left(\frac{\xi_h + \xi_h^*(\delta)}{a_2} + \frac{\xi_h + \xi_h^*(\delta - \delta_1)}{a_3 - \alpha H} \right) + M_v \left(\frac{\xi_v + \xi_v^*(\delta - \delta_1)}{b_1 - \alpha H} + \frac{\xi_v + \xi_v^*(\delta - \delta_1)}{b_2 - \alpha H} \right) \quad (\text{B.67})$$

The transition from one mode to the other will therefore take place at the particular penetration δ^* for which the folding resistance $P_f(\delta)$ calculated by (B.65) is equal to (B.67). After that, when $\delta > \delta^*$, denoting by ξ_h^* , $\tilde{\xi}_h^*$ and $\tilde{\xi}_v^*$ the particular values of $\xi_h^*(\delta^*)$, $\xi_h^*(\delta^* - \delta_1)$ and $\xi_v^*(\delta^* - \delta_1)$ respectively, it is clear that the contributions of the two vertical wings ② and ④ are the same as in equation (3.65), except that ξ_v^* has to be replaced by $\tilde{\xi}_v^*$. Regarding now the resistance of the horizontal elements ① and ③, the portion AC can also be seen as a continuous beam with three hinges. An analytical solution can be obtained by adapting (3.65). Doing so provides the following formula for the bending resistance:

$$\begin{aligned}
 P_b(\delta) &= M_h \left(\frac{\xi_h + \xi_h^*}{a_2} \left(1 - \frac{N_1^2}{N_h^2} \right) + \frac{\xi_h + \tilde{\xi}_h^*}{a_3 - \alpha H} \left(1 - \frac{\tilde{N}_1^2}{N_h^2} \right) \right) + (\delta - \delta^*) \left(\frac{N_1}{a_2} + \frac{\tilde{N}_1}{a_3 - \alpha H} \right) \\
 &+ \left(M_v (\xi_v + \tilde{\xi}_v^*) \left(1 - \frac{\tilde{N}_2^2}{N_v^2} \right) + \tilde{N}_2 (\delta - \delta^*) \right) \frac{b_1 + b_2 - 2\alpha H}{(b_1 - \alpha H)(b_2 - \alpha H)} \quad (\text{B.68})
 \end{aligned}$$

$$\text{with: } \tilde{N}_1 = \min \left\{ \frac{N_h^2 (\delta - \delta^*)}{2M_h (\xi_h + \tilde{\xi}_h^*)} ; N_h \right\} ; \tilde{N}_2 = \min \left\{ \frac{N_v^2 (\delta - \delta^*)}{2M_v (\xi_v + \tilde{\xi}_v^*)} ; N_v \right\}$$

$$\tilde{\xi}_h^* = \xi_h^*(\delta^* - \delta_1) ; \tilde{\xi}_v^* = \xi_v^*(\delta^* - \delta_1)$$

where N_1 is still given by (3.65). It is worth mentioning that (B.66), (B.67) and (B.68) are only applicable to cruciforms. These formulae could be easily extended to T-shaped intersections, but this should be done by accounting for some particularities, as discussed in section B.3.1.3.

B.3.2.3. Final resistance of the super-element

The final resistance $P(\delta)$ in case of a subsequent contact can be derived by combining $P_f(\delta)$ and $P_b(\delta)$ as detailed in section 3.5.2.3. Furthermore, the post-rupture behavior is treated in the same way.

B.4. Appendix B.4

B.4.1. Displacement fields before the transition

In equation (3.71) of section 3.6.2.2, the displacement field $u(Y_i, Z)$ in the elastoplastic regime (i.e. for $\delta \leq \delta_t$) involves the definition of a kinematically admissible function $g(Y, \delta)$ describing the deformed profile in the vertical impact plane $Z = Z_I$ (Figure 3.50). In this appendix, the definition of $g(Y, \delta)$ is extended to account for other collision configurations. As a linear interpolation is systematically used for each of them, the fundamental formulae for $g(Y, \delta)$ are as follows:

- For $0 \leq Y \leq Y_I$:
$$g(Y, \delta) = \delta \frac{Y}{Y_I} + g(0, \delta) \left(1 - \frac{Y}{Y_I}\right) \tag{B.69}$$
- For $Y_I < Y \leq h$:
$$g(Y, \delta) = \delta \frac{h - Y}{h - Y_I} + g(h, \delta) \frac{Y - Y_I}{h - Y_I}$$

where $g(0, \delta)$ and $g(h, \delta)$ are respectively the particular displacements of the lowermost and uppermost horizontal beams. Only these two parameters needs to be specified in order to have a complete determination of $g(Y, \delta)$. In case of bulbous bow, it is worth noting that (B.69) is only valid if the gate is first impacted by the stem and not by the bulb. If this is not the case, the equations given hereafter can be modified but for conciseness, the corresponding results are not presented here.

B.4.1.1. Raked bow

The situation of a raked bow impacting a structure that is not supported at the bottom has been treated in section 3.6.2.2, so the goal of this appendix is only to extend the definition of $g(Y, \delta)$ to the situation where the gate is resting against a sill. To do so, the displacement pattern of Figure B.17a may be postulated, from which it is clear that $g(0, \delta) = 0$. For the same reasons as those exposed in 3.6.2.2, the definition of $g(h, \delta)$ given by (3.72) is still holding in the present configuration. Therefore:

$$g(0, \delta) = 0 \quad ; \quad g(h, \delta) = \frac{Y_I}{h} \delta \tag{B.70}$$

which can be inserted in (B.69) to get the definition of $g(Y, \delta)$ over the entire height of the gate.

B.4.1.2. Bulbous bow

As a first step, the case of a bulbous bow impacting a gate free at the bottom is investigated. From Figure 3.8, it is recalled that the geometrical centre B of the bulb \mathcal{B} is located at a level Y_B that is simply related to the impact point by $Y_B = Y_I - h_b + R_Y$. Furthermore, from this picture, it also appears that \mathcal{B} reaches the initial plane of the gate when the penetration is equal to:

$$R_b = (h_b - 2R_Y) \cot \phi - R_X \tag{B.71}$$

Consequently, as long as $\delta < R_b$, the displacement pattern of Figure 3.50b and the definition (3.73) of $g(Y, \delta)$ are still valid. Nevertheless, for $\delta \geq R_b$, there is an additional local indentation imposed by the bulb (Figure B.17d) that should be taken into account when evaluating $g(Y, \delta)$. In particular, if there is no sill (Figure B.17b), the definition of $g(0, \delta)$

given in (3.72) is not relevant anymore because the displacement of the lowermost horizontal beam is greatly influenced by the local penetration of \mathcal{B} .

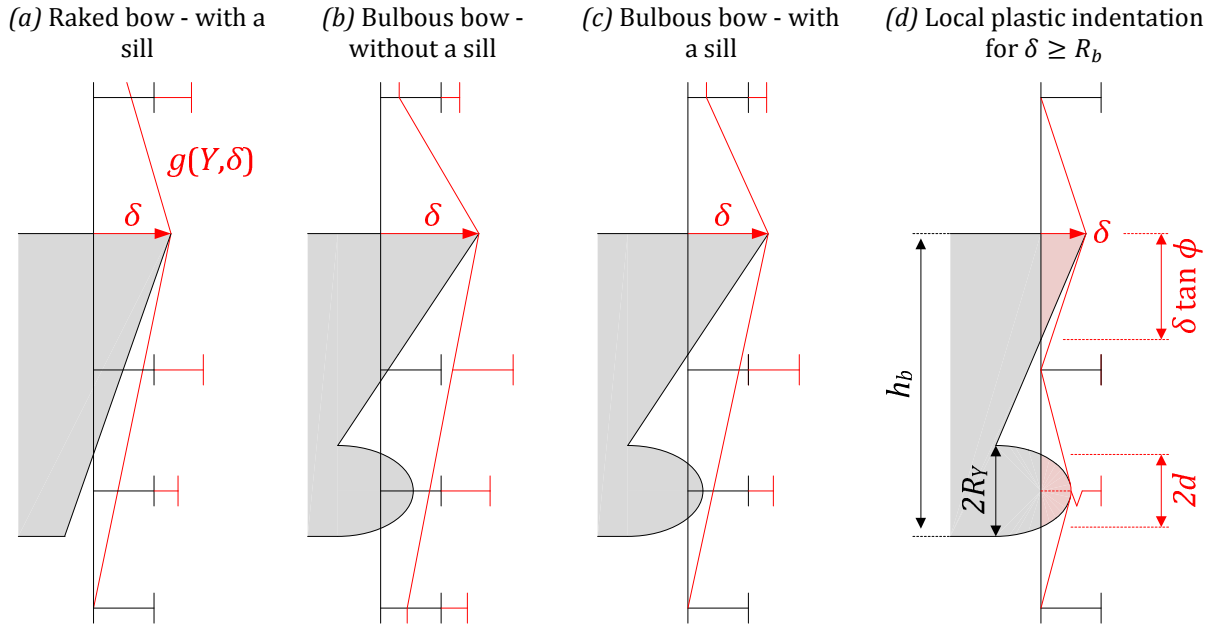


Figure B.17. Definition of the displacement profile for various impact configurations

By a similar reasoning than the one exposed in section 3.6.2.2, a convenient way to correct (3.72) is to assume that $g(0, \delta)$ is inversely proportional to the vertical distance Y_B separating the bottom of the gate from the centre of the bulb. Nevertheless, when \mathcal{B} is moving forward, this distance is progressively reduced from a factor d (Figure B.17d) that may be found by working equation (3.10):

$$d = R_Y \sqrt{(\delta - R_b)/R_X} \quad (\text{B.72})$$

Consequently, from the previous considerations, the coefficients $1 - Y_B/h$ and d/R_Y should be used to get a new evaluation of $g(0, \delta)$. On the other hand, it seems reasonable to think that the bulb has a negligible effect on the displacement of the uppermost beam, which implies that (3.72) is still valid to get $g(h, \delta)$. Finally, one should have:

$$g(0, \delta) = \frac{R_b^2 \tan \phi}{h_b} \left(1 - \frac{Y_I}{h}\right) + (\delta - R_b) \left(1 - \frac{Y_B}{h}\right) \min\left(\frac{d}{R_Y}; 1\right) ; \quad g(h, \delta) = \frac{Y_I}{h} \delta \quad (\text{B.73})$$

In this last equation, it is worth noticing that the first term in $g(0, \delta)$ corresponds to the penetration reached when $\delta = R_b$, i.e. when the bulb starts impacting the gate.

Of course, if there is a support at the bottom of the lock (Figure B.17c), then it is clear that the bulb does not have any effect on $g(Y, \delta)$. In this case, $g(0, \delta)$ and $g(h, \delta)$ may still be evaluated by (B.70).

B.4.2. Displacement field after the transition

The derivation of the displacement field after the transition is very similar to what has been done previously. The only difference comes from the subsequent contact that may occur between the stem or the bulb and the deforming gate, such as depicted on Figure 3.52d. Therefore, in order to avoid any redundancy, only the final expressions of $g(Y, \delta)$ are provided here (Table B.1).

| | Vertical position | Before subsequent contact ($\delta < \delta_1$) | After subsequent contact ($\delta \geq \delta_1$) |
|--|-----------------------------------|--|--|
| Raked bow Gate with a sill | For $0 \leq Y < Y_I - h_b$: | $g(Y, \delta) = (\delta - \delta_t) \frac{Y}{Y_I}$ | $g(Y, \delta) = (\delta_1 - \delta_t) \frac{Y}{Y_I} + (\delta - \delta_1) \frac{Y}{Y_I - h_b}$ |
| | For $Y_I - h_b \leq Y \leq Y_I$: | $g(Y, \delta) = (\delta - \delta_t) \frac{Y}{Y_I}$ | $g(Y, \delta) = (\delta_1 - \delta_t) \frac{Y}{Y_I} + \delta - \delta_1$ |
| | For $Y_I < Y \leq h$: | $g(Y, \delta) = (\delta - \delta_t) \left(1 - \frac{Y - Y_I}{h}\right)$ | $g(Y, \delta) = (\delta - \delta_t) \left(1 - \frac{Y - Y_I}{h}\right)$ |
| Bulbous bow Gate without a sill | For $0 \leq Y < Y_B$: | $g(Y, \delta) = (\delta - \delta_t) \left(1 + \frac{Y - Y_I}{Y_I} \left(1 - \left(1 - \frac{Y_I}{h}\right) \frac{\delta_t \tan \phi}{h_b}\right)\right)$ | $g(Y, \delta) = (\delta_1 - \delta_t) \left(\frac{Y}{Y_I} - \frac{Y - Y_I}{Y_I} \left(1 - \frac{Y_I}{h}\right) \frac{\delta_t \tan \phi}{h_b}\right) + (\delta - \delta_1) \left(1 + \frac{Y - Y_I}{h}\right)$ |
| | For $Y_B \leq Y \leq Y_I$: | $g(Y, \delta) = (\delta - \delta_t) \left(1 + \frac{Y - Y_I}{Y_I} \left(1 - \left(1 - \frac{Y_I}{h}\right) \frac{\delta_t \tan \phi}{h_b}\right)\right)$ | $g(Y, \delta) = (\delta_1 - \delta_t) \left(\frac{Y}{Y_I} - \frac{Y - Y_I}{Y_I} \left(1 - \frac{Y_I}{h}\right) \frac{\delta_t \tan \phi}{h_b}\right) + \delta - \delta_1$ |
| | For $Y_I < Y \leq h$: | $g(Y, \delta) = (\delta - \delta_t) \left(1 - \frac{Y - Y_I}{h}\right)$ | $g(Y, \delta) = (\delta - \delta_t) \left(1 - \frac{Y - Y_I}{h}\right)$ |
| Bulbous bow Gate with a sill | For $0 \leq Y < Y_B$: | $g(Y, \delta) = (\delta - \delta_t) \frac{Y}{Y_I}$ | $g(Y, \delta) = (\delta_1 - \delta_t) \frac{Y}{Y_I} + (\delta - \delta_1) \frac{Y}{Y_B}$ |
| | For $Y_B \leq Y \leq Y_I$: | $g(Y, \delta) = (\delta - \delta_t) \frac{Y}{Y_I}$ | $g(Y, \delta) = (\delta_1 - \delta_t) \frac{Y}{Y_I} + \delta - \delta_1$ |
| | For $Y_I < Y \leq h$: | $g(Y, \delta) = (\delta - \delta_t) \left(1 - \frac{Y - Y_I}{h}\right)$ | $g(Y, \delta) = (\delta - \delta_t) \left(1 - \frac{Y - Y_I}{h}\right)$ |
| Remarks: <ul style="list-style-type: none"> • In the case of a raked bow, a subsequent contact between the stem and the deforming gate is only possible if $\delta_t < h_b \cot \phi$, otherwise the second contact takes place during the local mode. • In the case of bulbous bow, a subsequent contact between the bulb and the deforming gate is only possible if $\delta_t < R_b$, otherwise the second contact takes place during the local mode. • The ratio $\delta_t \tan \phi / h_b$ should not be greater than unity in the case of bulbous bow impacting a gate that is not supported at the bottom. | | | |

Table B.1. Mathematical expressions of the central displacement after the transition from the local to the global deforming mode

B.5. Appendix B.5

In this appendix, comparisons between the numerical and analytical results are made for another gate than the one presented in section 3.7. The structure is depicted on Figure B.18. It is made of five horizontal girders and ten identical vertical frames. It has a total length l of 17.1 m and a total height h of 15 m. The geometrical and material properties are respectively listed in Table B.2 and in Table 3.2.

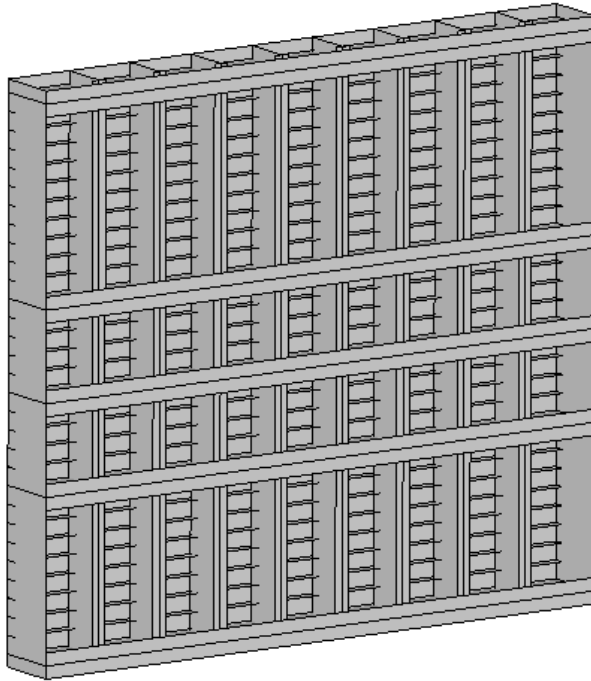


Figure B.18. Three dimensional view of gate 2

| <i>Horizontal girders</i> | | | | |
|------------------------------|-----------|----------------|-----------|-----------|
| Y (m) | h_w (m) | t_w (m) | h_f (m) | t_f (m) |
| 0 | 1.8 | 0.012 | 0.7 | 0.04 |
| 4.5 | 1.8 | 0.012 | 0.7 | 0.04 |
| 7 | 1.8 | 0.012 | 0.7 | 0.04 |
| 9.5 | 1.8 | 0.012 | 0.7 | 0.04 |
| 15 | 1.8 | 0.012 | 0.7 | 0.04 |
| <i>Vertical frames</i> | | | | |
| Z (m) | h_w (m) | t_w (m) | h_f (m) | t_f (m) |
| 0 | 1.8 | 0.012 | 0 | 0 |
| 1.9 | 1.4 | 0.012 | 0.4 | 0.03 |
| 3.8 | 1.4 | 0.012 | 0.4 | 0.03 |
| ⋮ | ⋮ | ⋮ | ⋮ | ⋮ |
| 15.2 | 1.4 | 0.012 | 0.4 | 0.03 |
| 17.1 | 1.8 | 0.012 | 0 | 0 |
| <i>Horizontal stiffeners</i> | | <i>Plating</i> | | |
| h_w (m) | t_w (m) | t_p (m) | | |
| 0.03 | 0.012 | 0.012 | | |

Table B.2. Geometrical properties of gate 2

The simulations are run using only vessel 1 (Figure 3.60a) and vessel 2 (Figure 3.63). The cases of a gate supported or free at the bottom are also treated separately for an impact initially located in $Y_l = 13$ m and $Z_l = 8.5$ m. For conciseness, only the curves showing the evolution of the resistance with the penetration are presented here as a matter of validation. The conclusions regarding the internal energy are identical to those developed in section 3.7.

All the results are reported on Figure B.19. From these graphs, it can be concluded that the analytical prediction provides a satisfactory overall agreement. Most of the time, the simplified method leads to a conservative approximation, except for the case of a gate resting against a sill and impacted by a bulbous bow (Figure B.19b). In this configuration, it appears once again that the membrane forces are overestimated for large values of δ . This conclusion is also partly valid for Figure B.19d, from which it can be observed that the analytical curve keeps on growing with the penetration while the numerical resistance tends to stabilize. In fact, the problem is essentially due to the difficulty of correctly assessing the influence of the bulb on the lateral displacements. Nevertheless, in the two other situations involving only a raked bow, the membrane effects seems to be more reasonably evaluated than in section 3.7. This may be explained by the fact that the distance between the lateral supports and the impact point is greater in the present case.

As a final observation, it is also worth noticing that there is no important instability during the impact on a gate that is not supported by a sill because the resistance curves of Figure B.19c

and d only slightly decrease for large values of δ . As already explained in section 3.7, this is essentially due to the fact that the vertical girders are weaker in the present case and therefore only provide a reduced in-plane collaboration of the horizontal beams.

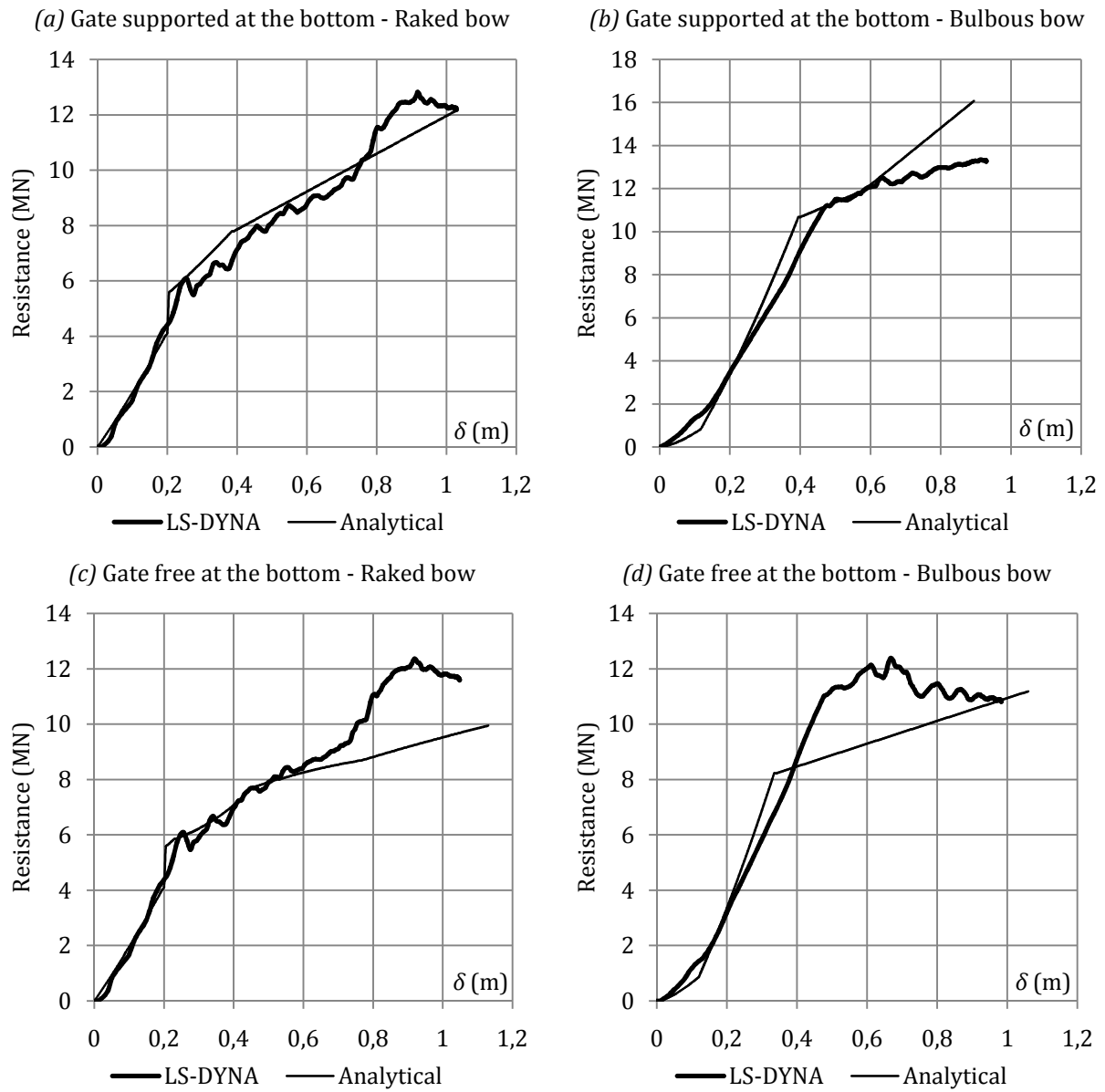


Figure B.19. Comparison of the numerical and analytical resistance curves

APPENDIX C. Additional developments for ship impacts on mitre lock gates

In this addendum to Chapter 4, some developments are presented to complete the derivation of the impact resistance for mitre lock gates. The different appendices are numbered coherently with the sections of Chapter 4.

Appendix C.1 has only an illustrative purpose. It presents some additional pictures in order to have a better understanding of the various components constituting a mitre gate.

In Appendix C.2, some mathematical developments are presented to complete the analytical derivations related to the three super-element types required to evaluate the local resistance. In particular, some results are detailed for the folding and bending mechanisms of SE2 and SE3.

Finally, complementary information is provided in Appendix C.3 about the global deforming mode and additional validation cases are provided in Appendix C.4.

C.1. Appendix C.1

This appendix is introduced in a purely illustrative purpose, in order to provide a clearer overview of the various components constituting a mitre lock gate. To do so, some pictures are proposed hereafter. These ones were all captured during the extraction of the lock gate in Evergem (Belgium) and are presented on Figure C.1.

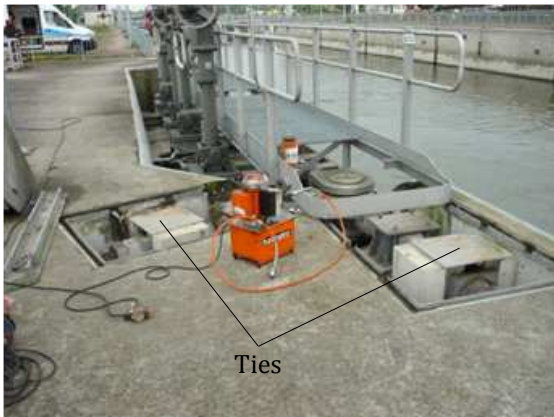
(a) Lateral contact blocks (closed position)



(b) Central contact block (open position)



(c) Ties placed at the top of the gate



(d) Ties placed at the top of the gate (details)



(e) Connection between the ties and the gate



(f) Connection between the ties and the gate



Figure C.1. Structural details of a mitre lock gate

C.2. Appendix C.2

C.2.1. Additional results for SE1

This part of the appendix provides more details on the way the displacement field and the internal energy rate should be calculated for the first super-element type in the case of a mitre gate.

C.2.1.1. Characterization of the displacement field

The displacements $U(z)$ in the plane of the uppermost deck are completely defined by equations (4.3) and (4.6) provided that the locations (x_1, z_1) and (x_2, z_2) of points A and B are known (Figure C.2). These parameters can be determined by imposing slope and displacement continuity conditions between $U_1(z)$, $U_2(z)$ and $U_3(z)$:

- If $z = z_1$: $U_1(z_1) = U_2(z_1)$ $\frac{\partial U_1}{\partial z} = \frac{\partial U_2}{\partial z}$
 - If $z = z_2$: $U_1(z_2) = U_3(z_2)$ $\frac{\partial U_1}{\partial z} = \frac{\partial U_3}{\partial z}$
- (C.1)

Unfortunately, trying to solve analytically the previous equations is not easy to do in the axes (x, z) . Therefore, one can consider first the reference frame (x_s, z_s) fixed to the initial position of the summit S of the stem (Figure C.2a). It is worth mentioning that these axes do not follow the striking vessel, which means that they are not moving with it (Figure C.2b). Working in this system provides more tractable equations.

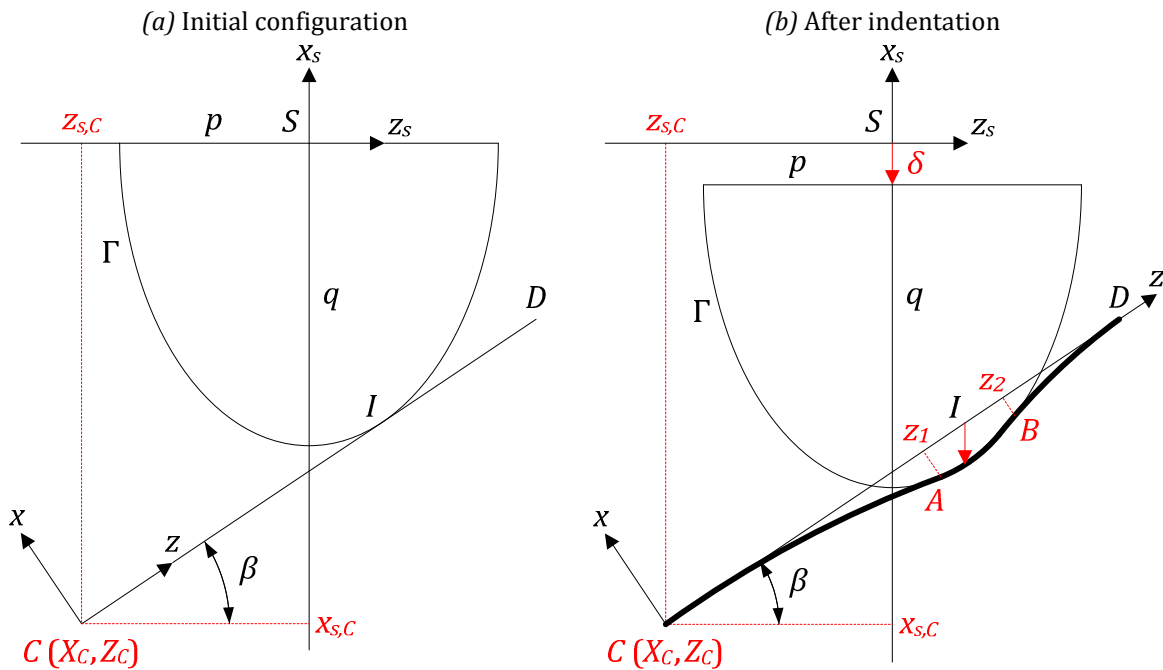


Figure C.2. Parameters defining the displacement field

As the coordinates (X_C, Z_C) and (X_S, Z_S) of points C and S in the global axes are defined in the collision scenario, it is obvious that the position of point C in this new system is given by (Figure C.2):

$$x_{s,c} = X_S - X_C \quad ; \quad z_{s,c} = Z_S - Z_C \quad (C.2)$$

In fact, it can be shown that $x_{s,C}$ and $z_{s,C}$ are not independent. Indeed, a relation can be found because of the requirement that the curve Γ describing the stem has to be initially tangent to the plate. Expressing this condition mathematically with the equation of Γ leads to:

$$z_{s,C} = x_{s,C} \tan \alpha - q - \frac{p^2 \tan^2 \beta}{4q} \quad (\text{C.3})$$

Once the coordinates of point C are known in the reference frame of the stem, the next step is to use (C.1) to determine the location $(x_{s,1}, z_{s,1})$ and $(x_{s,2}, z_{s,2})$ of points A and B in the same axes. However, working directly with (C.1) is not convenient because it leads to very cumbersome equations that are difficult to solve analytically. In order to overcome this difficulty, $U_1(z)$, $U_2(z)$ and $U_3(z)$ are first expressed in the (x_s, z_s) axes. This can be achieved with help of the following formulae:

$$\begin{aligned} x &= (x_s + x_{s,C}) \cos \beta - (z_s + z_{s,C}) \sin \beta \\ z &= (x_s + x_{s,C}) \sin \beta + (z_s + z_{s,C}) \cos \beta \end{aligned} \quad (\text{C.4})$$

Introducing (C.4) in (4.3) and (4.6) and solving with respect to x_s leads to an analytical description of $U_1(z_s)$, $U_2(z_s)$ and $U_3(z_s)$ that can be geometrically interpreted as being the longitudinal extrapolation of the displacement fields depicted on Figure 4.8. These latter are given by:

$$U_1(z_s) = q \left(\frac{z_s^2}{p^2} - \delta \right) \quad (\text{C.5})$$

$$U_2(z_s) = \left(z_{s,1} - x_{s,1} \tan \beta + \frac{p^2 \tan^2 \beta}{4q} + q \right) \left(\frac{x_s - x_{s,C}}{x_{s,1} - x_{s,C}} \right)^2 + z_s \tan \beta - \frac{p^2 \tan^2 \beta}{4q} - q \quad (\text{C.6})$$

$$U_3(z_s) = \left(z_{s,2} - x_{s,2} \tan \alpha + \frac{p^2 \tan^2 \beta}{4q} + q \right) \left(\frac{x_s - x_{s,D}}{x_{s,2} - x_{s,D}} \right)^2 + z_s \tan \beta - \frac{p^2 \tan^2 \beta}{4q} - q \quad (\text{C.7})$$

where $x_{s,D} = x_{s,C} + a \cos \beta$. Finally, expressing the displacement and slope compatibility conditions (C.1) in the (x_s, z_s) reference frame provides to the following results:

$$x_{s,1} = q \frac{z_{s,1}^2}{p^2} - \delta - q \quad \text{with:} \quad z_{s,1} = p^2 \frac{2(\delta + q + x_{s,C}) - z_{s,C} \tan \beta}{2q x_{s,C} - p^2 \tan \beta} \quad (\text{C.8})$$

$$x_{s,2} = q \frac{z_{s,2}^2}{p^2} - \delta - q \quad \text{with:} \quad z_{s,2} = p^2 \frac{2(\delta + q + x_{s,D}) - z_{s,D} \tan \beta}{2q x_{s,D} - p^2 \tan \beta} \quad (\text{C.9})$$

in which $z_{s,D} = z_{s,C} + a \sin \beta$. In order to get (x_1, z_1) and (x_2, z_2) , the last step consists in introducing the previous equations in (C.4). By so doing, the displacement field of section 4.2.1.1 is now completely characterized.

C.2.1.2. Derivation of the energy rate

The derivation of the internal energy rate can be done by introducing the displacement field $u(y, z)$ of section 4.2.1.1 in equation (3.18) to get the Green-Lagrange strain rates \dot{E}_{yy} and \dot{E}_{zz} . These latter have then to be integrated over the plate area to get the internal energy rate. In fact, three separated calculations have to be performed, as $u(y, z)$ is different for $0 \leq z < z_1$, $z_1 \leq z \leq z_2$ and $z_2 < z \leq a$. Doing so leads to:

$$\begin{aligned} \dot{E}_{int} = & \delta \frac{(b_1 + b_2) \cos \beta}{3K_4^2 \sin^2 \beta} I_1 + \delta \frac{b_1 + b_2}{K_4 b_1 b_2 \sin^2 \beta} I_2 + \delta \frac{K_2 (b_1 + b_2) \sin^3 \beta}{24} (I_3 - I_4) \\ & + \delta \frac{K_2^2 (b_1 + b_2) \sin^2 \beta}{2b_1 b_2} (I_5 - I_6) + \delta \frac{(b_1 + b_2) \cos \beta}{3K_4^2 \sin^2 \beta} I_7 + \delta \frac{b_1 + b_2}{K_4 b_1 b_2 \sin^2 \beta} I_8 \end{aligned} \quad (C.10)$$

where β is the mitre angle (β can be substituted by $\beta + \gamma_1$ or $\beta - \gamma_2$ according to the position of the super-element along the gate). The parameters I_1 to I_6 are given by the following formulae:

$$I_1 = \left(\frac{1 + K_4 z_1 \cos \beta}{\sqrt{1 + 2K_4 z_1 \cos \beta}} + \frac{K_4 z_1 \cos \beta}{2(1 + 2K_4 z_1 \cos \beta)} - \frac{1}{4} \ln(1 + 2K_4 z_1 \cos \beta) - 1 \right) \frac{\partial K_4}{\partial \delta} \quad (C.11)$$

$$I_2 = \left(\frac{\sqrt{1 + 2K_4 z_1 \cos \beta} (4 + 6K_4 z_1 \cos \beta + K_4^2 z_1^2 \cos^2 \beta) - 4}{5K_4 \cos \beta} - 2z_1 - K_4 z_1^2 \cos \beta \right) \frac{\partial K_4}{\partial \delta} \quad (C.12)$$

$$I_3 = \frac{K_2 \sin \beta - 4 \cot \beta \sqrt{K_3 + \delta \sin^2 \beta + z_2 \sin \beta}}{K_3 + \delta \sin^2 \beta + z_2 \sin \beta} \quad (C.13)$$

$$I_4 = \frac{K_2 \sin \beta - 4 \cot \beta \sqrt{K_3 + \delta \sin^2 \beta + z_1 \sin \beta}}{K_3 + \delta \sin^2 \beta + z_1 \sin \beta} \quad (C.14)$$

$$I_5 = z_2 - \frac{\sqrt{K_3 + \delta \sin^2 \beta + z_2 \sin \beta}}{K_2 \sin \beta} \left(K_1 - \frac{2 \cot \beta}{\sin \beta} (K_3 + \delta \sin^2 \beta) + \frac{z_2}{3} \cot \beta \right) \quad (C.15)$$

$$I_6 = z_1 - \frac{\sqrt{K_3 + \delta \sin^2 \beta + z_1 \sin \beta}}{K_2 \sin \beta} \left(K_1 - \frac{2 \cot \beta}{\sin \beta} (K_3 + \delta \sin^2 \beta) + \frac{z_1}{3} \cot \beta \right) \quad (C.16)$$

By symmetry, I_7 and I_8 have the same expression than I_1 and I_2 , except that z_1 and K_4 have to be replaced by $a - z_1$ and K_5 respectively. In the previous equations, the constant parameters K_1 , K_2 and K_3 are given by (4.4), while K_4 and K_5 have the subsequent definitions:

$$K_4 = \frac{(z_{s,c} - z_{s,1}) \tan \beta + x_{s,1} - x_{s,c}}{(z_{s,c} - z_{s,1})^2} \sin 2\beta \quad \frac{\partial K_4}{\partial \delta} = - \frac{\sin 2\beta}{(z_{s,c} - z_{s,1})^2} \quad (C.17)$$

$$K_5 = \frac{(z_{s,d} - z_{s,2}) \tan \beta + x_{s,2} - x_{s,d}}{(z_{s,d} - z_{s,2})^2} \sin 2\beta \quad \frac{\partial K_5}{\partial \delta} = - \frac{\sin 2\beta}{(z_{s,d} - z_{s,2})^2} \quad (C.18)$$

As a final result, introducing (C.10) in (4.7) allows for the calculation of the resistance provided by the plating elements of a mitre gate.

C.2.2. Additional results for SE2

C.2.2.1. Folding mechanism

A first complementary result that is needed to evaluate the resistance opposed by the super-element SE2 is the membrane energy rate. As briefly recalled in section 4.2.2, each horizontal fiber is only submitted to an axial straining along the z axis during the folding process. Under the conservative hypotheses that there is no shearing and only an internal dissipation over the triangles OAB and OBC (Figure 4.11), one should have:

$$\dot{E}_m = \iint_{OAB} \frac{\partial \dot{w}}{\partial z} dx dz + \iint_{OBC} \frac{\partial \dot{w}}{\partial z} dx dz \quad (\text{C.19})$$

where $\dot{E}_{zz} = \partial \dot{w} / \partial z$ is the Green-Lagrange strain rate that can be calculated by using the definition of $w(x, z)$ given in (4.10). Deriving (4.10) with respect to time and introducing it in (C.19) leads to the following result for the first wing:

$$\dot{E}_m = n_0 H \left| \frac{1}{2} \frac{\partial W_A}{\partial \delta} + \frac{\partial W_B}{\partial \delta} - \frac{a_1 + \delta \sin \beta + 2H}{(a_1 + \delta \sin \beta)^2} ((2 - \ln 2)W_A + 4W_B \ln 2) \right| \dot{\delta} \sin \beta \quad (\text{C.20})$$

where W_A and W_B are defined by (4.9). Because of the assumption that the folding height H is quite small in comparison with the length a_1 , the second term of the previous expression can be neglected. Doing so, one gets for the two wings:

$$\dot{E}_m = n_0 H \left(\frac{4a_1(\delta + 2H \cos \beta) + \delta^2 \sin 2\beta}{4(a_1 + \delta \sin \beta)^2} + \frac{4a_2(\delta + 2H \cos \beta) - \delta^2 \sin 2\beta}{4(a_2 - \delta \sin \beta)^2} \right) \dot{\delta} \cos \beta \quad (\text{C.21})$$

in which n_0 is the linear plastic resistance for a plate of thickness t_w . Regarding the bending energy rate \dot{E}_b , its definition is nearly the same as for a plane gate, but the definition of the angle θ (Figure 4.11) has to be corrected to account for the inclination β :

$$\theta = \arccos \left(1 - \frac{\delta \cos \beta}{2H} \right) \Leftrightarrow \dot{\theta} = \frac{\dot{\delta} \cos \beta}{2H \sqrt{1 - (\delta \cos \beta / 2H)^2}} \quad (\text{C.22})$$

Ideally, the bending dissipation has to be calculated for all the segments OA , OB , OC , AB and BC . Nevertheless, under the assumption that the folding height H is quite small with respect to the lengths a_1 and a_2 , the contributions of the moving hinges AB and BC can be neglected. Doing so has the advantage of simplifying the analytical derivation by skipping the theoretical questioning that is further discussed in section 4.2.2.2. Consequently, under the assumption that the rotation rate $\dot{\theta}$ is more or less the same for OA , OB and OC , it can be shown that:

$$\dot{E}_b = 4m_0(a_1 + a_2)\dot{\theta} = \frac{4m_0(a_1 + a_2)\dot{\delta} \cos \beta}{2H \sqrt{1 - (\delta \cos \beta / 2H)^2}} \quad (\text{C.23})$$

Nevertheless, from (C.23), it appears that $\dot{E}_b \rightarrow \infty$ when $\delta \rightarrow 0$, which is not acceptable as the folding process is in fact initiated after the elastoplastic buckling of the plate. Therefore, instead of using (C.23), a convenient way to overcome this difficulty is to smear the average dissipation rate over the indentation, which leads to:

$$\dot{E}_b = \frac{4m_0\pi(a_1 + a_2)}{H} \dot{\delta} \cos \beta \quad (\text{C.24})$$

where $m_0 = \sigma_0 t_w^2 / 4$ is the linear plastic moment characterizing the plate with a thickness equal to t_w . Summing up (C.21) and (C.24) leads to the total internal energy rate and the resistance given by (4.12). Nevertheless, in order to completely characterize the indentation process, it is still needed to evaluate the folding height H . As usual, this can be done by minimizing the mean resistance \bar{P}_f calculated for $0 \leq \delta \leq 2H / \cos \beta$. After integration, the subsequent result is obtained:

$$\bar{P}_f = \frac{\sigma_0 t_w}{2} (a_1 + a_2) \left(\frac{\pi t_w}{2H} + \frac{3H^2 \cos \beta}{(a_1 + 2H \tan \beta)(a_2 - 2H \tan \beta)} \right) \quad (\text{C.25})$$

To get the optimal value for H , a quite fastidious task is now to calculate the derivative of (C.25) and get the roots of the corresponding equation, i.e.:

$$\frac{\partial \bar{P}_f}{\partial H} = 0 \Leftrightarrow K_1 H^4 + K_2 H^3 + K_3 H^2 + K_4 H + K_5 = 0 \quad (\text{C.26})$$

$$\begin{aligned} \text{with: } K_1 &= -12(a_1 - a_2) \sin \beta - 16\pi t_w \tan^3 \beta & K_4 &= 4\pi t_w a_1 a_2 (a_1 - a_2) \tan \beta \\ K_2 &= 12a_1 a_2 \cos \beta - 16\pi t_w (a_1 - a_2) \tan^3 \beta & K_5 &= -\pi t_w a_1^2 a_2^2 \\ K_3 &= -4\pi t_w (a_1^2 + a_2^2 - 4a_1 a_2) \tan^2 \beta \end{aligned}$$

Of course, finding an analytical solution to the previous relation is unfortunately not possible, but the Newton-Raphson method can be a convenient way to obtain a numerical solution. However, under the hypothesis that the angle β is small, (C.26) shows that $K_1 \simeq K_3 \simeq K_4 \simeq 0$ and $K_2 \simeq 12a_1 a_2 \cos \beta$. Therefore, equation (C.26) becomes:

$$12H^3 a_1 a_2 \cos \beta - \pi t_w a_1^2 a_2^2 = 0 \Leftrightarrow H = \sqrt[3]{\frac{\pi}{12} a_1 a_2 t_w / \cos \beta} \quad (\text{C.27})$$

As a matter of illustration, the curves comparing the exact and approximate solutions for different values of β are plotted on Figure C.3. The geometrical data corresponding to this example are $a_1 = 2 \text{ m}$, $a_2 = 3 \text{ m}$ and $t_w = 0.03 \text{ m}$.

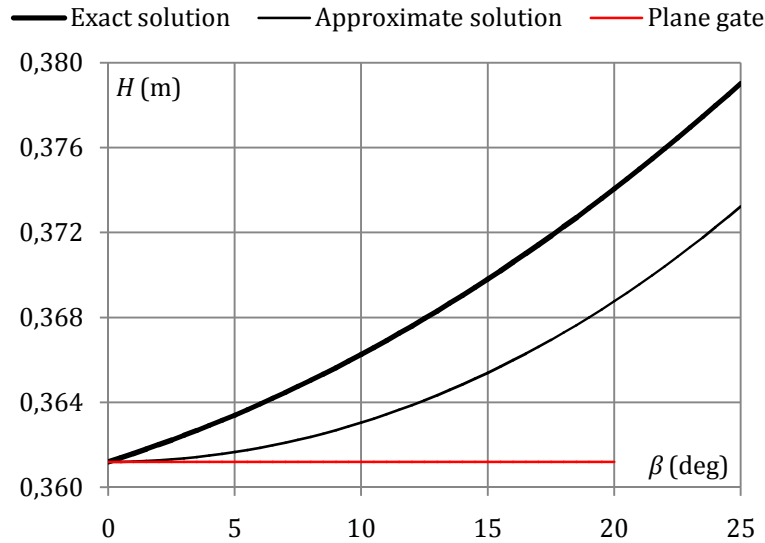


Figure C.3. Comparison of the exact and approximate folding heights

From this picture, it transpires that choosing (C.27) provides a convenient and sufficient estimation of the folding height.

C.2.2.2. Bending mechanism

The derivation of the collision force in this section is based on the hypothesis that the super-element web is of class 1, which allows for the development of the three-hinge mechanism of Figure 4.12b. If this is not the case, then another plastic collapse scheme has to be postulated, such as the one presented in section 4.3.

The theoretical calculation of the resistance during an oblique impact on a straight beam is a problem that is not easy to solve because it implies the use of travelling hinges. In an attempt

to study more precisely the oblique impact occurring on a cantilever beam, Yu [175] investigated the transient phase by working with plastic hinges propagating and interfering along the structure, but this is not of primary concern for low-velocity impacts such as those on lock gates. In order to derive a consistent theoretical solution to this problem, apart from the yield condition and the normality rule, the additional requirement of slope continuity has also to be fulfilled at each moving plastic hinge.

Nevertheless, as claimed by Stronge and Yu [146]: *"For a perfectly plastic structure with a yield condition that couples bending moment and axial tension, a model with discrete travelling hinges which combine bending and stretching deformations cannot satisfy both the flow rule and yield criterion throughout the deforming region"*. This assertion means that developing a theoretical solution to the present problem is not straightforward. Of course, one may argue that the concept of moving hinge has been successfully applied by many authors when dealing with plated structures, such as Simonsen [140], Amdahl [8] or Deshpande and Fleck [41] amongst others. However, it is worth bearing in mind that all these developments were based on the hypothesis that the bending moment and the axial force were decoupled within the yield criterion, i.e. that (3.17) may be used to evaluate the plastic dissipation. This idea has also been applied to beams by Symonds and Mentel [147].

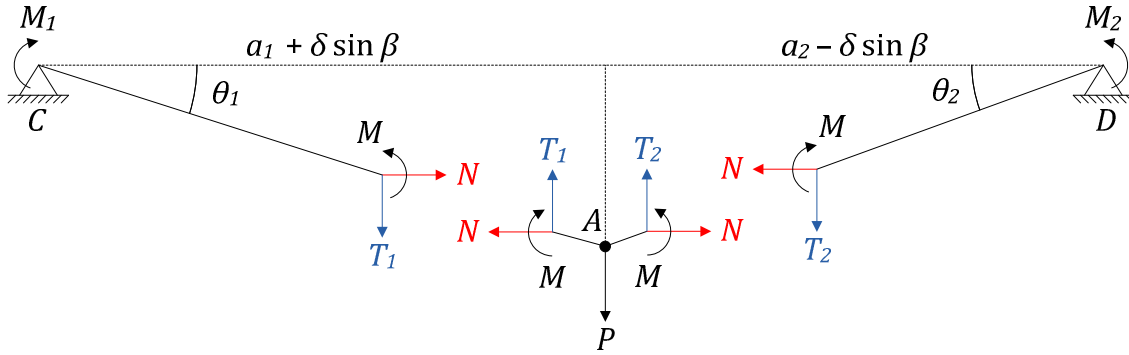


Figure C.4. Internal forces for the equilibrium method

The present developments are based on the idea that the slope continuity requirement may be neglected. Furthermore, as suggested by Tin-Loi [148], the normal and shear forces are supposed to act along the axes of the undeformed configuration, which is only valid under the assumption of moderately large displacements. Doing so, the yield condition and the normality rule can be respected within a kind of quasi-static approach by applying the equilibrium method. In this optic, the situation depicted on Figure C.4 is considered, where some of the external forces acting in sections A, C and D are represented.

As the bending moment $\xi^* M_0$ has to be continuous on both sides of A, the yield condition (B.28) implies that the axial force N is the same in the two arms of the beam. Consequently, satisfying the plastic criterion in A, C and D leads to:

$$\frac{M}{\xi^* M_0} = 1 - \left(\frac{N}{N_0}\right)^2 \quad \frac{M_1}{\xi_1 M_1} = 1 - \left(\frac{N}{N_0}\right)^2 \quad \frac{M_2}{\xi_2 M_2} = 1 - \left(\frac{N}{N_0}\right)^2 \quad (\text{C.28})$$

As a second requirement, the normality rule has also to be fulfilled for all the hinges. Consequently, the extension rates $\dot{\Delta}$, $\dot{\Delta}_1$ and $\dot{\Delta}_2$ at the sections A, C and D have to be related to the corresponding rotations $\dot{\theta}$, $\dot{\theta}_1$ and $\dot{\theta}_2$ (Figure C.4) in order to keep the combination of the bending moments and axial forces on the yield locus, i.e.:

$$\frac{\dot{\Delta}}{\theta} = \frac{2\xi^* M_0}{N_0^2} N \quad \frac{\dot{\Delta}_1}{\theta_1} = \frac{2\xi_1 M_0}{N_0^2} N \quad \frac{\dot{\Delta}_2}{\theta_2} = \frac{2\xi_2 M_0}{N_0^2} N \quad (\text{C.29})$$

where $\dot{\theta} = \dot{\theta}_1 + \dot{\theta}_2$ is the rotation rate at the central cross-section A . From simple geometrical considerations, because of the hypothesis of moderately large displacements, it is easy to show that:

$$\bullet \theta_1 = \frac{(\delta - \delta^*) \cos \beta}{l_1} \quad \dot{\theta}_1 = \frac{a_1 + \delta^* \sin \beta}{l_1^2} \dot{\delta} \cos \beta \quad (\text{C.30})$$

$$\bullet \theta_2 = \frac{(\delta - \delta^*) \cos \beta}{l_2} \quad \dot{\theta}_2 = \frac{a_2 - \delta \sin \beta}{l_2^2} \dot{\delta} \cos \beta \quad (\text{C.31})$$

where l_1 and l_2 are respectively the actual lengths of the segments AC and AD (Figure C.4) given by:

$$\bullet l_1 = a_1 + \delta \sin \beta + \frac{1}{2} \frac{(\delta - \delta^*)^2 \cos^2 \beta}{a_1 + \delta \sin \beta} \quad \dot{l}_1 = \frac{\partial l_1}{\partial \delta} \dot{\delta} \quad (\text{C.32})$$

$$\bullet l_2 = a_2 - \delta \sin \beta + \frac{1}{2} \frac{(\delta - \delta^*)^2 \cos^2 \beta}{a_2 - \delta \sin \beta} \quad \dot{l}_2 = \frac{\partial l_2}{\partial \delta} \dot{\delta} \quad (\text{C.33})$$

The total axial elongation of the beam can be easily found with help of the two previous formulae. Nevertheless, it is worth mentioning that another approach could be to follow the hypothesis made by Brown and Sajdak [15] or McDermott et al. [107], who state that the membrane stretching is only effective in the arm behind the impact point. Nevertheless, doing so is not in agreement with the observations made on numerical results. On the contrary, it transpires from finite element simulations that the normal force is more or less constant throughout the beam, which implies that the two arms are simultaneously submitted to a membrane extension. Therefore, accounting for this remark, it is now obvious for compatibility reasons that the total elongation of the beam has to be equal to the sum of the axial extensions in each individual plastic hinges, i.e.:

$$l_1 + l_2 - a_1 - a_2 = \Delta_1 + \Delta_2 + \Delta \quad (\text{C.34})$$

Deriving (C.34) with respect to time and using the relations detailed in equations (C.29) to (C.33) finally allows for the determination of the normal force N :

$$N = \min \left(\frac{N_0^2}{2M_0} \frac{l_1 + l_2}{(\xi_1 + \xi^*)\dot{\theta}_1 + (\xi_2 + \xi^*)\dot{\theta}_2} ; N_0 \right) \quad (\text{C.35})$$

Substituting (C.35) in (C.28) leads to the evaluation of the bending moments M , M_1 and M_2 in sections A , C and D respectively. Doing so, the shearing forces T_1 and T_2 (Figure C.4) may now be calculated by simply expressing the rotation equilibrium of the arms AC and CD :

$$T_1 = \frac{M + M_1 + N(\delta - \delta^*) \cos \beta}{a_1 + \delta \sin \beta} ; \quad T_2 = \frac{M + M_2 + N(\delta - \delta^*) \cos \beta}{a_2 - \delta \sin \beta} \quad (\text{C.36})$$

Finally, the formulae for P can be found by writing the translation equilibrium of the structure, i.e. $P = T_1 + T_2$. Using all the results established here above provides the relation given by (4.15). As a last comment, it is probably worth recalling that all the previous developments remain approximate. The problem of a beam impacted obliquely is quite difficult to solve on a theoretical point of view.

C.2.3. Additional results for SE3

In this appendix, it is assumed that a super-element of type 3 is activated by the subsequent contact occurring between the vessel and the left support of a horizontal girder, which happens when the penetration is equal to δ_1 . This particular value can be easily found analytically by considering the mathematical expression of the bow, but its derivation is not detailed here.

C.2.3.1. Folding mechanism

The situation during the folding process is as follows (Figure C.5). For $\delta < \delta_1$, the impacted super-element is simply crushed in accordance with the description made in section 4.2.2.1, until a new contact is established at point O . At this moment, $\delta = \delta_1$ and another deformation pattern is activated. It is made of three different regions numbered from *I* to *III* and characterized by a total height equal to $2H_1$ (Figure C.5a).

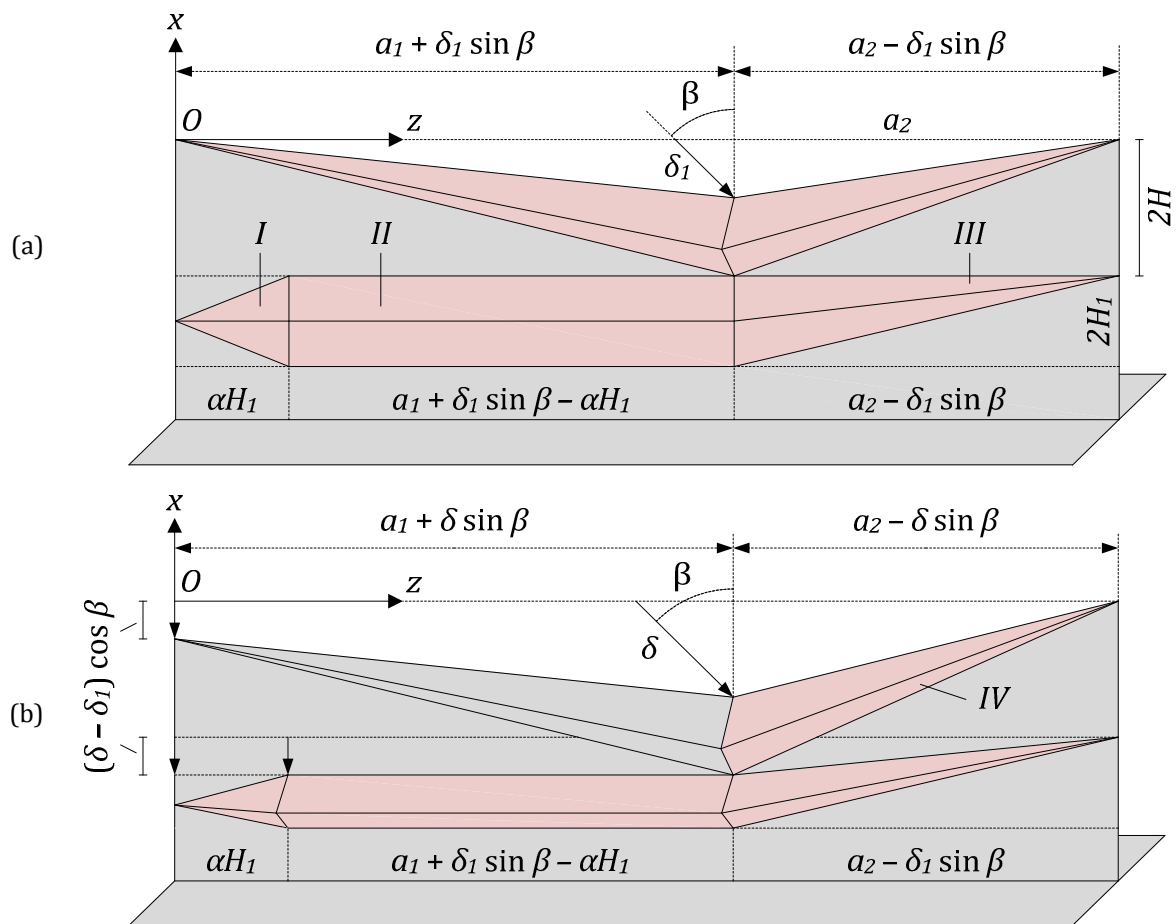


Figure C.5. Folding mechanism in the case of a subsequent contact

The first part has a constant length equal to αH_1 and simply follows the deformation scheme of Figure 3.37b. On the contrary, due to the inclination of the gate, the second and third parts have variable lengths, which means that a moving plastic hinge line should be placed at the junction between these two regions. When $\delta > \delta_1$, the mechanism is gradually closed (Figure C.5b), so there is a material flow between parts *II* and *III*, but there should be no slope discontinuity along the connection. In order to respect this requirement, it can be shown that an additional irregular toroidal surface may be used to make a compatible transition.

However, doing so is not really necessary, as the bending effects can be neglected if the folding height H_1 is sufficiently small with respect to a_1 and a_2 .

Due to the fact that the lengths are not constant, the analytical derivation of the resistance is quite fastidious. In order to facilitate the procedure, an additional simplification is introduced. Indeed, during the collision, the in-plane displacement of point O is not strictly equal to $(\delta - \delta_1) \cos \beta$ but should be calculated by taking the intersection between the bow and the perpendicular x axis. However, as the dimensions of the vessel may thought to be much larger than those of the super-element, this assumption is usually acceptable.

The resistance $P_I(\delta)$ associated to the first sub-area can still be evaluated by using equation (B.44), but one should account for some little modifications regarding the opening angle θ and the indentation to consider. Regarding the contribution of the second region, this latter can be easily found by evaluating the energy dissipated by the plastic rotation in the horizontal stationary hinges. Similarly, for region *III*, the internal dissipation due to the membrane and bending effects is also responsible for an additional resistance that can be simply found by accounting only for the right wing of the deforming mechanism in equation (C.21). From all the previous remarks, it may be shown that:

$$P_I(\delta) = n_0 H_1 \frac{\hat{G}(\theta)}{\sqrt{6}} + m_0 \pi \left(\sqrt{\alpha^2 + 1} + \frac{\alpha}{6} + \frac{2}{5} \right) ; \quad \theta = \arccos \left(1 - \frac{(\delta - \delta_1) \cos \beta}{2H_1} \right) \quad (\text{C.37})$$

$$P_{II}(\delta) = \frac{m_0 \pi}{H_1} (a_1 + \delta_1 \sin \beta + 2H_1 \tan \beta - \alpha H_1) \quad (\text{C.38})$$

$$P_{III}(\delta) = \frac{n_0 H_1}{2(a_2 - \delta \sin \beta)^2} \left((a_2 - \delta_1 \sin \beta)(2H_1 + (\delta - \delta_1) \cos \beta) - \frac{\delta - \delta_1}{4} \sin 2\beta \right) + \frac{m_0 \pi}{H_1} (a_2 - \delta_1 \sin \beta - 2H_1 \tan \beta) \quad (\text{C.39})$$

where $\hat{G}(\theta)$ is given by (B.37) and $\alpha = 0.8601$. Nevertheless, in order to find the total resistance associated to the folding process, it is still required to account for a last contribution. This one is coming from the membrane extension of the area previously damaged before the subsequent contact. Assuming that the internal dissipation only arises in part *IV* (Figure C.5b), a straightforward generalization of (B.63) leads to the subsequent approximate formula:

$$P_{IV}(\delta) = 2H_1 n_0 \frac{(\delta - \delta_1) \cos \beta}{2} \frac{2a_2 - (\delta + \delta_1) \sin \beta}{(a_2 - \delta \sin \beta)^2} \left| \frac{\delta_1 \cos \beta}{2H_1} \right| \quad (\text{C.40})$$

in which the last multiplying factor is introduced to account for the folds that have already been completely crushed before the subsequent contact. Summing up $P_I(\delta)$ to $P_{IV}(\delta)$ allows for the evaluation of the impacted wing resistance, provided that the folding height H_1 can be calculated. To do so, it is suggested to use the following simple relation obtained through a kind of minimization process:

$$H_1 = \sqrt[3]{\frac{\pi t_w (a_1 + a_2)(a_1 - \delta_1 \sin \beta)}{12 \cos \beta}} \quad (\text{C.41})$$

Finally, the folding resistance $P_f(\delta)$ of the cruciform has to be calculated by accounting also for the three remaining wings (or the two remaining wings for T-shaped intersections). These latter are numbered from ② to ④ on Figure 4.20 and are characterized by a contribution $P_{w,i}(\delta)$, with $i \in \{2, 3, 4\}$. Therefore, we have:

$$P_f(\delta) = P_I(\delta) + P_{II}(\delta) + P_{III}(\delta) + P_{IV}(\delta) + \sum_{i=2}^4 P_{w,i}(\delta) \quad (C.42)$$

where $P_{w,i}(\delta)$ can be evaluated by applying the recommendations made in section 4.2.3, except that $\delta - \delta_1$ has to be considered instead of δ .

C.2.3.2. Bending mechanism

This appendix focuses on the situation where a beam-like behavior is activated over the entire cruciform. It is first assumed that the activation of the bending mechanism occurs for a penetration δ^* such that the central cross-sections in point O (Figure C.6) have already been crushed by the bow, which means that $\delta^* > \delta_1$. On a mathematical point of view, the indentation at point O should be calculated by considering the intersection of the vessel with a vertical plane, such as shown on Figure 4.14. Doing so provides a function $c(\delta - \delta^*)$ for the penetration, but as the dimensions of the ship are usually quite large with respect to those of the impacted super-element, $c(\delta - \delta^*)$ may be conveniently approximated by $(\delta - \delta^*) \cos \beta$.

The collapse mechanism is the one depicted on Figure C.6a and is made of eight plastic hinges. The maximal bending moments in the horizontal and vertical elements are denoted by M_h and M_v respectively. At the supports, these latter have to be affected by reduction coefficients ξ_h and ξ_v to account for the partial rotational restraint. For the section immediately located under the impact point I , a coefficient ξ_h^* is also required because of the preliminary indentation δ^* preceding the activation of the bending mechanism. Finally, as $\delta_1 \leq \delta^*$, the central sections at point O are also crushed over a distance $\delta^* - \delta_1$ before the bending collapse, so the maximal bending moment is only equal to $\tilde{\xi}_h^* M_h$ or $\tilde{\xi}_v^* M_v$.

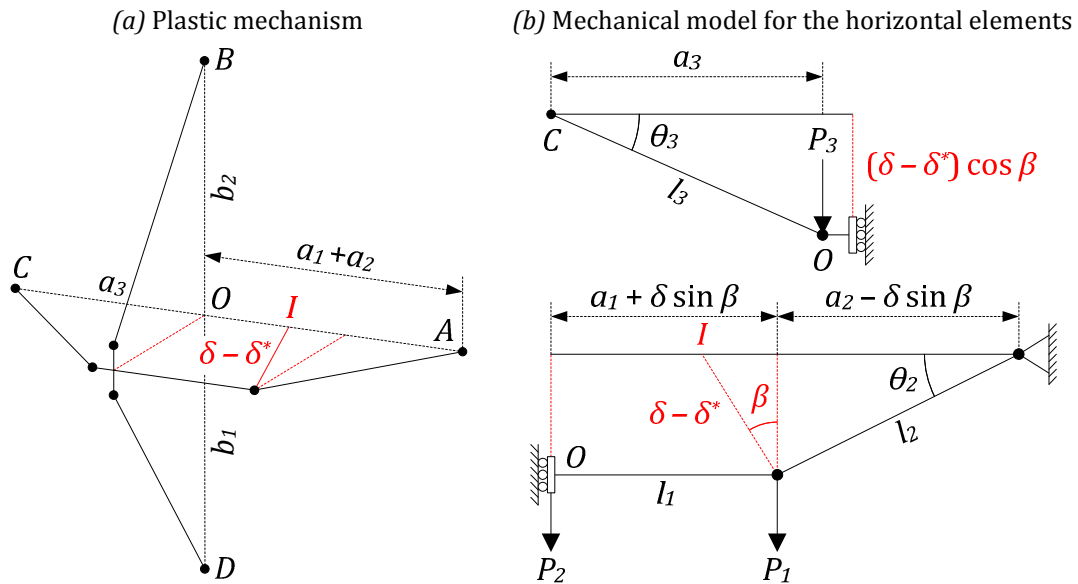


Figure C.6. Bending mechanism in case of a subsequent contact

The situation for the vertical wings OB and OD is exactly the same as on Figure B.16b, except that the central displacement is now equal to $(\delta - \delta^*) \cos \beta$, so their contribution to the

bending resistance can be obtained simply by adapting (B.68). For the horizontal wings OA and OC however, the approach is not straightforward. In order to solve this problem, a solution could be to generalize the method followed previously in section B.3.1.3 by analyzing the two wings individually. This way of doing is consistent with the hypothesis of having uncoupled super-elements, but is not entirely satisfactory as it does not respect the static requirements at the central point O . Nevertheless, as no major divergence with finite element simulations was found during the validation process, the approach has however been used for the analytical developments.

From the previous considerations, it results that the equilibrium method may be separately applied to both structures of Figure C.6b. The impact force acting on the horizontal elements has three different components, respectively denoted from P_1 , P_2 and P_3 . These ones can be determined by finding a set of statically admissible internal forces that respect both the yield locus and the normality requirement. Doing so, it can be shown that the bending resistance for the cruciform element is given by:

$$\begin{aligned}
 P_b(\delta) &= \frac{M_h(\xi_h + \xi_h^*)}{a_2 - \delta \sin \beta} \left(1 - \frac{N_1^2}{N_h^2}\right) + \frac{M_h(\xi_h + \xi_h^*)}{a_3 - \alpha H} \left(1 - \frac{\tilde{N}_1^2}{N_h^2}\right) + M_v(\xi_v + \xi_v^*) \left(1 - \frac{\tilde{N}_2^2}{N_v^2}\right) \\
 &+ (\delta - \delta^*) \left(\frac{N_1 \cos \beta}{a_2 - \delta \sin \beta} + \frac{\tilde{N}_1 \cos \beta}{a_3 - \alpha H} + \tilde{N}_2 \frac{b_1 + b_2 - 2\alpha H}{(b_1 - \alpha H)(b_2 - \alpha H)} \right)
 \end{aligned}$$

with:

$$\begin{aligned}
 N_1 &= \min \left\{ \frac{N_h^2}{4M_h(\xi_h + \xi_h^*)} \frac{2a_2 - (\delta - \delta^*) \sin \beta}{a_2 - \delta^* \sin \beta} (\delta - \delta^*) \cos \alpha ; N_h \right\} \\
 \tilde{N}_1 &= \min \left\{ \frac{N_h^2}{2M_h(\xi_h + \xi_h^*)} (\delta - \delta^*) \cos \beta ; N_h \right\} ; \quad \xi_h^* = \xi_v^*(\delta^* - \delta_1) \\
 \tilde{N}_2 &= \min \left\{ \frac{N_v^2}{2M_v(\xi_v + \xi_v^*)} (\delta - \delta^*) \cos \beta ; N_v \right\} ; \quad \xi_v^* = \xi_v^*(\delta^* - \delta_1)
 \end{aligned} \tag{C.43}$$

Of course, equation (C.43) is not valid if the beam-like behavior is activated before a subsequent contact occurs (i.e. if $\delta^* < \delta_1$). In this case, the resistance can be obtained by applying the same approach to the collapse mechanism of Figure B.16a.

As a final remark, it is worth bearing in mind that all the previous formulae are valid in case of a subsequent contact involving the left support. If the right one was first implicated, then equations (C.37) to (C.43) would be slightly modified. Furthermore, for a vertical SE2, all the formulae developed in section B.3.2 are still relevant, provided that $\delta - \delta_1$ is replaced by $(\delta - \delta_1) \cos \beta$.

C.3. Appendix C.3

C.3.1. Summary of some cross-section properties

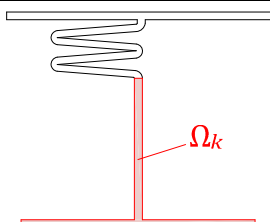
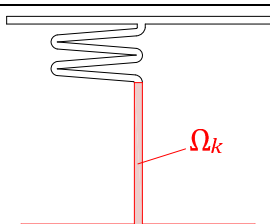
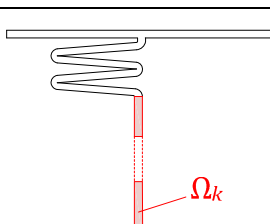
| Classification | Cross-section | | Bending resistance | | |
|--------------------|--|-------------|---|--|---|
| Class 1 Class 2 |  | | <p>M_k is the plastic bending resistance of the uncrushed T-shaped cross-section Ω_k when k folds are completely closed ($k \geq 1$). The bending capacity is as follows:</p> <ul style="list-style-type: none"> If $k < n$: $\xi_{p,i}(\delta)M_{p,i} = M_k + \frac{M_k - M_{k-1}}{2H}(\delta - 2kH)$ with $2(k-1)H \leq \delta \leq 2kH$ If $k = n$: $\xi_{p,i}(\delta)M_{p,i} = M_n$ with $\delta \geq 2nH$ | | |
| Class 3 |  | | <p>M_k is the elastic bending resistance of the uncrushed T-shaped cross-section Ω_k when k folds are completely closed ($k \geq 1$). The bending capacity is as follows:</p> <ul style="list-style-type: none"> If $k < n$: $\xi_{e,i}(\delta)M_{e,i} = M_k + \frac{M_k - M_{k-1}}{2H}(\delta - 2kH)$ with $2(k-1)H \leq \delta \leq 2kH$ If $k = n$: $\xi_{e,i}(\delta)M_{e,i} = M_n$ with $\delta \geq 2nH$ | | |
| Class 4 |  | | <p>M_k is the elastic bending resistance characterizing the efficient portion of the uncrushed T-shaped cross-section when k folds are completely closed ($k \geq 1$). If M_k is found to be higher than M_{k-1}, then the resistance is limited to M_{k-1} in order to keep a decreasing function. The bending capacity is as follows:</p> <ul style="list-style-type: none"> If $k < n$: $\bar{\xi}_{e,i}(\delta)\bar{M}_{e,i} = \min\left\{M_k + \frac{M_k - M_{k-1}}{2H}(\delta - 2kH); M_{k-1}\right\}$ with $2(k-1)H \leq \delta \leq 2kH$ If $k = n$: $\bar{\xi}_{e,i}(\delta)\bar{M}_{e,i} = M_n$ with $\delta \geq 2nH$ | | |
| Classification | Tension | Compression | Bending | Combination criteria | Comments |
| Class 1 Class 2 | $N_{p,i}$ | $N_{p,i}$ | $\xi_{p,i}(\delta)M_{p,i}$ | $\frac{M_i}{\xi_{p,i}(\delta)M_{p,i}} + \left(\frac{N_i}{N_{p,i}}\right)^2 = 1$ | $M_{p,i}$ and $N_{p,i}$ are calculated for the entire section. It is not required to account for buckling. |
| Class 3 | $N_{p,i}$ | $N_{p,i}$ | $\xi_{e,i}(\delta)M_{e,i}$ | $\frac{M_i}{\xi_{e,i}(\delta)M_{e,i}} + \frac{N_i}{N_{p,i}} = 1$ | $M_{e,i}$ and $N_{p,i}$ are calculated for the entire section. It is not required to account for buckling. |
| Class 4 | $N_{p,i}$ | $N_{p,i}$ | $\bar{\xi}_{e,i}(\delta)\bar{M}_{e,i}$ | $\frac{M_i}{\bar{\xi}_{e,i}(\delta)\bar{M}_{e,i}} + \frac{N_i}{\bar{N}_{p,i}} = 1$ | To account for buckling, $\bar{M}_{e,i}$ and $\bar{N}_{p,i}$ are calculated for the bending and compression effective cross-section respectively. |

Table C.1. Derivation of the bending resistance for a folded cross-section according to its class

C.3.2. Equilibrium method for a class 1 cross-section

As a reminder, it should be mentioned that the equilibrium method may be seen as an extension of the lower-bound theorem to moderate displacements. It leads to a solution that is statically admissible in the sense that the yield criterion and the equilibrium equations are simultaneously satisfied. However, the kinematic requirements are not necessarily fulfilled, in particular at the moving plastic hinge where the slope continuity is violated. For a complex situation such as the one depicted on Figure 4.28, it is claimed in section 4.3.2.2 that the equilibrium method leads to equations that are not tractable analytically. The aim of this appendix is to provide more details about this assertion.

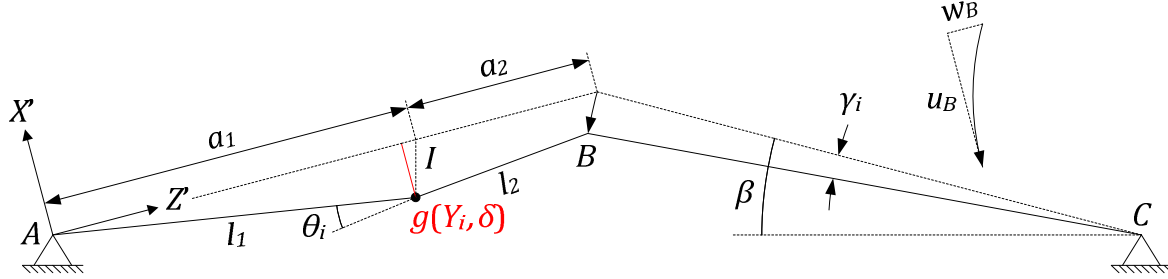


Figure C.7. Definition of the plastic collapse mechanism

To do so, one can consider the mechanism represented in Figure C.7 that involves one moving plastic hinge initially located at point I but travelling with a velocity $\dot{g}(Y_i, \delta) \tan \beta$ along the Z' axis. During the plastic collapse, it is postulated that the non-impacted leaf rotates as a rigid body, which means that the length of \overline{BC} is always equal to l . This forces point B to follow a circular trajectory having the following components along the X' and Z' axis:

$$u_B(\gamma_i) = l(\sin 2\beta - \sin(2\beta - \gamma_i)) ; w_B(\gamma_i) = l(\cos(2\beta - \gamma_i) - \cos 2\beta) \quad (C.47)$$

where γ_i is the rotation of BC for a given value of the penetration $g(Y_i, \delta)$. From these results, the current lengths l_1 and l_2 characterizing the two arms of the impacted beam are as follows:

$$l_1 = a_1 - g(Y_i, \delta) \tan \beta + \frac{g^2(Y_i, \delta)}{2(a_1 - g(Y_i, \delta) \tan \beta)} \quad (C.48)$$

$$l_2 = a_2 + g(Y_i, \delta) \tan \beta - w_B(\gamma_i) + \frac{(g(Y_i, \delta) - u_B(\gamma_i))^2}{2(a_2 + g(Y_i, \delta) \tan \beta - w_B(\gamma_i))}$$

where $a_1 = Z'_I$ and $a_2 = l - Z'_I$. From the previous results, it is easy to derive the total axial shortening $\Delta_i = a_1 + a_2 - l_1 - l_2$ and the relative rotation θ_i at the plastic hinge:

$$\Delta_i = w_B(\gamma_i) - \frac{g^2(Y_i, \delta)}{2(a_1 - g(Y_i, \delta) \tan \beta)} - \frac{(g(Y_i, \delta) - u_B(\gamma_i))^2}{2(a_2 + g(Y_i, \delta) \tan \beta - w_B(\gamma_i))} \quad (C.49)$$

$$\theta_i = \frac{g(Y_i, \delta)}{a_1 - g(Y_i, \delta) \tan \beta} - \frac{g(Y_i, \delta) - u_B(\gamma_i)}{a_2 + g(Y_i, \delta) \tan \beta - w_B(\gamma_i)}$$

The normal force that is required to produce the axial change of length Δ_i can be obtained by applying the normality rule. In this optic, the membrane and rotation rates are first calculated. These latter are found to be:

$$\dot{\Delta}_i = \left(\left(\frac{\partial \Delta_i}{\partial u_B} \cos(2\beta - \gamma_i) + \frac{\partial \Delta_i}{\partial w_B} \sin(2\beta - \gamma_i) \right) \frac{\partial \gamma_i}{\partial g} + \frac{\partial \Delta_i}{\partial g} \right) \dot{g}(Y_i, \delta) \quad (C.50)$$

$$\dot{\theta}_i = \left(\left(\frac{\partial \theta_i}{\partial u_B} \cos(2\beta - \gamma_i) + \frac{\partial \theta_i}{\partial w_B} \sin(2\beta - \gamma_i) \right) \frac{\partial \gamma_i}{\partial g} + \frac{\partial \theta_i}{\partial g} \right) \dot{g}(Y_i, \delta) \quad (\text{C.51})$$

where the derivatives with respect to u_B and w_B can be directly obtained by considering (C.49). Considering the previous results, the normal force N_i and the bending moment M_i associated to Δ_i and θ_i may be calculated to satisfy the plasticity equations (i.e. the normality rule and the yield criterion):

$$N_i = \min \left\{ \frac{N_{p,i}^2}{2\xi_{p,i} M_{p,i}} \frac{\dot{\Delta}_i}{\dot{\theta}_i}; N_{p,i} \right\} ; \quad M_i = \xi_{p,i} M_{p,i} \left(1 - \frac{N_i^2}{N_{p,i}^2} \right) \quad (\text{C.52})$$

Furthermore, because of static requirements, the shearing force T_i acting at the central contact block B and parallel to the X' axis (Figure C.8) has to be such that the rotational stability is verified, i.e.:

$$T_i = \frac{M_i - N_i(g(Y_i, \delta) - u_B(\gamma_i)) + p_i l_2^2 / 2}{a_2 + g(Y_i, \delta) \tan \beta - w_B(\gamma_i)} \quad (\text{C.53})$$

Substituting (C.50) and (C.51) in (C.52) allows to express N_i , M_i and T_i as functions of $g(Y_i, \delta)$, γ_i and $\partial \gamma_i / \partial g$, but a relation between γ_i and $g(Y_i, \delta)$ is still missing. This one will be derived hereafter.

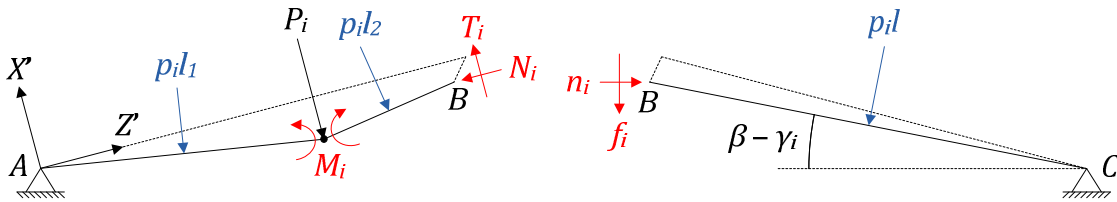


Figure C.8. Internal and external forces for the equilibrium method

In order to have a consistent application of the equilibrium method, a last requirement is to fulfill the static equations for the non-impacted leaf. For convenience, instead of working with N_i and T_i , the equivalent forces n_i and f_i are introduced (Figure C.8). Using these notations, it is obvious that the rotational equilibrium of BC leads to:

$$\frac{p_i l}{2} + f_i \cos(\beta - \gamma_i) - n_i \sin(\beta - \gamma_i) = 0 \quad \text{with:} \quad \begin{aligned} n_i &= N_i \cos \beta + T_i \sin \beta \\ f_i &= T_i \cos \beta - N_i \sin \beta \end{aligned} \quad (\text{C.54})$$

As a final result, it appears that (C.54) is a differential equation involving $g(Y_i, \delta)$, γ_i and $\partial \gamma_i / \partial g$ that allows for the derivation of γ_i as a function of $g(Y_i, \delta)$. Unfortunately, due to its excessive complexity, this equation cannot be solved analytically. Therefore, additional simplifications needs to be introduced in the model. As suggested by Paik and Thayamballi [121], an approximate solution can be found by disregarding the normality rule. However, doing so provides a result that is not entirely statically admissible. Consequently, the expression of $P_i(\delta)$ derived in section 4.3.2.2 fails to respect completely the static or kinematic requirements. For this reason, it has to be considered carefully, but comparisons with numerical solutions have shown that it was sufficient to model the gate behavior during the global deforming mode.

As a final comment, it is worth mentioning that the present solutions for $P_i(\delta)$ and those derived in section 4.3.2.2 are decreasing functions of the penetration δ , which is quite coherent as the plastic mechanisms corresponds to unstable configurations in the present case.

C.3.3. Plastic mechanism after buckling

C.3.3.1. Description of the folding process

As claimed in section 4.3.2.2, performing a rigid-plastic analysis is only valid for class 1 cross-sections because working with plastic hinges requires a sufficient rotation capacity. If this is not the case, then an early buckling is to fear when the relevant combination criteria of Table C.1 is satisfied. Once this instability occurs, the beam behavior may be studied by postulating a given folding mechanism. This approach has been largely applied in the literature to investigate thin-walled structures. Some application examples are provided by Kotelko [88] or Ungureanu et al. [151] who followed the upper-bound method to get the ultimate load for various cases.

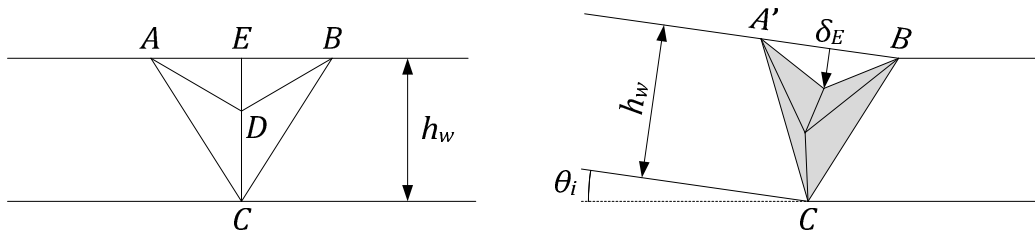


Figure C.9. Description of the folding mechanism

The approach followed here is exactly the same. The deformation pattern after buckling is depicted on Figure C.9 and is based on the one observed during finite element simulations. It is made of four different triangular surfaces ACD , BCD , ADE and BDE separated by various plastic hinges that allow for relative rotations between them. All these motions involve both bending and membrane deformations and it is precisely the aim of this section to evaluate the corresponding energy rates \dot{E}_b and \dot{E}_m . To do so, two parameters are introduced (Figure C.10). The first one is the length ℓ measured along the plating intersection, while the second one is the coefficient η such that the web is divided into two portions ηh_w and $(1 - \eta)h_w$ during the folding process.

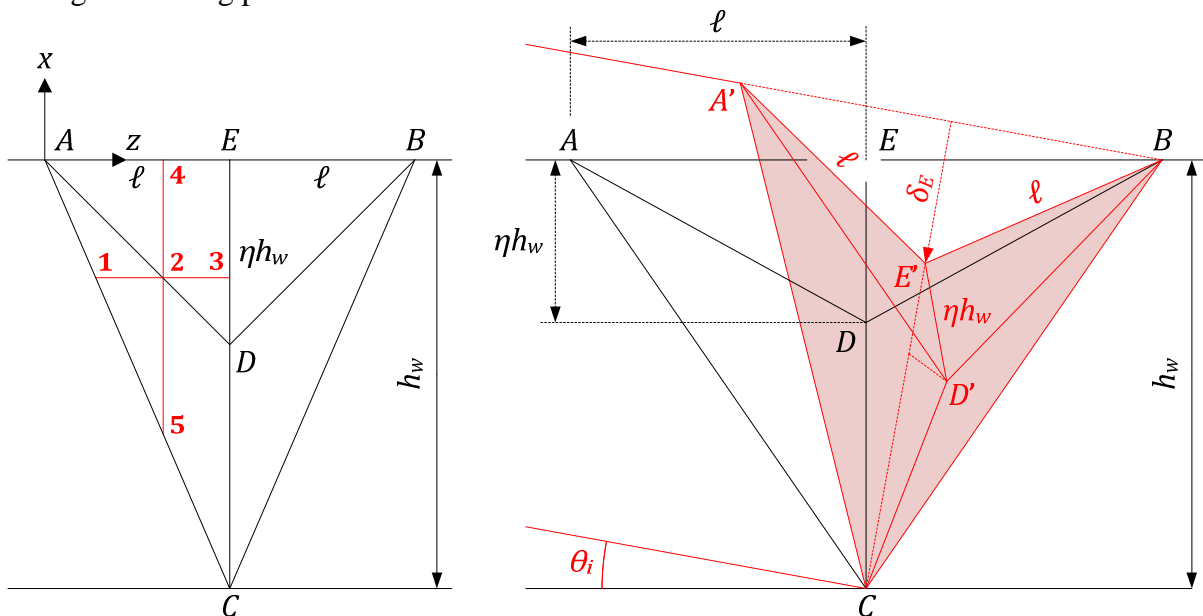


Figure C.10. Parameters defining the deformation pattern

The incremental variable governing the analytical approach is the relative rotation θ_i between the two arms of the beams (Figure C.9). When $\theta_i > 0$, the mechanism implies a relative

rotation of the four triangular surfaces such that the lengths of AE , EB , ED and CD remains unaffected. This last requirement involves an in-plane displacement δ_E of point E given by:

$$\delta_E = \sqrt{h_w \ell \sin \theta_i - (\ell^2 - h_w^2)(1 - \cos \theta_i)}/2 \quad (C.55)$$

which is a monotonically increasing function of θ_i . As in section 4.3.2.2, this latter may still be related to the penetration δ of the striking vessel.

C.3.3.2. Derivation of the displacement field

In an attempt to derive a kinematically admissible displacement field, the classical plate strip model is used. The folding mechanism is seen as a set of horizontal and vertical fibers that are weakly connected, which allows them to slide along each other without shearing. According to the hypotheses listed before, there is no deformation along the segments AE , EB , ED and CD , but for compatibility reasons this assumption has to be valid for any vertical fiber. In other words, the initial distance between the points 2, 4 and 5 of Figure C.10 is not modified when the beam is bent.

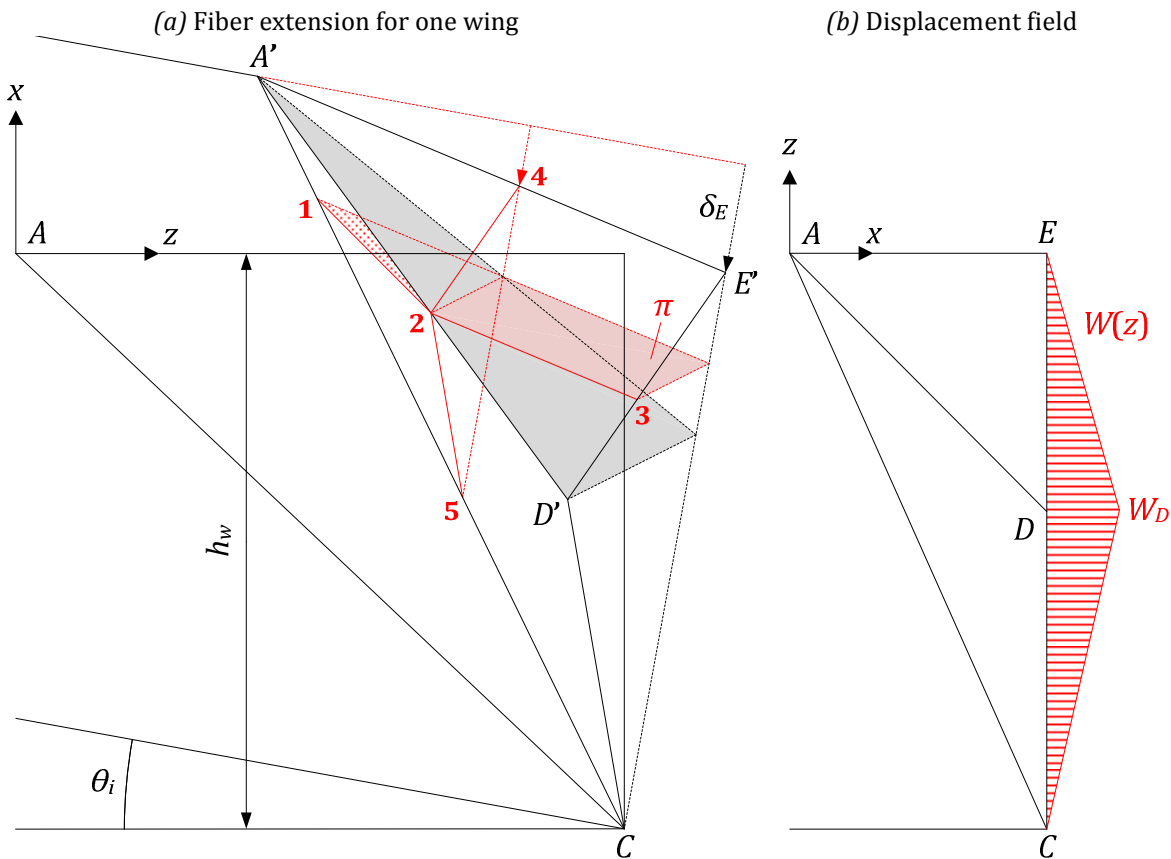


Figure C.11. Deformation and displacement field for one wing of the folding mechanism

Of course, if all the vertical fibers are inextensible, this cannot be the case for the horizontal ones. Because of the plate strip formulation, these latter may be seen as being only submitted to an axial elongation, which means that it is sufficient to impose only a displacement field $w(x,z)$ parallel to the x axis. In order to derive $w(x,z)$, a first step may be to get its particular profile $W(x) = w(x, \ell)$ along the central line EDC . An analytical expression for $W(x)$ can be found by evaluating the change of length between the points 1, 2 and 3 that are placed at a level x (Figure C.10). For a given indentation δ_E , due to geometrical considerations, these ones are found to be located in a inclined plane π that is always parallel

to the rotating segment $A'E'$ (Figure C.11a). This observation leads to the conclusion that $W(z)$ is the subsequent bilinear function:

- If $-h_w \leq x < \eta h_w$:
$$W(x) = \frac{x + h_w}{(1 - \eta)h_w} W_D$$
- If $-\eta h_w \leq x \leq 0$:
$$U(x) = -\frac{x}{\eta h_w} W_D$$

(C.56)

where W_D is the maximal in-plane displacement reached at point D (Figure C.11b). Of course, as the segments AE and AC are kept undeformed, $W(x)$ should be equal to zero for $x = 0$ and $x = -h_w$. In addition, the following result can be established:

$$W_D = (1 - \eta) \left(\sqrt{\ell^2 - 2\delta_E^2 + \frac{2\eta\delta_E}{1 - \eta} (h_w^2 + \delta_E^2)^{1/2}} - \ell \right) \quad (C.57)$$

where the indentation at point E is given by (C.55) and $\eta \leq 0.5$. With the previous equations, the derivation $w(x, z)$ is now quite straightforward. The only requirements are $w(x, z) = 0$ along AC and $w(x, \ell) = W(z)$. The easiest way to respect these conditions is to perform the subsequent linear interpolation:

$$w(x, z) = \frac{z + \ell x/h_w}{\ell(1 + x/h_w)} W(x) \quad (C.58)$$

which is reputed to be kinematically admissible as $w(x, z)$ satisfies the continuity and boundary conditions.

C.3.3.3. Derivation of the internal energy rate

Using equation (C.58), the membrane strain rate \dot{E}_m can be easily determined by integrating the axial strain rate \dot{E}_{zz} over the deforming triangles AED and ADC in accordance with the plate strip formulation recalled by formula (3.44). Doing so, we get:

$$\dot{E}_{zz} = \frac{\dot{W}(x)}{\ell(1 + x/h_w)} \Rightarrow \dot{E}_m = n_0 h_w \frac{\partial W_D}{\partial \delta_E} \frac{\partial \delta_E}{\partial \theta_i} \dot{\theta}_i \quad (C.59)$$

where the derivatives of W_D and δ_E can be obtained from (C.55) and (C.57). Once the membrane energy rate is known, the next step is to calculate the bending one. Due to the particular geometry of the fold, it is a very cumbersome process to establish the analytical formulae leading to \dot{E}_b . Therefore, only the final results are presented here. In fact, \dot{E}_b may be obtained by summing up two different terms $\dot{E}_{b,1}$ and $\dot{E}_{b,2}$.

The first contribution is coming from the folded web itself. From Figure C.10, it appears that the rotations are confined in six plastic hinges $A'C$, BC , $E'D'$, CD' , $A'E'$ and $E'B$, for which the internal dissipation is given by:

$$\dot{E}_{b,1} = 2m_0 \left(\sqrt{h_w^2 + \ell^2} \frac{\partial \zeta_1}{\partial \delta} + \ell_{eq} \left(\frac{\partial \zeta_1}{\partial \delta} + \frac{\partial \zeta_2}{\partial \delta} \right) + \ell \frac{\partial \zeta_2}{\partial \delta} \right) \frac{\partial \delta_E}{\partial \theta_i} \dot{\theta}_i \quad (C.60)$$

with:
$$\ell_{eq} = \sqrt{\ell^2 + \eta^2 h_w^2 + 2\eta\delta_E (h_w^2 + \delta_E^2)^{1/2} - 2\delta_E^2 (1 - \eta)}$$

where ζ_1 and ζ_2 are the relative rotations of the triangles constituting the fold. The second contribution is due to the bending effects arising in the flange and in the collaborating portion of plating. From Figure C.12, it can be seen that three plastic hinges are involved in the plating, while only one is present in the flange. They are responsible for the following dissipation:

$$\dot{E}_{b,2} = \left(\frac{\sigma_0 t_f^2}{4} h_f + \sigma_0 t_p^2 h_{eq} \frac{h_w \sqrt{1 + \cos \theta_i} + \ell \sqrt{1 - \cos \theta_i}}{2\sqrt{2}\delta_E} \right) \dot{\theta}_i \quad (\text{C.61})$$

where h_f is the flange width and h_{eq} is the collaborating length of the plating. As usual, t_f and t_p are the corresponding thicknesses of these elements. As a final result, \dot{E}_b is obtained by summing up (C.60) and (C.61).

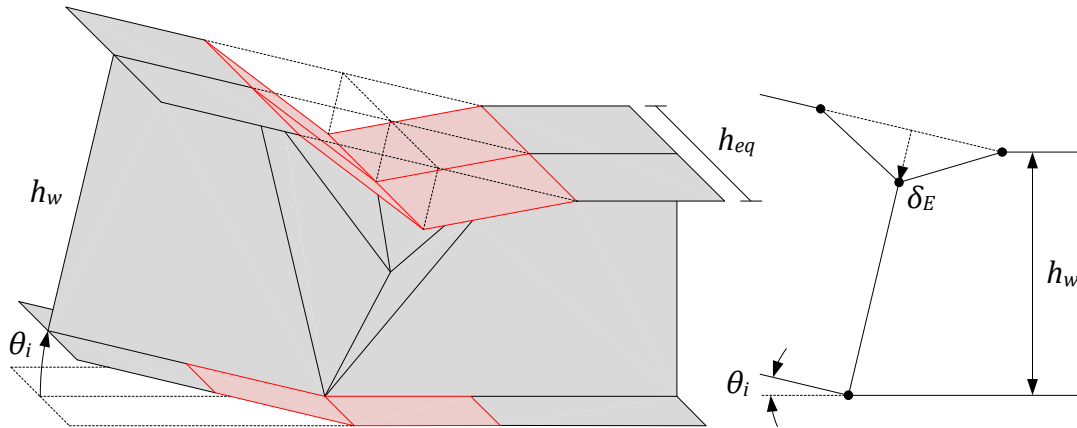


Figure C.12. Bending effects in the plating and in the flange

As a final result, the total internal energy rate \dot{E}_{int} is obtained by summing up E_m , $E_{b,1}$ and $E_{b,2}$ in accordance with equations (C.59), (C.60) and (C.61) respectively. This leads to an expression of \dot{E}_{int} as a function of θ_i and $\dot{\theta}_i$.

C.3.3.4. Derivation of the resistance

In accordance with the upper-bound method, the contribution $P_i(\delta)$ to the global resistance $P_G(\delta)$ has to be found by equating the work rate done by the external forces with the internal dissipation \dot{E}_{int} , i.e.:

$$P_i \frac{\partial g}{\partial \delta} \dot{\delta} + \dot{W}_h = \dot{E}_{int} \quad (\text{C.62})$$

where \dot{W}_h is the external power due to the hydrostatic pressure and \dot{E}_{int} has been derived in section C.3.3.3. However, solving (C.62) still requires to find a relation between the opening angle θ_i and the out-of-plane displacement $g(Y_i, \delta)$. To do so, one can consider the plastic mechanism depicted on Figure C.13. For a given position I' of the initial contact point, it can be seen that the three segments AI' , BI' and BC simply collapse by keeping their initial lengths, i.e.:

$$\overline{AI} = \overline{AI'} = Z'_l = a_1 \quad ; \quad \overline{BI} = \overline{BI'} = l - Z'_l = a_2 \quad ; \quad \overline{BC} = l \quad (\text{C.63})$$

which means that both points B and I follow a circular trajectory. In other words, the main difference with class 1 cross-sections lies in the fact that the hinge is not moving, so the folding mechanism of Figure C.9 remains located at its initial position where buckling first occurs.

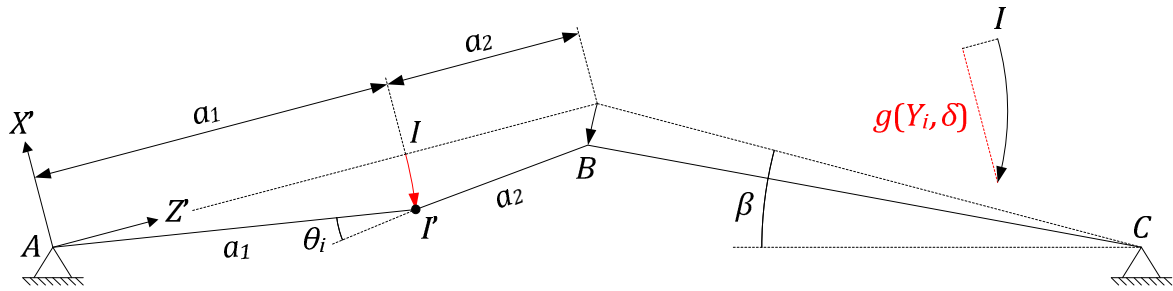


Figure C.13. Plastic mechanism for a class 2, 3 or 4 cross-section

Because of the requirements imposed by (C.63), it transpires that the position of the central point B is univocally determined, so a relation between θ_i and $g(Y_i, \delta)$ can be derived from geometrical considerations. This procedure being quite fastidious, it is not reported here.

As an additional result, the internal forces n_i and f_i at the central block B (Figure 4.30) can be found by expressing the rotation equilibrium of the two leaves. The solutions may then be introduced in the sliding criterion to know if the contact is still provided (see section 4.3.2.3).

C.4. Appendix C.4

This appendix provides additional comparisons to check the validity of the simplified approach in various other cases. These results are directly extracted from a publication made by Buldgen et al. [24] on the crashworthiness of lock mitre gates. They are all based on the structure presented in Figure 4.34, but four different models are investigated. For each of them, the main geometrical properties are the same as those listed in Table 4.5, but some parameters are varied (Table C.2).

| Property | | Gate 1 | Gate 2 | Gate 3 | Gate 4 |
|---------------------------------|-----------|--------|--------|--------|--------|
| Vertical position | $Y_S (m)$ | 7.15 | 7.15 | 7.15 | 7.15 |
| Transversal position | $Z_S (m)$ | 12.6 | 8.2 | 8.2 | 8.2 |
| Plating thickness | $t_p (m)$ | 0.022 | 0.015 | 0.012 | 0.022 |
| Web thickness of the girders | $h_w (m)$ | 0.016 | 0.012 | 0.02 | 0.01 |
| Web height of the girders | $t_w (m)$ | 1.5 | 1.5 | 1.5 | 1.2 |
| Flange thickness of the girders | $t_f (m)$ | 0.012 | 0.012 | 0.02 | 0.01 |

Table C.2. Parameters defining each gate model

In the first gate model (Table C.2), the impact point location is changed. Y_S is still equal to 7.15 m, but this time $Z_S = 12.6$ m. In this configuration, the collision occurs near the central stud. The results presented on Figure C.14 show that sliding occurs around $\delta = 0.7$ m, so it is not really a problem if the analytical curve is not conservative for $\delta \geq 0.7$ m.

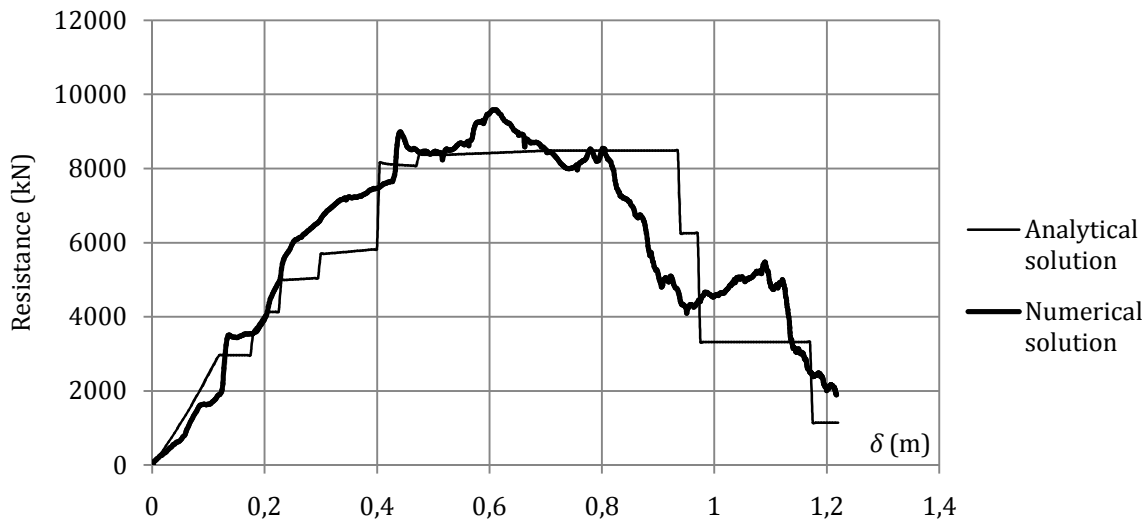


Figure C.14. Numerical and analytical resistance curves for the first gate model

For the second gate model (Table C.2), the importance of the stiffening system is reduced. To do so, in comparison with Table 4.5, the thickness of the plating and of the horizontal girders are respectively reduced to $t_p = 0.015$ m and $t_w = 0.012$ m, which implies that the beam cross-section may be of class 1 or 3 according to the collaborative part of the plating. The impact is kept at $Y_S = 7.15$ m and $Z_S = 8.2$ m. The curve obtained in this case is plotted on Figure C.15 and shows a rather good accordance with the numerical results of LS-DYNA. Nevertheless, the analytical approach appears to be too conservative when the global mode is activated, i.e. for $\delta > 0.45$ m. On a theoretical point of view, this may be justified by the two following reasons:

- When the overall plastic mechanism is activated over the whole lock gate, the contributions $P_i(\delta)$ of the beams having a class 3 cross-section are evaluated with help of

the unstable folding mechanism described in section C.3.3 of Appendix C.3, which explains why the curve is decreasing for $\delta > 0.45 \text{ m}$. Nevertheless, as mentioned in Eurocode 3 [53], a class 3 cross-section may still be bent beyond its elastic capacity, but this additional resistance is often conservatively neglected. Consequently, the folding mechanism only provides a lower estimation of the resistance during the post-buckling phase.

- Another reason is due to the fact that some beams are characterized by a class 1 cross-section for which it is possible to develop a plastic hinge. In reality, as all the horizontal girders are connected to each other by the vertical frames, it is likely that the collision efforts may be redistributed in order to compensate the lack of resistance exhibited by the beams where a folding process is initiated. Unfortunately, such a situation is not accounted for in the analytical model because all the elements are supposed to be decoupled.

As a conclusion for this second gate model, it can be said that evaluating the resistance of a gate with class 1 and class 3 cross-sections remains problematic but is achieved in a quite conservative manner.

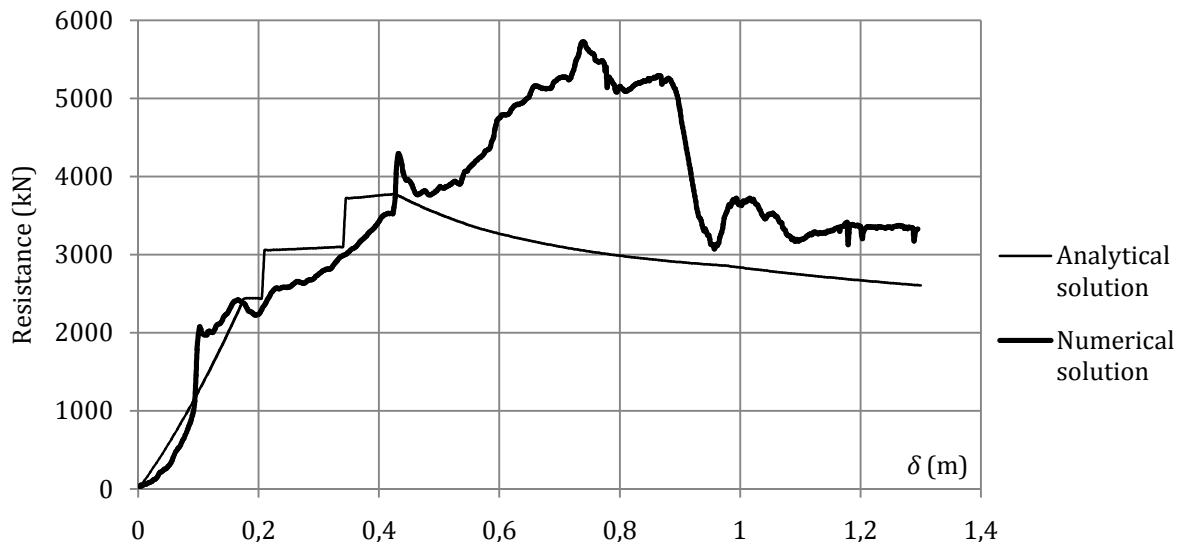


Figure C.15. Numerical and analytical resistance curves for the second gate model

For the third gate model (Table C.2), the importance of the stiffening system is this time increased by modifying the thicknesses of the horizontal girders to have $t_w = 0.02 \text{ m}$ and $t_f = 0.02 \text{ m}$. The impact is still located at $Y_S = 7.15 \text{ m}$ and $Z_S = 8.2 \text{ m}$. This leads to the curves depicted on Figure C.16. Conservative results are provided by the analytical procedure at the beginning of the penetration, but this is not always the case when $\delta > 0.2 \text{ m}$ where the crushing resistance tends to be overestimated in comparison with numerical results. This is partially due to the hypothesis that the local and global modes are strictly separated after the transition. Even when an overall plastic mechanism is activated, it is shown by the numerical simulations that the ship sometimes moves forward through an increased local indentation and sometimes through an increased overall bending of the gate. This phenomenon is not taken into account in the present simplified analytical approach. However, the discrepancy between the two curves remains quite acceptable.

For the fourth gate model (Table C.2), the influence of the vertical frames is now investigated. In the present approach, it is assumed that their role is only to transmit the displacement field

to the horizontal girders. However, this hypothesis may not be valid anymore if the vertical frames are too weak to force the collaboration between the beams. Therefore, the properties of the vertical frames are reduced to the following values: $t_w = 0.01\text{ m}$, $t_f = 0.01\text{ m}$ and $h_w = 1.2\text{ m}$. The impact is kept at $Y_S = 7.15\text{ m}$ and $Z_S = 8.2\text{ m}$. The corresponding results are plotted on Figure C.17 with a quite good agreement, which tends to corroborate the hypothesis made on the vertical components in the simplified approach.

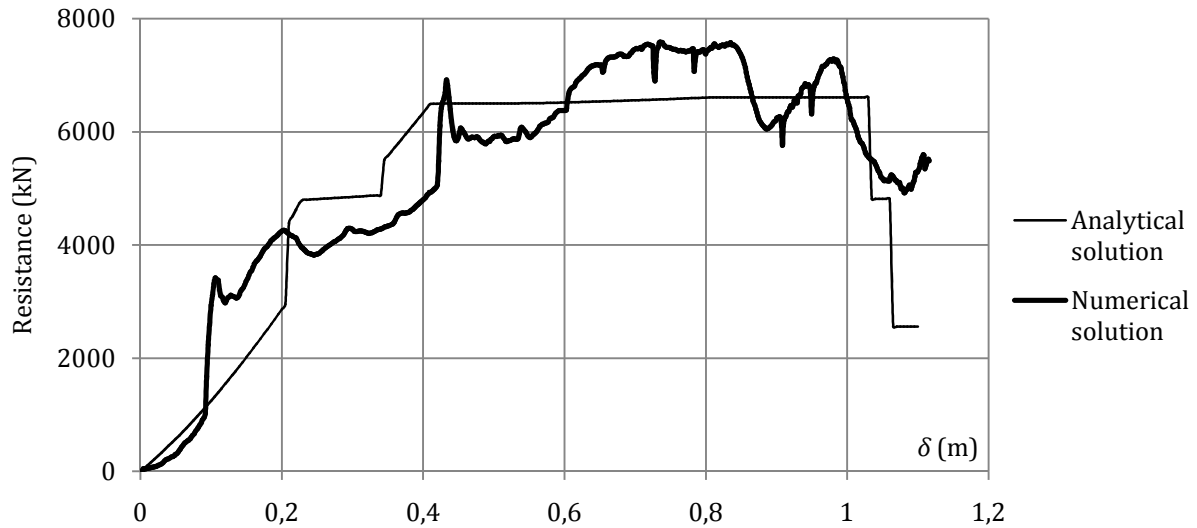


Figure C.16. Numerical and analytical resistance curves for the third gate model

It is shown by the comparisons performed in this appendix that the simplified procedure leads to quite acceptable curves in comparison with those obtained numerically with LS-DYNA. Most of the time, the approach appears to be conservative, which is an important point at a pre-design stage of the gate. The hypothesis made on the vertical frames is also confirmed by this study: even if they are weakened, they still play their role by transmitting the displacements from one girder to the others.

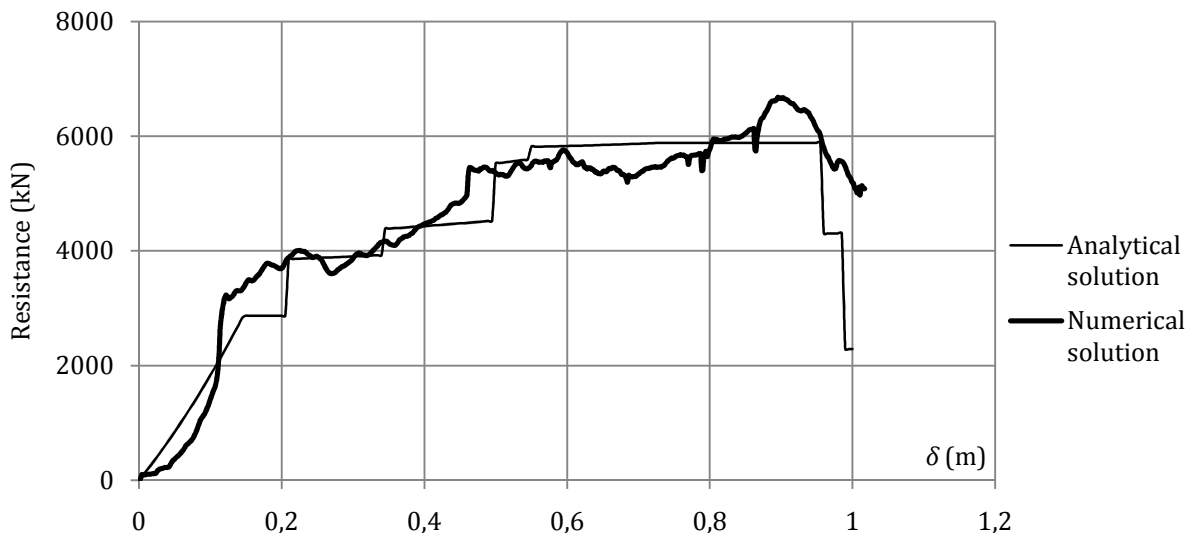


Figure C.17. Numerical and analytical resistance curves for gate the fourth gate model

APPENDIX D. Additional developments on the seismic analysis of large reservoirs

This addendum to Chapter 7 mainly provides some mathematical developments and other formulae that could be useful to implement the simplified approach detailed previously for large reservoirs.

In Appendix D.1, the equations of the Rayleigh quotient are first presented in the general form. After that, a non-dimensional analysis is performed to investigate the influence of the fluid-structure interaction on the modal analysis.

In Appendix D.2, the effect of the fluid during the seism is also pointed out. Some comparisons between rigid and flexible solutions are presented to stress the importance of the fluid-structure interaction during the dynamic analysis.

D.1. Appendix D.1

This appendix first provides the general form of the terms involved in the Rayleigh quotient. After that, they are reduced to non-dimensional expressions in order to perform a more detailed investigation of the fluid-structure interaction.

D.1.1. Derivation of the Rayleigh quotient

Let us start by deriving the mathematical expressions for \hat{T}_{jk} , \hat{W}_{jk} and \hat{U}_{jk} introduced in (7.38) and (7.39). All the parameters that are involved in these expressions have already been defined in section 7.2 dealing with dry mode shapes. As stated before, the matrices $[\hat{T}]$ and $[\hat{U}]$ are diagonal, which means that $\hat{T}_{jk} = \hat{U}_{jk} = 0$ if $j \neq k$. If $j = k$, the subsequent results may be established:

$$\hat{T}_{jj} = \frac{\rho t_p}{2} A_j^2 l (D_j + \bar{D}_j - 2B_j C_j) \quad (\text{D.1})$$

$$\hat{U}_{jj} = \frac{D}{2} A_j^2 l \left((\lambda_j^2 + \gamma_j^2)^2 (D_j - B_j C_j) + (\bar{\lambda}_j^2 - \gamma_j^2)^2 (\bar{D}_j - B_j C_j) \right) \quad (\text{D.2})$$

where ρ , D , t_p and l are respectively the mass density, the flexural rigidity, the thickness and the width of the plate. A_j is a parameter used to normalize the dry mode shape $\delta_j(y, z)$. The expressions of λ_j , $\bar{\lambda}_j$ and γ_j are given by (7.21), while B_j is defined in (7.23). For C_j , D_j and \bar{D}_j , one has the additional definitions:

$$C_j = \frac{\bar{\lambda}_j \cosh(\bar{\lambda}_j H) \sin(\lambda_j H) - \lambda_j \cos(\lambda_j H) \sinh(\bar{\lambda}_j H)}{\lambda_j^2 + \bar{\lambda}_j^2} \quad (\text{D.3})$$

$$D_j = \frac{H}{2} - \frac{\sin(2\lambda_j H)}{4\lambda_j} \quad (\text{D.4})$$

$$\bar{D}_j = B_j^2 \left(\frac{\sinh(2\bar{\lambda}_j H)}{4\bar{\lambda}_j} - \frac{H}{2} \right) \quad (\text{D.5})$$

The matrix $[\hat{W}]$ is not diagonal but is simply symmetric. The corresponding terms W_{jk} are given in (7.38), where $I_{mn}^{(j)}$ is as follows:

$$\hat{I}_{mn}^{(j)} = A_j \gamma_j \frac{1 - (-1)^m \cos(\gamma_j l)}{\gamma_j^2 - \bar{\gamma}_m^2} (E_n + B_j \bar{E}_n) \quad \text{if } \gamma_j \neq \bar{\gamma}_m \quad (\text{D.6})$$

$$\hat{I}_{mn}^{(j)} = 0 \quad \text{if } \gamma_j = \bar{\gamma}_m$$

where $\bar{\gamma}_m = m\pi/l$ as defined in (7.9). Remembering that $\gamma_j = n_j\pi/l$, it is clear from (D.6) that $\hat{I}_{mn}^{(j)} = 0$ for $m \neq n_j$ if $m + n_j + 1$ is an even number. So a lot of terms in $[\hat{W}]$ are in fact equal to 0. For E_n and \bar{E}_n , the following relations are valid, in which α_n is given in (7.9):

$$E_n = \frac{\lambda_j + \alpha_n (-1)^n \sin(\lambda_j h_s)}{\bar{\lambda}_j^2 - \alpha_n^2} \quad \bar{E}_n = \frac{\bar{\lambda}_j + \alpha_n (-1)^n \sinh(\bar{\lambda}_j h_s)}{\bar{\lambda}_j^2 + \alpha_n^2} \quad (\text{D.7})$$

Nevertheless, all these equations are expressed in terms of dimensional parameters, which is not convenient for qualitative analyses, so one may seek to have more harmonized relations.

D.1.2. Investigation of the fluid-structure interaction

D.1.2.1. Non-dimensional approach

If the water level is progressively reduced in such a way that $h_s \rightarrow 0$, it is obvious from equations (7.28) and (7.38) that all the terms \widehat{W}_{jk} also decrease and $[\widehat{W}] \rightarrow [0]$. In this case, it is clear that solving the generalized eigenvalues problem defined by (7.41) and (7.42) leads to solutions such that $\Omega_i \rightarrow \omega_i$. Moreover, the components of the eigenvector \mathbf{v}_i associated to Ω_i satisfy the following properties:

$$\begin{aligned} \text{If } i \neq j: \quad v_{ji} &\rightarrow 0 \\ \text{If } i = j: \quad v_{ji} &\rightarrow 1 \end{aligned} \tag{D.8}$$

Consequently, considering equation (7.35), it can be concluded that $\Delta_i(y, z) \rightarrow \delta_i(y, z)$, which means that the wet solution nears the dry one. If h_s tends to 0 in the Rayleigh quotient R given in (7.55), the previous reasoning shows that the term \mathcal{W} will be progressively reduced. Therefore, $R \rightarrow \mathcal{T}/\mathcal{U}$, where \mathcal{T} and \mathcal{U} have to be evaluated with the wet eigenmodes $\Delta_i(y, z)$ that are very close to the dry ones $\delta_i(y, z)$. To characterize the importance of the fluid-structure interaction, the Rayleigh quotient may be rewritten as:

$$R = \frac{\mathcal{T}}{\mathcal{U}} \left(1 - \frac{\mathcal{W}}{\mathcal{T}} \right) = \frac{\mathcal{T}}{\mathcal{U}} (1 + \text{FSI}) \quad ; \quad \text{FSI} = -\mathcal{W}/\mathcal{T} \tag{D.9}$$

where FSI is the fluid-structure interaction quotient. From equation (D.9), it is clear that the effect of the fluid may be neglected if $\text{FSI} \ll 1$. Nevertheless, it is important to bear in mind that the Rayleigh quotient is currently defined for a particular mode i , as stated in (7.40). In fact, if M admissible functions are used in (7.35), M wet eigenmodes $\Delta_i(y, z)$ can be obtained by solving (7.41) and (7.42). The FSI quotient may then be evaluated for each of these M modes of vibration, which means that the fluid-structure interaction can be neglected if the requirement $\text{FSI} \ll 1$ is satisfied for all the M possible $\Delta_i(y, z)$. In practice however, as the response of the structure is mainly affected by its first mode of vibration (as discussed in section 8.3.3, this is particularly true for a gate with a single plating), it is sufficient to check that $\text{FSI} \ll 1$ for $i = 1$.

| Geometrical properties | | Fluid properties | | Non-dimensional parameters | | |
|------------------------|-------------------------|-------------------------|---------------------|----------------------------|---------------|---------------------------|
| t_p | Thickness of the plate | ρ_f | Mass density | κ | h/l | Plate aspect ratio |
| l | Width of the plate | Solid properties | | μ | l/L | Reservoir narrowness |
| h | Height of the plate | E | Young modulus | ϕ | h_s/h | Filling coefficient |
| L | Length of the reservoir | ν | Poisson coefficient | \bar{t}_p | t_p/h | Non-dimensional thickness |
| h_s | Fluid level | ρ | Mass density | $\bar{\rho}$ | ρ_f/ρ | Non-dimensional density |

Table D.1. Geometrical, material and non-dimensional properties

In order to have a better characterization of the fluid-structure interaction, it may be interesting to express the FSI quotient as a function of non-dimensional parameters. To do so, let us start by considering Table D.1, where the initial geometrical and material properties are summarized. From the original geometrical data, four non-dimensional parameters may be defined: the plate aspect ratio $\kappa = h/l$, the reservoir narrowness $\mu = l/L$, the filling coefficient $\phi = h_s/h$ and the non-dimensional thickness $\bar{t}_p = t_p/h$. Additionally, the non-dimensional mass density $\bar{\rho} = \rho_f/\rho$ is also introduced. All these new notations are listed

with their definitions in Table D.1 and may now be used to transform the results obtained previously for \hat{T}_{jk} and \hat{W}_{jk} . This operation is done in the optic of allowing for easier qualitative analyses. To do so, the following notations are adopted:

$$\bar{c}_j^2 = c_j^2 l^2 \quad \lambda_j^* = \sqrt{\bar{c}_j^2 - n_j^2 \pi^2} \quad \bar{\lambda}_j^* = \sqrt{\bar{c}_j^2 + n_j^2 \pi^2} \quad (\text{D.10})$$

where c_j^2 and n_j have already been introduced in (7.21). It is worth noting that \bar{c}_j^2 has no dimension and is only a function of the aspect ratio κ (this is of course only valid for given values of the material properties E , ν and ρ). Introducing these new parameters in (7.21) and (7.23) leads to:

$$\lambda_j = \frac{\lambda_j^*}{l} \quad \bar{\lambda}_j = \frac{\bar{\lambda}_j^*}{l} \quad B_j = \frac{n_j^2 \pi^2 (1 - \nu) - \bar{c}_j^2 \sin(\kappa \lambda_j^*)}{n_j^2 \pi^2 (1 - \nu) + \bar{c}_j^2 \sinh(\kappa \bar{\lambda}_j^*)} \quad (\text{D.11})$$

It is now possible to write \hat{T}_{jk} using some of the above-mentioned notation. This derivation is quite straightforward and leads to:

$$\hat{T}_{jk} = \rho t_p H l \cdot \bar{T}_{jk} \quad ; \quad \bar{T}_{jj} = \frac{A_j^2}{2\kappa} (D_j^* + \bar{D}_j^* - 2B_j C_j^*) \quad (\text{D.12})$$

where A_j is still the modal amplitude. For $j \neq k$, it is evident that $\bar{T}_{jk} = 0$. For $j = k$, the following definitions are valid:

$$C_j^* = \frac{\bar{\lambda}_j^* \cosh(\kappa \bar{\lambda}_j^*) \sin(\kappa \lambda_j^*) - \lambda_j^* \cos(\kappa \lambda_j^*) \sinh(\kappa \bar{\lambda}_j^*)}{\kappa [(\lambda_j^* + \bar{\lambda}_j^*)^2 - 2\lambda_j^* \bar{\lambda}_j^*]} \quad (\text{D.13})$$

$$D_j^* = \frac{1}{2} - \frac{\sin(2\kappa \lambda_j^*)}{4\kappa \lambda_j^*} \quad (\text{D.14})$$

$$\bar{D}_j^* = B_j^2 \left(\frac{\sinh(2\kappa \bar{\lambda}_j^*)}{4\kappa \bar{\lambda}_j^*} - \frac{1}{2} \right) \quad (\text{D.15})$$

Similarly, the same job can be performed to get an harmonized form of \hat{W}_{jk} . To do so, $\hat{I}_{mn}^{(j)}$ has first to be rewritten with the notations introduced here over:

$$\hat{I}_{mn}^{(j)} = h_s l \cdot \bar{I}_{mn}^{(j)} \quad ; \quad \bar{I}_{mn}^{(j)} = \frac{A_j n_j}{\pi} \frac{1 - (-1)^m \cos(n_j \pi)}{n_j^2 - m^2} (E_n^* + B_j \bar{E}_n^*) \quad (\text{D.16})$$

The previous expression of $\bar{I}_{mn}^{(j)}$ is only valid for $m \neq n_j$, otherwise it is obvious that $\bar{I}_{mn}^{(j)} = 0$. For E_n^* and \bar{E}_n^* , one gets:

$$E_n^* = \frac{\kappa \phi \lambda_j^* + \alpha_n^* (-1)^n \sin(\kappa \phi \lambda_j^*)}{(\kappa \phi \lambda_j^* - \alpha_n^*)(\kappa \phi \lambda_j^* + \alpha_n^*)} \quad \bar{E}_n^* = \frac{\kappa \phi \bar{\lambda}_j^* + \alpha_n^* (-1)^n \sinh(\kappa \phi \bar{\lambda}_j^*)}{(\kappa \phi \bar{\lambda}_j^* + \alpha_n^*)^2 - 2\kappa \phi \alpha_n^* \bar{\lambda}_j^*} \quad (\text{D.17})$$

where $\alpha_n^* = (2n - 1)\pi/2$. These notations may now be utilized to seek for a more harmonize form of \hat{W}_{jk} . Accounting for (7.9) and (7.48), it is found that:

$$\hat{W}_{jk} = - \left(\frac{\rho_f h_s^2 l}{\phi^2} \right) \cdot \bar{W}_{jk} \quad ; \quad \bar{W}_{jk} = \sum_{m=0}^{+\infty} \sum_{n=1}^{+\infty} c_{mn}^* \phi^2 \frac{\chi_m \bar{I}_{mn}^{(j)} \bar{I}_{mn}^{(k)}}{\sqrt{(2n-1)^2 + 4m^2 \kappa^2 \phi^2}} \quad (\text{D.18})$$

where $\chi_m = 4/\pi$ if $m = 0$ and $\chi_m = 8/\pi$ if $m > 0$. In addition, the following definitions should also be mentioned:

$$c_{mn}^* = \frac{\cosh(\xi_{mn}^*) - 1}{\sinh(\xi_{mn}^*)} \quad ; \quad \xi_{mn}^* = \frac{\pi}{\mu} \sqrt{\left(\frac{2n-1}{2\kappa\phi}\right)^2 + m^2} \quad (\text{D.19})$$

Finally, to obtain a non-dimensional form for the FSI quotient (D.9), all the previous calculations simply have to be used in conjunction with (7.56):

$$\mathcal{T} = \frac{1}{2} \sum_{j=1}^M \sum_{k=1}^M v_{ji} \hat{T}_{jk} v_{ki} = \frac{\rho t_p H l}{2} \sum_{j=1}^M \sum_{k=1}^M v_{ji} \bar{T}_{jk} v_{ki} \quad (\text{D.20})$$

$$\mathcal{W} = \frac{1}{2} \sum_{j=1}^M \sum_{k=1}^M v_{ji} \hat{W}_{jk} v_{ki} = -\frac{\rho_f h_s^2 l}{2\phi^2} \sum_{j=1}^M \sum_{k=1}^M v_{ji} \bar{W}_{jk} v_{ki} \quad (\text{D.21})$$

As FSI is defined by the ratio $-\mathcal{W}/\mathcal{T}$, dividing (D.21) by (D.20) leads to the subsequent result:

$$\text{FSI} = \frac{\bar{\rho}}{\bar{t}_p} \left(\sum_{j=1}^M \sum_{k=1}^M v_{ji} \bar{W}_{jk}(\kappa, \mu, \phi) v_{ki} \right) \div \left(\sum_{j=1}^M \sum_{k=1}^M v_{ji} \bar{T}_{jk}(\kappa) v_{ki} \right) \quad (\text{D.22})$$

where \bar{T}_{jk} and \bar{W}_{jk} are the non-dimensional forms of the corresponding terms \hat{T}_{jk} and \hat{W}_{jk} defined in (7.38). It is interesting to note that \bar{T}_{jk} is only a function of the aspect ratio of the plate, but this is not the case for \bar{W}_{jk} which also depends on the reservoir properties μ and ϕ . Concerning the eigenvectors v_i , they are influenced by all the parameters of Table D.1.

D.1.2.2. Parametric study

In order to further investigate the importance of the fluid-structure interaction, it is of interest to analyze the evolution of the FSI quotient when the configuration of the reservoir is varied. This task is rather difficult to perform, because a lot of properties are involved in the problem. Moreover, the effect of all the above-mentioned parameters on the eigenvectors v_i is difficult to characterize, as the only way to get these vectors is to solve the generalized eigenvalues problem defined by (7.41) and (7.42). Therefore, in order to have a more concise investigation, only the particular case of a steel reservoir filled with water will be considered here. Doing so, the values of E , ν , ρ and ρ_f are the ones listed in Table 7.1. Furthermore, as the influence of the plate thickness has already been assessed through the examples in section 7.3.3, it will not be treated here again and it will be assumed that $\bar{t}_p = 0.02$. This choice is in accordance with equation (7.13), provided that $\kappa \leq 5$.

With the hypotheses listed before, only the variations of κ , μ and ϕ need to be considered. In order to have a configuration that is more or less similar to a lock chamber, these parameters are supposed to be varied within the following intervals:

$$0.5 \leq \kappa \leq 2 \quad 0.05 \leq \mu \leq 0.5 \quad 0 \leq \phi \leq 1 \quad (\text{D.23})$$

where it is obvious that ϕ may not be greater than unity, as this would correspond to an overtopping of the reservoir. The evolution of FSI is depicted on Figure D.1 for different values of κ , ϕ and μ . It is important to bear in mind that these curves are only valid under the

assumptions listed before, i.e. considering the values of Table 7.1 and the intervals of variation given by (D.23). From these results, the following conclusions may be drawn:

- The FSI quotient is always a monotonically increasing function of ϕ . Indeed, all the curves plotted on Figure D.1 for different values of κ and μ show that the fluid-structure interaction is more important if the liquid level is higher.
- The FSI quotient is an increasing value of κ , which means that a plate for which $h \gg l$ will be strongly influenced by the fluid. However, this not the case for all values of μ : as depicted on Figure D.1a for $\mu = 0.5$, this statement is not valid if the reservoir is more or less totally filled. This is due to the fact that \mathcal{T} and \mathcal{W} tend to stabilize when $\phi \rightarrow 1$. Nevertheless, as μ does usually not exceed 0.1 for classical lock chambers, such a situation is not really a problem.
- The FSI quotient is a decreasing function of μ . In other words, the interaction is reduced in a reservoir for which $L \ll l$. It is worth mentioning that for a classical lock chamber with $\mu \leq 0.1$, the effect of this parameter on FSI coefficient is negligible for all values of κ and ϕ .

This last statement is corroborated by Figure D.1d, where the maximal relative difference between the curves for $\mu = 0.1$ and $\mu = 0.2$ are listed for various values of κ . From these results, it transpires that evaluating the FSI quotient with $\mu = 0.1$ or $\mu = 0.2$ is practically similar. Consequently, it can be said that the FSI quotient is nearly independent on the narrowness of the reservoir, provided that $\mu \leq 0.2$ (which is almost the case for lock chambers).

Moreover, it appears from Figure D.1 that the requirement $\text{FSI} \ll 1$ is only satisfied for very small values of the filling coefficient ϕ . So most of the time, it is necessary to consider the presence of water while performing the modal analysis of an immersed plate.

D.1.2.3. Influence of the length of the reservoir

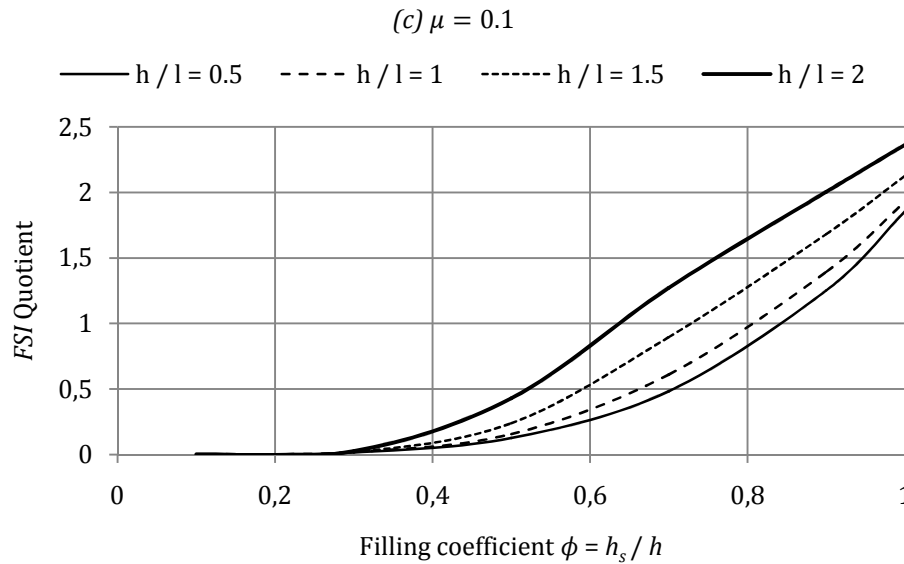
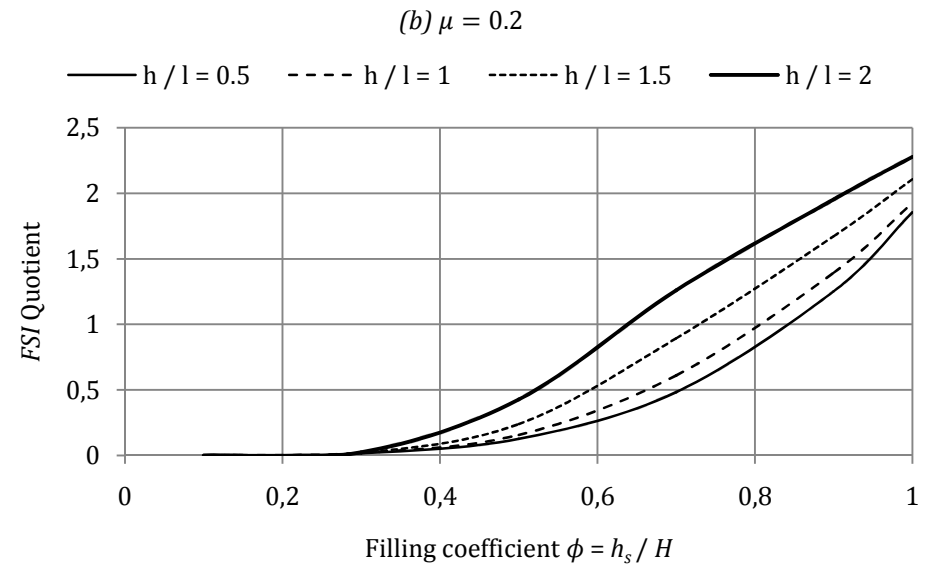
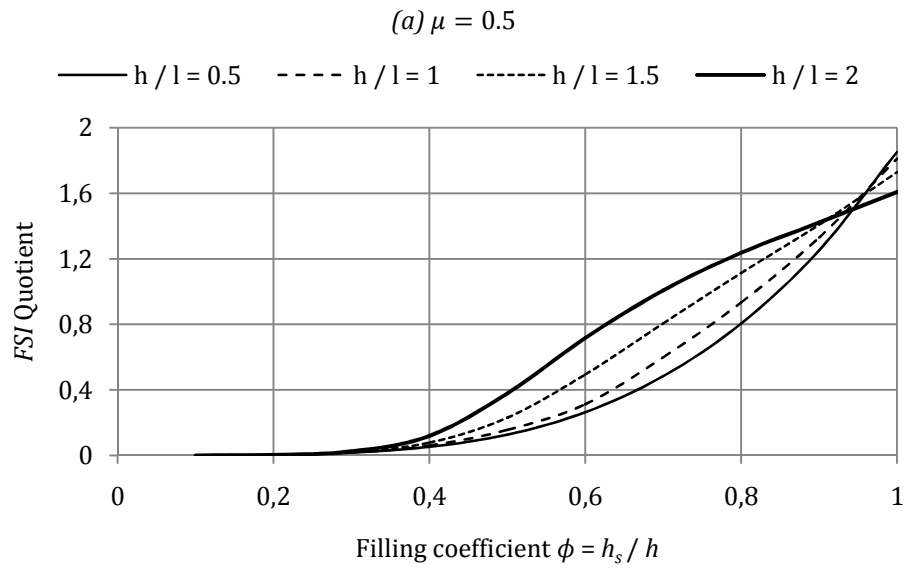
In fact, it is possible to explain mathematically why the reservoir narrowness μ has little influence, provided that it is sufficiently small. To do so, one needs to consider the results reported in section D.1.2.1. It is shown there that the term \bar{W}_{jk} involved in equation (D.22) is given by:

$$\bar{W}_{jk} = \sum_{m=0}^{+\infty} \sum_{n=1}^{+\infty} c_{mn}^* \frac{\phi^2 \chi_m \bar{\Gamma}_{mn}^{(j)} \bar{\Gamma}_{mn}^{(k)}}{\sqrt{(2n-1)^2 + 4m^2 \kappa^2 \phi^2}} \quad (\text{D.24})$$

where χ_m , $\bar{\Gamma}_{mn}^{(j)}$ and $\bar{\Gamma}_{mn}^{(k)}$ are only functions of κ and ϕ . In addition, the following relation is still holding for c_{mn}^* :

$$c_{mn}^* = \frac{\cosh(\xi_{mn}^*) - 1}{\sinh(\xi_{mn}^*)} \quad ; \quad \xi_{mn}^* = \frac{\pi}{\mu} \sqrt{\left(\frac{2n-1}{2\kappa\phi}\right)^2 + m^2} \quad (\text{D.25})$$

It is clear from (D.24) and (D.25) that the influence of μ on the FSI quotient is only hidden inside the coefficients c_{mn}^* . It may be easily shown that for $\mu \rightarrow 0$, $\xi_{mn}^* \rightarrow +\infty$ and $c_{mn}^* \rightarrow 1$. With such a property, putting $c_{mn}^* = 1$ in (D.24) immediately shows that \bar{W}_{jk} is now only a function of κ and ϕ , but it is no longer dependant on μ .



(d) Maximal relative difference on IFS between $\mu = 0.1$ and $\mu = 0.2$

$$\max_{\phi} \left| \frac{\text{FSI}(\mu = 0.2) - \text{FSI}(\mu = 0.1)}{\text{FSI}(\mu = 0.2)} \right| (\%)$$

| κ | Maximal difference (%) |
|----------|------------------------|
| 0.5 | 0.00 |
| 1 | 0.06 |
| 1.5 | 0.93 |
| 2 | 3.77 |

Figure D.1. Curves showing the evolution of FSI for different values of κ , ϕ and μ

As consequence, the FSI quotient is not influenced by the narrowness of the reservoir anymore. For practical reasons that will be discussed later, one may seek to know a kind of threshold value beyond which this statement is valid or not. So the purpose is now to find when the approximation:

$$c_{mn}^* = \frac{\cosh(\xi_{mn}^*) - 1}{\sinh(\xi_{mn}^*)} \approx 1 \quad \forall (m, n) \in [0, +\infty] \times [1, +\infty] \quad (\text{D.26})$$

is holding. According to (D.25), it transpires that ξ_{mn}^* is an increasing function of m and n , and therefore the validity of (D.26) needs only to be checked with $m = 0$ and $n = 1$:

$$\frac{\cosh(\pi/2\kappa\phi\mu) - 1}{\sinh(\pi/2\kappa\phi\mu)} \approx 1 \Leftrightarrow \frac{\cosh(\pi L/2h_s) - 1}{\sinh(\pi L/2h_s)} \approx 1 \quad (\text{D.27})$$

This last expression shows that μ has no influence on the FSI quotient, provided that the ratio L/h_s is sufficiently large. The evolution of c_{mn}^* (for $m = 0$ and $n = 1$) is plotted for different values of L/h_s on Figure D.2, where it can be seen that the curve quickly tends to its upper limit. This is due to the fact that c_{mn}^* invokes hyperbolic functions which have the property to increase rapidly. From the table on Figure D.2, it seems reasonable to consider that $c_{mn}^* \approx 1$ if $L/h_s \geq 3$.

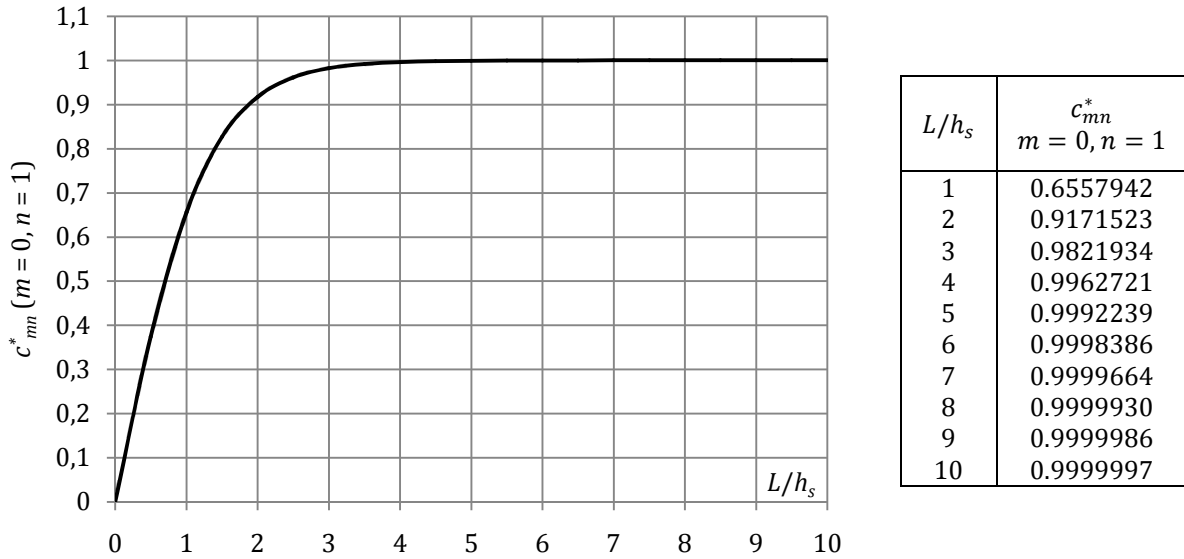


Figure D.2. Evolution of c_{mn}^* (with $m = 0$ and $n = 1$) with the ratio L/h_s .

As a conclusion, it can be said that the FSI quotient is no longer influenced by the narrowness μ of the reservoir if $L \geq 3h_s$. So for given values of E , ν , ρ and ρ_f , the following statement should be emphasized:

$$L \geq 3h_s \quad \rightarrow \quad \text{FSI} = \text{FSI}(\kappa, \phi, \bar{t}_p) = \text{FSI}(l, h_s, H, t_p) \quad (\text{D.28})$$

The direct consequence of (D.28) is that, for any value of E , ν , ρ , ρ_f , h , l and t_p , the length L does not play any role in the modal analysis of a reservoir, provided that $L \geq 3h_s$. In other words, for a given value of h_s , the vibration properties of a reservoir with $L = 3h_s$ are also valid for all reservoirs with $L \geq 3h_s$. To illustrate this last assertion, let us have a short application example and consider a reservoir with $\phi = 0.6$, $\kappa = 1.25$ and $\bar{t}_p = 0.02$. The material properties are still those listed in Table 7.1. The ratio L/h_s is progressively increased, which leads to the curves plotted on Figure D.3 and on Figure D.4.

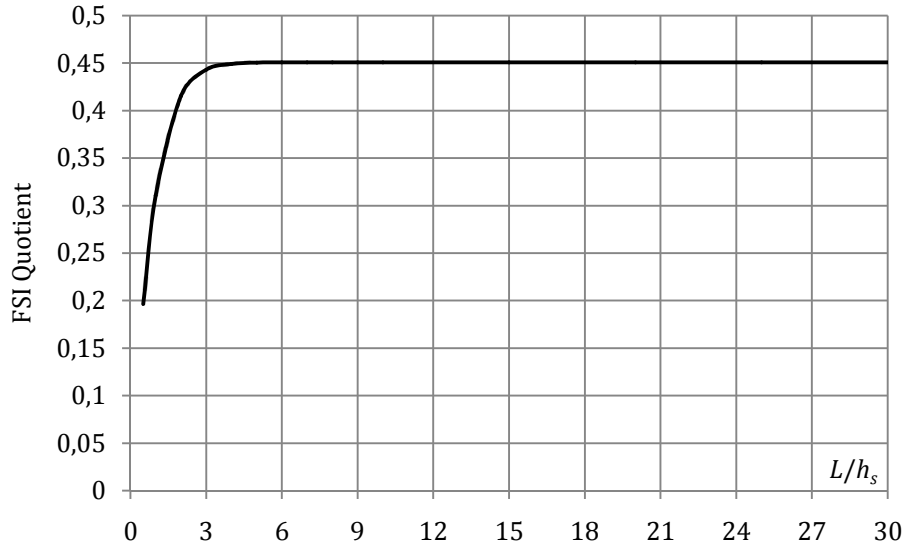


Figure D.3. Evolution of the FSI quotient with the ratio L/h_s

From Figure D.3, it is clear that the FSI quotient is no longer influenced by the length of the reservoir when the ratio L/h_s is progressively increased. In other words, it can be stated that the influence of the fluid is the same in any reservoir having a length L greater than $3h_s$. This is also corroborated by Figure D.4 depicting the evolution of the first wet frequency with the ratio L/h_s . This curve shows that the frequency tends to stabilize for $L/h_s \geq 3$, which confirms that the length of the reservoir does not influence the modal properties of the flexible walls beyond this limit.

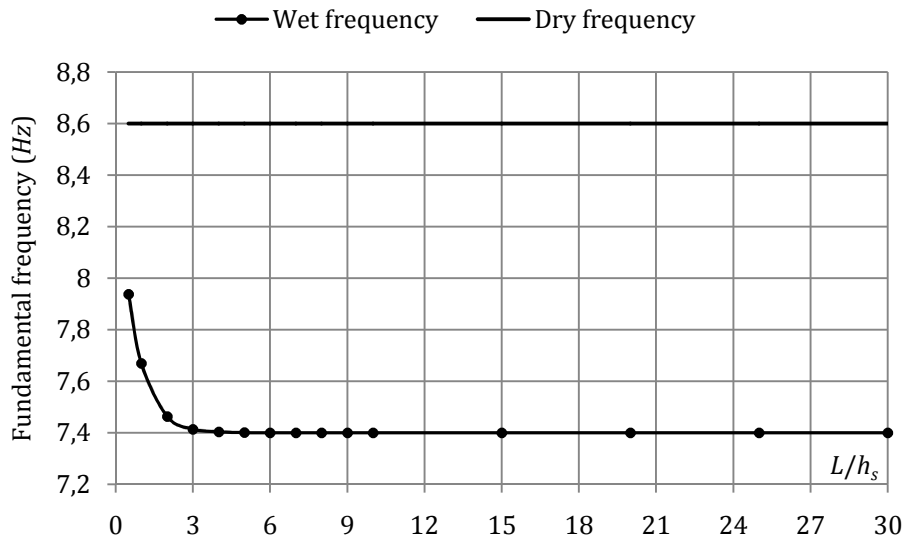


Figure D.4. Evolution of the first wet frequency with the ratio L/h_s

The property expressed in (D.28) may have some practical implications that will be considered later, in particular when dealing with dynamic analysis of flexible containers (section 7.4).

D.1.3. Derivation of the flexible pressure potential

The aim of this appendix is to establish equation (7.47) giving the potential \mathcal{W} associated to the hydrodynamic pressure $p_f(y, z, t)$ calculated in (7.25). To do so, the virtual work δW_f

performed by $p_f(y, z, t)$ during a virtual displacement $\delta u(y, z, t)$ needs first to be evaluated. The potential may then be found through the following definition:

$$\delta \left(\int_{t_1}^{t_2} \mathcal{W} dt \right) = - \int_{t_1}^{t_2} \delta W_f dt \quad (\text{D.29})$$

where the symbol δ is used to denote a virtual characteristic. $[t_1, t_2]$ is an arbitrary time period over which the integration is carried. From Figure D.5, it is clear that the pressure does not act in the same sense as the positive virtual displacement. Consequently, one should write:

$$\int_{t_1}^{t_2} \delta W_f dt = - \int_{t_1}^{t_2} \left(\iint_A p_f(y, z, t) \delta u(y, z, t) dA \right) dt = \sum_{n=1}^{+\infty} \sum_{m=0}^{+\infty} c_{mn} \int_{t_1}^{t_2} f(t) \dot{g}(t) dt \quad (\text{D.30})$$

where the two functions $f(t)$ and $g(t)$ are expressions integrated over the wet surface of the plate and are therefore only time-dependent:

$$f(t) = \iint_A \delta u \cos(\alpha_n y) \cos(\bar{\gamma}_m z) dA \quad g(t) = \iint_A \dot{u} \cos(\alpha_n y) \cos(\bar{\gamma}_m z) dA \quad (\text{D.31})$$

One may now simplify (D.30) by developing the equation through an integration by parts. Doing so leads to:

$$\int_{t_1}^{t_2} \delta W_f dt = \sum_{n=1}^{+\infty} \sum_{m=0}^{+\infty} c_{mn} \left(f(t_2)g(t_2) - f(t_1)g(t_1) - \int_{t_1}^{t_2} \dot{f}(t)g(t) dt \right) \quad (\text{D.32})$$

However, as the virtual displacements $\delta u(y, z, t)$ is arbitrary, it may be postulated that $\delta u(y, z, t) = 0$ for $t = t_1$ and $t = t_2$, which implies that $f(t_1) = f(t_2) = 0$. Moreover, noting that $\dot{f}(t) = \delta g(t)$, (D.32) becomes:

$$\int_{t_1}^{t_2} \delta W_f dt = - \sum_{n=1}^{+\infty} \sum_{m=0}^{+\infty} c_{mn} \int_{t_1}^{t_2} \delta g(t)g(t) dt = - \delta \left(\int_{t_1}^{t_2} \sum_{n=1}^{+\infty} \sum_{m=0}^{+\infty} \frac{c_{mn}}{2} g^2(t) dt \right) \quad (\text{D.33})$$

Comparing this last relation to (D.29), it is obvious that the potential \mathcal{W} has to fulfill the definition (7.47).

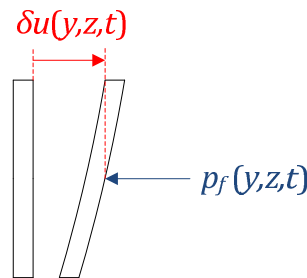


Figure D.5. Virtual displacement field

D.2. Appendix D.2

D.2.1. Dynamic analysis of a rigid reservoir

In this appendix, it is checked that simulations performed on a rigid reservoir are in quite good agreement with well-known theoretical formulae that are widely available in the literature. The goal is to have more confidence on the numerical model presented in 7.4.3.1, because having a proper representation of the fluid-structure interaction is a quite arduous task. To do so, the total resulting force $F_r(t)$ acting on the rigid wall will be numerically and analytically investigated for the reservoir introduced in section 7.4.3. It is worth noting that only the portion of the force due to the seismic hydrodynamic pressure is considered, the hydrostatic one being disregarded. In other words, one can more precisely define $F_r(t)$ as:

$$F_r(t) = \int_0^{h_s} \int_0^l p_r(y, t) dy dz = l \int_0^{h_s} p_r(y, t) dy \quad (\text{D.34})$$

where $p_r(y, t)$ is the rigid impulsive pressure given in (7.7). Figure D.6 shows the numerical and analytical curves of $F_r(t)$, for the acceleration $\ddot{X}(t)$ plotted on Figure 7.13 and for a water level h_s of 3.5 m. The agreement seems to be quite good, and this conclusion is also corroborated by Table D.2 showing the extreme values obtained in both cases. It can be seen that the relative difference with respect to the theoretical approach is satisfactory.

| | Analytical solution | Numerical solution | Relative difference |
|---------------|---------------------|--------------------|---------------------|
| Maximal value | 45.46 kN | 40.01 kN | 12 % |
| Minimal value | -38.07 kN | -36.19 kN | 5 % |

Table D.2. Comparison between the extreme values of the analytical and numerical rigid solutions

Another point that is important to stress is that the time evolution of pressure given by the finite element simulation follows more or less exactly the seismic acceleration $\ddot{X}(t)$, which is in accordance with classical formulae as well.

Apart from these purely numerical aspects, the differences noted in Table D.2 may be explained because of resonance phenomena. Indeed, the analytical solution (7.7) is developed under the assumption of an incompressible fluid, for which the bulk modulus K_f (and also the speed of sound c_f) tend to infinity. Nevertheless, by using LS-DYNA, these two parameters have the finite values shown in Table 7.1, which means that the liquid is in fact compressible. In this case, for a rigid reservoir of length L , it is possible to show that resonance may appear in the fluid if this is one is excited at the following frequencies:

$$(2n - 1) \frac{c_f}{2L} \quad ; \quad n \in \mathbb{N}_0 \quad (\text{D.35})$$

In the present case, as $c_f = 1500 \text{ m/s}$ and $L = 15 \text{ m}$, for $n = 1$, the first value of (D.35) is equal to 50 Hz. In order to exclude these resonant contributions, the numerical signal $F_r(t)$ has been filtered to eliminate all the harmonics greater than 50 Hz. This inevitably causes an artificial reduction of the total pressure force, as all the non-resonant harmonics greater than 50 Hz are also extracted from the signal. Nevertheless, as the composition of $\ddot{X}(t)$ in the large frequency range is quite modest (Figure 7.14), this operation should not affect dramatically the results presented here. So as a conclusion, it can be said, the quite good agreement found for the rigid case comfort the finite element model detailed in section 7.4.3.1.

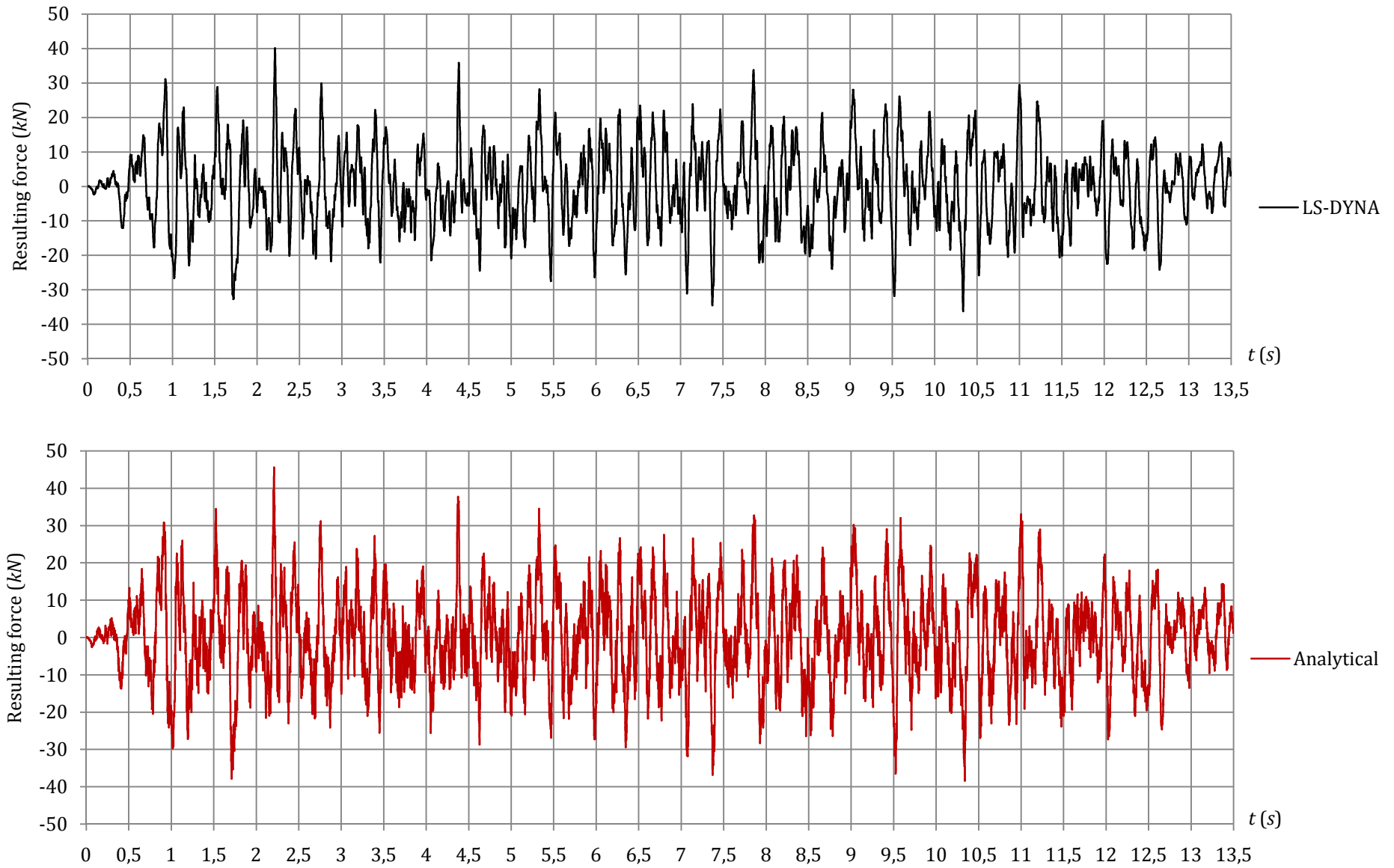


Figure D.6. Analytical and numerical resulting force for a rigid reservoir ($h_s = 3.5$ m)

D.2.2. Investigation of the fluid-structure interaction

D.2.2.1. Comparison of the rigid and flexible solutions

The goal of this section is to point out the importance of accounting for the fluid-structure interaction when performing the seismic analysis of flexible reservoirs. To do so, the theoretical solutions obtained when the walls are rigid or not can be compared for the reservoir used in section 7.4.3. For a water level of 3.5 m, Figure D.8 confronts the solutions derived in the two cases. From this figure, it is clear that the responses are totally different.

This observation is confirmed by the values listed in Table D.3, corresponding to the ratios between the extreme values given by the rigid and flexible solutions, i.e.:

$$\frac{\max_t \{F_r(t) + F_f(t)\}}{\max_t \{F_r(t)\}} ; \frac{\min_t \{F_r(t) + F_f(t)\}}{\min_t \{F_r(t)\}} \quad (\text{D.36})$$

where $F_r(t)$ and $F_f(t)$ are the total resulting forces due to the rigid and flexible impulsive pressures respectively. According to the analytical solution for $h_s = 3.5 \text{ m}$, it can be seen that the maximal rigid force applied on the wall has to be multiplied by a factor 1.66 to account for the flexibility. The situation is even worse for the lower extreme value, as the coefficient is this time equal to 2.19. The amplification is of the same order for the solutions given by LS-DYNA. It results from this brief comparison that performing the seismic design of this flexible reservoir while considering it as rigid may lead to an unsafe situation.

| $h_s = 3.5 \text{ m}$ | | |
|-----------------------|---------------------|--------------------|
| Result | Analytical solution | Numerical solution |
| Maximal value | 1.66 | 1.77 |
| Minimal value | 2.19 | 2.13 |
| $h_s = 5 \text{ m}$ | | |
| Result | Analytical solution | Numerical solution |
| Maximal value | 1.71 | 1.59 |
| Minimal value | 2.35 | 2.47 |

Table D.3. Ratios of the extreme values obtained for the flexible and rigid solutions

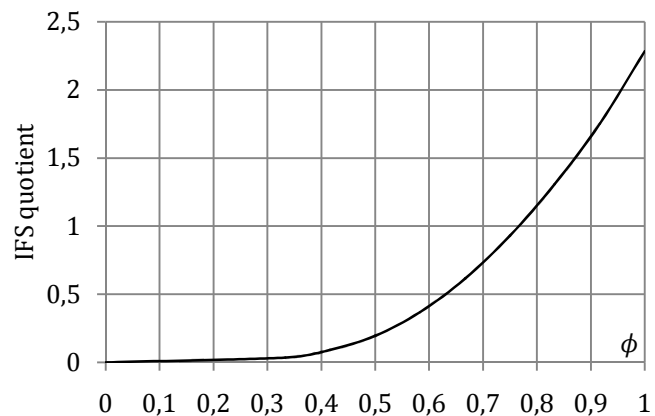


Figure D.7. Evolution of the FSI quotient with the filling coefficient $\phi = h_s/H$

Going back to the developments performed in section D.1.2 of Appendix D.1, the curve of Figure D.7 can be plotted to show the evolution of the FSI quotient as a function of the filling coefficient $\phi = h_s/h$. For $h_s = 3.5 \text{ m}$, $\phi = 0.6$ and FSI = 0.4, which is not negligible with respect to 1. Consequently, without performing any dynamic simulation, it was predictable that the fluid-structure interaction should be taken into account in the present case. The dynamic analysis and the results of Figure D.8 confirm this conclusion.

D.2.2.2. Influence of the length of the reservoir

In section D.1.2.3 of Appendix D.1, it was already mentioned that the length L has no influence on the modal properties of the immersed flexible plate, provided that $L \geq 3h_s$. The aim now is to see if this is also valid for the dynamic response of the reservoir.

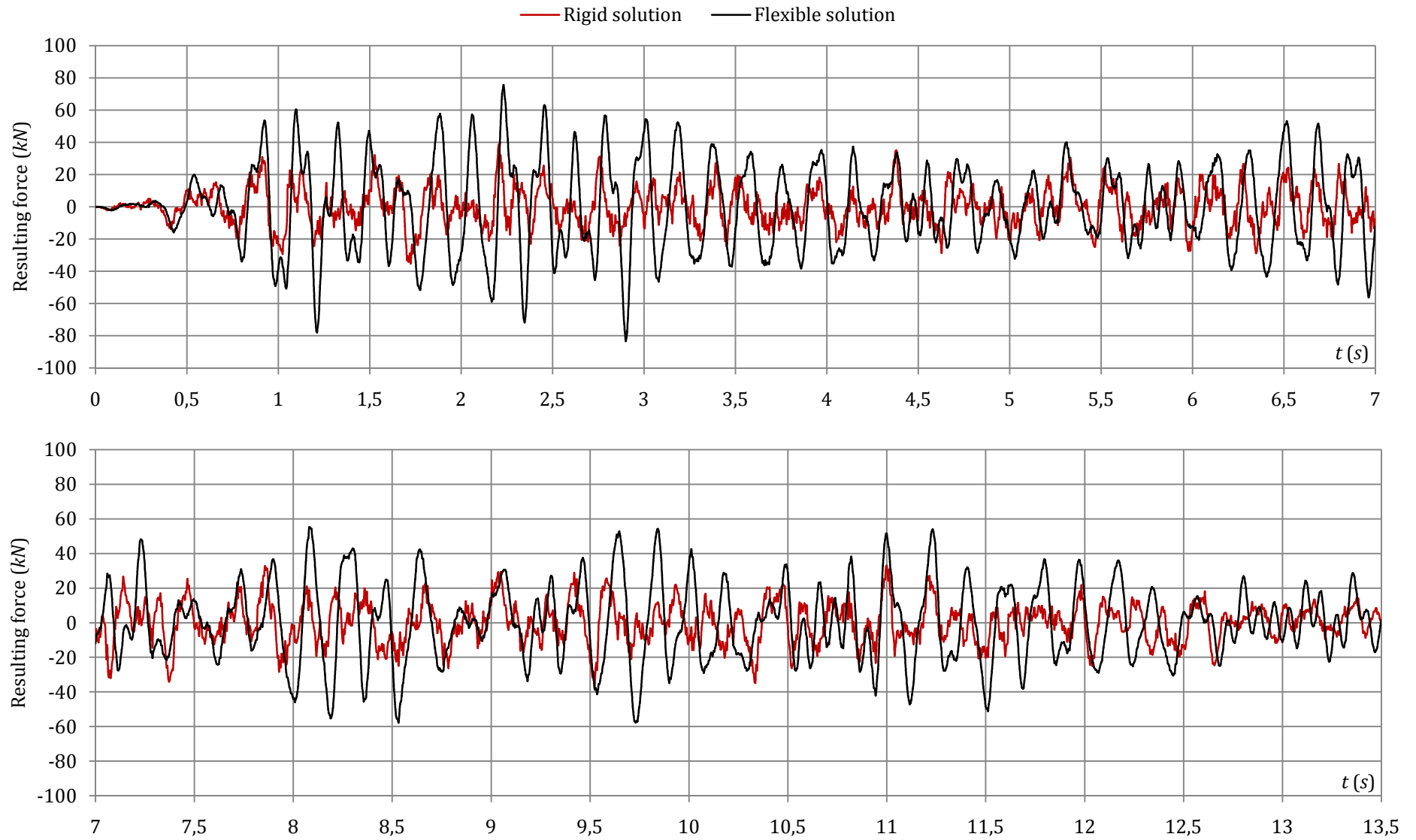


Figure D.8. Comparison of the theoretical rigid and flexible solutions ($h_s = 3.5 \text{ m}$)

To do so, it is worth examining the evolution of the total hydrodynamic pressure when the length L increases. Integrating the rigid and flexible contributions given by (7.7) and (7.8) over the wet area of the plate leads to:

$$F_r(t) = \frac{\rho_f h_s^2}{2} \left(\frac{L}{h_s} - \sum_{n=1}^{+\infty} \frac{8(L/h_s)^2}{(2n-1)^3 \pi^3} \tanh\left(\frac{(2n-1)\pi}{L/h_s}\right) \right) \ddot{X}(t) = \frac{\rho_f h_s^2}{2} \ddot{X}(t) g(L/h_s) \quad (\text{D.37})$$

$$F_f(t) = \frac{8\rho_f h_s}{2\pi^2} \left(\sum_{n=1}^{+\infty} \frac{\cosh(\alpha_n L)}{1 - \sinh(\alpha_n L)} \frac{(-1)^{n+1}}{(2n-1)^2} \int_0^{h_s} \int_0^l \ddot{u}(y, z, t) \cos(\alpha_n y) dy dz \right) \quad (\text{D.38})$$

where $\alpha_n = (2n-1)\pi/2h_s$. From a careful analysis of the total flexible pressure $F_f(t)$ given in (D.38), one may recognize the coefficient c_{mn}^* for which it was already shown in section D.1.2.3 that it tends to unity if $L \geq 3h_s$. Consequently, under the assumption of having a reservoir sufficiently long, (D.38) can be rewritten in the following form:

$$F_f(t) = \frac{8\rho_f h_s}{2\pi^2} \left(\sum_{n=1}^{+\infty} \frac{(-1)^{n+1}}{(2n-1)^2} \int_0^{h_s} \int_0^l \ddot{u}(y, z, t) \cos(\alpha_n y) dy dz \right) \quad (\text{D.39})$$

which does not depend on L anymore. So it can be said that the flexible impulsive pressure developed during the seismic excitation is not a function of L , provided that $L \geq 3h_s$.

The next step is now to see if this is also valid for the rigid impulsive pressure. It is clear that equation (D.37) is dominated by the function $g(L/h_s)$, but for a given value of h_s , it is analytically impossible to evaluate the limit of $g(L/h_s)$ when L tends to infinity. Consequently, even if this is not mathematically satisfactory, the evolution of the function $g(L/h_s)$ when the ratio L/h_s is progressively increased has to be studied numerically. Doing so leads to the results depicted on Figure D.9, where a stabilization may be observed¹⁸. Moreover, for $L/h_s \geq 3$, it can be considered that the curve does not change a lot, with an upper limitation of 1.086. Consequently, for $L \geq 3h_s$, the function $g(L/h_s)$ may be substituted by 1.086 in (D.37) to get:

$$F_r(t) = 1.086 \frac{\rho_f h_s^2}{2} \ddot{X}(t) \quad (\text{D.40})$$

which shows that the total rigid impulsive force developed during the earthquake does not depend on L anymore, provided that $L \geq 3h_s$.

It transpires from equations (D.39) and (D.40) that the total hydrodynamic pressure applied on the flexible walls during the seism is not a function of the length of the reservoir if $L \geq 3h_s$. In such a case, this conclusion means that the parameter L does not appear anymore in the dynamic equilibrium equation (7.61). Consequently, for a given value of h_s , working with a reservoir of length L is equivalent to working with a fictitious one of length $3h_s$ (Figure 7.18). For example, considering the lock chamber in the new Panama canal project, the approximate length L and water level h_s are respectively equal to 430 m and 30 m. Therefore, the hydrodynamic pressure obtained by doing a seismic analysis on a fictitious reservoir with $h_s = 30$ m and $L = 90$ m would be very close to the one obtained by performing the simulation with the real dimensions $h_s = 30$ m and $L = 430$ m.

¹⁸ This stabilization is not always valid: for very large values of the ratio L/h_s , the function starts increasing again. Nevertheless, the curve remains quite flat till $L/h_s = 5000$, which is sufficient for practical applications.

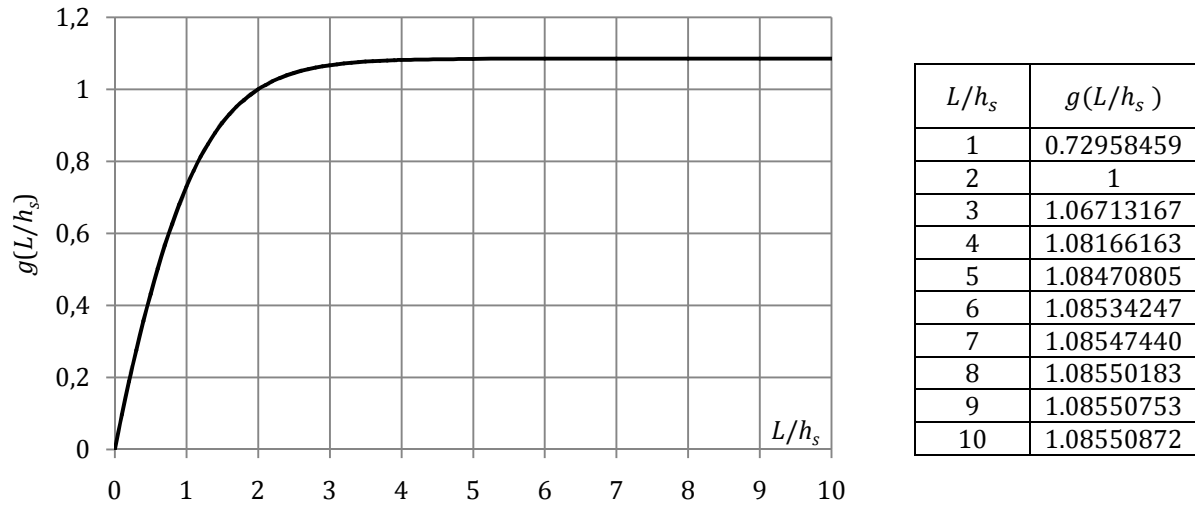


Figure D.9. Evolution of the function $g(L/h_s)$

On a practical point of view, all the previous mathematical developments allow for an important reduction of the computation effort required to perform finite element analyses because the fluid domain needs only to be modeled over a length $3h_s$ instead of L . Going back to the Panama canal situation, the size of a numerical model in such a case would be reduced more or less by a factor of $430/90 \approx 4.5$. So instead of using (for example) 10^6 finite element for the fluid part, working on a fictitious reservoir should not require more than $2.5 \cdot 10^5$ finite elements.

In the optic of consolidating the methodology explained here above, a short application example can be considered for a reservoir with a height h of 10 m, a width $l = 8$ m, a thickness $t_p = 20$ cm, a length $L = 80$ m and filled up to a level h_s of 6 m. The total number of elements involved in this real configuration ($L = 80$ m) is more or less equal to 424 000, as shown in Table D.4.

| | Number of shell elements | Number of solid elements | Number of nodes |
|--------------------------------|--------------------------|--------------------------|-----------------|
| Real model ($L = 80$ m) | 4000 | 419862 | 451122 |
| Fictitious model ($L = 18$ m) | 4000 | 94772 | 105972 |

Table D.4. Size of the real and fictitious models

In order to reduce the numerical effort, a fictitious model is also constructed, with a reservoir having this time a length of $3h_s = 18$ m. Doing so requires less than 100 000 elements, which represents a non negligible size reduction. Both the real and fictitious configurations are then submitted to a longitudinal acceleration $\ddot{X}(t)$ through a dynamic analysis performed with the software LS-DYNA. Doing so leads to a numerical evaluation of the hydrodynamic pressures acting on the flexible walls during the seism.

To check if it is correct to work with $L = 18$ m instead of the real length $L = 80$ m, the total hydrodynamic pressure $F(t)$ defined by (7.90) and calculated by LS-DYNA is compared for both the real and fictitious models. For convenience, the results are only plotted on Figure D.10 for a period of 7 seconds, which is approximately half of the total duration of the signal depicted on Figure 7.13. It is clear that the agreement between the numerical results is rather perfect. The maximal resulting pressures over this period of time are found to be 326.18 kN for $L = 80$ m and 311.44 kN for $L = 18$ m, which corresponds to a relative difference of 4 %. On the other hand, the total time required to perform the dynamic analysis has been reduced by a factor of 5.4.

The good coherence found in this example between the real and fictitious models tends to corroborate the simplified methodology detailed in this section. This will be quite useful later, when working on lock gates.

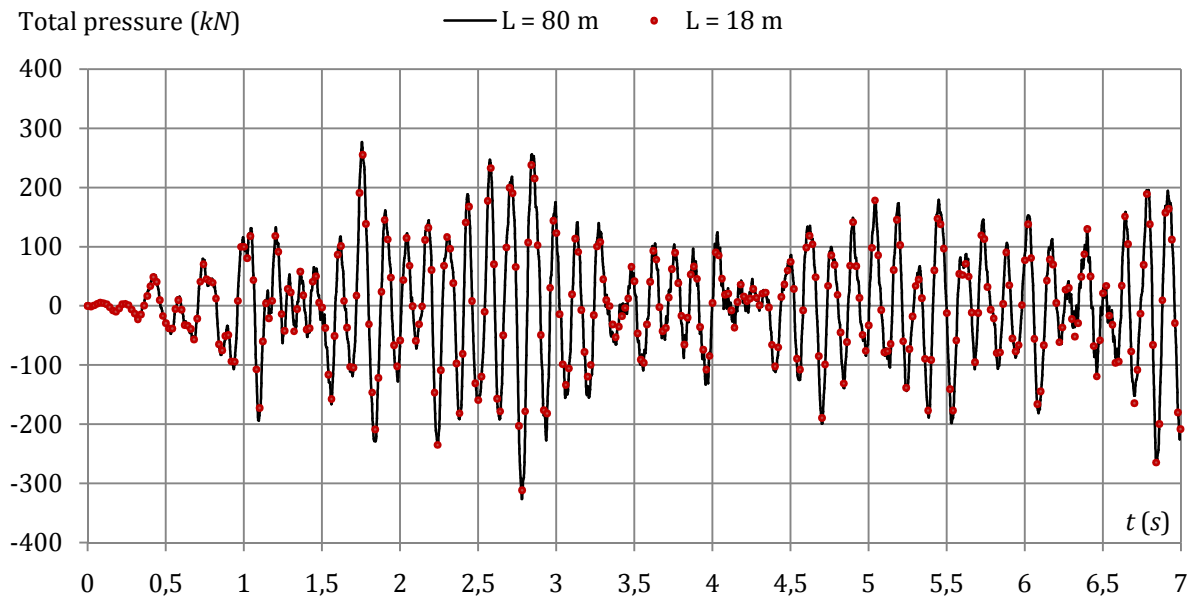


Figure D.10. Time evolution of the total hydrodynamic pressure for $L = 80\text{ m}$ and $L = 18\text{ m}$

APPENDIX E. Additional developments for the seismic analysis of lock gates

This addendum to Chapter 8 is divided in two main parts. In Appendix E.1, some complementary results to section 8.2 are presented. These ones are mainly additional formulae that are useful to derive the modal properties for both a gate supported or free at the bottom. Some other numerical comparisons are also performed for wide and high lock gates.

The information presented Appendix E.2 is directly related to section 8.3. It provides additional theoretical considerations about the dynamic analysis of lock gates.

Finally, in Appendix E.3, further developments are made to investigate some pending questions. The case of working with real boundary conditions for the sill is treated numerically, while additional indications are provided on the way to extend the analytical approach. In particular, the method to account for the presence of the upstream and downstream reaches is detailed. The case of the other components of the seismic action is also considered.

E.1. Appendix E.1

E.1.1. Additional formulae for the Rayleigh quotient

This appendix gives the mathematical forms of the terms \hat{T}_{jk} and \hat{U}_{jk} used in the Rayleigh quotient, but it is worth remembering that an additional coefficient of $1/2$ is introduced in (8.27). The expressions are provided for a structure supported at the bottom or not.

E.1.1.1. Case of a gate supported at the bottom

For such a situation of a gate supported by a sill at bottom, the pseudo-admissible functions $\psi_j(y, z)$ are calculated according to (8.3), with $g_j(z)$ and $f_j(y)$ given by (8.6) and (8.10) respectively. With these expressions, the terms \hat{T}_{jk} and \hat{U}_{jk} can be calculated by applying (8.28) and (8.29). In order to simplify the results, it is required to use the following more compact notations:

$$I_1 = l/2 \quad \text{if } \gamma_j = \gamma_k \qquad I_1 = 0 \quad \text{if } \gamma_j \neq \gamma_k \qquad (\text{E.1})$$

Furthermore, as the mathematical expressions are quite complex, let us introduced the next additional set of notations that are valid for any value of λ_j and λ_k :

$$I_3 = \frac{\lambda_k \cosh(\lambda_k h) \sin(\lambda_j h) - \lambda_j \cos(\lambda_j h) \sinh(\lambda_k h)}{\lambda_j^2 + \lambda_k^2} \qquad (\text{E.2})$$

$$I_4 = \frac{\lambda_j \cosh(\lambda_j h) \sin(\lambda_k h) - \lambda_k \cos(\lambda_k h) \sinh(\lambda_j h)}{\lambda_j^2 + \lambda_k^2} \qquad (\text{E.3})$$

$$I_{11} = \frac{\sin(\lambda_k h) + B_k \sinh(\lambda_k h)}{\lambda_k^2 h} - \frac{\cos(\lambda_k h) + B_k \cosh(\lambda_j h)}{\lambda_k} \qquad (\text{E.4})$$

$$I_{12} = \frac{\sin(\lambda_k h) - B_k \sinh(\lambda_k h)}{\lambda_k^2 h} - \frac{\cos(\lambda_k h) - B_k \cosh(\lambda_j h)}{\lambda_k} \qquad (\text{E.5})$$

$$I_{13} = \frac{\sin(\lambda_j h) + B_j \sinh(\lambda_j h)}{\lambda_j^2 h} - \frac{\cos(\lambda_j h) + B_j \cosh(\lambda_j h)}{\lambda_j} \qquad (\text{E.6})$$

$$I_{14} = \frac{\sin(\lambda_j h) - B_j \sinh(\lambda_j h)}{\lambda_j^2 h} - \frac{\cos(\lambda_j h) - B_j \cosh(\lambda_j h)}{\lambda_j} \qquad (\text{E.7})$$

In addition to equations (E.1) to (E.7), the following definitions are adopted. They are only holding if $\lambda_j = \lambda_k$:

$$I_2 = \frac{h}{2} - \frac{\sin(2\lambda_k h)}{4\lambda_k} \qquad I_5 = \frac{\sinh(2\lambda_k h)}{4\lambda_k} - \frac{h}{2} \qquad (\text{E.8})$$

$$I_7 = \frac{h}{2} + \frac{\sin(2\lambda_k h)}{4\lambda_k} \qquad I_{10} = \frac{\sinh(2\lambda_k h)}{4\lambda_k} + \frac{h}{2} \qquad (\text{E.9})$$

Finally, if the particular condition $\lambda_j \neq \lambda_k$ is fulfilled, it is quite convenient to introduce the expressions listed hereafter as they will be used in the next results:

$$I_2 = \frac{\lambda_k \sin(\lambda_j h) \cos(\lambda_k h) - \lambda_j \cos(\lambda_j h) \sin(\lambda_k h)}{\lambda_j^2 - \lambda_k^2} \quad (\text{E.10})$$

$$I_5 = \frac{\lambda_j \cosh(\lambda_j h) \sinh(\lambda_k h) - \lambda_k \sinh(\lambda_j h) \cosh(\lambda_k h)}{\lambda_j^2 - \lambda_k^2} \quad (\text{E.11})$$

$$I_7 = \frac{\lambda_j \sin(\lambda_j h) \cos(\lambda_k h) - \lambda_k \cos(\lambda_j h) \sin(\lambda_k h)}{\lambda_j^2 - \lambda_k^2} \quad (\text{E.12})$$

$$I_8 = \frac{\lambda_k \cos(\lambda_j h) \sinh(\lambda_k h) + \lambda_j \sin(\lambda_j h) \cosh(\lambda_k h)}{\lambda_j^2 + \lambda_k^2} \quad (\text{E.13})$$

$$I_9 = \frac{\lambda_j \sinh(\lambda_j h) \cos(\lambda_k h) + \lambda_k \cosh(\lambda_j h) \sin(\lambda_k h)}{\lambda_j^2 + \lambda_k^2} \quad (\text{E.14})$$

$$I_{10} = \frac{\lambda_j \sinh(\lambda_j h) \cosh(\lambda_k h) - \lambda_k \cosh(\lambda_j h) \sinh(\lambda_k h)}{\lambda_j^2 - \lambda_k^2} \quad (\text{E.15})$$

With all the notations given from (E.1) to (E.15), \hat{T}_{jk} and \hat{U}_{jk} can be calculated by summing up the individual contributions coming from both the plating and the entire reinforcing system:

$$\hat{T}_{jk} = \hat{T}_{jk}^{(p)} + \hat{T}_{jk}^{(h)} + \hat{T}_{jk}^{(v)} \quad \hat{U}_{jk} = \hat{U}_{jk}^{(p)} + \hat{U}_{jk}^{(h)} + \hat{U}_{jk}^{(v)} \quad (\text{E.16})$$

where the superscripts (p) , (h) and (v) respectively refer to the plating, to the horizontal stiffeners and to the vertical ones. These individual participations may be evaluated with help of the subsequent formulae, according to the values of λ_j and λ_k :

- If $\lambda_j \neq 0$ and $\lambda_k = 0$:

$$\hat{T}_{jk}^{(p)} = \rho t_p A_j I_1 I_{13} \quad (\text{E.17})$$

$$\hat{U}_{jk}^{(p)} = A_j D \left(\gamma_j^2 \gamma_k^2 I_{13} + 2(1-\nu) \gamma_j \gamma_k \frac{\sin(\lambda_j h) - B_j \sinh(\lambda_j h)}{h} + \nu \lambda_j^2 \gamma_k^2 I_{14} \right) I_1 \quad (\text{E.18})$$

$$\hat{T}_{jk}^{(h)} = \sum_{n=1}^{N_h} \rho A_{h,n} A_j (\sin(\lambda_j y_n) - B_j \sinh(\lambda_j y_n)) \frac{y_n}{h} I_1 \quad (\text{E.19})$$

$$\hat{U}_{jk}^{(h)} = \sum_{n=1}^{N_h} E I_{h,n} A_j \gamma_j^2 \gamma_k^2 (\sin(\lambda_j y_n) - B_j \sinh(\lambda_j y_n)) \frac{y_n}{h} I_1 \quad (\text{E.20})$$

$$\hat{T}_{jk}^{(v)} = \sum_{n=1}^{N_v} \rho A_{v,n} A_j \sin(\gamma_j z_n) \sin(\gamma_k z_n) I_{13} \quad (\text{E.21})$$

$$\hat{U}_{jk}^{(v)} = 0 \quad (\text{E.22})$$

- If $\lambda_j \neq 0$ and $\lambda_k \neq 0$:

$$\hat{T}_{jk}^{(p)} = \rho t_p A_j A_k (I_2 - B_k I_3 - B_j I_4 + B_j B_k I_5) I_1 \quad (\text{E.23})$$

$$\begin{aligned}
 \hat{U}_{jk}^{(p)} &= DA_j A_k (\lambda_j^2 \lambda_k^2 + \nu (\gamma_j^2 \lambda_k^2 + \gamma_k^2 \lambda_j^2) + \gamma_j^2 \gamma_k^2) I_1 I_2 \\
 &+ DA_j A_k B_j (\lambda_j^2 \lambda_k^2 + \nu (\gamma_k^2 \lambda_j^2 - \gamma_j^2 \lambda_k^2) - \gamma_j^2 \gamma_k^2) I_1 I_4 \\
 &+ DA_j A_k B_k (\lambda_j^2 \lambda_k^2 + \nu (\gamma_j^2 \lambda_k^2 - \gamma_k^2 \lambda_j^2) - \gamma_j^2 \gamma_k^2) I_1 I_3 \\
 &+ DA_j A_k B_j B_k (\lambda_j^2 \lambda_k^2 + \nu (\gamma_j^2 \lambda_k^2 + \gamma_k^2 \lambda_j^2) + \gamma_j^2 \gamma_k^2) I_1 I_5 \\
 &+ 2D(1 - \nu) A_j A_k \gamma_j \gamma_k \lambda_j \lambda_k (I_7 - B_k I_8 - B_j I_9 + B_j B_k I_{10}) I_1
 \end{aligned} \tag{E.24}$$

$$\hat{T}_{jk}^{(h)} = \sum_{n=1}^{N_h} \rho A_{h,n} A_j A_k (\sin(\lambda_j y_n) - B_j \sinh(\lambda_j y_n)) (\sin(\lambda_k y_n) - B_k \sinh(\lambda_k y_n)) I_1 \tag{E.25}$$

$$\begin{aligned}
 \hat{U}_{jk}^{(h)} &= \sum_{n=1}^{N_h} EI_{h,n} \gamma_j^2 \gamma_k^2 A_j A_k \sin(\lambda_j y_n) (\sin(\lambda_k y_n) - B_k \sinh(\lambda_k y_n)) I_1 \\
 &- \sum_{n=1}^{N_h} EI_{h,n} \gamma_j^2 \gamma_k^2 A_j A_k B_j \sinh(\lambda_j y_n) (\sin(\lambda_k y_n) - B_k \sinh(\lambda_k y_n)) I_1
 \end{aligned} \tag{E.26}$$

$$\hat{T}_{jk}^{(v)} = \sum_{n=1}^{N_v} \rho A_{v,n} A_j A_k \sin(\gamma_j z_n) \sin(\gamma_k z_n) (I_2 - B_k I_3 - B_j I_4 + B_j B_k I_5) \tag{E.27}$$

$$\hat{U}_{jk}^{(v)} = \sum_{n=1}^{N_v} EI_{v,n} A_j A_k \sin(\gamma_j z_n) \sin(\gamma_k z_n) (I_2 + B_k I_3 + B_j I_4 + B_j B_k I_5) \tag{E.28}$$

- If $\lambda_j = 0$ and $\lambda_k = 0$:

$$\hat{T}_{jk}^{(p)} = \rho t_p \frac{h}{3} I_1 \qquad \hat{U}_{jk}^{(p)} = D \frac{\gamma_j \gamma_k}{h} \left(\frac{\gamma_j \gamma_k}{3} h^2 + 2(1 - \nu) \right) I_1 \tag{E.29}$$

$$\hat{T}_{jk}^{(h)} = \sum_{n=1}^{N_h} \rho A_{h,n} \frac{y_n^2}{h^2} I_1 \qquad \hat{U}_{jk}^{(h)} = \sum_{n=1}^{N_h} EI_{h,n} \frac{y_n^2}{h^2} \gamma_j^2 \gamma_k^2 I_1 \tag{E.30}$$

$$\hat{T}_{jk}^{(v)} = \sum_{n=1}^{N_v} \rho A_{v,n} \frac{h}{3} \sin(\gamma_j z_n) \sin(\gamma_k z_n) \qquad \hat{U}_{jk}^{(v)} = 0 \tag{E.31}$$

- If $\lambda_j = 0$ and $\lambda_k \neq 0$:

$$\hat{T}_{jk}^{(p)} = \rho t_p A_k I_1 I_{11} \tag{E.32}$$

$$\hat{U}_{jk}^{(p)} = A_k D \left(\gamma_j^2 \gamma_k^2 I_{11} + 2(1 - \nu) \gamma_j \gamma_k \frac{\sin(\lambda_k h) - B_k \sinh(\lambda_k h)}{h} + \nu \lambda_j^2 \gamma_k^2 I_{12} \right) I_1 \tag{E.33}$$

$$\hat{T}_{jk}^{(h)} = \sum_{n=1}^{N_h} \rho A_{h,n} A_k (\sin(\lambda_k y_n) - B_k \sinh(\lambda_k y_n)) \frac{y_n}{h} I_1 \tag{E.34}$$

$$\hat{U}_{jk}^{(h)} = \sum_{n=1}^{N_h} EI_{h,n} A_k \gamma_j^2 \gamma_k^2 (\sin(\lambda_k y_n) - B_k \sinh(\lambda_k y_n)) \frac{y_n}{h} I_1 \tag{E.35}$$

$$\hat{T}_{jk}^{(v)} = \sum_{n=1}^{N_v} \rho A_{v,n} A_k \sin(\gamma_j z_n) \sin(\gamma_k z_n) I_{11} \quad (\text{E.36})$$

$$\hat{U}_{jk}^{(v)} = 0 \quad (\text{E.37})$$

All the previous results may be inserted in (E.16) to build the matrices $[\hat{T}]$ and $[\hat{U}]$, which are in turn useful to evaluate the modal properties by (8.32).

E.1.1.2. Case of a gate free at the bottom

For the situation of a gate that is not supported by a sill at the bottom, the pseudo-admissible functions $\psi_j(y, z)$ are still calculated according to (8.3), with $g_j(z)$ and $f_j(y)$ given by (8.6) and (8.13) respectively. Here again, \hat{T}_{jk} and \hat{U}_{jk} are to be found by applying (8.28) and (8.29). The results also have to be discussed according to the values of λ_j and λ_k , but this time two different rigid beam modes can be found for $\lambda_j = 0$, as shown by (II.3). For clarity, the first one will be related to $\lambda_j = 0$, while the second one will be associated to the dummy value $\lambda_j = -1$, i.e.:

$$f_j(y) = y/h \quad \text{if } \gamma_j = -1 \qquad f_j(y) = 1 \quad \text{if } \gamma_j = 0 \quad (\text{E.38})$$

Using the fictitious value $\lambda_j = -1$ has no consequence, as it is not a solution of (8.14). In addition to (E.1), it is also interesting to adopt the next convention:

$$S_j = 1 \quad \text{if } \sin(\lambda_j h) > 0 \qquad S_j = -1 \quad \text{if } \sin(\lambda_j h) < 0 \quad (\text{E.39})$$

Furthermore, in order to simplify the mathematical expressions of \hat{T}_{jk} and \hat{U}_{jk} , let us have the following definition of I_6 , which is only consistent if $\lambda_j = \lambda_k$:

$$I_6 = B_j \left(\lambda_j \gamma_j^2 (3 - 2\nu) + h \frac{C_j S_j - C_j^* \cos(\lambda_j h)}{\sin(\lambda_j h)} \right) \quad \text{with} \quad \begin{cases} C_j = (\gamma_j^2 + \gamma_j^2)^2 - 4\nu\gamma_j^2\gamma_j^2 \\ C_j^* = (\gamma_j^2 - \gamma_j^2)^2 + 4\nu\gamma_j^2\gamma_j^2 \end{cases} \quad (\text{E.40})$$

If $\lambda_j \neq \lambda_k$, the previous definition of I_6 is no longer valid and the subsequent one has to be adopted:

$$I_6 = \frac{\gamma_j^2 (S_{jk} - S_{kj})}{\lambda_j^2 - \lambda_k^2} \quad ; \quad S_{jk} = \lambda_j (\nu \lambda_j^4 - (2 - 3\nu) \lambda_k^4) \frac{S_j + S_k - (1 + S_j S_k) \cos(\lambda_k h)}{\sin(\lambda_k h)} \quad (\text{E.41})$$

As a final requirement, a kind of Kronecker delta will be designated by μ_{jk} , for which $\mu_{jk} = 0$ if $\lambda_j \neq \lambda_k$ and $\mu_{jk} = 1$ if $\lambda_j = \lambda_k$. With all the notations given from (E.38) to (E.41), \hat{T}_{jk} and \hat{U}_{jk} can be calculated by summing up the different contributions coming from the plating and the stiffening system, as it was done in (E.16). For the case of a gate supported at the bottom of the lock chamber, all these individual participations may be evaluated separately by applying the formulae listed hereafter, according to the particular values of λ_j and λ_k :

- If $\lambda_j = 0$ and $\lambda_k = 0$:

$$\hat{T}_{jk}^{(p)} = \rho t_p h I_1 \qquad \hat{U}_{jk}^{(p)} = Dh \gamma_j^2 \gamma_k^2 I_1 \quad (\text{E.42})$$

$$\hat{T}_{jk}^{(h)} = \sum_{n=1}^{N_h} \rho A_{h,n} I_1 \quad \hat{U}_{jk}^{(h)} = \sum_{n=1}^{N_h} E I_{h,n} \gamma_j^2 \gamma_k^2 I_1 \quad (\text{E.43})$$

$$\hat{T}_{jk}^{(v)} = \sum_{n=1}^{N_v} \rho A_{v,n} h \sin(\gamma_j z_n) \sin(\gamma_k z_n) \quad \hat{U}_{jk}^{(v)} = 0 \quad (\text{E.44})$$

- If $\lambda_j = 0$ and $\lambda_k = -1$:

$$\hat{T}_{jk}^{(p)} = \rho t_p \frac{h}{2} I_1 \quad \hat{U}_{jk}^{(p)} = \frac{Dh}{2} \gamma_j^2 \gamma_k^2 I_1 \quad (\text{E.45})$$

$$\hat{T}_{jk}^{(h)} = \sum_{n=1}^{N_h} \rho A_{h,n} \frac{y_n}{h} I_1 \quad \hat{U}_{jk}^{(h)} = \sum_{n=1}^{N_h} E I_{h,n} \frac{y_n}{h} \gamma_j^2 \gamma_k^2 I_1 \quad (\text{E.46})$$

$$\hat{T}_{jk}^{(v)} = \sum_{n=1}^{N_v} \rho A_{v,n} \frac{h}{2} \sin(\gamma_j z_n) \sin(\gamma_k z_n) \quad \hat{U}_{jk}^{(v)} = 0 \quad (\text{E.47})$$

- If $\lambda_j = -1$ and $\lambda_k = -1$:

$$\hat{T}_{jk}^{(p)} = \rho t_p \frac{h}{3} I_1 \quad \hat{U}_{jk}^{(p)} = Dh \left(\frac{\gamma_j^2 \gamma_k^2}{3} + \frac{2(1-\nu)}{h^2} \gamma_j \gamma_k \right) I_1 \quad (\text{E.48})$$

$$\hat{T}_{jk}^{(h)} = \sum_{n=1}^{N_h} \rho A_{h,n} \frac{y_n^2}{h^2} I_1 \quad \hat{U}_{jk}^{(h)} = \sum_{n=1}^{N_h} E I_{h,n} \frac{y_n^2}{h^2} \gamma_j^2 \gamma_k^2 I_1 \quad (\text{E.49})$$

$$\hat{T}_{jk}^{(v)} = \sum_{n=1}^{N_v} \rho A_{v,n} \frac{h}{3} \sin(\gamma_j z_n) \sin(\gamma_k z_n) \quad \hat{U}_{jk}^{(v)} = 0 \quad (\text{E.50})$$

- If $\lambda_j = -1$ and $\lambda_k > 0$:

$$\hat{T}_{jk}^{(p)} = 0 \quad \hat{U}_{jk}^{(p)} = 2\nu D A_k \gamma_j^2 \lambda_k (1 - S_k) I_1 \quad (\text{E.51})$$

$$\hat{T}_{jk}^{(h)} = \sum_{n=1}^{N_h} \rho A_{h,n} A_k (\sin(\lambda_k y_n) - B_k \sinh(\lambda_k y_n)) \frac{y_n}{h} I_1 \quad (\text{E.52})$$

$$\hat{U}_{jk}^{(h)} = \sum_{n=1}^{N_h} E I_{h,n} A_k \gamma_j^2 \gamma_k^2 (\sin(\lambda_k y_n) - B_k \sinh(\lambda_k y_n)) \frac{y_n}{h} I_1 \quad (\text{E.53})$$

$$\hat{T}_{jk}^{(v)} = 0 \quad \hat{U}_{jk}^{(v)} = 0 \quad (\text{E.54})$$

- If $\lambda_j = 0$ and $\lambda_k > 0$:

$$\hat{T}_{jk}^{(p)} = 0 \quad \hat{U}_{jk}^{(p)} = 2D A_k \gamma_j^2 \left((2-\nu) \frac{(1+S_k)(1-\cos(kh))}{H \sin(kh)} - \nu \lambda_k S_k \right) I_1 \quad (\text{E.55})$$

$$\hat{T}_{jk}^{(h)} = \sum_{n=1}^{N_h} \rho A_{h,n} A_k (\sin(\lambda_k y_n) - B_k \sinh(\lambda_k y_n)) I_1 \quad (\text{E.56})$$

$$\hat{U}_{jk}^{(h)} = \sum_{n=1}^{N_h} EI_{h,n} A_k \gamma_j^2 \gamma_k^2 (\sin(\lambda_k y_n) - B_k \sinh(\lambda_k y_n)) I_1 \quad (\text{E.57})$$

$$\hat{T}_{jk}^{(v)} = 0 \quad \hat{U}_{jk}^{(v)} = 0 \quad (\text{E.58})$$

- If $\lambda_j > 0$ and $\lambda_k > 0$:

$$\hat{T}_{jk}^{(p)} = \rho t_p I_1 A_j A_k B_j^2 h \mu_{jk} \quad \hat{U}_{jk}^{(p)} = 4 D A_j A_k I_{15} I_1 \quad (\text{E.59})$$

$$\hat{T}_{jk}^{(h)} = \sum_{n=1}^{N_h} \rho A_{h,n} A_j A_k (\sin(\lambda_j y_n) - B_j \sinh(\lambda_j y_n)) (\sin(\lambda_k y_n) - B_k \sinh(\lambda_k y_n)) I_1 \quad (\text{E.60})$$

$$\begin{aligned} \hat{U}_{jk}^{(h)} &= \sum_{n=1}^{N_h} EI_{h,n} \gamma_j^2 \gamma_k^2 A_j A_k \sin(\lambda_j y_n) (\sin(\lambda_k y_n) - B_k \sinh(\lambda_k y_n)) I_1 \\ &\quad - \sum_{n=1}^{N_h} EI_{h,n} \gamma_j^2 \gamma_k^2 A_j A_k B_j \sinh(\lambda_j y_n) (\sin(\lambda_k y_n) - B_k \sinh(\lambda_k y_n)) I_1 \end{aligned} \quad (\text{E.61})$$

$$\hat{T}_{jk}^{(v)} = \sum_{n=1}^{N_v} \rho A_{v,n} A_j A_k \sin(\gamma_j z_n) \sin(\gamma_k z_n) \lambda_j^4 B_j^2 h \mu_{jk} \quad (\text{E.62})$$

$$\hat{U}_{jk}^{(v)} = \sum_{n=1}^{N_v} EI_{v,n} A_j A_k \sin(\gamma_j z_n) \sin(\gamma_k z_n) \lambda_j^4 B_j^2 h \mu_{jk} \quad (\text{E.63})$$

The previous formulae may be inserted in (E.16) to build the matrices $[\hat{T}]$ and $[\hat{U}]$, which allows for the derivation of the modal properties through (8.32). It is worth noting that the solutions for:

$$\lambda_j = -1 ; \lambda_k = 0 \quad \lambda_j > 0 ; \lambda_k = -1 \quad \lambda_j = 0 ; \lambda_k > 0 \quad (\text{E.64})$$

have not been discussed here above, but they may be easily derived by inverting j and k in the appropriate corresponding results.

E.1.2. Additional comparisons for gate 2

In order to cover a certain category of lock gates, validations were also performed by comparing the numerical and analytical results for other configurations. This appendix deals with the second gate presented in section 8.2.3. As depicted on Figure E.1, this one has an extreme rectangular shape, with an important width l of 22.5 m and a reasonable height h equal to 8 m. So the lowest admissible value of h/l is almost reached.

The material properties are still those listed in Table 8.2, while the cross-sections characterizing the stiffening elements have the dimensions listed in Table E.2. The modal analysis performed with NASTRAN shows that the structure has two dominant global modes. This is particularly true for a gate that is free at the bottom.

If a sill is present, the importance of the first mode is found to be predominant, while the contribution from all the subsequent ones is negligible.

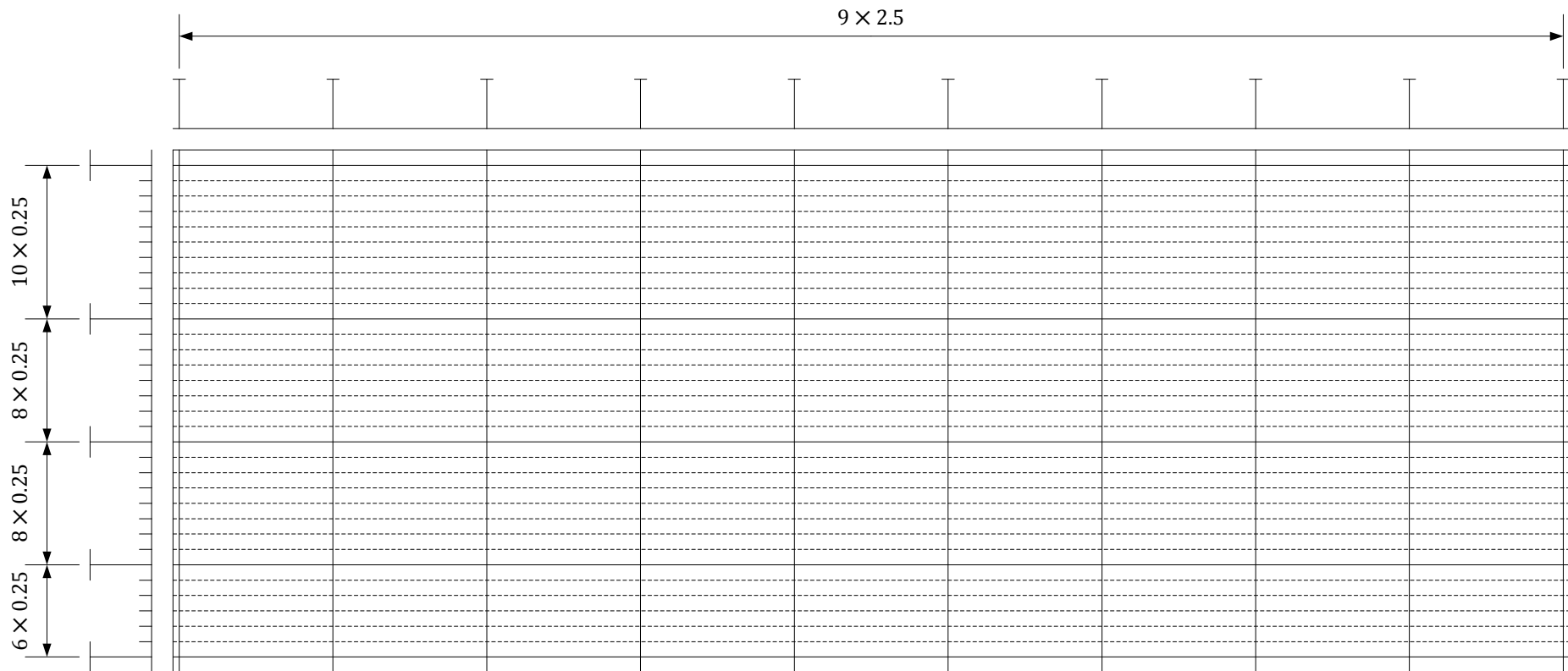


Figure E.1. Structural configuration and main dimensions (m) of gate 2

| Gate supported at the bottom | | | | | | Gate free at the bottom | | | | | |
|------------------------------|----------------|---------|------------|-----------|---------|-------------------------|----------------|---------|------------|-----------|---------|
| Mode | Frequency (Hz) | | | Error (%) | | Mode | Frequency (Hz) | | | Error (%) | |
| | NASTRAN | LS-DYNA | Analytical | NASTRAN | LS-DYNA | | NASTRAN | LS-DYNA | Analytical | NASTRAN | LS-DYNA |
| 1 | 7.34 | 7.57 | 7.49 | 2.07 | 1.05 | 1 | 7.19 | 7.33 | 7.37 | 2.51 | 0.55 |
| 2 | 39.15 | 38.47 | 44.55 | 14.25 | 15.81 | 2 | 8.48 | 8.43 | 8.63 | 1.77 | 2.37 |

Table E.1. Comparison of the natural frequencies obtained numerically and analytically for gate 2

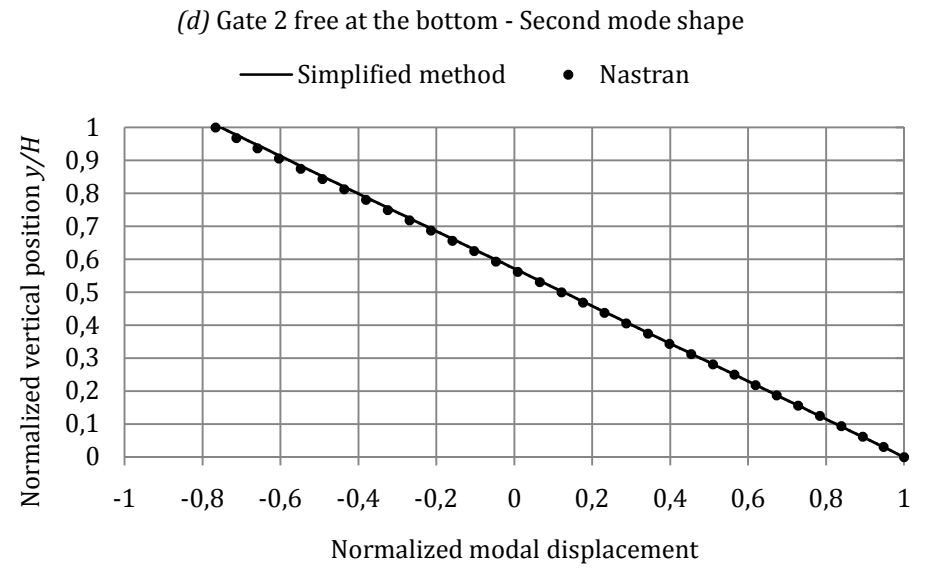
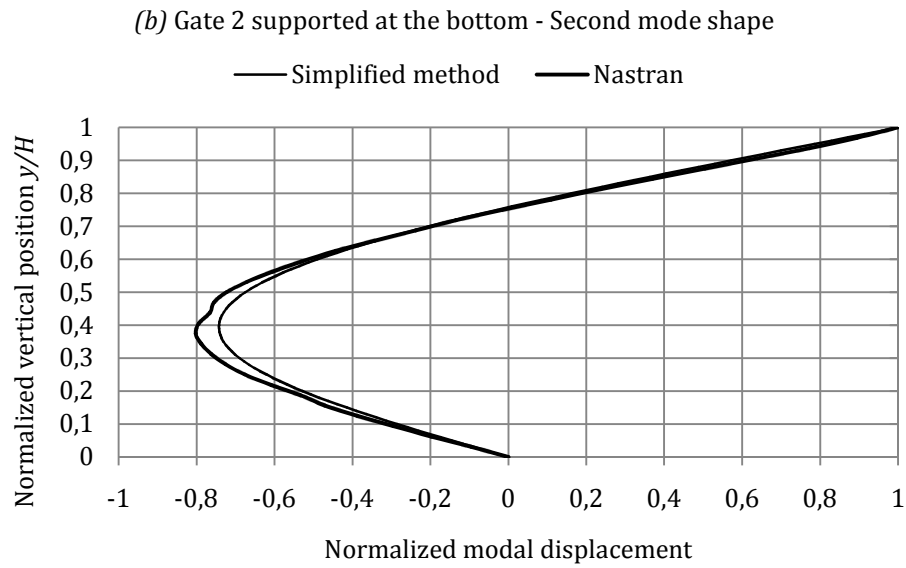
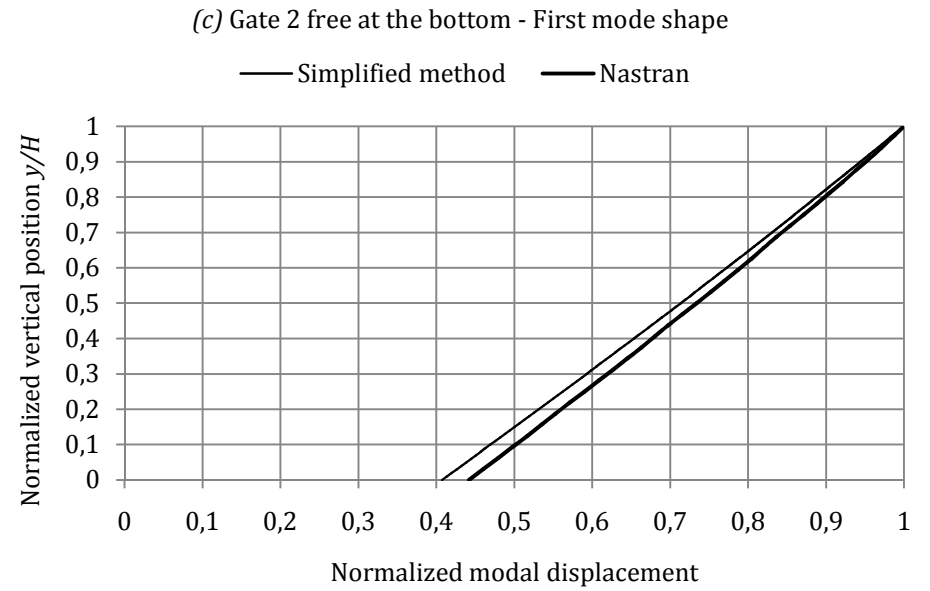
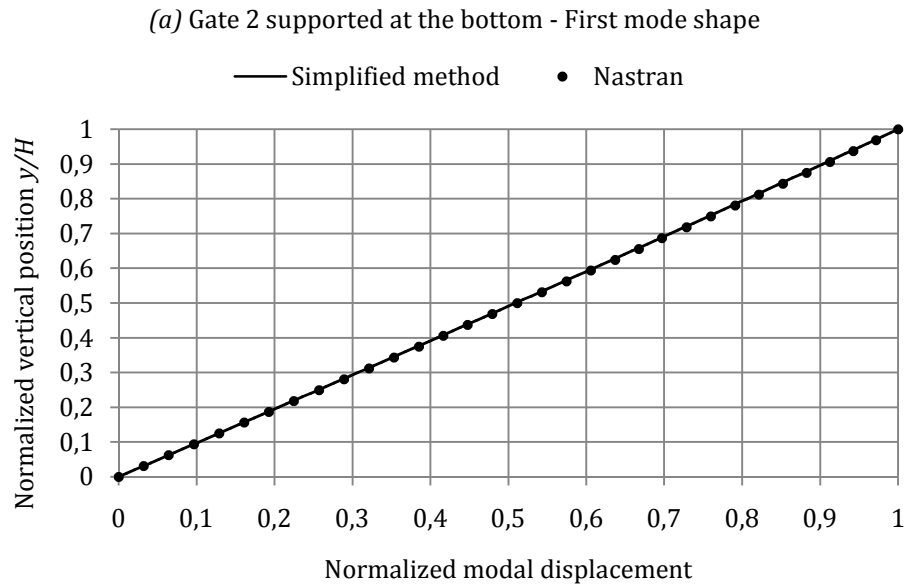


Figure E.2. Comparison of the vertical profiles in the plane $z = l/2$ obtained numerically and analytically for the two first modes of gate 2

The frequencies are listed in Table E.1, where a quite good agreement can be observed between the analytical and numerical results. This is particularly true if the structure is not supported at the bottom. On the contrary, the correlation on the second mode is not so good if it is resting against a sill, with a relative error of about 15 %. This discrepancy is however of minor importance, as the contributions coming from the higher modes is not really decisive in this case.

| | h_w (m) | t_w (m) | h_f (m) | t_f (m) |
|-----------------------|-----------|-----------|-----------|-----------|
| Horizontal girders | 0.98 | 0.02 | 0.4 | 0.025 |
| Vertical frames | 0.98 | 0.02 | 0.5 | 0.025 |
| Horizontal stiffeners | 0.21 | 0.006 | 0 | 0 |

Table E.2. Geometrical parameters for gate 2

The vertical profiles of the two first mode shapes in the plane $z = l/2$ (called π_1 on Figure 7.8) are plotted on Figure E.2 for the two support situations. Here again, the agreement is sufficient for a first approximation.

From all the observations made above, it transpires that the simplified analytical procedure may also be applied to the limit case of a gate with a ratio h/l close to its lowest practical value of 0.5. As smaller values of h/l are not really expected for gates with a single plating, such configurations have been disregarded.

E.1.3. Additional comparisons for gate 3

The third gate analyzed as an example is totally the opposite of the previous one. It has a very important height h of 21 m, with a much more modest width l of 10.5 m. For such values, the ratio h/l is equal to 2, which may be seen as the maximal practical value for structures with a single plating. The main dimensions and the positioning of the reinforcing system are represented on Figure E.3. From this picture, it is clear that the horizontal and vertical stiffening elements are disposed in a quite regular manner, but this is only motivated to simplify the construction of the finite element models. Indeed, the simplified analytical procedure perfectly allows for a non-uniform disposition of these elements.

The same comment is also valid for the cross sections, which may also be varied over the height h . However, for convenience, only three sets of sectional properties have been chosen, each of them characterizing the girders, the frames and the stiffeners respectively (see Table E.3).

For the material properties of Table 8.2, the modal analysis performed with NASTRAN gives the vibration frequencies listed in Table E.4. Comparing them to the analytical predictions leads to the conclusion that the discrepancy does not exceed 10 % on the two first dominant modes, which seems to be more or less acceptable. The approximate solutions provided by LS-DYNA are also shown in Table E.4 and are found to be in close agreement with the analytical ones.

The vertical profiles in the plane $z = l/2$ (called π_1 on Figure 7.8) are plotted on Figure E.4 for the two first modes. As it was already observed for gate 1, there is a global accordance between the numerical and analytical shapes, but with some indentations at very localized points. This particularity is totally similar to the one discussed in section 8.2.3.3, where it was pointed out that the beams were not strictly bent around the neutral fiber of the plating (see Figure 8.13).

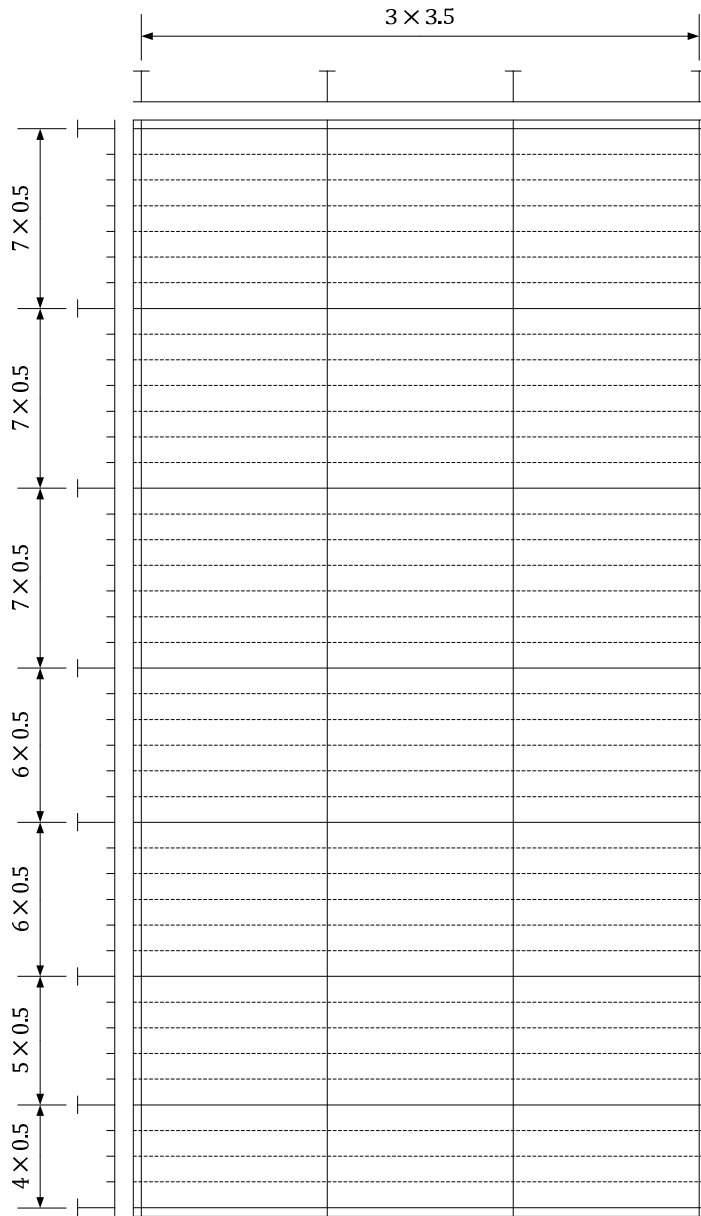


Figure E.3. Structural configuration and main dimensions (m) of gate 3

| Horizontal girders | | | |
|-----------------------|-----------|-----------|-----------|
| h_w (m) | t_w (m) | h_f (m) | t_f (m) |
| 0.7 | 0.018 | 0.35 | 0.018 |
| Vertical frames | | | |
| h_w (m) | t_w (m) | h_f (m) | t_f (m) |
| 0.6 | 0.016 | 0.3 | 0.016 |
| Horizontal stiffeners | | | |
| h_w (m) | t_w (m) | h_f (m) | t_f (m) |
| 0.14 | 0.08 | 0 | 0 |

Table E.3. Geometrical parameters for gate 3

| Gate 3 supported at the bottom | | | |
|--------------------------------|---------|------------|---------|
| | NASTRAN | Analytical | Error |
| 1 | 19 Hz | 20.79 Hz | 9.43 % |
| 2 | 21.5 Hz | 23.65 Hz | 10.01 % |
| | LS-DYNA | Analytical | Error |
| 1 | 19.7 Hz | 20.79 Hz | 5.76 % |
| 2 | 22.7 Hz | 23.65 Hz | 4.15 % |
| Gate 3 free at the bottom | | | |
| | NASTRAN | Analytical | Error |
| 1 | 19 Hz | 20.79 Hz | 9.48 % |
| 2 | 21.3 Hz | 23.41 Hz | 23.41 % |
| | LS-DYNA | Analytical | Error |
| 1 | 19.7 Hz | 20.79 Hz | 5.75 % |
| 2 | 22.3 Hz | 23.41 Hz | 4.74 % |

Table E.4. Comparison of the natural frequencies for gate 3

In other words, it can be said that the general flexural profile adopted by the gate is dominated by the horizontal girders (see the red dotted line on Figure E.4a for example), while the portions of plating located between two girders indeed suffer an additional bending around their neutral fiber. Another conclusion that may be drawn from Figure E.4 is that the mode shapes are very similar for the two types of support conditions. This seems logical: as the height h is quite important, the presence or the absence of a sill at the bottom has little influence on the mode shapes at the top of the structure. This last observation is also corroborated by comparing the natural frequencies obtained for the two support situations. From Table E.4, it appears that they are quite close to each other (they are even nearly identical for the first mode), whatever the presence of a sill.

All the comparisons made above show that the analytical approach is also applicable to treat the limit case of a gate having a h/l ratio more or less equal to its maximal value of 2. As greater values of h/l are not really expected in practice, such configurations have not been investigated.

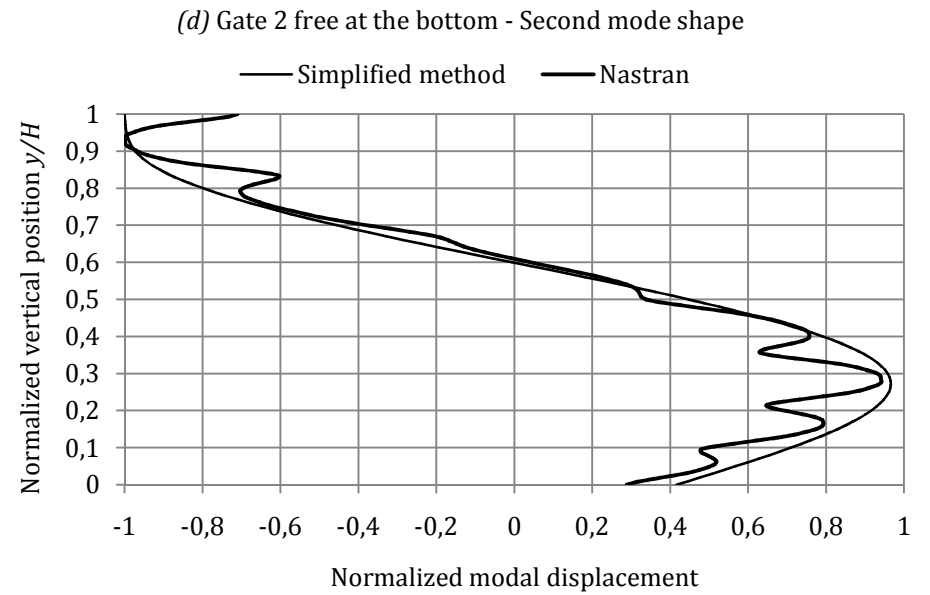
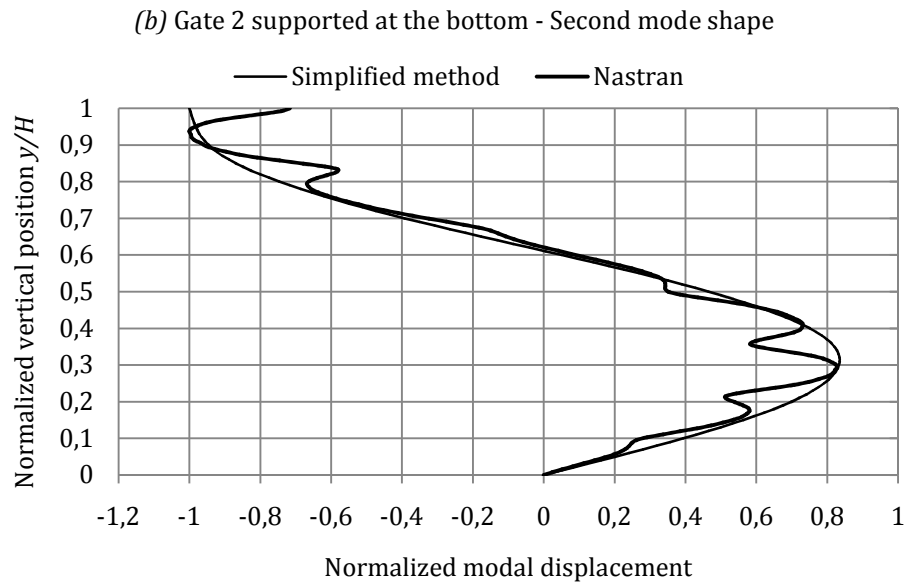
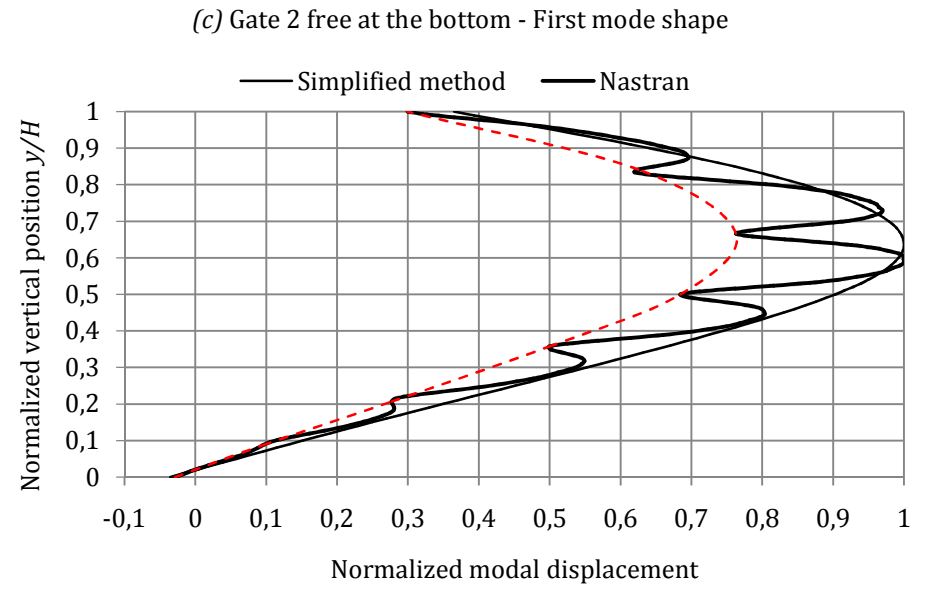
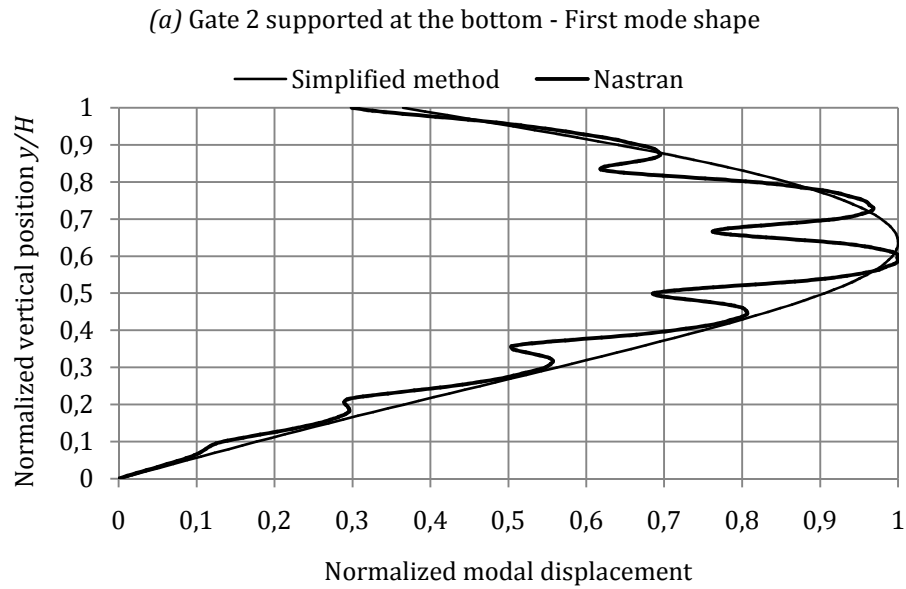


Figure E.4. Comparison of the vertical profiles in the plane $z = l/2$ obtained numerically and analytically for the two first modes of gate 3

E.2. Appendix E.2

E.2.1. Considerations about the wet modes

In this appendix, it is shown that deriving the wet modal properties of a lock gate is not really of primary importance. This can be justified by going back to Chapter 7, where applying the virtual work principle leads to (7.85). In this equation, the matrices $[T] - [W]$ and $[U]$ are diagonal, as the wet modes satisfy the orthogonality requirement (7.86).

Nevertheless, the presence of a mass-proportional damping term $\alpha[T]$ does not allow to decouple the set of equations expressed by (7.85) because this matrix is not diagonal. This was already explained in section 7.4.2.3. Therefore, working with the wet mode shapes is only profitable if the two following restrictions are satisfied:

- Mass-proportional damping forces are not involved in the equilibrium equation of the immersed structure. It should be noted however that considering the damping matrix $\alpha([T] - [W])$ instead of $\alpha[T]$ implies a diagonalization of the system (7.85) but this is not totally satisfactory.
- The boundary conditions have to be strictly satisfied by the wet modes, otherwise the orthogonality property (7.86) is not verified and consequently the matrices $[T] - [W]$ and $[U]$ are not diagonal.

From the two previous conditions, it transpires that working with the wet eigenmodes of a lock gate does not provide any substantial advantage, even for an undamped structure. Indeed, as it was explained in 8.2.1.3, it seems very difficult to find an analytical function that fully satisfies the boundary conditions associated to the stiffened plate, which is a serious objection for diagonalizing the equations given by the virtual work principle.

Nevertheless, one may argue that the displacements $u(y, z, t)$ affecting the structure should be better approximated if they were expressed as a function of the wet mode shapes $\Delta_i(y, z)$ instead of working with the dry ones $\delta_j(y, z)$. In fact, it can be shown that working with one of the two following modal decompositions:

$$u(y, z, t) = \sum_{i=1}^N q_i(t) \Delta_i(y, z) \quad u(y, z, t) = \sum_{j=1}^M \hat{q}_j(t) \delta_j(y, z) \quad (\text{E.65})$$

is strictly equivalent. Indeed, as stated by (7.35), $\Delta_i(y, z)$ may be related to $\delta_j(y, z)$ with help of the coefficients v_{ij} derived by the Rayleigh-Ritz method (this was already detailed in section 7.3.2.1 when dealing with the mathematical approach). Therefore, in the first part of equation (E.65), $\Delta_i(y, z)$ can be replaced by a linear combination of $\delta_j(y, z)$, as expressed by (7.35). Doing so leads to:

$$u(y, z, t) = \sum_{i=1}^N q_i(t) \Delta_i(y, z) = \sum_{j=1}^M \delta_j(y, z) \sum_{i=1}^N v_{ji} q_i(t) \quad (\text{E.66})$$

A further comparison of (E.66) with (E.65) shows that the coefficients $\hat{q}_j(t)$ affected to the dry modes may be expressed as a linear combination of $q_i(t)$:

$$\hat{q}_j(t) = \sum_{i=1}^N v_{ji} q_i(t) \quad \Leftrightarrow \quad \hat{\mathbf{q}}(t) = [\mathbf{v}]^T \mathbf{q}(t) \quad (\text{E.67})$$

where $[\mathbf{v}]$ is the matrix containing the Ritz factors v_{ij} . Now that (E.67) is established, one can go back to the virtual work principle expressed in (7.85). It is worth bearing in mind that the matrices $[\mathbf{T}]$, $[\mathbf{U}]$, $[\mathbf{W}]$ and \mathbf{V} calculated with the wet modes $\Delta_i(y, z)$ are directly related to the corresponding matrices $[\hat{\mathbf{T}}]$, $[\hat{\mathbf{U}}]$, $[\hat{\mathbf{W}}]$ and $\hat{\mathbf{V}}$ calculated with the dry ones $\delta_j(y, z)$. This was already stated in (7.88) and is recalled hereafter:

$$[\mathbf{T}] = [\mathbf{v}][\hat{\mathbf{T}}][\mathbf{v}]^T \quad [\mathbf{W}] = [\mathbf{v}][\hat{\mathbf{W}}][\mathbf{v}]^T \quad [\mathbf{U}] = [\mathbf{v}][\hat{\mathbf{U}}][\mathbf{v}]^T \quad \mathbf{V} = [\mathbf{v}]\hat{\mathbf{V}} \quad (\text{E.68})$$

As a final step, (E.68) can be introduced in (7.85) and the following simple developments can be performed:

$$\begin{aligned} & [\mathbf{v}][(\hat{\mathbf{T}}) - (\hat{\mathbf{W}})][\mathbf{v}]^T \frac{d^2 \mathbf{q}}{dt^2} + [\mathbf{v}](\alpha[\hat{\mathbf{T}}] + \beta[\hat{\mathbf{U}})][\mathbf{v}]^T \frac{d^2 \mathbf{q}}{dt^2} + [\mathbf{v}][\hat{\mathbf{U}}][\mathbf{v}]^T \frac{d^2 \mathbf{q}}{dt^2} = [\mathbf{v}]\hat{\mathbf{V}}\ddot{\mathbf{X}}(t) \\ \Leftrightarrow & ((\hat{\mathbf{T}}) - (\hat{\mathbf{W}})) \left([\mathbf{v}]^T \frac{d^2 \mathbf{q}}{dt^2} \right) + (\alpha[\hat{\mathbf{T}}] + \beta[\hat{\mathbf{U}}]) \left([\mathbf{v}]^T \frac{d\mathbf{q}}{dt} \right) + [\hat{\mathbf{U}}][\mathbf{v}]^T \mathbf{q} = \hat{\mathbf{V}}\ddot{\mathbf{X}}(t) \quad (\text{E.69}) \\ \Leftrightarrow & ((\hat{\mathbf{T}}) - (\hat{\mathbf{W}})) \frac{d^2 \hat{\mathbf{q}}}{dt^2} + (\alpha[\hat{\mathbf{T}}] + \beta[\hat{\mathbf{U}}]) \frac{d\hat{\mathbf{q}}}{dt} + [\hat{\mathbf{U}}]\hat{\mathbf{q}}(t) = \hat{\mathbf{V}}\ddot{\mathbf{X}}(t) \end{aligned}$$

where the last equivalence is justified by (E.67). It can be seen that (E.69) is precisely the virtual work principle equation expressed in the basis of the dry modes shapes. Consequently, solving (E.69) and rebuilding the displacements with the second relation in (E.65) is strictly equivalent to solving (7.85) and applying the first decomposition in (E.65). The short mathematical developments performed here above show that working with the wet modes is strictly equivalent to using the dry ones.

E.2.2. Considerations about the exactness of the solution

The goal of this short appendix is to explain why the exactness of the solution may be criticized when applying the virtual work principle to perform the dynamic analysis of a lock gate. In section 7.4.2, it is claimed that the displacements $u(y, z, t)$ obtained by applying the virtual work principle are simply an approximation of the exact theoretical solution because of the limited number N of wet modes considered in the decomposition process (7.67). Of course, as only N dry mode shapes are still used in (8.40), such a conclusion is also holding in the present case, but this is not the unique reason that may affect the exactness of the procedure.

Indeed, an additional approximation is also coming here from the fact that the functions $\psi_j(y, z)$ used in (8.2) are only pseudo-admissible. As discussed in 8.2.1.3, they do not satisfy the boundary conditions along the free edges. Because of (8.2) this is also the case for all of the N modes $\delta_i(y, z)$ in (8.40). Consequently, the solution found by applying (8.40) could not tend to the exact one simply by increasing N .

From the previous considerations, it appears that $u(y, z, t)$ fails to satisfy the virtual work principle for all kinematically admissible displacements $\delta u(y, z, t)$. In this case, it is quite common to work with a virtual field $\delta u(y, z, t)$ that is similar to $u(y, z, t)$, as given by (8.41). With this definition, $\delta u(y, z, t)$ can be used in the virtual work principle. Doing so, the

solution obtained for $u(y, z, t)$ only implies a global equilibrium, but the local one is not guaranteed. In other words, by considering (8.40) and (8.41), it is to fear that even if $u(y, z, t)$ meets the global equilibrium requirement expressed through the virtual work principle, it will not necessarily satisfy the local one given by equation (8.39).

The implications of the last conclusion can be detailed in a more explicit way. Going back to (8.39), this expression can be rewritten in the following condensed manner:

$$\mathcal{B}(u) = -p(u) \Leftrightarrow \mathcal{B}(u) + p(u) = 0 \quad (\text{E.70})$$

where $\mathcal{B}(\cdot)$ is the linear differential operator corresponding to the left-hand side of (8.39). The term $p(u)$ corresponds to the total seismic hydrodynamic pressure obtained by summing up (7.7) and (7.8) for $u(y, z, t)$ given by (8.40). Nevertheless, as $u(y, z, t)$ does not respect the virtual work principle for any kinematically admissible $\delta u(y, z, t)$, the local balance (E.70) is not verified. So instead of (E.70), one should write:

$$\mathcal{B}(u) + p(u) = p^*(u) \quad (\text{E.71})$$

where $p^*(u)$ may be seen as an additional pressure that has to be applied on the gate to reestablish the equilibrium (Figure E.5).

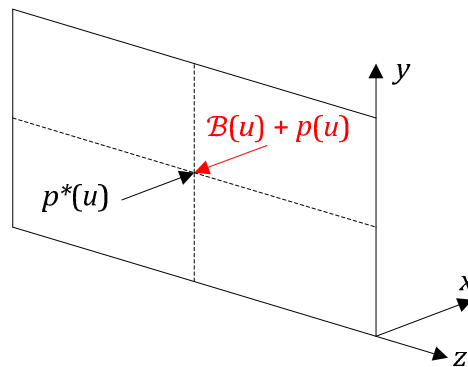


Figure E.5. Additional pressure for restoring the local equilibrium

As a conclusion, it is important to bear in mind that the solution derived analytically by applying the virtual work principle is only an approximation because the local balance and the static boundary conditions on the free edges are not respected. From (E.71), it is clear that this approximation is better if $p^* \ll p$. Such a requirement may be seen as a kind of criteria to assess the exactness of the solution.

In order to illustrate the importance of these unbalanced forces $p^*(y, z, t)$ with respect to $p(y, z, t)$, one can consider the examples presented in sections 8.3.3.1 and 8.3.3.2 for a gate resting against a sill or free at the bottom. To make sure that the analytical solutions are valid, it may be interesting to check if the resulting unbalanced force $F^*(t)$ satisfies the following condition:

$$F^*(t) = \int_0^h dy \int_0^l p^*(y, z, t) dz \ll F(t) \quad (\text{E.72})$$

where $F(t)$ is the total hydrodynamic pressure applied on the gate already introduced in expression (7.90). The curve showing the time evolutions of $F^*(t)$ and the one giving the total hydrodynamic pressure applied on the gate are depicted on Figure E.6 (if a sill is present) and on Figure E.7 (if no sill is present).

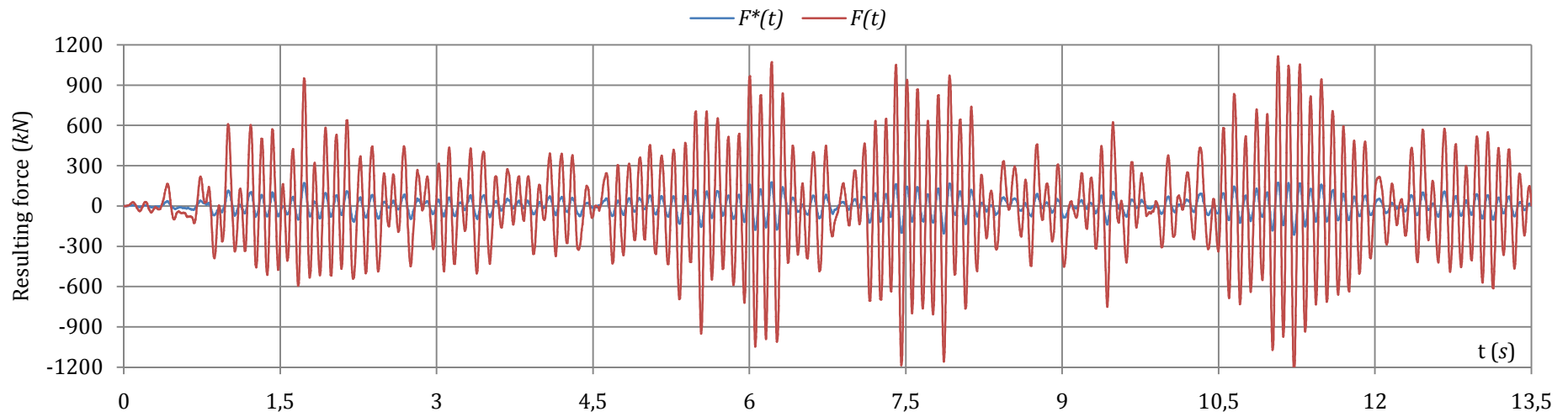


Figure E.6. Comparison between the unbalanced forces and the total pressure for gate 1 supported by a sill

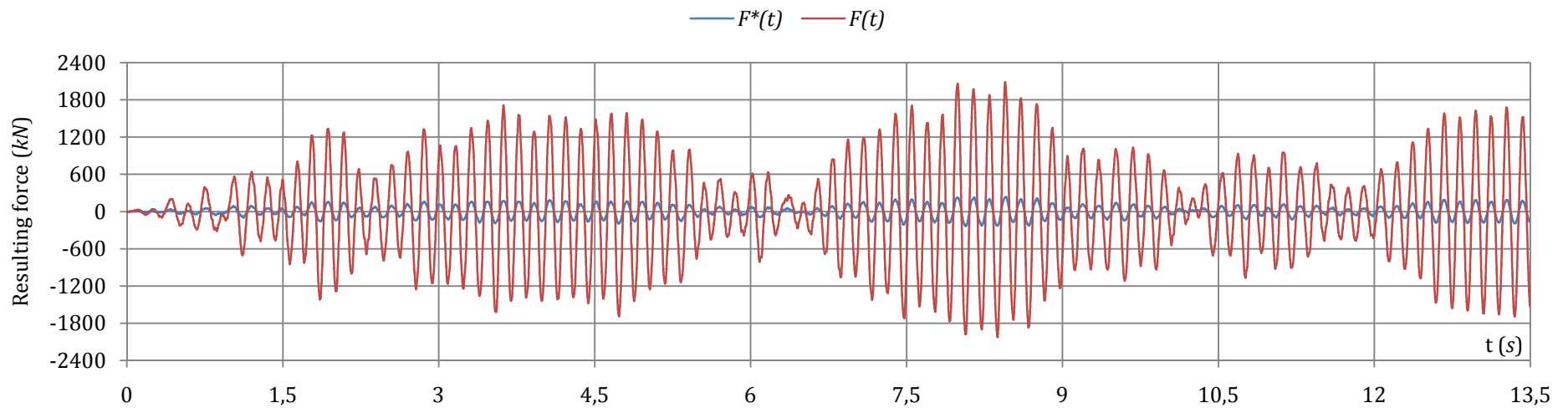


Figure E.7. Comparison between the unbalanced forces and the total pressure for gate 1 free at the bottom

From these curves, it appears that the requirement (E.72) is respected in a quite satisfactory way. Moreover, calculating the maximal value of the ratio $|F^*(t)/F(t)|$ shows that this latter is more or less equal to 0.11. Consequently, even if the functions $\psi_j(y, z)$ are only pseudo-admissible and simply satisfy the beams conditions, the analytical approach appears to be quite acceptable as the unbalanced pressures remain moderate. This seems to be logical: as a lock gate is mainly behaving like a set of beams, working with functions $\psi_j(y, z)$ derived from the beam theory should not be totally incoherent.

E.2.3. Additional formulae for the external work

This appendix briefly provides the analytical expressions allowing for the evaluation of the matrix $[\widehat{W}]$ given in (8.51). To evaluate \widehat{W}_{rs} , it appears from (8.51) that a closed-form expression for $\hat{I}_{mn}^{(r)}$ is required. For a gate supported at the bottom, one has:

$$\hat{I}_{mn}^{(r)} = 0 \quad ; \quad \gamma_r = \bar{\gamma}_m \quad \hat{I}_{mn}^{(r)} = \gamma_r \frac{1 - (-1)^m \cos(\gamma_r l)}{\bar{\gamma}_m^2 - \gamma_r^2} (E_n + \bar{E}_n) \quad ; \quad \gamma_r \neq \bar{\gamma}_m \quad (\text{E.73})$$

where $\bar{\gamma}_m = m\pi/l$ and γ_r is defined in (8.7). The function E_n is different for a rigid mode than for a flexible one. It has the following expressions:

- If $\lambda_r = 0$: $E_n = \frac{1 + \alpha_n (-1)^n h_s}{\alpha_n^2 h}$ (E.74)

$$\bar{E}_n = 0 \quad (\text{E.75})$$

- If $\lambda_r \neq 0$: $E_n = -A_r \frac{\lambda_r + \alpha_n (-1)^n \sin(\lambda_r h_s)}{\lambda_r^2 - \alpha_n^2}$ (E.76)

$$\bar{E}_n = -A_r B_r \frac{\lambda_r + \alpha_n (-1)^n \sin(\lambda_r h_s)}{\lambda_r^2 + \alpha_n^2} \quad (\text{E.77})$$

in which A_r is the modal amplitude. The two parameters λ_r and B_r are given by (8.11). Considering the situation where the gate is totally free at the bottom, it can be shown that:

- If $\lambda_r = -1$: $E_n = \frac{1 + \alpha_n (-1)^n h_s}{\alpha_n^2 h}$ (E.78) $\bar{E}_n = 0$

- If $\lambda_r = 0$: $E_n = \frac{(-1)^n}{\alpha_n}$ (E.79) $\bar{E}_n = 0$

- If $\lambda_r \neq 0$: $E_n = -A_r \frac{\lambda_r + \alpha_n (-1)^n (\sin(\lambda_r h_s) - B_r \cos(\lambda_r h_s))}{\lambda_r^2 - \alpha_n^2}$ (E.80)

$$\bar{E}_n = A_r \frac{\lambda_r + \alpha_n (-1)^n (\sinh(\lambda_r h_s) - B_r \cosh(\lambda_r h_s))}{\lambda_r^2 + \alpha_n^2} \quad (\text{E.81})$$

in which A_r is still the modal amplitude, but this time λ_r and B_r have to be found by the equations given in (8.14).

E.3. Appendix E.3

The comparisons performed in section 8.3.3 show that the simplified approach tends to provide a quite good approximation of the numerical results. Nevertheless, one has to bear in mind that the theoretical approach is based on hypotheses that are not always realistic. The aim of this appendix is to go a little bit further in the dynamic analysis of lock gates by discussing the following particular points:

- For a gate resting against a sill, the true support conditions are not those considered in 8.3.3.1, so it is interesting to investigate the consequences of working with the true ones.
- The flexible impulsive pressure is derived from equation (7.8), which is based on the hypothesis of a symmetric configuration. Nevertheless, this not necessarily the case in a real lock. Therefore, it is desirable to see the effects of not having two identical gates.
- All the developments performed in section 8.3 do not consider the presence of the upstream and downstream reaches, so it could be valuable to briefly detail the analytical and numerical procedures to realize the seismic analysis of an entire lock structure.
- Finally, as announced in section 8.1, only the longitudinal component $\ddot{X}(t)$ of the seismic acceleration has been considered so far. Nevertheless, the vertical and transversal ones still need to be treated analytically.

In this appendix, the only purpose is to have short analytical or numerical investigations of the topics listed here above. The aim is to briefly extend the analytical procedure detailed so far, but also to show some limitations of the simplified approach and maybe open the door for future researches.

E.3.1. Case of a gate with the real boundary conditions

In section 8.1.2, the true boundary conditions at the bottom of the lock chamber were briefly discussed. It is clear that the model considered in 8.3.3.1 is not entirely satisfactory, as both the positive and negative displacements along the x axis (Figure 8.3) are prohibited there. In reality, the gate is free to move backwards. To investigate this particularity, a solution is to perform numerical simulations with LS-DYNA in which the sill is really modeled (Figure E.8) and also submitted to the soil acceleration $\ddot{X}(t)$.

The contact between the gate and its support is automatically controlled by the software. In reality, this latter is provided by some particular pieces made of wood or of elastomers, so the material properties affected to the sill are those listed in Table E.5.

| | |
|---------------|-----------|
| Young modulus | 12500 MPa |
| Mass density | 710 MPa |
| Poisson Ratio | 0.3 |

Table E.5. Material properties of wood

The numerical results obtained by imposing these new boundary conditions to gate 1 are presented on Figure E.10 together with those already depicted on Figure 8.15 for a gate totally supported at the bottom. On this picture, the curve "True boundary" corresponds to the resulting pressure obtained for the model of Figure E.8.

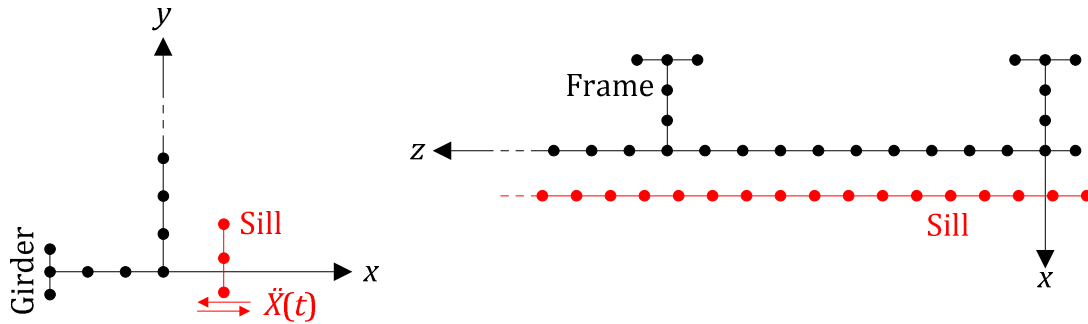


Figure E.8. Representation of the true boundary conditions by modeling the sill with shell elements

The extreme values on Figure E.10 are summarized in Table E.6, from which it appears that smaller pressures are reached when the sill is modeled. Consequently, one may consider that working with the true boundary at the bottom is not relevant when dealing with the seismic analysis of lock gates. Nevertheless, this conclusion has to be further investigated. Indeed, it is evident from Figure E.10 that the two curves are quite dissimilar. This sounds logical, as the structure does not have the same rigidity and support conditions. In other words, the vibration frequencies and mode shapes are not identical in both cases, which implies that the interaction between the fluid and the structure will be different as well. Consequently, one may not conclude a priori that the maximal resulting pressure is automatically lower if the true boundary conditions are used.

| | Solution with true boundary F_T | Solution with a sill F_S | Rigid solution F_R | Relative difference $ 1 - F_T/F_S $ | Ratio F_T/F_R |
|---------------|-----------------------------------|----------------------------|----------------------|-------------------------------------|-----------------|
| Maximal value | 1078.53 kN | 1382.8 kN | 375.2 kN | 22 % | 2.9 |
| Minimal value | -1079.15 kN | -1417.6 kN | -517.1 kN | 24 % | 2.1 |

Table E.6. Comparison between the extreme values for gate 1 supported by a sill or by cables

In order to investigate further this last assertion, one can perform similar analyses with gate 2 (Figure E.1). Indeed, in the previous case of gate 1, the structure was quite rigid and had a total width l of only 13.1 m (Figure 8.7). For this reason, the out-of-plane displacements u_b occurring in the horizontal plane $y = 0$ (see Figure E.9) were quite moderate, so the effect of allowing for free backwards motions may be limited. However, in the case of gate 2, the structure is this time much more flexible, with a total width of 22.5 m. For this reason, the relative displacements u_b between the gate and the sill may be attempted to be larger than for gate 1, leading to more severe consequences on the dynamic pressures induced by the seism. The results for gate 2 are depicted on Figure E.11. Even though they are quite dissimilar, it can be observed that the extreme values are not drastically different and are a bit smaller if the sill is properly modeled.

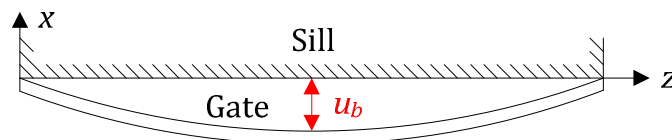


Figure E.9. Out-of-plane displacements in the horizontal plane $y = 0$

From the two cases presented above, it is hazardous to conclude that imposing a total restraint at the bottom of the lock automatically leads to a safe evaluation of the pressure field, even though this tends to be corroborated by the curves depicted on Figure E.10 and on Figure E.11. This is due to the fact the resulting hydrodynamic force is influenced by the contact conditions between the gate and the sill.

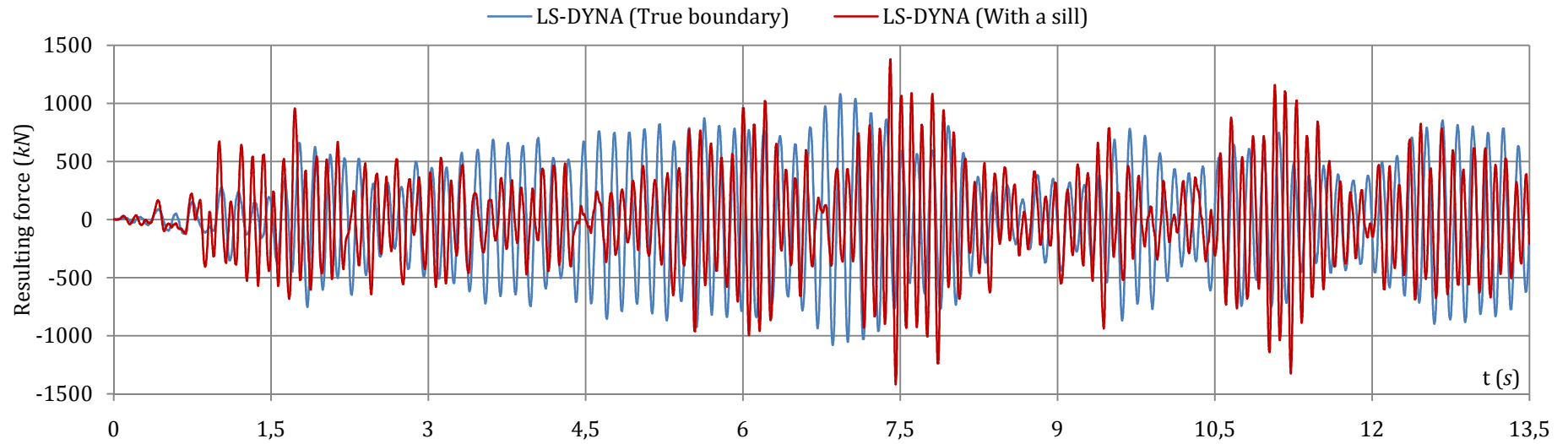


Figure E.10. Comparison of the numerical results for gate 1 if the boundary conditions are correctly modeled at the bottom

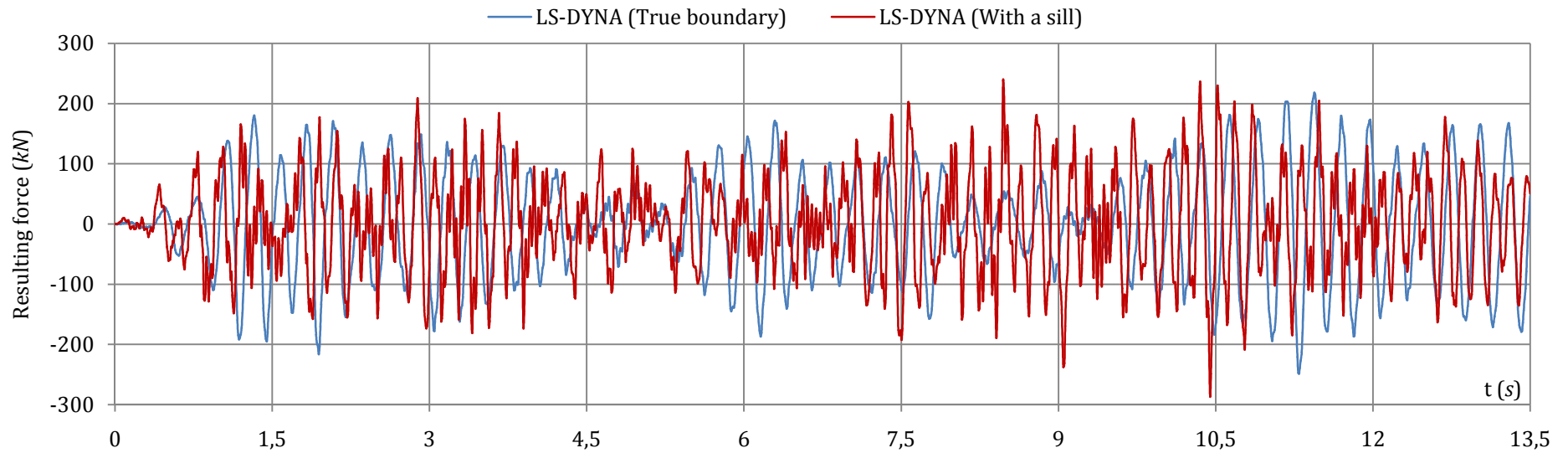


Figure E.11. Comparison of the numerical results for gate 2 if the boundary conditions are correctly modeled at the bottom

Indeed, if more stiffer material properties are used instead of those listed in Table E.5, numerical simulations performed with LS-DYNA have shown that higher water pressures were reached because of the shocks that take place between the gate and its support. Therefore, it can be said as a summary that assuming a perfect restraint at the bottom of the lock does not necessarily leads to a conservative evaluation of the seismic hydraulic forces. Doing so is only valid as a first approximation if the contact between the structure and the sill is provided by some flexible materials, such as wood or elastomers. If this is not the case, this approach may turn out to be unsafe¹⁹.

As a final remark, it should be noted that modeling the true boundary conditions is also questionable at the lock walls. This may be roughly explained from Figure E.12, where the lateral supports have been approximately represented. It can be seen that the positive displacements of the structure are prohibited, because of the contact provided by the sealing device. Nevertheless, the backward motions are not always totally restrained, as there might be a gap between the extreme vertical frame and the wall. For this reason, as for the sill, the support is also not perfectly restrained along the x direction (Figure E.12).

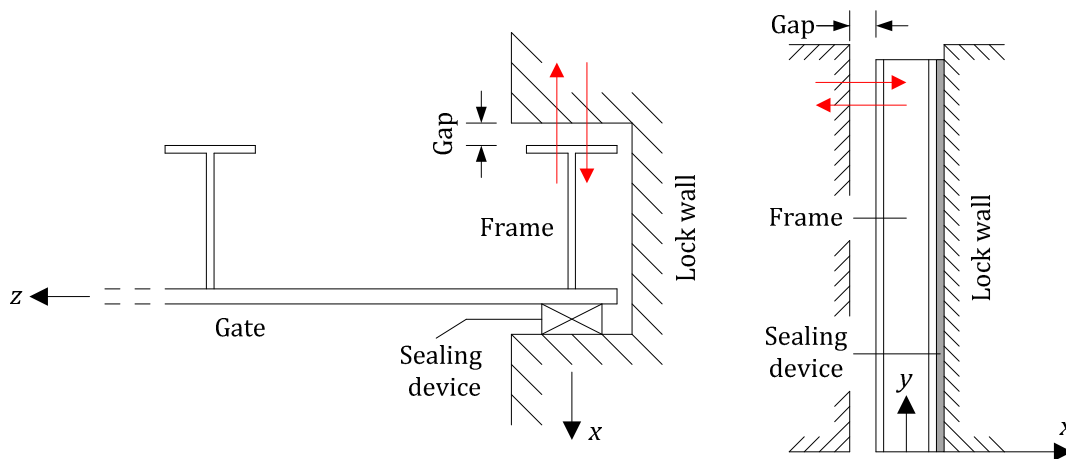


Figure E.12. Support conditions at lock wall

From all the previous developments, it transpires that modeling the real conditions of a lock gate is not easy. Indeed, one has to account for the shocks that may occur against the sill and the lock walls, but with due consideration for the elasticity of the contact materials. Nevertheless, finding an analytical procedure accounting for such non-linear phenomena is quite unrealistic and working with finite elements seems to be unavoidable. Such a numerical approach is probably not required for a preliminary study of the structure, where the present approximate method may still be relevant, but this topic has to be more thoroughly investigated during the upcoming design phases.

E.3.2. Case of an asymmetric configuration

All the results presented in Chapter 8 were obtained under the hypothesis of a symmetric configuration, which means that the two gates limiting the lock chamber were perfectly similar. These ones have of course the same modal properties and vibrates in unison, which implies that the proper accelerations $\ddot{u}(y, z, t)$ are the same for $x = 0$ and $x = L$. Consequently, this is also the case for the hydrodynamic pressure.

¹⁹ However, this last assertion has to be nuanced because of the damping effect due to the water confined between the gate and the sill.

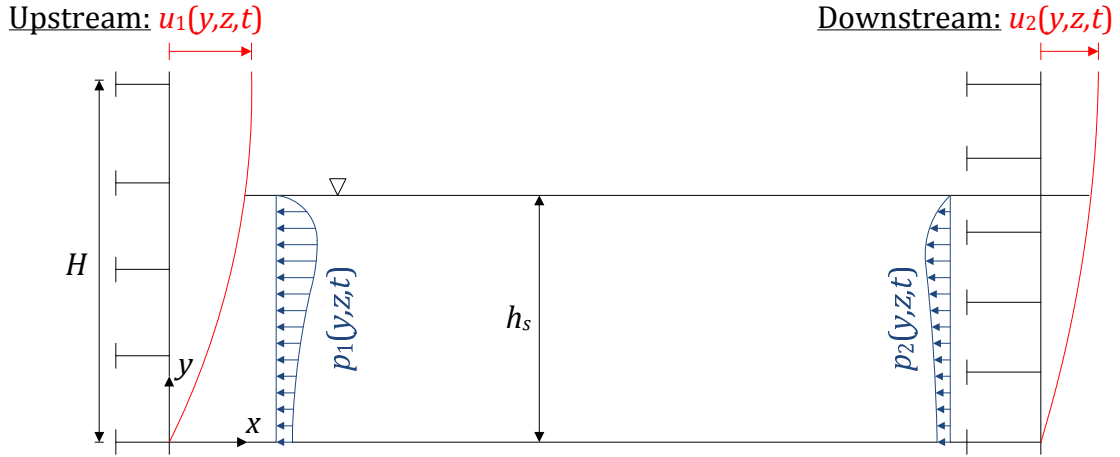


Figure E.13. Asymmetric configuration of the reservoir

Nevertheless, except for standardization purposes, there is no objective reason for having two identical structures. Therefore, it is quite relevant to analyze the case of an asymmetric situation, where the upstream and downstream gates (respectively located in $x = 0$ and $x = L$ on Figure E.13) are dissimilar. With such a situation, the accelerations $\ddot{u}_1(y, z, t)$ and $\ddot{u}_2(y, z, t)$ are not expected to be the same, which is also the case for the pressures $p_1(y, z, t)$ and $p_2(y, z, t)$.

On a mathematical point of view, it is obvious that (7.6) and (7.7) remain valid, but this is not the case for equation (7.8). Going back to the result given in (7.2), it can be seen that the hydrodynamic pressure has to be determined by finding a velocity potential $\mathcal{H}(x, y, z, t)$ that satisfies the Laplace equation (7.3) with the appropriate boundary conditions. It is clear that the restrictions (a) to (d) associated to (7.3) are still holding, but the conditions (e) and (f) have now to be modified to account for the asymmetry of the problem. Indeed, they have to be replaced by:

- (e) $\frac{\partial \mathcal{H}}{\partial x} = \dot{X}(t) + \frac{\partial u_1}{\partial t}$ for $x = 0$ The horizontal x component of the fluid velocity has to be equal to the one of the upstream gate.
- (f) $\frac{\partial \mathcal{H}}{\partial x} = \dot{X}(t) + \frac{\partial u_2}{\partial t}$ for $x = L$ The horizontal x component of the fluid velocity has to be equal to the one of the downstream gate.

Finding an analytical solution that satisfies all the previous requirements is not particularly difficult. For conciseness, the developments will not be provided here, but it can be shown that the flexible hydrodynamic pressure on the upstream gate (i.e. in $x = 0$ on Figure E.13) is given by:

$$p_f(y, z, t) = \sum_{m=0}^{+\infty} \sum_{n=1}^{+\infty} \frac{2\rho_f}{h_s l_m \xi_{mn}} f_{mn}(y, z) \left[\coth(\xi_{mn}L) \int_0^{h_s} dy \int_0^l \ddot{u}_1(y, z, t) f_{mn}(y, z) dz - \frac{1}{\sinh(\xi_{mn}L)} \int_0^{h_s} dy \int_0^l \ddot{u}_2(y, z, t) f_{mn}(y, z) dz \right] \quad (\text{E.82})$$

where $f_{mn}(y, z) = \cos(\alpha_n y) \cos(\bar{\gamma}_m z)$. In all the previous expressions, the notations α_n , $\bar{\gamma}_m$, ξ_{mn} and l_m have the same meaning than in section 7.1.2. It is worth noting that if $\ddot{u}_1(y, z, t) = \ddot{u}_2(y, z, t)$ as for a symmetric configuration, then (E.82) degenerates into (7.8) as it could be expected. Concerning the pressure acting on the downstream gate (i.e. in $x = L$

on Figure E.13), this one may simply be obtained by inverting the accelerations $\ddot{u}_1(y, z, t)$ and $\ddot{u}_2(y, z, t)$ in (E.82).

From (E.82), it appears that the total flexible pressure acting on the gate in $x = 0$ is influenced by the accelerations of both the upstream and downstream structures, which means that there is a kind of coupling between them. Consequently, all the developments performed so far in chapters 7 and 8 are no longer valid. In particular, the vibration frequencies and mode shapes have to be recalculated by accounting for (E.82) instead of (7.8). Realizing such an adaptation is quite fastidious but may be achieved through the Rayleigh-Ritz method, as it was done in sections 7.3 and 8.2. Nevertheless, before starting this quite long calculation, it is worth wondering if it is really useful or not. Indeed, from a careful analysis of (E.82), it can be stated that:

- the contribution coming from $\ddot{u}_1(y, z, t)$ is multiplied by the factor $\coth(\xi_{mn}L)$, which tends to unity if $L/h_s \rightarrow \infty$. Moreover, as $\coth(\xi_{mn}L)$ is an increasing function of m and n , the limit will be reached more rapidly for large values of these two parameters.
- the contribution due to $\ddot{u}_2(y, z, t)$ is weighted by $1/\sinh(\xi_{mn}L)$, which comes very close to 0 with increasing values of the ratio L/h_s . Once again, as $1/\sinh(\xi_{mn}L)$ is a decreasing function of m and n , the limit will be reached more rapidly if $m \gg$ and $n \gg$.

Consequently, following a similar approach as in section D.1.2.3 of Appendix D.1, it transpires from the previous considerations that it is sufficient to deal with the dominant term of the series in (E.82), which is found for $m = 0$ and $n = 1$. This one will be denoted by $\tilde{p}_f(y, z, t)$ and may be simply derived by limiting the development to $m = 0$ and $n = 1$ in (E.82), so it is easy to show that:

$$\tilde{p}_f(y, z, t) = \frac{4\rho_f}{\pi l} \left[\ddot{U}_1(t) \coth(\pi L/2h_s) - \frac{\ddot{U}_2(t)}{\sinh(\pi L/2h_s)} \right] \cos\left(\frac{\pi y}{2h_s}\right) \quad (\text{E.83})$$

where $\ddot{U}_1(t)$ and $\ddot{U}_2(t)$ may be seen as the mean accelerations exhibited by the upstream and downstream gates respectively. In fact, the definitions are as follows:

$$\ddot{U}_1(t) = \int_0^{h_s} dy \int_0^l \ddot{u}_1(y, z, t) \cos\left(\frac{\pi L}{2h_s}\right) dz \quad ; \quad \ddot{U}_2(t) = \int_0^{h_s} dy \int_0^l \ddot{u}_2(y, z, t) \cos\left(\frac{\pi L}{2h_s}\right) dz \quad (\text{E.84})$$

The curves showing the evolution of the two coefficients $\coth(\pi L/2h_s)$ and $1/\sinh(\pi L/2h_s)$ are plotted on Figure E.14, where it can be seen that they have already reached their asymptotic behavior for $L/h_s \geq 3$. In fact, for $L/h_s \geq 3$, $\coth(\pi L/2h_s) \approx 1$ and $1/\sinh(\pi L/2h_s) \leq 0.018$. Consequently, in (E.83), if we want the contributions coming from the downstream and upstream gates to be at least in a ratio of one tenth, the amplitudes $\ddot{U}_1(t)$ and $\ddot{U}_2(t)$ have to satisfy:

$$\frac{\ddot{U}_2(t)/\sinh(\pi L/2h_s)}{\ddot{U}_1(t) \coth(\pi L/2h_s)} \geq \frac{1}{10} \Leftrightarrow \frac{\ddot{U}_2(t)}{\ddot{U}_1(t)} \geq 5.5 \quad ; \quad L/h_s \geq 3 \quad (\text{E.85})$$

The previous relation means that the proper accelerations of the downstream structure should be at least 5 times greater than those of the upstream one to have a non-negligible effect on the pressures appearing in $x = 0$. Such a requirement is a bit unrealistic for classical lock configurations, where the gates vibration properties are somewhat similar.

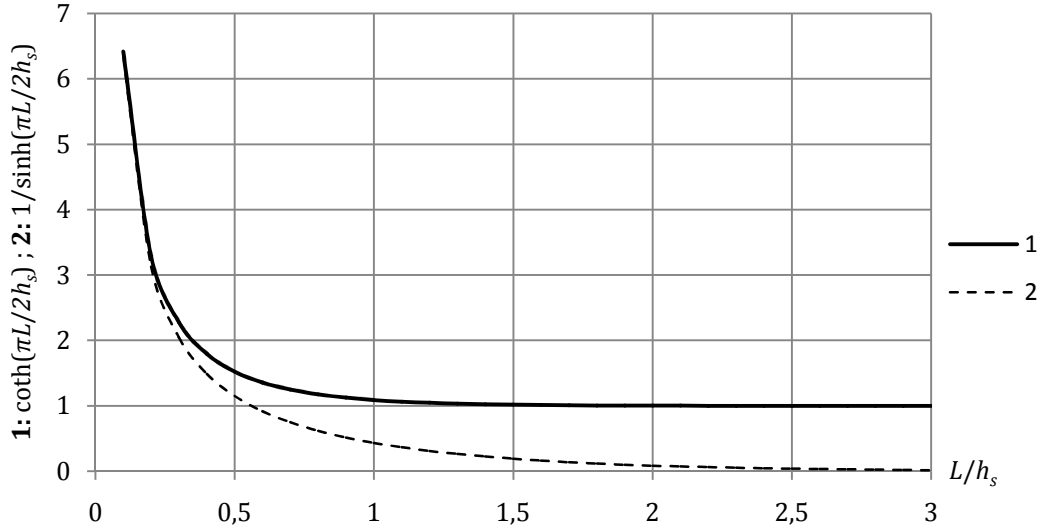


Figure E.14. Curves showing the evolution of $\coth(\pi L/2h_s)$ and $1/\sinh(\pi L/2h_s)$ with the ratio L/h_s

Consequently, under the hypothesis $L/h_s \geq 3$, it may be stated that the upstream and downstream gates do not influence each others. In other words, they may be said to be decoupled, which implies that the hydrodynamic pressure $p_1(y, z, t)$ in $x = 0$ (Figure E.13) only depends on the proper accelerations $\ddot{u}_1(y, z, t)$ of the upstream structure. This means that the second term in (E.82) may be omitted to get the following expression for the flexible contribution:

$$p_f = - \sum_{m=0}^{+\infty} \sum_{n=1}^{+\infty} c_{mn}^* \cos(\alpha_n y) \cos(\bar{\gamma}_m z) \int_0^{h_s} dy \int_0^l \ddot{u}_1(y, z, t) \cos(\alpha_n y) \cos(\bar{\gamma}_m z) dz \quad (\text{E.86})$$

in which $c_{mn}^* = -2\rho_f \coth(\xi_{mn}L)/h_s l_m \xi_{mn}$. A similar result may be derived for the flexible pressure in $x = L$ simply by substituting $\ddot{u}_1(y, z, t)$ by $\ddot{u}_2(y, z, t)$ in (E.86).

Furthermore, from a more careful analysis of (E.86), it appears that the expression is very closed to the solution (7.8) obtained for a symmetric configuration, except that this time the coefficient c_{mn}^* is used instead of c_{mn} . However, for $L/h_s \geq 3$, it may be shown that c_{mn}^* is practically equal to c_{mn} . Therefore, all the results obtained previously in chapters 7 and 8 for a symmetric situation are still applicable to an asymmetric one, provided that $L/h_s \geq 3$.

In order to corroborate the previous conclusions, the three following asymmetric situations can be considered (see Figure E.15):

- Configuration 1: as a starting case (Figure E.15a), one can examine a lock having a total length of 50 m and limited at the upstream side by the first gate described in 8.2.3. A flexible structure with a more important stiffening system is placed at the downstream location. The water level is of about 8 m, so as to have $L/h_s = 6.25 \geq 3$.
- Configuration 2: this intermediate situation (Figure E.15b) is the same as the previous one, except that the lock chamber has a length of only 16 m. Therefore, $L/h_s = 2 < 3$.
- Configuration 3: as an extreme disposition (Figure E.15c), the same lock chamber as in the first case is analyzed, but this time the downstream flexible gate is replaced by an infinitely rigid structure.

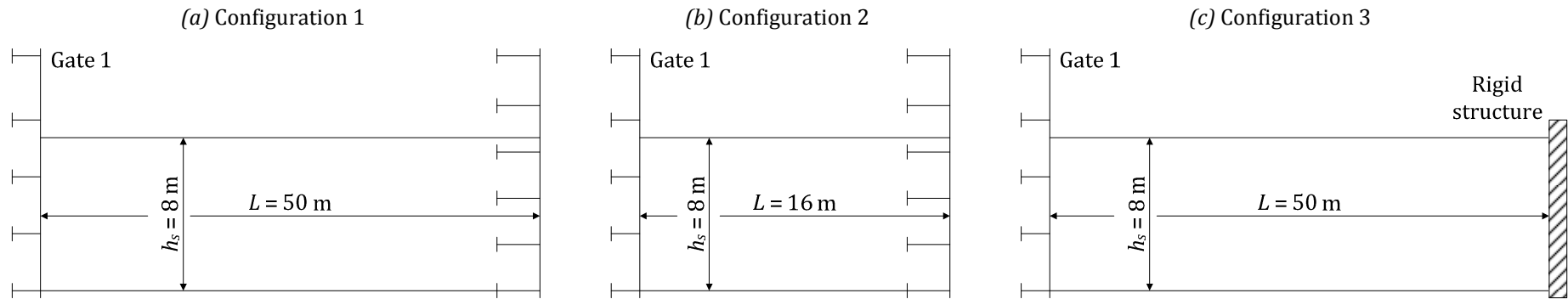


Figure E.15. Description of the three asymmetric configurations

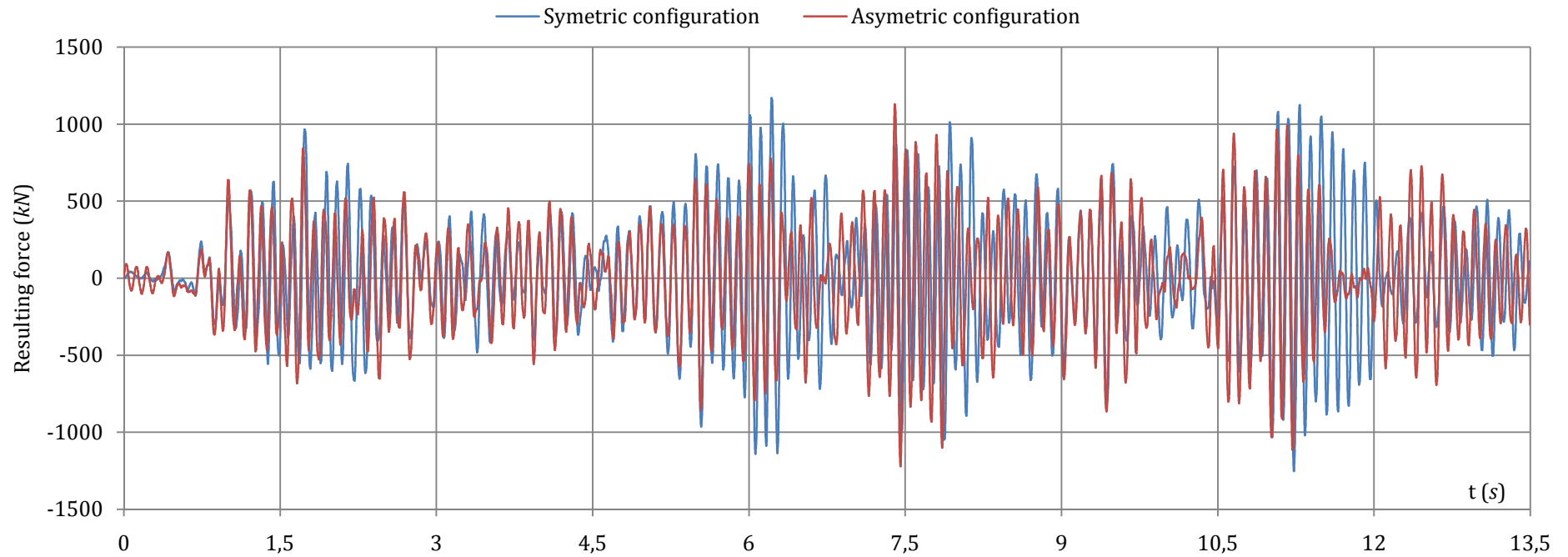


Figure E.16. Comparison between the numerical results obtained for a symmetric and asymmetric configuration ($L = 16 \text{ m}$)

The purpose now is to compare the numerical results obtained for each of these three asymmetric situations with those derived for the corresponding symmetric one. Concerning the configurations 1 and 3 for which $L/h_s \geq 3$, the curves showing the time evolution of the resulting pressure applied on gate 1 were found to be almost perfectly identical with the one obtained for the symmetric case and already presented on Figure 8.15. However, in the second configuration where $L/h_s < 3$, the discrepancy is much more important, as it can be observed on Figure E.16. In this case, it transpires that it is relevant to account for the coupling that may occur between the gates if the lock chamber is not long enough.

It is worth mentioning that for the three situations described here above, the gates were assumed to be perfectly restrained at the bottom. The same configurations were also tested with structures totally free at the bottom and the conclusions were very similar to those detailed previously.

E.3.3. Seismic analysis of an entire lock structure

So far, in sections 8.1 to 8.3 as well as in Chapter 7, we have been dealing with structures that were in contact with a fluid on one side only. Nevertheless, as depicted on Figure E.17, a lock chamber is preceded by the upstream reach and followed by the downstream one. Except during maintenance operations where cofferdams may be used, these ones are rarely totally empty, which implies that the gates are usually surrounded by water on both sides. Consequently, during the longitudinal seismic excitation $\ddot{X}(t)$, one should account for the hydrodynamic pressures in the chamber but also in the reach.

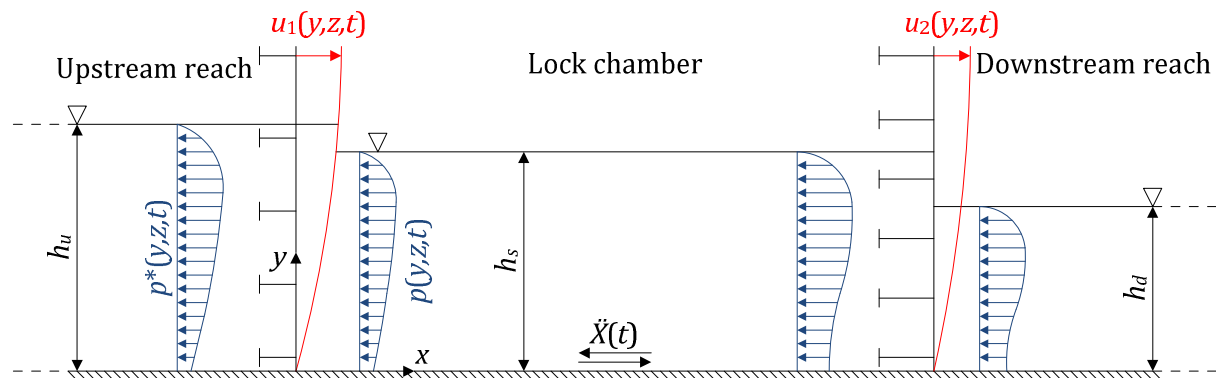


Figure E.17. Representation of a complete lock structure

In section 7.1.2, the total pressure $p(y, z, t)$ appearing inside the lock chamber was derived for a symmetric configuration. Here above, the results have been extended to an asymmetric situation, so the pressure $p(y, z, t)$ is already quite well characterized. The purpose is now to do the same work for the case of an infinite reach.

E.3.3.1. Hydrodynamic pressures in a reach

Before considering the seismic analysis of an entire lock gate, it is first required to go one step further by finding closed-form expressions for the total pressure $p^*(y, z, t)$ appearing in a reach. As in equation (7.1), this one is given by the sum of three different contributions:

$$p^*(y, z, t) = p_h^*(y) + p_r^*(y, t) + p_f^*(y, z, t) \quad (\text{E.87})$$

where $p_h^*(y)$ and $p_r^*(y, t) + p_f^*(y, z, t)$ are respectively the hydrostatic and hydrodynamic pressures acting on the gate. Once again, the hydrodynamic term can be derived from (7.2),

where the potential function $\mathcal{H}(x, y, z, t)$ may be found by solving the Laplace equation (7.3) with the appropriate boundary conditions. Working in the reference frame of Figure E.17, it is clear that the restrictions (a) to (d) introduced in 7.1.2 are still holding, but the requirements (e) and (f) have to be replaced by:

- (e) $\frac{\partial \mathcal{H}}{\partial x} = \dot{X}(t) + \frac{\partial u_1}{\partial t}$ for $x = 0$ The horizontal x component of the fluid velocity has to be equal to the one of the upstream gate.
- (f) $\frac{\partial \mathcal{H}}{\partial t} \rightarrow 0$ for $x \rightarrow -\infty$ In an infinite reach, the hydrodynamic pressure has to decrease when moving away from the gate.

The rigid solution to this problem was originally established by Westergaard [166] and has been applied by many other authors to treat the seismic behavior of dams with an infinite reservoir. As these equations have already been more formally redeveloped in [17], there is no need to reproduce them once again. Regarding the flexible contribution $p_f^*(y, z, t)$, this one may be evaluated in a very classical way by solving the Laplace equation. More information may be found in [17], where the derivation is performed in details. So gathering all these developments leads to the following results for the gate in $x = 0$:

$$p_h^*(y) = -\rho_f g(h_u - y) \quad (\text{E.88})$$

$$p_r^*(y, t) = \sum_{n=1}^{+\infty} (-1)^{n+1} \frac{8\rho_f h_u}{(2n-1)^2 \pi^2} \cos\left(\frac{(2n-1)\pi y}{2h_u}\right) \ddot{X}(t) \quad (\text{E.89})$$

$$p_f^*(y, z, t) = \sum_{n=1}^{+\infty} \sum_{m=0}^{+\infty} \frac{2\rho_f}{h_u l_m} \frac{\cos(\alpha_n y) \cos(\bar{\gamma}_m z)}{\xi_{mn}} \int_0^{h_u} dy \int_0^l \ddot{u}_1(y, z, t) \cos(\alpha_n y) \cos(\bar{\gamma}_m z) dz \quad (\text{E.90})$$

in which h_u is the water level in the upstream reach and where the other notations have the definitions already given in (7.9). It is worth noting that the pressure is positive if it is acting in opposition with the x axis (see Figure E.17). So it is interesting to note that the hydrodynamic pressures in the chamber and in the reach always act in the same sense. Of course, this is not holding for the hydrostatic pressures.

Now that all the pressures acting on a lock gate have been established, it is possible to realize the dynamic analysis of the structure depicted on Figure E.17. The approach is however slightly different from the one exposed in section 8.3. Indeed, this has to be done by accounting for some modifications on both analytical and numerical aspects. These ones are briefly described hereafter.

E.3.3.2. Analytical analysis of an entire lock

Concerning the simplified analytical approach, a similar procedure to the one exposed in section 8.3 can be applied. The goal here is not to perform this quite voluminous work, but simply to give some more information on the way to follow for achieving such an operation, which can be useful for future developments.

Under the assumption that $L/h_s \geq 3$ (which is usually the case for classical lock configurations), the upstream and downstream gates can be analyzed separately, without having to account for any coupling in the chamber. Consequently, for the upstream gate, going back to the equilibrium equation (8.39) leads to:

$$\rho t_p(\ddot{u}_1 + \ddot{X}) + f_d + D \left(\frac{\partial^4 u_1}{\partial y^4} + 2 \frac{\partial^4 u_1}{\partial y^2 \partial z^2} + \frac{\partial^4 u_1}{\partial z^4} \right) + \sum_{n=1}^{n_h} f_{h,n} + \sum_{n=1}^{n_v} f_{v,n} = -p_1 \quad (\text{E.91})$$

where $p_1(y, z, t)$ denotes the total hydrodynamic pressure acting on the gate. It is given by summing up the contributions coming from both sides:

$$p_1(y, z, t) = p_r(y, t) + p_f(y, z, t) + p_r^*(y, z, t) + p_f^*(y, z, t) \quad (\text{E.92})$$

where $p_r(y, t)$, $p_r^*(y, t)$ and $p_f^*(y, z, t)$ are given by (7.7), (E.89) and (E.90) respectively. The last term $p_f(y, z, t)$ may be evaluated by (7.8), (E.86) or even (E.82) as these three formulae are reputed to give similar results if $L/h_s \geq 3$.

Consequently, to account for an upstream reach, it is evident from (E.91) that the only modification is due to the pressure term in the equilibrium equation. Furthermore, keeping developing the proper displacements $u_1(y, z, t)$ in accordance with (8.40), applying the virtual work principle leads to an equation that is similar to (8.53). Nevertheless, in this expression, the terms $[W]$ and V have to be modified to include the additional contributions $p_r^*(y, t)$ and $p_f^*(y, z, t)$. Indeed, instead of using (7.78), the virtual work performed by the external pressure $p_1(y, z, t)$ has to be modified in the following way to include the contributions coming from both sides of the gate:

$$- \int_0^l dz \int_0^{h_s} \delta u (p_r + p_f) dy - \int_0^l dz \int_0^{h_u} \delta u (p_r^* + p_f^*) dy \quad (\text{E.93})$$

From this previous equation, it is clear that the new additional terms $p_r^*(y, t)$ and $p_f^*(y, z, t)$ have to be respectively integrated in the definitions of V and $[W]$. Apart from these two modifications, all the other mathematical developments performed in section 8.3 remain entirely applicable.

E.3.3.3. Numerical analysis of an entire lock

On a numerical point of view, the situation is more complex because representing an infinite upstream reach is not easy. Ideally, such an operation has to be achieved by modeling the fluid domain over a certain length L_u . Doing so, the liquid is in contact with the flexible gate on the downstream side, while a non-reflecting boundary is imposed on the upstream one (see Figure E.18). With this condition, the pressure waves moving away from the gate are absorbed after travelling a distance L_u and never go back in the direction of the vibrating structure, which is in fact what would happen in a true infinite reach.

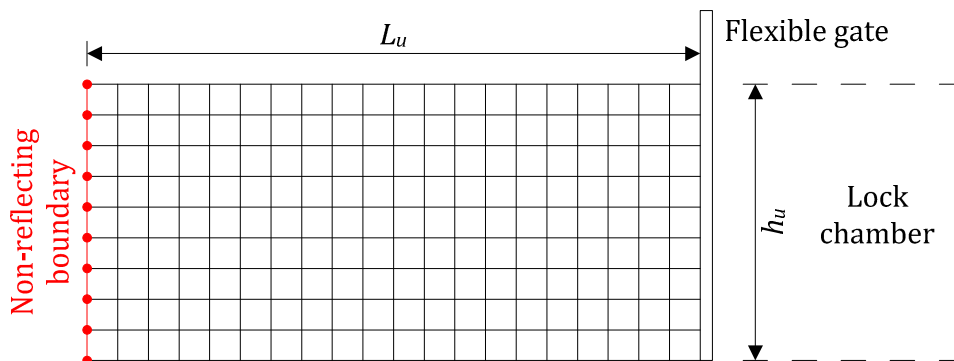


Figure E.18. Numerical model of an infinite reach

The problem is that LS-DYNA only provides that kind of boundary conditions with arbitrary Lagrangian-Eulerian (ALE) formulations, so they are not available if the fluid is modeled as an elastic medium. Nevertheless, this difficulty can be overcome by resorting to an approximate approach. Let us consider a lock chamber with a water level h_u and having a total length L_u , bounded by a flexible gate on one side and limited by a perfectly rigid structure on the other one. For this asymmetric configuration (see Figure E.19), the flexible pressure is given by (E.82), in which $\ddot{u}_1(y, z, t)$ and $\ddot{u}_2(y, z, t)$ have been inverted and where $\ddot{u}_1(y, z, t)$ is set to zero, as the upstream structure is assumed to be infinitely rigid. In other words, we have:

$$p_f(y, z, t) = \sum_{m=0}^{+\infty} \sum_{n=1}^{+\infty} \frac{2\rho_f \coth(\xi_{mn}L_u)}{h_u l_m \xi_{mn}} f_{mn}(y, z) \int_0^{h_u} dy \int_0^l \ddot{u}_2(y, z, t) f_{mn}(y, z) dz \quad (\text{E.94})$$

If it is further assumed that the lock chamber becomes infinitely long ($L_u \rightarrow +\infty$), then $\coth(\xi_{mn}L_u) \rightarrow 1$ in the previous relation and in such a case, (E.94) is identical to (E.82). In other words, the flexible pressure in an infinite reach is the same as the one generated in an infinite lock chamber. In fact, there is no need to have $L_u \rightarrow +\infty$ as it is obvious that the limit is already valid for $L_u \geq 3h_u$.

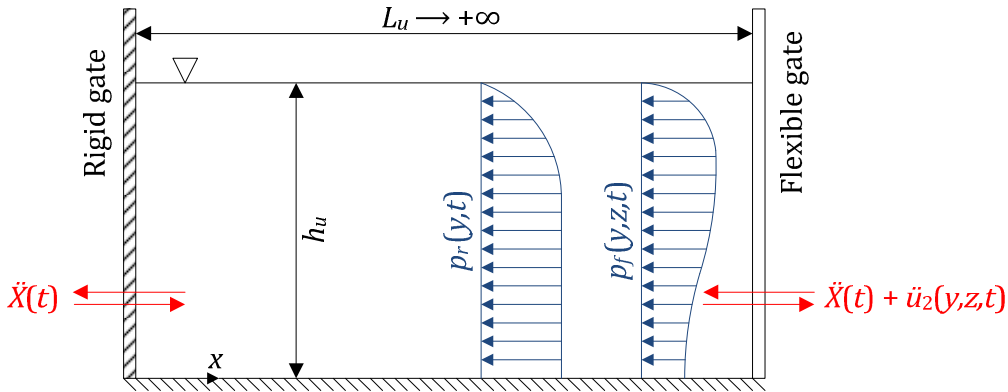


Figure E.19. Impulsive pressure in an infinite asymmetric lock chamber

Concerning the rigid pressure $p_r(y, t)$ appearing in the lock chamber of Figure E.19, it is still given by the initial formula (7.7), i.e.:

$$p_r(y, t) = -\rho_f \left(\sum_{n=1}^{+\infty} \frac{4L_u}{(2n-1)^2 \pi^2} \frac{\cosh((2n-1)\pi y/L_u)}{\cosh((2n-1)\pi h_u/L_u)} - \frac{L_u}{2} \right) \ddot{X}(t) \quad (\text{E.95})$$

Nevertheless, it is not so straightforward to show analytically that (E.95) degenerates into (E.89) when $L_u \rightarrow +\infty$. This was already discussed in section D.2.2.2 of Appendix D.2, where it was stated that the limit is also valid for $L_u \geq 3h_u$.

As a conclusion, it can be said that the rigid and flexible pressures appearing in the lock chamber of Figure E.19 with $L_u = 3h_u$ are the same as those generated in an infinite reach. Consequently, to study numerically the seismic behavior of an upstream lock gate, it is sufficient to consider the model depicted on Figure E.20 and submit it to a longitudinal acceleration $\ddot{X}(t)$. On this figure, it can be seen that fictitious rigid plates have been represented to close the fluid domains. In fact, it is not required to use real lock gates at these locations. Only non-flexible structures are simply needed there. Of course, doing so is only valid under the hypothesis of $L \geq 3h_s$, otherwise it is required to account for the coupling that

may occur between the upstream and downstream gates. This hypothesis also justifies the fact that the lock chamber is only modeled over a length of $3h_s$.

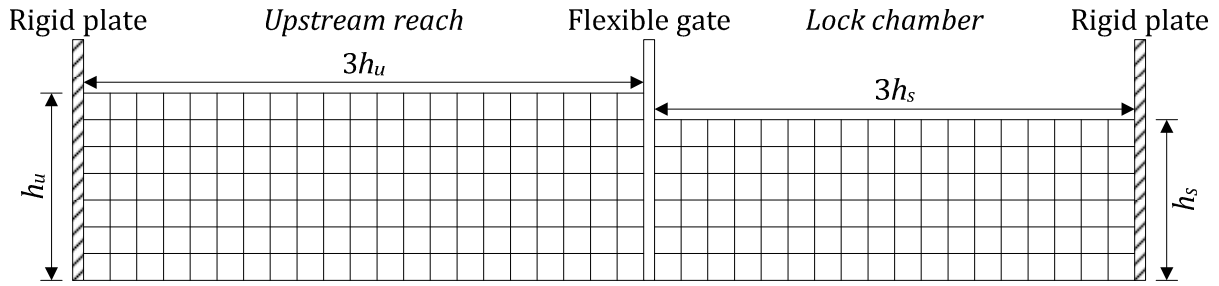


Figure E.20. Numerical model for studying the seismic behavior of an upstream lock gate

With the explanations given here above, it is possible to extend the simplified analytical approach to account for the presence of the upstream and downstream reaches. Moreover, realizing a numerical validation of these new developments seems to be quite accessible, as the model of Figure E.20 should be convenient to perform such an operation.

E.3.4. Other components of the seismic acceleration

So far, only the longitudinal component of the seismic acceleration has been considered. This one was denoted by $\ddot{X}(t)$ and oriented along the x axis on Figure 8.2). Nevertheless, it is also required to work with the vertical and transversal components because a seism is a spatial phenomenon. As already mentioned in 8.1.2, these ones are denoted by $\ddot{Y}(t)$ and $\ddot{Z}(t)$. They are supposed to act respectively along the y and z axes (Figure 8.2).

In the pre-design stage of a lock gate, it is quite common to neglect $\ddot{Y}(t)$ and $\ddot{Z}(t)$ because the associated pressures are smaller than those appearing under a longitudinal excitation $\ddot{X}(t)$. So it is not of prior importance to include them in an analytical approach. Nevertheless, in view of potential future developments, it is probably interesting to provide here some more information on the way to proceed to extend the simplified method.

E.3.4.1. Vertical ground acceleration

It is clear that under a vertical ground acceleration, the gate may be assumed to be quite rigid, so that the fluid-structure interaction should be relatively modest. Consequently, the flexible pressures $p_f(y, z, t)$ and $p_f^*(y, z, t)$ appearing in the chamber and in the reach respectively may be expected to be negligible. It can be shown [17] that the formulae (E.82) and (E.90) remain applicable to evaluate $p_f(y, z, t)$ and $p_f^*(y, z, t)$, even when dealing with a vertical acceleration. Furthermore, it is worth recalling that the pressure is positive when it is oriented in opposition with the x axis. Consequently, the flexible contributions induced on both sides of the gate always act in the same sense (see Figure E.21) and have additive effects.

Concerning the rigid impulsive contributions $p_r(y, t)$ and $p_r^*(y, t)$, it is demonstrated by Buldgen [17] that they simply vary linearly with the depth. For this reason, in static analyses, they are often applied in conjunction with the hydrostatic pressure. These terms have the following expressions:

$$p_r(y, t) = \rho_f(h_s - y)\ddot{Y}(t) \quad ; \quad p_r^*(y, t) = -\rho_f(h_u - y)\ddot{Y}(t) \quad (\text{E.96})$$

where h_s and h_u are the water levels in the chamber and in the reach respectively. This time, these two pressures act in opposition and partly compensate each others, which is a non negligible advantage for the design.

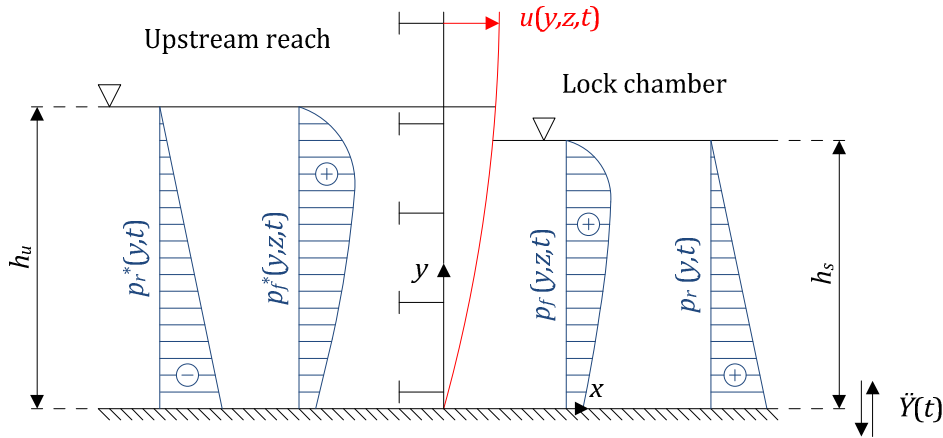


Figure E.21. Hydrodynamic pressures induced by a vertical seismic acceleration

From the previous developments, it is clear that the vertical acceleration is not attempted to be responsible for a large increase of the resulting forces acting on the gate. This is due to the fact that the vertical stiffness of the structure is quite important, but also because of the partial cancellation of the rigid pressures acting on its two sides. For this reason, it does not seem of prior importance to include $\ddot{Y}(t)$ in a pre-design tool for lock gates. However, this work is quite easy to realize, as only the vector \mathbf{V} in (8.53) has to be corrected to account for the new formulae (E.96) giving the rigid impulsive action in the present case.

E.3.4.2. Transversal ground acceleration

In the case of a ground acceleration $\ddot{Z}(t)$ acting along the horizontal z axis (Figure 8.2), it can also be argued that the structure has a sufficient transversal stiffness to neglect the fluid-structure interaction. However, for completeness, one can try to examine the flexible pressures $p_f(y, z, t)$ and $p_f^*(y, z, t)$ induced on both sides of the gate (see Figure E.22). Inside the lock chamber, it may be mathematically demonstrated that (E.82) is still valid, but the situation is more complicated in the reach. If this one has an infinite length, then is clear that the lock walls in $z = 0$ and $z = l$ will be submitted to a uniform seismic acceleration $\ddot{Z}(t)$ over a certain finite length L_u (see Figure E.23), but after this distance, the effects of the earthquake will progressively disappear.

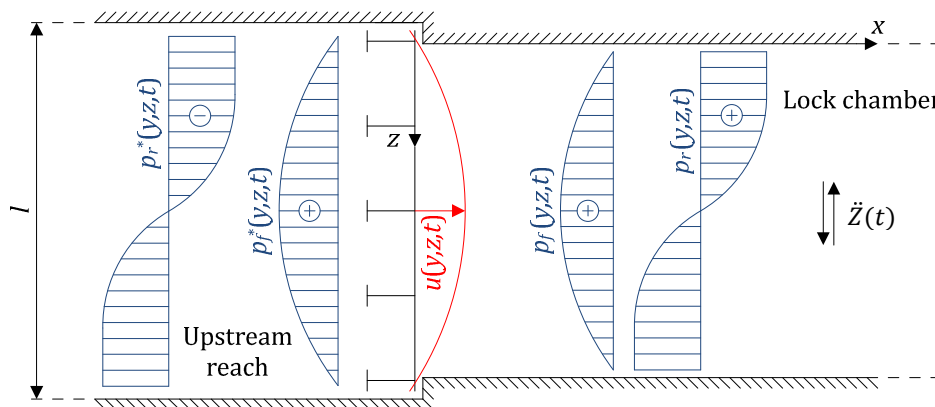


Figure E.22. Hydrodynamic pressures induced by a transversal seismic acceleration

Consequently, $\ddot{Z}(x, t)$ is a decreasing function of x and solving the Laplace equation (7.3) with the correct boundary conditions is mathematically quite difficult. Nevertheless, under the assumption that L_u is sufficiently large, (E.90) may still be used as an approximate solution for the flexible pressure in the reach. Doing so, it is worth noting that $p_f(y, z, t)$ and $p_f^*(y, z, t)$ act in the same sense, so their effects are additive.

Regarding the rigid contributions, the fluid equation (7.3) inside the lock chamber may be solved quite easily. The solution is very similar to the one obtained in the case of a longitudinal acceleration $\ddot{X}(t)$ and the following relation may be demonstrated [17]:

$$p_r(y, z, t) = -\rho \left(z - \frac{l}{2} + \sum_{n=1}^{+\infty} \frac{4}{\beta_n^2 l} \frac{\cosh(\beta_n y)}{\cosh(\beta_n h_s)} \cos(\beta_n z) \right) \ddot{Z}(t) \quad (\text{E.97})$$

where $\beta_n = (2n - 1)\pi/l$. The derivation of a closed-form expression for $p_r^*(y, z, t)$ is more difficult, as it should be accounted for a non-uniform distribution of the seismic acceleration $\ddot{Z}(x, t)$ along the lock walls. Once again, assuming that L_u is quite large, the hydrodynamic pressure near the gate should be correctly approximated by replacing h_s by h_u in (E.97).

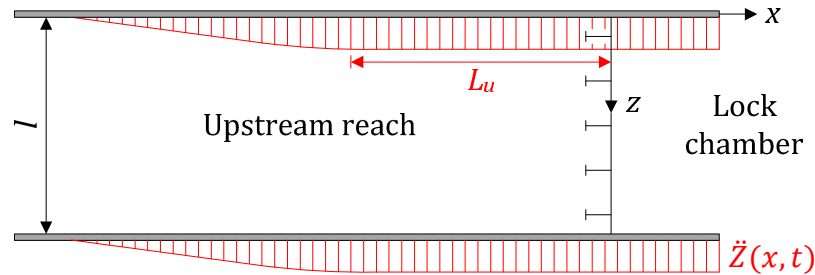


Figure E.23. Distribution of the seismic transversal acceleration along the lock walls

From the previous considerations, it transpires that some approximations are made to treat the case of a transversal acceleration, but it is not of prior importance to have a rigorous approach. This may be justified by the following arguments:

- The transversal gate stiffness is usually sufficient to limit the fluid-structure interaction. Therefore, the flexible pressures $p_f(y, z, t)$ and $p_f^*(y, z, t)$ should not be determinant.
- The rigid contributions $p_r(y, z, t)$ and $p_r^*(y, z, t)$ act in opposition (see Figure E.22), so there is a partial compensation.
- From a more careful analysis of (E.97), it appears that the pressure distribution along the transversal z axis is antisymmetric (see Figure E.22). Consequently, the resultant force applied on the entire gate is equal to zero.

For the three previous reasons, the transversal component of the seismic acceleration is not expected to produce an important increase of the resulting forces acting on the gate. Consequently, accounting for $\ddot{Z}(t)$ in the pre-design stage is probably not particularly relevant²⁰. However, this should not be an overwhelming task, as the only modification to realize in the virtual work equation (8.53) is to correct the vector \mathbf{V} to include (E.97).

²⁰ This component of the seismic acceleration was even neglected for the seismic pre-design of the new locks in the Panama canal.

References

All the references listed hereafter are sorted with respect to the alphabetic order of the authors. They are numbered accordingly.

A

- [1] W. Abramowicz, Crush resistance of T, Y and X sections, Joint MIT-Industry Project on Tanker Safety, Report 24, Cambridge, 1994.
- [2] H.N. Abramson, The dynamic behavior of liquids in moving containers, NASA Technical Reports, National Aeronautics and Space Administration, Washington, 1966.
- [3] Y. Akita, N. Ando, Y. Fujita, K. Kitamura, Studies on collision-protective structures in nuclear powered ships, Nuclear Engineering Design, 19 (1972), 365-401.
- [4] G. Aksu, Free vibration analysis of stiffened plates by including the effect of in-plane inertia, Journal of Applied Mechanics, 49 (1982), 206-212.
- [5] J.M. Alexander, An approximate analysis of the collapse of thin cylindrical shells under axial loading, Quarterly Journal of Mechanics and Applied Mathematics, 13 (1960), 10-15.
- [6] H.S. Alsos, J. Amdahl, On the resistance of stiffened plates, Part I - Experiments, International Journal of Impact Engineering, 36 (2009), 799-807.
- [7] H.S. Alsos, J. Amdahl, On the resistance of tanker bottom structures during stranding, Marine Structures, 20 (2007), 218-237.
- [8] J. Amdahl, Energy absorption in ship-platform impact, PhD Thesis, Norwegian Institute of Technologies, Trondheim, 1982.
- [9] J. Amdahl, D. Kavlie, A. Johansen, Tanker grounding resistance, Proceedings of the Sixth International Symposium on Practical Design of Ships and Mobile Units, Seoul, South Korea, 1995.
- [10] S.N. Amiri, A. Esmaily, Prediction of dynamic response of stiffened rectangular plates using hybrid formulation, Journal of Engineering Science and Technology, 5 (2010), 251-263.
- [11] J.R. Arroyo, R.M. Ebeling, B.C. Barker, Analysis of impact loads from full-scale, low velocity, controlled barge impact experiments, U.S. Army Corps of Engineers Research and Development Center, Vicksburg, 1998.

B

- [12] Y. Basar, D. Weichert, Nonlinear continuum mechanics of solids: fundamental concepts and perspectives, Springer Verlag, Berlin, 2000.

- [13] Z.P. Bazant, L. Cedolin, *Stability of structures: elastic, inelastic, fracture, and damage theories*, Oxford University Press, New York, 1991.
- [14] R.D. Blevins, *Formulas for natural frequencies and mode shape*, Krieger Publishing Company, Malabar, 1995.
- [15] A.J. Brown, J.A.W. Sajdak, *Modeling longitudinal damage in ship collisions*, Ship Structure Committee, Report SSC-437, Washington, 2005.
- [16] L. Brubak, J. Hellesland, *Semi-analytical postbuckling and strength analysis of arbitrarily stiffened plates in local and global bending*, *Thin-Walled Structures*, 45 (2007), 620-633.
- [17] L. Buldgen, *Analyse des portes d'écluse sous sollicitation sismique*, Master Thesis, University of Liège, Liège, 2010.
- [18] L. Buldgen, H. Degée, H. Le Sourne, P. Rigo, *A simplified procedure to assess the dynamic pressures on large reservoirs*, *Proceedings of the Ninth International Conference on Structural Dynamics*, Porto, Portugal, 2014.
- [19] L. Buldgen, H. Degée, H. Le Sourne, P. Rigo, *Simplified seismic analysis of lock gates*, *Proceedings of the Thirty-Third PIANC World Congress*, San Francisco, United States, 2014.
- [20] L. Buldgen, A. Gazerzadeh, A. Bela, H. Le Sourne, P. Rigo, *A simplified procedure to assess the dynamic pressures on lock gates*, *Proceedings of the Seventh International Conference on Thin-Walled Structures*, Busan, Korea, 2014.
- [21] L. Buldgen, H. Le Sourne, P. Rigo, *A simplified analytical method for estimating the crushing resistance of an inclined ship side*, *Marine Structures*, 33 (2013), 265-296.
- [22] L. Buldgen, H. Le Sourne, P. Rigo, *A simplified analytical method for estimating the resistance of lock gates to ship impacts*, *Journal of Applied Mathematics*, 2012 (2012), 1-39.
- [23] L. Buldgen, H. Le Sourne, P. Rigo, *A simplified procedure to assess the strength of a ship impacting a lock mitred gate*, *Proceedings of the Twenty-Second International Conference on Ocean, Offshore and Arctic Engineering*, Nantes, France, 2013.
- [24] L. Buldgen, H. Le Sourne, P. Rigo, *Fast strength assessment of mitre gates to ship impact*, *International Journal of Crashworthiness*, 18 (2013), 423-443.

C

- [25] Centre d'études techniques maritimes et fluviales, *Protection des portes d'écluses et des barrages contre les chocs de bateaux*, notice STC.VN 97.01, Paris, 1997.
- [26] Centre d'études techniques maritimes et fluviales, *Recommandations pour le calcul aux états-limites des ouvrages en site aquatique*, ROSA 2000, Paris, 2000.
- [27] J.Z. Chen, A.R. Ghaemmaghami, M.R. Kianoush, *Dynamic analysis of concrete rectangular liquid storage tanks*, *Proceedings of the Fourteenth World Conference on Earthquake Engineering*, Beijing, China, 2008.

- [28] W.F. Chen, D.J. Han, *Plasticity for structural engineers*, J. Ross Publishing, Fort Lauderdale, 2007.
- [29] J.Z. Chen, M.R. Kianoush, Seismic response of concrete rectangular tanks for liquid containing structures, *Canadian Journal of Civil Engineering*, 32 (2005), 739-752.
- [30] S.R. Cho, H.S. Lee, Experimental and analytical investigations on the response of stiffened plates subjected to lateral collisions, *Marine Structures*, 22 (2009), 84-95.
- [31] S.R. Cho, B.S. Seo, B.C. Cerik, H.K. Shin, Experimental and numerical investigations on the collision between offshore wind turbine support structures and service vessels, *Proceedings of the Sixth International Conference on Collision and Grounding of Ship and Offshore Structures*, Trondheim, Norway, 2013.
- [32] S.K. Choi, T. Wierzbicki, J. Culbertson-Driscoll, Crushing resistance of a web girder, *Joint MIT-Industry Project on Tanker Safety*, Report 23, Cambridge, 1994.
- [33] S.K. Choi, T. Wierzbicki, O. Goksy, J. Culbertson-Driscoll, Crushing resistance of a web girder with application to ship structures, *Joint MIT-Industry Project on Tanker Safety*, Report 38, Cambridge, 1995.
- [34] A.K. Chopra, Hydrodynamic pressures on dams during earthquakes, *Journal of the Engineering Mechanics Division*, 93 (1967), 205-223.
- [35] A.K. Chopra, Earthquake analysis, design and safety evaluation of concrete dams, *Proceedings of the Fifth Canadian Conference on Earthquake Engineering*, Ottawa, Canada, 1987.
- [36] M.A. Criesfield, *Non-linear finite element analysis of solids and structures*, John Wiley & Sons, Chichester, 1991.
- [37] I.G. Currie, *Fundamental mechanics of fluids*, Marcel Dekker Incorporated, New York 2003.

D

- [38] N.M. Dehousse, *Les écluses de navigation*, Lecture Notes, University of Liège, Liège, 1985.
- [39] N.M. Dehousse, J. Deprez, *Les bordages orthotropes plans: calcul d'une porte plane d'écluse*, Mémoires du CERES n°22 (nouvelle série), Centre d'études, de recherches et d'essais scientifiques du génie civil, Liège, 1967.
- [40] E.J.M. Delhez, *Analyse mathématique*, Lecture Notes, University of Liège, Liège, 2005.
- [41] V.S. Deshpande, N.A. Fleck, Energy absorption of an egg-box material, *Journal of the Mechanics and Physics of Solids*, 51 (2003), 187-208.
- [42] Deutsches Institut für Normung, *Locks for waterways for inland navigation- Principles for dimensioning and equipment*, Beuth Verlag, Berlin, 1995.
- [43] S. M. Dickinson, The buckling and frequency of flexural vibration of rectangular isotropic and orthotropic plates using Rayleigh's method, *Journal of Sound and Vibration*, 61 (1978), 1-8.

- [44] R. Donner, F. Besnier, H. Le Sourne, Numerical simulation of ship-submarine collisions, Proceedings of the Eighth International Symposium on Practical Design of Ships and Other Floating Structures, Shanghai, China, 2001.

E

- [45] S. Ehlers, Material relation to assess the crashworthiness of ship structures, Doctoral Dissertation, Helsinki University of Technology, Espoo, 2009.
- [46] S. Ehlers, Strain and stress relation until fracture for finite element simulations of a thin circular plate, *Thin-Walled Structures*, 48 (2010), 1-8.
- [47] S. Ehlers, J. Broekhuijsen, H.S. Alsos, F. Biehl, K. Tabri, Simulating the collision response of ship side structures: a failure criteria benchmark study, *International Shipbuilding Progress*, 55 (2008), 127-144.
- [48] S. Ehlers, P. Varsta, Strain and stress relation for non-linear finite element simulations, *Thin-Walled Structures*, 47 (2009), 1203-1217.
- [49] H.I. Epstein, Seismic design of liquid storage tanks, *Journal of the Structural Division*, 102 (1976), 1659-1673.
- [50] European Committee for Standardization, Eurocode 0 - Basis of structural design, EN 1990, Brussels, 2002.
- [51] European Committee for Standardization, Eurocode 1 - Actions on structures - Part 1.7: General actions and accidental actions, prEN 1991-1-7, Brussels, 2004.
- [52] European Committee for Standardization, Eurocode 3 - Design of steel structures - Part 1.5: Plated structural elements, prEN 1991-1-5, Brussels, 2003.
- [53] European Committee for Standardization, Eurocode 3 - Design of steel structures - Part 1.1: General rules and rules for buildings, prEN 1991-1-1, Brussels, 2005.
- [54] European Committee for Standardization, Eurocode 8 - Design of structures for earthquake resistance - Part 4: Silos, tanks and pipelines, prEN 1998-4, Brussels, 2006.
- [55] European Conference of Ministers of Transport, Resolution 92/2 on new classification of inland waterways, Athens, 1992.
- [56] European Environment Agency, Overall energy efficiency and specific CO₂ emissions for passenger and freight transport, Indicator factsheet, TERM 2003 27 EEA 31, Brussels, 2004.

F

- [57] D. F. Fischer, Dynamic fluid effects in liquid-filled flexible cylindrical tanks, *Earthquake Engineering and Structural Dynamics*, 7 (1979), 587-601.
- [58] D. Fischer, F.G. Rammerstorfer, The stability of liquid-filled cylindrical shells under dynamic loading, Proceedings of a State-of-Art Colloquium on Buckling of Shells, Stuttgart, Germany, 1982.

- [59] G. Forsyth, A. Porteous, The design and construction of seismically qualified steel caissons at Rosyth Royal Dockyard, *The Structural Engineer*, 78 (2000), 24-31.
- [60] K. Fujita, K. Shiraki, Approximate seismic response analysis of self-supported thin cylindrical liquid storage tanks, *Proceedings of the Fourth International Conference on Structural Mechanics in Reactor Technology*, San Francisco, United States, 1977.

G

- [61] A.R. Ghaemmaghami, M.R. Kianoush, Effect of wall flexibility on dynamic response of concrete rectangular liquid storage tanks under horizontal and vertical ground motions, *Journal of Structural Engineering*, 136 (2010), 441-451.
- [62] N.F. Grace, J.B. Kennedy, Dynamic analysis of orthotropic plate structures, *Journal of Engineering Mechanics*, 111 (1985), 1027-1037.
- [63] E.W. Graham, A.M. Rodriguez, The characteristics of fuel motion which affect airplane dynamics, *Journal of Applied Mechanics*, 19 (1952), 381-388.
- [64] A.E. Green, P.M. Naghdi, A general theory of an elastic-plastic continuum, *Archive for Rational Mechanics and Analysis*, 18 (1965), 251-281.
- [65] J.E. Greenspon, Vibration of cross-stiffened and sandwich plates with application to underwater sound radiators, *Journal of the Acoustical Society of America*, 33 (1961), 1485-1497.

H

- [66] J.O. Hallquist, *LS-DYNA theoretical manual*, Livermore Software Technology Corporation, Livermore, 2006.
- [67] M.A. Haroun, Stress analysis of rectangular walls under seismically induced hydrodynamic loads, *Bulletin of Seismological Society of America*, 74 (1984), 1031-1041.
- [68] M.A. Haroun, G.W. Housner, Earthquake response of deformable liquid storage tanks, *Journal of Applied Mechanics*, 48 (1981), 411-418.
- [69] R.M. Haythornthwaite, Beams with full end fixity, *Engineering*, 183 (1957), 110-112.
- [70] L. Hong, J. Amdahl, Crushing resistance of web girders in ship collision and grounding, *Marine Structures*, 21 (2008), 374-401.
- [71] L. Hong, J. Amdahl, Plastic design of laterally patch loaded plates for ships, *Marine Structures*, 20 (2007), 124-142.
- [72] L. Hong, J. Amdahl, Plastic mechanism analysis of the resistance of ship longitudinal girders in grounding and collision, *International Journal of Ships and Offshore Structures*, 3 (2008), 159-171.
- [73] H.G. Hopkins, On the plastic theory of plates, *Proceedings of the Royal Society A*, 241 (1957), 153-179.
- [74] G.W. Housner, Dynamic pressures on accelerated fluid containers, *Bulletin of Seismological Society of America*, 47 (1957), 15-37.

- [75] N.J. Huffington, Theoretical determination of rigidity properties of orthogonally stiffened plates, *Journal of Applied Mechanics*, 23 (1956), 15-20.

I

- [76] R.A. Ibrahim, *Liquid sloshing dynamics: theory and applications*, Cambridge University Press, Cambridge, 2005.
- [77] T. Irie, G. Yamada, H. Ida, Free vibration of a stiffened trapezoidal cantilever plate, *Journal of the Acoustical Society of America*, 72 (1982), 1508-1513.
- [78] K.T. Iyengar, R. Narayana, Determination of the orthotropic plate parameters of stiffened plates and grillages in free vibration, *Applied Sciences Research*, 17 (1967), 422-438.

J

- [79] N. Jones, Consistent equations for the large deflections of structures, *Bulletin of Mechanical Engineering Education*, 10 (1971), 9-20.
- [80] N. Jones, Influence of in-plane displacements at the boundaries of rigid-plastic beams and plates, *International Journal of Mechanical Sciences*, 15 (1973), 547-561.
- [81] N. Jones, *Structural impact*, Cambridge University Press, Cambridge, 2003.
- [82] N. Jones, T. Liu, J.J. Zheng, W.Q. Shen, Clamped beam grillages struck transversally by a mass at the centre, *International Journal of Impact Engineering*, 11 (1991), 379-399.

K

- [83] M.R. Kianoush, J.Z. Chen, Effect of vertical acceleration on response of concrete rectangular liquid storage tanks, *Engineering Structures*, 28 (2006), 704-715.
- [84] M.R. Kianoush, H. Mirzabozorg, M. Ghaemian, Dynamic analysis of rectangular liquid containers in three dimensional space, *Canadian Journal of Civil Engineering*, 33 (2006), 501-507.
- [85] J.K. Kim, H.M. Koh, I.J. Kwahk, Dynamic response of rectangular flexible fluid containers, *Journal of Engineering Mechanics*, 122 (1996), 807-817.
- [86] A.N. Kinkead, A method for analyzing cargo protection afforded by ship structures in collision and its application to an LNG carrier, *Transactions of the Royal Institution of Naval Architects*, 122 (1980), 299-323.
- [87] C.L. Kirk, Vibration characteristics of stiffened plates, *Journal of Mechanical Engineering Sciences*, 2 (1960), 242-253.
- [88] M. Kotelko, Load-capacity estimation and collapse analysis of thin-walled beams and columns: recent advances, *Thin-Walled Structures*, 42 (2004), 153-175.
- [89] M. Kotelko, V. Ungureanu, D. Dubina, M. Macdonald, Plastic strength of thin-walled plated members - Alternative solutions review, *Thin-Walled Structures*, 49 (2001), 636-644.

L

- [90] K.Y. Lam, K.M. Liew, A numerical model based on orthogonal plate functions for vibration of ring supported elliptical plates, *Computational Mechanics*, 9 (1992), 113-120.
- [91] H. Lamb, On the vibration of an elastic plate in contact with water, *Proceedings of the Royal Society of London*, 98 (1921), 205-216.
- [92] P.A. Laura, G.A. Smith, Vibrations of rib-stiffened thin elastic plates carrying concentrated masses, *Journal of the Acoustical Society of America*, 43 (1968), 332-335.
- [93] E. Lehmann, Peschmann J., Energy absorption by the steel structure of ships in event of collisions, *Marines Structures*, 15 (2002), 429-441.
- [94] E. Lehman, X. Yu, Progressive folding of bulbous bows, *Proceedings of the Sixth International Symposium on Practical Design of Ships and Mobile Units*, Seoul, South Korea, 1995.
- [95] A.W. Leissa, The free vibration of rectangular plates, *Journal of Sound and Vibration*, 31 (1973), 257-293.
- [96] S.G. Lekhnitskii, *Anisotropic plates*, Gordon and Breach Science Publishers, New York, 1968.
- [97] H. Le Sourne, A ship collision analysis program based on super-elements method coupled with large rotational ship movement analysis tool, *Proceedings of the Forth International Conference on Collision and Grounding of Ships*, Hamburg, Germany, 2007.
- [98] H. Le Sourne, N. Besnard, C. Cheylan, N. Buannic, A ship collision analysis program based on upper bound solutions and coupled with a large rotational ship movement analysis tool, *Journal of Applied Mathematics*, 2012 (2012), 1-28.
- [99] H. Le Sourne, J.C. Rodet, C. Clanet, Crashworthiness analysis of a lock gate impacted by two different river ships, *Internal Journal of Crashworthiness*, 7 (2002), 371-396.
- [100] C.C. Liang, C.C. Liao, Y.S. Tai, W.H. Lai, The free vibration analysis of submerged cantilever plates, *Ocean Engineering*, 28 (2001), 1225-1245.
- [101] K.M. Liew, C.M. Wang, Vibration analysis of plates by the pb-2 Rayleigh-Ritz method: mixed boundary conditions, reentrant corners and internal curved supports, *Mechanics of Structure and Machine: an International Journal*, 20 (2007), 281-292.
- [102] J. Lubliner, *Plasticity theory*, Dover Publications, New-York, 2008.
- [103] M. Lützen, *Ship collision damage*, PhD Thesis, Technical University of Denmark, Copenhagen, 2001.
- [104] M. Lützen, B.C. Simonsen, P.T. Pedersen, Rapid prediction of damage to struck and striking vessels in collision event, *Proceedings of Ship Structure Symposium for the New Millennium: Supporting Quality in Shipbuilding*, Arlington, United States, 2000.

M

- [105] P.K. Malhotra, Seismic response of soil-supported unanchored liquid-storage tanks, *Journal of Structural Engineering*, 123 (1997), 440-450.
- [106] C. Massonet, S. Cescotto, *Mécanique des matériaux*, Editions De Boeck Supérieur, Brussels, 1994.
- [107] J.F. Mc Dermott, R.G. Kline, E.L. Jones, N.M. Maniar, W.P. Chiang, Tanker structural analysis for minor collisions, *Transactions of the Society of Naval Architects and Marine Engineers*, 82 (1974), 382-414.
- [108] W. Meinhold, *Kollisionsbeanspruchungen im Stahlwasserbau - Untersuchungen zum Schiffsstoß auf Schleusentore und abzuleitende Maßnahmen*, Bundesanstalt für Wasserbau, Karlsruhe, 2011.
- [109] K. Meskouris, B. Holtschoppen, C. Butenweg, J. Rosin, Seismic analysis of liquid storage tanks, *Proceedings of the Second International Workshop on Active Tectonics, Earthquake Geology, Archaeology and Engineering*, Corinth, Greece, 2011.
- [110] M.M. Mikulas, J.A. McElman, On free vibrations of eccentrically stiffened cylindrical shells and flat plates, *NASA Technical Reports*, National Aeronautics and Space Administration, Washington, 1965.
- [111] Ministère des Transports de la République Française, *Sécurité des portes d'écluses sur les voies navigables à grand gabarit*, Circulaire ministérielle 1423, Paris, 1980.
- [112] A. Mitra, P. Sahoo, K. Saha, Effect of in-plane boundary conditions on forced vibration analysis of stiffened plates with a free edge, *Journal of Vibration and Control*, 19 (2013), 234-261.
- [113] S. Mitra, K.P. Sinhamahapatra, 2D simulation of fluid-structure interaction using finite element method, *Finite Elements in Analysis and Design*, 45 (2008), 52-59.
- [114] MSC Software, *MSC NASTRAN 2012 reference manual*, MSC Software Corporation, Santa Ana, 2012.
- [115] M. Muto, N. Von Gersdorff, Z. Duron, M. Knarr, Effective modeling of dam-reservoir interaction effects using acoustic finite elements, *Proceedings of Twenty-Second Annual US Society on Dams Conference*, New Orleans, United States, 2012.

O

- [116] M.H. Oh, J. H. Kim, Y. S. Jang, E. Bird, Impact analysis of greater plutonio FPSO considering ship collision, *Proceedings of the Fifteenth International Offshore and Polar Engineering Conference*, Seoul, Korea, 2005.
- [117] H. Ohtsubo, G. Wang, An upper-bound solution to the problem of plate tearing, *Journal of Marine Science Technology*, 1 (1995), 46-51.

P

- [118] J.K. Paik, P.T. Pedersen, Modeling of the internal mechanics in ship collisions, *Ocean Engineering*, 23 (1996), 107-142.

- [119] J.K. Paik, P.T. Pedersen, Ultimate and crushing strength of plated structures, *Journal of Ship Research*, 39 (1995), 250-261.
- [120] J.K. Paik, A.K. Thayamballi, A concise introduction to the idealized structural unit method for nonlinear analysis of large plated structures and its application, *Thin-Walled Structures*, 41 (2003), 329-355.
- [121] J.K. Paik, A.K. Thayamballi, *Ultimate limit state design of steel-plated structures*, John Wiley and Sons, Chichester, 2003.
- [122] J.K. Paik, A.K. Thayamballi, B.J. Kim, Large deflection orthotropic plate approach to develop ultimate strength formulations for stiffened panels under combined biaxial compression/tension and lateral pressure, *Thin Walled Structures*, 39 (2001), 215-246.
- [123] J.K. Paik, T. Wierzbicki, A benchmark study on crushing and cutting of plated structure, *Journal of Ship Research*, 41 (1997), 147-160.
- [124] Panama Canal Authority (ACP), *Design and construction of the third set of locks - Employer's requirements - Part 1: Locks performance and design criteria*, Panama, 2007.
- [125] Panama Canal Authority (ACP), *Atlantic locks complex: level I seismic analysis*, Panama, 2011.
- [126] P.K. Pani, S.K. Bhattacharyya, Finite element analysis of a vertical rectangular plate coupled with an unbounded fluid domain on one side using a truncated far boundary, *Journal of Hydrodynamics*, 21 (2009), 190-200.
- [127] P.K. Pani, S.K. Bhattacharyya, Fluid-structure interaction effects on dynamic pressure of a rectangular lock-gate, *Finite Elements in Analysis and Design*, 43 (2007), 739-748.
- [128] P.K. Pani, S.K. Bhattacharyya, Hydrodynamic pressure on a vertical gate considering fluid-structure interaction, *Finite Elements in Analysis and Design*, 44 (2008), 759-766.
- [129] R.C. Patev, B.C. Parker, L.V. Koestler, *Full-scale barge impact experiments*, U.S. Army Corps of Engineers Research and Development Center, Vicksburg, 2003.
- [130] P.T. Pedersen, S. Valsgaard, D. Olsen, S. Spangenberg, *Ship impacts: bow collisions*, *International Journal of Impact Engineering*, 13 (1993), 163-187.

Q

- [131] S. Qvist, K.B. Nielsen, M.H. Schmidt, S.H. Madsen, *Ship collision: experimental and numerical analysis of double hull models*, *Proceeding of the Ninth Technical Conference on Material and Structural Modelling in Collision Research*, Munich, Germany, 1995.

R

- [132] C. Rajalingham, R.B. Bhat, G.D. Xistris, *Vibration of rectangular plates using plate characteristic functions as shape functions in the Rayleigh-Ritz method*, *Journal of Sound and Vibration*, 193 (1996), 497-509.

- [133] F.G. Rammerstorfer, K. Scharf, F.D. Fischer, R. Seeber, Collapse of Earthquake Excited Tanks, *Res Mechanica*, 25 (1988), 129-143.
- [134] A.A. Rashed, W.D. Iwan, Dynamic analysis of short-length gravity dams, *Journal of Engineering Mechanics*, 111 (1985), 1067-1083.
- [135] K.A. Reckling, Mechanics of minor ship collisions, *International Journal of Impact Engineering*, 1 (1983), 281-299.
- [136] J. Rohacs, G. Simongati, The role of inland waterway navigation in a sustainable transport system, *Transport*, 22 (2010), 148-153.

S

- [137] I.H. Shames, C.L. Dym, *Energy and finite element methods in structural mechanics*, New Age International, New Delhi, 1995.
- [138] W.Q. Shen, Dynamic response of rectangular plates under drop mass impact, *International Journal of Impact Engineering*, 19 (1997), 207-229.
- [139] Z.A. Siddiqi, A.R. Kukreti, Analysis of eccentrically stiffened plates with mixed boundary conditions using differential quadrature method, *Applied Mathematical Modelling*, 22 (1998), 251-275.
- [140] B.C. Simonsen, Ship grounding on rock - I. Theory, *Marine Structures*, 10 (1997), 519-562.
- [141] B.C. Simonsen, Ship grounding on rock - II. Validation and application, 10 (1997), 563-584.
- [142] B.C. Simonsen, *The mechanics of ship grounding*, PhD Thesis, Technical University of Denmark, Copenhagen, 1997.
- [143] B.C. Simonsen, L. P. Lauridsen, Energy absorption and ductile failure in metal sheets under lateral indentation by a sphere, *International Journal of Impact Engineering*, 24 (2000), 1017-1039.
- [144] B.C. Simonsen, H. Ocakli, Experiments and theory on deck girder crushing, *Thin Walled Structures*, 34 (1999), 195-216.
- [145] Société Momentanée Bureau Greisch-Tractebel Engineering, *Note d'hypothèses pour le calcul de la nouvelle écluse d'Ivoz-Ramet*, Liège, 2009.
- [146] W.J. Stronge, T. Yu, *Dynamics models for structural plasticity*, Springer Verlag, London, 1995.
- [147] P.S. Symonds, T.J. Mentel, Impulsive loading of plastic beams with axial constraints, *Journal of the Mechanics and Physics of Solids*, 6 (1958), 186-202.

T

- [148] F. Tin-Loi, Post-yield analysis of rigid-plastic beams with variable restraints, *Journal of Engineering Mechanics*, 117 (1991), 54-69.

- [149] F. Tin-Loi, Post-yield behavior of a rigid-plastic beam with partial axial and rotational end fixities, *International Journal of Mechanical Sciences*, 32 (1990), 623-630.

U

- [150] Y. Ueda, S.M.H. Rashed, The idealized structural unit method and its application to deep girder structures, *Computers and Structures*, 18 (1984), 277-293.
- [151] V. Ungureanu, M. Kotelko, R.J. Mania, D. Dubina, Plastic mechanisms database for thin-walled cold-formed steel members in compression and bending, *Thin-Walled Structures*, 48 (2010), 818-826.
- [152] U.S. Army Corps of Engineers, Design of hydraulic steel structures, EM 1110-2-2105, Washington, 1993.
- [153] U.S. Army Corps of Engineers, Lock gates and operating equipment, EM 1110-2-2105, Washington, 1994.
- [154] U.S. Department of Transportation, U.S. Coast Guard 1995 oil pollution research grants publications, Report CG-D-22-97, Cambridge, 1997.

V

- [155] A.S. Veletsos, Seismic effect in flexible liquid storage tanks, *Proceedings of the Fifth World Conference of the International Association for Earthquake Engineering*, Rome, Italy, 1974.
- [156] K. Vijayakumar, Natural frequencies of rectangular orthotropic plates with a pair of parallel edges simply supported, *Journal of Sound and Vibration*, 35 (1974), 379-394.
- [157] V. de Ville de Goyet, L'analyse statique non linéaire par la méthode des éléments finis des structures spatiales formées de poutres à section non symétrique, PhD Thesis, University of Liège, Liège, 1989.
- [158] K.Y. Volokh, An approach to elastoplasticity at large deformations, *European Journal of Mechanics and Solids*, 39 (2013), 153-162.
- [159] G.Z. Voyiadjis, P.D. Kioussis, Stress rate and the lagrangian formulation of the finite-strain plasticity for a Von Mises kinematic hardening model, *International Journal of Solids and Structures*, 23 (1987), 95-109.
- [160] A.W. Vredeveldt, J.H.A. Schipperen, Q.H.A. Nassar, C.A. Spaans, Safe jacket configurations to resist boat impact, *Collision and Grounding of Ships and Offshore Structures*, J. Leira Editors, London, 2013.

W

- [161] T. Wah, Vibration of stiffened plates, *The Aeronautical Quarterly*, 15 (1964), 285-298.
- [162] G. Wang, Some recent studies on plastic behavior of plates subjected to large impact loads, *Journal of Offshore Mechanics and Arctic Engineering*, 124 (2002), 125-131.
- [163] G. Wang, K. Arita, D. Liu, Behavior of a double hull in a variety of stranding or collision scenarios, *Marine Structures*, 13 (2000), 147-187.

- [164] G. Wang, H. Ohtsubo, Deformation of ship plate subjected to very large load, Proceedings of the Sixteenth International Conference on Offshore Mechanics and Arctic Engineering, Yokohama, Japan, 1997.
- [165] G. Wang, H. Ohtsubo, Impact load of a supply vessel, Proceedings of the Ninth International Offshore and Polar Engineering Conference, Brest, France, 1999.
- [166] H.M. Westergaard, Water pressure on dams during earthquakes, Transactions of the American Society of Civil Engineers, 98 (1933), 418-433.
- [167] T. Wierzbicki, Concertina tearing of metal plates, International Journal of Solids and Structures, 32 (1995), 2923-2943.
- [168] T. Wierzbicki, W. Abramowicz, On the crushing mechanics of thin-walled structures, Journal of Applied Mechanics, 50 (1983), 727-734.
- [169] T. Wierzbicki, J. Culbertson-Driscoll, Crushing damage of web girders under localized static loads, Journal of Constructional Steel Research, 33 (1995), 199-235.
- [170] World Association for Waterborne Transport and Infrastructure (PIANC), Innovation in navigation lock design, PIANC, Brussels, 2009.
- [171] World Association for Waterborne Transport and Infrastructure (PIANC), Rapport final de la commission internationale pour l'étude des écluses, PIANC, Brussels, 1986.

Y

- [172] J.Y. Yang, Dynamic behavior of fluid-tank systems, PhD Thesis, Rice University, Houston, 1976.
- [173] Y. Yamada, P.T. Pedersen, A benchmark study of procedures for analysis of axial crushing of bulbous bows, Marine Structures, 21 (2008), 257-293.
- [174] P.D.C. Yang, J.B. Caldwell, Collision energy absorption of ship's bow structures, International Journal of Impact Engineering, 7 (1988), 181-196.
- [175] T. Yu, An analytical model of the cantilever beam subjected to oblique impact, Sciences in China, 34 (1991), 191-200.

Z

- [176] C.N. Zangar, Hydrodynamic pressures on dams due to horizontal earthquakes, Proceedings of the Society for Experimental Stress Analysis, 10 (1953), 93-102.
- [177] H. Zeng, C.W. Bert, A differential quadrature analysis of vibration for rectangular stiffened plates, Journal of Sound and Vibration, 241 (2001), 247-252.
- [178] H. Zeng, C.W. Bert, Free vibration analysis of discretely stiffened skew plates, International Journal of Structural Stability and Dynamics, 1 (2001), 125-144.
- [179] S. Zhang, Plate tearing and bottom damage in ship grounding, Marine Structures, 15 (2002), 101-117.
- [180] S. Zhang, The mechanics of ship collisions, PhD Thesis, Technical University of Denmark, Copenhagen, 1999.